Eruption dynamics and frequency-magnitude relationships of explosive eruptions at Mt. Ruapehu, New Zealand over the past 1800 years

A thesis presented in partial fulfilment of the requirements for the degree of

Doctor of Philosophy

in

Earth Science

at Massey University, Palmerston North, New Zealand

Marija Voloschina

2020

This thesis is dedicated to my mother

Mt. Ruapehu as seen from the southwestern Round the Mountain Track in February 2018.

Abstract

Small to moderate explosive eruptions (VEI ≤ 3) constitute the most frequent eruptions and often involve several phases characterised by different eruption dynamics. Deposits associated with small-scale multi-phase eruptions tend to be underrepresented in geological records and the resulting probabilistic eruption forecast models. This PhD research presents a refined high-resolution tephrostratigraphic framework for the 1800-year Tufa Trig Formation at one of New Zealand's most active volcanoes, Mt. Ruapehu. This framework is used to characterise short- and long-term changes in eruption behaviour aiming to identify time-variable processes in the volcanic system of a long-lived andesite volcano.

Systematic mapping and lithosedimentological characterisation of tephra deposits are combined with geochemical fingerprinting and radiocarbon dating to create a detailed frequency-magnitude record of single- and multi-phase eruptions of the last 1800 years. At least 32 eruptions can be identified, ranging from low to mid-intensity single-phase eruptions ($1–10 \times 10^6$ m^3 deposit volumes) to complex multi-phase eruptions up to two magnitudes larger. The largest eruption is the T13-sequence that comprises at least 5 eruption phases. Multi-lobate dispersal pattern and componentry analyses show that individual eruption phases represent multiple fall events of similar eruption style and magnitude. Major and trace element analyses of juvenile glass display limited syn-sequence variability, while heterogeneous pyroclast and textural characteristics suggest that short-term changes in eruption behaviour are predominantly controlled by shallow conduit processes. The frequency-magnitude record is integrated with geochemistry and statistical modelling, identifying time-variable pattern in Mt. Ruapehu's eruption behaviour: the time span 1718–1300 cal BP involves low-intensity single-phase eruptions every ~40 years and is followed by a low rate regime (one eruption every 125 years). The largest multi-phase eruptions of the last two millennia occur between 610 and 370 cal BP, while the past 370 years are dominated by smaller multi-phase eruptions every ~40 years, suggesting that long-term changes in Mt. Ruapehu's eruption behaviour are related to changes in magma supply. This research adds critical complexity to the understanding of the processes and timescales controlling eruption behaviour in the southern Taupo Volcanic Zone and provides insights into the dynamic behaviour of small to moderate multi-phase eruptions. These results will constitute the framework for refining dynamic eruption forecast models at Mt. Ruapehu and other similar volcanoes globally.

Acknowledgements

First of all, I would like to thank my main supervisor Gert Lube (Massey University) for providing me with the opportunity to come to New Zealand and to work at Mt. Ruapehu. I am grateful for his on-point contributions to discussions and his detailed feedback on written manuscripts. Many thanks also to my co-supervisor Jonathan Procter (Massey University) for his help with proposal writing and his comments during discussions and thesis writing. I would like to thank my co-supervisor Christian Timm (GNS Science) for his positivity, enthusiasm and his support with the geochemical sections of this thesis. Furthermore, I am grateful to Mark Bebbington (Massey University) for statistical modelling and for the time he dedicated during manuscript writing.

This research would not have been possible without the support of Anja Moebis (Massey University), who aided with field work, coring, laboratory work and discussions. Thank you for sharing your time, your knowledge and your love for the Tongariro National Park during these years.

I would also like to thank Kate Arentsen and Fiona Bardell for their help with logistics, organisation and support. I am particularly grateful to Kate Arentsen for the final proof-reading of this thesis. During different stages of this research, many people have contributed their knowledge and experience and their help is hugely appreciated. This regards in particular David Feek (Massey University) for his help with coring and Ian Furkert and Bob Toes (Massey University) for their support in the laboratory. Ian Schipper's (Victoria University of Wellington) help with microprobe analysis in Wellington is acknowledged. Bruce Charlier (Victoria University of Wellington) is thanked for his aid with acquiring trace element data at the LA-ICP-MS. Alan Hogg's (University of Waikato) support with radiocarbon dating is greatly acknowledged. Matt Irwin is thanked for help with GIS. Niki Minards, Raoul Solomon, and Matthew Savoian (Massey Microscopy Imaging Centre) are thanked for their help with the Scanning Electron Microscope.

The field work part of this thesis would have not been possible without the help and support of Keith Wood (Ernslaw Karioi Forest), Hollei Gabrielsen (Department of Conservation) and staff from the Waiouru Military Training Area who facilitated access to respective field sites. Also, Ngāti Rangi's and Ngāti Uenuku's permission for access and sampling is greatly appreciated.

Funding for this research was provided by the Natural Hazards Research Platform and the Resilience to Nature's Challenges Volcano program. Furthermore, I am grateful for receiving the Memorial Award from the Tongariro Natural History Society.

During these years, individuals from the Volcanic Risk Solutions Group have contributed time and feedback to the realisation of this thesis and I would like to thank Georg Zellmer, Stuart Mead and Gabor Kereszturi for discussion and their assistance with different

practical problems. Furthermore, I would like to thank Charline Lormand, Braden Walsh, Raimundo Brahm Scott and Kevin Kreutz for discussion and field work assistance. I would also like to acknowledge Leandra Roither for assistance with field work and grain size analysis and Courtney Durham for her assistance with image analysis.

A particular big thanks goes to Ermanno Brosch, who not only managed to make late working nights and weekend work fun, but who has also supported me throughout these years. Thank you for being a driving instructor, for your scientific and logistic help, for our Italian-Denglish, for listening to presentations, commenting on written drafts and figures, for sharing the office and, most of all, thank you for your friendship.

Andrea Todde, I am hugely grateful for your support and your friendship during these years. Thank you for innumerable scientific (and non-scientific) discussions, your comments on figures and presentations, for sharing your knowledge and passion for volcanology.

I am hugely indebted to Clel Wallace and Nicki Banks for their warmth and support during these years. Thank you for welcoming me and making me feel at home far away from home.

Over the years, I have crossed paths with many different people, who contributed to making the time outside of the PhD memorable. Florentine van Noppen, Aniek Hilkens, Ivan Ordoñez Vasquez, thank you for brief and long escapes, for hikes, runs, climbs, hugs, laughter, for sharing food and beer and, most of all, thank you for your friendship! Another big thanks goes to Diana Cabrera for her continuing friendship and for receiving me in Palmy with open arms and a huge smile. Darius Siljee, thank you for your support, enthusiasm and positivity during the last months. Magret Damaschke, Kevin Kreutz, Jasper Hoffmann, Doreen Montesclaros, Ivayla Yozova, Mirjam De Oude, Shahista Nisa, Christian Schneider, Leandra Roither, Nico Tapia, Sebastian Rivera Smith, Micaela Paz, Dimitrios Rados, Caroline Giezenaar, Sarah Priour, Gonzalo Martinez Hermosilla, Raimundo Brahm Scott, Daniel Coulthard Jr., Daniel Uhle, Thomas Mackay-Smith, Fernando Avendano, Sarah Tapscott, Paul Ogbuigwe, thank you all for sharing stories, smiles, food, music and for providing support and distraction!

Finally, I would not be where I am without the people, who had my back all along. Nataliya Voloshina, Mark Voloshin, Quan-Troung Ngo, Wilmut Benesch, Lara Heuchmer and Lisa Goebel: each one of you has been a source of inspiration and strength and I am truly grateful for your ongoing support. I could not have done this without your love and encouragement.

Table of contents

Abstract i

Acknowledgements ii

Table of contents iv

List of tables ix

List of figures xi

Chapter 1 .... **1**

Introduction 1

1.1 Introduction 1

1.1.1 Overall aim and objectives of this research 2

1.2 Literature Review 6

1.2.1 Explosive eruptions 6

1.2.2 Classification of explosive eruptions 6

1.2.3 Regional geological background 11

1.2.4 The Taupo Volcanic Zone (TVZ) 13

1.3 Eruptive record of Mt. Ruapehu 13

1.3.1 Local geological framework 13

1.3.2 Holocene and late Holocene stratigraphic record 14

1.3.3 The Tufa Trig Formation 18

1.3.4 Historical record 19

1.4 Existing models of Mt. Ruapehu’s magmatic system 22

1.4.1 Geochemical characterisation of Mt. Ruapehu’s eruptive products 22

1.4.2 Characteristics of the shallow magma storage system 23

1.4.3 Ascent characteristics 24

1.5 Mt. Ruapehu’s vent system 25

1.5.1 Eruption styles 25

1.6 Volcanic hazards 26

1.6.1 Volcanic hazards at Mt. Ruapehu 26

References 29

Chapter 2 .... **38**

Methodology 38

2.1 Field work 38

2.2 Sample characterisation 39

2.2.1 Grain size analyses 39

2.2.2 Componentry 40

2.2.2.1 Point counting 40

2.2.3 Pyroclast characterisation 41

2.2.3.1 Ash morphologies 41
2.2.3.2 Image analysis and clast textures 41
2.2.4 Tephra dispersal and volume calculations 42
2.2.4.1 Isopach construction and volume calculation 42
2.2.4.2 Isopleths 43
2.3 Age constraints 44
2.3.1 Stratigraphic markers and known ages 44
2.3.2 Radiocarbon dating 44
2.4 Geochemical analysis 45
2.4.1 Electron Microprobe Analyser (EMPA) 45
2.4.1.1 Massey University microprobe 46
2.4.1.2 Victoria University of Wellington microprobe 47
2.4.2 Laser ablation inductively coupled plasma mass spectroscopy (LA-ICP-MS) 47
References 49
Chapter 3 51
Tephrostratigraphy of the Tufa Trig Formation 51
Lithosedimentological and tephrostratigraphical characterisation of small-volume, low-intensity eruptions: The 1800 years Tufa Trig Formation, Mt. Ruapehu (New Zealand) 53
3.1 Abstract 54
3.2 Introduction 55
3.2.1 Late Holocene tephrostratigraphic framework 56
3.2.2 Previous work on the Tufa Trig Formation 57
3.3 Methodology 59
3.3.1 Terminology and field methodology 59
3.3.2 Sample characterisation 62
3.3.3 Age constraints 62
3.3.3.1 Stratigraphic markers 62
3.3.3.2 Radiocarbon dating 64
3.3.4 Major element characterisation 64
3.4 Results 65
3.4.1 Mt. Ruapehu’s eruptive record for the past 1800 years 65
3.4.2 Lithosedimentological characterisation of fall sequences of small-volume, low-intensity eruptions 66
3.4.2.1 Tephra appearance and dispersal 67
3.4.2.2 Grain size characteristics 67
3.4.2.3 Pyroclast assemblage 68
3.4.3 Tephra characteristics of the Tufa Trig Formation members 71
3.4.4 Tephra volume estimates 90
3.5 Discussion 94
3.5.1 Insights into the Tufa Trig Formation 94

3.5.2 Magnitude and dispersal patterns 97
3.5.3 Frequency patterns 98
3.6 Conclusions and outlook 99
3.7 Acknowledgements 101
References 102
Supplementary material 107

Chapter 4 .... **113**
Reconstructing the T13 multi-phase eruption 113
Reconstructing the largest eruption of Mt. Ruapehu (New Zealand) in the last two millennia- a case study of prolonged multi-phase eruptions at long-lived composite volcanoes 115
4.1 Abstract 115
4.2 Introduction 117
4.2.1 Eruptive history 118
4.3 Methodology 121
4.3.1 Field work 121
4.3.2 Grain size and componentry 121
4.3.3 Tephra volumes 122
4.3.4 Image analysis and ash morphologies 122
4.3.5 Geochemical characterisation 123
4.3.5.1 EMPA and LA-ICP-MS 123
4.4 Results 129
4.4.1 Stratigraphy and tephra dispersal 129
Subunit T13-1 131
Subunit T13-2 131
Subunit T13-3 132
Subunit T13-4 133
Subunit T13-5 133
Subunit T13-6 134
4.4.2 Componentry 136
4.4.2.1 Juvenile clasts 136
4.4.2.2 Crystals and lithics 140
4.4.2.3 Lateral variation 140
4.4.2.4 Sequence variation 142
4.4.3 Geochemical characterisation 144
4.4.3.1 Major elements 145
4.4.3.2 Trace element compositions 146
4.5 Discussion 151
4.5.1 Tephra dispersal 151
4.5.1.1 Tephra volume 151

4.5.2 Syn-eruptive variation and eruption progression 153
4.5.2.1 The opening phase P1 154
4.5.2.2 Violent Strombolian phase P2 155
4.5.2.3 Main violent Strombolian to subplinian phase P3 155
4.5.2.4 Violent Strombolian phase P4 156
4.5.2.5 Violent Strombolian to subplinian phase P5 156
4.5.3 Temporal patterns in the magmatic system of an andesitic composite volcano 158
4.5.3.1 Temporal patterns within an eruption sequence 158
4.5.3.2 Temporal patterns between eruption sequences 163
4.5.4 Limitations in characterising the deposits of small to moderate multi-phase eruptions.... 165
4.6 Conclusions and outlook 169
References 172
Supplementary material 177
Chapter 5 .... **178**
Modelling multi-phase eruptions 178
Probabilistic modelling of multi-phase eruptions in geological records: An example from Mt Ruapehu, New Zealand. 180
5.1 Abstract 180
5.2 Introduction 181
5.2.1 Geological background 183
5.2.2 Tufa Trig Formation 184
5.2.3 Major historical eruptions 185
5.3 Methods 188
5.3.1 Linking the most recent tephra member T31 to a historical eruption 188
5.3.2 Tephra dispersal and volume calculations 189
5.3.3 Geochemical characterisation 192
5.4 Results 192
5.4.1 Age model 192
5.4.2 Minimum volume estimates for subunits 193
5.4.3 Frequency-magnitude record 194
5.4.4 Variation in the geochemical signature 197
5.5 Statistical Modelling 199
5.5.1 Statistical modelling of inter-sequence onsets 200
5.5.2 Statistical Modelling of intra-eruption sequences 203
5.5.2.1 Number of subunits 203
5.5.2.2 Volumes 205
5.6 Discussion 208
5.6.1 Insights into long-term variation in Mt. Ruapehu’s eruption behaviour 208
5.6.2 Changes in eruptive regime 210
5.6.3 Implications for eruption forecast 211

5.7 Conclusions 213
References 215
Supplementary material 219

Chapter 6 222
Synthesis 222
6.1 Synthesis 222
6.1.1 Research objectives revisited 223
6.2 Key research findings 224
6.2.1 A high-resolution tephra record for the last two millennia at Mt. Ruapehu and re-definition of the Tufa Trig Formation 224
6.2.2 New age constraints and stratigraphic markers for the post-Taupo eruptive history of the Tongariro Volcanic Centres 226
6.2.3 Time-variable eruption behaviour at Mt. Ruapehu 227
6.2.4 Time-variable pattern in glass compositions of the 1800-year tephra record at Mt. Ruapehu 227
6.2.5 Time-variable pattern in the Mg-number as indicator of upcoming regime changes 228
6.2.6 Characterisation of the largest multi-phase eruption of the last 1800 years – a possible worst-case scenario for future eruptions 229
6.2.7 Insights into the magmatic system feeding prolonged multi-phase eruptions 231
6.2.8 Probabilistic modelling of small to moderate multi-phase eruptions 232
6.2.9 Implications for eruption styles associated with small to moderate explosive eruptions .. 233
6.2.10 Preservation bias from merging historical datasets with geological dataset 234
6.3 Implications for the late Holocene history at Mt. Ruapehu 237
6.3.1 Eruption frequencies at the Tongariro Volcanic Centres 237
6.3.2 Inception of Crater Lake 239
6.3.3 Implications for hazard assessment and future eruptions 242
6.4 Conclusive remarks 247
References 248

Chapter 7 252
Conclusions 252
7.1 Conclusions 252
7.2 Future perspectives 255
References 258
List of appendices 259

List of tables

Table 1.1 (next page): Holocene tephrostratigraphy of the Tongariro and Tukino subgroups after Donoghue et al. (1995). Where available, calibrated ages are reported as cal BP. Selected rhyolitic stratigraphic markers from TVC and OVC are reported in italics. Sources are abbreviated as follows: R=Mt. Ruapehu, N=Mt. Ngauruhoe, TL=Tama Lakes, T=Mt. Tongariro. References for definition of tephra formations and tephra members with respective ages are: [1] Donoghue et al. (1995) [2] Donoghue et al. (1997) [3] Moebis (2010) [4] Lowe et al. (2013) [5] Topping (1974) [6] Pardo et al. (2011) [7] Topping (1973) [8] Heinrich et al. (2020). 16

Table 1.2: Overview of major eruptions in the historical record with details on eruption sequences and event magnitude. 21

Table 1.3: Summary of volcanic hazards at Mt. Ruapehu, as inferred from eruptive activity during the past 27,000 years. 28

Table 3.1: Selected key samples of this study with sampling location, distances from source and sedimentological parameters. 61

Table 3.2: Overview of radiocarbon ages presented in this study. For comparison, previously published ages for the Burrell Lapilli and the Taupo Pumice, which are used as stratigraphic markers, are reported as well. 65

Table 3.3: Overview of Tufa Trig Formation showing the new refined nomenclature, dispersal, deposit type, eruption classification, age constraints and the previous nomenclature after Donoghue et al. (1997). 89

Table 3.4: Parameters used for deposit volume calculations for members T2, T14 and T15 91

Table 4.1 (continues on next page): Key samples of the T13-tephra sequence, detailing sampling location, distances from source, main grain size parameters and componentry 125

Table 4.2: Parameters used for deposit volume calculations for T13 132

Table 4.3 (continues on next page): Main features of subunits within the T13-tephra sequence 149

Table 5.1: Deposit volumes calculated for key subunits to illustrate how volumes based on simplified ellipse compare with volumes obtained from detailed isopachs. 191

Table 5.2: Tephra units with number of subunits and estimated tephra ages. Cumulative volumes are reported for units based on idealised ellipses and are estimated following Legros (2000) 194

Table 5.3: Number of subunits per eruption 204

Table 5.4: Summary statistics of deposit volume (km^3) by subunit number. Pooled data for subunit numbers 4-6 is included in the last row. N marks the number of subunits for the respective class. Note that T28 and T26 are excluded from these statistics. 205

List of figures

Fig. 1.1: Classification of fallout deposits modified after Walker (1973) and Houghton & Carey (2015) showing different eruption types and their relationship with tephra dispersal and fragmentation efficiency. 10

Fig. 1.2: Overview of New Zealand's setting on the plate boundaries. Taupo Volcanic Zone (TVZ) boundaries after Wilson et al. (1995). Tongariro Volcanic Centre volcanoes (TgVC) are marked by white box........ 12

Fig. 1.3: Overview of the ring plain tephrostratigraphy involving lahar and tephra formations at Mt. Ruapehu for the past 27,000 years. For comparison, tephra formations from the adjacent Tongariro and Ngauruhoe volcanoes are reported as well. Rhyolitic stratigraphic markers from the northward Taupo Volcanic Centre (TVC) and the Okataina Volcanic Centre (OVC) are shown with respective age constraints. 17

Fig. 3.1: a) Overview of the study area and the investigated field locations, showing the Tongariro Volcanic Centres (TgVC) Mt. Tongariro, Mt. Ngauruhoe and the object of this study, Mt. Ruapehu. Positions of nearby townships (N: National Park; O: Ohakune; Wa: Waiouru) and skifields (W: Whakapapa; T: Tukino; t: Turoa) are marked by green and white polygons, respectively. Main state highways are shown by a white line, while the Round the Mountain hiking track is represented by a black dashed line. The underlying hillshade view is based on an 8 m digital elevation model from the LINZ Data Service (https://data.linz.govt.nz), based on the 2012 LINZ Topo50 map series. b) Inset shows NZ land mass and its relative position to the Hikurangi-Kermadec (HKSZ) and the Puysegur subduction zones (PSZ). The Taupo Volcanic Zone (TVZ) is marked after Wilson et al., 1995. Andesitic-dacitic volcanic centres (crosses) are as follows: T: Mt. Taranaki, TgVC: Tongariro Volcanic Centres, E: Mt. Edgecumbe (Putauaki), WhI: Whale Island (Moutohora), WI: White Island (Whakaari). c) Inset highlights the key sections, which are used for the lateral correlation of the Tufa Trig tephra members. 57

Fig. 3.2: Lateral correlation showing stratigraphic key sections for the members of the Tufa Trig Formation from West to North-West in an anti-clockwise sense. Specific members at different sections are linked by coloured bands. Small inset highlights the position of key sections relative to source. The inset's black line represents the equidistant lateral correlation. Below each section, the location name and the distance to the Crater Lake are reported. Correlated tephra members of the Tufa Trig Formation are marked by prefix "T" plus number. Caret indicates a tephra member that could not be correlated between more than one location. Where present, the deposit of the Taupo eruption (1718 ± 10 cal BP, Lowe et al., 2013) is shown with a standard thickness of 100 mm, which is not representative of the actual deposit thickness. Tephra member T26, which contains glass shards of the Taranaki-sourced Burrell Lapilli as well as juvenile Mt. Ruapehu-sourced glass is highlighted in red. Radiocarbon ages (cal BP) are reported in italics after [1] Lowe et al. (2013), [2] Moebis (2010) and [3] Druce (1966). 59

Fig. 3.3: Correlation of selected sections in NE direction, away from source. Inset shows the position of key sections relative to the lateral correlation (grey line) shown in Fig. 3.2. Correlated members of the Tufa Trig Formation are marked by prefix "T" plus number and are linked by coloured bands. Location names and respective distance to the Crater Lake are indicated below the sections while distances between sections are shown as well. Where present, the deposit of the Taupo eruption (1718 ± 10 cal BP, Lowe et al., 2013) is shown with a standard thickness of 100 mm, which is not representative of the actual deposit thickness. The stratigraphic position of tephra member T26, which contains glass shards of the Taranaki-sourced Burrell Lapilli and Mt. Ruapehu-sourced juvenile glass is highlighted in red. Radiocarbon ages (cal BP) are reported in italics and follow [1] Lowe et al. (2013) and [2] Druce (1966). 63

Fig. 3.4: Stratigraphic profile and lithosedimentological description of tephra members observed at key section Loc. 3. This location corresponds to the type location of the Tufa Trig Formation (after Donoghue et al., 1997). Members and subunits are reported for the correlated tephra members. The beds observed in the field are numbered and shown with depositional subunits. Observations illustrate field descriptions as well as median grain size and sorting parameters, obtained from grain size analysis for individual beds. Median grain size and sorting parameters are calculated after Inman (1952), and follow the nomenclature of White & Houghton (2006). 69

Fig. 3.5 (next page): a) Overview of members T2 to T11 in south-eastern direction at WP297. While T2 and T7 occur as continuous beds, T5 appears as sparse juvenile fragments at the same stratigraphic position relative to over and underlying members, which are highlighted by circles. b) Overview of centimetre-sized juvenile pyroclasts of T5 and multi-bed ash member T11 at Loc. 3. c) Overview of T15 to T17 and the soil/weathered ash between them at WP262. T17 has an indistinct upper contact, while T15 shows a disturbed lower contact. d) Close-up on member T17 at Loc. 3. Several distinct beds and bedsets can be identified with subunit T17-2 being significantly coarser than the encompassing beds. e) Overview over tephra members T19, T20, T21, T22, T23 and T24 at WP290. Interbedded andisol is of similar thickness between all members. f) Close-up on T19 and T20 at Loc. 1. Image shows internal textures and sharp internal contacts. Upper contact of T19 shows a gradual transition into overlying soil, while T20 has a disturbed lower contact. g) Overview of T17, T19, T20, T21 and T24 at Loc. 2. T18 appears as pockets with indistinct contacts. T21 contains coarse ash at this location. h) Zoom on T25 highlighting the coarse lower bed and the overlying very fine ash bed with a weathered upper contact at Loc. 1. i) Characteristic pocketing appearance of T26, which contains juvenile Taranaki-sourced glass shards, associated with the AD 1655 Burrell eruption, as well as juvenile Mt. Ruapehu-sourced pyroclasts. Note the distinct pinkish-light grey colour and the pocketing appearance. j) Zoom on T27 at Loc. 2, which is characterised by fine lapilli-sized white and orange-coloured pyroclasts overlain by dark grey fine ash without distinct contact. The above member T28 consists in dark grey pockets of very fine ash. k) Close-up on T29 at Loc. 1 showing three distinct beds, each characterised by different grain size and texture. 72

Fig. 3.6: Grain size characteristics of analysed Tufa Trig tephra members and selected key samples. The symbols represent the classification of members according to their lithosedimentological characteristics. Multi-bed ash beds (MBA) are represented by triangles with key samples being outlined (Table 3.1); single

bed ash units (SBA) are shown as circles with key samples highlighted by outlined circles; lapilli-dominated units (L) are shown as diamonds and the MBA (L) unit is marked by a grey diamond. a) Sorting σ(Φ) and median grain size Md(Φ) parameters of Tufa Trig tephras follow Inman (1952). Grey lines and grey dashed lines represent the fields for fall and flow deposits after Walker (1971). b) Plot shows descriptive grain size parameters F1 (wt% of sample that is >0 Φ or <1 mm) and F2 (wt% of sample that is >4 Φ or <63 μm). 76

Fig. 3.7: Images of selected ash fragments. Insets a) to i) show secondary electron images with the bar in each image representing 300 μm. Images j) to k) show optical images. a) Blocky dense dark (D-type) juvenile clast showing conchoidal fractures on the surface. b) D clast with sharp edges and step-like features. c) Blocky D shard of light colour, partially with smooth glassy surface. d) DV clast with thick vesicle walls and isolated round vesicles. e) DV clast with heterogeneous vesicles, thin bubble walls and slightly deformed vesicles. f) Light-coloured glassy BV shard with smooth surface and heterogeneous deformed vesicles. g) Vesicular beige shard with elongated vesicles and thin bubble walls. h) BV juvenile with small round vesicles that are closely spaced to each other. i) BV shard with smooth glassy surface and isolated large and slightly deformed vesicles. j) Optical image of dense dark D clasts with blocky morphologies and sparse transparent phenocrysts. k) Scoriaceous DV clasts of dark colour with irregular morphologies and heterogeneous vesicles. l) Vesicular beige and brown BV glass, showing pumiceous morphologies and small vesicles. 78

Fig. 3.8: K_2O vs FeO discrimination diagram, used to fingerprint glass compositions after Moebis et al. (2011). Major element groundmass glass compositions are reported as averages and normalised to 100 on a volatile-free basis. Grey plus signs mark compositions for individual subunits of the 31 tephra members of the Tufa Trig Formation. Glass compositions of tephra member T26 are marked by black stars. Note the two different compositions. Reference data is reported [1]after Platz et al. (2007a) for the Taranaki-sourced Burrell Lapilli and [2]after Moebis et al. (2011) for the Tongariro Volcanic Centres. Circles mark glass compositions from the historical 2007 and 1995–1996 eruptions from Mt. Ruapehu, diamonds mark historical Ngauruhoe eruptions from 1954 and 1975 and squares represent eruptive material from Red Crater. *Glass shards from historical Mts. Ruapehu, Ngauruhoe and Red Crater eruptions were re-analysed together with Tufa Trig glass shards and are reported for comparison. Values shown in this graph are reported in Supplementary Tables S3.2 and S3.3. 85

Fig. 3.9: Ternary plots showing the results of componentry analysis for selected key samples as summarised in Table 3.1. Single bed ash (SBA) unit T14 is shown as grey circles. Lapilli (L) units T2 and T7 are shown as empty diamonds. Multi-bed ash unit T27 (MBA (L)) is shown by a grey diamond. Key samples representing individual subunits of the multi-bed ash (MBA) unit T15 are shown for their main dispersal directions as follows: T15-1 (black circle) at Loc. 1, T15-2 (half circle) at Loc. 1 and T15-3 (plus signs) at WP250 and WP219, in line with the bilobate dispersal of this subunit. T15-4 (WP290) is represented by squares and T15-5 is shown at Loc. 3 (triangles). a) Componentry is shown as percentages of lithic clasts (Lith), juvenile clasts (Juv) and crystals (C) calculated relative to number of clasts counted. b) Percentages of the different types of juvenile clasts calculated relative to the number of juvenile shards with D: dark dense clasts, DV: dark vesicular clasts and BV: light-coloured vesicular glass. 86

Fig. 3.10: Thickness (mm) and maximum clast (mm) distribution for characteristic tephra members T2, T14 and T15. a) Total thickness distribution of lapilli-bearing member T2. Isopach pattern shows narrow distribution towards the E-ESE. b) Distribution of maximal clast diameters of member T2. c) Total thickness distribution of single bed ash member T14. d) Cumulative multi-lobate thickness distribution of multi-bed ash unit T15. Insets show the stratigraphic succession and grain size characterisation at selected key locations and are colour-coded according to subunits. e) Thickness distribution of main subunits T15-3 (red line) and T15-4 (dark grey line). T15-3 shows a slightly bilobate distribution towards the NE, while T15-4 has a main dispersal towards the SE. f) Isopleths of subunits T15-3 (red line) towards the NE and T15-4 (dark grey line) towards the SE. Grain size of the coarsest clast class is indicated in mm. 88

Fig. 3.11: Composite idealised stratigraphic profile illustrating combined field descriptions for individual tephra members, associated deposit types based on their lithosedimentological characteristics, and a qualitative interpretation of eruption intensity and style. Single bed ash units are abbreviated as SBA, multi-bed ash units are abbreviated as MBA and lapilli units are marked by L. Multi-bed ash units containing a dominant lapilli bed are marked as MBA (L). Soil and tephra thicknesses are not to scale. 92

Fig. 3.12: Schematic representation of the 1800 years tephra record of Mt. Ruapehu, integrated with new and existing radiocarbon ages and the lithosedimentological classification of the 31 Tufa Trig tephra members. Members classified as single bed ash units (SBA) are reported in light grey and lapilli units (L) are shown in brown. Multi-bed ash units (MBA) with 2 to 3 subunits are reported in medium grey while complex MBAs with ≥4 subunits are shown in dark grey. For further details, see the legend in the figure. 96

Fig. 4.1: Overview of studied area showing field locations, key sections and main geographical features. Major townships are shown by green hexagons (O: Ohakune; Wa: Waiouru; N: National Park). Skifields are marked by white hexagons (t: Turoa; T: Tukino; W: Whakapapa). Main state highways are marked in white and hiking tracks are represented by black dashed lines. The underlying hillshade view is based the 8 m digital elevation model from the LINZ Data service (https://data.linz.govt.nz) that is based on the 2012 LINZ Topo50 map series. Investigated field locations that do not contain discrete tephra units, are reported as empty circles. Inset b) shows a close-up on the key locations discussed in this study. 120

Fig. 4.2 (previous page): Stratigraphic profiles at key sections showing the main depositional features, such as texture, median grain size Md(Φ) (dark grey crosses) and sorting σ(Φ) (red plus signs). Grain size and sorting parameters follow Inman (1952). Depositional subunits T13-2, -3, -4, -5 and -6 are correlated throughout the different sections from SSE to NNE as shown in Fig. 4.1b. Distances between locations are reported below each location. Sampled beds are marked by black triangles. Photo insets illustrate the lateral variation of the field appearance of the T13-sequence. Bed boundaries are marked by white lines, while coloured bars show subunits. a) Loc. 3 is located 9.2 km from source in SSE direction. Note the absence of T13-3 in this location. b) WP290 is located at 9.4 km distance from source in SE direction. Subunits T13-2, -3, -4, -5 and -6 can be identified here, while T13-1 is not preserved. T13-5 contains several distinct, but not correlatable beds. c) Loc. 1 is situated at 8.9 km E from source and comprises the sequence with the greatest cumulative thickness. Note the absence of T13-1. d) WP250 lies in NE direction, 9.6 km from source. e) Loc. 2 is positioned in NNE direction, 8.9 km from source. Only subunits T13-2, -3, -4 and -6 are preserved. 128

Fig. 4.3: Thickness distribution in mm of the T13-tephra sequence and selected individual subunits. Field locations, where thickness measurements were obtained are marked by filled circles, while field locations without discrete tephra units are marked by empty circles. a) Cumulative thickness for the T13-sequence shows a strongly irregular, multi-lobate dispersal. b) Thickness distribution for subunit T13-1 shows a limited dispersal towards the SE. c) Isopachs for subunit T13-3 indicate an extensive, asymmetrical dispersal towards the East. d) Isopachs for subunit T13-4 show several thickness maxima in different directions and are characterised by irregular shapes. The main lobe goes towards the East. e) The dispersal of subunit T13-6 shows a distinct bilobate shape with one main dispersal direction towards the NE and a second lobe towards the SE. Where subunits T13-5 and T13-6 cannot be separated unequivocally, joined thicknesses are reported (half coloured circles). 130

Fig. 4.4: Maximum clast distribution shown in mm for the T13-sequence and selected subunits T13-3, T13-4 and T13-6. Field locations where grain size data was obtained are marked by filled circles, while locations where no discrete tephra could be observed are reported by empty circles. a) Irregular multi-lobate distribution is shown for the maximum clast size from the whole T13-sequence b) Maximum grain size for subunit T13-3. Note the asymmetrical, slightly bilobate dispersal. c) Irregular maximum clast dispersal for subunit T13-4, characterised by several thickness maxima in different directions. d) Asymmetric, slightly bilobate isopleths for subunit T13-6. Note that maximum grain sizes are coarser in NE locations compared to SE locations at similar distance from source. At locations, where subunits T13-5 and -6 cannot be distinguished unequivocally, maximum grain size was determined for the joined subunit. These locations are marked by half coloured circles. 135

Fig. 4.5: Grain size characteristics of individual beds of the T13-sequence at key locations shown in Fig. 4.2. Data is colour-coded according to subunits: T13-1 is shown by black circles, T13-2 is marked by grey circles, T13-3 is marked by white circles, T13-4 is represented by blue circles and T13-5 and T13-6 are shown in orange and yellow, respectively. a) This inset illustrates the median grain size Md(Φ) and sorting σ(Φ) following Inman (1952). b) F1 and F2 are descriptive parameters where F1 represents the proportion of the sample that is >0 Φ (<1 mm) and F2 represents the proportion of the sample that is >4 Φ (<63 μm). 136

Fig. 4.6: Scanning electron microscope images of selected representative juvenile shards in the 2 Φ fraction. Scale bar in each image corresponds to 300 μm. a) D-type, blocky clast with irregular surface and conchoidal fractures. b) S-type juvenile with a smooth, glassy surface and heterogeneous vesicles, typical of subunits T13-1 and T13-2. c) Irregular S-type juvenile from T13-5 with thick bubble walls and large vesicles. Note the step-like fractures. d) T-type shard with a smooth surface and fluidal morphology. e) D-type clast from T13-4 displaying small vesicles on the breakage plane. f) S-type clast from T13-4 that is characterised by a smooth, glassy surface and large deformed vesicles. g) Pumiceous T-type shard as found in subunits T13-4, -5 and -6. h) Dense juvenile shard with an irregular surface showing step-like fractures. i) T-type shard showing high vesicle density, a fluidal morphology and a smooth surface. 138

Fig. 4.7: Overview of different juvenile types, their groundmass crystallinities and textures. a) 2D-groundmass crystallinities obtained from image analysis on back-scattered electron images. Different glass types are summarised as follows: Tan vesicular juveniles comprise both beige vesicular (BEV) and brown vesicular (BRV) clasts, marked by white and grey squares, respectively. Dense clasts include beige dense (BD) and dark dense (DD) juveniles and are represented by grey and white circles, respectively. Scoriaceous juveniles (DV) are represented by triangles. Insets b) to e) show backscattered electron images where groundmass glass is of medium grey colour, whereas dark grey areas represent feldspar microlites and bright areas mark pyroxene microlites. Scale bar corresponds to 100 µm for a, b and c, while in d the scale bar represents 300 µm. b) T-type glass from T13-4, showing medium-sized coalescent and slightly deformed vesicles and large feldspar microlites. Pyroxene microlites are subordinate and overall groundmass crystallinity lies at 41.73%. c) T-type juvenile from T13-3, displaying large deformed vesicles and large feldspar microlites. Few large pyroxene microlites (long axis 30-40 µm) can be seen, while most pyroxene microlites are small (<10 µm). Groundmass crystallinity is gmc=50.50%. d) D-type microcrystalline juvenile that exhibits a high groundmass crystallinity of gmc=60.19%. Feldspar and pyroxene microlites are small and closely spaced. e) Scoriaceous juvenile from T13-4 showing both high vesicularity and high groundmass crystallinity (gmc=75%). Vesicles are large, coalescent and deformed and the groundmass is characterised by large feldspar microlites and closely spaced, groundmass-filling pyroxene microlites. 139

Fig. 4.8: Pyroclast assemblage obtained from point counting of the 2 Φ fraction of individual subunits from the T13-tephra sequence. Point counting data is reported for key sections to illustrate lateral variability, with locations being the same as in Fig. 4.2 and Fig. 4.1b. Where a subunit contains more than one sampled bed, the pyroclast assemblage for each sampled bed is reported. The distinguished componentry classes are: dark dense clasts (D-type, black), scoriaeous clasts (S-type, grey), tan dense clasts (orange), tan vesicular clasts (T-type, yellow), plagioclase (light grey), pyroxenes (striped), lithics (white). Note that for inset a) Loc. 3, tan dense clasts are included within the tan vesicular glass class, slightly increasing relative proportions of T clasts by ≤5.92%. 141

Fig. 4.9: Idealised composite profile illustrating the main variations in componentry at the representative key location Loc. 1. Componentry is shown for the 2 Φ size class. Note that data for T13-1 is taken from Loc. 3, given the limited dispersal of T13-1. a) Percentage of lithic clasts (grey) and free crystals (black) is calculated relative to total number of clasts counted per sample. b) Ratio of free pyroxenes over free plagioclase. c) Vesicular juvenile over dense juveniles with vesicular juveniles containing both tan vesicular (T) and scoriaceous (S) clasts, while D marks dense clasts. d) Variation in vesicular clast types calculated relative to total number of counted juvenile glass. Insets e to l) show grain size distributions for individual beds at Loc. 1 and at Loc. 3 for T13-1. Note the bimodality in subunits T13-1 (l) and T13-2 (k). 144

Fig. 4.10: Overall 2D-groundmass crystallinity (gmc in %, calculated on a vesicle- and phenocryst-free basis) for different componentry classes and their relationship with selected major element oxide and trace element compositions. Major element compositions are normalised on a volatile-free basis. Error bars mark respective analytical errors (see Appendix G-1 for major element data and Appendix G-2 for trace element

data). Different juvenile types are represented by the following symbols: white circles- dense microcrystalline juveniles (D-type), light grey squares- tan vesicular juveniles (T-type), dark grey triangles- scoriaceous juveniles (S-type) a) Groundmass crystallinity vs K_2O. Note the constant K_2O values with increasing groundmass crystallinity. b) Groundmass crystallinity vs MgO. Note the weak negative correlation between gmc and MgO. c) Groundmass crystallinity vs Th. Thorium compositions are variable but lack an evident correlation with groundmass crystallinity. d) Groundmass crystallinity vs incompatible trace element ratio Zr/Y. Note that Zr/Y remains constant with variable gmc....................................... 145

Fig. 4.11: Geochemical characterisation of individual subunit throughout the T13-sequence. Major elements are normalised on a volatile-free basis. Symbols are grouped according to their corresponding juvenile class: circles show dense juveniles, squares mark tan vesicular clasts and triangles mark scoriaceous juveniles. Individual subunits are colour-coded with T13-2 data being reported in grey, T13-3 in white, T13-4 in blue and T13-5 and -6 in orange and yellow, respectively. Note the absence of T13-1. Error bars mark accuracy for major element oxides (Appendix G-1.4). Stippled field in b, d, f, h and j mark compositional field for subunits T13-2,-3 and -4 as reported in insets a, c, e, g and i. Assuming 10% of fractionation of each phase, fractionation vectors are reported by grey dashed arrows for orthopyroxene (O), clinopyroxene (C) and plagioclase (P), following phenocryst compositions in Nakagawa et al., (1999) and Price et al., (2012). a) MgO vs SiO_2 for subunits T13-2, -3 and -4 b) MgO vs SiO_2 for subunits T13-5 and -6. c) CaO vs SiO_2 for subunits T13-2, -3 and -4. d) CaO vs SiO_2 for subunits T13-5 and -6. e) K_2O vs SiO_2 for subunits T13-2, -3 and -4. f) K_2O vs SiO_2 for subunits T13-5 and -6. g) Trace element ratios Zr/Y vs La/Sm for subunits T13-2, -3 and -4. h) Trace element ratios Zr/Y vs La/Sm for subunits T13-5 and -6. i) Trace element ratios Rb/Sm vs Ba/Y are shown for subunits T13-2, -3 and -4. j) Trace element ratios Rb/Sm vs Ba/Y are reported for subunits T13-5 and -6.. 148

Fig. 4.12: Semi-log plot showing deposit thickness in cm vs √(isopach area A) in km. a) The distribution of the cumulative thickness for the T13-sequence (plus signs) is compared with the thickness distribution of the Fuego 1974 eruption (circles, data from Rose et al., 2008) and the distribution for the June 1996 Mt. Ruapehu eruption (data from Bonadonna and Houghton, 2005). For comparison, exponential equations that describe the exponential fitting line are reported as well. b) Thickness distribution for individual subunits: T13-1 (black plus signs), T13-3 (grey plus signs), T13-4 (blue plus signs) and T13-6 (orange plus signs). Note the steep thickness distribution for subunits T13-1 and T13-3. Assuming, that our field data represents only the medial segment (cf. Bonadonna et al., 1998), T13-4 and T13-6 show similar k-factors of $k_{T13\text{-}4}= -0.117$ and $k_{T13\text{-}6}= -0.126$ that describe the thickness thinning rate following Pyle (1989); Fierstein et al. (1992). Based on the known thickness distribution from the June 1996 Mt. Ruapehu eruption after Bonadonna and Houghton, 2005 and assuming similar break-in-slope distances (b_{is}=28.41 km) between the medial and the distal segment, we extrapolate the distal segment for subunits T13-4 and T13-6, using a distal k-factor of $k_d= -0.047$. Extrapolated distal segments are marked by blue and orange crosses and dashed lines for T13-4 and T13-6, respectively. The exponential equations that describe the observed medial and extrapolated distal segments are shown as well. For comparison, the June 1996 Mt. Ruapehu distribution (after Bonadonna and Houghton, 2005) is also shown. 153

Fig. 4.13: Overview of an idealised composite stratigraphic profile of the T13-tephra sequence. The variability of selected parameters throughout the sequence is reported. Subunit averages are marked by plus signs, are connected by a grey line and are calculated based on the relative proportions of the different juvenile types. Major element compositions are normalised on a volatile-free basis. Groundmass crystallinity is shown as gmc (%). The temporal evolution of major element oxides SiO_2, K_2O and CaO is reported, showing averaged compositions for the three main juvenile classes: dense clasts (D, circles), tan vesicular clasts (T, squares) and scoriaceous clasts (S, triangles). The temporal evolution of selected trace element ratios Zr/Y and Rb/Sm is shown as well, using the same symbology as for major elements. 157

Fig. 4.14: Schematic illustration of the magmatic system feeding the T13-eruption sequence. a) Deeper parental magma arrives into pre-existing crustal, shallow sill-dike system, prior to T13-eruption onset. b) Eruption phases P1 to P3 are fed by magma with similar major and trace element composition, deriving from the same parental magma and affecting increasingly less evolved magma portions. c) After a time break, eruption recommences with P4, which involves similar major and trace element compositions to P1 to P3. Final eruption phase P5 involves slightly more evolved major element compositions compared to P4. Note that potential "fresh" magma replenishing the shallow system is not erupted but leads to a destabilisation of the magma already residing in the system. Size of magma batches and depths are not representative of actual dimensions. 162

Fig. 4.15 (next page): Illustration of SiO_2, K_2O and CaO groundmass variability throughout different eruption sequences over the last 22,000 years. T13 groundmass glass (black with grey plus signs) is integrated with glass data on Tufa Trig tephra sequences T5, T15 and T31 and with existing literature data on the historical 1995–1996 eruptions and tephra deposits from the Bullot Formation. Note the breaks in the time axis. Compositional ranges are marked by horizontal bars, while crosses show the average, where available. Literature data on tephra is marked by grey bars. Additional compositions obtained from the analysis of groundmass glass in lava bombs and scoriae is shown in black. Eruption ages are reported where available. Compositional ranges have been previously published as follows: [1]Mgt- Mangatoetoenui eruption (Pardo et al., 2012); Sw- Shawcroft compositions follow Pardo et al. (2012), while the age is obtained from [2]Donoghue et al. (1995); [+]ages for tephra sequences T5, T13 and T15 are from Voloschina et al., (2020); [3]Groundmass glass compositions for historical eruptions were obtained on scoriae and are described in Kilgour et al. (2013) and [4]Nakagawa et al. (2002); groundmass glass compositions on volcanic ash from historical eruptions follow [5]Moebis et al. (2011), [6]Moebis (2010) and [7]Donoghue et al. (1997). Compositions for other Tufa Trig tephra members are reported after [8]Donoghue et al. (2007), while trace element compositions for the Shawcroft and Mangatoetoenui members are published in [9]Pardo et al. (2014). Trace element compositions on lava flows from the Whakapapa Formation are reported for selected lava flows from the Crater Lake and Iwikau members, both younger than 10,000 years and follow [10]Conway et al. (2018), while trace element compositions for the historical 1995–1996 eruptions are from [11]Gamble et al. (1999). 167

Fig. 5.1: Overview geographical setting based on a 8 m digital elevation model from the LINZ Data Service (https://data.linz.govt.nz) and is based on the LINZ Topo50 map series from 2012. a) The North Island of

New Zealand. The Taupo Volcanic Zone (TVZ) is delimited following Wilson et al 1995. The position of the Tongariro Volcanic Centre (TgVC) is marked by a box and the position of the andesitic volcano Mt. Taranaki and the rhyolitic caldera Taupo are reported for comparison. Inset b) shows an overview of the Tongariro Volcanic Centres (TgVC), which include Mt. Tongariro and Mt. Ngauruhoe to the North and Mt. Ruapehu. Field locations that were investigated for this research are marked by grey circles. The white lines represent major roads. Red lines show major fault lines and are modified after Villamor et al., (2007). 184

Fig. 5.2: Composite stratigraphic profile showing idealised tephra and soil thicknesses of the Tufa Trig Formation in mm at ~10 km distance from source. The three main types of deposit, classified in Voloschina et al. (2020) are reported by different colours with light grey units corresponding to single bed ash unit (SBA), medium grey units showing multi-bed ash units with 2 to 3 subunits, dark grey units representing multi-bed ash units with ≥4 subunits and orange marking lapilli units. The stratigraphic position of four uncorrelated tephra units is reported as well (“^”). Insets show images of typical tephra sequences, representative of the different lithosedimentological types. 186

Fig. 5.3: Overview showing tephra dispersal during major historical eruption episodes at Mt. Ruapehu. Inset a) shows the dispersal of ash associated with the 1945 eruptions modified after Johnston et al. (2000) with green area marking tephra dispersal after Beck (1950), while the blue area extends the dispersal area following Johnston et al. (2000). b) Tephra dispersal for major magmatic phases during 1995-1996 episodes shows the NE-isopachs for October 11th in blue, the SE-isopachs of Oct 14th after Cronin et al. (1998) with stippled lines and the isomass dispersal from the 17 Jun 1996 subplinian phase after Bonadonna and Houghton (2005) are reported by dashed lines. 187

Fig. 5.4: Comparison of idealised and detailed isopachs to approximate tephra dispersal. Thicknesses are in mm. a) Lapilli unit T2 is approximated by an idealised ellipse of 35 mm thickness. b) Detailed isopachs constructed for the same unit T2 after Voloschina et al. (2020). c) Idealised ellipse of 2 mm thickness to approximate the dispersal of subunit T13-1. d) Detailed isopach for subunit T13-1 as shown in Chapter 4. e) Tephra dispersal of main subunit T13-4 approximated by an idealised ellipse and f) by detailed isopachs as shown in Chapter 4. 190

Fig. 5.5: Tephra age interpolation based on cumulative soil depth in mm. Each tephra age is indicated by a boxplot at the profile depth. The 1945 eruption (see text) is indicated by a circle. 193

Fig. 5.6: Frequency-magnitude relationships for the Tufa Trig Formation showing tephra unit deposit volumes for individual members. Ages for members are based on the age model. Different lithosedimentological deposit types are marked by different colours with lapilli-units in orange, single bed ash units in light, multi-bed ash units with 2-3 subunits in medium grey and multi-bed ash units with more than 4 subunits in dark grey. Time-dependent average Mg-number (Mg#) for individual tephra members is calculated as $Mg\#=100*MgO/(MgO+FeO_{Tot})$ and is shown in blue. No data is available for members T1 and T7. For comparison, the Mg-number for the historical 1995-1996 eruptions is reported as well, following the dataset of Moebis et al. (2011). 196

Fig. 5.7: Major element groundmass compositions for individual subunits reported relative to their stratigraphic position. Compositions for SiO_2, CaO and K_2O are normalised to 100, on a volatile-free basis. Grey squares represent individual analyses (cf. Appendix H-3.2), while plus signs show averaged compositions with number of analyses reported in Appendix H-3.3. No data is available for tephra members T1 and T7 and subunits T13-3, T19-1, T20-3, -5 and -6. Data for the historical 1995–1996 eruptions is reported as T32 and follows Moebis et al. (2011). 198

Fig. 5.8: Flow chart illustrating the data sets and models used for the statistical modelling and discussed in the following sections. Solid arrows show the employed process, while dashed lines mark potential alternatives that were discarded. The final applied model is highlighted by a box. a) Inter-sequence modelling is discussed in 5.5.1 Statistical modelling of inter-sequence onsets. Abbreviations are as follows: AIC - Akaike Information Criterion, HMM - Hidden Markov model, MMPP - Markov Modulated Poisson Process with S denoting the number of hidden states. b) Intra-sequence modelling is discussed in 5.5.2 Statistical Modelling of intra-eruption sequences. 199

Fig. 5.9: a) The cumulative number of eruptions is shown against eruption ages in AD ages following the age model. Constant slopes indicate stationarity of the data over the duration of an unobserved hidden state. Data is obtained from averaging 1000 age realisations. b) Estimated mean hidden state path of the three-state Weibull hidden Markov model. Data represents averages of 1000 age realisations. 201

Fig. 5.10: Measured subunit volumes (all subunits), compared with an exponential distribution (mean 0.002768 km^3). The 95% significance in line with the Kolmogorov-Smirnov test is reported for comparison. 206

Fig. 5.11: Exponential volume distributions grouped according to their respective subunit number. Following the Kolmogorov-Smirnov test, the 95% significance limit is reported as well. Note that subunits 4-6 are grouped in inset d. 207

Fig. 5.12: Frequency distributions of the inter-sequence repose lengths preceding each eruption are shown for different number of phases. “n” represents the number of eruptions with that specific number of subunits. 207

Fig. 5.13: Overview over time-variable changes in cumulative frequency and magnitude data. Ages are reported in cal BP following the previously introduced age model. The number of subunits is shown in black and deposit volumes for individual tephra units are represented by the grey curve. For comparison, the extent of the regimes as identified by previous statistical analysis is reported as well. 211

Fig. 5.14: Probability forecast of eruption onset time of the next commensurate (VEI 3+) event, starting from 1945. Based on a dataset that includes the tephra record of the Tufa Trig Formation up to and including the 1945 eruptions. Red and blue lines mark the onset date of the 1995–1996 eruptions that were classified as VEI 3. 212

Fig. 5.15: Temporal forecast for the eruption onset of the next commensurate (VEI 3+) event, considering that no commensurate event was observed prior to AD 2020. The forecast is based on a dataset that includes the tephra record of the Tufa Trig Formation and the 1995–1996 eruptions. 213

Fig. 6.1: Cumulative eruption frequency distributions for the TgVC volcanoes Mt. Ruapehu (black), Mt. Ngauruhoe (grey) and Red Crater (red). Inset a) shows explosive eruption behaviour over the past ~6000 years, while b) shows only the past 2000 years, excluding historical eruptions. Note that, for Mt. Ruapehu, the historical 1945 eruption is included in the cumulative eruption frequency. 239

Fig. 6.2: Schematic overview of the post-Taupo timeline integrating the Tufa Trig tephra record with previously published studies on the lahar deposits of the Onetapu Formation (Donoghue et al., 2001; Lecointre et al., 2004; Hodgson et al., 2007). CL marks the evolution of Crater Lake. Radiocarbon ages are marked by stars for tephras and by plus signs for lahars and are reported in cal BP (Hodgson et al., 2007). 241

Fig. 6.3: Eruption scenario as inferred from the historically most frequent small-scale, short-lived phreatic and phreatomagmatic eruptions (Scott, 2013). Note that these eruptions typically affect the summit area. 242

Fig. 6.4 (next page): Schematic visualisation of the main eruption scenarios as inferred from the 1800-year tephra record. For comparison, 10 and 15 km distances are indicated by red circles and the position of State Highway 1 is shown by a yellow line. Column heights are not to scale. a) Low-intensity small volume eruption resulting in single bed ash units. The extent of associated ash-rich deposits is limited to the most proximal ~10 km. b) Moderate intensity eruption leading to lapilli deposits. This type of eruptions is probably associated with the absence of Crater Lake in the active vent leading to short-lived eruptions dominated by magmatic fragmentation and the dispersal of lapilli-sized material to distances >15 km. Insets c), d), e) and f) show different phases of a multi-phase eruption leading to a multi-bed deposit. c) shows the opening phase(s), which are of low intensity and dominated by phreatomagmatic activity. Syn-eruptive changes in wind patterns lead to the dispersal of ash-sized material in different directions. d) The pre-climactic phase(s) is associated with a change in eruption intensity compared to the opening phase(s) and leads to ashfall in different directions and, depending on the eruption intensity, at different distances. d) The climactic, semi-continuous phase of the multi-phase eruption is associated with irregular multi-lobate deposits that are associated with changes in eruption intensity such as waning and waxing, multiple individual fall events and syn-eruptive changes in wind pattern. f) Following the climactic phase, a post-climactic phase emits ash over prolonged periods leading to mostly local ashfall that might affect large areas depending on the prevailing wind conditions... 245

Chapter 1

Introduction

This chapter introduces the hypothesis and the objectives that guide this PhD research. Furthermore, a literature review presents the geological background and current state of knowledge.

1.1 Introduction

Volcanic eruptions are amongst the most lethal and far-reaching natural hazards on Earth, directly affecting more than 800 million people globally (Sigurdsson et al., 2015). In New Zealand, these hazards pose potential threat to life – ranging from our iconic national parks to our largest city. The impacts of volcanic hazards have the potential to disrupt infrastructure, as well as tourism and primary industries that underpin the NZ economy. Over the past decades, our fundamental understanding of individual eruption processes and our ability to simulate them numerically have progressed considerably (e.g., Carey et al., 1986; Pallister et al., 2013). However, we have yet to address one of the key risk dimensions of volcanic eruptions: their dynamic evolution with eruption progression, and the correlated changes in the associated hazards. The complex dynamics, and the often-unforeseen impacts, of multi-phase eruptions cannot be accounted for in current short- and long-term forecast and hazard models. Almost every eruption on Earth involves multiple eruption phases, while simple single-phase eruptions are extremely rare (Jenkins et al., 2007). In particular, small-scale, low to mid-intensity multi-phase eruptions tend to be underrepresented in long-term records. Despite these small to moderate explosive eruptions constituting the most frequent eruptions (Siebert et al., 2015), our understanding of the complexity of the eruption dynamics is currently limited due to the low preservation potential of the associated deposits as well as the low number of detailed time-resolved studies (Taddeucci et al., 2002; Cioni et al., 2014; Miyabuchi et al., 2019). As a result, forecast models tend to be biased toward eruption scenarios that do not account for the hazards that are associated with small-scale prolonged multi-phase eruptions.

This research aims to improve our understanding of the eruptive dynamics during small-scale multi-phase eruptions. To address this, a detailed frequency-magnitude record of small-scale multi-phase eruptions will be created. Mt. Ruapehu is the southernmost andesitic volcano within the Taupo Volcanic Zone on New Zealand's North Island (Wilson et al., 1995). It is considered one of New Zealand's historically most active volcanoes with recent eruptions in 2007 and 1995–1996. Over the past 250,000 years (Gamble et al., 2003), Mt. Ruapehu has exhibited a broad range of eruption styles and processes (Houghton et al., 1987), leading to proximal hazards such as the expulsion of ballistic blocks (Kilgour et al., 2010) and dome extrusion (Oliver, 1945; Johnston et al., 1995) to proximal-medial hazards such as ice-slurry lahars (e.g., Lube et al., 2009) and dense pyroclastic density currents (e.g., Cowlyn, 2016), as well as distal hazards such as widespread ash fall (Cronin et al., 2003; Pardo et al., 2012), debris avalanches (Palmer et al., 1989) and voluminous lahars (Houghton et al., 1987; Hodgson, 1993; Hodgson et al., 2007). The 1995–1996 multi-phase eruptions resulted in major economic losses to tourism and agricultural industries (Johnston et al., 2000). They also highlighted the need for a better understanding of the eruptive dynamics as well as the eruption styles, magnitudes and timescales involved during prolonged eruption episodes to enable reliable decision-tools for stakeholders.

1.1.1 Overall aim and objectives of this research

Despite previous studies on both historic (Scott, 2013) and geological eruption frequency records (Topping, 1973; Donoghue et al., 1995; Donoghue et al., 1997), no detailed frequency record exists for Mt. Ruapehu's small to moderate single-phase and multi-phase explosive eruptions in the last few thousand years. Similarly, detailed information on eruption style and magnitude and their evolution during eruption progression is lacking. This research aims to fill this gap by creating a detailed frequency-magnitude record for the past 1800 years at Mt. Ruapehu. This record will form the basis for probabilistic analysis with the aim to estimate probabilities of future eruptive activity. An overarching hypothesis for this work is proposed as follows:

A detailed frequency-magnitude record, characterising information on eruption style, magnitude and recurrence as well as the number and order of individual single- and multi-phase eruptions will be developed and can be used to identify short- and long-term patterns in eruption behaviour that provide insights into time-variant physico-chemical processes within the volcanic system and will constitute the basis for short- and long-term eruption forecasts.

To test this hypothesis, three main research objectives are defined:

Objective 1: Creating a detailed frequency-magnitude record for Mt. Ruapehu, detailing eruption style, frequency and magnitude for multi-phase and single-phase eruptions over the past two millennia.

Approach: Detailed tephrostratigraphic field work together with geochemical fingerprinting, componentry analysis and new constraints on eruption ages.

Goals:

- Creating a detailed eruption record for the last two thousand years, detailing eruption style, magnitude and dispersal as well as the number and order of eruptions in multi-phase sequences. Characterising the range in deposit features associated with small to moderate explosive single-phase and multi-phase eruptions and relating this variability to different eruption styles and magnitudes.
- Obtaining additional age constraints that provide the base for a statistical age model and the frequency-magnitude record. Integrating this new dataset with existing frequency records over the last ~6000 years to characterise long-term patterns in frequency distributions.
- Comparison of the frequency distribution to other Tongariro Volcanic Centre (TgVC) volcanoes.

Objective 2: Characterising switches in eruption behaviour during multi-phase eruptions and relating them to changes in the source-conduit system.

Approach: Investigation of a selected key tephra sequence by determining eruption progression through the study of lithosedimentological parameters in combination with geochemical and textural characterisation of juvenile material.

Goals:

- Quantifying lateral and vertical variability of multi-bed tephra sequences, including deposit characteristics, pyroclast assemblages, tephra dispersal as well as the time-variable magma evolution in terms of textural and geochemical characteristics.
- Identifying the factors that control eruption dynamics and eruption succession/progression during prolonged multi-phase eruptions.

Objective 3: Identifying patterns and long-term changes in eruption behaviour and the volcanic system.

Approach: Integration of the new frequency-magnitude eruption record with the geochemical dataset to characterise long-term behaviour of the magmatic system during the past 1800 years. Probabilistic modelling of long-term frequency-magnitude trends and eruption progression during multi-phase eruptions.

Goals:

- Constraining the inception of a permanent Crater Lake in the currently active vent system.
- Discussing long-term processes in the magmatic system that control changes in eruption behaviour.
- Testing whether patterns identified by probabilistic modelling can be used to forecast the dynamic evolution during a multi-phase eruption event.

This thesis is subdivided into seven chapters with the first providing a review of previous work. Chapter two discusses the methodology and techniques that are employed during this research. Chapter three presents the tephrostratigraphic framework, detailing the lithosedimentological characteristics of the tephra units and leads to the refined definition of the Tufa Trig Formation. In Chapter four the characteristic multi-bed tephra sequence of the largest eruptions of the past two millennia is analysed in terms of physical parameters such as tephra dispersal, lithosedimentological characteristics and pyroclast assemblages. This information is then integrated with geochemical analyses of juvenile components to reconstruct eruption progression. Time-variable patterns in eruption frequency, magnitude and geochemical characteristics are discussed in Chapter five, which also outlines the value of long-term geological records for probabilistic modelling of multi-phase eruptions. The findings of this thesis are summarised in Chapter six, where the contributions of this research are discussed in the context of the current knowledge in this field and the overarching research questions are answered. Finally, Chapter seven summarises the specific findings of this research and presents possibilities for future research. In addition to this, the underlying datasets are contained in electronic appendices.

1.2 Literature Review

1.2.1 Explosive eruptions

Explosive volcanic eruptions involve the fragmentation of magma and produce pyroclasts which can be transported over great distances by strongly or weakly buoyant eruption plumes and the wind (e.g., the Taupo Pumice AD 232, Walker, 1980; Tambora AD 1815, Self et al., 2004). The explosivity of an eruption depends on a number of factors that control the characteristics of the magma at source, during magma ascent and finally during the fragmentation processes. The most active and frequent volcanoes on Earth are related to subduction zones (e.g., the Pacific "Ring of Fire", Simkin et al., 2000) where the subduction of one plate beneath the other leads to partial melting of the overlying mantle due to slab dehydration. This melt has a lower density compared to the surrounding rocks and thus ascends. During this process, it can stall at various levels of the crust (Marsh, 1996; Marsh, 2015), where important processes such as differentiation or mixing/mingling occur (e.g., Civetta et al., 1991; Annen et al., 2005). Additionally, assimilation of surrounding rocks (i.e., limestone at Vesuvius, Barberi et al., 1981) or crystallisation leads to the accumulation or loss of volatiles (e.g., CO_2, H_2O, S, Cl, F) and/or to the nucleation of crystals. These processes control the magma's rheology and density and therefore determine further ascent behaviour. Whatever the final trigger leading to the eruption will be (i.e., injection of new, hot magma; decompression due to flank collapse; volatile oversaturation), the processes occurring along the source-ascent-vent system will fundamentally influence the eruption progression.

1.2.2 Classification of explosive eruptions

Based on the mechanisms that generate them, explosive eruptions can be subdivided into two "ideal" end members: (1) "dry" magmatic eruptions and (2) "wet" phreatomagmatic eruptions (e.g. Freundt et al., 1998; Parfitt et al., 2008; Cashman et al., 2015).

For **"dry" magmatic eruptions**, the main factor controlling eruption explosivity is the amount and the composition of the volatiles dissolved in the magma. The volatile content in combination with the magma composition and the pressure-temperature-conditions at which the different volatile species exsolve will determine the explosivity of an eruption (Cashman, 2004). The energy of a volcanic eruption is generated during fragmentation, where a single liquid phase (magma) with sparse gas bubbles is transformed into individual fragments (pyroclasts) with a gas phase (Sparks, 1978; Wilson et al., 1980). The potential energy of the expanding magma is converted into kinetic energy as the pyroclasts and the surrounding gas phase erupt (Freundt et al., 1998). The main factors leading to magmatic fragmentation are: rapid acceleration, rapid decompression (e.g., during a collapse of the volcanic edifice or a lava dome) or shear processes occurring along the conduit walls (Cashman et al., 2015).

The interplay of bubble nucleation and growth with magma rheology and volatile solubility are crucial factors that influence magma rise speed and magmatic fragmentation (Cashman et al., 2004; 2015). The different types and processes of nucleation and bubble growth are further described in detail in Parfitt et al. (2008) and Freundt et al. (1998). Magma composition plays a very important role, e.g., if magma viscosity is low (in the case of a basalt for example) bubbles can grow very quickly and can also escape easily, leading to a high gas:magma ratio and smaller eruptions, often accompanied by effusive volcanism. On the other hand, more viscous magmas like rhyolites tend to retain the exsolved gas until very shallow depths, leading to high porosity clasts, high degrees of fragmentation, smaller clast sizes and bigger eruption plumes (Wilson et al., 1980; Sparks, 1986). In the past, different eruption types have been classified in various ways, often using the characteristics of the associated fallout deposits; the most common classifications use tephra dispersal and degree of fragmentation (Walker, 1973; Walker, 1980; Cas et al., 1987). Here, an increase in eruption intensity and tephra dispersal is associated with increasing magma viscosity and volatile content, ranging from the less dispersed and generally basaltic Hawaiian and Strombolian eruptions to subplinian and Plinian eruptions that typically involve more silicic compositions (Fig. 1.1, Walker, 1973). The most violent eruptions are associated with widely dispersed deposits and comprise high amounts of fine-grained pyroclastic material due to high fragmentation efficiency. At the same time, efficient and violent fragmentation can result in fine-grained deposits with relatively small dispersal areas, leading to Violent Strombolian and Surtseyan eruptions and Vulcanian eruptions for silicic compositions (Fig. 1.1; Walker, 1973). The terminology describing the different eruption types is based on type localities and well-described, observed eruptions (e.g. Kilauea, Hawaii, Head et al., 1987;

Stromboli, Italy, Rosi et al., 2013; Vulcano, Italy, Mercalli and Silvestri, 1891; Plinian after the AD 79 Vesuvius eruption, cf. Cioni et al., 2015). Other classification schemes approximate eruption intensity and magnitude through parameters that can be obtained from deposits such as the clast and thickness half-distance (Pyle, 1989) or plume height, mass eruption rate and deposit volume (Bonadonna et al., 2013b). For the classification of historically observed eruptions, the relation between explosive magnitude and intensity is used to define the Volcanic Explosivity Index (VEI, Newhall et al., 1982). While this classification provides a useful scheme to classify observed eruptions, its application to eruptions that are preserved only in the geological record is limited.

Eruptions that involve deposit volumes $\leq 10^8$ m^3 are classified as "small to moderate explosive eruptions" (Cioni et al., 2008b; Bonadonna et al., 2013b) and are associated with VEI ≤ 3 (Newhall et al., 1982). Small to moderate explosive eruptions encompass a range of different eruption styles, intensities and fragmentation mechanisms (Bonadonna et al., 2013b, 2016). As this thesis focuses on small to moderate explosive eruptions, in the following, an overview will be provided over the main eruption types, emphasising key differences in eruption style, magnitude and the resulting tephra deposits. The different eruption types involve characteristic, underlying fragmentation mechanisms such as normal *Strombolian* activity that comprises periodic explosions of gas slugs (e.g. Stromboli, Italy, Burton et al., 2007; Rosi et al., 2013). In comparison to Hawaiian activity, Strombolian activity is generally associated with high gas:magma ratios and a higher magma rise speed (Parfitt et al., 1995). Associated deposits are characterised by limited dispersal and relatively low fragmentation indices, resulting in coarse-grained pyroclastic deposits (Valentine & Gregg, 2008; Bertagnini et al., 2011; D'Oriano et al., 2011). Contrastingly, the term that describes "*violent Strombolian*" eruptions is more ambiguous and not evidently linked to typical "Strombolian" activity (Francis et al., 1990; Valentine & Gregg, 2008). Generally, "*violent Strombolian*" is considered to describe explosive activity that is more energetic compared to normal Strombolian activity, resulting in more dispersed deposits with high percentages of ash-sized material (Fig. 1.1, Walker, 1973). In line with eruptions observed at Parícutin (Pioli et al., 2008) and from deposit descriptions at Vesuvius (Arrighi et al. 2001; Cioni et al., 2008a), eruption columns are described to reach maximum heights of ~10 km and magma eruption rates are intermediate between Strombolian and subplinian eruptions.

Another eruption style that is associated with small to moderate explosive eruptions, is described as *Vulcanian* (Nairn et al., 1978, Bonadonna et al., 2013b). Vulcanian eruptions involve intermittent, violent explosions due to periodic sealing of magma in the conduit and are dominated by brittle fragmentation due to rapid decompression resulting from the downward propagation of a shockwave (e.g. Kennedy et al., 2005. Clarke et al., 2015). This eruption style is typically associated with intermediate and more volatile-rich magmas and type localities involve Vulcano, Italy (Mercalli & Silvestri, 1891; Clarke et al., 2015), Ngauruhoe, New Zealand (Nairn, 1976) or Soufrière Hills, Montserrat (Giachetti et al., 2010). Associated erupted material is characterised by the ejection of meter-sized ballistic bombs in proximal areas and high amounts of often microcrystalline and dense, ash-sized material (Fig. 1.1, Walker, 1973, Clarke et al., 2015). Other eruption styles that are associated with small to moderate explosive eruptions involve prolonged continuous ash emission and subplinian II-activity as has been described for Vesuvius in Cioni et al. (2008a). Generally, *subplinian* to *Plinian* eruptions are associated with larger deposit volumes >10^8 m^3, VEIs>4 (Newhall et al., 1982) and are more dispersed. Compared to small to moderate explosive eruptions they involve higher eruption intensity and are mostly associated with intermediate to evolved, volatile-rich magma. Here, volatile exsolution leads to extensive fragmentation and small, highly vesicular clasts (e.g. Taupo Pumice, Walker, 1980). The fine-grained pyroclasts feed high, sustained eruption columns (e.g. 40 km during 1991 Pinatubo eruption; Holasek et al., 1996) and lead to wide dispersal areas (Walker, 1973; Cioni et al., 2015; Houghton & Carey, 2015).

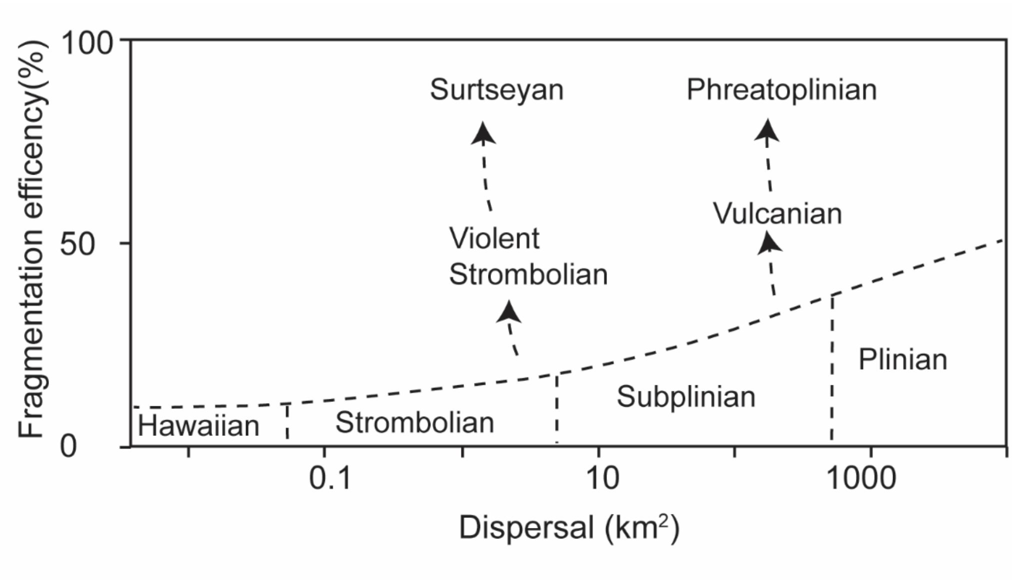

Fig. 1.1: Classification of fallout deposits modified after Walker (1973) and Houghton & Carey (2015) showing different eruption types and their relationship with tephra dispersal and fragmentation efficiency.

For **“wet” phreatomagmatic eruptions**, the factor that leads to fragmentation is external water. This can be either groundwater from aquifers and fractures or surface water from rivers, lakes or oceans. The term “Surtseyan” describes a scenario where the injection of magma into a standing water body (e.g. Crater Lake) leads to the violent evaporation of water, leading to magma fragmentation and involving high water:magma ratios (Kokelaar, 1983; Moore, 1985; Houghton et al., 2015). This eruption type has been observed during historical eruptions at e.g. Surtsey Island (Kokelaar, 1983; Moore, 1985) or Nakadake (Miyabuchi et al., 2018) and is typically associated with small-scale pyroclastic density current (PDC) base surges (Moore, 1967) and “cock’s tail jets” (Houghton et al., 2015) in the most proximal area. Another type of phreatomagmatic eruption involves the violent fragmentation of magma driven by its interaction with water. These eruptions are described as molten fuel coolant interaction (MFCI) processes and have been extensively studied by means of experiments (Zimanowski et al., 1991; Wohletz et al., 1995; Zimanowski et al., 1997). Features, typical for deposits associated with phreatomagmatic eruptions include accretionary lapilli and relatively high amounts of fine grain-sized clasts (Fig. 1.1, Fisher et al., 1984). Clast features include conchoidal fractures, ash coatings due to brittle fracturing and blocky shapes with low vesicularities (Wohletz, 1983a; Wohletz, 1983b; Heiken et al., 1985).

A different kind of eruption, involving water but without the expulsion of fresh magma, are termed phreatic or hydrothermal eruptions (Barberi et al., 1992). It is often a matter of debate to unambiguously identify fresh magmatic glass and the extent to which fresh magma contributed to the eruption as e.g., injection of magma in the hydrothermal system increases the overpressure, thus destabilising the hydrothermal system as inferred for the 2012 Te Maari eruption (Pardo et al., 2014a) or the 2014 Ontake eruption (Maeno et al., 2016; Miyagi et al., 2020). Ejecta from hydrothermal eruptions is usually characterised by hydrothermally altered lithic clasts, which include a large proportion of clay minerals and zeolites (Heiken et al., 1985; Barberi et al., 1992; Miyagi et al., 2020).

Finally, it is important to keep in mind, that the above described eruption styles, mechanisms and classifications describe “ideal” eruption scenarios and processes and are mostly based on well-observed eruptions. In line with this, the application of existing eruption style and classification schemes to quantify deposit characteristics is often complex due to discrepant definitions between observed processes and deposit features (cf. Francis et al., 1990; Houghton & Gonnermann, 2008; Valentine & Gregg, 2008). This is particularly problematic for small to moderate explosive eruptions that often involve an interplay between different eruption styles and mechanisms rather than representing one main process (cf. Bonadonna et al., 2016).

1.2.3 Regional geological background

New Zealand’s landmass sits astride a plate boundary between the Pacific plate and the Australian plate. It is part of the “Ring of Fire”, a nearly circular zone surrounding the Pacific Ocean, where the convergence of tectonic plates leads to frequent and explosive volcanism. North of the New Zealand landmass, the plate boundary is marked by the Hikurangi-Kermadec subduction system where the Australian plate overrides the Pacific plate (Fig. 1.2). To the south of the South Island, the Australian plate subducts beneath the Pacific plate in the Puysegur subduction system. Between the two opposed subduction zones, the Alpine fault, a dextral transform fault, dominates plate motions (Nakagawa et al., 2002; Graham, 2008), shifting the Pacific plate southward relative to the Australian plate (Fig. 1.2). Convergence of the plates is slightly oblique, moving at rates of 35–50 mm/y (Graham, 2008). The Hikurangi-Kermadec subduction zone is characterised by a clockwise rotation with the pole close to New Zealand (Wallace et al., 2004), leading to the back-arc extension of the North Island continental crust at rates of c. 7–20 mm/y (Houghton et al., 1995; Beavan et al., 2001; Villamor et al., 2007; Graham, 2008). The Taupo Volcanic Zone (TVZ) is a c. 200 km long and maximum 60 km wide zone onshore, characterised by high heat flow (~700 mW/m^3 average heat flux in the central zone, Bibby et al., 1995) and extensive volcanism (Houghton et al., 1995; Wilson et al., 1995).

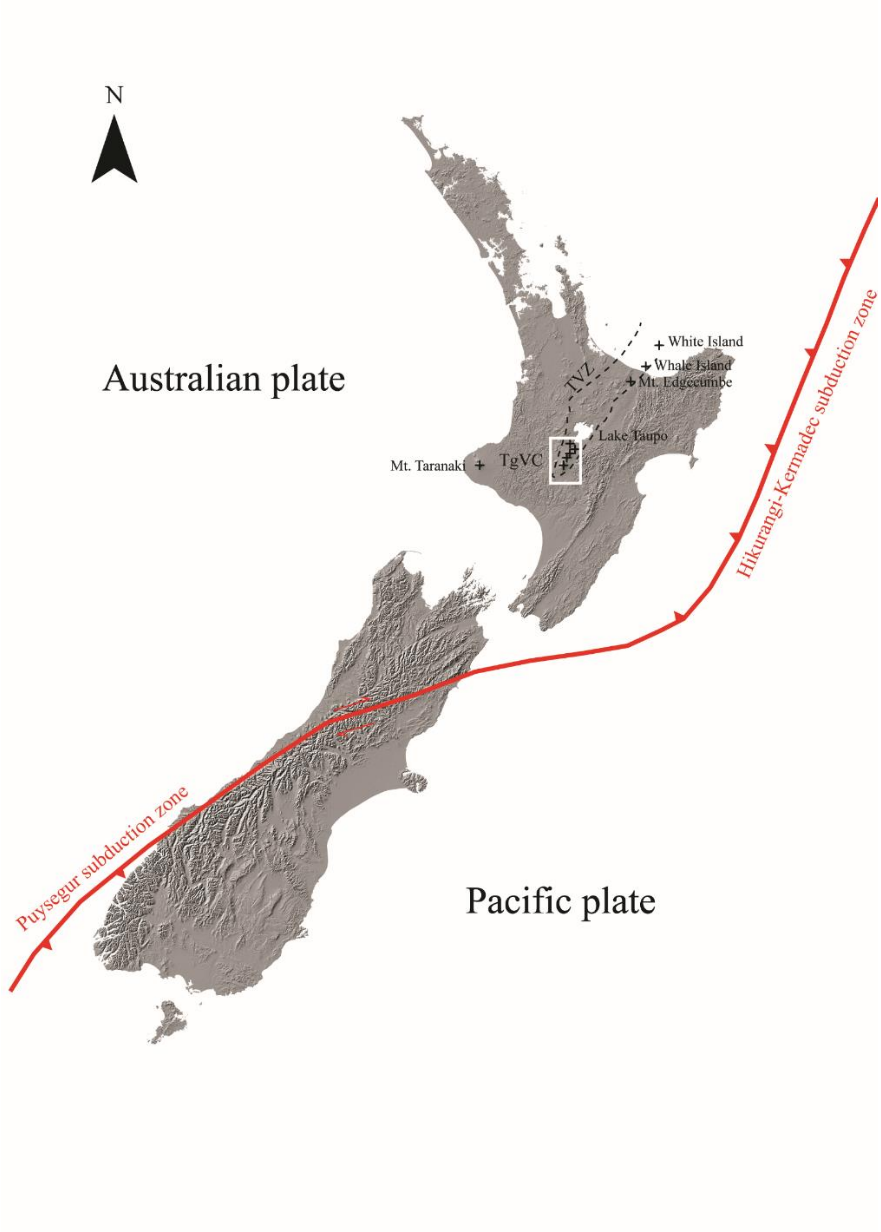

Fig. 1.2: Overview of New Zealand's setting on the plate boundaries. Taupo Volcanic Zone (TVZ) boundaries after Wilson et al. (1995). Tongariro Volcanic Centre volcanoes (TgVC) are marked by white box.

1.2.4 The Taupo Volcanic Zone (TVZ)

The Taupo Volcanic Zone (TVZ) extends offshore for 1350 km along the Kermadec arc (Graham, 2008). The onshore TVZ is defined by a graben structure (Houghton et al., 1995; Wilson et al., 1995) with crustal thicknesses increasing towards the south, compared to the central segment (Villamor et al., 2006; Salmon et al., 2011). The TVZ can be subdivided into three segments; the central segment is 125 km long and is dominated by caldera-forming, mainly rhyolitic eruptions from at least 8 centres (Houghton et al., 1995; Wilson et al., 1995). The northern segment is dominated by andesitic-dacitic volcanism from Whakaari (White Island), Moutohora (Whale Island) and Putauaki (Mt. Edgecumbe), (Fig. 1.2). The southern andesitic-dacitic segment comprise the Tongariro Volcanic Centre (TgVC), which embraces Kakaramea-Tihia, Pihanga and the composite volcanoes Mt. Tongariro (including Mt. Ngauruhoe) and Mt. Ruapehu (Wilson et al., 1995).

Most recent eruptions from the central segment of the TVZ originated from the two most active calderas of the TVZ: the Okataina Volcanic Centre (OVC) and the Taupo Volcanic Centre (TVC). The historical basaltic Plinian eruption from the Tarawera Volcanic Complex (AD 1886, OVC) dispersed ~2 km^3 of fall deposits over 200 km^2 (Walker et al., 1984). The other voluminous eruption was the Kaharoa eruption, AD 1314 ± 12 (OVC, Lowe et al., 2013) that erupted ~4 km^3 of magma and is considered New Zealand’s largest rhyolitic eruption within the last 1000 years (Leonard et al., 2002). The last eruption from Taupo occurred in AD 232 ± 10 (Lowe et al., 2013) and dispersed the ~30 km^3 Taupo Pumice (Unit Y7, Wilson, 1985; Wilson, 1993) over most of the North Island.

1.3 Eruptive record of Mt. Ruapehu

1.3.1 Local geological framework

Mt. Ruapehu (from Te Reo Māori language: Rua- pit, pehu- to explode) is the highest peak (2797 m asl) of the North Island of New Zealand and the largest of the Tongariro Volcanic Centre volcanoes (110 km^3, Hackett et al., 1989). It lies within the 40 km wide Ruapehu graben, which is filled by tertiary sediments (Price et al., 2012) and is bounded by the Rangipo fault to the east and the Raurimu fault to the west (Villamor et al., 2007). The basement consists of mainly greywacke and argillite of the Mesozoic Torlesse Terrane and, to the west of the volcanic arc basement of the mafic Waipapa terrane (Price et al., 2012). Compared to the central TVZ, the crust beneath Mt. Ruapehu is thicker (Salmon et al., 2011) and extension rates are lower (Villamor et al., 2006).

Mt. Ruapehu’s volcanic lifespan has recently been extended to 340,000 years, based on mass flow deposits that contain andesitic lava clasts from Mt. Ruapehu (Tost et al., 2015). The current volcanic edifice has been built during four major cone-forming episodes from at least six summit and flank vents over the last 250,000 years (Hackett, 1985; Hackett et al., 1989; Tanaka et al., 1997; Gamble et al., 2003; Price et al., 2012; Conway et al., 2018). The most recent cone-building formation is the Whakapapa Formation and includes lava flows erupted during the past 15,000 years (Hackett et al., 1989; Gamble et al., 2003; Conway et al., 2016; Conway et al., 2018).

Mt. Ruapehu is surrounded by an extensive ring plain, volumetrically similar to the cone (Hackett et al., 1989). Since the last glacial maximum (23–13 ka BP), primary medial-distal pyroclastics and secondary reworked material (e.g., lahars) have contributed to the construction of the ring plain (Topping, 1973, 1974). Five formations in the ring plain were defined to represent the different periods of ring plain aggradation: the Te Heuheu Formation (>22.6–14.7 ka), Tangatu Formation (14.7–5.4 ka), Mangaio Formation (4.6 ka), Manutahi Formation (5370–3200 years BP; Donoghue et al., 2001) and the most recent Onetapu Formation (<1850 years BP, Fig. 1.3). Generally, the ring plain preserves a more complete record of distal explosive products than the steep flanks in the proximal cone area which are subjected to erosion and reworking processes, inhibiting clear identification of explosive products (Hackett et al., 1989).

1.3.2 Holocene and late Holocene stratigraphic record

Most of Mt. Ruapehu’s explosively erupted pyroclastics have been deposited on the eastern and north-eastern ring plain, due to prevailing westerly to south westerly winds (Donoghue et al., 1995). Holocene tephras from Mt. Ruapehu were classified within the Tongariro Subgroup, including all TgVC-sourced tephras from the last 14,000 years (Grindley, 1960). Topping (1973, 1974) further distinguished between five tephra formations, which were later redefined in Donoghue et al. (1995). Additionally, the Tukino Subgroup was defined to include all TgVC tephras erupted between ~12 ka BP and ~25 ka BP (Donoghue et al., 1995; Lowe et al., 2013). Defined formations included multiple discrete tephra members interbedded with soil, andisoil or peat and thus represent soil formations bounded by paleosols or erosion breaks (Topping, 1973; Donoghue et al., 1995). Previously defined formations are presented in Table 1.1 together with individual tephra members and ages, and an overview of relevant formations that are preserved in Mt. Ruapehu’s ring plain is shown in Fig. 1.3.

The tephrostratigraphic framework suggests that Mt. Ruapehu’s eruptive activity has not been uniform throughout time, neither regarding magnitude nor frequency. The eruptive period, which deposited the tephras of the Bullot Formation (~27,000 to 10,000 cal BP, Pardo et al., 2011), was characterised by large Plinian eruptions with eruption column heights of up to 37 km (Pardo et al., 2012). These eruptions involved magnitudes of VEI 4 to VEI 5 and represent the largest eruptions known from Mt. Ruapehu (Pardo et al., 2012). Deposits generally consist of fallout deposits containing pumice lapilli, and are sometimes interbedded with thin pyroclastic density current deposits (Pardo et al., 2011; Pardo, 2012; Pardo et al., 2012). Isopach and isopleth maps indicate Mt. Ruapehu’s North Crater as the main source (Pardo et al., 2012). Deposit volumes for the five largest eruptions (erupted between ~13.6 and ~10 ka BP) were estimated as at least 0.3 km^3 to 0.6 km^3 (Pardo et al., 2012).

The time span ranging from ~10,000 cal BP to the eruption of the Taupo Ignimbrite (AD 232, Lowe et al., 2013), is characterised by less voluminous activity from Mt. Ruapehu; this period is poorly constrained in terms of eruption style and distribution (Donoghue et al., 1995). The Papakai Formation contains several Mt. Ruapehu-sourced tephra members (Table 1.1, Fig. 1.3, Topping, 1973; Donoghue et al., 1995), whereas the Mangatawai Formation is considered to be mainly Ngauruhoe-sourced (Gregg, 1960; Topping, 1973; Donoghue et al., 1995) and consists of thinly bedded, grey to black ash layers, often containing leaves of the beech tree *Nothofagus sp.* (Topping, 1973; Moebis, 2010). However, studies on glass chemistry have shown that some of the ash layers are Mt. Ruapehu-sourced (Table 1.1, Fig. 1.3, Moebis, 2010; Moebis et al., 2011).

Table 1.1 (next page): Holocene tephrostratigraphy of the Tongariro and Tukino subgroups after Donoghue et al. (1995). Where available, calibrated ages are reported as cal BP. Selected rhyolitic stratigraphic markers from TVC and OVC are reported in italics. Sources are abbreviated as follows: R=Mt. Ruapehu, N=Mt. Ngauruhoe, TL=Tama Lakes, T=Mt. Tongariro. References for definition of tephra formations and tephra members with respective ages are: [1] Donoghue et al. (1995) [2] Donoghue et al. (1997) [3] Moebis (2010) [4] Lowe et al. (2013) [5] Topping (1974) [6] Pardo et al. (2011) [7] Topping (1973) [8] Heinrich et al. (2020).

Formation	Formation age	Tephra members	Ages	Source	Selected rhyolitic stratigraphic markers
Tongariro Subgroup					
Tufa Trig Formation (TTF) [2]	AD 232 to present [2], [4]	Tf19	AD 1995–1996 [2]	R	*Kaharoa Tephra (OVC, AD 1314±12) [4]*
		Tf18			
		Tf17			
		Tf16			
		Tf15			
		Tf14			
		Tf13			
		Tf12			
		Tf11			
		Tf10			
		Tf9			
		Tf8			
		Tf7			
		Tf6			
		Tf5	~650±50–830±60 yBP, [2])		
		Tf4			
		Tf3			
		Tf2	1338±45 cal BP, [3]		
		Tf1	1555±135 cal BP, [3]		
Ngauruhoe Tephra Formation (NF) [1], [3]		Unit A-G	AD 1954/1955, AD 1975 [3]	N	
		Nh 1-6	~980 cal BP–AD 1890 [3]		
Mangatawai Tephra Formation [3]	AD 232 to ~3500 cal BP [3], [4]	Mw 62	~1790 cal BP [3]	R	*Taupo Pumice (TVC, AD 232±10) [4]*
		Mw 61-9	~3694–2485 cal BP [3]	N	
		Mw 8-1	~3520–3470 cal BP [3]	R	
Papakai Tephra Formation [1]	~3500–11,000 cal BP [3]	Black ash-2	<4,510±20 yBP [1]	R	
		Black ash-1	>4,510±20 yBP [1]	R	
		Orange lapilli-2		R	
		Orange lapilli-1	<4830±20 yBP [1]	R	
Mangamate Formation [1]	11,165±31 to 11,410±190 cal BP [3]	Poutu Lapilli	~9700 yBP [7]	TL, N	*Hinemaiaia Tephra (Unit K, TVC ~5111±210 cal BP) [4]*
		Wharepu Lapilli			
		Ohinepango Lapilli	<9810±50 yBP [1]		
		Waihohonu Lapilli			
		Unnamed tephra			
		Oturere Lapilli			
		Te Rato Lapilli	9780±170 yBP [7]		
Pahoka Tephra [5],[1]	12,079±76 cal BP [3]			T	
Tukino Subgroup					
Bullot Formation [6]	27,097±957 to ~10,000 cal BP [6]			R	*Kawakawa/Oruanui (TVC 25,358±162 cal BP) [4]*

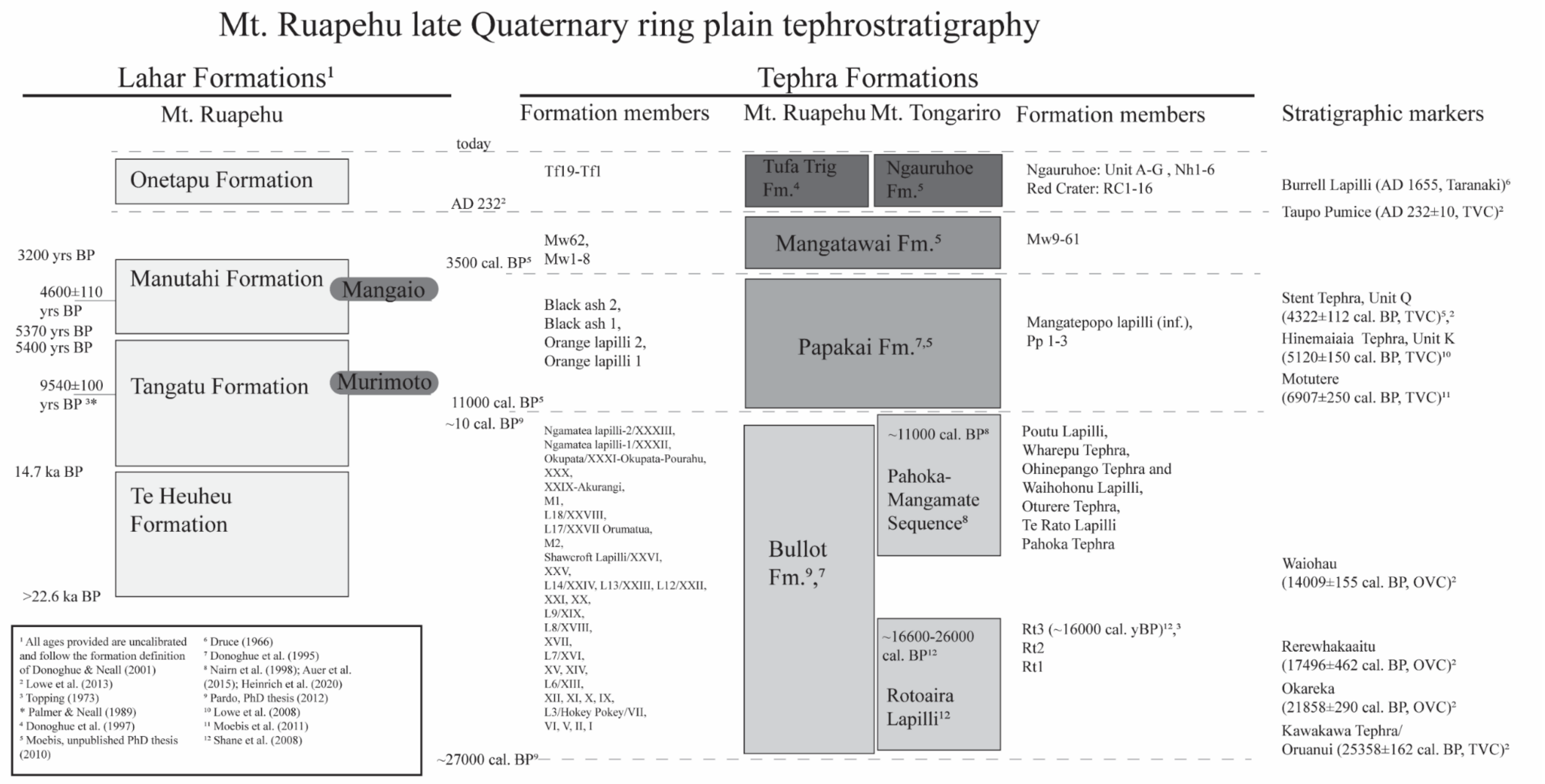

Fig. 1.3: Overview of the ring plain tephrostratigraphy involving lahar and tephra formations at Mt. Ruapehu for the past 27,000 years. For comparison, tephra formations from the adjacent Tongariro and Ngauruhoe volcanoes are reported as well. Rhyolitic stratigraphic markers from the northward Taupo Volcanic Centre (TVC) and the Okataina Volcanic Centre (OVC) are shown with respective age constraints.

1.3.3 The Tufa Trig Formation

The most recent Mt. Ruapehu-sourced tephra formation is the Tufa Trig Formation (TTF) and includes all deposits that overlie the AD 232 Taupo Pumice. It was firstly defined in Grange et al. (1929) and was named *Ngauruhoe ash* and included not only Mt. Ruapehu-sourced tephras but also tephras from Te Maari, Red Crater and Ngauruhoe (Topping, 1973, 1974). Later, Donoghue et al. (1995) grouped Mt. Ruapehu-sourced tephras within the newly defined Tufa Trig Formation (Donoghue et al., 1997), whereas Tongariro and Ngauruhoe sourced andesitic tephras remain grouped within the previous Ngauruhoe Formation (Table 1.1, Fig. 1.3).

The TTF appears as multiple discrete tephra layers deposited through fallout from an eruption plume. Individual tephra layers are interbedded with andisoils, aeolian Makahikatoa Sands or with the Ngauruhoe Formation (Donoghue et al., 1995). Makahikatoa Sands often contain reworked material, both from Taupo Pumice as well as from Mt. Ruapehu tephras (Purves, 1990; Donoghue et al., 1997). Seventeen tephra members (Tf2 to Tf18) were defined at the type location (T20/378045 in Donoghue et al., 1997). Until this date, the restricted thickness (mm to few cm, often pocketing) and lack of unique features of the individual tephra members hindered an unequivocal identification of individual members in different locations (Donoghue et al., 1995). However, some members were described as sufficiently thick to be correlated and/or to show particularly distinctive deposit features, such as members Tf1, Tf2, Tf5, Tf6, Tf8 and Tf14. Tf5 has been described as the most prominent and largest member of the TTF, showing relatively greater thicknesses and an extensive eastward dispersal. Volume calculations based on cumulative isopachs yield values of <0.1 km^3 for individual tephra members (Donoghue, 1991; Donoghue et al., 1995). Peat sampled above and beneath Tf5 in the Ngamatea Swamp (T21/413874 in Donoghue et al., 1995) provided a minimum age of 650 ± 50 years BP (Wk1488, Donoghue et al., 1995) and a maximum age of 830 ± 60 years BP (Wk1489, Donoghue et al., 1995).

Overall, tephra members are described as “coarse, black sandy ash and lapilli beds” (Donoghue et al., 1995) and contain juvenile clasts of varying vesicularity, few lithic clasts and some free pyroxenes and feldspars (Donoghue et al., 1997). Members Tf3 to Tf18 have been related to mainly phreatomagmatic eruptive mechanisms, as juvenile vitric clasts show a predominantly fine grain size (<2 mm), limited vesicularity and blocky morphology (Donoghue et al., 1997). Features such as conchoidal fractures and vesicles with adhering dust are commonly known to form during magma-water interaction (Wohletz, 1983b; e.g., Heiken et al., 1985) and have been identified among TTF glass shards. The first two members, Tf1 and Tf2, on the other hand, were described to be much coarser and to contain vesiculated pumice and scoria clasts, suggesting other eruption and fragmentation mechanisms, more similar to Strombolian eruptions (Wohletz, 1983b; Donoghue et al., 1997). The combination of Strombolian and phreatomagmatic eruptions leads to intervals of interbedded ash-sized tephra sequences, where weathering of individual layers has been slowed down due to frequent activity (Cole et al., 1986).

The 18 defined members of the Tufa Trig Formation, erupted since AD 232, suggest an eruption frequency of ~one eruption every 100 years (Hackett et al., 1989; Donoghue et al., 1997). It needs to be considered, however, that even the most dispersed eruptions (i.e., Tf5 and Tf8) account only for individual deposit volumes of <0.1 km^3 (Donoghue et al., 1997).

1.3.4 Historical record

Historical activity is sourced from the present-day vent, which is currently occupied by the Crater Lake. The presence of a crater lake influences the type of activity, being dominated by both small and frequent phreatic eruptions, as well as phreatomagmatic eruptions and Strombolian to subplinian eruptions following lake displacement (Scott, 2013). The most recent eruption took place in 2007 and consisted in a short-lived phreatomagmatic explosion which affected mostly the summit area (Kilgour et al., 2010). Less frequent but more prolonged magmatic eruptions occurred in 1945 (Oliver, 1945; Reed, 1945; Beck, 1950; Johnston et al., 1995), 1969 (Healy et al., 1978), 1971 (Latter, 1985) and 1995–1996 (Cronin et al., 1997a; Cronin et al., 1997c; Bryan et al., 1999; Nakagawa et al., 1999). A disappearance of the Crater Lake was observed only during the 1945 and the 1995–1996 episodes (Johnston et al., 1995; Cronin et al., 1997a; Scott, 2013). In total, 603 days of activity have been reported since 1830 and a detailed report on all documented eruptive events is presented in Scott (2013). Detailed descriptions of major eruption successions are summarised in Table 1.2.

Eruption frequency for the historical record is dependent on the observed events, with the 1945 and 1995–1996 episodes strongly influencing the overall frequency due to their high number of observations (Scott, 2013). The long-term eruption recurrence for events that are potentially large enough to affect areas outside the crater basin is 1.79 per year and 4 per year when taking in to account the whole dataset since 1830 and since 1940, respectively (Scott, 2013). Considering major episodes of sustained activity like 1945 and 1995–1996, eruption periodicity lies around ~ 20–30 years (Gamble et al., 1999). Additionally, more than 50 lahars were recorded in the Whangaehu Valley since AD 1861 (Graettinger et al., 2009).

Table 1.2: Overview of major eruptions in the historical record with details on eruption sequences and event magnitude.

Eruption	Description of eruptive sequence	Other comments
Mar–Dec 1945	Various small-moderate eruptions throughout March (Johnston, 1997). Lava dome in Crater Lake from Mar 19th (Reed, 1945). Eruption columns up to 2500 m high (Reed, 1945) during eruption on Mar 26th. Second larger dome from May (Oliver, 1945). Violent explosions on May14th (Scott, 2013). Major magmatic explosions through June, leading to wide ash dispersal (Johnston, 1997; Scott, 2013). Ash column of 6000 m during magmatic explosion on Jul 20th (Johnston, 1997). High ash columns and major activity throughout Aug, Sep and Oct with ash dispersal to Whakatane and Wellington (Johnston, 1997; Scott, 2013). Declining activity throughout Nov, last strong eruption reported on Dec 15th and smaller steam and ash eruptions continuing until Dec 31st (Johnston, 1997; Scott, 2013).	Overall erupted volume was estimated at ~0.1 km^3 (Johnston et al., 2000), but no deposits were associated to this eruption so far (Cole et al., 1986). Moebis (2010) suggests that Tf18 might correlate with the 1945 episode, but no proof has been provided yet.
22 Jun 1969	Major phreatomagmatic eruption, several lahars in the Whakapapanui, Whakapapa, Mangaturuturu and Whangaehu valleys, ash dispersal up to 25 km distance (Healy et al., 1978; Latter, 1985). Pyroclastic surge in summit area (Houghton et al., 1987).	
Apr–Nov 1971	Small phreatic eruptions in Apr, moderate phreatomagmatic eruption and Whangaehu lahar on May 8th (Latter, 1985). Numerous moderate eruptions and lahars (Scott, 2013) on May 16th. From May to Nov predominantly small phreatic events and sporadic phreatomagmatic eruptions, leading to small base surges and minor lahars (Scott, 2013).	
Apr 1975	Major phreatomagmatic eruption on Apr 24th, accompanied by several major lahars in Whakapapanui, Whakapapaiti, Mangaturuturu and Whangaehu valleys and ash 130 km from vent (Nairn et al., 1979; Latter, 1985). Upper flanks and summit area affected by pyroclastic surges (Houghton et al., 1987). Major phreatomagmatic eruption on Apr 27th with lahars in Whangaehu valley (Scott, 2013).	
2nd Nov 1977	Moderate phreatomagmatic eruption, accompanied by lahar in Whangaehu valley (Latter, 1985; Scott, 2013).	
7th Mar 1978	Moderate phreatic eruption, dispersing ash up to 2 km from vent (Latter, 1985)	
Jan 1995–Sep 1996	Numerous small phreatic eruptions throughout 1995, large phreatomagmatic eruption on Sep 18th, producing a lahar in the Whangaehu Valley (Cronin et al., 1997c; Scott, 2013). On Sep 23rd another major phreatomagmatic eruption produces an eruption column of 10 km (Cronin et al., 2003) and leads to lahars in the Whakapapanui, Mangaturuturu and Whangaehu valleys (Scott, 2013). Activity continues with phreatomagmatic eruptions and some smaller surtseyan type eruptions throughout Sep producing lahars and gradually expelling the water from Crater Lake (Bryan et al., 2003; Scott, 2013). A sustained magmatic eruption with a subplinian plume >10 km forms on Oct 11th, accompanied by voluminous ash emissions to the NE (~0.02 km^3, Nairn et al., 1996) which empty the Crater Lake (Bryan et al., 1999; Cronin et al., 2003). Between Sep 18th and Oct 11th, 26 lahars with a total volume of 10.2×10^6 m^3 were recorded at a distance of 56.5 km from source (Cronin et al., 1997c). Another subplinian magmatic event (>11 km plume, ~0.01 km^3) occurs on Oct 14th, leading to a lahar and ash fall 200 km SE of Crater Lake. During Oct, minor eruptions continue emitting ash and gas (Nairn et al., 1996; Scott, 2013). A second period of enhanced activity begins on 17th-18th Jun 1996with initial major phreatomagmatic eruptions and, with progressive Crater Lake emptying, Strombolian to subplinian eruptions (~10 km eruption plume, 0.04 km^3, Cronin et al., 2003; Bonadonna et al., 2005). Large magmatic eruption on Jun 27th (Bryan et al., 2003; Scott, 2013). During Jul and the first Aug week smaller, Strombolian eruptions distribute ash over large parts of the North Island, with large magmatic eruptions on Jul 4th , Jul 15th (7000 m plume), Jul 20th (plume 7500 m, fire fountaining) and Jul 27th (9700 m eruption plume, Bryan et al., 2003; Scott, 2013). Subsequent minor activity until Sep (Bryan et al., 2003; Scott, 2013).	Considered as Tf19, though no deposit has been associated yet (Donoghue et al., 1997). Total volume of all eruptions in 1995 and 1996 accounts for <0.1 km^3 (Johnston et al., 2000) Primary lahars accompanying the eruptive activity are eruption-related and influenced by the Crater Lake (Cronin et al., 1997c). Another type of lahar occurs when the Crater Lake is empty; they can be attributed to secondary remobilisation e.g., by rainfall (Cronin et al., 1997c; Hodgson et al., 1999).
25th Sep 2007	Moderate phreatomagmatic eruption without major precursors (Christenson et al., 2010; Scott, 2013). Northerly directed blast spread ballistics over an area of 2.5 km^2 (Christenson et al., 2010; Kilgour et al., 2010) and several lahars go down the Whangaehu and the Whakapapaiti side of the mountain (Lube et al., 2009; Christenson et al., 2010; Jolly et al., 2010; Kilgour et al., 2010). Ash deposition is restricted to the summit area and deposit volume is estimated to ~1×10^5 m^3 (Kilgour et al., 2010). Two small very-long period seismic signals (VLP) within 10 minutes were recorded before the eruption and were accompanied by some tremor and minor volcano-tectonic earthquakes (VT, Jolly et al., 2010).	Typical eruption with little or no warning, small volumes and local dispersal, making them only minor events in the geological record of a volcano (e.g., Barberi et al., 1992).

1.4 Existing models of Mt. Ruapehu’s magmatic system

Recent eruptions such as the 2007 event and the 1995–1996 eruptions have highlighted that volcanic activity at Mt. Ruapehu is preceded by only minor precursory activity (Bryan et al., 1999; Christenson et al., 2010; Jolly et al., 2010). This makes prediction and the management of volcanic crises very difficult and stresses the need for a better understanding of the magmatic system and potential eruption progression. Geochemical investigation of eruptive products can provide valuable insights into magma dynamics within the storage system, as well as information on processes during magma ascent. Numerous studies have constrained magma dynamics based on the older lava formations (Hackett, 1985; Cole et al., 1986; Graham et al., 1987; Hackett et al., 1989; Gamble et al., 1999; Gamble et al., 2003; Price et al., 2012), while there is little information on the late Holocene magmatic system following the switch from voluminous Plinian eruptions (Pardo et al., 2011; Pardo et al., 2012) to frequent, small volume phreatic and phreatomagmatic-magmatic eruptions (Donoghue et al., 1995; Donoghue et al., 1997). In contrast, various petrological studies were conducted on the 2007 eruption (Christenson et al., 2010; Kilgour et al., 2010), on the 1995–1996 episode (Nakagawa et al., 1999; Nakagawa et al., 2002; Kilgour et al., 2013), and on historic magmatic eruptions such as 1945, 1969, 1971, 1977 (Gamble et al., 1999; Kilgour et al., 2013; Kilgour et al., 2014) but studied samples consisted of predominantly proximal scoria and juvenile lava bombs. Similarly, there is no data available for historical eruptions older than 1945.

1.4.1 Geochemical characterisation of Mt. Ruapehu’s eruptive products

Mt. Ruapehu’s magmas are best described as arc-andesites, with water contents <2–3 wt% H_2O and <1000 ppm CO_2 (Kilgour et al., 2013; Kilgour et al., 2014). Groundmass glasses are andesitic to dacitic (Donoghue et al., 1997) and show systematic temporal variations in major elements for the major eruptive phases of historical magmatic eruptions (Gamble et al., 1999; Nakagawa et al., 1999) with respect to both whole rock compositions as well as matrix glass compositions (Kilgour et al., 2013). Major element geochemistry of historic eruptions shows the same variability as the entire geological record (Gamble et al., 1999).

Petrographic studies of lava bombs and scoria indicate a strongly porphyritic character with 30 to >40 vol% crystals (Nakagawa et al., 1999). The dominant phenocryst phases are plagioclases followed by clinopyroxene and orthopyroxene and rare Fe-Ti oxides (Donoghue et al., 1997; Gamble et al., 1999; Nakagawa et al., 1999). Plagioclases show often variable zoning patterns, mostly with Ca-rich cores and Na-rich rims, and are often oscillatory (Nakagawa et al., 2002). Pyroxenes contain melt inclusions and show various zoning and resorption patterns (Gamble et al., 1999; Nakagawa et al., 2002; Kilgour et al., 2013; Kilgour et al., 2014). Microlites are abundant and consist mostly in pyroxenes and plagioclases (Kilgour et al., 2014; Kilgour et al., 2016).

Isotope data on Sr, Nd and Pb span a wide compositional range for historical eruptions without clear systematic variations and rare earth element (REE) patterns are similar, showing a negative Eu anomaly, depletion of Nb and Ti, and enrichment in elements mobile in aqueous fluids (large ion lithophile elements, such as Cs, Rb, Ba, Pb) compared to less mobile elements (e.g., REE, Zr, Y, Hf) as typical for arc-related magmas (Gamble et al., 1999).

1.4.2 Characteristics of the shallow magma storage system

Several studies on the petrology and geochemistry of Mt. Ruapehu’s eruptive products were performed on lavas (Hackett, 1985; Hackett et al., 1989) or lava bombs and scoria (Gamble et al., 1999; Nakagawa et al., 1999) and suggest a complex magmatic system, located between ~2 to > 9 km depth (Kilgour et al., 2013). Here, short-term events of magma mixing and recharge (Price et al., 1997) overlap with long-term evolution involving assimilation of the surrounding Torlesse Terrane and fractional crystallisation (Graham et al., 1987; Gamble et al., 1999). Various authors suggest a complex open system, similar to a magma mush (Nakagawa et al., 1999; Nakagawa et al., 2002; Kilgour et al., 2013). However, historical magmas show no relationship to prehistoric magmas that can be explained by simple differentiation but rather involve the same magmatic source (Gamble et al., 1999). Periodic reinjections provide hotter (~1000–1200°C), fresh magma which leads to the destabilisation of the system and acts as the trigger for an eruption (Sparks et al., 1977). These injections generate small discrete, dike-like magma pockets within the mush (Gamble et al., 1999; Nakagawa et al., 1999), which can grow together and result in mixing and mingling (Gamble et al., 1999). In fact, melt inclusions in pyroxenes and plagioclases of historical eruptions indicate that most phenocrysts were incorporated from the mush and did not crystallise in equilibrium with the surrounding melt (Kilgour et al., 2013).

The nested mush system hinders the ascent of fresh magma, thus increasing the heat flow of the system and favouring local assimilation-fractional crystallisation (AFC) processes (Nakagawa et al., 1999). This accounts for differences in major element compositions between distinct magma batches and favours an unstable system, which could be triggered by e.g., the coalescence of magma pockets (Nakagawa et al., 2002). This model is consistent with the 1995–1996 eruption episode, where slightly different magma compositions were observed within the time span of weeks (Nakagawa et al., 1999) but were not always accompanied by major seismic signals, as e.g., volcanic earthquakes (Bryan et al., 1999). Nakagawa et al. (2002) suggest that while the October 1995 eruptions were indeed triggered by magma injection (preceded by volcanic earthquakes and tremor), the September 1995 eruptions can be ascribed to the conjunction of magma pockets or to a very small injection (tremor but no significant volcanic earthquakes).

1.4.3 Ascent characteristics

Processes affecting the magma during its ascent from the storage zone are poorly constrained for the Tufa Trig Formation, as well as for most of historical eruptions due to the lack of textural analyses. Several authors (Gamble et al., 1999; Kilgour et al., 2013) suggest an open or ductile conduit system based on the absence of major precursor seismic activity (Bryan et al., 1999). On the other hand, changes in the chemistry of Crater Lake were commonly observed after eruption, suggesting that some impermeable zone within the hydrothermal system inhibits fluid and gas flow (Kilgour et al., 2014). Zoning patterns in clinopyroxenes were used in combination with a multi-parameter monitor dataset (Sherburn et al., 1999; Christenson et al., 2010) to constrain timescales for magma ascent (Kilgour et al., 2014). Diffusion profiles of outer rims reveal perturbations of the magmatic system up to 7 months prior to eruption (Kilgour et al., 2014). In the case of the 2007 eruptions these perturbations could be related to deep seismic swarms (~8–18 km), observed 5–7 months in advance (Kilgour et al., 2014). Interaction of pyroxenes with the crystal mush appears to have increased within the last weeks before eruption (<12 days, Nakagawa et al., 2002) and continues in some cases syn-eruptively, suggesting fast magma ascent (Kilgour et al., 2016). Generally, ascent rates are strongly influenced by crystallisation and bubble growth. However, Mt. Ruapehu magmas are water poor, thus crystallisation is suppressed until water saturation is reached on magma ascent at ~50–100 MPa (Kilgour et al., 2016). Here, crystal growth greatly increases melt viscosity, impeding bubble growth and potentially forming a magma plug, resulting in an explosive eruption. Lower crystallisation rates on the other hand would favour Strombolian eruptions (Kilgour et al., 2016).

1.5 Mt. Ruapehu’s vent system

The current vent system is located in the southwestern part of the Summit Plateau and hosts two active vents (Hurst et al., 1991; Christenson et al., 2010; Kilgour et al., 2010), and is filled by a ~10 × 10^6 m^3 acidic Crater Lake at 2540 m asl. This vent system is thought to be active since ~11.6 ka cal BP, when the position of the active vent switched from the previous northern crater to the current vent (Pardo et al., 2012). Crater Lake presumably formed ~3000–2000 years ago as inferred from lahar distribution (Topping, 1974; Hackett et al., 1989; Palmer, 1991) and the character of tephra deposits (Donoghue et al., 1997). The lake-vent zone is characterised by a hydrothermal system up to 1 km below the lake floor, where a layer of liquid sulphur regulates the heat and gas flow from the underlying heat pipe (Hurst et al., 1991; Christenson et al., 1993; Hurst, 1998). Crater Lake temperatures vary cyclically between 10 to 60°C and changes in lake chemistry can be generally correlated to eruptions, although several eruptions have occurred through a cold Crater Lake (e.g., the 2007 eruption, Christenson et al., 1993; Christenson et al., 2010).

1.5.1 Eruption styles

The signature of Mt. Ruapehu’s frequent, small volume explosive eruptions is related to low volatile content (Kilgour et al., 2013) and to late, shallow crystallisation, explaining the high explosivity and the short duration (Kilgour et al., 2016). The eruption style is strongly influenced by the current vent system (Hackett et al., 1989; Donoghue et al., 1997) and the presence of a hydrothermal system, resulting in phreatomagmatic and phreatic eruptions through Crater Lake (CL) and activity described as “Strombolian” when CL is emptied (Donoghue et al., 1997; Gamble et al., 1999; Cronin et al., 2003). Sustained magmatic eruptions during the 1995–1996 event resulted in continuous eruption plumes, up to 12 km high that were classified as “subplinian” (Cronin et al., 2003). Historic eruptions show similar volatile contents independent of eruption magnitude, suggesting that factors other than volatiles must be considered to explain the variation in magma volumes and eruption style between individual eruptions (Kilgour et al., 2013).

1.6 Volcanic hazards

Volcanic eruptions are considered among the most dangerous, potentially lethal, natural hazards on Earth and can severely impact life, infrastructure and the economy (e.g. Auker et al., 2013; Wilson et al., 2014). The hazard posed by a specific volcano depends mainly on the volcano type, its location and the recurrence time of eruptions. However, the risk an area is subjected to is a combination of the volcano-specific hazards, their intensity and the vulnerability and exposure of the area (Blong, 2000). Different volcanic hazards are traditionally investigated individually. This results in individual hazard assessments for each volcanic hazard, which can then inform event trees (Newhall et al., 2002; Sandri et al., 2014) or be used to create specific hazard maps (Cioni et al., 2003; Orsi et al., 2004). In reality, however, a volcanic eruption can result in a combination of various, often linked or simultaneous, volcanic processes and thus should be described by a model that accounts for the dynamic evolution during the eruption, resulting in a series of inter-related multiple hazards.

1.6.1 Volcanic hazards at Mt. Ruapehu

Mt. Ruapehu, being part of the Tongariro National Park, is a popular destination for hikers and climbers during the summer months. During winter months the three ski fields on the upper flanks can host thousands of skiers per day. The closest inhabited centres are Ohakune, Whakapapa Village, National Park Village as well as the military base

Waiouru. The ring plain hosts the country's major electricity transmission line, as well as the principal national road (State Highway 1, 15 km from Crater Lake) and the main Auckland-Wellington train route. Major volcanic hazards as inferred from Holocene and historical activity at Mt. Ruapehu are summarised in Table 1.3.

Table 1.3: Summary of volcanic hazards at Mt. Ruapehu, as inferred from eruptive activity during the past 27,000 years.

Hazard	Description
Ballistic ejecta (>64 mm)	Large to small blocks in summit region, associated with all eruption styles, typical for phreatic and phreatomagmatic eruptions, as e.g., during 2007 eruption (Christenson et al., 2010; Kilgour et al., 2010)
Tephra fall (here referring to lapilli and ash-sized particles <64 mm)	Dispersal and area affected depends on eruption style (limited in case of phreatic eruptions, dispersed for dry magmatic eruptions), magnitude and main wind direction (up to 300 km on 17th June 1996, Cronin et al., 2003). Highly abrasive. Ash thickness (uncompacted) determines the impacts, ranging from nuisance to respiratory, minor damage to infrastructure or water contamination to roof collapses, loading/breakage of power and communication lines, severe damage and death of aquatic life, livestock, and vegetation.
Pyroclastic flows and surges	Pyroclastic flows are known to be associated with the unsteady and oscillating eruption columns of the Bullot Formation (Neall et al., 1999; Pardo et al., 2011; Pardo et al., 2014b; Cowlyn, 2016). Similarly, modelling by Degruyter et al. (2013) suggests that during the 17th June 1996 eruption conditions for column collapse were reached theoretically but that the plume was kept buoyant by strong winds. However, studies on PDCs are strongly limited by the preservation potential of the related deposits (Hackett et al., 1989) and are scarce for the late Holocene (Gillies et al., 2020). Small scale fully dilute pyroclastic surges are typically associated with phreatic and phreatomagmatic eruptions (Moore, 1967; Scott, 2013) and were observed historically, i.e., during the 2007 eruption (Kilgour et al., 2010). Dispersal would be rather limited (< 3 km, Houghton et al., 1987) and strongly influenced by topography.
Lava flows and dome extrusion	During the Holocene, lava flows occurred from summit and flank vents; their distribution would be limited to topographic valleys (Neall et al., 1999). Lava flows played a subordinate role during the late Holocene. The most recent known lava flow is dated at 0.2 ka ± 2.2 ka (Conway, 2016) and is thought to represent the effusive complementary part of the Tufa Trig Formation but the stratigraphic relationship to specific tephra members remains unknown. No lava flows are documented during historical times Lava dome (or tholoid) emplacement has been observed throughout the 1945 episode as well as in 1996 and possibly in 1861 (Neall et al., 1999). No deposits were found, suggesting similar events might be underestimated in the eruptive record due to low preservation potential (Hackett et al., 1989).
Lahars	Major hazard at Mt. Ruapehu and characteristic of late Holocene activity. The most recent Onetapu Formation (post-Taupo, Fig. 1.3) involves at least 17 events in the Whangaehu River, of which 4 are historical (Hodgson et al., 2007). Lahars can be eruption-related (syn-eruptive or post-eruption tephra remobilisation, Cronin et al., 1997b; Hodgson et al., 1999) but can also be non-eruptive, due to i.e., partial collapses of the cone (e.g., 18 March 2007 lahar). They are very erosive, very fast (9 m/s in 1995, Cronin et al., 1997c), and follow valleys and river streams. Lahars pose the greatest risk to human life on ski fields and due to damage of bridges (e.g. Tangiwai disaster, 1953). They have the potential to overtop riverbanks, leading to damages of vehicles, crops, buildings. Lahars accompany nearly every eruptive event (Houghton et al., 1987; Scott, 2013).
Cone collapse and debris avalanche	A major sector collapse, ascribed to a gravitational collapse, occurred on the NW flank of the volcano, leading to the Murimoto Formation 9500 years ago (Topping, 1973; Palmer et al., 1989). A second debris avalanche 4600 years ago is described in the Whangaehu Catchment (Fig. 1.3, Mangaio Formation, Donoghue, 1991; Donoghue et al., 2001).

References

Annen, C., Blundy, J. D., & Sparks, R. S. J. (2005). The Genesis of Intermediate and Silicic Magmas in Deep Crustal Hot Zones. *Journal of Petrology, 47*(3), 505-539. doi:https://doi.org/10.1093/petrology/egi084

Arrighi, S., Principe, C., & Rosi, M. (2001). Violent strombolian and subplinian eruptions at Vesuvius during post-1631 activity. *Bulletin of Volcanology, 63*(2), 126-150. doi:https://doi.org/10.1007/s004450100130

Auer, A., Martin, C. E., Palin, J. M., White, J. D. L., Nakagawa, M., & Stirling, C. (2015). The evolution of hydrous magmas in the Tongariro Volcanic Centre: the 10 ka Pahoka-Mangamate eruptions. New Zealand Journal of Geology and Geophysics, 58(4), 364-384. doi:10.1080/00288306.2015.1089913

Auker, M. R., Sparks, R. S. J., Siebert, L., Crosweller, H. S., & Ewert, J. (2013). A statistical analysis of the global historical volcanic fatalities record. Journal of Applied Volcanology, 2(1), 2.

Barberi, F., Bizouard, H., Clocchiatti, R., Metrich, N., Santacroce, R., & Sbrana, A. (1981). The Somma-Vesuvius Magma Chamber: a Petrological and Volcanological Approach. *Bulletin volcanologique, 44*(3), 295-315. doi:https://doi.org/10.1007/bf02600566

Barberi, F., Bertagnini, A., Landi, P., & Principe, C. (1992). A review on phreatic eruptions and their precursors. *Journal of Volcanology and Geothermal Research, 52*(4), 231-246. doi:https://doi.org/10.1016/0377-0273(92)90046-G

Beavan, J., & Haines, J. (2001). Contemporary horizontal velocity and strain rate fields of the Pacific-Australian plate boundary zone through New Zealand. *Journal of Geophysical Research: Solid Earth, 106*(B1), 741-770. doi:https://doi.org/10.1029/2000jb900302

Beck, A. (1950). Volcanic activity at Mt. Ruapehu from August to December, 1945. *New Zealand Journal of Science and Technology, 31*, 1-13.

Bertagnini, A., Di Roberto, A., & Pompilio, M. (2011). Paroxysmal activity at Stromboli: lessons from the past. Bulletin of Volcanology, 73(9), 1229-1243. doi:10.1007/s00445-011-0470-3

Bibby, H. M., Caldwell, T. G., Davey, F. J., & Webb, T. H. (1995). Geophysical evidence on the structure of the Taupo Volcanic Zone and its hydrothermal circulation. *Journal of Volcanology and Geothermal Research, 68*(1), 29-58. doi:https://doi.org/10.1016/0377-0273(95)00007-H

Blong, R. (2000). Volcanic Hazards and Risk Management In H. Sigurdsson, B. Houghton, S. R. McNutt, H. Rymer, & J. Stix (Eds.), *Encyclopedia of volcanoes* (pp. 1215-1227).

Bonadonna, C., Phillips, J. C., & Houghton, B. F. (2005). Modeling tephra sedimentation from a Ruapehu weak plume eruption. *Journal of Geophysical Research, 110*(B08209). doi:https://doi.org/10.1029/2004jb003515

Bonadonna, C., & Costa, A. (2013b). Plume height, volume, and classification of explosive volcanic eruptions based on the Weibull function. *Bulletin of Volcanology, 75*(8), 742. doi:https://doi.org/10.1007/s00445-013-0742-1

Bonadonna, C., Cioni, R., Costa, A., Druitt, T., Phillips, J., Pioli, L., Andronico, D., Harris, A., Scollo, S., Bachmann, O., Bagheri, G., Biass, S., Brogi, F., Cashman, K., Dominguez, L., Dürig, T., Galland, O., Giordano, G., Gudmundsson, M., Hort, M., Höskuldsson, A., Houghton, B., Komorowski, J. C., Küppers, U., Lacanna, G., Le Pennec, J. L., Macedonio, G., Manga, M., Manzella, I., Vitturi, M. d. M., Neri, A., Pistolesi, M., Polacci, M., Ripepe, M., Rossi, E., Scheu, B., Sulpizio, R., Tripoli, B., Valade, S., Valentine, G., Vidal, C., & Wallenstein, N. (2016). MeMoVolc report on classification and dynamics of volcanic explosive eruptions. Bulletin of Volcanology, 78(11), 84. doi:10.1007/s00445-016-1071-y

Bryan, C. J., & Sherburn, S. (1999). Seismicity associated with the 1995–1996 eruptions of Ruapehu volcano, New Zealand: narrative and insights into physical processes. *Journal of Volcanology and Geothermal Research, 90*(1–2), 1-18. doi:https://doi.org/10.1016/S0377-0273(99)00016-5

Bryan, C. J., & Sherburn, S. (2003). Eruption-induced modifications to volcanic seismicity at Ruapehu, New Zealand, and its implications for eruption forecasting. *Bulletin of Volcanology, 65*(1), 30-42. doi:https://doi.org/10.1007/s00445-002-0236-z

Burton, M., Allard, P., Muré, F., & La Spina, A. (2007). Magmatic gas composition reveals the source depth of slug-driven Strombolian explosive activity. *Science, 317*(5835), 227-230. doi:https://doi.org/10.1126/science.1141900

Carey, S., & Sigurdsson, H. (1986). The 1982 eruptions of El Chichon volcano, Mexico (2): Observations and numerical modelling of tephra-fall distribution. *Bulletin of Volcanology, 48*(2), 127-141. doi:https://doi.org/10.1007/BF01046547

Cas, R. A. F., & Wright, J. V. (1987). *Volcanic successions: modern and ancient: a geological approach to processes, products and successions*. London: Allen & Unwin/Chapman & Hall.

Cashman, K. V. (2004). Volatile Controls on Magma Ascent and Eruption. In R. S. J. Sparks & C. Hawkesworth (Eds.), *The State of the Planet: Frontiers and Challenges in Geophysics* (pp. 109-124): American Geophysical Union.

Cashman, K. V., & Scheu, B. (2015). Magmatic fragmentation. In H. Sigurdsson (Ed.), *The Encyclopedia of Volcanoes (Second Edition)* (pp. 459-471). Amsterdam: Academic Press.

Christenson, B. W., & Wood, C. P. (1993). Evolution of a vent-hosted hydrothermal system beneath Ruapehu Crater Lake, New Zealand. *Bulletin of Volcanology, 55*(8), 547-565. doi:https://doi.org/10.1007/bf00301808

Christenson, B. W., Reyes, A. G., Young, R., Moebis, A., Sherburn, S., Cole-Baker, J., & Britten, K. (2010). Cyclic processes and factors leading to phreatic eruption events: Insights from the 25 September 2007 eruption through Ruapehu Crater Lake, New Zealand. *Journal of Volcanology and Geothermal Research, 191*(1–2), 15-32. doi:http://dx.doi.org/10.1016/j.jvolgeores.2010.01.008

Cioni, R., Longo, A., Macedonio, G., Santacroce, R., Sbrana, A., Sulpizio, R., & Andronico, D. (2003). Assessing pyroclastic fall hazard through field data and numerical simulations: Example from Vesuvius. *Journal of Geophysical Research: Solid Earth, 108*(B2). doi:https://doi.org/10.1029/2001JB000642

Cioni, R., Bertagnini, A., Santacroce, R., & Andronico, D. (2008a). Explosive activity and eruption scenarios at Somma-Vesuvius (Italy): Towards a new classification scheme. *Journal of Volcanology and Geothermal Research, 178*(3), 331-346. doi:https://doi.org/10.1016/j.jvolgeores.2008.04.024

Cioni, R., D'Oriano, C., & Bertagnini, A. (2008b). Fingerprinting ash deposits of small scale eruptions by their physical and textural features. *Journal of Volcanology and Geothermal Research, 177*(1), 277-287. doi:https://doi.org/10.1016/j.jvolgeores.2008.06.003

Cioni, R., Pistolesi, M., Bertagnini, A., Bonadonna, C., Hoskuldsson, A., & Scateni, B. (2014). Insights into the dynamics and evolution of the 2010 Eyjafjallajökull summit eruption (Iceland) provided by volcanic ash textures. *Earth and Planetary Science Letters, 394*, 111-123. doi:https://doi.org/10.1016/j.epsl.2014.02.051

Cioni, R., Pistolesi, M., & Rosi, M. (2015). Plinian and subplinian eruptions The Encyclopedia of Volcanoes (pp. 519-535): Elsevier.

Civetta, L., Galati, R., & Santacroce, R. (1991). Magma mixing and convective compositional layering within the Vesuvius magma chamber. *Bulletin of Volcanology, 53*(4), 287-300. doi:https://doi.org/10.1007/BF00414525

Clarke, A. B., Ongaro, T. E., & Belousov, A. (2015). Vulcanian eruptions The Encyclopedia of Volcanoes (pp. 505-518): Elsevier.

Cole, J., Graham, I., Hackett, W., & Houghton, B. (1986). Volcanology and petrology of the Quaternary composite volcanoes of Tongariro volcanic centre, Taupo volcanic zone *Late Cenozoic Volcanism in New Zealand* (Vol. 23, pp. 224-250): Royal Society of New Zealand Bulletin.

Conway, C. E., Leonard, G. S., Townsend, D. B., Calvert, A. T., Wilson, C. J. N., Gamble, J. A., & Eaves, S. R. (2016). A high-resolution 40Ar/39Ar lava chronology and edifice construction history for Ruapehu volcano, New Zealand. *Journal of Volcanology and Geothermal Research, 327*, 152-179. doi:https://doi.org/10.1016/j.jvolgeores.2016.07.006

Conway, C. E., Gamble, J. A., Wilson, C. J., Leonard, G. S., Townsend, D. B., & Calvert, A. T. (2018). New petrological, geochemical, and geochronological perspectives on andesite-dacite magma genesis at Ruapehu volcano, New Zealand. *American Mineralogist: Journal of Earth and Planetary Materials, 103*(4), 565-581. doi:ttps://doi.org/10.2138/am-2018-6199

Cowlyn, J. D. (2016). *Pyroclastic density currents at Ruapehu volcano; New Zealand.* (Doctor of Philosophy), University of Canterbury.

Cronin, S. J., Hedley, M. J., Smith, R. G., & Neall, V. E. (1997a). Impact of Ruapehu ash fall on soil and pasture nutrient status 1. October 1995 eruptions. *New Zealand Journal of Agricultural Research, 40*(3), 383-395. doi:https://doi.org/10.1080/00288233.1997.9513260

Cronin, S. J., Hodgson, K. A., Neall, V. E., Palmer, A. S., & Lecointre, J. A. (1997b). 1995 Ruapehu lahars in relation to the late Holocene lahars of Whangaehu River, New Zealand. *New Zealand Journal of Geology and Geophysics, 40*(4), 507-520. doi:https://doi.org/10.1080/00288306.1997.9514780

Cronin, S. J., Neall, V. E., Lecointre, J. A., & Palmer, A. S. (1997c). Changes in Whangaehu river lahar characteristics during the 1995 eruption sequence, Ruapehu volcano, New Zealand. *Journal of*

Volcanology and Geothermal Research, 76(1), 47-61. doi:https://doi.org/10.1016/S0377-0273(96)00064-9

Cronin, S. J., Neall, V. E., Lecointre, J. A., Hedley, M. J., & Loganathan, P. (2003). Environmental hazards of fluoride in volcanic ash: a case study from Ruapehu volcano, New Zealand. *Journal of Volcanology and Geothermal Research, 121*, 271-291. doi:https://doi.org/10.1016/S0377-0273(02)00465-1

Degruyter, W., & Bonadonna, C. (2013). Impact of wind on the condition for column collapse of volcanic plumes. *Earth and Planetary Science Letters, 377*, 218-226. doi:https://doi.org/10.1016/j.epsl.2013.06.041

D'Oriano, C., Bertagnini, A., & Pompilio, M. (2011). Ash erupted during normal activity at Stromboli (Aeolian Islands, Italy) raises questions on how the feeding system works. Bulletin of Volcanology, 73(5), 471-477. doi:10.1007/s00445-010-0425-0

Donoghue, S. L. (1991). *Late Quaternary Volcanic Stratigraphy of the Southeastern Sector of the Mount Ruapehu Ring Plain New Zealand.* (Doctor of Philosophy), Massey University.

Donoghue, S. L., Neall, V. E., & Palmer, A. S. (1995). Stratigraphy and chronology of late Quaternary andesitic tephra deposits, Tongariro Volcanic Centre, New Zealand. *Journal of the Royal Society of New Zealand, 25*(2), 115-206. doi:https://doi.org/10.1080/03014223.1995.9517487

Donoghue, S. L., Neall, V. E., Palmer, A. S., & Stewart, R. B. (1997). The volcanic history of Ruapehu during the past 2 millenia based on the record of Tufa Trig tephras. *Bulletin of Volcanology, 59*, 136-146. doi:https://doi.org/10.1007/s004450050181

Donoghue, S. L., & Neall, V. E. (2001). Late Quaternary constructional history of the southeastern Ruapehu ring plain, New Zealand. *New Zealand Journal of Geology and Geophysics, 44*(3), 439-466. doi:https://doi.org/10.1080/00288306.2001.9514949

Druce, A. (1966). Tree-ring dating of recent volcanic ash and lapilli, Mt Egmont. New Zealand journal of botany, 4(1), 3-41.

Fisher, R., & Schmincke, H. (1984). *Pyroclastic rocks*.

Francis, P., Glaze, L., Pieri, D., Oppenheimer, C., & Rothery, D. (1990). Eruption terms. Nature, 346(6284), 519-519.

Freundt, A., & Rosi, M. (1998). *From magma to tephra: modelling physical processes of explosive volcanic eruptions*: Elsevier.

Gamble, J. A., Wood, C. P., Price, R. C., Smith, I. E. M., Stewart, R. B., & Waight, T. (1999). A fifty year perspective of magmatic evolution on Ruapehu Volcano, New Zealand: verification of open system behaviour in an arc volcano. *Earth and Planetary Science Letters, 170*, 301-314. doi:https://doi.org/10.1016/S0012-821X(99)00106-5

Gamble, J. A., Price, R. C., Smith, I. E. M., McIntosh, W. C., & Dunbar, N. W. (2003). ^{40}Ar/^{39}Ar geochronology of magmatic activity, magma flux and hazards at Ruapehu volcano, Taupo Volcanic Zone, New Zealand. *Journal of Volcanology and Geothermal Research, 120*, 271-287. doi:https://doi.org/10.1016/S0377-0273(02)00407-9

Giachetti, T., Druitt, T. H., Burgisser, A., Arbaret, L., & Galven, C. (2010). Bubble nucleation, growth and coalescence during the 1997 Vulcanian explosions of Soufrière Hills Volcano, Montserrat. Journal of Volcanology and Geothermal Research, 193(3), 215-231. doi:https://doi.org/10.1016/j.jvolgeores.2010.04.001

Gillies, J., Kennedy, B., Gravley, D., Leonard, G., & Cowlyn, J. (2020). Identifying Pyroclastic Density Currents From Partial Outcrop Exposure on Mt. Ruapehu, New Zealand. Frontiers in Earth Science, 8(402). doi:10.3389/feart.2020.542932

Graettinger, A. H., Manville, V., & Briggs, R. M. (2009). Depositional record of historic lahars in the upper Whangaehu Valley, Mt. Ruapehu, New Zealand: implications for trigger mechanisms, flow dynamics and lahar hazards. *Bulletin of Volcanology, 72*(3), 279-296. doi:https://doi.org/10.1007/s00445-009-0318-2

Graham, I. J., & Hackett, W. R. (1987). Petrology of Calc-alkaline Lavas from Ruapehu Volcano and Related Vents, Taupo Volcanic Zone, New Zealand. *Journal of Petrology, 28*(3), 531-567. doi:https://doi.org/10.1093/petrology/28.3.531

Graham, I. J. (2008). *A continent on the move: New Zealand geoscience into the 21st century*: Geological Society of New Zealand.

Grange, L. I., & Hurst, J. A. (1929). Tongariro Subdivision. *New Zealand Geological Survey 23rd Annual Report*, 5-8.

Gregg, D. R. (1960). *The geology of Tongariro Subdivision* (Vol. 40).

Grindley, G. (1960). Sheet 8 Taupo-Geological Map of New Zealand 1: 250,000. *Department of Scientific and Industrial Research, Wellington, New Zealand*.

Hackett, W. R. (1985). *Geology and petrology of Ruapehu volcano and related vents.* (Doctor of Philosophy), Victoria University of Wellington.

Hackett, W. R., & Houghton, B. F. (1989). A facies model for a quaternary andesitic composite volcano: Ruapehu, New Zealand. *Bulletin of Volcanology, 51*(1), 51-68. doi:https://doi.org/10.1007/bf01086761

Head, J. W., & Wilson, L. (1987). Lava fountain heights at Pu'u'O'o, Kilauea, Hawaii: Indicators of amount and variations of exsolved magma volatiles. *Journal of Geophysical Research: Solid Earth, 92*(B13), 13715-13719. doi:https://doi.org/10.1029/JB092iB13p13715

Healy, J., Lloyd, E., Rishworth, D., Wood, C., Glover, R., & Dibble, R. (1978). The eruption of Ruapehu on 22 June 1969. *DSIR Bulletin, 217*.

Heiken, G., & Wohletz, K. (1985). *Volcanic Ash* Univ. of Calif. Press, Berkeley.

Heinrich, M., Cronin, S. J., & Pardo, N. (2020). Understanding multi-vent Plinian eruptions at Mt. Tongariro Volcanic Complex, New Zealand. *Bulletin of Volcanology, 82*(3), 30. doi:https://doi.org/10.1007/s00445-020-1369-7

Hodgson, K. A. (1993). *Late Quaternary Lahars from Mount Ruapehu in the Whangaehu River Valley, North Island, New Zealand.* (Doctor of Philosophy), Massey University.

Hodgson, K. A., & Manville, V. R. (1999). Sedimentology and flow behavior of a rain-triggered lahar, Mangatoetoenui Stream, Ruapehu volcano, New Zealand. *GSA Bulletin, 111*(5), 743-754. doi:http://dx.doi.org/10.1130/0016-7606(1999)111<0743:SAFBOA>2.3.CO;2

Hodgson, K. A., Lecointre, J. A., & Neall, V. E. (2007). Onetapu Formation: The last 2000 yr of laharic activity at Ruapehu volcano, New Zealand. *New Zealand Journal of Geology and Geophysics, 50*(2), 81-99. doi:https://doi.org/10.1080/00288300709509823

Holasek, R. E., Self, S., & Woods, A. W. (1996). Satellite observations and interpretation of the 1991 Mount Pinatubo eruption plumes. *Journal of Geophysical Research: Solid Earth, 101*(B12), 27635-27655. doi:https://doi.org/10.1029/96JB01179

Houghton, B. F., Latter, J. H., & Hackett, W. R. (1987). Volcanic hazard assessment for Ruapehu composite volcano, Taupo Volcanic Zone, New Zealand. *Bulletin of Volcanology, 49*(6), 737-751. doi:http://dx.doi.org/10.1007/BF01079825

Houghton, B. F., Wilson, C. J. N., McWilliams, M. O., Lanphere, M. A., Weaver, S. D., Briggs, R. M., & Pringle, M. S. (1995). Chronology and dynamics of a large silicic magmatic system: Central Taupo Volcanic Zone, New Zealand. *Geology, 23*(1), 13-16. doi:https://doi.org/10.1130/0091-7613(1995)023<0013:cadoal>2.3.co;2

Houghton, B. F., & Gonnermann, H. M. (2008). Basaltic explosive volcanism: Constraints from deposits and models. Geochemistry, 68(2), 117-140. doi:https://doi.org/10.1016/j.chemer.2008.04.002

Houghton, B., & Carey, R. J. (2015). Pyroclastic fall deposits The Encyclopedia of Volcanoes (pp. 599-616): Elsevier.

Houghton, B. F., White, J. D. L., & Van Eaton, A. R. (2015). Phreatomagmatic and related eruption styles. In H. Sigurdsson (Ed.), *The Encyclopedia of Volcanoes (Second Edition)* (pp. 537-552). Amsterdam: Academic Press.

Hurst, A. W., Bibby, H. M., Scott, B. J., & McGuinness, M. J. (1991). The heat source of Ruapehu crater lake; deductions from the energy and mass balances. *Journal of Volcanology and Geothermal Research, 46*(1), 1-20. doi:http://dx.doi.org/10.1016/0377-0273(91)90072-8

Hurst, A. W. (1998). Shallow seismicity beneath Ruapehu Crater Lake: results of a 1994 seismometer deployment. *Bulletin of Volcanology, 60*(1), 1-9. doi:https://doi.org/10.1007/s004450050212

Jenkins, S. F., Magill, C. R., & McAneney, K. J. (2007). Multi-stage volcanic events: A statistical investigation. *Journal of Volcanology and Geothermal Research, 161*(4), 275-288. doi:https://doi.org/10.1016/j.jvolgeores.2006.12.005

Johnston, D. M. (1997). *Physical and social impacts of past and future volcanic eruptions in New Zealand.* (Doctor of Philosophy), Massey University, Palmerston North.

Johnston, D. M., & Neall, V. E. (1995). *Ruapehu Awakens: the 1945 eruption of Ruapehu*. Palmerston North, New Zealand: Science Centre and Manawatu Museum Scientific Monograph No. 1.

Johnston, D. M., Houghton, B. F., Neall, V. E., Ronan, K. R., & Paton, D. (2000). Impacts of the 1945 and 1995-1996 Ruapehu eruptions, New Zealand: An example of increasing societal vulnerability. *Geological Society of America Bulletin, 112*(5), 720-726. doi:https://doi.org/10.1130/0016-7606(2000)112<720:IOTARE>2.0.CO;2

Jolly, A. D., Sherburn, S., Jousset, P., & Kilgour, G. (2010). Eruption source processes derived from seismic and acoustic observations of the 25 September 2007 Ruapehu eruption—North Island, New Zealand. *Journal of Volcanology and Geothermal Research, 191*(1–2), 33-45. doi:https://doi.org/10.1016/j.jvolgeores.2010.01.009

Kennedy, B., Spieler, O., Scheu, B., Kueppers, U., Taddeucci, J., & Dingwell, D. B. (2005). Conduit implosion during Vulcanian eruptions. Geology, 33(7), 581-584. doi:10.1130/g21488.1

Kilgour, G., Manville, V., Pasqua, F. D., Graettinger, A., Hodgson, K. A., & Jolly, G. E. (2010). The 25 September 2007 eruption of Mount Ruapehu, New Zealand: Directed ballistics, surtseyan jets, and ice-slurry lahars. *Journal of Volcanology and Geothermal Research, 191*(1–2), 1-14. doi:http://dx.doi.org/10.1016/j.jvolgeores.2009.10.015

Kilgour, G., Blundy, J., Cashman, K., & Mader, H. M. (2013). Small volume andesite magmas and melt–mush interactions at Ruapehu, New Zealand: evidence from melt inclusions. *Contributions to Mineralogy and Petrology, 166*(2), 371-392. doi:https://doi.org/10.1007/s00410-013-0880-7

Kilgour, G., Saunders, K., Blundy, J., Cashman, K., Scott, B., & Miller, C. (2014). Timescales of magmatic processes at Ruapehu volcano from diffusion chronometry and their comparison to monitoring data. *Journal of Volcanology and Geothermal Research, 288*, 62-75. doi:https://doi.org/10.1016/j.jvolgeores.2014.09.010

Kilgour, G., Mader, H., Blundy, J., & Brooker, R. (2016). Rheological controls on the eruption potential and style of an andesite volcano: A case study from Mt. Ruapehu, New Zealand. *Journal of Volcanology and Geothermal Research, 327*, 273-287. doi:https://doi.org/10.1016/j.jvolgeores.2016.08.001

Kokelaar, B. (1983). The mechanism of Surtseyan volcanism. *Journal of the Geological Society, 140*(6), 939-944. doi:https://doi.org/10.1144/gsjgs.140.6.0939

Latter, J. (1985). Frequency of eruptions at New Zealand volcanoes. *Bulletin of the NZ National Society for Earthquake Engineering, 18*(1).

Leonard, G. S., Cole, J. W., Nairn, I. A., & Self, S. (2002). Basalt triggering of the c. AD 1305 Kaharoa rhyolite eruption, Tarawera Volcanic Complex, New Zealand. *Journal of Volcanology and Geothermal Research, 115*(3–4), 461-486. doi:https://doi.org/10.1016/S0377-0273(01)00326-2

Lowe, D. J., Shane, P. A. R., Alloway, B. V., & Newnham, R. M. (2008). Fingerprints and age models for widespread New Zealand tephra marker beds erupted since 30,000 years ago: a framework for NZ-INTIMATE. Quaternary Science Reviews, 27(1), 95-126. doi:https://doi.org/10.1016/j.quascirev.2007.01.013

Lowe, D. J., Blaauw, M., Hogg, A. G., & Newnham, R. M. (2013). Ages of 24 widespread tephras erupted since 30,000 years ago in New Zealand, with re-evaluation of the timing and palaeoclimatic implications of the Lateglacial cool episode recorded at Kaipo bog. *Quaternary Science Reviews, 74*, 170-194. doi:https://doi.org/10.1016/j.quascirev.2012.11.022

Lube, G., Cronin, S. J., & Procter, J. N. (2009). Explaining the extreme mobility of volcanic ice-slurry flows, Ruapehu volcano, New Zealand. *Geology, 37*(1), 15-18. doi:https://doi.org/10.1130/g25352a.1

Maeno, F., Nakada, S., Oikawa, T., Yoshimoto, M., Komori, J., Ishizuka, Y., Takeshita, Y., Shimano, T., Kaneko, T., & Nagai, M. (2016). Reconstruction of a phreatic eruption on 27 September 2014 at Ontake volcano, central Japan, based on proximal pyroclastic density current and fallout deposits. *Earth, Planets and Space, 68*(1), 82. doi:https://doi.org/10.1186/s40623-016-0449-6

Marsh, B. D. (1996). Solidification fronts and magmatic evolution. *Mineralogical Magazine, 60*(1), 5-40. doi:https://doi.org/10.1180/minmag.1996.060.398.03

Marsh, B. (2015). Magma chambers. In H. Sigurdsson (Ed.), *The Encyclopedia of Volcanoes (Second Edition)* (Vol. 1, pp. 184-201). Amsterdam: Academic Press.

Mercalli, G., & Silvestri, O. (1891). Le eruzioni dell'Isola di Vulcano incominciate il 3 agosto 1888 e terminate il 22 marzo 1890, relazione scientifica. Ann Ufficio Centrale Metereol Geodin Ital, 10, 1-213.

Miyabuchi, Y., Iizuka, Y., Hara, C., Yokoo, A., & Ohkura, T. (2018). The September 14, 2015 phreatomagmatic eruption of Nakadake first crater, Aso Volcano, Japan: Eruption sequence inferred from ballistic, pyroclastic density current and fallout deposits. *Journal of Volcanology and Geothermal Research, 351*, 41-56. doi:https://doi.org/10.1016/j.jvolgeores.2017.12.009

Miyabuchi, Y., & Hara, C. (2019). Temporal variations in discharge rate and component characteristics of tephra-fall deposits during the 2014–2015 eruption of Nakadake first crater, Aso Volcano, Japan. *Earth, Planets and Space, 71*(1), 44. doi:https://doi.org/10.1186/s40623-019-1018-6

Miyagi, I., Geshi, N., Hamasaki, S., Oikawa, T., & Tomiya, A. (2020). Heat source of the 2014 phreatic eruption of Mount Ontake, Japan. *Bulletin of Volcanology, 82*(4), 33. doi:https://doi.org/10.1007/s00445-020-1358-x

Moebis, A. (2010). *Understanding the Holocene explosive eruption record of the Tongariro Volcanic Centre, New Zealand.* (Doctor of Philosophy), Massey University, Palmerston North.

Moebis, A., Cronin, S. J., Neall, V. E., & Smith, I. E. (2011). Unravelling a complex volcanic history from fine-grained, intricate Holocene ash sequences at the Tongariro Volcanic Centre, New Zealand. *Quaternary International, 246*(1–2), 352-363. doi:http://dx.doi.org/10.1016/j.quaint.2011.05.035

Moore, J. G. (1967). Base surge in recent volcanic eruptions. *Bulletin volcanologique, 30*(1), 337. doi:https://doi.org/10.1007/bf02597678

Moore, J. G. (1985). Structure and eruptive mechanisms at Surtsey Volcano, Iceland. *Geological Magazine, 122*(6), 649-661. doi: https://doi.org/10.1017/S0016756800032052

Nairn, I. A. (1976). Atmospheric shock waves and condensation clouds from Ngauruhoe explosive eruptions. *Nature, 259*(5540), 190-192. doi:https://doi.org/10.1038/259190a0

Nairn, I. A., & Self, S. (1978). Explosive eruptions and pyroclastic avalanches from Ngauruhoe in February 1975. *Journal of Volcanology and Geothermal Research, 3*(1), 39-60. doi:https://doi.org/10.1016/0377-0273(78)90003-3

Nairn, I. A., Wood, C. P., & Hewson, C. A. Y. (1979). Phreatic eruptions of Ruapehu: April 1975. *New Zealand Journal of Geology and Geophysics, 22*(2), 155-170. doi:https://doi.org/10.1080/00288306.1979.10424215

Nairn, I. A., & Group, R. S. (1996). Volcanic eruption at a New Zealand ski resort prompts reevaluation of hazards. *Eos, Transactions American Geophysical Union, 77*(20), 189-191. doi:http://dx.doi.org/10.1029/96EO00129

Nairn, I. A., Kobayashi, T., & Nakagawa, M. (1998). The ~10 ka multiple vent pyroclastic eruption sequence at Tongariro Volcanic Centre, Taupo Volcanic Zone, New Zealand:: Part 1. Eruptive processes during regional extension. Journal of Volcanology and Geothermal Research, 86(1–4), 19-44. doi:https://doi.org/10.1016/S0377-0273(98)00085-7

Nakagawa, M., Wada, K., Thordarson, T., Wood, C. P., & Gamble, J. A. (1999). Petrologic investigations of the 1995 and 1996 eruptions of Ruapehu volcano, New Zealand: formation of discrete and small magma pockets and their intermittent discharge. *Bulletin of Volcanology, 61*, 15-31. doi:https://doi.org/10.1007/s004450050259

Nakagawa, M., Wada, K., & Wood, C. P. (2002). Mixed Magmas, Mush Chambers and Eruption Triggers: Evidence from Zoned Clinopyroxene Phenocrysts in Andesitic Scoria from the 1995 Eruptions of Ruapehu Volcano, New Zealand. *Journal of Petrology, 43*(12), 2279-2303. doi:https://doi.org/10.1093/petrology/43.12.2279

Neall, V. E., Houghton, B. F., Cronin, S. J., Donoghue, S. L., Hodgson, K. A., Johnston, D. M., Lecointre, J. A., & Mitchell, A. R. (1999). Volcanic Hazards at Ruapehu Volcano. *Ministry of Civil Defense, Volcanic Hazards Information Series No. 8*.

Newhall, C. G., & Self, S. (1982). The volcanic explosivity index (VEI) an estimate of explosive magnitude for historical volcanism. *Journal of Geophysical Research: Oceans, 87*(C2), 1231-1238. doi: https://doi.org/10.1029/JC087iC02p01231

Newhall, C., & Hoblitt, R. (2002). Constructing event trees for volcanic crises. *Bulletin of Volcanology, 64*(1), 3-20. doi:https://doi.org/10.1007/s004450100173

Oliver, R. (1945). Further activity of Mount Ruapehu, May-July 1945. *New Zealand Journal of Science and Technology, 26*, 24-33.

Orsi, G., Di Vito, M. A., & Isaia, R. (2004). Volcanic hazard assessment at the restless Campi Flegrei caldera. *Bulletin of Volcanology, 66*(6), 514-530. doi:https://doi.org/10.1007/s00445-003-0336-4

Pallister, J. S., Schneider, D. J., Griswold, J. P., Keeler, R. H., Burton, W. C., Noyles, C., Newhall, C. G., & Ratdomopurbo, A. (2013). Merapi 2010 eruption—Chronology and extrusion rates monitored with satellite radar and used in eruption forecasting. *Journal of Volcanology and Geothermal Research, 261*, 144-152. doi:https://doi.org/10.1016/j.jvolgeores.2012.07.012

Palmer, B. A., & Neall, V. E. (1989). The Murimotu Formation—9500 year old deposits of a debris avalanche and associated lahars, Mount Ruapehu, North Island, New Zealand. *New Zealand Journal of Geology and Geophysics, 32*(4), 477-486. doi:https://doi.org/10.1080/00288306.1989.10427555

Palmer, B. A. (1991). Holocene lahar deposits in the Whakapapa catchment, northwestern ring plain, Ruapehu volcano (North Island, New Zealand). *New Zealand Journal of Geology and Geophysics, 34*(2), 177-190. doi:https://doi.org/10.1080/00288306.1991.9514455

Pardo, N. (2012). *Andesitic Plinian eruptions at Mt. Ruapehu (New Zealand): from lithofacies to eruption dynamics.* (Doctor of Philosophy), Massey University, Palmerston North.

Pardo, N., Cronin, S. J., Palmer, A. S., & Németh, K. (2011). Reconstructing the largest explosive eruptions of Mt. Ruapehu, New Zealand: lithostratigraphic tools to understand subplinian–plinian eruptions at andesitic volcanoes. *Bulletin of Volcanology, 74*(3), 617-640. doi:https://doi.org/10.1007/s00445-011-0555-z

Pardo, N., Cronin, S., Palmer, A., Procter, J., & Smith, I. (2012). Andesitic Plinian eruptions at Mt. Ruapehu: quantifiying the uppermost limits of eruptive parameters. *Bulletin of Volcanology, 74*, 1161-1185. doi:https://doi.org/10.1007/s00445-012-0588-y

Pardo, N., Cronin, S. J., Németh, K., Brenna, M., Schipper, C. I., Breard, E., White, J. D. L., Procter, J., Stewart, B., Agustín-Flores, J., Moebis, A., Zernack, A., Kereszturi, G., Lube, G., Auer, A., Neall, V., & Wallace, C. (2014a). Perils in distinguishing phreatic from phreatomagmatic ash; insights into the eruption mechanisms of the 6 August 2012 Mt. Tongariro eruption, New Zealand. *Journal of Volcanology and Geothermal Research, 286*, 397-414. doi:http://dx.doi.org/10.1016/j.jvolgeores.2014.05.001

Pardo, N., Cronin, S. J., Wright, H. M., Schipper, C. I., Smith, I., & Stewart, B. (2014b). Pyroclast textural variation as an indicator of eruption column steadiness in andesitic Plinian eruptions at Mt. Ruapehu. *Bulletin of Volcanology, 76*(5), 822. doi:https://doi.org/10.1007/s00445-014-0822-x

Parfitt, E. A., & Wilson, L. (1995). Explosive volcanic eruptions—IX. The transition between Hawaiian-style lava fountaining and Strombolian explosive activity. *Geophysical Journal International, 121*(1), 226-232. doi:http://dx.doi.org/10.1111/j.1365-246X.1995.tb03523.x

Parfitt, E., & Wilson, L. (2008). The role of volatiles *Fundamentals of Physical Volcanology* (pp. 64-76): Blackwell Science.

Pioli, L., Erlund, E., Johnson, E., Cashman, K., Wallace, P., Rosi, M., & Delgado Granados, H. (2008). Explosive dynamics of violent Strombolian eruptions: The eruption of Parícutin Volcano 1943–1952 (Mexico). *Earth and Planetary Science Letters, 271*(1), 359-368. doi:https://doi.org/10.1016/j.epsl.2008.04.026

Price, R., Waight, T., Chapman, J., Beyer, E., Smith, I., & Stewart, R. (1997). The geochemical evolution of arc magmas in a continental setting: Evidence from detailed chemo-stratigraphy at Ruapehu, New Zealand. *Geological Society of Australia Abstracts, 45*, 79-81.

Price, R. C., Gamble, J. A., Smith, I. E. M., Maas, R., Waight, T., Stewart, R. B., & Woodhead, J. (2012). The Anatomy of an Andesite Volcano: a Time-Stratigraphic Study of Andesite Petrogenesis and Crustal Evolution at Ruapehu Volcano, New Zealand. *Journal of Petrology, 53*(10), 2139-2189. doi:https://doi.org/10.1093/petrology/egs050

Purves, A. (1990). *Landscape ecology of the Rangipo Desert.* (Master), Massey University, Palmerston North.

Pyle, D. M. (1989). The thickness, volume and grainsize of tephra fall deposits. *Bulletin of Volcanology, 51*(1), 1-15. doi:https://doi.org/10.1007/bf01086757

Reed, J. (1945). Activity at Ruapehu, March-April, 1945. *New Zealand Journal of Science and Technology, 26*, 17-23.

Rosi, M., Pistolesi, M., Bertagnini, A., Landi, P., Pompilio, M., & Di Roberto, A. (2013). Stromboli volcano, Aeolian Islands (Italy): present eruptive activity and hazards. *Geological Society, London, Memoirs, 37*(1), 473-490.

Salmon, M., Stern, T., & Savage, M. K. (2011). A major step in the continental Moho and its geodynamic consequences: the Taranaki-Ruapehu line, New Zealand. *Geophysical Journal International, 186*(1), 32-44. doi:https://doi.org/10.1111/j.1365-246X.2011.05035.x

Sandri, L., Thouret, J.-C., Constantinescu, R., Biass, S., & Tonini, R. (2014). Long-term multi-hazard assessment for El Misti volcano (Peru). *Bulletin of Volcanology, 76*(2), 771. doi:https://doi.org/10.1007/s00445-013-0771-9

Scott, B. J. (2013). A revised catalogue of Ruapehu volcano eruptive activity: 1830-2012. *GNS Science Report, 2013/45*.

Self, S., Gertisser, R., Thordarson, T., Rampino, M., & Wolff, J. (2004). Magma volume, volatile emissions, and stratospheric aerosols from the 1815 eruption of Tambora. *Geophysical Research Letters, 31*(20). doi: https://doi.org/10.1029/2004GL020925

Shane, P., Doyle, L. R., & Nairn, I. A. (2008). Heterogeneous andesite–dacite ejecta in 26–16.6 ka pyroclastic deposits of Tongariro Volcano, New Zealand: the product of multiple magma-mixing events. Bulletin of Volcanology, 70(4), 517-536.

Sherburn, S., Bryan, C. J., Hurst, A. W., Latter, J. H., & Scott, B. J. (1999). Seismicity of Ruapehu volcano, New Zealand, 1971–1996: a review. *Journal of Volcanology and Geothermal Research, 88*(4), 255-278. doi:https://doi.org/10.1016/S0377-0273(99)00014-1

Sigurdsson, H, Houghton, B., McNutt, S., Rymer, H., & Stix, J. (2015). *The Encyclopedia of Volcanoes (Second Edition).* Amsterdam: Academic Press.

Siebert, L., Cottrell, E., Venzke, E., & Andrews, B. (2015). Earth's Volcanoes and Their Eruptions: An Overview. In H. Sigurdsson (Ed.), *The Encyclopedia of Volcanoes (Second Edition)* (pp. 239-255). Amsterdam: Academic Press.

Simkin, T., & Siebert, L. (2000). Earth's volcanoes and eruptions: an overview *Encyclopedia of volcanoes* (pp. 249-262).

Sparks, S. R., Sigurdsson, H., & Wilson, L. (1977). Magma mixing: a mechanism for triggering acid explosive eruptions. *Nature, 267*(5609), 315-318.

Sparks, R. S. J. (1978). The dynamics of bubble formation and growth in magmas: A review and analysis. *Journal of Volcanology and Geothermal Research, 3*(1), 1-37. doi:https://doi.org/10.1016/0377-0273(78)90002-1

Sparks, R. S. J. (1986). The dimensions and dynamics of volcanic eruption columns. *Bulletin of Volcanology, 48*(1), 3-15. doi:https://doi.org/10.1007/BF01073509

Taddeucci, J., Pompilio, M., & Scarlato, P. (2002). Monitoring the explosive activity of the July–August 2001 eruption of Mt. Etna (Italy) by ash characterization. *Geophysical Research Letters, 29*(8). doi:https://doi.org/10.1029/2001GL014372

Tanaka, H., Kawamura, K. i., Nagao, K., & Houghton, B. F. (1997). K-Ar Ages and Paleosecular Variation of Direction and Intensity from Quaternary Lava Sequences in the Ruapehu Volcano, New Zealand. *Journal of geomagnetism and geoelectricity, 49*(4), 587-599. doi:https://doi.org/10.5636/jgg.49.587

Topping, W. W. (1973). Tephrostratigraphy and chronology of late quaternary eruptives from the Tongariro Volcanic Centre, New Zealand. *New Zealand Journal of Geology and Geophysics, 16*(3), 397-423. doi:https://doi.org/10.1080/00288306.1973.10431368

Topping, W. W. (1974). *Some aspects of quaternary history of Tongariro volcanic centre.* (Doctor of Philosophy), Victoria University of Wellington.

Tost, M., & Cronin, S. J. (2015). Linking distal volcaniclastic sedimentation and stratigraphy with the development of Ruapehu volcano, New Zealand. *Bulletin of Volcanology, 77*(11). doi:https://doi.org/10.1007/s00445-015-0977-0

Valentine, G. A., & Gregg, T. K. P. (2008). Continental basaltic volcanoes — Processes and problems. Journal of Volcanology and Geothermal Research, 177(4), 857-873. doi:https://doi.org/10.1016/j.jvolgeores.2008.01.050

Villamor, P., & Berryman, K. R. (2006). Evolution of the southern termination of the Taupo Rift, New Zealand. *New Zealand Journal of Geology and Geophysics, 49*(1), 23-37. doi:https://doi.org/10.1080/00288306.2006.9515145

Villamor, P., Van Dissen, R., Alloway, B. V., Palmer, A. S., & Litchfield, N. (2007). The Rangipo fault, Taupo rift, New Zealand: An example of temporal slip-rate and single-event displacement variability in a volcanic environment. *GSA Bulletin, 119*(5-6), 529-547. doi:https://doi.org/10.1130/B26000.1

Walker, G. P. (1973). Explosive volcanic eruptions—a new classification scheme. *Geologische Rundschau, 62*(2), 431-446.

Walker, G. P. L. (1980). The Taupo pumice: Product of the most powerful known (ultraplinian) eruption? *Journal of Volcanology and Geothermal Research, 8*(1), 69-94. doi:https://doi.org/10.1016/0377-0273(80)90008-6

Walker, G. P. L., Self, S., & Wilson, L. (1984). Tarawera 1886, New Zealand — A basaltic plinian fissure eruption. *Journal of Volcanology and Geothermal Research, 21*(1), 61-78. doi:https://doi.org/10.1016/0377-0273(84)90016-7

Wallace, L. M., Beavan, J., McCaffrey, R., & Darby, D. (2004). Subduction zone coupling and tectonic block rotations in the North Island, New Zealand. *Journal of Geophysical Research: Solid Earth (1978–2012), 109*(B12). doi:https://doi.org/10.1029/2004JB003241

Wilson, L., Sparks, R. S. J., & Walker, G. P. L. (1980). Explosive volcanic eruptions - IV. The control of magma properties and conduit geometry on eruption column behaviour. *Geophysical Journal International, 63*(1), 117-148. doi:https://doi.org/10.1111/j.1365-246X.1980.tb02613.x

Wilson, C. J. N. (1985). The Taupo eruption, New Zealand. II. The Taupo Ignimbrite. *Philosophical Transactions of the Royal Society of London. Series A, Mathematical and Physical Sciences, 314*(1529), 229-310. doi:https://doi.org/10.1098/rsta.1985.0020

Wilson, C. J. N. (1993). Stratigraphy, Chronology, Styles and Dynamics of Late Quaternary Eruptions from Taupo Volcano, New Zealand. *Philosophical Transactions: Physical Sciences and Engineering, 343*(1668), 205-306. doi:https://doi.org/10.1098/rsta.1993.0050

Wilson, C. J. N., Houghton, B. F., McWilliams, M. O., Lanphere, M. A., Weaver, S. D., & Briggs, R. M. (1995). Volcanic and structural evolution of Taupo Volcanic Zone, New Zealand: a review. *Journal of Volcanology and Geothermal Research, 68*, 1-28. doi:https://doi.org/10.1016/0377-0273(95)00006-G

Wilson, G., Wilson, T. M., Deligne, N. I., & Cole, J. W. (2014). Volcanic hazard impacts to critical infrastructure: A review. *Journal of Volcanology and Geothermal Research*, 286, 148-182. doi:https://doi.org/10.1016/j.jvolgeores.2014.08.030

Wohletz, K. H. (1983a). *Chemical and textural surface features of pyroclasts from hydrovolcanic eruption sequences*. Retrieved from

Wohletz, K. H. (1983b). Mechanisms of hydrovolcanic pyroclast formation: grain-size, scanning electron microscopy, and experimental studies. *Journal of Volcanology and Geothermal Research, 17,* 31-63.

Wohletz, K., McQueen, R., & Morrissey, M. (1995). Analysis of fuel-coolant interaction experimental analogs of hydrovolcanism. *Intense multiphase interactions. Proceedings of US (NSF) Japan (JSPS) Joint Seminar, Santa Barbara, CA*, 8-13.

Zimanowski, B., Fröhlich, G., & Lorenz, V. (1991). Quantitative experiments on phreatomagmatic explosions. *Journal of Volcanology and Geothermal Research*, 48(3), 341-358. doi:https://doi.org/10.1016/0377-0273(91)90050-A

Zimanowski, B., Büttner, R., & Lorenz, V. (1997). Premixing of magma and water in MFCI experiments. *Bulletin of Volcanology*, 58(6), 491-495. doi:https://doi.org/10.1007/s004450050157

Chapter 2

Methodology

This chapter aims to introduce and discuss the methodology and the approaches that were used throughout this research.

2.1 Field work

In order to construct a solid tephrostratigraphic framework, several field visits were undertaken to the ring plain around Mt. Ruapehu. Discrete tephras were identified at a total of 91 field sections, while 18 additional sections did not contain macroscopic tephras but are reported to mark the limit of tephra dispersal (Field locations are shown in Appendix A). At 29 selected sections (Appendix A), tephra thicknesses were measured and units were described in detail, stating sedimentological features such as grain size, colour, componentry, contacts, and bed succession (Pardo et al., 2011; Torres-Orozco et al., 2017). These sections were used for the lateral and radial correlation of tephra members and individual subunits. At a number of locations, tephra samples were taken for further investigation, such as geochemical fingerprinting, grain size analysis and further analysis of key sequences.

Generally, deposits from other volcanic processes, such as PDCs, lahars and lava flows, are distinguished from fall deposits by the presence of flow textures, the presence of a matrix and other characteristic sedimentological features (Wright et al., 1980; Fisher et al., 1984). All deposits discussed in this thesis are fall deposits.

2.2 Sample characterisation

2.2.1 Grain size analyses

In this study, grain size terminology follows the nomenclature of White et al. (2006), while descriptive terms, such as median grain size and sorting, adhere to the nomenclature and calculations of Inman (1952).

Bulk tephra samples, representative of individual beds and subunits, were dried at ~50 °C. For sieving, dry samples were weighed and then manually dry sieved at 1 Φ intervals between 4 Φ and –2 Φ. Dry sieving was preferred over wet sieving to preserve eruption-style related characteristics as e.g., adhering dust (Heiken et al., 1985). Gentle hand-sieving was used, to avoid the breakage of pumice clasts that can result from machine sieving. Individual grain size classes were weighed and normalised to the total sample weight for obtaining comparable distributions in wt% (Appendix D).

For selected samples, the >4 Φ size fraction was analysed with a Laser Scattering Particle Size Distribution Analyser of Horiba (LPA), model Partica LA-950V2. It uses two different wavelengths of light to analyse different particle sizes, for which the refractive index must be known normally. A measuring routine based on the Fraunhofer approximation, which does not need information on the refraction index and discards particles smaller than 2 μm, was used. This brings good results for larger particles and makes the problematic identification of the refraction index unnecessary. Measurements were performed three times and the results were subsequently averaged.

LPA results were merged with those from the manually sieved grain size analyses and the resulting grain size distributions were analysed using the software Gradistat, version 8 (Blott et al., 2001). Various methods for reporting statistical parameters of grain size distributions such as median diameter (Md_Φ), sorting (σ_Φ), skewness (Sk_Φ) and kurtosis (K_Φ) are available (e.g. Krumbein et al., 1938; Inman, 1952; Folk et al., 1957). In the research presented here, the methods of Inman (1952) are used with the median being defined as $Md_\Phi=\Phi_{50}$ and sorting being defined as $\sigma_\Phi=0.5*(\Phi_{84}-\Phi_{16})$. Results are presented in Appendix D.

2.2.2 Componentry

The characterisation of the pyroclast assemblage is one of the parameters (together with e.g., grain size distributions and ash morphologies) that were used to characterise fall deposits (Fisher et al., 1984; Pistolesi et al., 2017). The ratio of juvenile volcanic glass, lithics (accidental, accessory and cognate) and crystals at any location depends on the fragmentation mechanisms and the eruption style. To not bias componentry ratios, point counting needed to be performed prior to any further analyses that remove clasts from the sample.

2.2.2.1 Point counting

To obtain a representative overview of the componentry, at least 300 grains were counted from the 2 Φ fraction under a binocular microscope by using a point counter. The 2 Φ fraction is considered to be the representative grain size for further analysis as it is present in all samples and allows the comparison of lapilli-bearing beds with predominantly ash-bearing beds. Where applicable, the coarser classes up to –2 Φ were point counted as well to investigate grain size-related changes in componentry. These are further discussed in Appendix E-1.

Component classes were normalised to the total number of particles counted for each grain size class and calculated as percentages to make them comparable. The distinguished componentry classes were juvenile glass, lithics and phenocrysts. Additionally, several juvenile glass classes could be further subdivided based on glass colour, shard morphology and vesicularity (Appendix E). The term “lithics” was used for accidental and accessory clasts, meaning clasts with obvious signs of alteration or clearly different provenance. Cognate lithics, meaning juvenile material from older eruptions or juvenile material that was subsequently recycled (cf. D'Oriano et al., 2014), are often difficult to distinguish from juvenile glass and were identified based on particularly rounded clast shapes or evidence of hydrothermal alteration. Phenocrysts were distinguished based on their colour, transparency and habits (cf., Fisher et al., 1984; Philpotts et al., 2009).

2.2.3 Pyroclast characterisation

2.2.3.1 Ash morphologies

Different eruption styles are associated with different transport and fragmentation mechanisms that in turn influence the shape and surface characteristics of pyroclasts (Heiken et al., 1985; Freundt et al., 1998; Dellino et al., 2001). For example, conchoidal fractures or dust adhering to the surface indicate the influence of water during fragmentation (Heiken et al., 1985; Buttner et al., 1999). High resolution images of pyroclast morphologies and textures were obtained by Scanning Electron Microscopy (SEM). The principle behind this technique involves the acceleration of an electron beam on the sample. The signals resulting from the electron-sample interaction are then counted and can be used either for imaging purposes by scanning the sample or for qualitative data acquisition, when equipped with a detector system (e.g., energy dispersive; EDS). Analytical precision is rather low, compared to other qualitative techniques such as the microprobe, but the advantage lies in high resolution images and fast sample preparation. For the study of clast morphologies, 31–45 glass shards, representative of the juvenile glass types in selected key units, were manually picked from the 2 Φ fraction under a binocular microscope and placed on a 20 mm wide stub, which was subsequently gold-coated. Images were taken with a FEI Quanta 200 Scanning Electron Microscope at the Manawatu Microscopy and Imaging Centre (MMIC), Massey University. Analysing conditions were a high vacuum, voltage of 25 kV, a beam width of 2.5 μm and measuring distances ranging from 8.3 to 9.5 mm.

2.2.3.2 Image analysis and clast textures

For investigating the variability in groundmass textures, back scattered electron images were obtained of polished, carbon-coated juvenile shards from the 2 Φ fraction at the Manawatu Microscopy and Imaging Centre, Massey University by using a FEI Quanta 200 Scanning Electron Microscope. Subsequently, image analysis was performed on representative images of each glass type by means of the trainable Weka segmentation plugin in ImageJ/Fiji, following the methodology described in Lormand et al. (2018). Here, a combination of machine learning and image segmentation was used to separate the image in areas with distinct pixel attributes. Based on the relative grey scales, which are indicative of the composition in backscattered electron mode, the distinguished phases involved phenocrysts, microlites of plagioclase and pyroxenes (<100 µm), groundmass glass and vesicles. The percentage of each of the phases was obtained in two dimensions by counting the pixels with Adobe Photoshop with the relative proportions of glass and microlites being re-calculated on a vesicle- and phenocryst-free basis. Images and results are presented in Appendix F.

2.2.4 Tephra dispersal and volume calculations

2.2.4.1 Isopach construction and volume calculation

Isopach data for selected individual subunits and tephra units is a combination of tephra thickness and tephra dispersal and provides the basis for volume calculations. Isopachs were constructed based on average bed and unit thicknesses as they were measured in the field (Appendix C). Isopachs were drawn manually on an 8 m digital elevation model from LINZ Data Service (https://data.linz.govt.nz), based on the 2012 LINZ Topo50 map series. Different methods to calculate deposit volumes were applied to the constructed isopachs, and the data and the estimated key parameters for the different methods are detailed in the respective appendix files. The methods of Fierstein et al. (1992) and Pyle (1989) use exponential thinning where the tephra thickness is plotted against the square root area of the isopach (SQRT(A)). Assuming a single segment, the volume can be obtained from

$$V = \frac{2 * T_0}{k^2} \tag{2.1}$$

with T_0 being the extrapolated maximum thickness and k representing the slope of the regression line on a ln(T) vs SQRT(A) plot (Pyle, 1989; Fierstein et al., 1992). Fierstein et al. (1992) suggest that the decay can be described better by two segments with different slopes, leading to the following volume calculation:

$$V = \frac{2 * T_0}{k^2} + 2 * T_0 * \left[\frac{\left(k_1 * A_{ip}^{\frac{1}{2}} + 1\right)}{k_1^2} - \frac{\left(k * A_{ip}^{\frac{1}{2}} + 1\right)}{k^2} \right] * \exp\left(-kA_{ip}^{\frac{1}{2}}\right) \tag{2.2}$$

with T_0 being the extrapolated maximum thickness, k and k_1 being the slopes of the two segments, respectively and A_{ip} marking the isopach area at which the two segments intercept. Those two methods are classically applied in volcanology, although they do not take in account the distal (fine grain-sized) tephras, and hence potentially underestimate the total deposit volume (see also e.g., Walker, 1980). While the approach of Fierstein et al (1992) and Pyle (1989) provide a good estimate, thickness variations of tephra deposits usually do not follow simple exponential thinning, and are instead characterised by multiple straight-line segments (Bonadonna et al., 1998). Accordingly, Bonadonna et al. (2012) suggest that the thickness distribution can be approximated by the Weibull function and the fitting of three empirical parameters λ, θ and n:

$$V = \frac{2\theta_{th}\lambda_{th}^{2}}{n_{th}} \tag{2.3}$$

Finally, another method can be used to estimate a minimum volume based on a single isopach (Legros, 2000). This method has established an empirical relationship between thickness and area, which results in the volume that can be calculated as:

$$V = 3.69 * T * A \tag{2.4}$$

with T representing the thickness of the given isopach and A the area that is enclosed by it.

Given the simplicity of the Legros-method, this formula is used to provide volume estimates for the entire dataset based on idealised ellipses in Chapter 5. Here, ellipses for individual subunits are constructed from as few as one data point.

2.2.4.2 Isopleths

Given the limited deposit thicknesses and the fine-grained nature of the studied deposits, in-situ large clast determination after Bonadonna et al. (2013a) is impracticable. Instead, in order to provide minimum estimates of the dispersal patterns and to estimate the largest grain size class, a slightly different approach was taken: for selected key samples and for grain size fractions <0 Φ, grain size analysis was performed at half Φ steps. The isopleths that are presented in Chapter 3 and Chapter 4 accordingly report the coarsest half Φ size fraction that contains ≥5 clasts. The correspondent data is summarised in Appendix C.

2.3 Age constraints

To investigate time-variant patterns in the eruption behaviour, absolute age constraints are needed. These age constraints can be obtained from different sources, such as the identification of external, dated, stratigraphic markers, as well as through radiocarbon dating. These absolute age constraints can then provide the framework for statistical age models.

2.3.1 Stratigraphic markers and known ages

In the time span investigated in this research, several eruptions sourced from other New Zealand volcanoes deposited tephra over the Tongariro National Park. These tephras provide valuable time constraints: (1) Deposits from the AD 232 Taupo eruption (or 1718 ± 10 cal BP; Hogg et al., 2012; Lowe et al., 2013) can be readily identified and mark the lowermost end of the Tufa Trig Formation. (2) The rhyolitic Kaharoa tephra, sourced from the Okataina Volcanic Centre (AD 1314; Lowe et al., 2013), has been described to be interbedded with the Tufa Trig Formation members in previous studies (Donoghue et al., 1995). However, no evidence of the associated deposit could be identified unequivocally at any location. (3) The andesitic Burrell Lapilli is associated with the AD 1655 eruption from the 130 km westward Mt. Taranaki (Druce, 1966; Platz et al., 2007). (4) Tephras from the simultaneous Ngauruhoe Formation include eruptions from Red Crater, Te Maari and Ngauruhoe and are known to be interbedded with the Tufa Trig Formation members (Topping, 1973; Donoghue et al., 1995; Moebis et al., 2011). Associated deposits have similar lithosedimentological characteristics to the units of the Tufa Trig Formation, but show different major element compositions (Moebis et al., 2011)

2.3.2 Radiocarbon dating

Radiocarbon dating is based on the decay of the radioactive carbon-isotope ^{14}C into the stable nitrogen isotope ^{14}N under the emission of an electron. ^{14}C is one of the three naturally occurring carbon isotopes ^{12}C, ^{13}C and ^{14}C, with ^{12}C constituting 99% of all existing carbon. Throughout their lifetime, living organisms are in permanent exchange of carbon with the atmosphere, having a more or less constant amount of ^{14}C. After their death, however, no new carbon is incorporated and the ^{14}C decay begins. The half-life has been defined at 5730 ± 40 years (Godwin, 1962) and indicates the time at which half of the atoms will have decayed. Accelerator Mass Spectrometry (AMS) is a technique to separate and count isotopes with different mass. The different carbon isotopes are separated by their mass and are counted directly, thus making it a very fast method. Another advantage is that generally little sample material is needed.

Samples for radiocarbon dating involved individual pieces of charcoal, selected from a humus-rich horizon interbedded with Makahikatoa sands at the type section (1703-107, Loc. 3), as well as soil samples containing organic material from a soil core taken at Ngamatea Swamp close to Waiouru (WP251, Appendix B). Samples were analysed by Accelerator Mass Spectrometry (AMS) at the Waikato Radiocarbon Dating Laboratory in Hamilton. Ages were reported as calibrated ages (cal BP) and calibration was performed using OxCal v4.3.2 (Bronk Ramsey, C., 2017. OxCal 4.3.2. Web Interface Build No. 105, last updated 11/11/2017) and the Southern Hemisphere curve SH Cal13 for atmospheric calibration (Hogg et al., 2013).

2.4 Geochemical analysis

Geochemical data obtained on juvenile glass is combined with textural data and integrated within the tephrostratigraphic framework. With this, variations in the magmatic system can be investigated at different timescales, providing insights into the processes during and before magma ascent.

2.4.1 Electron Microprobe Analyser (EMPA)

Major element glass compositions on juvenile groundmass glass are obtained by microprobe (Nakagawa et al., 1999; Smith et al., 2011). This is a non-destructive method, yielding quantitative elemental analyses on small spot sizes down to 1-2 μm. A focused electron beam is accelerated onto the solid sample, leading to the emission of different types of electrons from the sample. The x-rays resulting from this interaction are element-specific and can be determined and counted by either an energy-dispersive (EDS) or a wavelength-dispersive (WDS) detector system. Juvenile glass shards selected for microprobe analyses were hand-picked from subsamples of the 250 μm–500 μm (2 Φ) and the 125 μm–250 μm (3 Φ) fractions. They were embedded in epoxy resin (EPO-TEK), mixed at 4:1 resin to hardener ratios, to form a 24 mm diameter plug. The epoxy plugs were subsequently smoothed with powder of different grain sizes (220, 400, 600, 1000) and polished with 3 μm and 1 μm diamond paste. Carbon coating prevented charging of the plug by electrons. At least 10 points were analysed per sample. Due to the highly microcrystalline nature of the samples, some data points were discarded during post-analysis data processing as they indicated contamination by microlite analysis. Data was filtered and discarded for the following factors: (1) Al_2O_3>16 wt% (cf. Platz et al. 2007b), (2) totals <94 wt% and (3) MgO>5 wt% and <0.5 wt%. Compositions were normalised to 100 on a volatile-free basis, and were averaged for each sample; spot analyses are reported as wt% in Appendix G-1 and G-3.

During this study, major element compositions were acquired by two instruments: (1) a JEOL JXA-840 microprobe, equipped with an EDS system at Massey University and (2) a JEOL JXA-8230 SuperProbe EMPA at Victoria University of Wellington, which is equipped with a WDS system.

2.4.1.1 Massey University microprobe

As described in the section 2.3.1 Stratigraphic markers and known ages, several tephra deposits from other volcanic sources are interbedded with the Tufa Trig Formation (TTF). While in particular the Ngauruhoe Formation is very similar to the TTF, major element glass compositions are different (Moebis et al., 2011). To obtain a long-term record of major element variations during the past 1800 years and to verify whether the tephra units are actually Mt. Ruapehu-sourced, individual subunits were sampled at four key locations Loc. 1, Loc. 2, Loc. 3 and WP306. Analysis was performed at Massey University by means of a JEOL JXA-840 electron microprobe, which is equipped with an energy-dispersive system (EDS, Princeton Gamma Tech Prism 2000 Si(Li)), allowing a simultaneous spectrum acquisition which makes it faster than a wavelength dispersive system (WDS).

Analytical conditions involved a voltage of 15 kV with a beam current of 900 pA and counting times of 100 s. A defocused beam with diameters of 8 to15 μm, depending on microlite density, was used to minimize alkali loss in glass. To ensure probe precision and to quantify instrument drift, the standard minerals albite and olivine were analysed regularly during the session. Accuracy was well below 5 % for SiO_2, Al_2O_3, Na_2O and MgO and slightly worse for FeO, reaching maximum values of -18%. Standards consist of Astimex mineral mount MINM 25-43 (serial number 98-048) and Astimex Metal Mount (serial number 00-006). Oxides below the respective detection limits were excluded during post-analysis data processing and the whole dataset can be found in Appendix G-3.

2.4.1.2 Victoria University of Wellington microprobe

While the EDS system allows faster analysis, detection limits are generally higher compared to a WDS system. Accordingly, in addition to the analysis obtained on the entire tephra record, more detailed analyses on selected key units were performed at the JEOL JXA-8230 SuperProbe EMPA at Victoria University of Wellington (VUW), New Zealand, which is equipped with a WDS system. Selected key units were T5, T13, T15 and T31, with T5 samples deriving from Loc. 3, while T13, T15 and T31 samples were taken at Loc. 1.

Analytical conditions at the VUW microprobe included a ~8 nA probe current, an acceleration voltage of 15 kV and counting times of 30/15 s (On/Off peak) for all elements except Na (10/5 s On/Off peak). Spot size was varied according to microlite density, involving 5, 8 and 10 µm diameter spots. To control instrumental drift, the rhyolitic glass standard VG-568 (Jarosewich, 2002) was analysed every 20–30 points. Accuracy lies generally below ±6% with the exception of TiO_2 (15%) and MnO (19%). The corresponding data can be found in Appendix G-1.

2.4.2 Laser ablation inductively coupled plasma mass spectroscopy (LA-ICP-MS)

Trace element compositions were obtained on selected key samples, including T5, T13, T15 and T31, using the same samples that were analysed at the VUW microprobe. Laser ablation inductively coupled plasma mass spectroscopy (LA-ICP-MS) is a destructive technique where a laser source converts the solid sample to an aerosol and ionizes it. The ions are then brought into the mass spectrometer, where they are separated by their mass/charge ratio and can be detected.

Analyses were obtained in-situ at VUW, using a LA-ICP-MS Agilent 7900 coupled to a Resonetics 193 nm excimer laser ablation system. Analytical conditions involved a 10 Hz repetition rate and measuring times of 45 s and 60 s for ablation and background, respectively. The carrier gas involved a mixture of He (400 mL/min) and N_2 (1.5 mL/min). Reference glasses NIST610 and NIST612 (Pearce et al., 1997) were measured every 10–15 analyses to quantify analysis accuracy. For NIST610, accuracy lies generally within 15%, while it lies within 7% for NIST612. The exception is Mg, which has an accuracy of 46% and 14% for NIST610 and NIST612, respectively. Trace element compositions were acquired on spots with 30 μm diameter. While phenocrysts and xenocrysts could be avoided by careful spot selection, microlites could not be avoided. The presented data therefore represents semi bulk-rock (glass and microlites) compositions.

Semi-quantitative results were obtained through applying the data reduction scheme in the Iolite software (Paton et al., 2011). Here, ^{43}Ca was used as the internal standard, while NIST612 constituted the reference material. Post-analysis assessment and filtering was necessary due to the microlite-rich nature of the sample and involved the manual selection of integration windows in Iolite to avoid contaminated sections of the spectrum. Enhanced peaks in characteristic elements such as Mg, Sr, Cr, Ca indicated the ablation of sub-surface plagioclase and pyroxene crystals and were cut out. Similarly, data points with very high compositions of Ca (>110,000 ppm), combined with high Sr (>700 ppm) and high Mg (>60,000 ppm) and Cr (>50 ppm) were excluded. Ablation-related element fractionation effects are minimised by discussing trace element ratios rather than individual trace elements. The whole dataset can be found in Appendix G-2.

References

Blott, S. J., & Pye, K. (2001). GRADISTAT: a grain size distribution and statistics package for the analysis of unconsolidated sediments. *Earth Surface Processes and Landforms, 26*(11), 1237-1248. doi:https://doi.org/10.1002/esp.261

Bonadonna, C., Cioni, R., Pistolesi, M., Connor, C., Scollo, S., Pioli, L., & Rosi, M. (2013). Determination of the largest clast sizes of tephra deposits for the characterization of explosive eruptions: a study of the IAVCEI commission on tephra hazard modelling. *Bulletin of Volcanology, 75*(1), 680. doi:https://doi.org/10.1007/s00445-012-0680-3

Bonadonna, C., & Costa, A. (2012). Estimating the volume of tephra deposits: A new simple strategy. *Geology, 40*(5), 415-418. doi:https://doi.org/10.1130/G32769.1

Bonadonna, C., Ernst, G., & Sparks, R. (1998). Thickness variations and volume estimates of tephra fall deposits: the importance of particle Reynolds number. *Journal of Volcanology and Geothermal Research, 81*(3), 173-187. doi:https://doi.org/10.1016/S0377-0273(98)00007-9

Buttner, R., Dellino, P., & Zimanowski, B. (1999). Identifying magma-water interaction from the surface features of ash particles. *Nature, 401*(6754), 688-690. doi:https://doi.org/10.1038/44364

D'Oriano, C., Bertagnini, A., Cioni, R., & Pompilio, M. (2014). Identifying recycled ash in basaltic eruptions. *Scientific Reports, 4*, 5851. doi:https://doi.org/10.1038/srep05851

Dellino, P., Isaia, R., Volpe, L. L., & Orsi, G. (2001). Statistical analysis of textural data from complex pyroclastic sequences: implications for fragmentation processes of the Agnano-Monte Spina Tephra (4.1 ka), Phlegraean Fields, southern Italy. *Bulletin of Volcanology, 63*(7), 443-461. doi:https://doi.org/10.1007/s004450100163

Donoghue, S. L., Neall, V. E., & Palmer, A. S. (1995). Stratigraphy and chronology of late Quaternary andesitic tephra deposits, Tongariro Volcanic Centre, New Zealand. *Journal of the Royal Society of New Zealand, 25*(2), 115-206. doi:https://doi.org/10.1080/03014223.1995.9517487

Fierstein, J., & Nathenson, M. (1992). Another look at the calculation of fallout tephra volumes. *Bulletin of Volcanology, 54*(2), 156-167. doi:https://doi.org/10.1007/bf00278005

Fisher, R., & Schmincke, H. (1984). *Pyroclastic rocks*.

Folk, R. L., & Ward, W. C. (1957). Brazos River bar: a study in the significance of grain size parameters. *Journal of Sedimentary Research, 27*(1). doi:http://dx.doi.org/10.1306/74D70646-2B21-11D7-8648000102C1865D

Freundt, A., & Rosi, M. (1998). *From magma to tephra: modelling physical processes of explosive volcanic eruptions*: Elsevier.

Godwin, H. (1962). Half-life of Radiocarbon. *Nature, 195*, 984. doi:https://doi.org/10.1038/195984a0

Heiken, G., & Wohletz, K. (1985). *Volcanic Ash* Univ. of Calif. Press, Berkeley.

Hogg, A., Lowe, D. J., Palmer, J., Boswijk, G., & Ramsey, C. B. (2012). Revised calendar date for the Taupo eruption derived by 14C wiggle-matching using a New Zealand kauri 14C calibration data set. *The Holocene, 22*(4), 439-449. doi:https://doi.org/10.1177/0959683611425551

Hogg, A. G., Hua, Q., Blackwell, P. G., Niu, M., Buck, C. E., Guilderson, T. P., Heaton, T. J., Palmer, J. G., Reimer, P. J., & Reimer, R. W. (2013). SHCal13 Southern Hemisphere calibration, 0–50,000 years cal BP. *Radiocarbon, 55*(4), 1889-1903. doi:https://doi.org/10.2458/azu_js_rc.55.16783

Inman, D. L. (1952). Measures for describing the size distribution of sediments. *Journal of Sedimentary Research, 22*(3).

Jarosewich, E. (2002). Smithsonian microbeam standards. *Journal of Research of the National Institute of Standards and Technology, 107*(6), 681. doi:https://doi.org/10.6028/jres.107.054

Krumbein, W. C., & Pettijohn, F. J. (1938). Manual of sedimentary petrography.

Legros, F. (2000). Minimum volume of a tephra fallout deposit estimated from a single isopach. *Journal of Volcanology and Geothermal Research, 96*(1-2), 25-32. doi:https://doi.org/10.1016/S0377-0273(99)00135-3

Lormand, C., Zellmer, G. F., Németh, K., Kilgour, G., Mead, S., Palmer, A. S., Sakamoto, N., Yurimoto, H., & Moebis, A. (2018). Weka Trainable Segmentation Plugin in ImageJ: A Semi-Automatic Tool Applied to Crystal Size Distributions of Microlites in Volcanic Rocks. *Microscopy and Microanalysis, 24*(6), 667-675. doi:https://doi.org/10.1017/S1431927618015428

Lowe, D. J., Blaauw, M., Hogg, A. G., & Newnham, R. M. (2013). Ages of 24 widespread tephras erupted since 30,000 years ago in New Zealand, with re-evaluation of the timing and palaeoclimatic implications of the Lateglacial cool episode recorded at Kaipo bog. *Quaternary Science Reviews, 74*, 170-194. doi:https://doi.org/10.1016/j.quascirev.2012.11.022

Moebis, A., Cronin, S. J., Neall, V. E., & Smith, I. E. (2011). Unravelling a complex volcanic history from fine-grained, intricate Holocene ash sequences at the Tongariro Volcanic Centre, New Zealand. *Quaternary International, 246*(1–2), 352-363. doi:http://dx.doi.org/10.1016/j.quaint.2011.05.035

Nakagawa, M., Wada, K., Thordarson, T., Wood, C. P., & Gamble, J. A. (1999). Petrologic investigations of the 1995 and 1996 eruptions of Ruapehu volcano, New Zealand: formation of discrete and small magma pockets and their intermittent discharge. *Bulletin of Volcanology, 61*, 15-31. doi:https://doi.org/10.1007/s004450050259

Pardo, N., Cronin, S. J., Palmer, A. S., & Németh, K. (2011). Reconstructing the largest explosive eruptions of Mt. Ruapehu, New Zealand: lithostratigraphic tools to understand subplinian–plinian eruptions at andesitic volcanoes. *Bulletin of Volcanology, 74*(3), 617-640. doi:https://doi.org/10.1007/s00445-011-0555-z

Paton, C., Hellstrom, J., Paul, B., Woodhead, J., & Hergt, J. (2011). Iolite: Freeware for the visualisation and processing of mass spectrometric data. *Journal of Analytical Atomic Spectrometry, 26*(12), 2508-2518. doi:https://doi.org/10.1039/C1JA10172B

Pearce, N. J. G., Perkins, W. T., Westgate, J. A., Gorton, M. P., Jackson, S. E., Neal, C. R., & Chenery, S. P. (1997). A Compilation of New and Published Major and Trace Element Data for NIST SRM 610 and NIST SRM 612 Glass Reference Materials. *Geostandards Newsletter, 21*(1), 115-144. doi:https://doi.org/10.1111/j.1751-908X.1997.tb00538.x

Philpotts, A., & Ague, J. (2009) *Principles of igneous and metamorphic petrology*: Cambridge University Press.

Pistolesi, M., Bertagnini, A., Di Roberto, A., Isaia, R., Vona, A., Cioni, R., & Giordano, G. (2017). The Baia–Fondi di Baia eruption at Campi Flegrei: stratigraphy and dynamics of a multi-stage caldera reactivation event. *Bulletin of Volcanology, 79*(9), 67. doi:https://doi.org/10.1007/s00445-017-1149-1

Pyle, D. M. (1989). The thickness, volume and grainsize of tephra fall deposits. *Bulletin of Volcanology, 51*(1), 1-15. doi:https://doi.org/10.1007/bf01086757

Smith, V., Isaia, R., & Pearce, N. (2011). Tephrostratigraphy and glass compositions of post-15 kyr Campi Flegrei eruptions: implications for eruption history and chronostratigraphic markers. *Quaternary Science Reviews, 30*(25), 3638-3660. doi:https://doi.org/10.1016/j.quascirev.2011.07.012

Topping, W. W. (1973). Tephrostratigraphy and chronology of late quaternary eruptives from the Tongariro Volcanic Centre, New Zealand. *New Zealand Journal of Geology and Geophysics, 16*(3), 397-423. doi:https://doi.org/10.1080/00288306.1973.10431368

Torres-Orozco, R., Cronin, S. J., Pardo, N., & Palmer, A. S. (2017). New insights into Holocene eruption episodes from proximal deposit sequences at Mt. Taranaki (Egmont), New Zealand. *Bulletin of Volcanology, 79*(1), 3. doi:https://doi.org/10.1007/s00445-016-1085-5

Walker, G. P. L. (1980). The Taupo pumice: Product of the most powerful known (ultraplinian) eruption? *Journal of Volcanology and Geothermal Research, 8*(1), 69-94. doi:https://doi.org/10.1016/0377-0273(80)90008-6

White, J. D. L., & Houghton, B. F. (2006). Primary volcaniclastic rocks. *Geology, 34*(8), 677-680. doi:https://doi.org/10.1130/G22346.1

Wright, J. V., Smith, A. L., & Self, S. (1980). A working terminology of pyroclastic deposits. *Journal of Volcanology and Geothermal Research, 8*(2), 315-336. doi:https://doi.org/10.1016/0377-0273(80)90111-0

Chapter 3

Tephrostratigraphy of the Tufa Trig Formation

This chapter introduces the tephrostratigraphical framework of the 1800-year Tufa Trig Formation at Mt. Ruapehu and identifies 13 additional, previously unknown tephra members. Three main types of deposits are distinguished based on their lithosedimentological deposit features and represent different eruption styles and magnitudes. Characteristic key units for the three main deposit types are further described in terms of their pyroclast assemblage and tephra dispersal and add complexity to the existing understanding of deposits associated with small to moderate explosive eruptions.

All of chapter 3 is contained within the manuscript Lithosedimentological and tephrostratigraphical characterisation of small-volume, low-intensity eruptions: The 1800 years Tufa Trig Formation, Mt. Ruapehu (New Zealand) by M. Voloschina, G. Lube, J. Procter, A. Moebis & C. Timm. The manuscript was published as a research article in *Journal of Volcanology and Geothermal Research* (https://doi.org/10.1016/j.jvolgeores.2020.106987). The format of the manuscript has been adapted to match the thesis format and to ensure consistency within the thesis. In the following, the contributions of individual authors are outlined (DRC 16 - Statement of Contribution is contained in Appendix I-1 and on page 262):

Principal author: M Voloschina

Carried out: Field work, mapping, sampling

Laboratory analysis

Data analysis and interpretation

Manuscript and figure preparation, manuscript submission and handling of reviews

Co-authors: G. Lube

Contributed to the study by: Data discussion and interpretation

Commenting and reviewing manuscript

J. Procter

Contributed to the study by: Discussion of manuscript

Commenting manuscript

A. Moebis

Contributed to the study by: Assistance with field and laboratory work

Data discussion and interpretation

Commenting manuscript

C. Timm

Contributed to the study by: Commenting manuscript

Lithosedimentological and tephrostratigraphical characterisation of small-volume, low-intensity eruptions: The 1800 years Tufa Trig Formation, Mt. Ruapehu (New Zealand)

Marija Voloschina[1*], Gert Lube[1], Jonathan Procter[1], Anja Moebis[1], Christian Timm[2]

[1]Volcanic Risk Solutions, Massey University, Private Bag 11222, Palmerston North, New Zealand

[2]GNS Science, PO Box 30368, Lower Hutt 5035, New Zealand

*corresponding author (e-mail address: M.Voloschina@massey.ac.nz)

Keywords: Andesitic composite volcano; Tephrostratigraphy; Small to moderate explosive eruptions; Ash deposits; Fall deposits; Multi-phase eruptions

3.1 Abstract

Low to moderate-intensity eruptions (VEI ≤ 3) constitute the most frequent eruptions on historical timescales and can last from days to years. Direct observations of historical eruptions (e.g. Mt. Ruapehu 1995–1996, Nakadake 2003–2005, Etna 2002–2003) have highlighted the complexity of these eruptions, which often involve multiple phases and sudden changes in eruption behaviour. Eruptive products associated with low to moderate-intensity eruptions are typically characterised by small erupted volumes $\ll 1$ km^3 and a significant amount of ash-sized material, making their preservation subject to local environmental conditions. Accordingly, long-term (1000s of years) eruptive records tend to be biased towards the usually less frequent but better-preserved, more intense eruptions with VEI > 4 and deposit volumes >1 km^3, leading to an underestimation of the complexity and frequency of small-scale eruptions. This research presents a high-resolution tephrostratigraphic framework for the Tufa Trig Formation, formed during the last 1800 years of activity of the 2797 m high andesitic composite volcano Mt. Ruapehu in New Zealand. Systematic mapping and characterisation of macroscopic lithosedimentological features and tephra dispersal are combined with further studies on selected characteristic sequences to add complexity to the 1800 years tephra record of one of New Zealand’s historically most active volcanoes. Tephra deposits display a range of deposit textures, componentry and dispersal, with eruptive activity showing a time-variant distribution. Based on lithosedimentological deposit features, three main eruption types can be distinguished to have formed the Tufa Trig Formation: (1) ash-dominated low-intensity eruptions having deposit volumes of ~1×10^6 m^3 and leading to the deposition of single bed ash units; (2) small-volume (5–10×10^6 m^3) moderate intensity eruptions, which distributed lapilli-sized material up to distances of 20 km; and (3) multi-phase eruptions that were associated with multi-bed ash sequences, involved a magnitude larger tephra volumes (15.19–68.89×10^6 m^3), and whose tephra dispersal shows multiple thickness maxima in different directions. The here presented framework extends existing knowledge on the complexity of tephra deposits associated with low to moderate-intensity eruptions and provides the fundamental base for further, more detailed studies at Mt. Ruapehu and similar volcanoes worldwide. To guide future studies on similar records of detailed VEI ≤ 3 volcanic sequences elsewhere, several key lessons and challenges in the characterisation of such fall units are summarised also.

3.2 Introduction

Recent eruption episodes, such as Popocatepetl 1994–1997 (Martin-Del Pozzo et al., 2008), Etna 2002–2003 (Andronico et al., 2005), Nakadake 2003–2005 (Miyabuchi et al., 2008) and Eyjafjallajökull 2010 (Bonadonna et al., 2011) have been classified as low to moderate-intensity eruptions and have highlighted the severe impacts of ash-rich eruptions on modern society. Eruptions of this type have resulted in disturbances of aerial traffic (Miller, 2011), damage of infrastructure (Wilson et al., 2012; 2014) and constituted a health hazard to humans and animals (Cronin et al., 1998; 2003; Stewart et al., 2006). This is particularly important given that their tephra volumes are significantly smaller (generally <0.1 km^3; Newhall & Self, 1982; Siebert et al., 2015) compared to large cataclysmic events such as Pinatubo 1991 (5.3 km^3, VEI 6; Holasek et al., 1996). Fine-grained ejecta can be distributed over large distances (100s of km cf. Bonadonna et al., 2005; 2011) with dispersal patterns being strongly affected by the characteristics of the eruption plume (weak vs strong) and by prevailing wind conditions (Turner & Hurst, 2001; Bonadonna et al., 2005; Andronico et al., 2008). Similar to large eruptions (cf. Jenkins et al., 2007), low to moderate-intensity eruptions often comprise multiple eruption phases, each of which can involve different durations and follow characteristic eruption patterns (opening vs climactic vs post-climactic phases; Cioni et al., 2008a; Torres-Orozco et al., 2017b).

Traditionally, the quantification of short and long-term patterns in eruption behaviour is approached through deposit-based studies, which link these patterns to magmatic, tectonic and environmental factors (e.g. Ngauruhoe, Hobden et al., 1999; Vesuvius, Cioni et al., 2008a; Cotopaxi, Pistolesi et al., 2011). For low to moderate-intensity eruptions, however, the Holocene record of many volcanoes remains poorly constrained and fragmentary, due to limited tephra preservation and vegetation cover (Cutler et al., 2018; Dugmore et al., 2018). This limits the refinement of critical datasets behind statistical eruption forecast and impedes the understanding of the characteristics and syn-eruptive progression of low to moderate-intensity eruptions.

Mt. Ruapehu in New Zealand is an exemplary study target, as it shows both historically (603 days of eruptive activity since 1830; Scott, 2013) and prehistorically high eruption frequencies. The most recent tephra formation is known as the Tufa Trig Formation, which has been formed by small volume (<0.1 km^3) pyroclastic fall deposits, produced by mainly phreatic to Strombolian eruptions (Donoghue et al., 1997). This formation also includes the 1995–1996 eruptions, which comprised numerous eruptive events from September 1995 to September 1996, separated by a break in eruptive activity between November 1995 and June 1996 (Cronin et al., 2003; Scott, 2013). Eruption styles were dominated by small phreatomagmatic eruptions and magmatic violent Strombolian eruptions (VEI 1 to 3), but purely magmatic subplinian eruption phases (VEI 3 to 4) have been observed on several occasions (Cronin et al., 2003; Bonadonna et al., 2005; Scott, 2013).

We use the 1800 years tephra record of Mt. Ruapehu to reconstruct a high-resolution framework of tephra deposits associated with low to moderate-intensity eruptions. Tephrostratigraphic observations and lithosedimentological descriptions are complemented by studies of characteristic key sequences to determine componentry, tephra volume and dispersal. Based on this record, we refine the previous definition of the Tufa Trig Formation by adding thirteen tephra members. Tephra deposits are classified according to their main macroscopic and lithosedimentological features, suggesting different degrees of complexity and eruption dynamics. The results of this paper amplify the existing knowledge on Mt. Ruapehu's past eruption behaviour and set the framework for future detailed studies on small volume tephra deposits.

3.2.1 Late Holocene tephrostratigraphic framework

Mt. Ruapehu is a composite andesitic stratovolcano (2797 m asl) belonging to the Tongariro Volcanic Centres (TgVC) in the southernmost segment of the Taupo Volcanic Zone (a, b) on the North Island of New Zealand. The ring plain of Mt. Ruapehu preserves an extensive tephra record of the past ~27,000 years, evidencing a range of eruption styles, magnitudes and frequencies. The Bullot Formation (27,000–10,000 years) is dominated by voluminous subplinian to small Plinian eruptions (VEI 4–5; 0.3–0.6 km^3; Topping, 1973; Donoghue et al., 1995; Pardo et al., 2011; 2012). Associated deposits are fall deposits, comprising pumice lapilli beds, occasionally interbedded with thin pyroclastic density current deposits (Pardo et al., 2011; 2014). For the time span between ~10,000 years and AD 232, the existing tephrostratigraphic record suggests sporadic activity of yet poorly constrained style and magnitude, represented by millimetric to centimetric ash or lapilli deposits (Donoghue, 1991; Donoghue et al., 1995).

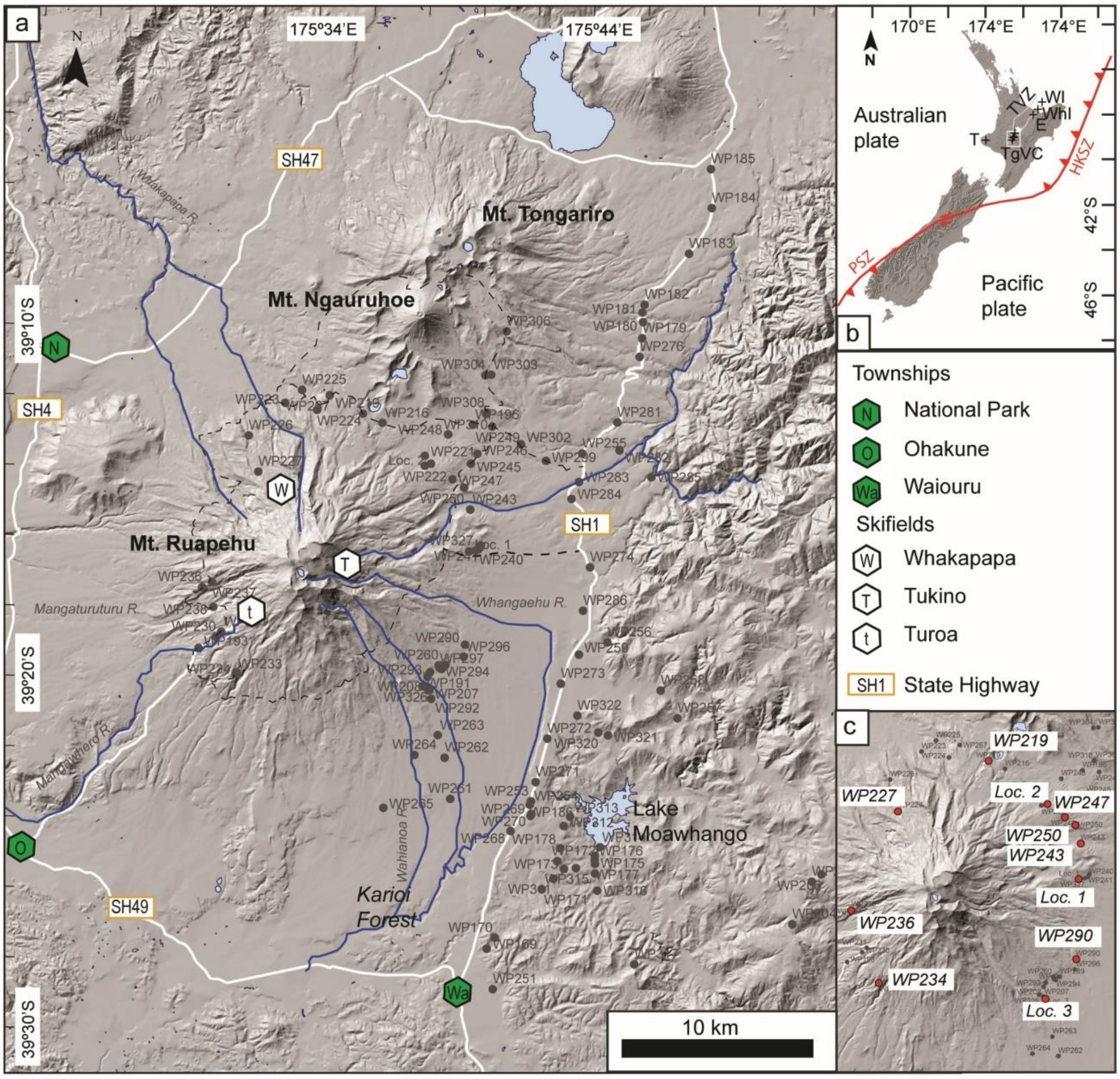

Fig. 3.1: a) Overview of the study area and the investigated field locations, showing the Tongariro Volcanic Centres (TgVC) Mt. Tongariro, Mt. Ngauruhoe and the object of this study, Mt. Ruapehu. Positions of nearby townships (N: National Park; O: Ohakune; Wa: Waiouru) and skifields (W: Whakapapa; T: Tukino; t: Turoa) are marked by green and white polygons, respectively. Main state highways are shown by a white line, while the Round the Mountain hiking track is represented by a black dashed line. The underlying hillshade view is based on an 8 m digital elevation model from the LINZ Data Service (https://data.linz.govt.nz), based on the 2012 LINZ Topo50 map series. b) Inset shows NZ land mass and its relative position to the Hikurangi-Kermadec (HKSZ) and the Puysegur subduction zones (PSZ). The Taupo Volcanic Zone (TVZ) is marked after Wilson et al., 1995. Andesitic-dacitic volcanic centres (crosses) are as follows: T: Mt. Taranaki, TgVC: Tongariro Volcanic Centres, E: Mt. Edgecumbe (Putauaki), WhI: Whale Island (Moutohora), WI: White Island (Whakaari). c) Inset highlights the key sections, which are used for the lateral correlation of the Tufa Trig tephra members.

3.2.2 Previous work on the Tufa Trig Formation

The current vent system of Mt. Ruapehu hosts a 10 million m^3 acidic Crater Lake, contained by hydrothermally altered volcanic breccia and lava flows. Previous studies relate the inception of the Crater Lake at ~2000–3000 years (Palmer, 1991) leading to a switch in eruption style to the predominantly phreatomagmatic to Strombolian eruption styles of the Tufa Trig Formation (Donoghue et al., 1995; 1997). Until this study, nineteen discrete tephra members (Donoghue, 1991; Donoghue et al., 1995, 1997) were known to overlie the AD 232 Taupo eruption (Lowe et al., 2013). Seventeen members (Tf2 to Tf18) are defined at the type location (Loc. 3 in Fig. 3.1c) as “coarse, black sandy ash and lapilli beds” (Donoghue et al., 1995), containing juvenile clasts of varying vesicularity, few lithic clasts and sparse pyroxenes and feldspars (Donoghue et al., 1997). Tephra member Tf19 corresponds to the 14 Oct 1995 eruption, while Tf1 underlies Tf2 in the Southern Rangipo Desert (Donoghue, 1991; Donoghue et al., 1997). Restricted deposit thicknesses (millimetres to few centimetres), the lack of unique features and univocal identification of individual members have hindered further correlations throughout the ring plain (Donoghue et al., 1995). Few members display distinctive features, such as relatively greater thickness or particular componentry assemblage and were used to construct broadscale isopach maps based on total tephra member thicknesses, yielding tephra volumes <0.1 km^3 (Donoghue et al., 1995). Volumes were calculated as cumulative volumes, therefore neglecting potential syn-eruptive changes in eruption dynamics and dispersal, as they were documented from observed eruptions (i.e. Cronin et al., 2003). Similarly, while existing descriptions report member-internal differences in componentry, grain size and texture (Donoghue, 1991; Donoghue et al., 1995), these have not yet been explored in terms of eruption progression and dynamics.

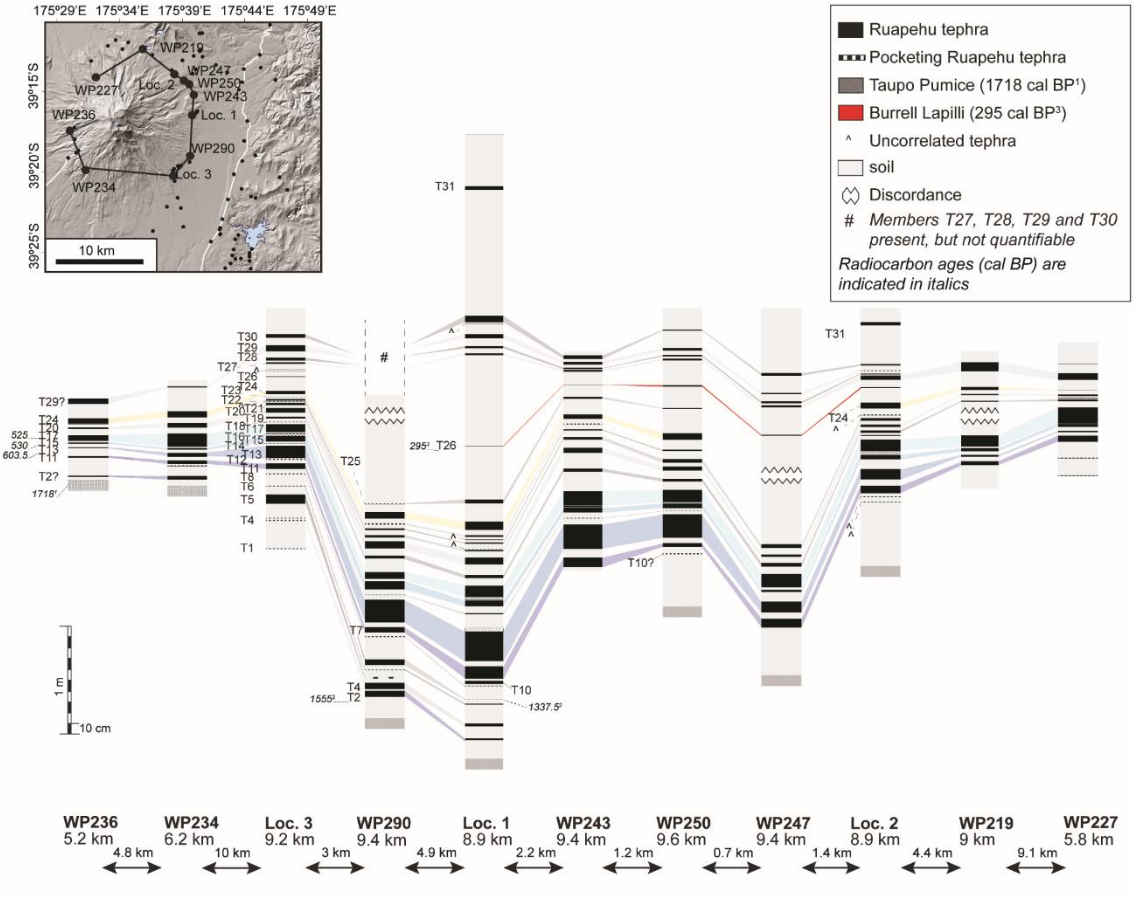

Fig. 3.2: Lateral correlation showing stratigraphic key sections for the members of the Tufa Trig Formation from West to North-West in an anti-clockwise sense. Specific members at different sections are linked by coloured bands. Small inset highlights the position of key sections relative to source. The inset's black line represents the equidistant lateral correlation. Below each section, the location name and the distance to the Crater Lake are reported. Correlated tephra members of the Tufa Trig Formation are marked by prefix "T" plus number. Caret indicates a tephra member that could not be correlated between more than one location. Where present, the deposit of the Taupo eruption (1718 ± 10 cal BP, Lowe et al., 2013) is shown with a standard thickness of 100 mm, which is not representative of the actual deposit thickness. Tephra member T26, which contains glass shards of the Taranaki-sourced Burrell Lapilli as well as juvenile Mt. Ruapehu-sourced glass is highlighted in red. Radiocarbon ages (cal BP) are reported in italics after ^{1} Lowe et al. (2013), ^{2} Moebis (2010) and ^{3} Druce (1966).

3.3 Methodology

3.3.1 Terminology and field methodology

Macroscopic observations of lithosedimentological characteristics from well-preserved tephra deposits provide information on eruption dynamics, fragmentation mechanisms and style (e.g. Arrighi et al., 2001; Pardo et al., 2011, 2012; Torres-Orozco et al., 2017a). However, given the small volume and limited distribution of deposits from low to moderate-intensity eruptions, correlation and interpretation are often complex. The classification of associated tephra deposits into macroscopically defined lithosedimentological units can improve the understanding of these complex eruptions and their eruption dynamics (cf. Pardo et al., 2011; Torres-Orozco et al., 2018).

In terms of descriptive terminology, we use the general terms *tephra unit*, *bedsets*, *beds* and *laminae*. A *tephra unit* is bounded by the continuous presence of andisoils and can be associated with the formal term *member* within a formal *formation* (Murphy & Salvador, 1999; Salvador, 1994). *Tephra units* can comprise either one individual bed/bedset or several beds/bedsets. *Bedsets* describe a sequence of beds, which are characterised by similar to identical lithosedimentological features. Here, this term is used mainly for correlation purposes, as in some cases, the correlation of bedsets is more achievable than the correlation of beds. The term *bed* describes the smallest quantifiable lithosedimentological entity, in accordance with Salvador (1994) and Murphy and Salvador (1999). A bed differs in its lithosedimentological characteristics from the encompassing beds, with its boundaries being marked by a sharp contact (i.e. change in grain size, lithology, texture) that is continuous on decimetre to metre scales. Observed lithosedimentological features at bed-level include: matrix- or clast-supported facies, grain size characteristics (following White & Houghton, 2006), grading, bed geometry, internal texture and stratification, sorting (following Inman 1952), componentry and contact type (cf. Torres-Orozco et al., 2017a). The term *laminae* describes layers with millimetric to sub-millimetric thicknesses.

To construct a detailed tephrostratigraphic framework, 109 field sections in different areas of Mt. Ruapehu's ring plain were measured and used to correlate individual tephra units and beds between locations (Fig. 3.1). Amongst all sections, eleven sites were identified to be representative of the different directions of the laterally variable tephra dispersal (Fig. 3.2). An overview over the relevant sections in this study is given in Supplementary Table S3.1.

Table 3.1: Selected key samples of this study with sampling location, distances from source and sedimentological parameters.

Sample ID	Unit	Subunit	Deposit type	Location	Distance to source (km); heading (°)	Latitude	Longitude	Md(Φ)	σ(Φ)	F1	F2	Juv	C	Lith	D	DV	BV	Analysed Φ-classes
1902-47	T2	–	L	WP296	9.6; 115.7	39 19 07.2 S	175 39 54.9 E	–1.15	1.71	23.13	nd	16.93	11.87	71.20	59.07	12.44	28.50	–1 to 1 (61.48 wt%)
1902-48	T7	–	L	WP296	9.6; 115.7	39 19 07.2 S	175 39 54.9 E	–1.15	2.15	23.11	nd	24.00	11.75	64.25	44.57	7.49	47.94	–1 to 1 (63.09 wt%)
1712-33	T27	–	MBA (L)	L2	8.9; 48.4	39 13 39.9 S	175 38 30.7 E	–1.54	2.86	34.55	2.09	42.26	9.33	48.41	49.32	24.03	26.65	–2 to 2 (57.22 wt%)
1703-21	T14	–	SBA	L1	8.9; 81.0	39 16 7.54 S	175 39 59.67 E	2.88	1.14	97.77	13.63	60.90	22.92	16.18	63.06	32.84	4.10	2 (13.58 wt%)
1703-67	T14	–	SBA	L3	9.2; 130.7	39 20 05.9 S	175 38 41.7 E	3.03	1.00	100.00	16.53	64.40	17.90	17.70	49.20	35.14	15.65	2 (12.80 wt%)
1703-68	T15	-1, -2	MBA	L3	9.2; 130.7	39 20 05.9 S	175 38 41.7 E	2.47	1.44	98.33	17.41	73.40	13.06	13.54	43.59	45.42	10.98	1 to 2 (36.52 wt%)
1703-69	T15	-4	MBA	L3	9.2; 130.7	39 20 05.9 S	175 38 41.7 E	1.17	0.89	90.24	2.42	88.87	6.49	4.64	45.29	32.01	22.69	0 to 2 (84.49 wt%)
1703-70	T15	-5	MBA	L3	9.2; 130.7	39 20 05.9 S	175 38 41.7 E	2.67	1.39	98.29	18.87	67.40	23.56	8.77	50.41	34.96	14.63	2 (23.80 wt%)
1703-71	T15	-5	MBA	L3	9.2; 130.7	39 20 05.9 S	175 38 41.7 E	3.27	1.18	98.29	26.07	65.35	25.63	8.73	43.10	33.62	23.28	2 (10.02 wt%)
1902-16	T15	-4	MBA	WP290	9.4; 112.0	39 18 46.6 S	175 39 56.9 E	0.86	1.00	82.39	3.47	82.01	14.66	3.33	41.54	42.68	15.78	0 to 2 (84.38 wt%)
1703-22	T15	-1	MBA	L1	8.9; 81.0	39 16 7.54 S	175 39 59.67 E	2.91	1.17	100.00	20.65	74.10	12.23	12.95	48.54	43.69	7.77	2 (17.13 wt%)
1703-23	T15	-2	MBA	L1	8.9; 81.0	39 16 7.54 S	175 39 59.67 E	2.41	1.07	99.84	9.91	75.70	16.07	7.66	54.07	36.54	9.38	2 (30.46 wt%)
1703-24	T15	-4	MBA	L1	8.9; 81.0	39 16 7.54 S	175 39 59.67 E	1.30	1.38	88.52	8.24	72.70	16.99	7.80	61.69	26.05	12.26	2 (31.75 wt%)
1803-22	T15	-3	MBA	WP250	9.6; 60.6	39 14 19.0 S	175 39 44.8 E	0.16	1.71	53.50	3.82	81.07	12.76	6.16	40.07	36.63	23.30	0 to 2 (62.51 wt%)
1712-12	T15	-1, -2	MBA	L2	8.9; 48.4	39 13 39.9 S	175 38 30.7 E	2.46	1.26	99.45	14.02	79.18	12.88	8.37	59.12	30.66	10.22	2 (26.58 wt%)
1712-13	T15	-3	MBA	L2	8.9; 48.4	39 13 39.9 S	175 38 30.7 E	0.59	1.54	66.59	2.63	75.65	12.50	11.85	49.93	22.39	27.69	1 to 2 (45.26 wt%)
1712-14	T15	-4	MBA	L2	8.9; 48.4	39 13 39.9 S	175 38 30.7 E	0.77	1.01	81.10	2.42	73.76	15.46	10.77	41.93	32.46	25.61	0 to 2 (85.20 wt%)
1712-15	T15	-5	MBA	L2	8.9; 48.4	39 13 39.9 S	175 38 30.7 E	2.53	1.33	96.60	13.70	67.51	22.22	10.27	63.98	30.75	5.28	2 (18.82 wt%)
1901-4	T15	-3	MBA	WP219	9.0; 19.6	39 12 17.8 S	175 35 58.3 E	–0.35	1.31	39.24	1.23	80.33	11.84	7.84	47.22	31.24	21.55	0 to 2 (63.45 wt%)

Notes: Associated deposit type classification is abbreviated as follows: L corresponds to lapilli-bearing tephra members, MBA marks multi-bed ash units and SBA represents single bed ash units. MBA (L) marks multi-bed units which contain a dominant lapilli bed. Median grain size Md(Φ) and sorting σ(Φ) follow Inman (1952). F1 and F2 represent percentage of material finer than 1 mm and 63 µm, respectively. Results from point counting are reported as percentage, calculated for the three main componentry classes juvenile clasts (Juv), crystals (C) and lithics (Lith), relative to the total number of counted shards. Juvenile clasts are further subdivided in dense clasts (D), scoriaceous clasts (DV) and beige vesicular glass (BV), with relative percentages being normalised to the total number of juvenile shards. The grain size classes that were point counted are reported in the last column, together with their weight relative to the total sample weight.

3.3.2 Sample characterisation

Grain size analysis, investigation of ash morphologies and point counts were performed on selected key samples (Table 3.1). Dry samples were manually sieved at 1 Φ intervals between –2 and >4 Φ and individual classes were weighted and normalised to 100. The 2 Φ fraction is chosen as the representative grain size for further sample characterisation, allowing the analysis and comparison of both fine grained, predominantly ash-sized beds with predominantly lapilli-bearing beds. Representative juvenile pyroclasts (31–45 clasts) from the 2 Φ fraction were imaged by Scanning Electron Microscopy (SEM) for selected tephra members and different componentry classes. Point counting was performed on at least 300 grains from the 2 to –2 Φ fractions of selected key samples (Table 3.1). For some fine-grained samples, point counting was only possible for the 2 Φ fraction, as this fraction constituted the coarsest grain size. The percentages of individual componentry classes were calculated relative to the total number of clasts counted between the analysed grain size fractions, distinguishing between juvenile clasts, crystals and lithics (Juv, C and Lith in Table 3.1). Percentages of different juvenile clast types were calculated relative to the total number of juvenile shards counted.

3.3.3 Age constraints

3.3.3.1 Stratigraphic markers

During the past 2000 years, several, well-studied eruptions from other New Zealand volcanic centres dispersed their tephra over the North Island; (1) the eruption of the Taupo Ignimbrite (AD 232 or 1718 ± 10 cal BP; Hogg et al., 2012; Lowe et al., 2013) provides a valuable and distinct stratigraphic marker, which marks the base of the Tufa Trig Formation; (2) the AD 1314 rhyolitic Kaharoa tephra from the Okataina Volcanic Centre (Lowe et al., 2013) has been previously described to be interbedded with the Tufa Trig Formation members (Donoghue et al., 1995), but could not be identified unequivocally at any location; (3) the AD 1655 (295 cal BP) eruption from the 130 km westward Mt. Taranaki resulted in the deposition of the andesitic Burrell Lapilli (Druce, 1966; Platz et al., 2007a); (4) eruptions from the contemporaneous Ngauruhoe-Formation are sourced from the adjacent Red Crater, Te Maari and Ngauruhoe vents and are known to be interbedded with the Tufa Trig Formation (Topping 1973; Donoghue et al., 1995; Moebis et al., 2011). These eruptions are represented by ash and lapilli layers, which are very similar to Tufa Trig tephra units, but are characterised by slightly different major element composition (Moebis et al., 2011).

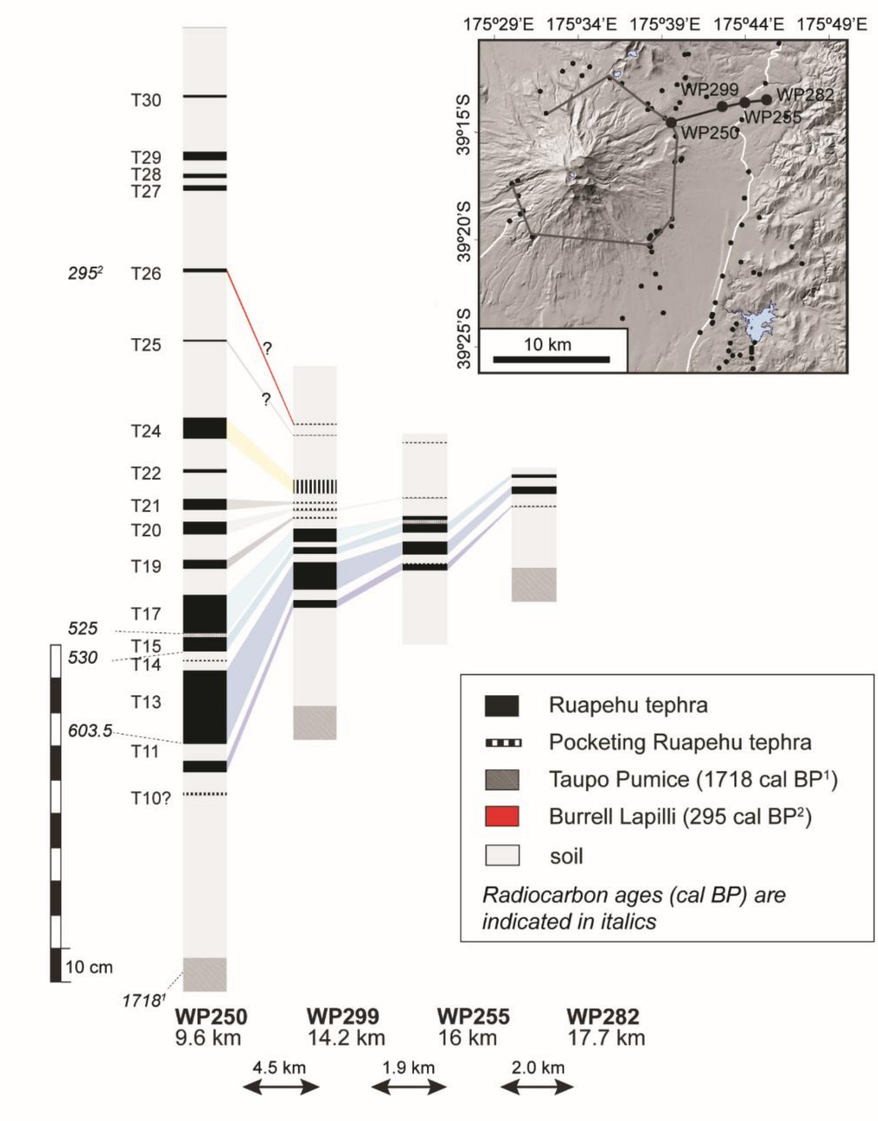

Fig. 3.3: Correlation of selected sections in NE direction, away from source. Inset shows the position of key sections relative to the lateral correlation (grey line) shown in Fig. 3.2. Correlated members of the Tufa Trig Formation are marked by prefix "T" plus number and are linked by coloured bands. Location names and respective distance to the Crater Lake are indicated below the sections while distances between sections are shown as well. Where present, the deposit of the Taupo eruption (1718 ± 10 cal BP, Lowe et al., 2013) is shown with a standard thickness of 100 mm, which is not representative of the actual deposit thickness. The stratigraphic position of tephra member T26, which contains glass shards of the Taranaki-sourced Burrell Lapilli and Mt. Ruapehu-sourced juvenile glass is highlighted in red. Radiocarbon ages (cal BP) are reported in italics and follow ^{1} Lowe et al. (2013) and ^{2} Druce (1966).

3.3.3.2 Radiocarbon dating

Three samples below tephra members T13, T15 and T17 were taken from a core from Ngamatea Swamp, close to Waiouru (WP251, Fig. 3.1) and were used for radiocarbon dating (Table 3.2). Furthermore, charcoal above tephra member T26 was sampled at type location Loc. 3 (Fig. 3.1c). Samples were analysed with Accelerator Mass Spectrometry (AMS) at the Radiocarbon Dating Laboratory at Waikato University in Hamilton. Ages are reported as calibrated ages (cal BP), based on calibration using OxCal v4.3.2 (Bronk Ramsey, 2017) and the Southern Hemisphere curve SH Cal13 for atmospheric calibration (Hogg et al., 2013). In addition, we introduce new age constraints for tephra members T2 and T7 from radiocarbon dating of charcoal at a location close to our WP256 (Fig. 3.1a, Supplementary Table S3.1), based on a previous unpublished research (Moebis, 2010).

3.3.4 Major element characterisation

To verify that the tephra units discussed in this study are Mt. Ruapehu-sourced, individual units were characterised in terms of their major element compositions and compared with the fingerprint presented in Moebis et al. (2011). Juvenile shards were picked manually from the 2 and 3 Φ size fractions of individual subunits. They were embedded in epoxy and at least 10 juvenile shards were analysed for each sample by means of a JEOL JXA-840 electron microprobe, equipped with a Priceton Gamma Tech Prism 2000 Si(Li) energy-dispersive system at Massey University. Analytical conditions involved 15 kV voltage, ~900 pA beam current and 100s counting times. Depending on microlite density, a defocused beam of 8 to 15 µm was used. Data points which show evidence of microlite contamination such as Al_2O_3 > 16 wt%, MgO > 5 wt% and <0.5 wt% (cf. Platz et al., 2007b) were excluded from the dataset. Compositions were normalised to 100 on a volatile-free basis and are reported as averages with respective standard deviations in Supplementary Table S3.2 (Appendix H-1), together with representative reference compositions for the adjacent Mts. Ngauruhoe and Tongariro (Red Crater) following Moebis et al. (2011) and the westward Mt. Taranaki (Platz et al., 2007a, Supplementary Table S3.3, Appendix H-1). With Loc. 1 showing the most complete tephra record, the majority of samples derives from this location, but is complemented by samples from other locations, yielding major element characterisation of overall sixty-six subunits.

Table 3.2: Overview of radiocarbon ages presented in this study. For comparison, previously published ages for the Burrell Lapilli and the Taupo Pumice, which are used as stratigraphic markers, are reported as well.

Age (cal BP)	error	C^{14} age (BP)	error	Sample ID	Material	Location	Reference	Stratigraphic position
295[a]						-	Druce (1966); Platz et al. (2007a)	T26/Burrell
410	85	401	23	1703-107	Charcoal	Loc. 3	Wk46601	Above T26
525	25	537	22	1803-3a-20	Pollen, leaves, seed pods from soil in core	WP251	Wk48878	Below T17
530	20	551	17	1805-3a-23	Pollen, leaves, seed pods from soil in core	WP251	Wk48634	Below T15
603.5	46.5	671	14	1805-3a-27	Pollen, leaves, seed pods from soil in core	WP251	Wk48586	Below T13
1337.5[b]	44.5	1490	30	30875	Charcoal	Loc. 73 in Moebis (2010)	NZA29921, Moebis (2010)	T7
1555[b]	135	1713	25	30874	Charcoal	Loc. 73 in Moebis (2010)	NZA29887, Moebis (2010)	T2
1718[c]	10					-	Lowe et al. (2013), Hogg et al. (2012)	Taupo

Notes: [a]Calibrated age for the Taranaki-sourced Burrell Lapilli corresponds to the AD 1655 age from Druce (1966), which was obtained by tree ring dating. [b]Ages for T2 and T7 are unpublished. Dated samples derive from Location 73 in Moebis (2010), which is located close to WP256 in this study (Fig. 3.1). [c]Age for Taupo eruption derives from Lowe et al. (2013) and Hogg et al. (2012) and corresponds to AD 232 ± 10.

3.4 Results

3.4.1 Mt. Ruapehu's eruptive record for the past 1800 years

The majority of the investigated outcrops lie within a distance of ~6–15 km from source (Fig. 3.1, Fig. 3.2). Within this distance interval, the presence of vegetation and soil sequences ensure the preservation of the fine-grained pyroclastic material, while at distances <6 km, the steep and exposed flanks of the volcanic edifice impede the preservation of discrete tephra beds. The most distant outcrop where tephra members are sufficiently preserved in order to measure their thickness and to distinguish specific characteristics is ~21 km ESE from source (Fig. 3.1). The east and southeast sectors of Mt. Ruapehu are covered by an extensive volcaniclastic fan between Loc. 1, WP290 and WP273 (Fig. 3.1). This fan highlights the role of the Whangaehu River Valley as a highly active lahar path and preserves deposits of numerous historical and prehistorical lahars (Donoghue & Neall, 2001; Lecointre et al., 2004; Hodgson et al., 2007; Graettinger et al., 2009). While several studies use the Tufa Trig Formation to constraint the ages for the lahar deposits of the contemporaneous Onetapu Formation (e.g. Donoghue & Neall, 2001; Lecointre et al., 2004; Hodgson et al., 2007), this study focuses solely on primary fall deposits to refine the existing tephrostratigraphic framework. Accordingly, the key locations used for the identification and correlation of tephra members are carefully chosen to represent depositional environments, which have been stable over timescales of at least 1800 years and show no evidence of lahar deposits or other major secondary reworking events. With this, thirty-one tephra members, separated by andisoils or sand can be identified (Fig. 3.2). This includes both the previously defined eighteen members after Donoghue et al. (1997) as well as thirteen new members. Accordingly, the previous definition of the Tufa Trig Formation is updated and re-numbered. The new nomenclature and the previous definition after Donoghue et al. (1997) are summarised in Table 3.3. Formal members of the Tufa Trig Formation include tephra units that are correlated between more than one section. The majority of the tephra members can be traced laterally at similar distances from source (Fig. 3.2). This lateral consistency, in combination with deposit characteristics such as consistent thickness variation between locations, overall good sorting and parallel bedding features suggest that the here presented members represent fall deposits. In line with this, no evidence of flow-like structures could be identified. With increasing distance from source, tephra thickness decreases rapidly, reducing the preserved tephra record to only few members at distances >15 km (Fig. 3.3). Some members are characterised by laterally restricted dispersals and can be identified only along their main dispersal axis. Few tephra units remain uncorrelated due to either limited thickness, limited dispersal or the lack of diagnostic features. They are marked as unnamed (“^”) and their position and characteristics are noted in the section description (Fig. 3.2, Fig. 3.4).

3.4.2 Lithosedimentological characterisation of fall sequences of small-volume, low-intensity eruptions

The lithosedimentological characteristics of the Tufa Trig tephra deposits cover a variable range of deposit textures, deposit features and dispersal characteristics (Fig. 3.4, Fig. 3.5). Beds and/or bedsets can be correlated throughout multiple sections and can be related to subunits within individual tephra units (Fig. 3.4). Accordingly, three main deposit types can be distinguished: single bed ash units (SBA), multi-bed ash units (MBA) and lapilli-bearing units (L). In the following, typical dispersal, grain size characteristics and pyroclast assemblage are illustrated for the different deposit types.

3.4.2.1 Tephra appearance and dispersal

Single bed ash (SBA) units are characterised by deposit thicknesses smaller than 10 mm at distances <15 km. Strong lateral and radial thinning with increasing distance is typical (Fig. 3.2, Fig. 3.3). Locally, they form pockets and show a wavy appearance, with unit boundaries characterised by the presence of andisoils and disturbed or blurred contacts. Internal variations are not quantifiable or form discontinuous laminae of sub-millimetric thickness. Given the limited thickness and lack of distinct features, correlation of SBA units is restricted to the main dispersal direction with closely spaced exposures and depends on the encompassing stratigraphic marker units.

Multi-bed ash (MBA) units contain multiple beds/bedsets, separated by clear contacts that are marked by sub-millimetric changes in lithosedimentological features such as grain size, lithology, colour or deposit texture. Individual beds/bedsets form a depositional subunit, which can be correlated between several field locations. Associated deposits are extensively distributed around source with cumulative dispersal showing unusual round isopachs, which are characterised by multiple thickness maxima in different directions, which can be related to individual subunits. Characteristics of the tephra sequence, such as median grain size, thickness or number and appearance of subunits change laterally.

Unit contacts for lapilli (L) units are marked by the sudden decrease in grain size from lapilli to soil. Associated deposits are characterised by a narrow dispersal, reaching distances up to 20 km. With increasing distance from source, unit thickness and grain size decrease. Both perpendicular to the main dispersal axis as well as with increasing distance, lapilli-sized pyroclasts continue appearing as sparse clasts, embedded in various proportions of smaller-grain sized pyroclastic material. Where the unit is characterised by the absence of ash-sized material, lapilli-sized clasts appear as sparse clasts embedded in the surrounding soil.

3.4.2.2 Grain size characteristics

Tephra units represent fall deposits, in agreement with the field defined by Walker (1971, Fig. 3.6a). For single bed and multi-bed ash units, the median grain size lies in the ash fraction (Fig. 3.6a). For SBA units, median grain sizes range between 1.6 and 3.8 Φ, with the average lying in the fine ash fraction (Md = 2.7 Φ) and average well sorting (σ = 1.2 Φ). The proportion of the sample, which is smaller than 1 mm (0 Φ) is described by the parameter F1, which is >76 wt% for SBA units, while the proportions of the sample that lie within the extremely fine ash fraction (>4 Φ, F2, Fig. 3.6b) range between ~8 and 40 wt% (Fig. 3.6b). Grain size characteristics for individual beds within MBA units span a wider range, ranging from fine ash to lapilli fractions (–1.5 to 3.5 Φ, Fig. 3.6a), with the average grain size at medial-distal distances being 2.1 Φ and showing slightly lower extremely fine ash fractions (F2 = 0.9–30.5 wt%, Fig. 3.6b), compared to SBA units. Sorting is variable (σ = 0.7–2.9 Φ), generally being classified as well sorted. Lapilli units are characterised by median grain sizes < –1 Φ and are well to poorly sorted. The proportion of ash-sized material constitutes ≤25 wt% of the total sample (F1, Fig. 3.6b), while extremely fine ash is ≤2 wt%.

3.4.2.3 Pyroclast assemblage

The different deposit types show variable proportions of juvenile clasts, free crystals and lithics. Juvenile clasts can be further subdivided in different components, based on morphology, texture and colour (Fig. 3.7): (1) Dark dense clasts (D), (2) dark scoriaceous clasts (DV) and (3) beige to brown vesicular glass (BV).

Dense (D) clasts are opaque and have a strongly microcrystalline groundmass. Clast morphologies involve chip-like and blocky morphologies with sharp breakage planes, step-like fractures and rough surfaces (e.g., Fig. 3.7a, b, j). Often, pyroclasts are covered by adhering ash (Fig. 3.7a, c).

Dark vesicular (DV) clasts have a microcrystalline groundmass and variable vesicularity. These clasts are scoriaceous, characterised by thick vesicle walls with sparse isolated round to slightly elongated vesicles (Fig. 3.7d, k), which sometimes show evidences of coalescence (Fig. 3.7e). Vesicles are typically medium-sized (20–50 μm in diameter) or small (~10–20 μm). Edges are sharp and show step-like features and fractures. Vesicles are often filled with extremely fine ash particles.

Beige vesicular juveniles (BV) are of a tan or brown colour and show generally lower microcrystallinity compared to D and DV clasts. Clast edges and breakage surfaces are often irregular and show step-like fractures, while surfaces are fluidal and smooth. Vesicle distributions are variable, ranging from strongly deformed or coalescent vesicles (Fig. 3.7f, g) to pumiceous morphologies with closely spaced small round vesicles (Fig. 3.7h) to thick bubble walls and a predominantly glassy groundmass (Fig. 3.7i, l).

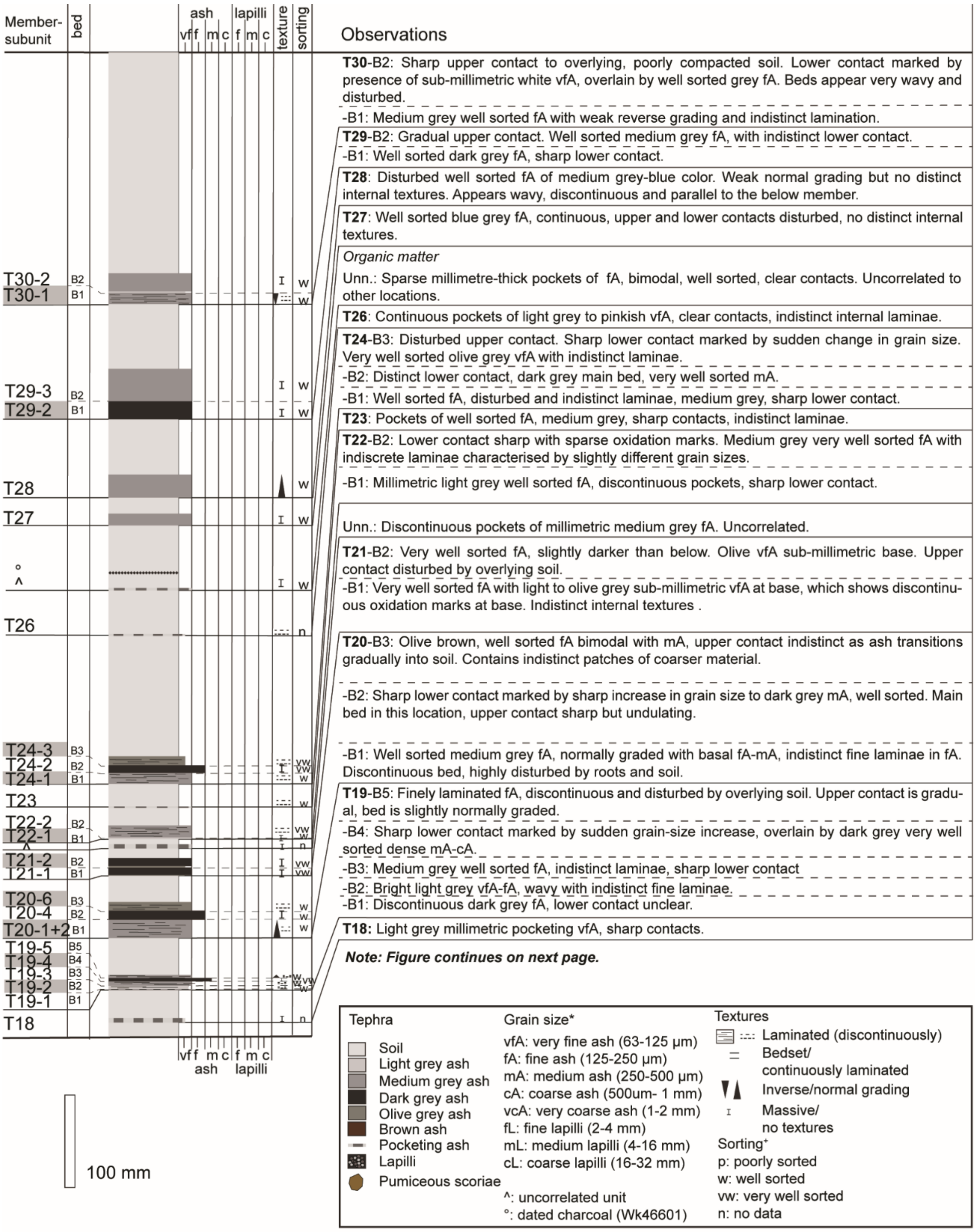

T30-B2: Sharp upper contact to overlying, poorly compacted soil. Lower contact marked by presence of sub-millimetric white vfA, overlain by well sorted grey fA. Beds appear very wavy and disturbed.

-B1: Medium grey well sorted fA with weak reverse grading and indistinct lamination.

T29-B2: Gradual upper contact. Well sorted medium grey fA, with indistinct lower contact.

-B1: Well sorted dark grey fA, sharp lower contact.

T28: Disturbed well sorted fA of medium grey-blue color. Weak normal grading but no distinct internal textures. Appears wavy, discontinuous and parallel to the below member.

T27: Well sorted blue grey fA, continuous, upper and lower contacts disturbed, no distinct internal textures.

Organic matter

Unn.: Sparse millimetre-thick pockets of fA, bimodal, well sorted, clear contacts. Uncorrelated to other locations.

T26: Continuous pockets of light grey to pinkish vfA, clear contacts, indistinct internal laminae.

T24-B3: Disturbed upper contact. Sharp lower contact marked by sudden change in grain size. Very well sorted olive grey vfA with indistinct laminae.

-B2: Distinct lower contact, dark grey main bed, very well sorted mA.

-B1: Well sorted fA, disturbed and indistinct laminae, medium grey, sharp lower contact.

T23: Pockets of well sorted fA, medium grey, sharp contacts, indistinct laminae.

T22-B2: Lower contact sharp with sparse oxidation marks. Medium grey very well sorted fA with indiscrete laminae characterised by slightly different grain sizes.

-B1: Millimetric light grey well sorted fA, discontinuous pockets, sharp lower contact.

Unn.: Discontinuous pockets of millimetric medium grey fA. Uncorrelated.

T21-B2: Very well sorted fA, slightly darker than below. Olive vfA sub-millimetric base. Upper contact disturbed by overlying soil.

-B1: Very well sorted fA with light to olive grey sub-millimetric vfA at base, which shows discontinuous oxidation marks at base. Indistinct internal textures .

T20-B3: Olive brown, well sorted fA bimodal with mA, upper contact indistinct as ash transitions gradually into soil. Contains indistinct patches of coarser material.

-B2: Sharp lower contact marked by sharp increase in grain size to dark grey mA, well sorted. Main bed in this location, upper contact sharp but undulating.

-B1: Well sorted medium grey fA, normally graded with basal fA-mA, indistinct fine laminae in fA. Discontinuous bed, highly disturbed by roots and soil.

T19-B5: Finely laminated fA, discontinuous and disturbed by overlying soil. Upper contact is gradual, bed is slightly normally graded.

-B4: Sharp lower contact marked by sudden grain-size increase, overlain by dark grey very well sorted dense mA-cA.

-B3: Medium grey well sorted fA, indistinct laminae, sharp lower contact

-B2: Bright light grey vfA-fA, wavy with indistinct fine laminae.

-B1: Discontinuous dark grey fA, lower contact unclear.

T18: Light grey millimetric pocketing vfA, sharp contacts.

Note: Figure continues on next page.

Fig. 3.4: Stratigraphic profile and lithosedimentological description of tephra members observed at key section Loc. 3. This location corresponds to the type location of the Tufa Trig Formation (after Donoghue et al., 1997). Members and subunits are reported for the correlated tephra members. The beds observed in the field are numbered and shown with depositional subunits. Observations illustrate field descriptions as well as median grain size and sorting parameters, obtained from grain size analysis for individual beds. Median grain size and sorting parameters are calculated after Inman (1952), and follow the nomenclature of White & Houghton (2006).

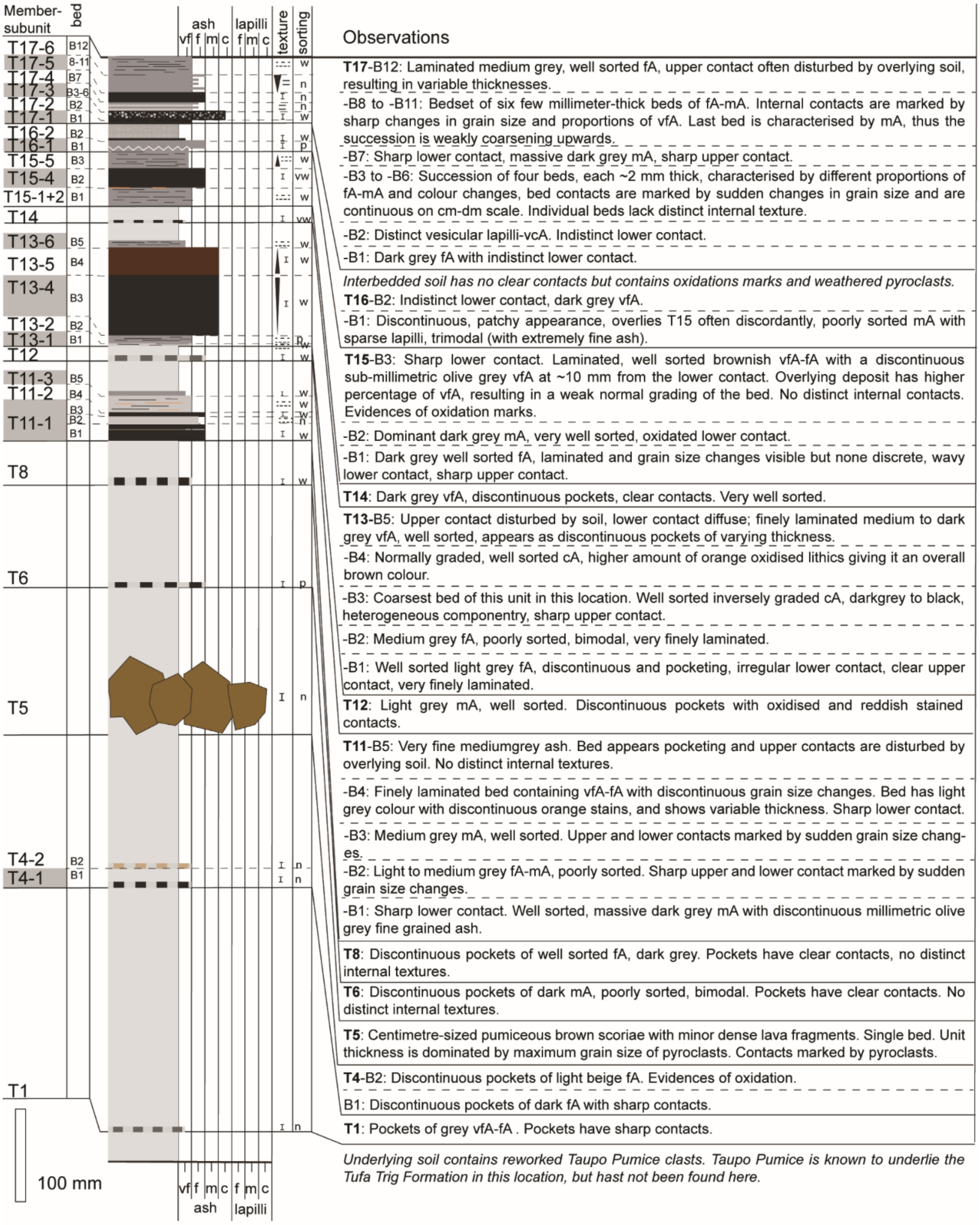

Observations

T17-B12: Laminated medium grey, well sorted fA, upper contact often disturbed by overlying soil, resulting in variable thicknesses.

-B8 to -B11: Bedset of six few millimeter-thick beds of fA-mA. Internal contacts are marked by sharp changes in grain size and proportions of vfA. Last bed is characterised by mA, thus the succession is weakly coarsening upwards.

-B7: Sharp lower contact, massive dark grey mA, sharp upper contact.

-B3 to -B6: Succession of four beds, each ~2 mm thick, characterised by different proportions of fA-mA and colour changes, bed contacts are marked by sudden changes in grain size and are continuous on cm-dm scale. Individual beds lack distinct internal texture.

-B2: Distinct vesicular lapilli-vcA. Indistinct lower contact.

-B1: Dark grey fA with indistinct lower contact.

Interbedded soil has no clear contacts but contains oxidations marks and weathered pyroclasts.

T16-B2: Indistinct lower contact, dark grey vfA.

-B1: Discontinuous, patchy appearance, overlies T15 often discordantly, poorly sorted mA with sparse lapilli, trimodal (with extremely fine ash).

T15-B3: Sharp lower contact. Laminated, well sorted brownish vfA-fA with a discontinuous sub-millimetric olive grey vfA at ~10 mm from the lower contact. Overlying deposit has higher percentage of vfA, resulting in a weak normal grading of the bed. No distinct internal contacts. Evidences of oxidation marks.

-B2: Dominant dark grey mA, very well sorted, oxidated lower contact.

-B1: Dark grey well sorted fA, laminated and grain size changes visible but none discrete, wavy lower contact, sharp upper contact.

T14: Dark grey vfA, discontinuous pockets, clear contacts. Very well sorted.

T13-B5: Upper contact disturbed by soil, lower contact diffuse; finely laminated medium to dark grey vfA, well sorted, appears as discontinuous pockets of varying thickness.

-B4: Normally graded, well sorted cA, higher amount of orange oxidised lithics giving it an overall brown colour.

-B3: Coarsest bed of this unit in this location. Well sorted inversely graded cA, darkgrey to black, heterogeneous componentry, sharp upper contact.

-B2: Medium grey fA, poorly sorted, bimodal, very finely laminated.

-B1: Well sorted light grey fA, discontinuous and pocketing, irregular lower contact, clear upper contact, very finely laminated.

T12: Light grey mA, well sorted. Discontinuous pockets with oxidised and reddish stained contacts.

T11-B5: Very fine mediumgrey ash. Bed appears pocketing and upper contacts are disturbed by overlying soil. No distinct internal textures.

-B4: Finely laminated bed containing vfA-fA with discontinuous grain size changes. Bed has light grey colour with discontinuous orange stains, and shows variable thickness. Sharp lower contact.

-B3: Medium grey mA, well sorted. Upper and lower contacts marked by sudden grain size changes.

-B2: Light to medium grey fA-mA, poorly sorted. Sharp upper and lower contact marked by sudden grain size changes.

-B1: Sharp lower contact. Well sorted, massive dark grey mA with discontinuous millimetric olive grey fine grained ash.

T8: Discontinuous pockets of well sorted fA, dark grey. Pockets have clear contacts, no distinct internal textures.

T6: Discontinuous pockets of dark mA, poorly sorted, bimodal. Pockets have clear contacts. No distinct internal textures.

T5: Centimetre-sized pumiceous brown scoriae with minor dense lava fragments. Single bed. Unit thickness is dominated by maximum grain size of pyroclasts. Contacts marked by pyroclasts.

T4-B2: Discontinuous pockets of light beige fA. Evidences of oxidation.

B1: Discontinuous pockets of dark fA with sharp contacts.

T1: Pockets of grey vfA-fA . Pockets have sharp contacts.

Underlying soil contains reworked Taupo Pumice clasts. Taupo Pumice is known to underlie the Tufa Trig Formation in this location, but hast not been found here.

Fig. 3.4: (continued)

3.4.3 Tephra characteristics of the Tufa Trig Formation members

Major element fingerprinting of sixty-six samples representing individual subunits shows that all tephra members have compositions, which are typical of Mt. Ruapehu (cf. Moebis et al., 2011, Fig. 3.8). To further illustrate internal textures of members, such as bed succession, texture and lithosedimentological characteristics, in the following section, the members of the refined Tufa Trig Formation are described in terms of their deposit characteristics, their distinguishing features and their main dispersal directions. The correlations of individual beds and bedsets allow us to investigate lateral changes in deposit characteristics and tephra dispersal, which are illustrated for three key locations at similar distances of ~9 km from source. The field sections are located in different directions of the ring plain: SE (Loc. 3, Fig. 3.4), E (Loc. 1, Fig. S3.1) and NE (Loc. 2, Fig. S3.2). Furthermore, members T2, T14 and T15 are characterised in terms of their pyroclast assemblage and dispersal patterns to illustrate the main differences between the three dominant lithosedimentological types L, SBA and MBA.

T1: This member is an indistinct discontinuous SBA of grey colour, often preserved in pockets of maximum 5 mm thickness. The main grain size range lies in the very fine to fine ash fraction. T1 shows a limited dispersal in SE direction (e.g., Loc. 3, Fig. 3.1, Fig. 3.4). Generally, this member lacks distinct characteristics, but can be identified due to its stratigraphic position relative to the overlying distinct T2 unit.

T2 ("Tf1") is a characteristic lapilli-bearing (L) unit with a subdominant ash-sized component (Fig. 3.6b). It shows a distinct overall orange colour accounted for by ~71% lithics (Table 3.1, Fig. 3.9a). Lithics consist of predominantly dense and hydrothermally altered lava, reddish oxidised altered pumices and rounded glassy particles. The latter component is characterised by round to sub-rounded shapes and have a sub-millimetric outer layer of hydrothermally altered glass, which is covered in extremely fine ash particles. Conversely, the inner portions appear vesicular and glassy. Juvenile clasts are subordinate (<17%) and increase slightly towards smaller grain sizes. Juvenile clasts are dominated by light-coloured microvesicular BV glass and D clasts, with the latter being represented within the finer grain size fraction, while BV glass dominates in coarser size fractions (<0 Φ). BV glass is of white colour and is extremely vesicular with thin bubble walls and smooth fluidal surfaces covered by adhering ash. Vesicle size distribution is heterogeneous and involves mostly round shapes. D clasts display irregular rough to smooth surfaces with scattered tiny vesicles and morphologies range from blocky to slightly cuspate, involving step-like fractures. DV clasts constitute ≤10% (Fig. 3.9b) and show sharp and planar fracture surfaces, which cut tiny vesicles (<10 µm diameter), while large vesicles (~100 µm diameter) are cut by grain boundaries, resulting in thick dense vesicle walls.

The spatial distribution is characterised by a narrow dispersal towards the E-ESE, with WP290 being the key section. Here this unit shows a thickness of 55 mm (e.g., Fig. 3.10a) and maximum clast diameters of 31 mm (Fig. 3.10b). Radiocarbon dating of charcoal within a lapilli unit that is correlated to T2 ("Tf1" in Moebis, 2010) yields an age of 1555 ± 135 cal BP (NZA29887, Moebis, 2010). The charcoal is not eruption-related but derives from local natural wildfires, which occurred within the same age range.

Fig. 3.5 (next page): a) Overview of members T2 to T11 in south-eastern direction at WP297. While T2 and T7 occur as continuous beds, T5 appears as sparse juvenile fragments at the same stratigraphic position relative to over and underlying members, which are highlighted by circles. b) Overview of centimetre-sized juvenile pyroclasts of T5 and multi-bed ash member T11 at Loc. 3. c) Overview of T15 to T17 and the soil/weathered ash between them at WP262. T17 has an indistinct upper contact, while T15 shows a disturbed lower contact. d) Close-up on member T17 at Loc. 3. Several distinct beds and bedsets can be identified with subunit T17-2 being significantly coarser than the encompassing beds. e) Overview over tephra members T19, T20, T21, T22, T23 and T24 at WP290. Interbedded andisol is of similar thickness between all members. f) Close-up on T19 and T20 at Loc. 1. Image shows internal textures and sharp internal contacts. Upper contact of T19 shows a gradual transition into overlying soil, while T20 has a disturbed lower contact. g) Overview of T17, T19, T20, T21 and T24 at Loc. 2. T18 appears as pockets with indistinct contacts. T21 contains coarse ash at this location. h) Zoom on T25 highlighting the coarse lower bed and the overlying very fine ash bed with a weathered upper contact at Loc. 1. i) Characteristic pocketing appearance of T26, which contains juvenile Taranaki-sourced glass shards, associated with the AD 1655 Burrell eruption, as well as juvenile Mt. Ruapehu-sourced pyroclasts. Note the distinct pinkish-light grey colour and the pocketing appearance. j) Zoom on T27 at Loc. 2, which is characterised by fine lapilli-sized white and orange-coloured pyroclasts overlain by dark grey fine ash without distinct contact. The above member T28 consists in dark grey pockets of very fine ash. k) Close-up on T29 at Loc. 1 showing three distinct beds, each characterised by different grain size and texture.

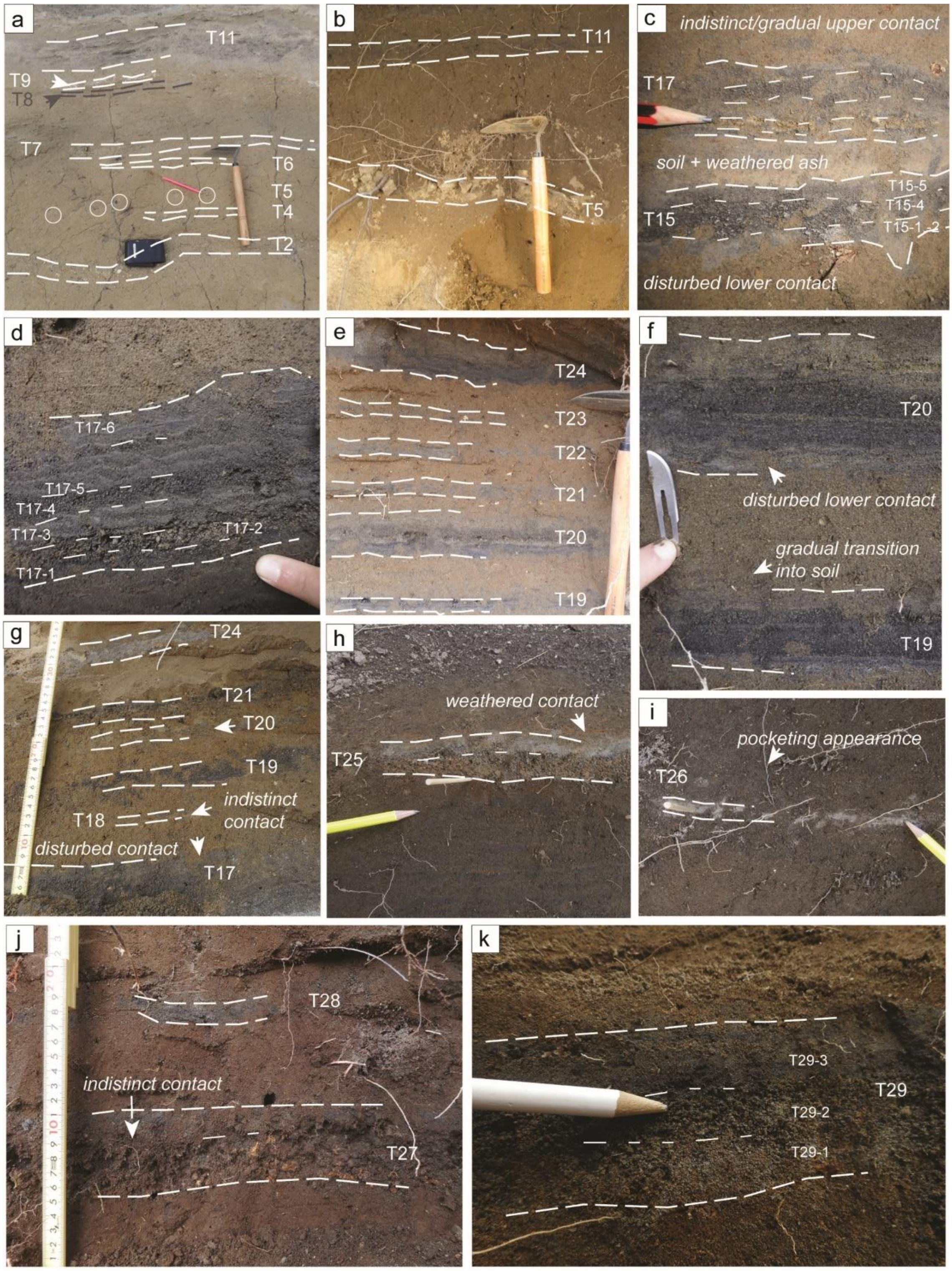

T3: This member consists of a SBA unit with thicknesses <10 mm, which often forms pockets. The dispersal is limited to SE directions (WP296, Loc. 1) and maximum distances of ~12 km. Here, it contains a discontinuous white base of sub-millimetre thickness, composed of very fine to fine ash.

T4 is a distinct MBA member in the SE-E areas of the ring plain between Loc. 3 and Loc. 1, showing a maximum total thickness of ~50 mm at WP290 (Fig. 3.2, Fig. 3.5a). In most sections it appears as a characteristic twofold unit with a lower dark grey fine to medium ash bed (T4-1) and an upper bright-coloured beige bed (T4-2). The upper bed is characterised by an abundance of highly vesicular beige to transparent juvenile glass. At WP290 in the southern Rangipo Desert, T4-2 contains fine lapilli-sized pumiceous clasts. Here, T4-2 is overlain by another light grey fine ash bed (T4-3) that is characterised by an abundance of hydrothermally altered pyroclasts. Contacts between individual beds are diffuse and show evidences of incipient soil formation and weathering, suggesting that associated eruption phases were separated in time but that the involved timescales were shorter than those necessary to form a distinct soil horizon.

T5 (“Tf2”) is a distinct L-type member, comprising highly vesicular, fragile pyroclasts of brown colour (Fig. 3.5b) that are usually significantly coarser than other members. Clast’s vesicles are generally round. Lithics constitute <30% of the unit and consist of dense lava fragments. Unit thickness is generally restricted by the maximum clast size (up to 47.5 mm in diameter at Loc. 3). Perpendicular to the main SE dispersal axis and with increasing distances, this unit appears as sparsely dispersed individual clasts, appearing continuously at the same stratigraphic position relative to under or overlying units (i.e., circles in Fig. 3.5a).

T6 is a dark fine to medium ash that forms pockets of max. 5 mm thickness without distinct features. It has a characteristic stratigraphic position relative to overlying member T7. The main dispersal is in SE direction (i.e., Loc. 3, Fig. 3.4).

T7 (“Tf2”) is a ~52 mm thick, heterolithologic lapilli-dominated unit with a subdominant ash-sized component and a characteristic narrow dispersal along the main E-SE dispersal axis (e.g., WP290). Componentry consists of ~64% hydrothermally altered lithics, comprising dense and pumiceous components with alterated surfaces as well as dense, red oxidised lava fragments. Juvenile clasts constitute ~24% of the assemblage and contain light-coloured white and beige vesicular glass, at times with slightly elongated and deformed vesicles. Additionally, the ash fraction contains dark dense microcrystalline juvenile clasts. Perpendicular to the main dispersal axis (i.e., Loc. 1, Fig. S3.1, WP293), this member occurs as a dark ash containing sparse lapilli-sized pyroclasts and shows discontinuous lamination. This member has been previously falsely correlated to “Tf2”

(T5 in this study) in outcrops in the Rangipo Desert (WP296, Fig. 3.1, equivalent to Missile Ridge Dune location in Donoghue et al. 1997). However, several observations contradict the previously established correlation; (1) the discrepancy between the distinct lithosedimentological characteristics of T5, such as the type and quantity of lithic fragments and the fragile, highly vesicular nature of the juveniles compared to the lithosedimentological characteristics of T7 at Missile Ridge Dune; (2) at several locations between Loc. 3 and WP296, pyroclasts with T5-like characteristics occur stratigraphically between T2 and T7. Here, sparse cm-sized vesicular scoriae and dense lithic lava fragments are embedded in soil at a continuous distance from the underlying T2 (circles, Fig. 3.5a). T7, on the contrary, generally appears as a continuous massive lapilli unit (Fig. 3.5b). Aligning with these observations, we interpret T5 and T7 as two distinct tephra members. Unpublished data suggests a radiocarbon age of 1337.5 ± 44.5 cal BP for T7 (NZA29921, Moebis 2010; Table 3.2).

T8 (“Tf3”) is a SBA and forms a dark grey fine ash with a main dispersal towards SE-E (e.g., WP290, Fig. 3.1), where it has thicknesses of <10 mm. It lacks distinguishing features and can be identified mainly due to its stratigraphic position relative to overlying members T9 or T11.

T9 is a distinct white fine ash bed, which overlies T8 closely in the SE areas of the ring plain (e.g., WP297, Fig. 3.5a). The pyroclast assemblage consists of white-coloured lithics, dense and scoriaceous juvenile clasts. This member shows a very irregular appearance; i.e. it does not appear at any of the key locations but at other nearby locations (such as WP292 or WP207), where it shows a pocketing appearance of <5 mm thickness.

T10 forms indistinct pockets of medium grey fine ash in ESE direction. Main dispersal is towards Loc.1 (Fig. S3.1), where it appears as a continuous, strongly oxidised and weathered, discontinuously laminated unit and shows a maximum thickness of 22 mm.

T11 (“Tf4”) is an MBA, which forms a complex succession of at least eight beds and displays a notably widespread distribution. In S to E directions, it appears as an overall twofold tephra unit composed of a lower dark and coarser-grained bedset and upper, fine-grained bedsets of light grey to orange colour. This member can be subdivided into four subunits with a lower bedset of three beds containing massive dark medium ash, which form subunit T11-1. Subunit T11-1 is dispersed in all directions, and appears as a massive medium ash to the East (Loc. 1, Fig. S3.1), while to the NE, it can be subdivided into three beds separated by distinct contacts, which are marked by sudden changes in grain size (e.g., Loc. 2, Fig. S3.2). The contact with the overlying subunit T11-2 is sharp and marked by the presence of a white-orange, oxidised sub-millimetric very fine ash bed in the East (Loc. 1, Fig. S3.1). Subunit T11-2 contains at least three beds, best exposed at Loc. 1 (Fig. S3.1) and has an overall distinct light grey-orange colour due to orange oxidised contacts between individual beds. Individual beds are fine-grained (very fine to fine ash) and join to form a single, vaguely laminated bed to the SE (Loc. 3, Fig. 3.4) and the NE (Loc. 2, Fig. S3.2). T11-3 constitutes a laminated fine-grained bed, which can be found from SE (Loc. 3, Fig. 3.4) to the NE (Loc. 2, Fig. S3.2). No distinct internal contacts can be identified. In N-NE areas, T11-3 is overlain by a distinct orange to dark-coloured coarse ash to fine lapilli (T11-4, Fig. S3.2, Fig. 3.11).

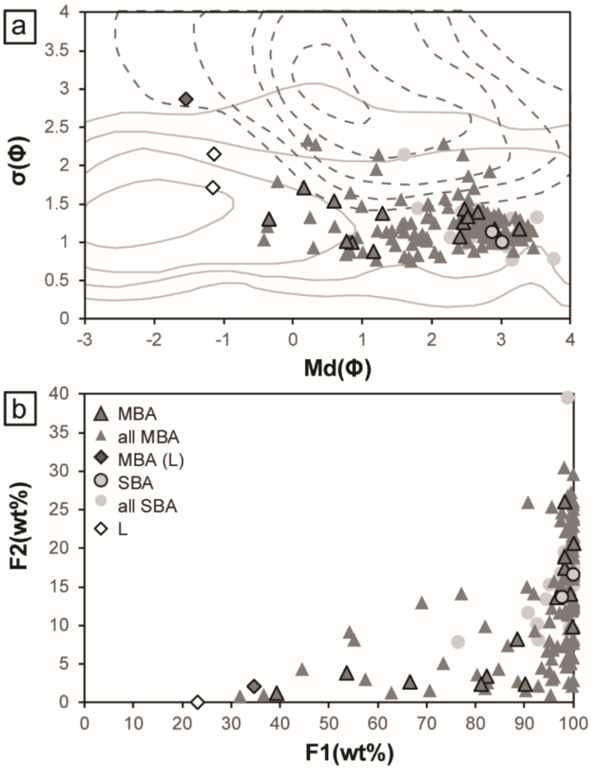

Fig. 3.6: Grain size characteristics of analysed Tufa Trig tephra members and selected key samples. The symbols represent the classification of members according to their lithosedimentological characteristics. Multi-bed ash beds (MBA) are represented by triangles with key samples being outlined (Table 3.1); single bed ash units (SBA) are shown as circles with key samples highlighted by outlined circles; lapilli-dominated units (L) are shown as diamonds and the MBA (L) unit is marked by a grey diamond. a) Sorting σ(Φ) and median grain size Md(Φ) parameters of Tufa Trig tephras follow Inman (1952). Grey lines and grey dashed lines represent the fields for fall and flow deposits after Walker (1971). b) Plot shows descriptive grain size parameters F1 (wt% of sample that is >0 Φ or <1 mm) and F2 (wt% of sample that is >4 Φ or <63 µm).

T12 is a single bed ash unit, which is characterised by pocketing light grey fine to medium ash of <3 mm thickness and is distinct due to the encompassing tephra members T11 and T13. It shows a main dispersal towards the SE (Loc. 3, Fig. 3.4).

T13 (Tf5): Organic matter in soil underlying this member in a core, yields a radiocarbon age of 603.5 ± 46.5 cal BP (95.4% probability; Wk48586, Table 3.2). T13 is distinct by its thickness (270 mm at Loc. 1, Fig. S3.1) and the presence of a dominant coarse bed, containing dark coarse ash and pumiceous beige fine lapilli. It consists of a complex succession of several bedsets, whose thickness and characteristics vary around source (cf. Fig. 3.4 with Fig. S3.1 and Fig. S3.2). Different bedsets are dominant or pinch out in different directions. T13-1 constitutes the basal sub-millimetric, light grey, fine ash, distinct at Loc. 3, while pocketing or absent in other directions. T13-2 is a medium grey, fine ash, overlying the bed below. It appears as a distinct bed between Loc. 3 and Loc. 1, while it forms pockets and sub-millimetre layers in the NE (e.g., Loc. 2, Fig. S3.2). T13-3 is characterised by massive medium to coarse ash capped by a discontinuous millimetre-thick, olive-coloured fine ash, which is best exposed to the E-NE, at WP250 and Loc. 2 (Fig. S3.2). T13-4 is the most dominant subunit, which can be found in all directions from source. At Loc. 3, it comprises a six centimetre-thick bed, composed of dark coarse ash (Fig. 3.4). Going towards Loc. 1, this subunit shows at least two distinct reversely graded parts (medium ash to fine lapilli), which are best exposed at WP290 and Loc. 1 (Fig. S3.1). The similarity in lithology and lack of evident contacts complicates any correlation of individual beds for this subunit. The upper bed contact is marked by a sudden decrease in grain size. T13-5: This subunit is marked by a dominant massive brownish to dark medium ash, slightly fining upwards. It contains dark dense juveniles and brownish vesicular scoriae of coarse ash to fine lapilli size. It is characterised by a relatively high amount of brownish lithics, giving it a distinct brownish colour. This subunit rapidly thins out towards Loc. 2, while the best preserved exposures can be found between Loc. 3 and WP290. Here, T13-5 is capped by a characteristic orange coarse ash, marking the upper contact. T13-6 consists in a normally graded dark to medium grey medium ash, which is best exposed at Loc. 2 (Fig. S3.2). The upper part shows indistinct lamination, with the upper contact being affected by soil formation.

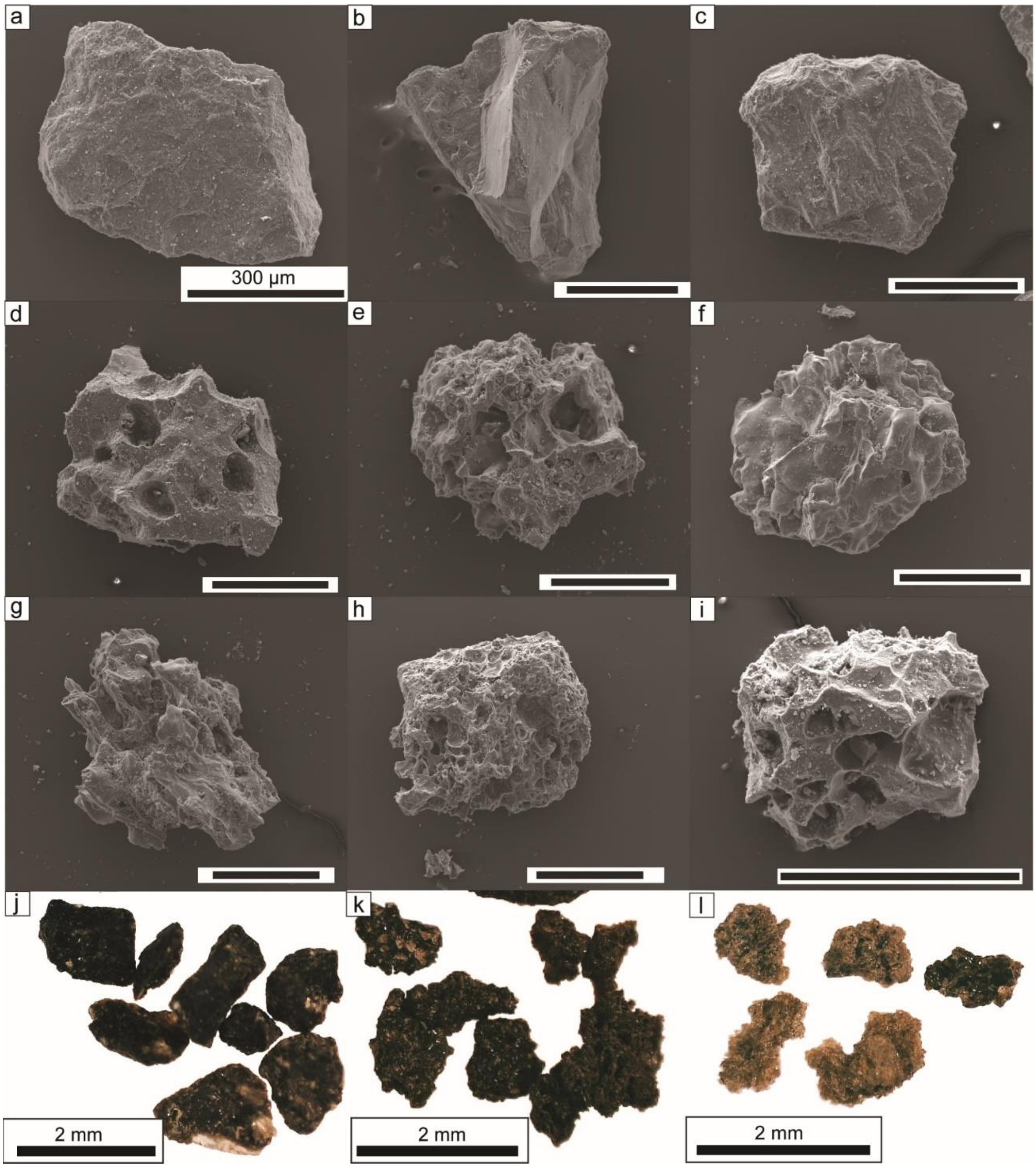

Fig. 3.7: Images of selected ash fragments. Insets a) to i) show secondary electron images with the bar in each image representing 300 µm. Images j) to k) show optical images. a) Blocky dense dark (D-type) juvenile clast showing conchoidal fractures on the surface. b) D clast with sharp edges and step-like features. c) Blocky D shard of light colour, partially with smooth glassy surface. d) DV clast with thick vesicle walls and isolated round vesicles. e) DV clast with heterogeneous vesicles, thin bubble walls and slightly deformed vesicles. f) Light-coloured glassy BV shard with smooth surface and heterogeneous deformed vesicles. g) Vesicular beige shard with elongated vesicles and thin bubble walls. h) BV juvenile with small round vesicles that are closely spaced to each other. i) BV shard with smooth glassy surface and isolated large and slightly deformed vesicles. j) Optical image of dense dark D clasts with blocky morphologies and sparse transparent phenocrysts. k) Scoriaceous DV clasts of dark colour with irregular morphologies and heterogeneous vesicles. l) Vesicular beige and brown BV glass, showing pumiceous morphologies and small vesicles.

T14: This member is a characteristic SBA with a maximum thickness of ~10 mm. The main dispersal of this dark grey unit is towards the E (Fig. 3.10c, Loc. 1, Fig. S3.1), while it is preserved as pockets in ENE (e.g., WP250) and SE directions (e.g., Loc. 3, Fig. 3.4). The unit has discontinuous, internal lamination and an indistinct sub-millimetre light grey base in SE. The analysed key samples highlight that juvenile clasts constitute the main component (60.9–64.4%, Fig. 3.9a, Table 3.1) and lithic percentages are slightly higher (16.2–17.7%), compared to a typical MBA unit (Fig. 3.9a). Juvenile clasts are dominated by D (49.2–63.1%) and DV clasts (32.8–35.1%), while BV clasts are subordinate (4.1–15.7%).

T15, T16 and T17: These tephra units appear as a distinct sequence, which can be identified by the interbedded soil of 5–15 mm thickness between T15/T16 and T17. This soil is characterised by the presence of weathered ash, which does not form any continuous, discrete beds (Fig. 3.5c). The stratigraphic uniqueness of the T15–T17 sequence makes it a useful marker sequence around the ring plain.

T15 (“Tf6”) is a characteristic MBA. Radiocarbon dating of organic matter in soil underlying this member in the Ngamatea Swamp core (WP251, Fig. 3.1), indicates a maximum age of 530 ± 20 cal BP (Wk48634, 95.4% probability, Table 3.2). This member generally appears as a trifold tephra unit (Fig. 3.5c, Fig. 3.10d). Owing to its stratigraphic position between T13 and T17 and its distinct characteristics, T15 can be readily identified in many sections. The cumulative dispersal shows unusual round isopachs with multiple thickness maxima in different directions (SE, NE and NNE, Fig. 3.10d). It is worth noting that the tephra sequence changes laterally (insets in Fig. 3.10d). It is best exposed at Loc. 3, while complexity increases towards Loc. 1, WP250 and Loc. 2 (Fig. 3.10d, Fig. S3.1, Fig. S3.2).

T15-1 is a massive, vaguely laminated medium grey, fine ash, sometimes with a basal millimetre to sub-millimetre light grey bed. T15-2 consists in a massive and weakly laminated medium grey to brownish fine ash with the lower contact being marked by the presence of light grey fine ash. The unit is capped by a millimetre-thick olive grey very fine to fine ash. While T15-2 and T15-1 can be clearly distinguished at WP290 and Loc. 1 (Fig. 3.10d), they thin out rapidly towards the NE (WP250, Loc. 2) and form a conjunct, indistinctly laminated bed at Loc. 3. T15-3: This bed is characterised by a brownish to dark grey colour and an abundance of beige vesicular juvenile clasts. Isopach and isopleth data for T15-3 indicate a bilobate dispersal towards Loc. 2 and WP219 (Fig. 3.10e, f), while it is difficult to identify in E and SE directions (WP290 and Loc. 1, Fig. 3.10e, f). T15-4: This subunit consists of an often reversely graded dark medium to coarse ash with a distinct sharp lower contact. The main dispersal is towards the SE (Loc. 3 to WP290, Fig. 3.5c, Fig. 3.10e, f), as inferred from isopach and isopleth construction. T15-5 is a finely laminated medium grey to brown very fine to fine ash with a sharp lower contact and main dispersal towards Loc. 3 (Fig. 3.10d).

To illustrate the variability of the pyroclast assemblage within a typical multi-bed ash unit, Fig. 3.9a and b report relative proportions for individual subunits, compared to L and SBA units. Overall, T15 is similar to SBA unit T14, but is characterised by higher juvenile percentages, ranging between 65.4 and 88.9% (Fig. 3.9a, Table 3.1). Subunits T15-1 and -2 are characterised by higher proportions of lithics and D clasts. T15-3 and -4 show the highest percentage of juvenile clasts of the entire tephra sequence as well as relatively higher proportions of BV glass. The pyroclast assemblages of the two T15-3 lobes are similar, containing 21.5–23.3% BV glass (Fig. 3.9b), which is characterised by high vesicularity with thin, fluidal bubble walls and coalescent heterogeneous vesicles (Fig. 3.7h). T15-4 is dominated by DV clasts compared to D juveniles. Both DV and BV clasts show heterogeneous vesicles, thin vesicle walls and smooth surfaces (Fig. 3.7e, g). Vesicles are generally coalescent and slightly deformed. T15-5 is characterised by relatively higher proportions of free crystals (Fig. 3.9a). Clast surfaces are smooth compared to T15-1 dense clasts but show step-like features and sharp edges. Scoriaceous clasts show both clasts with dense groundmass and isolated large vesicles (Fig. 3.7d) as well as clasts with thin vesicle walls and closely spaced homogeneous vesicles. BV juveniles display dense, smooth-fluidal groundmass with sparse medium-sized vesicles (Fig. 3.7i).

T16 (“Tf7”) overlies T15 directly at Loc. 3 and WP295, while it is separated by millimetric soil/weathered ash in sections WP290 and Loc. 1. The best exposures are in the SE, where it comprises a thin (<10 mm) bed of medium, pumiceous ash with sparse fine lapilli (T16-1) and an indistinct overlying bed of dark fine ash (T16-2, Fig. 3.4). This member is difficult to identify anywhere else due to the lack of distinct characteristics and the absence of distinct encompassing soil.

T17 (“Tf8”): A maximum age for this member is constrained by a radiocarbon age of 525 ± 25 cal BP (Wk48878, 95.4% probability). The main part of this member is composed of repeated alternations of millimetre- to sub-millimetre-thick, light grey and dark grey fine to medium ashes (Fig. 3.5d) with few lapilli-sized pumiceous beds. The best preserved and most detailed tephra sequences occur at Loc. 3 (Fig. 3.4, Fig. 3.5d), where twelve beds can be distinguished. T17 is subdivided into six subunits: T17-1 consists of a dark massive medium ash, mainly dispersed to the East (Loc. 1, Fig. S3.1). T17-2 is the most distinct bed of this unit, consisting of lapilli-sized white pumice pyroclasts with the main dispersal towards the SE (Loc. 3, Fig. 3.4). T17-3: Bedset of laminated medium grey, fine to medium ash, with four clearly distinct beds at Loc. 3 (Fig. 3.5d). The uppermost bed contains lapilli-sized clasts at location WP290 and has a sharp upper contact, marked by oxidised material at some outcrops. T17-4 is represented by a massive dark medium ash at Loc. 3, which is generally of greater thickness than the other beds. T17-5: Bedset of medium grey to brownish fine to medium ash showing variable thickness (usually <10 mm). Where contacts are distinct, beds appear to be capped by lighter coloured sub-millimetric very fine to fine ash. Some beds are more distinct and can be correlated throughout several outcrops. At the type location Loc. 3, at least four beds, separated by sharp contacts can be distinguished (Fig. 3.4, Fig. 3.5d). T17-6 is represented by the uppermost weakly laminated bed that gradually fades into the juxtaposed soil. It is characterised by a distinct basal beige fine ash, occurring mainly between Loc. 1 and Loc. 2.

T18 is an indistinct SBA, forming pockets of ~5 mm thickness at Loc. 3 (Fig. 3.4). This member is composed of light grey very fine ash and is correlated based on its stratigraphic position relative to the encompassing members T17 and T19. At Loc. 2, a tephra unit in the same stratigraphic position comprises pockets (<10 mm thickness) of medium grey fine ash with a millimetric light grey basal very fine ash (Fig. S3.2).

T19, T20, T21, T22 and T23 are separated by soil sequences of similar thickness (Fig. 3.5e) and are best exposed in the SE. T19 and T20 show distinguishing characteristics (Fig. 3.5f) and exhibit a wider dispersal, compared to the other members:

T19 (“Tf9”) contains several beds with multiple distinct light grey beds at the base, overlain by dark coarse ash and intercalated sub-millimetric very fine ash (Fig. 3.5f). T19-1 is a thin, massive, medium grey, fine ash, which can be clearly distinguished only in sections to the SE (e.g., Loc. 3, WP293, WP290, Fig. 3.1). T19-2: This subunit is a distinct light grey-coloured very fine to fine ash bed that has a wavy aspect and variable thickness (generally <5 mm). At Loc. 1, which is perpendicular to the main SE-directed dispersal axis, T19-1 and T19-2 appear as a single, indistinctly laminated bed with a characteristic light grey millimetric lamina in the middle (Fig. 3.5f). T19-3: Dark, massive bed, composed of fine ash, which shows traces of laminations and is capped by a distinct olive brown very fine to fine ash layer at WP290 and Loc. 1. T19-4 constitutes the main bed of this unit and is composed of dark, medium to coarse ash. It is 12 mm thick at WP250 and 16 mm at Loc. 2 and shows a massive texture with sharp upper and lower contacts. The main dispersal is between Loc. 1 and Loc. 2. T19-5: This subunit comprises of faintly laminated, olive brown to grey, very fine to fine ash, with main dispersal between Loc. 3 and Loc. 1, where it is <5 mm thick.

T20 (“Tf10”): This MBA member forms a complex succession containing several beds of dark ash interbedded with light-coloured coarser pyroclasts with grain size up to fine lapilli. T20-1: Medium grey, very fine to fine ash that is indistinctly laminated. It shows a sharp upper contact and is best exposed in sections to the E, where it is 12 mm thick (Loc. 1, Fig. S3.1). T20-2 is represented by massive, dark, fine to medium ash. In the SE and NE, T20-1 and T20-2 form a conjunct laminated bed of 20 mm without distinct internal contacts (i.e., Loc. 3, Fig. 3.4). T20-3: This bed contains beige, very fine to fine ash and shows a sharp lower contact. Along the main axis in SE direction, this bed has a thickness of 20 mm and contains lapilli-sized clasts (e.g., WP290). T20-4 consists in a distinct dark grey medium ash, which is capped by a weakly laminated fine to medium ash, without sharp internal contact. It shows a broad dispersal, ranging from Loc. 3 to Loc. 1. T20-5: A characteristic feature of this member is the presence of a yellowish-coloured very fine to fine ash (Fig. 3.5f), which can be correlated throughout most of the directions, but is dominant in the E-NE with a thickness of ~20 mm (e.g., Loc. 2, Fig. S3.2). This subunit is faintly laminated and has sharp contacts. T20-6 is a discontinuous light grey very fine to fine ash that is usually disturbed by overlying soil. Main dispersal is to the ESE, where it has a thickness of ~10 mm (e.g., Loc. 3, WP290).

T21, **T22** and **T23** thin out rapidly and lack distinct diagnostic features. They are correlated based on their relative stratigraphic positions to encompassing members T24 and T20 and are best exposed in ESE directions, between Loc. 3 and Loc. 1.

T21 (“Tf11”): Finely laminated unit that comprises both light grey, very fine ash and dark grey fine ash. Individual beds are best exposed in the SE (Loc. 3, WP293, Fig. 3.1), where it has a cumulative thickness of 20 mm, while at Loc. 1 in the East, no distinct features can be identified and this unit rapidly thins out, forming 13 mm thick pockets of wavy, faintly laminated ash. At Loc. 2 (Fig. S3.2), an 18 mm thick, coarse-grained lapilli-bearing unit with a dark-ash top overlies T20 (Fig. 3.5g) and is tentatively correlated with T21, based on its stratigraphic position. Here, T21 contains two beds with the lower one being associated with subunit T21-1. T21-1 consists of very poorly sorted coarse ash of brown-white colour, with subdominant fine ash. The above subunit T21-2 consists of dark fine ash.

T22 (“Tf12”): This MBA member is an indistinct, wavy unit, often preserved as 10 mm thick pockets. The main dispersal is between Loc. 3 and Loc. 1, where it shows a twofold character: At Loc. 3, T22-1 is a poorly sorted, light grey, fine ash of millimetric to sub-millimetric thickness, while the overlying T22-2 consists of a weakly laminated moderately sorted fine ash. This member is rapidly thinning towards the NE (e.g., WP250, Loc. 2), where it consists of a faintly laminated, grey, very fine to fine ash.

T23 (“Tf13”) comprises a finely laminated dark grey fine ash without distinct beds or continuous changes in deposit features, such as texture, grain size or sorting. Generally, it is preserved in pockets of maximum 10 mm thickness with a main dispersal towards the East (Loc. 1, Fig. S3.1).

T24 (“Tf14”) constitutes a dominant and widely dispersed marker unit due to stratigraphic position, thickness and distinct bed succession. The best exposures are in the ESE, between Loc. 3 and WP290, where it appears as a 30 and 62 mm thick threefold unit (e.g., Fig. 3.2, Fig. 3.4). T24-1 comprises indistinctly laminated medium grey fine ash, which is widely dispersed between Loc. 1 and Loc. 3. T24-2: This subunit shows two main dispersal directions: towards the SE (e.g., Loc. 3), it comprises massive, dark, medium ash with sharp contacts, while between Loc. 1 and Loc. 2 (Fig. S3.1, Fig. S3.2), it appears as massive, dark, medium ash with indistinct lamination. T24-3 is a finely laminated, medium grey, very fine to fine ash that contains several distinct olive green and brown-coloured sub-millimetric bands that represent a distinct feature. This bed is widely dispersed throughout the SE-E and NE. Towards Loc. 1 and Loc. 2 (E-NE), T24 appears as a 53 mm thick, predominantly twofold unit, featuring T24-2 and -3 (Fig. 3.5e).

T25 is a distinct tephra mainly dispersed between Loc. 1 and WP250 (Fig. 3.1). This MBA member is characterised by coarse ash containing fine lapilli (T25-1, Fig. S3.1) and has a bright light grey-orange colour (Fig. 3.5h). At Loc. 1, T25-2 consists of an 8 mm-thick bed of light grey-orange, fine ash, and is separated by a sharp contact from T25-1, which is 27 mm thick and has a median grain size in the coarse ash fraction. The contact between the two subunits is indistinct perpendicular to the main dispersal axis, resulting in pockets of light grey-orange, very fine ash with sparse fine lapilli.

T26 shows a distinct pinkish-grey colour and is characterised by pocketing appearance and thicknesses <10 mm (Fig. 3.5i). The median grain size lies in the very fine ash fraction (Fig. 3.4) and the deposit shows discontinuous lamination. This SBA unit contains a notably wide range of components, including white-transparent pumiceous glass as well as dark dense and glassy beige to brown juveniles. Also, sparse biotite can be identified, additional to the ubiquitous plagioclase and pyroxenes. Major element analysis of juvenile glass shows that the transparent pumiceous glass is characterised by higher K_2O contents (4–6 wt%) and lower FeO compositions (2–4 wt%, Fig. 3.8), compared to the known composition for TgVC volcanoes (Fig. 3.8, Moebis et al., 2011). Together with the observation that biotite is rare in Mt. Ruapehu andesites, this suggest that this tephra contains pyroclastic material from the Mt. Taranaki-sourced Burrell eruption (dated at AD 1655; Druce, 1966; Platz et al., 2007a). Interestingly, other juvenile glasses show a composition, typical of Mt. Ruapehu, suggesting the two volcanoes erupted either contemporaneous or within short timescales.

This tephra unit constitutes an important chronostratigraphic marker as it can be readily identified by its stratigraphic position between the two dominant marker units T24 and T27 (Fig. 3.4, Fig. S3.1, Fig. S3.2) as well as by its distinct light grey-pinkish appearance and fine grain size (Fig. 3.5i).

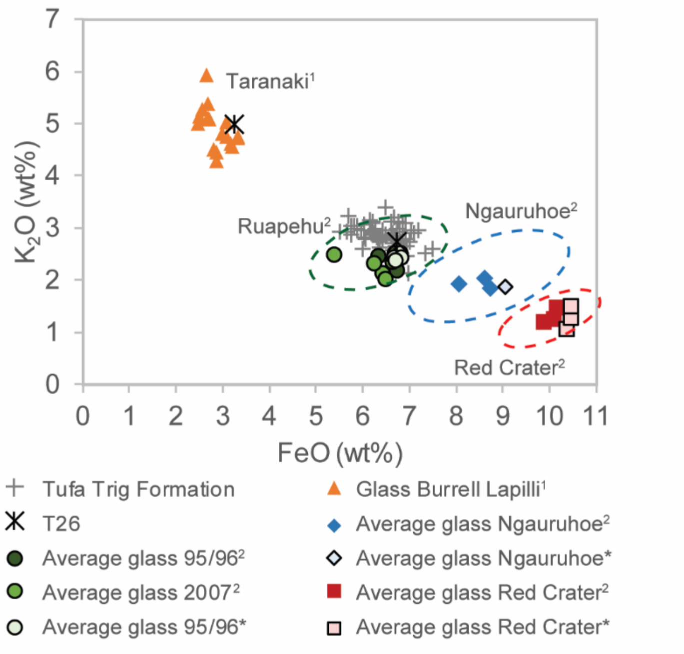

Fig. 3.8: K_2O vs FeO discrimination diagram, used to fingerprint glass compositions after Moebis et al. (2011). Major element groundmass glass compositions are reported as averages and normalised to 100 on a volatile-free basis. Grey plus signs mark compositions for individual subunits of the 31 tephra members of the Tufa Trig Formation. Glass compositions of tephra member T26 are marked by black stars. Note the two different compositions. Reference data is reported ¹after Platz et al. (2007a) for the Taranaki-sourced Burrell Lapilli and ²after Moebis et al. (2011) for the Tongariro Volcanic Centres. Circles mark glass compositions from the historical 2007 and 1995–1996 eruptions from Mt. Ruapehu, diamonds mark historical Ngauruhoe eruptions from 1954 and 1975 and squares represent eruptive material from Red Crater. *Glass shards from historical Mts. Ruapehu, Ngauruhoe and Red Crater eruptions were re-analysed together with Tufa Trig glass shards and are reported for comparison. Values shown in this graph are reported in Supplementary Tables S3.2 and S3.3.

T27 (“Tf15”): In SE and E sections (Loc. 3 to Loc. 1), this member consists of a medium grey-blueish, fine ash with indistinct light grey laminae. In the NE however, such as Loc. 2, T27 is 40 mm thick and contains ash and fine pumiceous lapilli of white and orange colour, which often show evidence of alteration (Fig. 3.5j, Fig. S3.2).

T28 (“Tf16”) is a fine ash-dominated member. Between Loc. 3 and Loc. 1 (SE-E), this MBA unit is 20 to 25 mm thick and shows discontinuous sub-millimetre to millimetre laminae that are characterised by oscillating grain size. In other locations, such as WP250 or Loc. 2, it occurs as a faintly laminated, often wavy and pocketing unit. In few locations to the E (e.g., WP327, Fig. 3.1), it displays a millimetre-thick light grey base (T28-1).

T29 (“Tf17”) is found mainly between Loc. 1 and Loc. 2 (Fig. S3.1, Fig. S3.2), where it contains three distinct beds. T29-1 is a characteristic bright, light grey, fine ash bed that is weakly laminated and widely dispersed between Loc. 1 and Loc. 2 (Fig. 3.5k). T29-2: At Loc. 1, this bed is characterised by orange to dark-coloured coarse ash and has a thickness of 12 mm. T29-3 is represented by a finely laminated dark to medium grey fine ash, with a main dispersal towards the ESE (WP290).

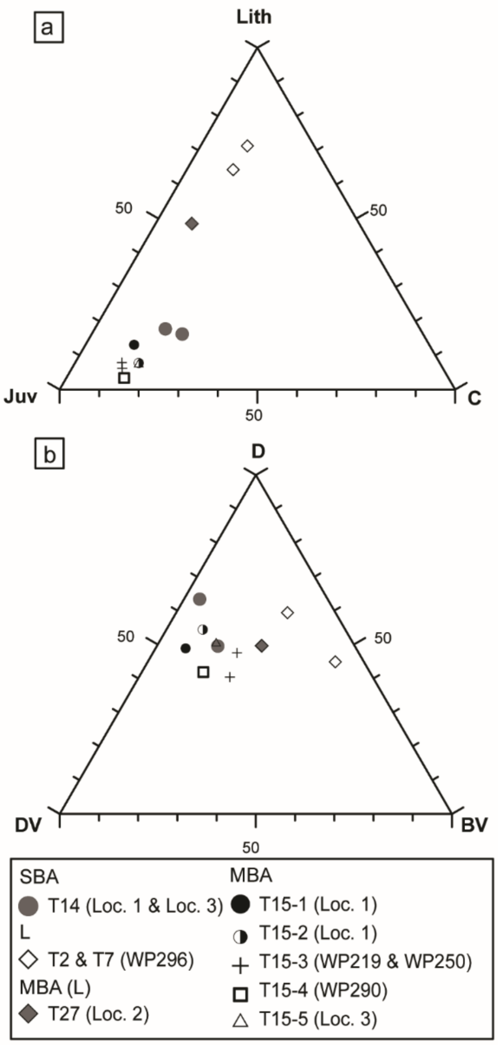

Fig. 3.9: Ternary plots showing the results of componentry analysis for selected key samples as summarised in Table 3.1. Single bed ash (SBA) unit T14 is shown as grey circles. Lapilli (L) units T2 and T7 are shown as empty diamonds. Multi-bed ash unit T27 (MBA (L)) is shown by a grey diamond. Key samples representing individual subunits of the multi-bed ash (MBA) unit T15 are shown for their main dispersal directions as follows: T15-1 (black circle) at Loc. 1, T15-2 (half circle) at Loc. 1 and T15-3 (plus signs) at WP250 and WP219, in line with the bilobate dispersal of this subunit. T15-4 (WP290) is represented by squares and T15-5 is shown at Loc. 3 (triangles). a) Componentry is shown as percentages of lithic clasts (Lith), juvenile clasts (Juv) and crystals (C) calculated relative to number of clasts counted. b) Percentages of the different types of juvenile clasts calculated relative to the number of juvenile shards with D: dark dense clasts, DV: dark vesicular clasts and BV: light-coloured vesicular glass.

T30 and T31 are close to the surface where poor soil compaction and vegetation (i.e. roots) perturbate the deposits, hindering the identification of discrete features and individual beds. Accordingly, the correlation of these units is tentative and is based mainly on their stratigraphic position relative to the topsoil and to other members.

T30 (“Tf18”): This MBA member consists of a thick, finely laminated sequence of medium and light grey, predominantly fine ash, with indistinct pockets of dark medium ash. A general fining upwards can be observed, constituting the twofold character of the unit, but a discrete contact can be identified only at Loc. 3 (Fig. 3.4). Here, it is marked by the presence of a millimetric light grey very fine to fine ash bed and shows an overall thickness of 34 mm (Fig. 3.4), while it is 60 mm thick at Loc. 1 (Fig. S3.1).

T31 occurs in the uppermost 10–20 cm from today’s surface. It is in a distinct stratigraphic position relative to the members below, from which T31 is separated by a thick soil sequence at Loc. 1 (Fig. S3.1) and Loc. 2 (Fig. S3.2). At Loc. 1, this member contains at least three distinct beds (Fig. S3.1) and is 33 mm thick. T31-1 consists of a poorly compacted, light grey, very fine ash with sharp contacts. T31-2 is represented by inversely graded, fine ash. T31-3: This subunit is associated with a bed containing massive, medium grey, poorly compacted, fine ash that gradually fades into soil. Based on its stratigraphic position, T31 is correlated between Loc. 1 and Loc. 2.

T32 corresponds, in agreement with Donoghue et al. (1997), to the subplinian eruptions of 11–12 and 14–15 October 1995. However, even with careful investigations of the upper topsoil of stratigraphic sections located along downwind directions, described in Cronin et al. (2003), we were not able to identify unambiguous, discrete tephra deposits. Some unconsolidated pockets of medium grey fine ash suggest the presence and preservation of erupted material, but the deposits cannot be linked clearly to any observed events. We speculate that, in the future, compaction and burial of the topsoil and the contained tephra material might bring out discrete distinct tephra units.

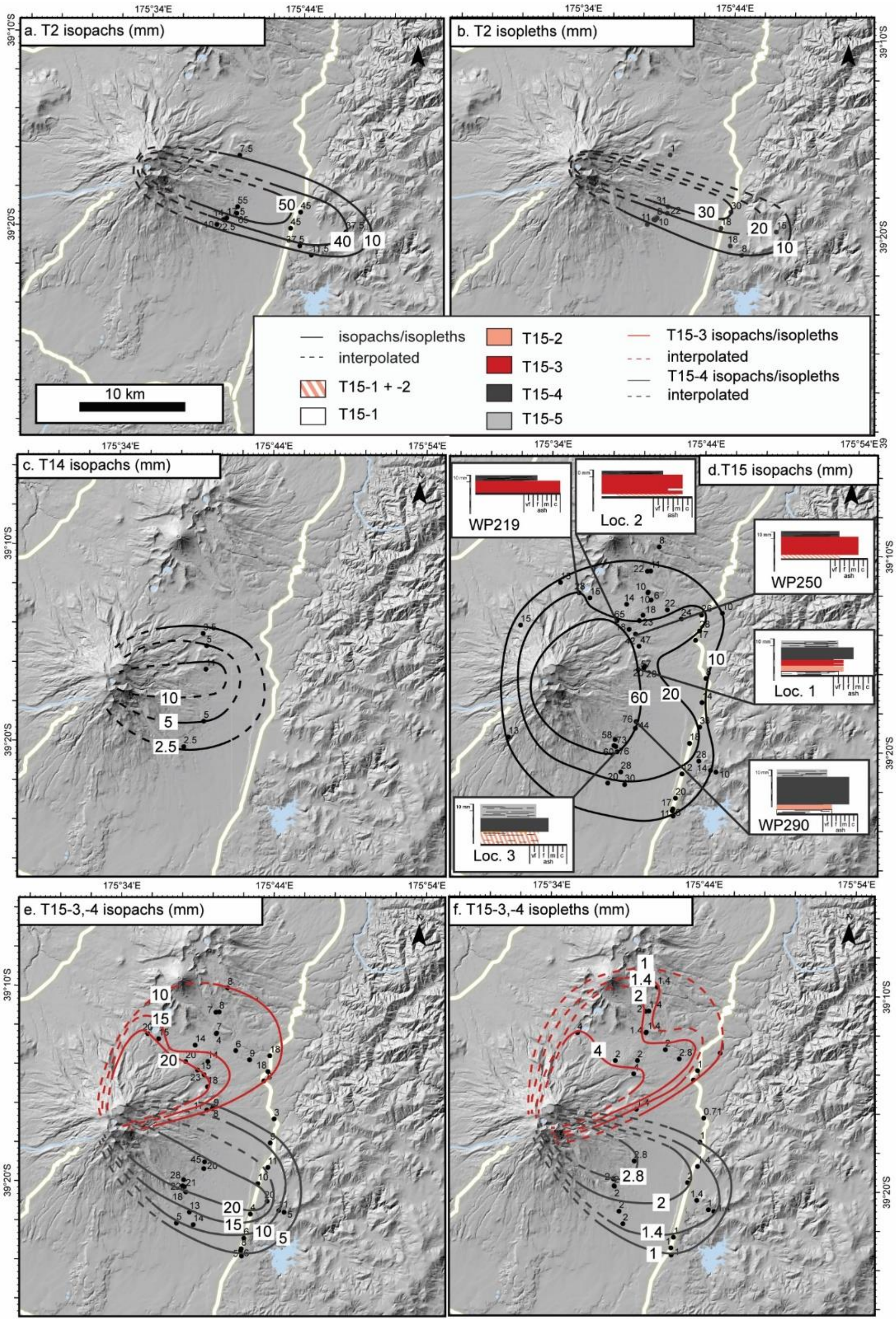

Fig. 3.10: Thickness (mm) and maximum clast (mm) distribution for characteristic tephra members T2, T14 and T15. a) Total thickness distribution of lapilli-bearing member T2. Isopach pattern shows narrow distribution towards the E-ESE. b) Distribution of maximal clast diameters of member T2. c) Total thickness distribution of single bed ash member T14. d) Cumulative multi-lobate thickness distribution of multi-bed ash unit T15. Insets show the stratigraphic succession and grain size characterisation at selected key locations and are colour-coded according to subunits. e) Thickness distribution of main subunits T15-3 (red line) and T15-4 (dark grey line). T15-3 shows a slightly bilobate distribution towards the NE, while T15-4 has a main dispersal towards the SE. f) Isopleths of subunits T15-3 (red line) towards the NE and T15-4 (dark grey line) towards the SE. Grain size of the coarsest clast class is indicated in mm.

Table 3.3: Overview of Tufa Trig Formation showing the new refined nomenclature, dispersal, deposit type, eruption classification, age constraints and the previous nomenclature after Donoghue et al. (1997).

New nomenclature	Subunits	Main dispersal	Max. number of beds at one location	Deposit type	Eruption style	Ages	Nomenclature after Donoghue et al. (1997)
T32				MBA	Low to moderate-intensity multi-phase, PM and M	AD 1995–1996	Tf19
T31	3	E	3	MBA	Small volume low-intensity multi-phase, PM-M		previously unidentified
T30	2	SE	2	MBA	Small volume low-intensity multi-phase, PM-M		Tf18
uncorrelated	1	E	1	SBA	Small volume low-intensity, PM-M		previously unidentified
T29	3	E-NE	3	MBA	Low to moderate-intensity multi-phase, PM and M		Tf17
T28	2	SE	2	MBA	Small volume low-intensity, PM-M		Tf16
T27	2	NE	2	MBA (L)	Low-intensity and moderate-intensity with different dispersal, PM and M		Tf15
uncorrelated	1	SE	1	SBA	Small volume low-intensity, PM-M		previously unidentified
T26	1	–	1	SBA	Small volume low-intensity, PM-M	AD 1655 or 295 cal BP [6]	previously unidentified
T25	2	E	2	MBA	Moderate and low-intensity, PM, H and M		previously unidentified
T24	3	SE	3	MBA	Low-moderate-intensity multi-phase, PM and M		Tf14
T23	1	SE	1	SBA	Small volume low-intensity, PM-M		Tf13
uncorrelated	1	E	1	SBA	Small volume low-intensity, PM-M		previously unidentified
T22	2	SE	2	MBA	Small volume low-intensity multi-phase, PM-M		Tf12
uncorrelated	1	SE	1	SBA	Small volume low-intensity, PM-M		previously unidentified
T21	2	L2 + SE	1	MBA	Low and moderate-intensity with different dispersal, PM-M		Tf11
T20	6	E-SE	6	MBA	Low and moderate-intensity multi-phase, PM, H and M		Tf10
T19	5	E-SE	5	MBA	Low and moderate-intensity multi-phase, PM and M		Tf9
T18	1	SE	1	SBA	Small volume low-intensity, PM-M		previously unidentified
T17	6	E-SE	12	MBA	Prolonged eruption period with semi-continuous ash venting and at least three major multi-phase eruptions of low and moderate-intensity, PM and M	525 ± 25 cal BP [5]	Tf8
T16	2	SE	2	MBA			Tf7
T15	5	E-SE	5	MBA		530 ± 20 cal BP [4]	Tf6
T14	1	E-SE	1	SBA	Small volume low-intensity eruption, PM-M		previously unidentified
T13	6	E	12	MBA	Low and moderate-intensity multi-phase eruption, PM and M	603.5 ± 46.5 cal BP [3]	Tf5
T12	1	SE	1	SBA	Small volume low-intensity, PM-M		previously unidentified
T11	4	SE + NE	6	MBA	Low and moderate-intensity multi-phase eruption, PM, H and M		Tf4
T10	1	L3	1	SBA	Small volume low-intensity, PM-M		previously unidentified
T9	1	SE	1	SBA	Small volume low-intensity, H-PM		previously unidentified
T8	1	SE	1	SBA	Small volume low-intensity, PM-M		Tf3
T7	1	SE	1	L	Small volume moderate-intensity, H-M	1337.5 ± 44.5 cal BP [2]	falsely correlated with Tf2
T6	1	SE	1	SBA	Small volume low-intensity, PM-M		previously unidentified
T5	1	SE	1	L	Small volume moderate-intensity, M		Tf2
T4	3	SE	3	MBA	Low and moderate-intensity multi-phase eruptions, PM and M		previously unidentified
T3	1	SE	1	SBA	Small volume low-intensity, PM-M		previously unidentified
T2	1	SE	1	L	Small volume moderate-intensity, H-M	1555 ± 135 cal BP [2]	Tf1
T1	1	SE	1	SBA	Small volume low-intensity, PM-M		previously unidentified
						AD 232 or 1718 ± 10 cal BP [1]	Taupo

Notes: MBA: Multi-bed ash unit; SBA: Single bed ash unit; L: Single bed lapilli unit. PM marks phreatomagmatic eruptions, while H highlights a strong excavation of the hydrothermal system and M indicates magmatic eruption styles. References for radiocarbon ages are as follows: [1] Lowe et al. (2013) and Hogg et al. (2012); [2] NZA29887 and NZA29921, unpublished data, Moebis (2010); [3] This study, Wk48586, 95.4% probability; [4] This study, Wk48634, 95.4% probability; [5] This study, Wk48878, 95.4% probability; [6] Tree-ring dating in Druce (1966), details on Burrell eruption in Platz et al. (2007a)

3.4.4 Tephra volume estimates

Deposit volumes are calculated for the three key units T2, T14 and T15 and are based on the isopachs, presented in Fig. 3.10. Different approaches for volume calculations are applied and compared in Table 3.4, including the single segment method as well as the two segment method after Fierstein and Nathenson (1992); Pyle (1989) and the Weibull function after Bonadonna and Costa (2012; 2013). Minimum volumes are estimated by the single isopach method of Legros (2000).

The different methods yield deposit volumes between 5.17 and 9.52 × 10^6 m^3 for lapilli-dominated member T2. Deposit volumes of SBA unit T14 are smaller but range in the same order of magnitude (1.10–1.35 × 10^6 m^3; Table 3.4). For MBA unit T15, volume calculations are complicated by the irregular dispersal patterns (Fig. 3.10d). Not surprisingly, volumes obtained by different methods yield quite diverging values; while the single segment and the two segment methods give similar values of 20.92–25.59 × 10^6 m^3, the single isopach method after Legros (2000) gives a smaller value of 15.19 × 10^6 m^3. The Weibull method, contrarily, gives a significantly larger volume (68.89 × 10^6 m^3, Table 3.4). Volume calculations for individual subunits give deposit volumes of 6.4–15.9 × 10^6 m^3 and 3.63–4.89 × 10^6 m^3 for the two phases T15-3 and T15-4.

Table 3.4: Parameters used for deposit volume calculations for members T2, T14 and T15

Tephra member	No. isopachs	k	1 segment (km^3) [1],[2]	k1	k2	2 segments (km^3) [1],[2]	Single isopach (km^3) [3]	θ	λ	n	R2	Weibull (km^3) [4]	Average (km^3)	Average(m^3)	SD (%)
T2	3	–0.299	0.009518	–0.081	–0.538	0.006121	0.005165	11.218	7.748	2.000	0.904	0.006735	0.006885	6.88E+06	23.528
T14	3	–0.239	0.001348	–0.206	–0.273	0.001248	0.001099	1.452	8.560	1.859	1.000	0.001145	0.001210	1.21E+06	7.978
Cumulative T15	3	–0.174	0.020924	–0.218	–0.132	0.025588	0.015193	120.173	3.879	0.525	0.999	0.068895	0.032650	3.26E+07	65.077
T15-3	3	–0.113	0.006786	–0.183	–0.094	0.008393	0.006398	5.536	15.306	1.632	0.993	0.015896	0.009368	9.37E+06	41.015
T15-4	4	–0.195	0.004894	–0.097	–0.368	0.003626	0.003672	3.560	10.314	2.000	0.977	0.003787	0.003995	3.99E+06	13.083
15-3 and 15-4			0.011680			0.012020	0.010070					0.019683	0.013363		

Notes: References for volume calculations are as follows: [1] Pyle (1989); [2] Fierstein and Nathenson (1992); [3] Legros (2000); [4] Bonadonna and Costa (2013)

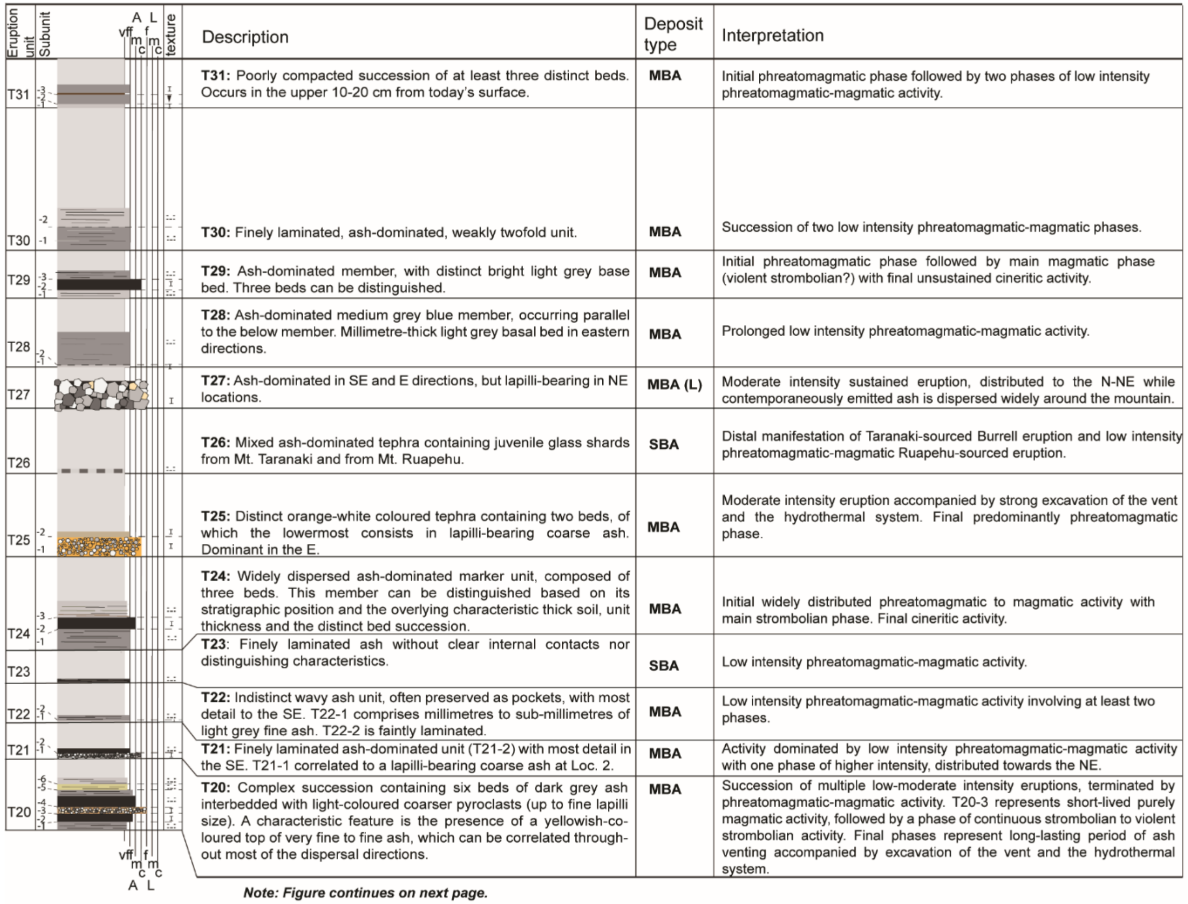

Eruption unit	Description	Deposit type	Interpretation
T31	**T31:** Poorly compacted succession of at least three distinct beds. Occurs in the upper 10-20 cm from today's surface.	**MBA**	Initial phreatomagmatic phase followed by two phases of low intensity phreatomagmatic-magmatic activity.
T30	**T30:** Finely laminated, ash-dominated, weakly twofold unit.	**MBA**	Succession of two low intensity phreatomagmatic-magmatic phases.
T29	**T29:** Ash-dominated member, with distinct bright light grey base bed. Three beds can be distinguished.	**MBA**	Initial phreatomagmatic phase followed by main magmatic phase (violent strombolian?) with final unsustained cineritic activity.
T28	**T28:** Ash-dominated medium grey blue member, occurring parallel to the below member. Millimetre-thick light grey basal bed in eastern directions.	**MBA**	Prolonged low intensity phreatomagmatic-magmatic activity.
T27	**T27:** Ash-dominated in SE and E directions, but lapilli-bearing in NE locations.	**MBA (L)**	Moderate intensity sustained eruption, distributed to the N-NE while contemporaneously emitted ash is dispersed widely around the mountain.
T26	**T26:** Mixed ash-dominated tephra containing juvenile glass shards from Mt. Taranaki and from Mt. Ruapehu.	**SBA**	Distal manifestation of Taranaki-sourced Burrell eruption and low intensity phreatomagmatic-magmatic Ruapehu-sourced eruption.
T25	**T25:** Distinct orange-white coloured tephra containing two beds, of which the lowermost consists in lapilli-bearing coarse ash. Dominant in the E.	**MBA**	Moderate intensity eruption accompanied by strong excavation of the vent and the hydrothermal system. Final predominantly phreatomagmatic phase.
T24	**T24:** Widely dispersed ash-dominated marker unit, composed of three beds. This member can be distinguished based on its stratigraphic position and the overlying characteristic thick soil, unit thickness and the distinct bed succession.	**MBA**	Initial widely distributed phreatomagmatic to magmatic activity with main strombolian phase. Final cineritic activity.
T23	**T23**: Finely laminated ash without clear internal contacts nor distinguishing characteristics.	**SBA**	Low intensity phreatomagmatic-magmatic activity.
T22	**T22:** Indistinct wavy ash unit, often preserved as pockets, with most detail to the SE. T22-1 comprises millimetres to sub-millimetres of light grey fine ash. T22-2 is faintly laminated.	**MBA**	Low intensity phreatomagmatic-magmatic activity involving at least two phases.
T21	**T21:** Finely laminated ash-dominated unit (T21-2) with most detail in the SE. T21-1 correlated to a lapilli-bearing coarse ash at Loc. 2.	**MBA**	Activity dominated by low intensity phreatomagmatic-magmatic activity with one phase of higher intensity, distributed towards the NE.
T20	**T20:** Complex succession containing six beds of dark grey ash interbedded with light-coloured coarser pyroclasts (up to fine lapilli size). A characteristic feature is the presence of a yellowish-coloured top of very fine to fine ash, which can be correlated throughout most of the dispersal directions.	**MBA**	Succession of multiple low-moderate intensity eruptions, terminated by phreatomagmatic-magmatic activity. T20-3 represents short-lived purely magmatic activity, followed by a phase of continuous strombolian to violent strombolian activity. Final phases represent long-lasting period of ash venting accompanied by excavation of the vent and the hydrothermal system.

Note: Figure continues on next page.

Fig. 3.11: Composite idealised stratigraphic profile illustrating combined field descriptions for individual tephra members, associated deposit types based on their lithosedimentological characteristics, and a qualitative interpretation of eruption intensity and style. Single bed ash units are abbreviated as SBA, multi-bed ash units are abbreviated as MBA and lapilli units are marked by L. Multi-bed ash units containing a dominant lapilli bed are marked as MBA (L). Soil and tephra thicknesses are not to scale.

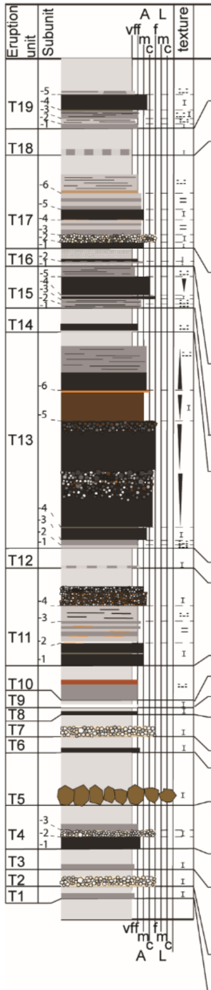

Description	Deposit type	Interpretation
T19: Five distinct, ash-dominated beds, dispersed in different directions.	**MBA**	Succession of several phases with initial phreatomagmatic and several strombolian to violent strombolian phases with intercalated ash emission.
T18: Pockets of indistinct light grey very fine ash, occurring generally in the SE.	**SBA**	Low intensity phreatomagmatic-magmatic eruption.
T17: The main part of this member is composed of repeated alterations of millimetric to sub-millimetric light grey and dark grey fine to medium ash (Fig. 5d), which coarsen and thicken in different directions. An estimated minimum number of beds, separated by sharp contacts is 12. Two beds are characterised by lapilli-sized pumiceous clasts. Radiocarbon dating yields an age of 525±25 cal BP.	**MBA**	Initial predominantly strombolian to phreatomagmatic phase progressing into violent strombolian phase. The third phase contains a series of several low intensity cineritic explosions possibly due to alternations of open and closed vent. Subsequent more sustained magmatic phase followed by a prolonged period of small-scale cineritic activity with unstable degassing conditions. Decreasing eruption energy is accompanied by ash venting.
T16: This member directly overlies T15 in few locations in the SE sectors, while it is separated from the underlying member by millimetric soil/weathered ash to the E. It consists in a thin (<10 mm) bed of medium ash to fine lapilli-sized pumices and an indistinct overlying bed of dark grey fine ash.	**MBA**	Almost continuous eruptive activity between T15 and T17, including mainly ash emission. T16 represents a major magmatic phase of larger intensity compared to the intermittent ash expulsion.
T15: Characteristic MBA tephra unit (Fig. 5c), with the main subunit marked by an often reversely graded dark grey coarse ash. Increased complexity in other sectors, resulting in at least five beds with different dispersal axes. Radiocarbon dating yields an age of 530±20 cal BP.	**MBA**	Initial phases of phreatomagmatic-magmatic character followed by a major sustained eruption phase, distributed to the NE and subsequently to the SE. Final intermittent cineritic phase leading to multiple low intensity eruptions.
T14: Characteristic SBA unit. Dark grey unit of limited thickness and dispersal with indistinct internal lamination. Light grey base in SE.	**SBA**	Low intensity phreatomagmatic-magmatic eruption.
T13: Tephra member distinct by its thickness and the presence of dominant coarse beds, containing dark grey coarse ash and pumiceous beige fine lapilli. Complex succession of at least eight beds, whose order, thickness and characteristics vary laterally. Dating of underlying soil yields age of 603.5±46.5 cal BP.	**MBA**	Phreatomagmatic opening phase. Main eruption phase with several waxing-waning phases over a relatively short time span, suggesting a semi-sustained eruption column. Short time break followed by phase T13-5 with strong vent excavation. Another predominantly magmatic phase and a final waning phase of low intensity ash emission.
T12: Light grey fA-mA of pocketing appearance.	**SBA**	Low intensity phreatomagmatic-magmatic eruption.
T11: Complex succession of at least eight beds, associated with four subunits. Beds associated with T11-2 show evidences of hydrothermal alteration. Notably widespread distribution around the ring plain. In N-NE directions, the topmost bed consists in an orange to black cA-fL.	**MBA**	Initial predominantly magmatic phase, followed by several small cineritic hydrothermal-phreatomagmatic eruptions over prolonged period of time. Subsequent ash emission. Final short-lived moderate intensity event, distributed predominantly in N-NE direction, following a short time break.
T10: Indistinct ash of pocketing appearance.	**SBA**	Low intensity phreatomagmatic-magmatic eruption.
T9: Distinct white fine ash bed.	**SBA**	Phreatomagmatic eruption strongly excavating the hydrothermal system.
T8: Ash-dominated unit with limited dispersal.	**SBA**	Low intensity phreatomagmatic-magmatic eruption.
T7: Heterolithologic lapilli-dominated unit with subdominant ash-sized components.	**L**	Moderate intensity hydrothermal-magmatic eruption.
T6: Dark fine to medium ash of pocketing appearance.	**SBA**	Low intensity phreatomagmatic-magmatic eruption.
T5: Highly vesicular, fragile pyroclasts of brown colour (Fig. 5b). Lithics consist in dense lava fragments.	**L**	Magmatic eruption of moderate intensity.
T4: Sequence of three beds. Predominant occurence as a distinct doubleband (T4-1 and -2, Fig. 5a). Middle bed is lapilli-bearing in some locations, while the encompassing beds are ash-dominated.	**MBA**	Initial phreatomagmatic cineritic phase, followed by magmatic phase and final ash venting. Breaks between individual phases.
T3: Grey very fine to fine ash pockets, characterised by discontinuous white basal pyroclasts.	**SBA**	Low intensity phreatomagmatic-magmatic eruption.
T2: Characteristic lapilli-bearing member, characterised by an orange colour, dense lithics and rounded pumices. Juvenile clasts are subordinate and consist in variable proportions of dense and vesicular glass.	**L**	Moderate intensity hydrothermal-magmatic eruption.
T1: Indistinct discontinuous grey very fine to fine ash, generally pocketing.	**SBA**	Low intensity phreatomagmatic-magmatic eruption.

Fig. 3.11: (continued)

3.5 Discussion

3.5.1 Insights into the Tufa Trig Formation

The combination of tephrostratigraphic analysis with lithosedimentological characterisation adds complexity to the existing understanding on the most recent tephra formation of Mt. Ruapehu. A broad range of deposit types is associated with low to moderate-intensity eruptions, as shown by a schematic representation of the individual sequences over the 1800 years stratigraphic record (Fig. 3.11, Fig. 3.12). This variability in deposit patterns agrees very well with the complexity known for small-volume low to moderate-intensity eruptions at other volcanoes, which includes strongly heterogeneous pyroclastic assemblages within individual beds, sudden changes in eruption style and steadiness as well as the influence of syn-eruptive changes in wind during long-lasting ash emission (i.e., Vesuvius; Cioni et al., 2008a; Cioni et al., 2008b).

The majority (~55%) of the 1800-year eruptive record is associated with MBA units, containing more than one distinct bed. This agrees well with existing studies on historically observed eruptions, showing that most volcanic eruptions comprise more than one eruption phase (Jenkins et al., 2007). In Fig. 3.12, we use the previously introduced lithosedimentological characterisations to illustrate short-term patterns and eruption progression within MBA units. Two main types of MBAs can be distinguished based on the number of beds, associated subunits and the complexity of the tephra sequence: (1) Multi-bed ash units that involve two to three phases, constitute ~35% of the known eruptive record. They contain predominantly ash-sized material that forms either indistinctly laminated beds or massive beds, composed of well sorted ash-sized material. More than one third of these sequences start with a light grey basal layer. In three cases, the ash-sized material is associated with the expulsion of coarser, up to lapilli-sized material (T21, T25 and T27). (2) Multi-bed ash units that contain four or more phases make up for 19% of the total tephra record. Two-thirds display a basal light grey ash bed, while the two sequences T11 and T17 lack this bed. Typically, at least one bed of up to lapilli-sized material can be observed, which generally follows an initial highly fragmented phase and a phase of massive ash-sized material (Fig. 3.12). Finally, 5 out of 6 sequences exhibit a finely laminated bed on top of the sequence (Fig. 3.5c, T15-5).

The similarity of patterns within the different MBA tephra sequences suggests similar underlying eruption mechanisms and allows for qualitative interpretations on eruption style. Fine grained, highly fragmented basal beds have been observed at other volcanic systems (e.g., White Island and Vesuvius), where they have been related to the opening phase (Houghton et al., 1991; Cioni et al., 1992; 2000), in some cases associated with phreatomagmatic activity. In the case of Mt. Ruapehu, the highly fragmented nature of the basal beds can be related to the presence of the Crater Lake within the active vent, which leads to violent interaction between hot magma and cool water, in particular during initial eruption phases. This agrees with the occurrence of high percentages (>60%) of blocky dense clasts with step-like and conchoidal features, accompanied by adhering dust and vesicle fillings, which are known as characteristic features linked to fuel-coolant interaction (Wohletz, 1983; Zimanowski et al., 1997; Buttner et al., 1999; Wohletz et al., 2013). Accordingly, the presence of coarse, lapilli-sized subunits in complex MBA units is typically accompanied by an increase in overall clast vesicularity while proportions of dense microcrystalline clasts decrease. This suggests an increase in the influence of magmatic fragmentation styles throughout the eruptive progression. During historical observations at Mt. Ruapehu, long-lasting or large eruption progressions have been seen to be accompanied by a displacement of the Crater Lake, leading to increasingly magmatic Strombolian and/or subplinian eruption styles (i.e. 1945 and 1995–1996, Johnston et al., 2000; Cronin et al., 2003; Scott, 2013).

Single bed ash units constitute about 35% of the 1800 years record. Generally, the lack of continuous distinct internal features suggests that these deposits are related to a single eruption phase. However, three single bed ash members show evidences of a sub-millimetric light grey basal layer, similar to that observed in MBA units. Considering also the ubiquitous discontinuous lamination, this may indicate that SBA units can represent poorly preserved manifestations of multi-phase eruptions that are at least one order of magnitude smaller than those eruptions preserved as MBA type deposits. Accordingly, SBA units could be associated with semi-continuous, low-intensity, predominantly phreatomagmatic activity.

Lapilli-bearing eruptions form ~10% of the eruptive record. Similar to SBA units, they represent one predominant eruption phase, without evidences of preserved ensuing phases. On the contrary to SBA units, however, the high vesicularity of juvenile components coupled with the significantly larger pyroclast size hints towards more magmatic fragmentation mechanisms characterised by higher energy and shorter duration. At the same time, the high proportions of alterated pumiceous and dense fragments in T2 and T7 suggest that a major component of the deposit can be related to an enhanced excavation of the hydrothermal area and pre-existing juvenile deposits. Despite this observation, the narrow dispersal patterns which distribute clasts of up to 15 mm diameter to distances of ~20 km witness relatively higher eruption energy. More detailed analysis of the componentry is needed to unequivocally prove the proportions of the hydrothermal versus magmatic component of these eruptions. For lapilli member T5, on the other hand, the highly vesicular, juvenile character of the pyroclasts in combination with subdominant proportions of monolithologic lithic dense lava fragments and clast diameters of up to 12 mm at a distance of 27 km, indicate that this member in fact represents a purely magmatic moderate intensity eruption.

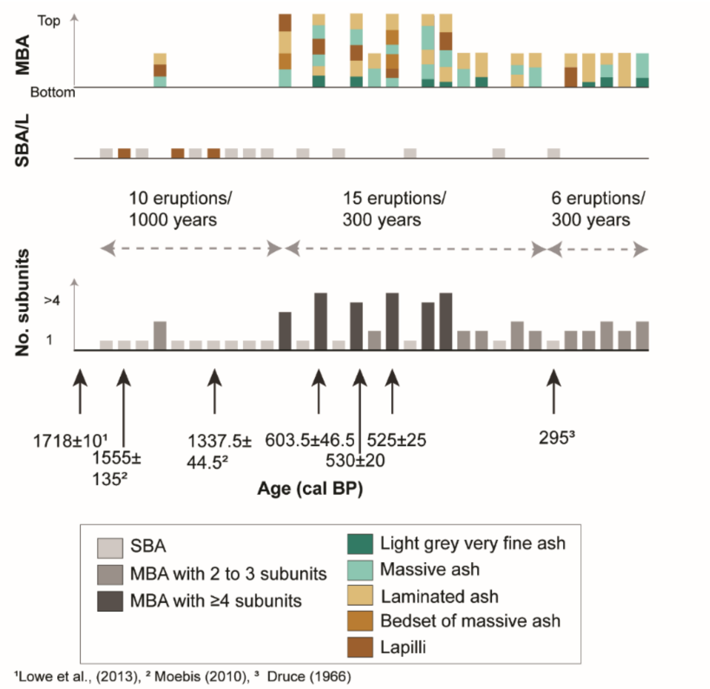

Fig. 3.12: Schematic representation of the 1800 years tephra record of Mt. Ruapehu, integrated with new and existing radiocarbon ages and the lithosedimentological classification of the 31 Tufa Trig tephra members. Members classified as single bed ash units (SBA) are reported in light grey and lapilli units (L) are shown in brown. Multi-bed ash units (MBA) with 2 to 3 subunits are reported in medium grey while complex MBAs with ≥4 subunits are shown in dark grey. For further details, see the legend in the figure.

3.5.2 Magnitude and dispersal patterns

Most of the existing literature on the estimation of eruptive parameters and classification schemes are based on Plinian-type eruption dynamics with VEI > 4 (Walker, 1973; Carey & Sparks, 1986; Wilson & Walker, 1987; Sparks et al., 1992). One major problem with applying these models to the ash-rich deposits lies in the different settling behaviour of particles <1 mm (Bonadonna et al., 1998). The low energy associated with these eruptions results in weak plumes, whose dispersal is strongly dependent on wind strength and direction (Turner & Hurst, 2001; Bonadonna et al., 2005). This results in irregular, often strongly elongated deposit distributions (Bonadonna et al., 2011; Cioni et al., 2011; Oishi et al., 2018), which cannot be adequately represented by ellipses. The deposit volumes calculated in this study represent minimum values due to several limitations: (1) the variation of preservation features and their fine-grained character complicate the identification of deposits with thicknesses <5 mm for isopach construction, (2) the distal segment is not resolved and is lacking in volume calculations and similarly, (3) no proximal segment is preserved. Nonetheless, the calculated volumes align well with the different orders of eruption magnitudes preserved in the Tufa Trig Formation. Single bed ash unit T14 shows the smallest deposit volume of 1.10–1.35 × 10^6 m^3, followed by lapilli unit T2 (5.17–9.52 × 10^6 m^3). These volumes are a magnitude smaller, compared to the cumulative volume of T15 (15.19–68.89 × 10^6 m^3, Table 3.4). Generally, the volume obtained for T15 compares very well with the previously obtained volume of ~33 × 10^6 m^3 (Tf6 in Donoghue et al., 1995; Donoghue, 1990), but it needs to be kept in mind that the previous volume is based on elliptic isopachs (cf. Fig. 5a in Donoghue et al., 1995) and does not account for the multiple lobes of the deposit (Fig. 3.10d). Isopach construction for individual phases, by contrast, has the advantage that it allows to estimate volumes during phases of different intensity. For the example of T15, the main phases T15-3 and T15-4 contribute about 40% of the total deposit volume (Table 3.4). This has important implications for the understanding of the syn-eruptive evolution of this eruption. The other implication is that both the N-NE as well as SE were affected by a significant amount of pyroclastic material (≥4 × 10^6 m^3 each, Table 3.4), over short timescales or possibly even contemporaneous. Similar scenarios are well known for Mt. Ruapehu, both for past more voluminous eruptions (Pardo et al., 2012), as well as during historical eruptions (e.g., 1945, Johnston et al., 2000; 1995–1996, Cronin et al., 2003).

3.5.3 Frequency patterns

To this stage, Mt. Ruapehu's most recent eruptive record has been considered to consist in small phreatomagmatic to magmatic eruptions, with a recurrence rate of ~100 years (Donoghue et al., 1997). In the present study, addition of thirteen members significantly increases the previously assumed frequency. Newly obtained radiocarbon ages and the identification of the Burrell Lapilli as chronostratigraphic marker allow for qualitative statements about temporal relationships between different types of deposits and their frequency, which appears to be highly variable through time (Fig. 3.12). Three main periods can be distinguished; the oldest period includes ten members T1 to T10, erupted over a time range of ~1000 years, yielding one eruption/100 years. Associated tephra members involve eruptions with predominantly one and up to three subunits (T4). The majority of tephras classify as SBA with three L-type members. The following time interval covers approximately 300 years and includes the six complex multi-bed eruptions that comprise ≥4 phases. Considering the nine SBA units that are interbedded with the MBA members, this yields an average eruption frequency of one eruption every 20 years. Eruption magnitude seems to decrease in the final 100 years of this period, resulting in the deposition of SBA and less complex MBA. The most recent time period spans a ~400-year timeframe and includes MBA units with 2 to 3 phases and SBA units, with eruptions every 60–70 years.

Studies on comparably detailed tephra records for individual volcanoes are rare and generally depend on the quality and availability of historical accounts (e.g., Vesuvius, Cioni et al., 2008a; Cotopaxi, Pistolesi et al., 2011). Conversely, deposit-based studies tend to cover larger timescales of several 1000s to 10,000s of years and focus on identifying long-term periodicities in eruption behaviour and frequency (Shiveluch, Ponomareva et al., 2007; Taranaki, Turner et al., 2009; Damaschke et al., 2017). However, recent studies at Mt. Taranaki display similar time-variant complexities in the tephra record, highlighting the importance of proximal tephra records in realistic eruption scenarios for multi-phase eruptions (Torres-Orozco et al., 2017a, 2018) and in assessing variability in eruption frequency over shorter timescales of 100s of years (Lerner et al., 2019).

3.6 Conclusions and outlook

This study presents a refined high-resolution tephrostratigraphic record of the 1800 years eruptive record of one of New Zealand's most active volcanoes, Mt. Ruapehu. A combination of lithosedimentological characterisation with tephrostratigraphy and component characterisation allows investigating the broad range of deposits associated with frequent low to moderate-intensity eruptions. Three main deposit types can be distinguished: single bed ash units, multi-bed ash units and lapilli units. Single bed ash units are characterised by small deposit volumes ($1.10–1.35 \times 10^6$ m^3) and dispersals that are limited to one main direction. Lapilli units involve similar erupted deposit volumes ($5.17–9.52 \times 10^6$ m^3) but exhibit typically narrow, elongated dispersals, reaching greater distances. Associated deposits typically consist of single beds composed almost entirely of lapilli-sized material without distinct internal changes. Multi-bed ash units comprise the most complex depositional units; they involve multiple subunits with the most detailed members containing at least 4 subunits. Total deposit volumes are an order of magnitude larger ($15.19–68.89 \times 10^6$ m^3), with the main phases typically involving volumes of $3.63–15.9 \times 10^6$ m^3. Tephra dispersal is characterised by multiple lobes in different directions.

While low to moderate-intensity eruptions make up for the most frequently observed eruptions, there are a limited number of studies that target the complexity of the associated deposits (e.g., Cioni et al., 2011, D'Oriano et al., 2011; Miyabuchi et al 2013). In the following, we outline a number of key lessons and caveats that we believe will facilitate future studies on comparable tephra sequences elsewhere and improve the existing understanding of the complexity of small to moderate explosive eruptions.

(1) In order to account for the heterogeneity of deposits associated with small to moderate explosive eruptions, creating a systematic network of field sites that manages to adequately describe the complex, limited, wind-controlled dispersal patterns proofed essential to add complexity to the existing Tufa Trig tephra record. At Mt. Ruapehu, we found that sections located in the distance range of 6 to 15 km represent and preserve tephra sequences spanning several orders of magnitude, from 1.10×10^6 m^3 to 68.89×10^6 m^3. This observation implies that erupted tephra volumes $<<1 \times 10^6$ m^3 might not be preserved as discrete units and therefore cannot be recognised with the here applied resolution. It is likely that

this threshold and the optimum distance ranges vary between different volcanoes and future studies should discuss this preservation issue.

(2) Lithosedimentological characterisation stating sequence-internal variations at bed level as well as their lateral and radial variability allows identifying and characterising individual eruption phases in detailed multi-bed units and to account for syn-eruptive changes in eruption progression of the associated multi-phase eruptions.

(3) Multi-phase eruptions constitute ~55% of the geologically preserved 1800 years record at Mt. Ruapehu. The dispersal of the here examined multi-phase eruption sequences is strongly controlled by the prevailing winds, showing complex multi-lobate deposits. Bilobate dispersal patterns can be created within a single eruption through i.e., plume-bifurcation in crosswinds (Ernst et al., 1994) or multi-directional plume dispersal due to vertically variable wind directions with plume height (Rose et al., 2008). However, in the here examined case, individual lobes can be associated with individual subunits within the multi-phase tephra sequence. Further examination of deposits from historically observed multi-phase eruptions that are characterised by marked changes in wind-direction could add a better understanding to interpreting similar dispersal patterns here and elsewhere. At Mt. Ruapehu, however, potential candidates for such studies, e.g. the 1995–1996 multi-phase eruptions, cannot yet be identified unambiguously in soil profiles.

(4) The <1800 years eruption frequency at Mt. Ruapehu appears to be variable over time, with periods of enhanced activity that comprise more complex multi-phase eruptions and periods of less frequent, less complex eruptions. This observation bears potential for future petrogenetic studies on time-variant processes in the magmatic system that control eruption frequency and magnitude over short and long-term scales.

This study illustrates how a high-resolution tephrostratigraphic framework can aid at addressing some of the challenges that come with the characterisation of fine-grained, small volume tephra deposits and help to unravel the complexity of deposits associated with low to moderate-intensity eruptions. With regards to late Holocene volcanism at Mt. Ruapehu and the Tongariro Volcanic Centres, Mt. Ruapehu’s revised two millennia tephra record adds critical detail and complexity to existing eruption frequency records, aiding hazard modelling and future risk forecasts.

3.7 Acknowledgements

This research is part of MV’s PhD research, which is funded through the research program “Quantifying exposure to specific and multiple volcanic hazards” from the Natural Hazards Research Platform (2015-MAU-PC-01) and the Resilience to Nature’s Challenges Volcano program (GNS-RNC047). MV is grateful for the Memorial Award from the Tongariro Natural History Society, which contributed to field work costs and thanks E. Brosch, R. Brahm Scott, K. Kreutz, L. Roither, A. Todde and A. Zemeny for field assistance. The authors would like to thank staff at Waiouru Military Training Area, H. Gabrielsen (Department of Conservation) and K. Wood at Ernslaw Karioi Forest for granting access to field sites. D. Feek is greatly acknowledged for help with coring and A. Hogg is thanked for radiocarbon dating. Furthermore, the authors thank two anonymous reviewers for their detailed comments, which improved the clarity of the manuscript. J. L. Macìas is thanked for editorial handling.

References

Andronico, D., Branca, S., Calvari, S., Burton, M., Caltabiano, T., Corsaro, R. A., Del Carlo, P., Garfì, G., Lodato, L., Miraglia, L., Murè, F., Neri, M., Pecora, E., Pompilio, M., Salerno, G., & Spampinato, L. (2005). A multi-disciplinary study of the 2002–03 Etna eruption: insights into a complex plumbing system. Bulletin of Volcanology, 67(4), 314-330. doi:https://doi.org/10.1007/s00445-004-0372-8

Andronico, D., Scollo, S., Caruso, S., & Cristaldi, A. (2008). The 2002–03 Etna explosive activity: Tephra dispersal and features of the deposits. Journal of Geophysical Research: Solid Earth, 113(B4).

Arrighi, S., Principe, C., & Rosi, M. (2001). Violent strombolian and subplinian eruptions at Vesuvius during post-1631 activity. Bulletin of Volcanology, 63(2), 126-150. doi:https://doi.org/10.1007/s004450100130

Bonadonna, C., & Costa, A. (2012). Estimating the volume of tephra deposits: A new simple strategy. Geology, 40(5), 415-418. doi:https://doi.org/10.1130/G32769.1

Bonadonna, C., & Costa, A. (2013). Plume height, volume, and classification of explosive volcanic eruptions based on the Weibull function. Bulletin of Volcanology, 75(8), 742. doi:https://doi.org/10.1007/s00445-013-0742-1

Bonadonna, C., Ernst, G., & Sparks, R. (1998). Thickness variations and volume estimates of tephra fall deposits: the importance of particle Reynolds number. Journal of Volcanology and Geothermal Research, 81(3), 173-187. doi:https://doi.org/10.1016/S0377-0273(98)00007-9

Bonadonna, C., Genco, R., Gouhier, M., Pistolesi, M., Cioni, R., Alfano, F., Hoskuldsson, A., & Ripepe, M. (2011). Tephra sedimentation during the 2010 Eyjafjallajökull eruption (Iceland) from deposit, radar, and satellite observations. Journal of Geophysical Research: Solid Earth, 116(B12). doi:https://doi.org/10.1029/2011jb008462

Bonadonna, C., Phillips, J. C., & Houghton, B. F. (2005). Modeling tephra sedimentation from a Ruapehu weak plume eruption. Journal of Geophysical Research, 110(B08209). doi:https://doi.org/10.1029/2004jb003515

Bronk Ramsey, C. (2017). OxCal 4.3. 2. 2017.

Buttner, R., Dellino, P., & Zimanowski, B. (1999). Identifying magma-water interaction from the surface features of ash particles. Nature, 401(6754), 688-690. doi:https://doi.org/10.1038/44364

Carey, S., & Sparks, R. S. J. (1986). Quantitative models of the fallout and dispersal of tephra from volcanic eruption columns. Bulletin of Volcanology, 48(2), 109-125. doi:10.1007/bf01046546

Cioni, R., Bertagnini, A., Andronico, D., Cole, P. D., & Mundula, F. (2011). The 512 AD eruption of Vesuvius: complex dynamics of a small scale subplinian event. Bulletin of Volcanology, 73(7), 789-810. doi:https://doi.org/10.1007/s00445-011-0454-3

Cioni, R., Bertagnini, A., Santacroce, R., & Andronico, D. (2008a). Explosive activity and eruption scenarios at Somma-Vesuvius (Italy): Towards a new classification scheme. Journal of Volcanology and Geothermal Research, 178(3), 331-346. doi:https://doi.org/10.1016/j.jvolgeores.2008.04.024

Cioni, R., D'Oriano, C., & Bertagnini, A. (2008b). Fingerprinting ash deposits of small scale eruptions by their physical and textural features. Journal of Volcanology and Geothermal Research, 177(1), 277-287. doi:https://doi.org/10.1016/j.jvolgeores.2008.06.003

Cioni, R., Gurioli, L., Sbrana, A., & Vougioukalakis, G. (2000). Precursors to the Plinian Eruptions of Thera (Late Bronze Age) and Vesuvius.

Cioni, R., Sbrana, A., & Vecci, R. (1992). Morphologic features of juvenile pyroclasts from magmatic and phreatomagmatic deposits of Vesuvius. Journal of Volcanology and Geothermal Research, 51(1), 61-78. doi:https://doi.org/10.1016/0377-0273(92)90060-Q

Cronin, S. J., Hedley, M. J., Neall, V. E., & Smith, R. G. (1998). Agronomic impact of tephra fallout from the 1995 and 1996 Ruapehu Volcano eruptions, New Zealand. Environmental Geology, 34(1), 21-30.

Cronin, S. J., Neall, V. E., Lecointre, J. A., Hedley, M. J., & Loganathan, P. (2003). Environmental hazards of fluoride in volcanic ash: a case study from Ruapehu volcano, New Zealand. Journal of Volcanology and Geothermal Research, 121, 271-291. doi:https://doi.org/10.1016/S0377-0273(02)00465-1

Cutler, N. A., Streeter, R. T., Marple, J., Shotter, L. R., Yeoh, J. S., & Dugmore, A. J. (2018). Tephra transformations: variable preservation of tephra layers from two well-studied eruptions. Bulletin of Volcanology, 80(11), 77. doi:https://doi.org/10.1007/s00445-018-1251-z

D'Oriano, C., Cioni, R., Bertagnini, A., Andronico, D., & Cole, P. D. (2011). Dynamics of ash-dominated eruptions at Vesuvius: the post-512 AD AS1a event. Bulletin of Volcanology, 73(6), 699-715. doi:10.1007/s00445-010-0432-1

Damaschke, M., Cronin, S. J., Holt, K. A., Bebbington, M. S., & Hogg, A. G. (2017). A 30,000 yr high-precision eruption history for the andesitic Mt. Taranaki, North Island, New Zealand. Quaternary Research, 87(1), 1-23. doi:https://doi.org/10.1017/qua.2016.11

Donoghue, S. L. (1991). Late Quaternary Volcanic Stratigraphy of the Southeastern Sector of the Mount Ruapehu Ring Plain New Zealand. (Doctor of Philosophy), Massey University.

Donoghue, S. L., & Neall, V. E. (2001). Late Quaternary constructional history of the southeastern Ruapehu ring plain, New Zealand. New Zealand Journal of Geology and Geophysics, 44(3), 439-466. doi:https://doi.org/10.1080/00288306.2001.9514949

Donoghue, S. L., Neall, V. E., & Palmer, A. S. (1995). Stratigraphy and chronology of late Quaternary andesitic tephra deposits, Tongariro Volcanic Centre, New Zealand. Journal of the Royal Society of New Zealand, 25(2), 115-206. doi:https://doi.org/10.1080/03014223.1995.9517487

Donoghue, S. L., Neall, V. E., Palmer, A. S., & Stewart, R. B. (1997). The volcanic history of Ruapehu during the past 2 millenia based on the record of Tufa Trig tephras. Bulletin of Volcanology, 59, 136-146. doi:https://doi.org/10.1007/s004450050181

Druce, A. (1966). Tree-ring dating of recent volcanic ash and lapilli, Mt Egmont. New Zealand journal of botany, 4(1), 3-41.

Dugmore, A., Streeter, R., & Cutler, N. (2018). The role of vegetation cover and slope angle in tephra layer preservation and implications for Quaternary tephrostratigraphy. Palaeogeography, Palaeoclimatology, Palaeoecology, 489, 105-116. doi:https://doi.org/10.1016/j.palaeo.2017.10.002

Ernst, G. G. J., Davis, J. P., & Sparks, R. S. J. (1994). Bifurcation of volcanic plumes in a crosswind. Bulletin of Volcanology, 56(3), 159-169. doi:10.1007/bf00279601

Fierstein, J., & Nathenson, M. (1992). Another look at the calculation of fallout tephra volumes. Bulletin of Volcanology, 54(2), 156-167. doi:https://doi.org/10.1007/bf00278005

Graettinger, A. H., Manville, V., & Briggs, R. M. (2009). Depositional record of historic lahars in the upper Whangaehu Valley, Mt. Ruapehu, New Zealand: implications for trigger mechanisms, flow dynamics and lahar hazards. Bulletin of Volcanology, 72(3), 279-296. doi:https://doi.org/10.1007/s00445-009-0318-2

Hobden, B. J., Houghton, B. F., Davidson, J. P., & Weaver, S. D. (1999). Small and short-lived magma batches at composite volcanoes: time windows at Tongariro volcano, New Zealand. Journal of the Geological Society, 156(5), 865-868. doi:https://doi.org/10.1144/gsjgs.156.5.0865

Hodgson, K. A., Lecointre, J. A., & Neall, V. E. (2007). Onetapu Formation: The last 2000 yr of laharic activity at Ruapehu volcano, New Zealand. New Zealand Journal of Geology and Geophysics, 50(2), 81-99. doi:https://doi.org/10.1080/00288300709509823

Hogg, A., Lowe, D. J., Palmer, J., Boswijk, G., & Ramsey, C. B. (2012). Revised calendar date for the Taupo eruption derived by 14C wiggle-matching using a New Zealand kauri 14C calibration data set. The Holocene, 22(4), 439-449. doi:https://doi.org/10.1177/0959683611425551

Hogg, A. G., Hua, Q., Blackwell, P. G., Niu, M., Buck, C. E., Guilderson, T. P., Heaton, T. J., Palmer, J. G., Reimer, P. J., & Reimer, R. W. (2013). SHCal13 Southern Hemisphere calibration, 0–50,000 years cal BP. Radiocarbon, 55(4), 1889-1903. doi:https://doi.org/10.2458/azu_js_rc.55.16783

Holasek, R. E., Self, S., & Woods, A. W. (1996). Satellite observations and interpretation of the 1991 Mount Pinatubo eruption plumes. Journal of Geophysical Research: Solid Earth, 101(B12), 27635-27655. doi:https://doi.org/10.1029/96JB01179

Houghton, B. F., & Nairn, I. A. (1991). The 1976–1982 Strombolian and phreatomagmatic eruptions of White Island, New Zealand: eruptive and depositional mechanisms at a 'wet' volcano. Bulletin of Volcanology, 54(1), 25-49. doi:https://doi.org/10.1007/BF00278204

Inman, D. L. (1952). Measures for describing the size distribution of sediments. Journal of Sedimentary Research, 22(3).

Jenkins, S. F., Magill, C. R., & McAneney, K. J. (2007). Multi-stage volcanic events: A statistical investigation. Journal of Volcanology and Geothermal Research, 161(4), 275-288. doi:https://doi.org/10.1016/j.jvolgeores.2006.12.005

Johnston, D. M., Houghton, B. F., Neall, V. E., Ronan, K. R., & Paton, D. (2000). Impacts of the 1945 and 1995-1996 Ruapehu eruptions, New Zealand: An example of increasing societal vulnerability. Geological Society of America Bulletin, 112(5), 720-726. doi:https://doi.org/10.1130/0016-7606(2000)112<720:IOTARE>2.0.CO;2

Lecointre, J., Hodgson, K., Neall, V., & Cronin, S. (2004). Lahar-Triggering Mechanisms and Hazard at Ruapehu Volcano, New Zealand. Natural Hazards, 31(1), 85-109. doi:https://doi.org/10.1023/B:NHAZ.0000020256.16645.eb

Legros, F. (2000). Minimum volume of a tephra fallout deposit estimated from a single isopach. Journal of Volcanology and Geothermal Research, 96(1-2), 25-32. doi:https://doi.org/10.1016/S0377-0273(99)00135-3

Lerner, G. A., Cronin, S. J., Bebbington, M. S., & Platz, T. (2019). The characteristics of a multi-episode volcanic regime: the post-AD 960 Maero Eruptive Period of Mt. Taranaki (New Zealand). Bulletin of Volcanology, 81(11), 61. doi:https://doi.org/10.1007/s00445-019-1327-4

Lowe, D. J., Blaauw, M., Hogg, A. G., & Newnham, R. M. (2013). Ages of 24 widespread tephras erupted since 30,000 years ago in New Zealand, with re-evaluation of the timing and palaeoclimatic implications of the Lateglacial cool episode recorded at Kaipo bog. Quaternary Science Reviews, 74, 170-194. doi:https://doi.org/10.1016/j.quascirev.2012.11.022

Martin-Del Pozzo, A. L., González-Morán, T., Espinasa-Pereña, R., Butron, M. A., & Reyes, M. (2008). Characterization of the recent ash emissions at Popocatepetl Volcano, Mexico. Journal of Volcanology and Geothermal Research, 170(1), 61-75. doi:https://doi.org/10.1016/j.jvolgeores.2007.09.004

Miller, S. A. (2011). April 2010 UK Airspace closure: Experience and impact on the UK's air-travelling public and implications for future travel. Journal of Air Transport Management, 17(5), 296-301. doi:https://doi.org/10.1016/j.jairtraman.2011.03.008

Miyabuchi, Y., Hanada, D., Niimi, H., & Kobayashi, T. (2013). Stratigraphy, grain-size and component characteristics of the 2011 Shinmoedake eruption deposits, Kirishima Volcano, Japan. Journal of Volcanology and Geothermal Research, 258, 31-46. doi:https://doi.org/10.1016/j.jvolgeores.2013.03.027

Miyabuchi, Y., Ikebe, S.-i., & Watanabe, K. (2008). Geological constraints on the 2003–2005 ash emissions from the Nakadake crater lake, Aso Volcano, Japan. Journal of Volcanology and Geothermal Research, 178(2), 169-183. doi:https://doi.org/10.1016/j.jvolgeores.2008.06.025

Moebis, A. (2010). Understanding the Holocene explosive eruption record of the Tongariro Volcanic Centre, New Zealand. (Doctor of Philosophy), Massey University, Palmerston North.

Moebis, A., Cronin, S. J., Neall, V. E., & Smith, I. E. (2011). Unravelling a complex volcanic history from fine-grained, intricate Holocene ash sequences at the Tongariro Volcanic Centre, New Zealand. Quaternary International, 246(1–2), 352-363. doi:http://dx.doi.org/10.1016/j.quaint.2011.05.035

Murphy, M. A., & Salvador, A. (1999). International stratigraphic guide—an abridged version. Episodes., 22(4), 255.

Newhall, C. G., & Self, S. (1982). The volcanic explosivity index (VEI) an estimate of explosive magnitude for historical volcanism. Journal of Geophysical Research: Oceans, 87(C2), 1231-1238. doi: https://doi.org/10.1029/JC087iC02p01231

Oishi, M., Nishiki, K., Geshi, N., Furukawa, R., Ishizuka, Y., Oikawa, T., Yamamoto, T., Nanayama, F., Tanaka, A., Hirota, A., Miwa, T., & Miyabuchi, Y. (2018). Distribution and mass of tephra-fall deposits from volcanic eruptions of Sakurajima Volcano based on posteruption surveys. Bulletin of Volcanology, 80(4), 42. doi:https://doi.org/10.1007/s00445-018-1215-3

Palmer, B. A. (1991). Holocene lahar deposits in the Whakapapa catchment, northwestern ring plain, Ruapehu volcano (North Island, New Zealand). New Zealand Journal of Geology and Geophysics, 34(2), 177-190. doi:https://doi.org/10.1080/00288306.1991.9514455

Pardo, N., Cronin, S., Palmer, A., Procter, J., & Smith, I. (2012). Andesitic Plinian eruptions at Mt. Ruapehu: quantifiying the uppermost limits of eruptive parameters. Bulletin of Volcanology, 74, 1161-1185. doi:https://doi.org/10.1007/s00445-012-0588-y

Pardo, N., Cronin, S. J., Palmer, A. S., & Németh, K. (2011). Reconstructing the largest explosive eruptions of Mt. Ruapehu, New Zealand: lithostratigraphic tools to understand subplinian–plinian eruptions at andesitic volcanoes. Bulletin of Volcanology, 74(3), 617-640. doi:https://doi.org/10.1007/s00445-011-0555-z

Pardo, N., Cronin, S. J., Wright, H. M., Schipper, C. I., Smith, I., & Stewart, B. (2014). Pyroclast textural variation as an indicator of eruption column steadiness in andesitic Plinian eruptions at Mt. Ruapehu. Bulletin of Volcanology, 76(5), 822. doi:https://doi.org/10.1007/s00445-014-0822-x

Pistolesi, M., Rosi, M., Cioni, R., Cashman, K. V., Rossotti, A., & Aguilera, E. (2011). Physical volcanology of the post–twelfth-century activity at Cotopaxi volcano, Ecuador: Behavior of an andesitic central volcano. GSA Bulletin, 123(5-6), 1193-1215. doi:http://dx.doi.org/10.1130/B30301.1

Platz, T., Cronin, S. J., Cashman, K. V., Stewart, R. B., & Smith, I. E. M. (2007a). Transition from effusive to explosive phases in andesite eruptions — A case-study from the AD1655 eruption of Mt.

Taranaki, New Zealand. Journal of Volcanology and Geothermal Research, 161(1–2), 15-34. doi:https://doi.org/10.1016/j.jvolgeores.2006.11.005

Platz, T., Cronin, S. J., Smith, I. E. M., Turner, M. B., & Stewart, R. B. (2007b). Improving the reliability of microprobe-based analyses of andesitic glasses for tephra correlation. The Holocene, 17(5), 573-583. doi:https://doi.org/10.1177/0959683607078982

Ponomareva, V., Kyle, P., Pevzner, M., Sulerzhitsky, L., & Hartman, M. (2007). Holocene eruptive history of Shiveluch volcano, Kamchatka Peninsula, Russia.

Pyle, D. M. (1989). The thickness, volume and grainsize of tephra fall deposits. Bulletin of Volcanology, 51(1), 1-15. doi:https://doi.org/10.1007/bf01086757

Rose, W. I., Self, S., Murrow, P. J., Bonadonna, C., Durant, A. J., & Ernst, G. G. J. (2008). Nature and significance of small volume fall deposits at composite volcanoes: Insights from the October 14, 1974 Fuego eruption, Guatemala. Bulletin of Volcanology, 70(9), 1043-1067. doi:https://doi.org/10.1007/s00445-007-0187-5

Salvador, A. (1994). International stratigraphic guide: a guide to stratigraphic classification, terminology, and procedure: Geological Society of America.

Scott, B. J. (2013). A revised catalogue of Ruapehu volcano eruptive activity: 1830-2012. GNS Science Report, 2013/45.

Siebert, L., Cottrell, E., Venzke, E., & Andrews, B. (2015). Earth's Volcanoes and Their Eruptions: An Overview. In H. Sigurdsson (Ed.), The Encyclopedia of Volcanoes (Second Edition) (pp. 239-255). Amsterdam: Academic Press.

Sparks, R. S. J., Bursik, M. I., Ablay, G. J., Thomas, R. M. E., & Carey, S. N. (1992). Sedimentation of tephra by volcanic plumes. Part 2: controls on thickness and grain-size variations of tephra fall deposits. Bulletin of Volcanology, 54(8), 685-695. doi:https://doi.org/10.1007/bf00430779

Stewart, C., Johnston, D. M., Leonard, G. S., Horwell, C. J., Thordarson, T., & Cronin, S. J. (2006). Contamination of water supplies by volcanic ashfall: A literature review and simple impact modelling. Journal of Volcanology and Geothermal Research, 158(3), 296-306. doi:https://doi.org/10.1016/j.jvolgeores.2006.07.002

Topping, W. W. (1973). Tephrostratigraphy and chronology of late quaternary eruptives from the Tongariro Volcanic Centre, New Zealand. New Zealand Journal of Geology and Geophysics, 16(3), 397-423. doi:https://doi.org/10.1080/00288306.1973.10431368

Torres-Orozco, R., Cronin, S. J., Damaschke, M., & Pardo, N. (2017a). Diverse dynamics of Holocene mafic-intermediate Plinian eruptions at Mt. Taranaki (Egmont), New Zealand. Bulletin of Volcanology, 79(11), 76. doi:10.1007/s00445-017-1162-4

Torres-Orozco, R., Cronin, S. J., Pardo, N., & Palmer, A. S. (2017b). New insights into Holocene eruption episodes from proximal deposit sequences at Mt. Taranaki (Egmont), New Zealand. Bulletin of Volcanology, 79(1), 3. doi:https://doi.org/10.1007/s00445-016-1085-5

Torres-Orozco, R., Cronin, S. J., Pardo, N., & Palmer, A. S. (2018). Volcanic hazard scenarios for multiphase andesitic Plinian eruptions from lithostratigraphy: Insights into pyroclastic density current diversity at Mount Taranaki, New Zealand. GSA Bulletin, 130(9-10), 1645-1663. doi:https://doi.org/10.1130/B31850.1

Turner, M. B., Bebbington, M. S., Cronin, S. J., & Stewart, R. B. (2009). Merging eruption datasets: building an integrated Holocene eruptive record for Mt Taranaki, New Zealand. Bulletin of Volcanology, 71(8), 903-918. doi:10.1007/s00445-009-0274-x

Turner, R., & Hurst, T. (2001). Factors Influencing Volcanic Ash Dispersal from the 1995 and 1996 Eruptions of Mount Ruapehu, New Zealand. Journal of Applied Meteorology, 40(1), 56-69. doi:https://doi.org/10.1175/1520-0450(2001)040<0056:FIVADF>2.0.CO;2

Walker, G. P. (1973). Explosive volcanic eruptions—a new classification scheme. Geologische Rundschau, 62(2), 431-446.

Walker, G. P. L. (1971). Grain-Size Characteristics of Pyroclastic Deposits. The Journal of Geology, 79(6), 696-714. doi:https://doi.org/10.1086/627699

White, J. D. L., & Houghton, B. F. (2006). Primary volcaniclastic rocks. Geology, 34(8), 677-680. doi:https://doi.org/10.1130/G22346.1

Wilson, C. J. N., Houghton, B. F., McWilliams, M. O., Lanphere, M. A., Weaver, S. D., & Briggs, R. M. (1995). Volcanic and structural evolution of Taupo Volcanic Zone, New Zealand: a review. Journal of Volcanology and Geothermal Research, 68, 1-28. doi:https://doi.org/10.1016/0377-0273(95)00006-G

Wilson, G., Wilson, T. M., Deligne, N. I., & Cole, J. W. (2014). Volcanic hazard impacts to critical infrastructure: A review. Journal of Volcanology and Geothermal Research, 286, 148-182. doi:https://doi.org/10.1016/j.jvolgeores.2014.08.030

Wilson, L., & Walker, G. P. L. (1987). Explosive volcanic eruptions - VI. Ejecta dispersal in plinian eruptions: the control of eruption conditions and atmospheric properties. Geophysical Journal of the Royal Astronomical Society, 89(2), 657-679. doi:10.1111/j.1365-246X.1987.tb05186.x

Wilson, T. M., Stewart, C., Sword-Daniels, V., Leonard, G. S., Johnston, D. M., Cole, J. W., Wardman, J., Wilson, G., & Barnard, S. T. (2012). Volcanic ash impacts on critical infrastructure. Physics and Chemistry of the Earth, Parts A/B/C, 45-46, 5-23. doi:https://doi.org/10.1016/j.pce.2011.06.006

Wohletz, K., Zimanowski, B., & Büttner, R. (2013). Magma-water interactions Modeling volcanic processes: The physics and mathematics of volcanism (pp. 230-257): Cambridge University Press, New York.

Wohletz, K. H. (1983). Mechanisms of hydrovolcanic pyroclast formation: grain-size, scanning electron microscopy, and experimental studies. Journal of Volcanology and Geothermal Research, 17, 31-63.

Zimanowski, B., Büttner, R., & Lorenz, V. (1997). Premixing of magma and water in MFCI experiments. Bulletin of Volcanology, 58(6), 491-495. doi:https://doi.org/10.1007/s004450050157

Supplementary material

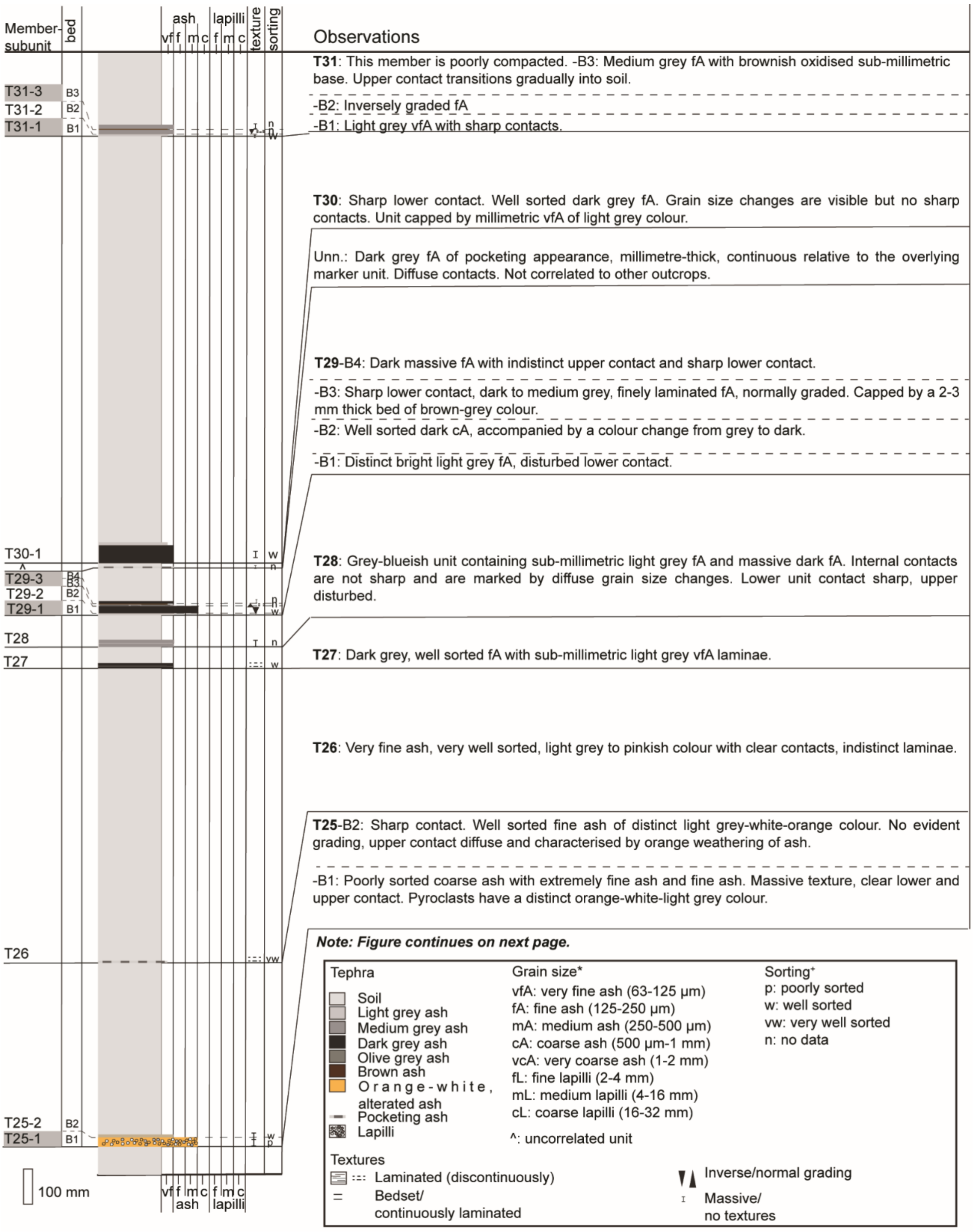

Observations

T31: This member is poorly compacted. -B3: Medium grey fA with brownish oxidised sub-millimetric base. Upper contact transitions gradually into soil.

-B2: Inversely graded fA

-B1: Light grey vfA with sharp contacts.

T30: Sharp lower contact. Well sorted dark grey fA. Grain size changes are visible but no sharp contacts. Unit capped by millimetric vfA of light grey colour.

Unn.: Dark grey fA of pocketing appearance, millimetre-thick, continuous relative to the overlying marker unit. Diffuse contacts. Not correlated to other outcrops.

T29-B4: Dark massive fA with indistinct upper contact and sharp lower contact.

-B3: Sharp lower contact, dark to medium grey, finely laminated fA, normally graded. Capped by a 2-3 mm thick bed of brown-grey colour.

-B2: Well sorted dark cA, accompanied by a colour change from grey to dark.

-B1: Distinct bright light grey fA, disturbed lower contact.

T28: Grey-blueish unit containing sub-millimetric light grey fA and massive dark fA. Internal contacts are not sharp and are marked by diffuse grain size changes. Lower unit contact sharp, upper disturbed.

T27: Dark grey, well sorted fA with sub-millimetric light grey vfA laminae.

T26: Very fine ash, very well sorted, light grey to pinkish colour with clear contacts, indistinct laminae.

T25-B2: Sharp contact. Well sorted fine ash of distinct light grey-white-orange colour. No evident grading, upper contact diffuse and characterised by orange weathering of ash.

-B1: Poorly sorted coarse ash with extremely fine ash and fine ash. Massive texture, clear lower and upper contact. Pyroclasts have a distinct orange-white-light grey colour.

Note: Figure continues on next page.

Tephra
- Soil
- Light grey ash
- Medium grey ash
- Dark grey ash
- Olive grey ash
- Brown ash
- Orange-white, alterated ash
- Pocketing ash
- Lapilli

Grain size*
- vfA: very fine ash (63-125 µm)
- fA: fine ash (125-250 µm)
- mA: medium ash (250-500 µm)
- cA: coarse ash (500 µm-1 mm)
- vcA: very coarse ash (1-2 mm)
- fL: fine lapilli (2-4 mm)
- mL: medium lapilli (4-16 mm)
- cL: coarse lapilli (16-32 mm)

^: uncorrelated unit

Sorting⁺
- p: poorly sorted
- w: well sorted
- vw: very well sorted
- n: no data

Textures
- ::: Laminated (discontinuously)
- = Bedset/ continuously laminated
- Inverse/normal grading
- I Massive/ no textures

Fig. S3.1: (continues on next page)

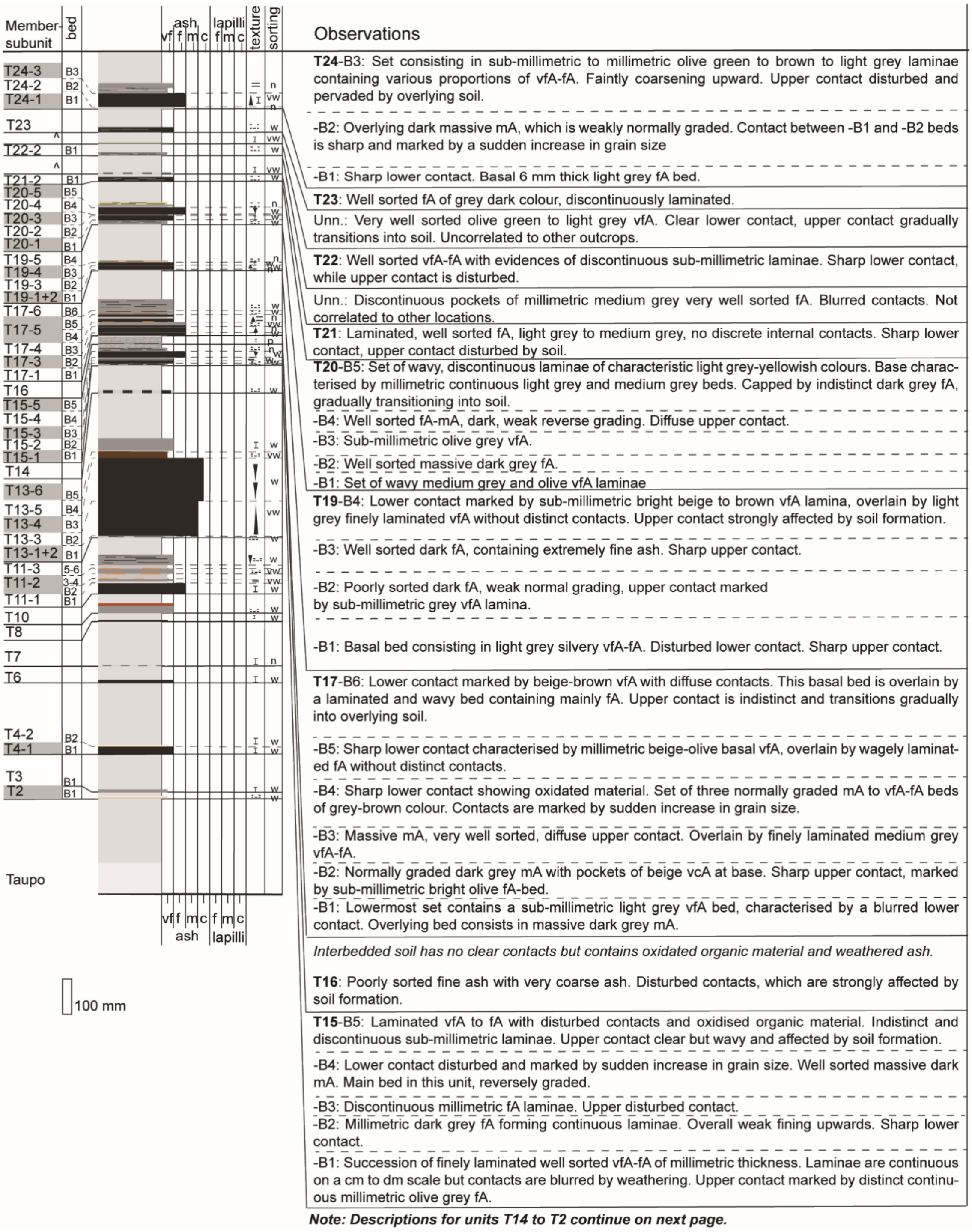

Observations

T24-B3: Set consisting in sub-millimetric to millimetric olive green to brown to light grey laminae containing various proportions of vfA-fA. Faintly coarsening upward. Upper contact disturbed and pervaded by overlying soil.

-B2: Overlying dark massive mA, which is weakly normally graded. Contact between -B1 and -B2 beds is sharp and marked by a sudden increase in grain size

-B1: Sharp lower contact. Basal 6 mm thick light grey fA bed.

T23: Well sorted fA of grey dark colour, discontinuously laminated.

Unn.: Very well sorted olive green to light grey vfA. Clear lower contact, upper contact gradually transitions into soil. Uncorrelated to other outcrops.

T22: Well sorted vfA-fA with evidences of discontinuous sub-millimetric laminae. Sharp lower contact, while upper contact is disturbed.

Unn.: Discontinuous pockets of millimetric medium grey very well sorted fA. Blurred contacts. Not correlated to other locations.

T21: Laminated, well sorted fA, light grey to medium grey, no discrete internal contacts. Sharp lower contact, upper contact disturbed by soil.

T20-B5: Set of wavy, discontinuous laminae of characteristic light grey-yellowish colours. Base characterised by millimetric continuous light grey and medium grey beds. Capped by indistinct dark grey fA, gradually transitioning into soil.

-B4: Well sorted fA-mA, dark, weak reverse grading. Diffuse upper contact.

-B3: Sub-millimetric olive grey vfA.

-B2: Well sorted massive dark grey fA.

-B1: Set of wavy medium grey and olive vfA laminae

T19-B4: Lower contact marked by sub-millimetric bright beige to brown vfA lamina, overlain by light grey finely laminated vfA without distinct contacts. Upper contact strongly affected by soil formation.

-B3: Well sorted dark fA, containing extremely fine ash. Sharp upper contact.

-B2: Poorly sorted dark fA, weak normal grading, upper contact marked by sub-millimetric grey vfA lamina.

-B1: Basal bed consisting in light grey silvery vfA-fA. Disturbed lower contact. Sharp upper contact.

T17-B6: Lower contact marked by beige-brown vfA with diffuse contacts. This basal bed is overlain by a laminated and wavy bed containing mainly fA. Upper contact is indistinct and transitions gradually into overlying soil.

-B5: Sharp lower contact characterised by millimetric beige-olive basal vfA, overlain by wagely laminated fA without distinct contacts.

-B4: Sharp lower contact showing oxidated material. Set of three normally graded mA to vfA-fA beds of grey-brown colour. Contacts are marked by sudden increase in grain size.

-B3: Massive mA, very well sorted, diffuse upper contact. Overlain by finely laminated medium grey vfA-fA.

-B2: Normally graded dark grey mA with pockets of beige vcA at base. Sharp upper contact, marked by sub-millimetric bright olive fA-bed.

-B1: Lowermost set contains a sub-millimetric light grey vfA bed, characterised by a blurred lower contact. Overlying bed consists in massive dark grey mA.

Interbedded soil has no clear contacts but contains oxidated organic material and weathered ash.

T16: Poorly sorted fine ash with very coarse ash. Disturbed contacts, which are strongly affected by soil formation.

T15-B5: Laminated vfA to fA with disturbed contacts and oxidised organic material. Indistinct and discontinuous sub-millimetric laminae. Upper contact clear but wavy and affected by soil formation.

-B4: Lower contact disturbed and marked by sudden increase in grain size. Well sorted massive dark mA. Main bed in this unit, reversely graded.

-B3: Discontinuous millimetric fA laminae. Upper disturbed contact.

-B2: Millimetric dark grey fA forming continuous laminae. Overall weak fining upwards. Sharp lower contact.

-B1: Succession of finely laminated well sorted vfA-fA of millimetric thickness. Laminae are continuous on a cm to dm scale but contacts are blurred by weathering. Upper contact marked by distinct continuous millimetric olive grey fA.

Note: Descriptions for units T14 to T2 continue on next page.

Fig. S3.1: (continues on next page)

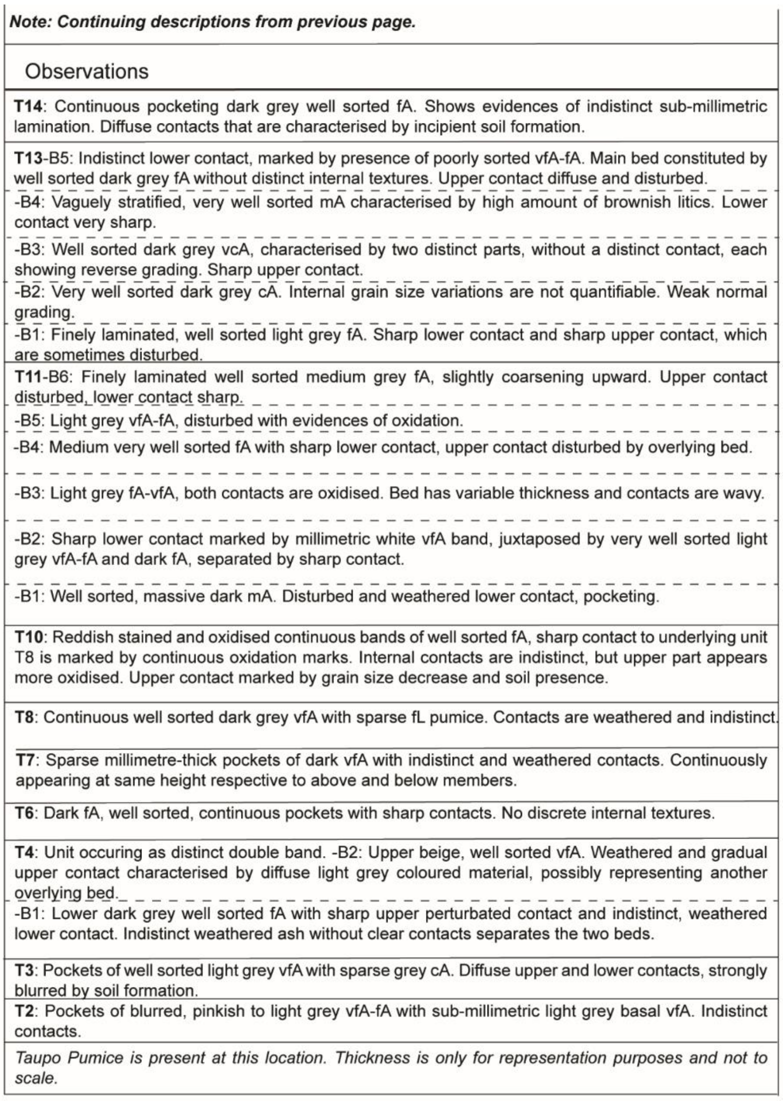

Note: Continuing descriptions from previous page.

Observations

T14: Continuous pocketing dark grey well sorted fA. Shows evidences of indistinct sub-millimetric lamination. Diffuse contacts that are characterised by incipient soil formation.

T13-B5: Indistinct lower contact, marked by presence of poorly sorted vfA-fA. Main bed constituted by well sorted dark grey fA without distinct internal textures. Upper contact diffuse and disturbed.

-B4: Vaguely stratified, very well sorted mA characterised by high amount of brownish litics. Lower contact very sharp.

-B3: Well sorted dark grey vcA, characterised by two distinct parts, without a distinct contact, each showing reverse grading. Sharp upper contact.

-B2: Very well sorted dark grey cA. Internal grain size variations are not quantifiable. Weak normal grading.

-B1: Finely laminated, well sorted light grey fA. Sharp lower contact and sharp upper contact, which are sometimes disturbed.

T11-B6: Finely laminated well sorted medium grey fA, slightly coarsening upward. Upper contact disturbed, lower contact sharp.

-B5: Light grey vfA-fA, disturbed with evidences of oxidation.

-B4: Medium very well sorted fA with sharp lower contact, upper contact disturbed by overlying bed.

-B3: Light grey fA-vfA, both contacts are oxidised. Bed has variable thickness and contacts are wavy.

-B2: Sharp lower contact marked by millimetric white vfA band, juxtaposed by very well sorted light grey vfA-fA and dark fA, separated by sharp contact.

-B1: Well sorted, massive dark mA. Disturbed and weathered lower contact, pocketing.

T10: Reddish stained and oxidised continuous bands of well sorted fA, sharp contact to underlying unit T8 is marked by continuous oxidation marks. Internal contacts are indistinct, but upper part appears more oxidised. Upper contact marked by grain size decrease and soil presence.

T8: Continuous well sorted dark grey vfA with sparse fL pumice. Contacts are weathered and indistinct.

T7: Sparse millimetre-thick pockets of dark vfA with indistinct and weathered contacts. Continuously appearing at same height respective to above and below members.

T6: Dark fA, well sorted, continuous pockets with sharp contacts. No discrete internal textures.

T4: Unit occuring as distinct double band. -B2: Upper beige, well sorted vfA. Weathered and gradual upper contact characterised by diffuse light grey coloured material, possibly representing another overlying bed.

-B1: Lower dark grey well sorted fA with sharp upper perturbated contact and indistinct, weathered lower contact. Indistinct weathered ash without clear contacts separates the two beds.

T3: Pockets of well sorted light grey vfA with sparse grey cA. Diffuse upper and lower contacts, strongly blurred by soil formation.

T2: Pockets of blurred, pinkish to light grey vfA-fA with sub-millimetric light grey basal vfA. Indistinct contacts.

Taupo Pumice is present at this location. Thickness is only for representation purposes and not to scale.

Fig. S3.1: Stratigraphic profile and lithosedimentological description of tephra members at Loc. 1, which is located 8.9 km from source to the East. Members and subunits are reported for tephra members, which are correlated between more than one location. Beds, observed in the field are numbered and shown with depositional subunits. Tephra units that could not be correlated to other locations are marked by "^". Observations include field descriptions and state median grain size and sorting parameters, obtained from grain size analysis for individual beds. Median grain size and sorting parameters are calculated after Inman (1952). Grain size classification follows the nomenclature of White & Houghton (2006).

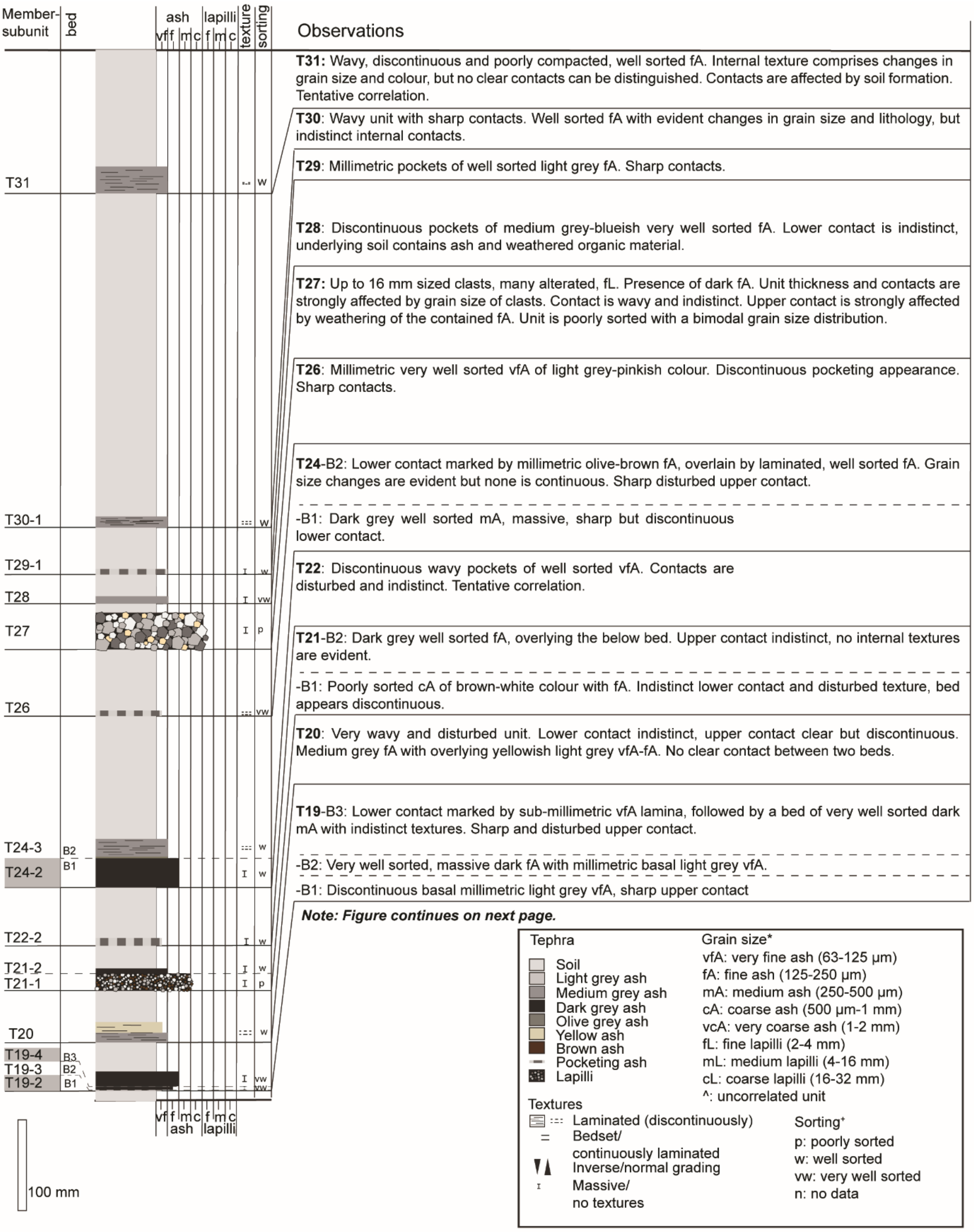

T31: Wavy, discontinuous and poorly compacted, well sorted fA. Internal texture comprises changes in grain size and colour, but no clear contacts can be distinguished. Contacts are affected by soil formation. Tentative correlation.

T30: Wavy unit with sharp contacts. Well sorted fA with evident changes in grain size and lithology, but indistinct internal contacts.

T29: Millimetric pockets of well sorted light grey fA. Sharp contacts.

T28: Discontinuous pockets of medium grey-blueish very well sorted fA. Lower contact is indistinct, underlying soil contains ash and weathered organic material.

T27: Up to 16 mm sized clasts, many alterated, fL. Presence of dark fA. Unit thickness and contacts are strongly affected by grain size of clasts. Contact is wavy and indistinct. Upper contact is strongly affected by weathering of the contained fA. Unit is poorly sorted with a bimodal grain size distribution.

T26: Millimetric very well sorted vfA of light grey-pinkish colour. Discontinuous pocketing appearance. Sharp contacts.

T24-B2: Lower contact marked by millimetric olive-brown fA, overlain by laminated, well sorted fA. Grain size changes are evident but none is continuous. Sharp disturbed upper contact.

-B1: Dark grey well sorted mA, massive, sharp but discontinuous lower contact.

T22: Discontinuous wavy pockets of well sorted vfA. Contacts are disturbed and indistinct. Tentative correlation.

T21-B2: Dark grey well sorted fA, overlying the below bed. Upper contact indistinct, no internal textures are evident.

-B1: Poorly sorted cA of brown-white colour with fA. Indistinct lower contact and disturbed texture, bed appears discontinuous.

T20: Very wavy and disturbed unit. Lower contact indistinct, upper contact clear but discontinuous. Medium grey fA with overlying yellowish light grey vfA-fA. No clear contact between two beds.

T19-B3: Lower contact marked by sub-millimetric vfA lamina, followed by a bed of very well sorted dark mA with indistinct textures. Sharp and disturbed upper contact.

-B2: Very well sorted, massive dark fA with millimetric basal light grey vfA.

-B1: Discontinuous basal millimetric light grey vfA, sharp upper contact

Note: Figure continues on next page.

Fig. S3.2: (continues on next page)

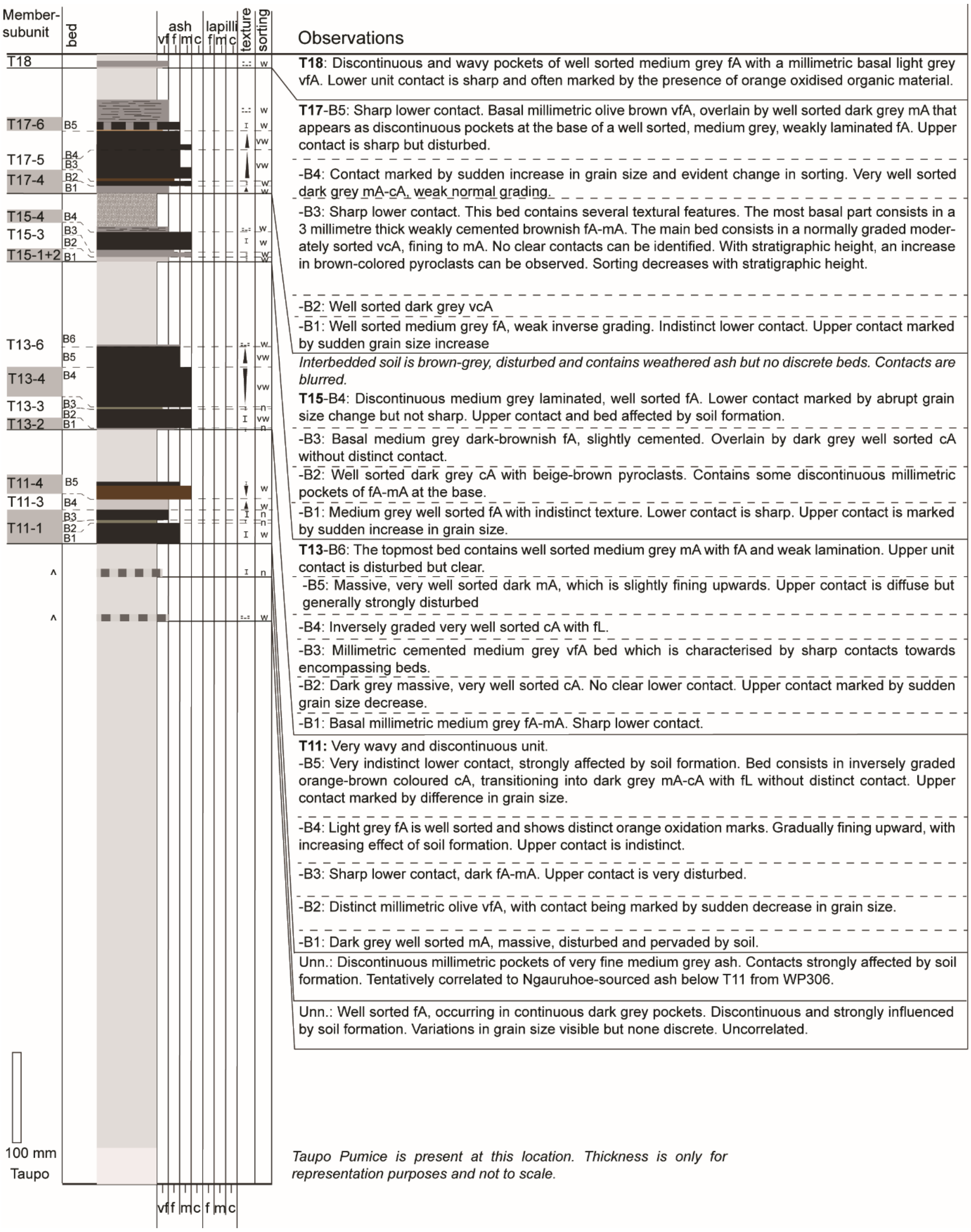

T18: Discontinuous and wavy pockets of well sorted medium grey fA with a millimetric basal light grey vfA. Lower unit contact is sharp and often marked by the presence of orange oxidised organic material.

T17-B5: Sharp lower contact. Basal millimetric olive brown vfA, overlain by well sorted dark grey mA that appears as discontinuous pockets at the base of a well sorted, medium grey, weakly laminated fA. Upper contact is sharp but disturbed.

-B4: Contact marked by sudden increase in grain size and evident change in sorting. Very well sorted dark grey mA-cA, weak normal grading.

-B3: Sharp lower contact. This bed contains several textural features. The most basal part consists in a 3 millimetre thick weakly cemented brownish fA-mA. The main bed consists in a normally graded moderately sorted vcA, fining to mA. No clear contacts can be identified. With stratigraphic height, an increase in brown-colored pyroclasts can be observed. Sorting decreases with stratigraphic height.

-B2: Well sorted dark grey vcA

-B1: Well sorted medium grey fA, weak inverse grading. Indistinct lower contact. Upper contact marked by sudden grain size increase

Interbedded soil is brown-grey, disturbed and contains weathered ash but no discrete beds. Contacts are blurred.

T15-B4: Discontinuous medium grey laminated, well sorted fA. Lower contact marked by abrupt grain size change but not sharp. Upper contact and bed affected by soil formation.

-B3: Basal medium grey dark-brownish fA, slightly cemented. Overlain by dark grey well sorted cA without distinct contact.

-B2: Well sorted dark grey cA with beige-brown pyroclasts. Contains some discontinuous millimetric pockets of fA-mA at the base.

-B1: Medium grey well sorted fA with indistinct texture. Lower contact is sharp. Upper contact is marked by sudden increase in grain size.

T13-B6: The topmost bed contains well sorted medium grey mA with fA and weak lamination. Upper unit contact is disturbed but clear.

-B5: Massive, very well sorted dark mA, which is slightly fining upwards. Upper contact is diffuse but generally strongly disturbed

-B4: Inversely graded very well sorted cA with fL.

-B3: Millimetric cemented medium grey vfA bed which is characterised by sharp contacts towards encompassing beds.

-B2: Dark grey massive, very well sorted cA. No clear lower contact. Upper contact marked by sudden grain size decrease.

-B1: Basal millimetric medium grey fA-mA. Sharp lower contact.

T11: Very wavy and discontinuous unit.

-B5: Very indistinct lower contact, strongly affected by soil formation. Bed consists in inversely graded orange-brown coloured cA, transitioning into dark grey mA-cA with fL without distinct contact. Upper contact marked by difference in grain size.

-B4: Light grey fA is well sorted and shows distinct orange oxidation marks. Gradually fining upward, with increasing effect of soil formation. Upper contact is indistinct.

-B3: Sharp lower contact, dark fA-mA. Upper contact is very disturbed.

-B2: Distinct millimetric olive vfA, with contact being marked by sudden decrease in grain size.

-B1: Dark grey well sorted mA, massive, disturbed and pervaded by soil.

Unn.: Discontinuous millimetric pockets of very fine medium grey ash. Contacts strongly affected by soil formation. Tentatively correlated to Ngauruhoe-sourced ash below T11 from WP306.

Unn.: Well sorted fA, occurring in continuous dark grey pockets. Discontinuous and strongly influenced by soil formation. Variations in grain size visible but none discrete. Uncorrelated.

Taupo Pumice is present at this location. Thickness is only for representation purposes and not to scale.

Fig. S3.2: Stratigraphic profile and lithosedimentological description of tephra members at Loc. 2, which is located 8.9 km from source to the Northeast. Members and subunits are reported for tephra members, which are correlated between more than one location. Beds, observed in the field are numbered and shown with depositional subunits. Uncorrelated tephra units are marked by "^". Observations include field descriptions and state median grain size and sorting parameters, obtained from grain size analysis for individual beds. Median grain size and sorting parameters are calculated after Inman (1952). Grain size classification follows the nomenclature of White & Houghton (2006).

Supplementary Table S3.1: Overview of key field locations, mentioned in this study

Location	Latitude	Longitude	Distance (km)	Heading (°)	Type	Comments
Loc. 1	39 16 7.5 S	175 39 59.7 E	8.9	81	Stable vegetated pedestal in Rangipo Desert	
Loc. 2	39 13 39.9 S	175 38 30.7 E	8.9	48.4	Stable vegetated pedestal	
Loc. 3	39 20 05.9 S	175 38 41.7 E	9.2	130.7	Type location after Donoghue et al. (1997)	
WP207	39 20 04.6 S	175 38 40.1 E	9.1	130.7	Edge of natively forested area	Upper part above T17 disturbed
WP219	39 12 17.8 S	175 35 58.3 E	9	19.6	Roadside outcrop in area characterised by shrub vegetation	Discordance between T17 and T19
WP227	39 14 01.6 S	175 32 12.2 E	5.8	335.9	Roadside outcrop in area characterised by shrub vegetation	
WP234	39 19 45.0 S	175 31 36.7 E	6.2	211.5	Roadside outcrop in area characterised by shrub vegetation	
WP236	39 17 21.1 S	175 30 16.2 E	5.2	260.6	Roadside outcrop in area characterised by shrub vegetation	
WP243	39 14 55.9 S	175 39 59.8 E	9.4	67.3	Stable vegetated pedestal	
WP247	39 14 05.3 S	175 39 19.1 E	9.4	56.4	Stable vegetated pedestal	Discordance between T21 and T26
WP250	39 14 19.0 S	175 39 44.8 E	9.6	60.6	Stable vegetated pedestal	
WP251	39 28 32.5 S	175 41 20.3 E	24.4	154.6	Core for radiocarbon dating in Ngamatea Swamp, Waiouru	
WP256	39 18 35.4 S	175 45 09.6 E	16.3	102.5	Roadside outcrop on side of shrub vegetated hill	Waypoint close to original Loc. 73 of Moebis (2010)
WP262	39 22 00.3 S	175 39 19.5 E	12.2	140.6	Forested area	
WP273	39 19 48.4 S	175 43 30.0 E	14.9	111.5	Roadside outcrop in area characterised by shrub vegetation	
WP290	39 18 46.6 S	175 39 56.9 E	9.4	112	Stable vegetated pedestal in Rangipo Desert	Upper part of outcrop could not be quantified, but T27, T28, T29 and T30 are present
WP292	39 20 20.6 S	175 38 46.1 E	9.6	132.4	Forested area	Above T24 disturbed
WP293	39 19 43.3 S	175 38 36.7 E	8.6	127.8	Stable vegetated pedestal in Rangipo Desert	
WP295	39 19 27.0 S	175 38 59.2 E	8.8	123.5	Stable vegetated pedestal in Rangipo Desert	Below T8 reworked
WP296	39 19 07.2 S	175 39 54.9 E	9.6	115.7	Stable vegetated pedestal in Rangipo Desert	Corresponds to the Missile Ridge Dune location in Donoghue et al. (1997). Section is disturbed.
WP297	39 19 29.2 S	175 39 07.2 E	9	123.2	Stable vegetated pedestal in Rangipo Desert	Only part below T11 characterised
WP327	39 16 05.7 S	175 40 13.9 E	9.2	81.1	Stable vegetated pedestal in Rangipo Desert	

Additional supplementary material:

Supplementary Table S3.2 (Appendix H-1): Averaged groundmass glass major element compositions for individual subunits of the Tufa Trig Formation, obtained from electron microprobe analysis. Available at https://doi.org/10.1016/j.jvolgeores.2020.106987.
Supplementary Table S3.3 (Appendix H-1): Compilation of re-normalised groundmass glass major element compositions. a) for the Taranaki-sourced Burrell Lapilli after Platz et al. (2007a) and b) for the Tongariro Volcanic Centres (TgVC) after Moebis et al. (2011). Available at https://doi.org/10.1016/j.jvolgeores.2020.106987.

Chapter 4

Reconstructing the T13 multi-phase eruption

This chapter uses a multi-parameter approach to reconstruct the eruption progression of the multi-phase T13-tephra sequence, which constitutes the largest eruption of the past two millennia. Six depositional subunits represent five eruption phases, which show consistent syn-sequence variations in terms of tephra volume and lithosedimentological characteristics, while major and trace element compositions of juvenile glass show limited variability.

Chapter 4 contains the manuscript Reconstructing the largest eruption of Mt. Ruapehu (New Zealand) in the last two millennia- a case study of prolonged multi-phase eruptions at long-lived composite volcanoes by M. Voloschina, G. Lube, C. Timm, A. Moebis & J. Procter. The manuscript is intended to be published as a research article in *Bulletin of Volcanology*. The format of the manuscript has been adapted to match the format of the thesis. In the following, the contributions of individual authors are outlined (DRC 16 - Statement of Contribution is contained in Appendix I-2 and on page 263):

Principal author: M Voloschina

Carried out: Field work, mapping, sampling

Laboratory analysis

Data analysis and interpretation

Manuscript and figure preparation

Co-authors: G. Lube

Contributed to the study by: Data discussion and interpretation

Commenting and reviewing manuscript

C. Timm

Contributed to the study by: Data discussion and interpretation

Commenting and reviewing manuscript

A.Moebis

Contributed to the study by: Assistance with field and laboratory work

Commenting manuscript

J. Procter

Contributed to the study by: Commenting manuscript

Reconstructing the largest eruption of Mt. Ruapehu (New Zealand) in the last two millennia- a case study of prolonged multi-phase eruptions at long-lived composite volcanoes

4.1 Abstract

Small to moderate explosive eruptions involve tephra volumes <0.1 km^3 and eject often a significant amount of ash-sized pyroclastic material. This limits the preservation potential of associated deposits and leads to an underrepresentation of these low to mid-intensity explosive eruptions in long-term frequency-magnitude datasets.

Mt. Ruapehu is one of New Zealand's most active volcanoes, having produced at least thirty-two small-scale eruptions over the past 1800 years. The largest of these eruptions deposited the wide-spread T13-sequence and represents a prolonged multi-phase eruption that lasted several months to years. The total deposit volume of the T13-sequence is estimated at 0.05 km^3, thus being a magnitude larger than the average deposit volumes of the past 1800 years. The T13-tephra sequence is subdivided in six depositional subunits that represent at least five eruption phases: (1) an opening phase P1 involving multiple low energy eruptions, (2) a semi-continuous violent Strombolian phase P2, (3) the prolonged violent Strombolian to subplinian phase P3, concluded by a time break of less than a year. Then, the eruption recommences with (4) a violent Strombolian phase P4 accompanied by enhanced conduit excavation and (5) a violent Strombolian to subplinian phase P5 with final ash emission. The complex ash-lapilli sequence displays a range in deposit textures, pyroclast characteristics and dispersal. While the initial phase P1 is characterised by dispersal limited to the proximal 11 km and a tephra volume of 5.61×10^5 m^3 (±33.83%), the high-intensity phase P3 constitutes about 65% of the total tephra volume, involving an average deposit volume of 3.2×10^7 m^3 (±15.07%). Multi-lobate irregular dispersal patterns together with a lateral variance of the pyroclast assemblage of individual depositional subunits suggest that the majority of the T13 subunits represent the record of several individual fall events of similar eruption style and intensity.

Throughout the sequence, minor systematic variations in major and trace element data can be recognized although overall compositions show limited variability. This is different compared to the compositional heterogeneity that has been described for recent historical products. The combination of geochemical data with textural analysis on different types of juvenile glass suggests that eruption style changes during eruption progression are mainly controlled by shallow processes in the conduit, such as late-stage crystallisation, and changes in melt viscosity and degassing. This study adds complexity on how the multi-parameter characterisation of tephra sequences associated with small-volume multi-phase eruptions can provide insights into the processes acting at different stages of the magmatic evolution. Several limitations arise from characterising this deposit type and are outlined to provide guidelines for future deposit-based studies on similarly detailed small-volume, ash-rich tephra sequences.

4.2 Introduction

The study of detailed eruption sequences from recent small-scale, ash-rich eruptions at Etna 2001, Taddeucci et al. (2002); Popocatepetl 1994–1997, Martin-Del Pozzo et al. (2008); Eyjafjallajökull 2010, Cioni et al. (2014); Shinmoedake 2011, (Miyabuchi et al., 2013; Nakada et al., 2013; Suzuki et al., 2013); Nakadake 2014–2015 (Miyabuchi et al., 2018, 2019) have contributed to improve our understanding of small to moderate explosive activity and the eruption dynamics associated with small-scale multi-phase sequences. Using the most common methods to classify volcanic eruptions, these eruptions would be classified as small to moderate explosive eruptions or low to mid-intensity eruptions (Cioni et al., 2008b; Bonadonna et al., 2013b). However, many of the existing classifications struggle to account for the complexity of syn-eruptive progression and the associated sudden changes in eruption style and intensity, thus overlooking the multi-phase character of these eruptions. Generally, the quantification of eruption magnitude and style focuses on the peak phase, with eruption styles associated with small to moderate explosive eruptions being classified as Strombolian or Vulcanian activity (Rose et al., 2008; Cioni et al., 2011; Oishi et al., 2018), or less often violent Strombolian activity (Arrighi et al., 2001; Pioli et al., 2008). In some occasions, key eruption parameters, such as column height, tephra volume or mass discharge rates can reach subplinian scales (Rose et al., 1978; Cioni et al., 2011). As opposed to the peak phases, the associated low-intensity activity often involves intermittent and prolonged ash emission (Cioni et al., 2008a) as well as one or several phases of phreatic to phreatomagmatic activity (White Island, Houghton et al., 1991; Vesuvius, Cioni et al., 2008a; Popocatepetl, Martin-Del Pozzo et al., 2008; Nakadake, Miyabuchi et al., 2019). Recent small to moderate multi-phase eruptions have addressed the syn-eruptive changes in eruption dynamics (e.g., style, magnitude and dispersal) by discussing time-resolved changes in e.g., ash characteristics (Taddeucci et al., 2002; Suzuki et al., 2013; Gaunt et al., 2016; Miyabuchi et al., 2019), ash textures (Miwa et al., 2009; 2013; Cioni et al., 2014; Miyabuchi et al., 2018), tephra dispersal (Cioni et al., 2011; Barsotti et al., 2015; Bustillos et al., 2016; Oishi et al., 2018) or geochemical signatures (Miwa et al., 2009; Cioni et al., 2011; Suzuki et al. 2013). By contrast, the small volume of the associated deposits and the fine-grained nature of the pyroclastic ejecta has, until this point, hampered the number of comparable studies on geologically preserved multi-phase tephra sequences.

Mt. Ruapehu on the North Island of New Zealand constitutes an excellent target for the study of small-volume, ash-rich tephra sequences associated with small to moderate multi-phase eruptions. Over the past 1800 years, at least thirty-one small to moderate eruptions associated with a range of eruption styles are represented in the well-preserved tephra record of the Tufa Trig Formation (Donoghue et al., 1997; Voloschina et al., 2020). About 55% of the tephra units of the past 1800 years are classified as multi-bed ash units and have been interpreted to represent multi-phase eruptions of predominantly phreatomagmatic-magmatic eruption activity (Donoghue et al., 1997; Voloschina et al., 2020). However, until this point, little information is known about eruption progression and intra-eruption changes in eruption style of these small-scale multi-phase eruptions.

In this contribution, we present a multi-parameter characterisation of the multi-bed ash-rich T13-tephra sequence, which is considered to be the deposit associated with the largest event of Mt. Ruapehu in the past 2000 years (Donoghue et al., 1997). In the following, we use the T13-sequence as a case study to provide insights into the temporal and spatial variations of a geologically preserved multi-phase tephra sequence by characterising the lateral variability in tephra dispersal, deposit characteristics and pyroclast assemblage. In a second step, we quantify variations in tephra volume, ash morphology, texture as well as in the major and trace element composition between individual eruption subunits and use this information to reconstruct the eruption progression of the T13-multi-phase eruption. This yields new insights into eruption dynamics of the largest eruption at Mt. Ruapehu in the last 2000 years and contributes to the understanding of the factors that control sudden changes in eruption style during small to moderate multi-phase eruptions at Mt. Ruapehu and similar volcanoes elsewhere.

4.2.1 Eruptive history

Mt. Ruapehu is a frequently active andesitic stratovolcano on the North Island of New Zealand, associated with the Pacific Ring of Fire. It is located on the southernmost extension of the Taupo Volcanic Zone (TVZ), where crustal thickness increases to 15–20 km (Hurst et al., 1999; Hayes, 2004; Villamor et al., 2006) compared to the central TVZ (6–8 km crustal thickness, Bryan et al., 1999). Similarly, the rift system is less evolved in the southern TVZ compared to the central segment (Villamor et al., 2006; Salmon et al., 2011). Mt. Ruapehu’s eruptive activity has undergone significant changes throughout the past ~30,000 years, regarding both eruption magnitude and frequency. Between 27,000 and 10,000 years the predominant eruption style consisted of the large Plinian eruptions of the Bullot Formation (Pardo et al., 2011; Pardo et al., 2012). These eruptions have been attributed to Mt. Ruapehu's North Crater (Pardo et al., 2011) and estimated eruption parameters involve Volcanic Explosivity Indices (VEI) of 4 to 5 and eruption column heights of up to 37 km (Pardo et al., 2012). Transitions in eruption dynamics (i.e., steady and oscillatory non-collapsing columns vs wet and dry collapsing columns) have been inferred from variations in textural and compositional characteristics (i.e., microcrystallinity, vesicle texture, groundmass glass composition; Pardo et al., 2014). From ~10,000 years to the eruption of the Taupo Ignimbrite (AD 232, Lowe et al., 2013), eruption behaviour is characterised by less voluminous activity. Twenty-two Mt. Ruapehu-sourced eruptions are known for the Mangatawai and Papakai Formations but are poorly constrained in terms of eruption style and distribution (Donoghue et al., 1995; Moebis et al., 2011). The most recent tephra formation is the Tufa Trig Formation, involving at least 32 explosive eruptions (Voloschina et al., 2020). These intermittent, small-volume eruptions (deposit volume <0.1 km^3) are characterised by an average recurrence rate of ~60 years. The presence of the 10 × 10^6 m^3 Crater Lake in the active vent system is believed to influence eruption style, resulting in predominantly small phreatic to phreatomagmatic eruptions with rare magmatic, Strombolian eruptions as inferred in Donoghue et al., 1997. However, recent studies show that about 55% of the tephras erupted in the past 1800 years are characterised by more complex patterns, involving more than one eruption phase (Voloschina et al., 2020). Lithosedimentological characterisation of the deposits and analysis of pyroclast assemblage suggests that the associated multi-bed sequences represent a range of eruption styles and intensities. The variable characteristics of individual beds within multi-bed sequences underline how dynamic the associated multi-phase eruption sequences are on timescales as short as individual eruption sequences.

Similar complexity has also been documented during the most recent eruptive episodes in 1945 (Oliver, 1945; Reed, 1945; Beck, 1950; Johnston, 1997) and 1995–1996 (Nairn et al., 1996; Cronin et al., 1998; Cronin et al., 2003; Scott, 2013). In particular the 1995–1996 eruptions involved a series of explosive events spanning phreatomagmatic to increasingly magmatic Strombolian activity with progressive Crater Lake displacement (Cronin et al., 2003). In several occasions, subplinian, semi-continuous eruption plumes were documented, involving column heights of up to ~11 km (Turner et al., 2001; Cronin et al., 2003). Petrological studies on scoria ejecta point out distinct major element signature in whole rock, matrix glass and phenocrystal compositions (i.e., SiO_2, FeO, MgO) between individual phases, indicating that the eruptions of the 1995–1996 were fed by multiple individual magma pockets and involved the injection of hot magma into crystallised small-volume magma batches, residing at shallow depth (Nakagawa et al., 1999; Nakagawa et al., 2002).

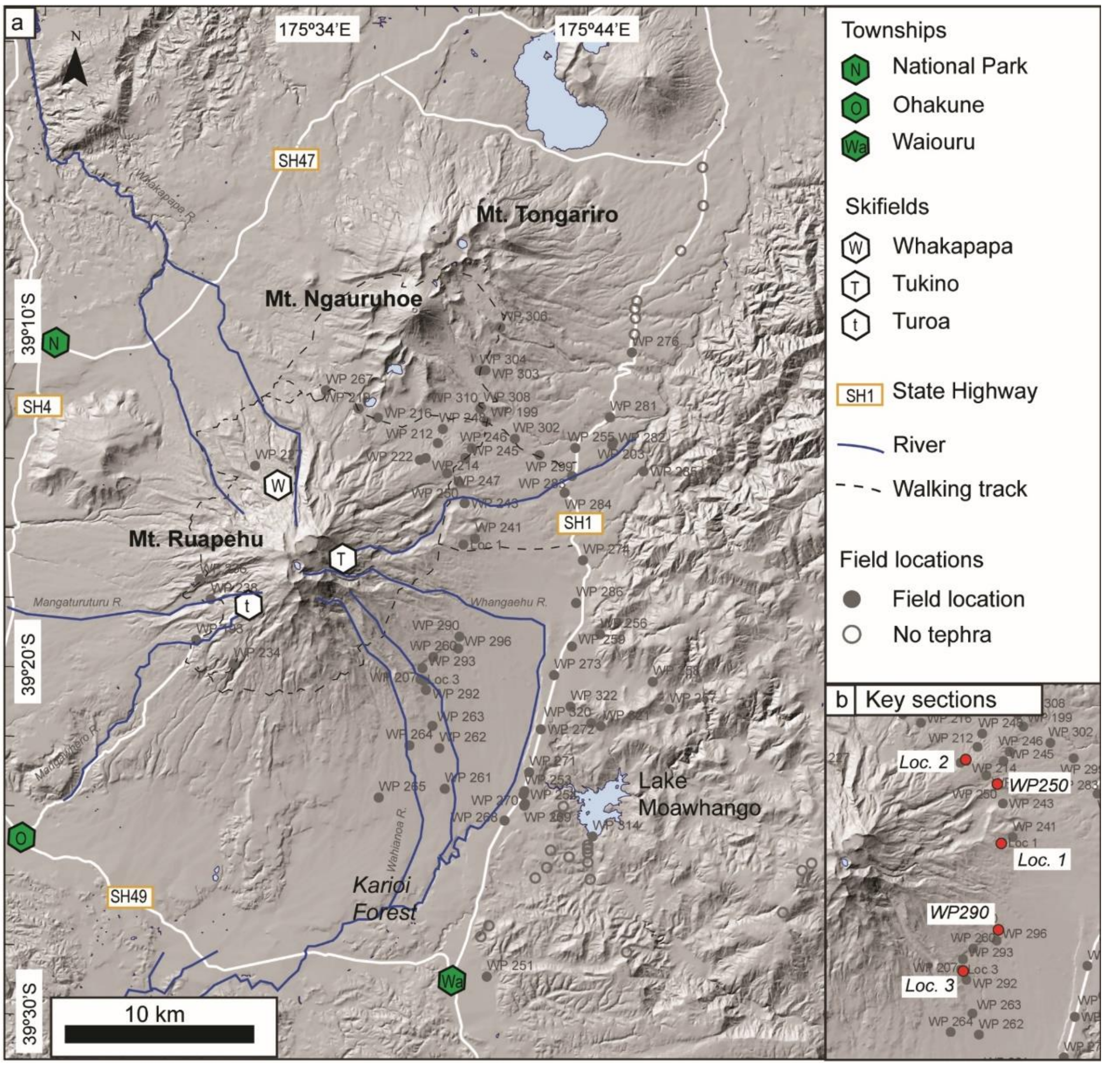

Fig. 4.1: Overview of studied area showing field locations, key sections and main geographical features. Major townships are shown by green hexagons (O: Ohakune; Wa: Waiouru; N: National Park). Skifields are marked by white hexagons (t: Turoa; T: Tukino; W: Whakapapa). Main state highways are marked in white and hiking tracks are represented by black dashed lines. The underlying hillshade view is based the 8 m digital elevation model from the LINZ Data service (https://data.linz.govt.nz) that is based on the 2012 LINZ Topo50 map series. Investigated field locations that do not contain discrete tephra units, are reported as empty circles. Inset b) shows a close-up on the key locations discussed in this study.

4.3 Methodology

4.3.1 Field work

Field work was carried out at ninety locations around the ring plain of Mt. Ruapehu (Fig. 4.1). Five key sections at distances between 8.9 and 9.7 km from source were chosen to be representative of the different dispersal directions of the T13-sequence (Fig. 4.1b) and were sampled and analysed in terms of their componentry and grain size characteristics (Fig. 4.2). Loc. 1 (Fig. 4.1b) was sampled for image analysis and geochemical studies on major and trace element compositions.

4.3.2 Grain size and componentry

Samples were sieved manually at 1 Φ steps down to 4 Φ. Grain size nomenclature follows White et al. (2006), while descriptive parameters such as median and sorting were calculated following Inman (1952, Fig. 4.2). In addition, descriptive parameters F1 and F2 represent the percentage in wt% of the sample that is >0 Φ and >4 Φ, respectively. For samples, which contained ≥25 wt% in the >4 Φ grain size fraction, this fraction was additionally analysed with a Laser Scattering Particle Size Distribution Analyser of Horiba (LPA), model Partica LA-950V2 at Massey University. Measurements were performed three times and averaged subsequently. Results were merged with those from manually sieved grain size analyses.

At least 300 grains were counted from the 2 Φ fraction for each bed. This grain size fraction occurs in all samples subunits and allows the unambiguous identification of main component classes. Component classes were normalised to the total number of particles counted and numerical percentages were calculated (Table 4.1). While the main components could be classified as juvenile clasts, lithics or phenocrysts, juvenile shards were further subdivided based on characteristics such as vesicle content, colour and morphology. The term “lithics” is used for accidental and accessory clasts, meaning clasts with obvious signs of alteration or clearly different provenance. Phenocrysts were distinguished based on colour, transparency and habit.

4.3.3 Tephra volumes

Isopachs were constructed using average bed and unit thicknesses measured in the field (Fig. 4.3). Thickness measurements are available for 66 locations at a distance range between 4.9 and 21.4 km. At further 24 locations, T13 could not be identified as a discrete tephra layer; these locations are reported as empty circles in Fig. 4.3 and mark the limit of the macroscopic T13 dispersal. Isopachs were drawn manually for cumulative T13 thicknesses and for selected subunits T13-1, -3, -4 and -6 (Fig. 4.3). For subunits T13-2 and T13-5 no coherent isopachs could be constructed due to their discontinuous appearance and due to evident lateral changes in deposit texture between locations (cf. Fig. 4.2). The following methods were adopted to calculate deposit volumes: the single segment and two segment methods after Pyle (1989) and Fierstein et al. (1992), the single isopach minimum deposit volume estimate after Legros (2000) and the Weibull function method after Bonadonna et al. (2012) and Bonadonna et al. (2013b).

Maximum clast data was obtained for 47 locations (Fig. 4.4). Limited deposit thickness and the fine-grained nature of deposits makes in-situ large clast determination after Bonadonna et al. (2013a) impracticable. To provide minimum estimates of the dispersal and values for the largest size class, a slightly different approach was used: grain size analysis was performed at half Φ steps for size fractions <0 Φ and the maximum clast size, reported in Fig. 4.4, corresponds to the coarsest half Φ size fraction that contains at least five clasts.

4.3.4 Image analysis and ash morphologies

Backscattered electron (BSE) images of polished and carbon coated juvenile shards for image analysis were taken at the FEI Quanta 200 Scanning Electron Microscope (SEM) at the Manawatu Microscopy and Imaging Centre, Massey University. Image analysis was performed on 1-3 representative images of each glass type and used the trainable Weka segmentation plugin in ImageJ/Fiji, following the procedure described in Lormand et al. (2018). The distinguished phases were phenocrysts and microlites of plagioclase and pyroxenes (<100 µm), groundmass glass and vesicles. Two dimensional modal percentages for each of the classes were obtained from counting the pixels with Adobe Photoshop, with the relative proportions of glass and microlites being calculated on a vesicle-free and phenocryst-free basis. In addition to this, 30–40 representative clasts were picked from the 2 Φ fractions of key samples and were imaged in secondary electron mode to investigate ash morphologies.

4.3.5 Geochemical characterisation

4.3.5.1 EMPA and LA-ICP-MS

Individual juvenile shards for subunits of T13 were manually selected from the 2 Φ fraction. Glass shards were embedded in EPO-TEK epoxy plugs, mixed at 4:1 resin to hardener ratios, and were polished with 3 µm and 1 µm diamond paste. Major element analysis was performed on carbon coated plugs using a JEOL JXA-8230 SuperProbe Electron Probe Microanalyser equipped with a WDS at Victoria University of Wellington, New Zealand. Analytical conditions included a ~8 nA probe current, a 15 kV acceleration voltage and counting times of 30/15 s (On/Off peak) for all elements except Na (10/5 s On/Off peak). Spot sizes included diameters of 5, 8 and 10 µm, and were varied according to microlite densities of the analysed glass type. The rhyolitic glass standard VG-568 (Jarosewich, 2002) was analysed every 20–30 points to assess instrumental drift. Accuracy lies below ±6% excluding TiO_2 (15%) and MnO (19%). At least ten analyses were performed for every glass type and averages are reported with standard deviation. Analyses with Al_2O_3 > 16 wt% were excluded, due to contamination by microlites (cf. Platz et al., 2007) as were analyses with totals <94%. Major element data were normalised to 100% on a volatile-free basis, excluding Cl (Appendix H-2).

Trace element compositions were acquired on analyses spots of 30 µm diameter that were carefully chosen, avoiding phenocrysts and xenocrysts. Given the spot size, microlites could not be avoided and the data therefore represent semi bulk-rock (glass and microlites) compositions. Trace element compositions were obtained in-situ, using an LA-ICP-MS Agilent 7900 coupled to a Resonetics 193 nm excimer laser ablation system at Victoria University of Wellington. Data acquisition conditions involve a 10 Hz repetition rate, and 45 s and 60 s for ablation and background, respectively. A mixture of He (400 mL/min) and N2 (1.5 mL/min) were used as carrier gas. Reference glasses NIST612 and NIST610 (Pearce et al., 1997) were analysed every 10–15 analyses and were used to calculate analysis accuracy. Accuracy for NIST610 lies within 15% except for Mg (46%), while NIST612 accuracy is below 7%, with Mg accuracy at 14%.

The applied data reduction scheme yields semi-quantitative results, obtained from the Iolite software (Paton et al., 2011), using ^{43}Ca as internal standard and NIST612 as reference material. Due to the complex, microlite-rich nature of the samples, careful post-analysis assessment and filtering was necessary, including the manual selection of integration windows in Iolite. Here, sections of the spectrum, which showed enhanced peaks in key elements such as Sr, Cr, and Mg were cut out, as they indicated the ablation of sub-surface plagioclase and pyroxene crystals. Data points with excessively high values of Ca (>110,000 ppm) in combination with high values of Sr (>700 ppm) and Mg values in excess of 60,000 ppm, as well as Cr values > 50 ppm were excluded being indicative of the ablation of a significant portion of a crystal. Similarly, data points with SiO_2 values of >80 wt% and <50 wt% were excluded as these values are unrealistic for andesite “bulk” glass and indicate errors in data acquisition (Appendix G-2).

Table 4.1 (continues on next page): Key samples of the T13-tephra sequence, detailing sampling location, distances from source, main grain size parameters and componentry

						Grain size parameters				Componentry analysis						
Sample ID	Subunit	Section	Lat	Long	Distance from source; heading	Md(Φ)	σ(Φ)	F1	F2	Juv	D (+BD*)	S	T	C	Lith	% total sample
1703-62	T13-1	L3	39 20 05.9 S	175 38 41.7 E	9.2 km; 130.7°	2.54	1.87	97.76	24.68	60.26	29.79	41.49	28.72	17.63	22.12	24.46
1703-63	T13-2	L3	39 20 05.9 S	175 38 41.7 E	9.2 km; 130.7°	2.45	2.15	95.68	25.37	68.7	38.71	37.9	23.39	21.33	9.97	23.27
1703-64	T13-4	L3	39 20 05.9 S	175 38 41.7 E	9.2 km; 130.7°	0.25	1.32	57.51	3.01	81.16	38.21	36.43	25.36	13.91	4.93	15.09
1703-65	T13-5	L3	39 20 05.9 S	175 38 41.7 E	9.2 km; 130.7°	0.93	1.07	84.74	4.37	61.39	27.34	43.75	28.91	16.07	22.54	29.82
1703-66	T13-6	L3	39 20 05.9 S	175 38 41.7 E	9.2 km; 130.7°	3.45	1.15	99.52	27.33	63.45	40.4	23.2	36.4	28.68	7.87	8.89
1902-8	T13-3	WP290	39 18 46.6 S	175 39 56.9 E	9.4 km; 112.0°	1.39	1.16	93.08	4.93	71.46	58.92	28.9	12.18	18.02	10.53	38.57
1902-9	T13-4	WP290	39 18 46.6 S	175 39 56.9 E	9.4 km; 112.0°	0	0.91	49.91	1	55.58	56.62	24.66	18.72	39.59	4.82	8.84
1902-10	T13-4	WP290	39 18 46.6 S	175 39 56.9 E	9.4 km; 112.0°	–0.25	1.27	41.2	3.08	60.09	47.08	37.59	15.33	27.85	12.06	6.68
1902-11	T13-4	WP290	39 18 46.6 S	175 39 56.9 E	9.4 km; 112.0°	–0.33	1.13	37.2	3.85	58.49	50	30.36	19.64	29.5	12.01	5.99
1902-12	T13-5	WP290	39 18 46.6 S	175 39 56.9 E	9.4 km; 112.0°	1.59	1.6	95.38	13.47	55.47	44.39	29.6	26.01	12.44	32.09	37.37
1902-13	T13-5	WP290	39 18 46.6 S	175 39 56.9 E	9.4 km; 112.0°	1.37	0.96	96.05	6.1	61.24	46.33	37.16	16.51	21.35	17.42	48.43
1902-14	T13-5	WP290	39 18 46.6 S	175 39 56.9 E	9.4 km; 112.0°	1.09	0.91	90.81	3.39	45.11	47.77	30.57	21.66	7.47	47.41	37.59
1902-15	T13-6	WP290	39 18 46.6 S	175 39 56.9 E	9.4 km; 112.0°	1.4	1.67	75.09	8.29	60.93	48.39	31.05	20.56	22.6	16.46	40.56
1703-13	T13-2	L1	39 16 07.5 S	175 39 59.7 E	8.9 km; 81.0°	2.62	1.32	100	18.76	73.62	37.61	43.36	19.03	17.59	8.79	26.41
1703-14	T13-3	L1	39 16 07.5 S	175 39 59.7 E	8.9 km; 81.0°	0.86	0.99	82.5	2.59	72.92	48.53	27.04	24.43	24.7	2.38	32.55

Notes: Median grain size Md(Φ) and sorting σ(Φ) are calculated after Inman (1952). F1 and F2 represent the relative percentage of sample that is >0 Φ (1 mm) and >4 Φ (63 µm), respectively. Componentry refers to the 2 Φ grain size fraction and indicates relative percentages of Juv (juvenile clasts), Lith (lithics) and C (crystals), calculated to total number of counted shards, while the different juvenile classes are calculated relative to total number of juveniles with D: dense clasts, S: scoriaceous clasts and T: tan vesicular clasts. The percentage of the total sample that was analysed for componentry is indicated in the last column. * BD marks beige dense clasts. These clasts are included in the dense clast (D) class. For samples at Loc. 3, BD is contained within the T-type class.

Table 4.1 (continued): Key samples of the T13-tephra sequence, detailing sampling location, distances from source, main grain size parameters and componentry

						Grain size parameters				Componentry analysis						
Sample ID	Subunit	Section	Lat	Long	Distance from source; heading	Md(Φ)	σ(Φ)	F1	F2	Juv	D (+BD*)	S	T	C	Lith	% total sample
1703-15	T13-4	L1	39 16 07.5 S	175 39 59.7 E	8.9 km; 81.0°	–0.42	1.04	31.86	0.92	63.17	44.94	27.53	27.53	29.67	7.16	5.08
1703-16	T13-4	L1	39 16 07.5 S	175 39 59.7 E	8.9 km; 81.0°	–0.38	1.21	36.62	1.02	64.94	35.2	41.6	23.2	24.68	10.39	7.15
1703-17	T13-5	L1	39 16 07.5 S	175 39 59.7 E	8.9 km; 81.0°	1.66	0.8	99.02	2.62	70.92	44.06	36.4	19.54	19.57	9.51	52.65
1703-18	T13-6	L1	39 16 07.5 S	175 39 59.7 E	8.9 km; 81.0°	3.05	1.3	100	21.47	72.31	29.37	42.38	28.25	18.55	9.14	16.4
1703-19	T13-6	L1	39 16 07.5 S	175 39 59.7 E	8.9 km; 81.0°	2.24	1.46	95.1	10.45	65.97	32.28	34.65	33.07	13.77	20.26	25.44
1803-18	T13-3	WP250	39 14 19.0 S	175 39 44.8 E	9.7 km; 60.6°	0.75	1.02	80.66	2.63	69.54	54.83	34.14	11.03	23.26	7.19	28.35
1803-19	T13-4	WP250	39 14 19.0 S	175 39 44.8 E	9.7 km; 60.6°	0.79	0.86	85.23	0.69	57.34	47.87	39.34	12.8	40.22	2.45	32.28
1803-20	T13-4	WP250	39 14 19.0 S	175 39 44.8 E	9.7 km; 60.6°	0.36	1.32	61.2	3.64	54.66	46.64	33.63	19.73	33.58	11.76	20.77
1803-21	T13-6	WP250	39 14 19.0 S	175 39 44.8 E	9.7km; 60.6°	1.34	1.23	88.96	4.41	67.13	53.13	31.25	15.63	23.78	9.09	35.5
1712-8	T13-3	L2	39 13 39.9 S	175 38 30.7 E	8.9 km; 48.4°	0.83	0.87	90.34	1.64	76.05	56.27	30.28	13.46	16.98	6.98	29.48
1712-9	T13-4	L2	39 13 39.9 S	175 38 30.7 E	8.9 km; 48.4°	0.29	0.93	62.86	1.38	65.41	53.24	34.89	11.87	30.59	4	13.18
1712-10	T13-6	L2	39 13 39.9 S	175 38 30.7 E	8.9 km; 48.4°	1.2	0.77	95.36	1.09	63.81	51.27	35.27	13.45	32.48	3.71	51.28
1712-11	T13-6	L2	39 13 39.9 S	175 38 30.7 E	8.9 km; 48.4°	1.82	1.04	98.24	5.35	63.5	52.23	34.01	13.77	31.88	4.63	39.74

Notes: Median grain size Md(Φ) and sorting σ(Φ) are calculated after Inman (1952). F1 and F2 represent the relative percentage of sample that is >0 Φ (1 mm) and >4 Φ (63 µm), respectively. Componentry refers to the 2 Φ grain size fraction and indicates relative percentages of Juv (juvenile clasts), Lith (lithics) and C (crystals), calculated to total number of counted shards, while the different juvenile classes are calculated relative to total number of juveniles with D: dense clasts, S: scoriaceous clasts and T: tan vesicular clasts. The percentage of the total sample that was analysed for componentry is indicated in the last column. * BD marks beige dense clasts. These clasts are included in the dense clast (D) class. For samples at Loc. 3, BD is contained within the T-type class.

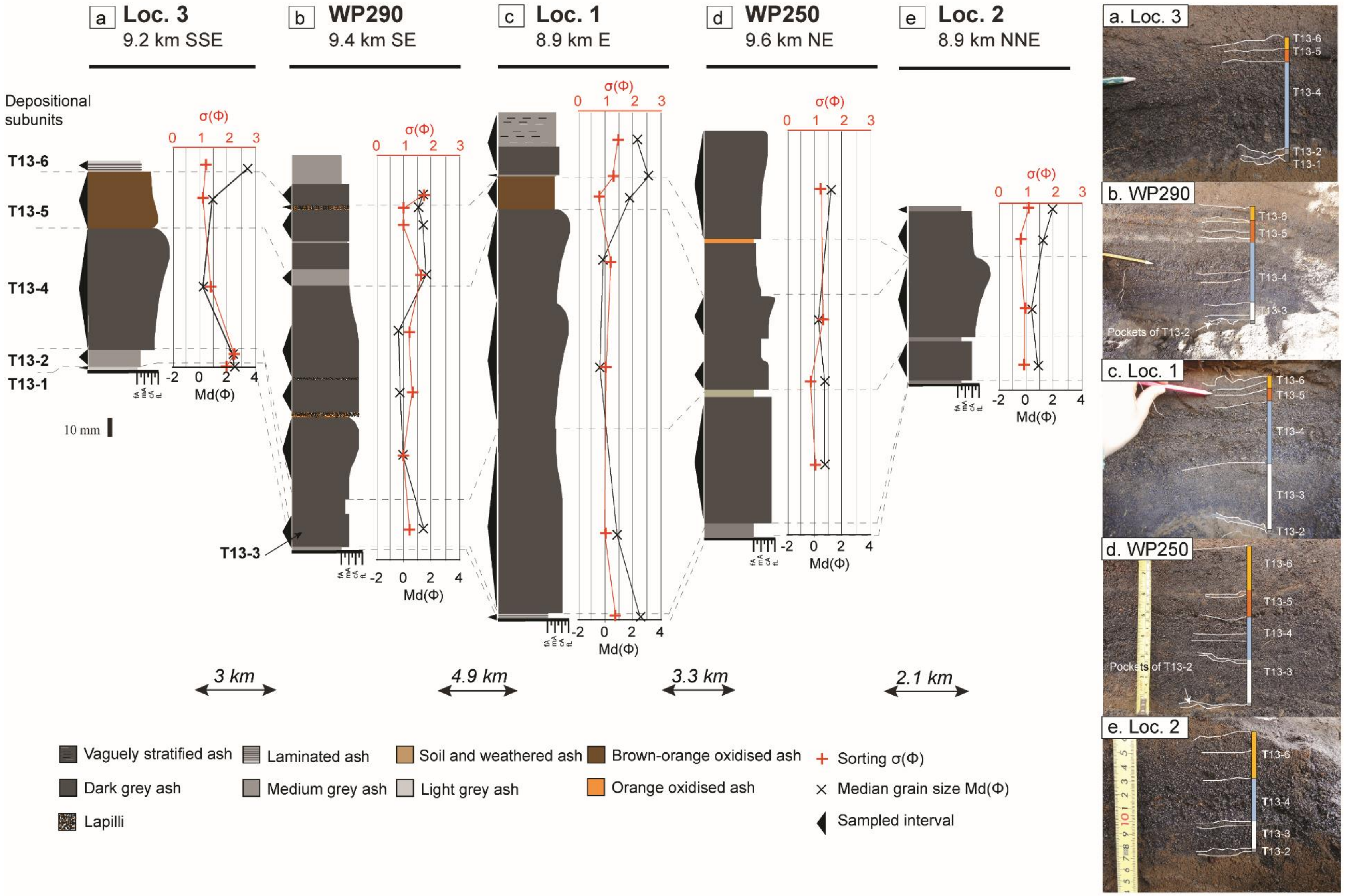
a Loc. 3 9.2 km SSE
b WP290 9.4 km SE
c Loc. 1 8.9 km E
d WP250 9.6 km NE
e Loc. 2 8.9 km NNE
Depositional subunits
T13-6
T13-5
T13-4
T13-3
T13-2
T13-1
σ(Φ)
0 1 2 3
-2 0 2 4
Md(Φ)
fA mA cA fL
10 mm
3 km
4.9 km
3.3 km
2.1 km
Vaguely stratified ash
Laminated ash
Soil and weathered ash
Brown-orange oxidised ash
Dark grey ash
Medium grey ash
Light grey ash
Orange oxidised ash
Lapilli
Sorting σ(Φ)
Median grain size Md(Φ)
Sampled interval
a. Loc. 3
b. WP290
Pockets of T13-2
c. Loc. 1
d. WP250
e. Loc. 2

Fig. 4.2 (previous page): Stratigraphic profiles at key sections showing the main depositional features, such as texture, median grain size Md(Φ) (dark grey crosses) and sorting σ(Φ) (red plus signs). Grain size and sorting parameters follow Inman (1952). Depositional subunits T13-2, -3, -4, -5 and -6 are correlated throughout the different sections from SSE to NNE as shown in Fig. 4.1b. Distances between locations are reported below each location. Sampled beds are marked by black triangles. Photo insets illustrate the lateral variation of the field appearance of the T13-sequence. Bed boundaries are marked by white lines, while coloured bars show subunits. a) Loc. 3 is located 9.2 km from source in SSE direction. Note the absence of T13-3 in this location. b) WP290 is located at 9.4 km distance from source in SE direction. Subunits T13-2, -3, -4, -5 and -6 can be identified here, while T13-1 is not preserved. T13-5 contains several distinct, but not correlatable beds. c) Loc. 1 is situated at 8.9 km E from source and comprises the sequence with the greatest cumulative thickness. Note the absence of T13-1. d) WP250 lies in NE direction, 9.6 km from source. e) Loc. 2 is positioned in NNE direction, 8.9 km from source. Only subunits T13-2, -3, -4 and -6 are preserved.

4.4 Results

4.4.1 Stratigraphy and tephra dispersal

T13 is the most prominent member of the Tufa Trig Formation (Donoghue et al., 1997; Voloschina et al., 2020). The tephra sequence is widespread throughout the ring plain and comprises a multi-bed ash sequence. Following the previous definition of the Tufa Trig Formation this member is also known as “Tf5” (Donoghue et al., 1997), but has been subsequently renamed to T13 (Voloschina et al., 2020). Radiocarbon dating of organic matter in soil underlying this member in a core at Ngamatea Swamp (WP251, Fig. 4.1) yields an age of 603 ± 46.5 cal BP (Wk48586, Voloschina et al., 2020).

The stratigraphic sequence can be subdivided into six depositional subunits, which are distinct in their appearance and lithosedimentological characteristics, such as grain size distribution, sorting (Fig. 4.5a, b) and deposit features (i.e., laminated vs massive) and can be correlated laterally at similar distances from source (Fig. 4.2). With increasing distance from source, beds and subunits join to form laminated depositional units without clear internal contacts. Cumulative thickness data for T13 unit shows an irregular distribution with a dominant eastward dispersal (100 mm at 16.5 km distance, Fig. 4.3a) and secondary thickness maxima to the NE (42 mm at 14.2 km distance), SE (52 mm at 17.4 km distance) and a minor WSW-lobe (55 mm at 6.7 km distance, Fig. 4.3a). Isopachs can be constructed for subunits T13-1, T13-3, T13-4 and T13-6 (Fig. 4.3b, c, d, e), while isopleths can be drawn only for T13-3, T13-4 and T13-6 (Fig. 4.4b, c and d). The different methods for volume calculations yield consistent results and are reported with their key parameters in Table 4.2. Cumulative deposit volumes for T13 range between 24.4 and 60.4×10^6 m^3, while deposit volumes calculated for individual subunits span several orders of magnitude between 0.38×10^6 m^3 and 36.97×10^6 m^3.

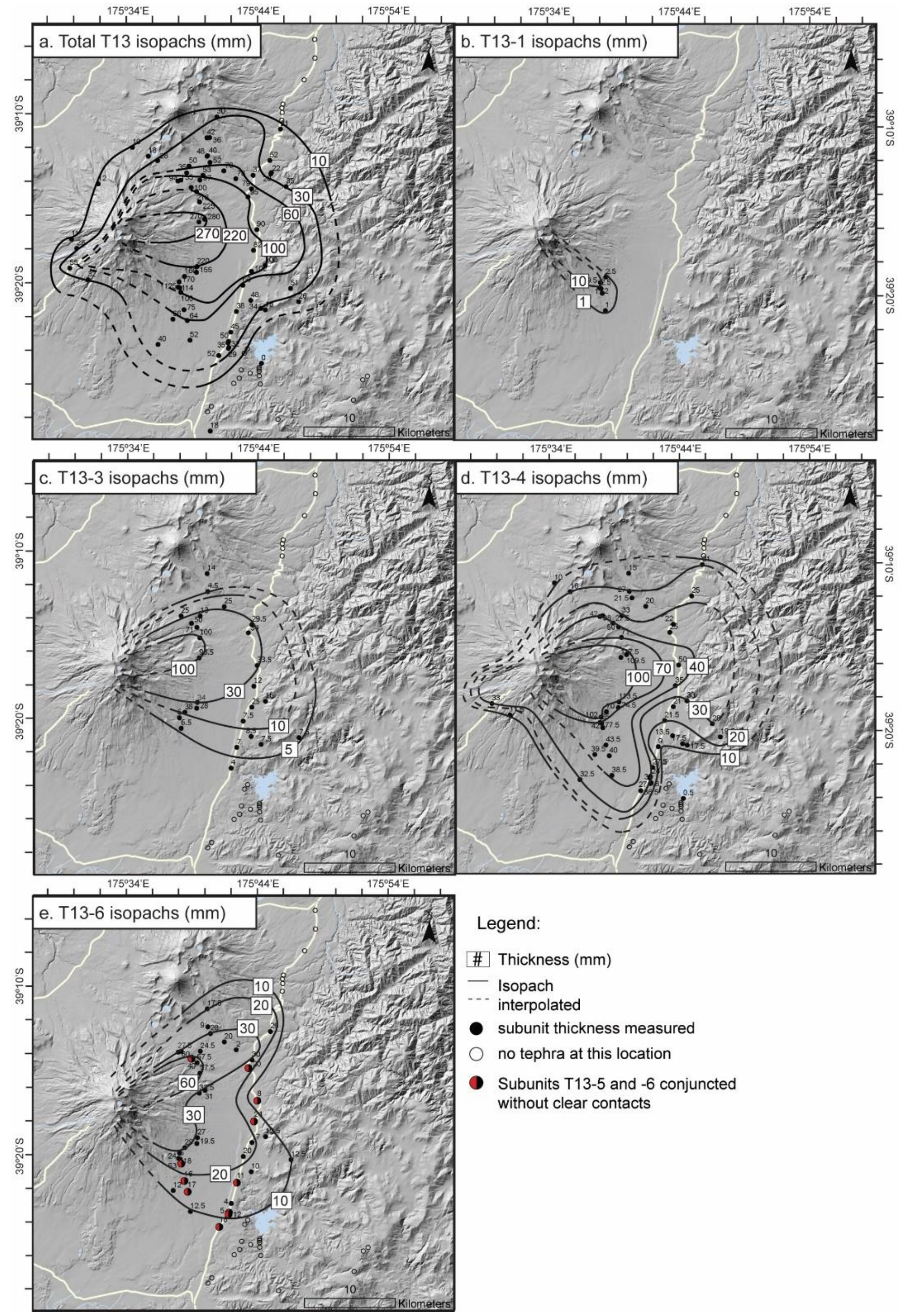

Fig. 4.3: Thickness distribution in mm of the T13-tephra sequence and selected individual subunits. Field locations, where thickness measurements were obtained are marked by filled circles, while field locations without discrete tephra units are marked by empty circles. a) Cumulative thickness for the T13-sequence shows a strongly irregular, multi-lobate dispersal. b) Thickness distribution for subunit T13-1 shows a limited dispersal towards the SE. c) Isopachs for subunit T13-3 indicate an extensive, asymmetrical dispersal towards the East. d) Isopachs for subunit T13-4 show several thickness maxima in different directions and are characterised by irregular shapes. The main lobe goes towards the East. e) The dispersal of subunit T13-6 shows a distinct bilobate shape with one main dispersal direction towards the NE and a second lobe towards the SE. Where subunits T13-5 and T13-6 cannot be separated unequivocally, joined thicknesses are reported (half coloured circles).

Subunit T13-1

The lowermost subunit consists in a single bed, appearing as a millimetric well sorted, light grey, very fine to fine ash layer. This bed comprises highly fragmented pyroclasts (F1=97.76 wt% of the sample >0 Φ), with 24.68 wt% of the sample being >4 Φ (F2, Fig. 4.5). The grain size distribution is slightly bimodal with a primary mode at 2 Φ and a secondary mode at 6 Φ. Pyroclast assemblage is dominated by variably vesiculated juvenile clasts, followed by lithics (22.12%) and free crystals (17.63%) with components being covered in light grey to white adhering dust. Lithic clasts are of white and orange colour representing alterated and rounded fragments of the hydrothermal system and of older eruptive products. The dispersal of this subunit is limited to south-eastern sections and is characterised by a narrow dispersal (Fig. 4.3b), thinning out rapidly at distances >11 km. Volume calculations yield a deposit volume ranging between $3.83–8.23 \times 10^5$ m^3.

Subunit T13-2

The overlying subunit T13-2 is dispersed in various directions around source and forms the base of the T13-sequence, where T13-1 is absent (Fig. 4.2, Fig. 4.3). T13-2 comprises medium grey well to poorly sorted fine ash with discontinuous sub-millimetric laminations (Fig. 4.2). It is of slightly greater thickness compared to T13-1 but shows similar grain size characteristics (Fig. 4.2), with high proportions of extremely fine ash (F2=25.37 wt% of the sample are >4 Φ, Fig. 4.5) and bimodal grain size distributions with modes at 2 and 6 Φ. Its identification as the basal subunit in different locations suggests multiple pulses towards NE, E, SE and W directions, but bed thicknesses of <10 mm at 10 km from source, pocketing preservation and lack of distinguishing features limit the correlation and the construction of useful isopach maps for this subunit. The pyroclast assemblage is similar to T13-1 with pyroclasts being covered in light grey to white adhering dust, and dense blocky clasts and scarcely vesiculated scoria constituting the dominant components. Lithics are less abundant compared to T13-1 and consist of white and orange alterated and rounded dense and pumiceous fragments of older eruptive products, as well as sparse reddish oxidised lava fragments.

Table 4.2: Parameters used for deposit volume calculations for T13

	T13 cumulative	T13-1	T13-3	T13-4	T13-6
Isopachs no.	6	2	4	6	4
k	–0.16	–1.078	–0.24	–0.117	–0.126
1 seg (m^3) [1],[2]	6.04E+07	8.23E+05	1.28E+07	3.42E+07	1.46E+07
k1	–0.121		–0.21	–0.171	–0.15
k2	–0.187		–0.235	–0.11	–0.17
2 seg (m^3) [1],[2]	5.85E+07		1.17E+07	3.70E+07	1.19E+07
Single isopach (m^3) [3][a]	2.44E+07	4.75E+05	8.11E+06	2.41E+07	1.34E+07
θ	27.41	4.44	12.20	8.45	4.34
λ	13.62	2.94	8.92	17.11	15.73
n	1.80	2.00	1.56	1.47	1.54
R2	0.99	1.00	1.00	0.99	1.00
Weibull (m^3) [4]	5.64E+07	3.83E+05	1.25E+07	3.37E+07	1.39E+07
Average (m^3)	4.99E+07	5.61E+05	1.13E+07	3.23E+07	1.35E+07
SD (%)	29.64	33.83	16.50	15.07	7.38

Notes: References for calculations are as follows: [1] Pyle (1989); [2] Fierstein and Nathenson (1992); [3] Legros (2000); [4] Bonadonna and Costa (2013); [a]based on extent of 10 mm isopach

Subunit T13-3

This subunit comprises at least two parts, which can be best distinguished to the East but are not separated by any discrete contact. The lower part is composed of well sorted, coarse to medium ash, which is weakly normally graded (Fig. 4.2). The upper part consists in medium ash, which appears as a capping discontinuous millimetric fine ash of an olive colour in locations to the N (Fig. 4.2). Isopachs cover areas from NE to SE with a maximum discrete extent of ~21 km (Fig. 4.3c) and yield tephra volume estimates of 8.11–12.76 × 10^6 m^3. It is noteworthy, that while grain size distributions are unimodal, the modes slightly change between NE and E directions, with coarser grain sizes appearing in NE directions (Table 4.3, Fig. 4.4b). The proportion of extremely fine ash is low with F2 < 4.93 wt%, despite 80.66–93.08 wt% of the sample being <0 Φ (Fig. 4.5, Table 4.1). This subunit is characterised by higher amounts of free crystals, compared to T13-1 and -2 and shows a significant decrease in lithic components and adhering dust. Lithics consist mainly in rounded cognate components and few white, hydrothermally altered clasts. Dense juvenile clasts are as abundant as vesicular juvenile clasts in the ash fraction.

Subunit T13-4

Subunit T13-4 is easily identified by its relative coarser grain size and the presence of lapilli-sized dark scoriae and tan vesicular lapilli and constitutes the most dominant and widely dispersed subunit of the T13-sequence. The subunit is represented by well sorted coarse ash to very coarse ash, which show 2–3 cycles of inverse grading, depending on the location (Fig. 4.2). The proportion of material >0 Φ varies laterally and is significantly lower compared to the other subunits (F1=31.86–85.23 wt%, Table 4.1, Fig. 4.5). Extremely fine ash constitutes less than 3.85 wt%.

The dispersal is complex and dominated by multiple irregular thickness maxima (Fig. 4.3d). To the E-SE, where the tephra sequence shows the most detail (Fig. 4.2), the isopach distribution is bilobate with a narrow lobe towards the Southeast and a wide lobe towards the East (Fig. 4.3d). Subunit tephra volume estimates range between 24.12 and 36.97 × 10^6 m^3 and constitute ~65% of the cumulative deposit volume of T13. In eastern directions, the subunit is the coarsest (Fig. 4.4c), with maximum grain sizes of –3 Φ and only 31.86–49.91 wt% being finer than 1 Φ. The grain size distribution is unimodal with a clear mode at 0 Φ, reaching maximum grain sizes of –3 Φ. Conversely, the NE lobe contains increasingly finer material, with modes at 1 Φ and F1=61.20–62.86 wt%. However, this lobe is similarly characterised by the lack of extremely fine ash, with F2 < 3.64 wt%. Adhering ash and lithics are subordinate (Lith=2.45–12.06%), giving this subunit a “fresh” appearance, compared to T13-1 and -2. Lithics consist of white-orange hydrothermally alterated pumiceous clasts, dense red-brown lava fragments, grey dull glass fragments covered in oxidised dust as well as rounded and weakly alterated cognate lithics.

The contact between subunits T13-4 and T13-5 is very prominent (Fig. 4.2c). It is marked by both a sudden decrease in grain size from the coarse ash to very coarse ash of T13-4 to the medium to coarse ash of T13-5 and a sudden increase in brown lithics in T13-5. In some locations the contact shows evidences of weathering and alteration, but no soil formation is evident (Fig. 4.2c).

Subunit T13-5

T13-5 shows a characteristic overall brown-orange colour (Fig. 4.2a, b), given by relatively higher proportions of brown-orange lithics, red oxidised lava fragments and adhering dust of the same colour. To the SE, it contains multiple beds of millimetre to centimetre thickness (Fig. 4.2b), which cannot be correlated laterally. To the SSE and E, T13-5 consists in massive medium to coarse ash, which is characterised by a generally better sorting than other subunits in the sequence (Fig. 4.2, Fig. 4.5a, Table 4.1). In the SE-E, the bedset is capped by a distinct millimetre-thick orange-coloured medium ash (Fig. 4.2b). Grain size distributions vary laterally from being unimodal (1 Φ) at Loc. 3 to individual beds showing variable distributions at WP290 (Fig. 4.2), with a main mode at 2 Φ, and a subdominant secondary mode at >4 Φ (F2 < 13.47 wt%, Fig. 4.5b).

T13-5 and the overlying T13-6 are separated by distinct contacts in SE and NE directions, but they cannot be distinguished unequivocally in locations, which lie off-axis or with increasing distance from source. Fig. 4.3e highlights where T13-5 and -6 can only be measured as a joined bed, as well as those locations, where the topmost T13-6 can be clearly distinguished.

Subunit T13-6

T13-6 shows a clearly bilobate dispersal with thickness maxima of 30 mm at 15.4 km in the NE and 20 mm at 14.9 km in the SE. The maximum distance at which it can be identified macroscopically is 19.9 km (WP258). Tephra volume estimates for this subunit range between 11.91–14.60 × 10^6 m^3. At Loc. 1, the lower contact to the underlying T13-5 is distinct and is marked by the presence of a millimetre-thick bed of very fine to fine ash, which is absent in other locations (Fig. 4.2c). Similarly, the contact is marked by a distinct change in colour from the brownish T13-5 to the distinctly juvenile-looking, medium to dark grey T13-6. The depositional features of T13-6 are best exposed in SE and E directions, where the subunit is represented by medium grey to dark grey medium ash. Here it is normally graded, with the upper part consisting in indistinctly laminated well to very well sorted fine ash. Grain size distributions are mainly unimodal with modes in the medium to fine ash classes. In other directions (e.g., Loc. 3, SSE), the entire subunit appears as an indistinctly laminated grey very fine to extremely fine ash, which gradually transitions into the overlying soil (Fig. 4.2a). Towards the NE (Loc. 2), on the other hand, T13-6 comprises massive well sorted fine to medium ash, without clear internal textures and low extremely fine ash contents. Here, T13-6 overlies T13-4 due to the absence of T13-5 and the contact is generally indistinct as the two subunits show similar lithosedimentological characteristics in these locations, such as subdominant extremely fine ash and the dominance of dark dense blocky fragments over vesicular clasts in the ash size fraction.

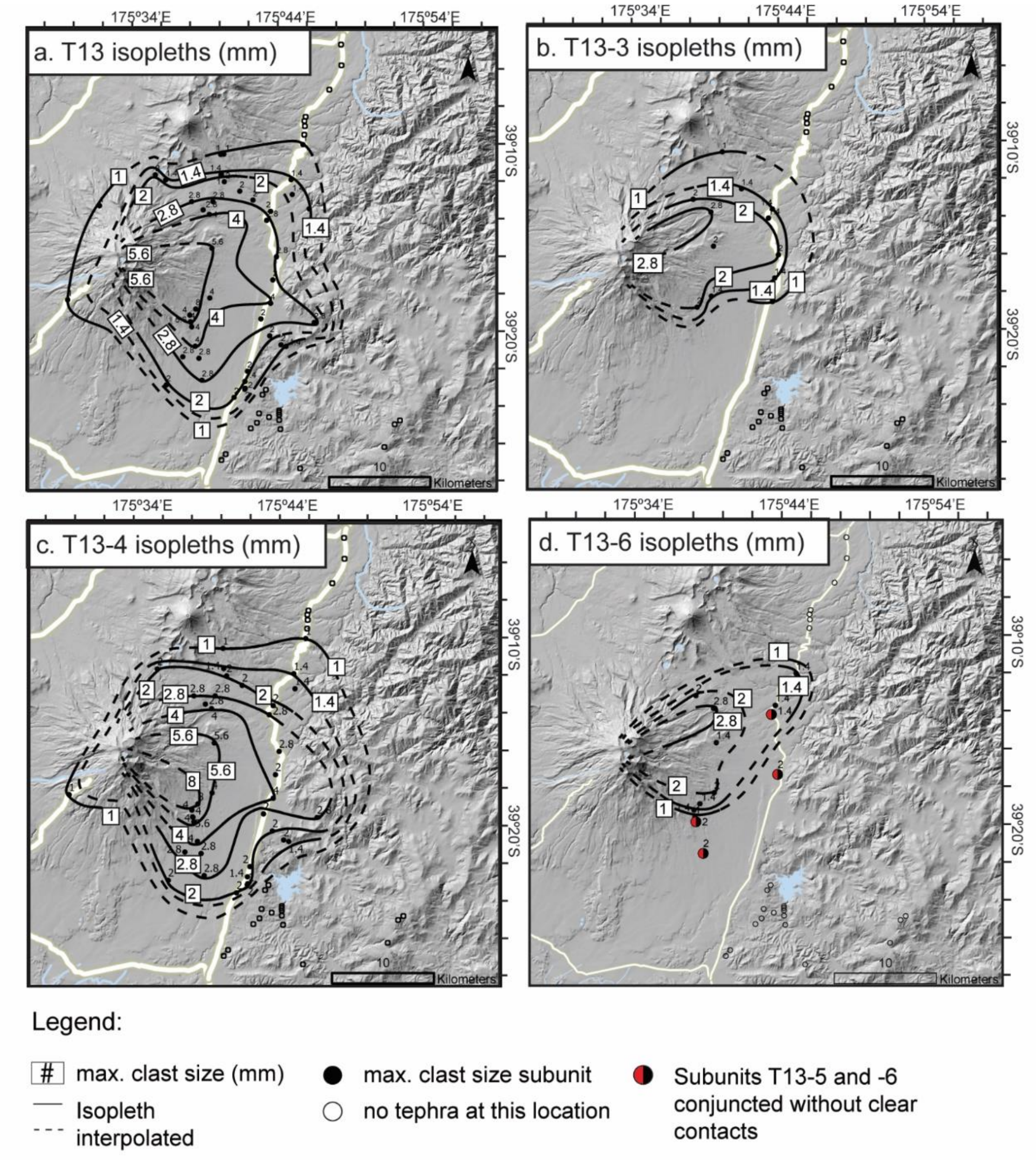

Fig. 4.4: Maximum clast distribution shown in mm for the T13-sequence and selected subunits T13-3, T13-4 and T13-6. Field locations where grain size data was obtained are marked by filled circles, while locations where no discrete tephra could be observed are reported by empty circles. a) Irregular multi-lobate distribution is shown for the maximum clast size from the whole T13-sequence b) Maximum grain size for subunit T13-3. Note the asymmetrical, slightly bilobate dispersal. c) Irregular maximum clast dispersal for subunit T13-4, characterised by several thickness maxima in different directions. d) Asymmetric, slightly bilobate isopleths for subunit T13-6. Note that maximum grain sizes are coarser in NE locations compared to SE locations at similar distance from source. At locations, where subunits T13-5 and -6 cannot be distinguished unequivocally, maximum grain size was determined for the joined subunit. These locations are marked by half coloured circles.

4.4.2 Componentry

The pyroclast assemblage of the T13-sequence comprises three main components: (1) juvenile clasts, (2) free crystals and (3) lithics. Juvenile clasts constitute the dominant component (54.66–81.16%), followed by lithics (2.38–32.09%) and spare crystals (12.44–40.22%, Table 4.1). Relative proportions vary within the tephra sequence.

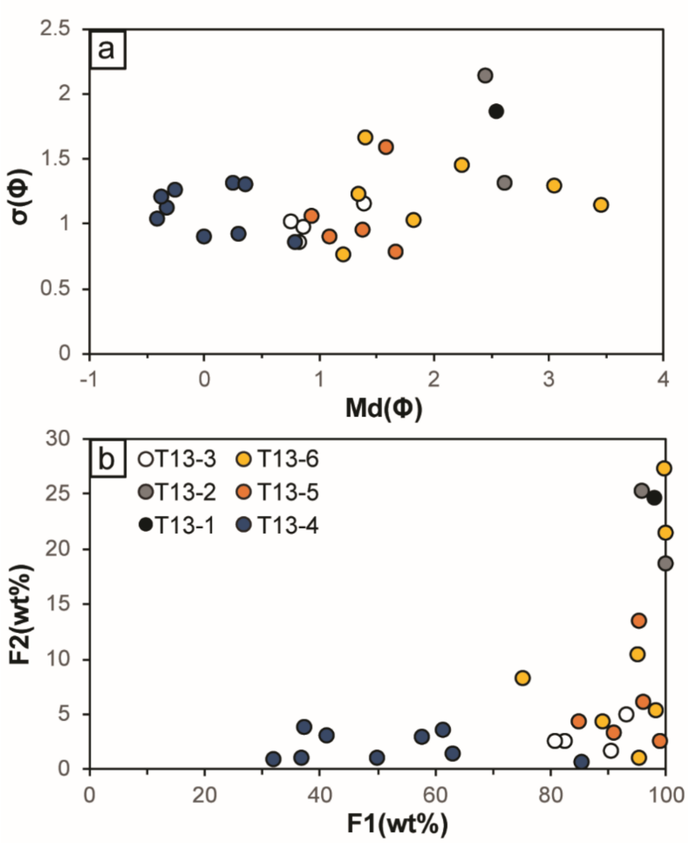

Fig. 4.5: Grain size characteristics of individual beds of the T13-sequence at key locations shown in Fig. 4.2. Data is colour-coded according to subunits: T13-1 is shown by black circles, T13-2 is marked by grey circles, T13-3 is marked by white circles, T13-4 is represented by blue circles and T13-5 and T13-6 are shown in orange and yellow, respectively. a) This inset illustrates the median grain size Md(Φ) and sorting σ(Φ) following Inman (1952). b) F1 and F2 are descriptive parameters where F1 represents the proportion of the sample that is >0 Φ (<1 mm) and F2 represents the proportion of the sample that is >4 Φ (<63 µm).

4.4.2.1 Juvenile clasts

Juvenile clasts display a range of clast characteristics and ash morphologies, allowing for the distinction of three main types: (a) dense clasts, (b) scoriaceous clasts and (3) tan vesicular glass.

(a) Dense juvenile clasts (D) are opaque, showing blocky to subordinate platy morphologies (Fig. 4.6a, h). Clast edges are sharp and display conchoidal and step-like features. Pyroclasts are microcrystalline, displaying groundmass crystallinities 58.14–73.18% (Table 4.3, Fig. 4.7a). The clast surface is often irregular due to the high percentages of microlites (Fig. 4.6a). Microlite assemblage is dominated by plagioclase microlites (>40% of groundmass) and 10–20% of pyroxene microlites. This class also includes tan-coloured dense clasts, which constitute a minor component (<5%) in all subunits of the T13-sequence (Fig. 4.8). Generally, groundmass crystallinity is less extensive in tan dense clasts (37.80–62.94% Fig. 4.7a). Morphological characteristics of tan-coloured dense clasts are similar to those of dark dense clasts with few tan dense shards showing smooth surfaces and small subordinate vesicles (Fig. 4.6e). In the following, tan dense clasts will be integrated within the dense juvenile class.

(b) Scoriaceous clasts (S) comprise black to dark grey opaque glass with a high amount of groundmass crystallinity (43.05–75.0 %, Fig. 4.7a, Table 4.3). Clast morphologies span a range from smooth and fluidal (Fig. 4.7b) to irregular morphologies with conchoidal fractures and step-like features (Fig. 4.6c). Sometimes vesicles are filled with extremely fine ash. Vesicles are generally isolated and form thick bubble walls (Fig. 4.6b). Vesicle shape and size vary along the tephra sequence, ranging from round vesicles of medium size (30–50 µm) to large deformed, coalescent (~70–100 µm) vesicles.

(c) Tan vesicular juvenile clasts (T) include vesicular glass of different optical colours, such as beige, white and brown, which vary in vesicularity, morphology and groundmass crystallinity but are not abundant enough to be counted as individual classes. Beige and brown glass are generally most abundant and have smooth glassy surfaces, occasionally showing fluidal morphologies (Fig. 4.6d, i) and higher vesicularity, compared to D- and S-clasts. On the contrary, associated groundmass crystallinities are lower compared to D- and S-type clasts, with beige glass (BEV) showing groundmass crystallinities of 39.98–53.28 % (Table 4.3, Fig. 4.7a), while brown glass (BRV) shows slightly higher groundmass crystallinities of 43.93–69.29% (Fig. 4.7a). Microlite assemblage is dominated by plagioclase with subdominant pyroxene (Fig. 4.7a, b). In subunits, where this class contains highly vesicular white-transparent pumiceous glass the vesicles are closely-spaced and vesicle walls are thin (e.g., Fig. 4.6g).

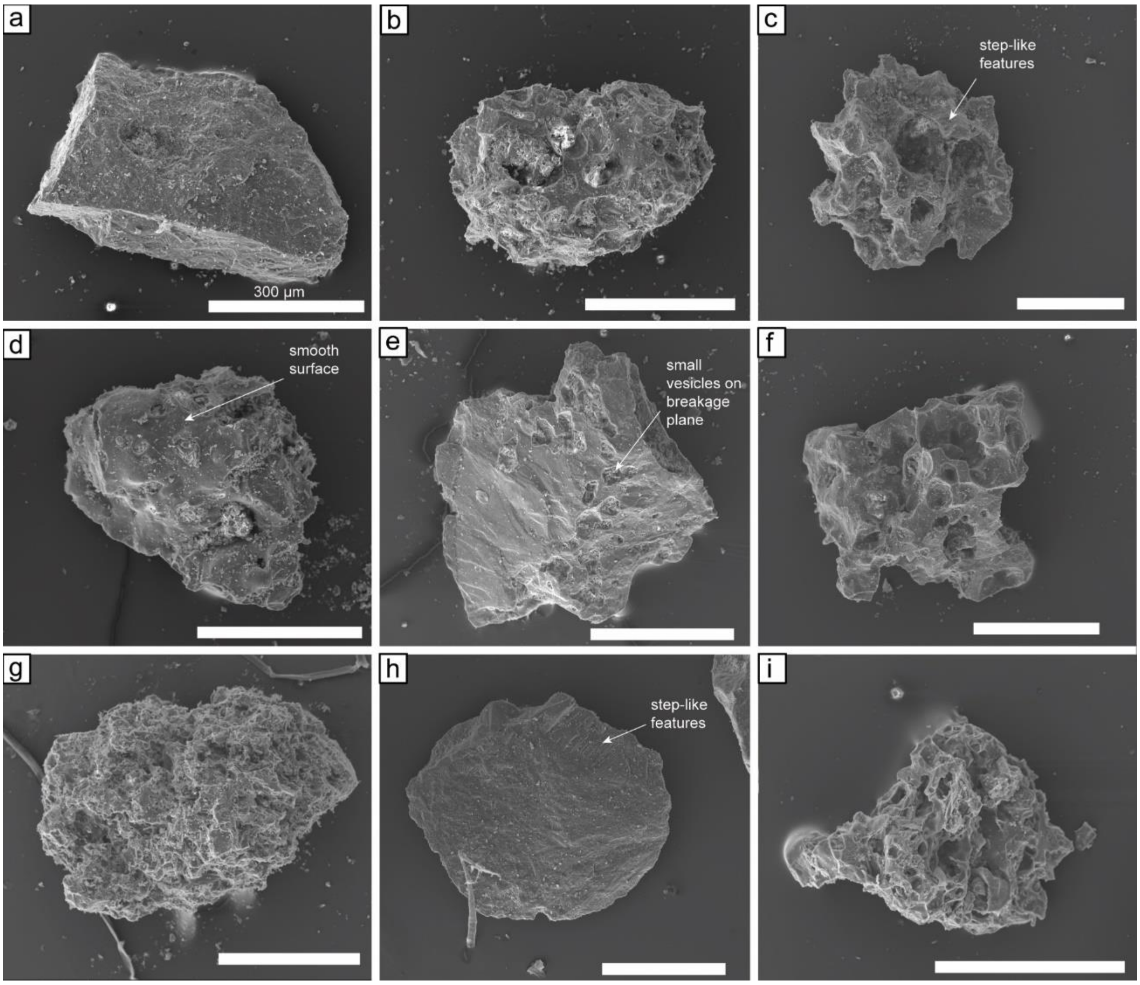

Fig. 4.6: Scanning electron microscope images of selected representative juvenile shards in the 2 Φ fraction. Scale bar in each image corresponds to 300 µm. a) D-type, blocky clast with irregular surface and conchoidal fractures. b) S-type juvenile with a smooth, glassy surface and heterogeneous vesicles, typical of subunits T13-1 and T13-2. c) Irregular S-type juvenile from T13-5 with thick bubble walls and large vesicles. Note the step-like fractures. d) T-type shard with a smooth surface and fluidal morphology. e) D-type clast from T13-4 displaying small vesicles on the breakage plane. f) S-type clast from T13-4 that is characterised by a smooth, glassy surface and large deformed vesicles. g) Pumiceous T-type shard as found in subunits T13-4, -5 and -6. h) Dense juvenile shard with an irregular surface showing step-like fractures. i) T-type shard showing high vesicle density, a fluidal morphology and a smooth surface.

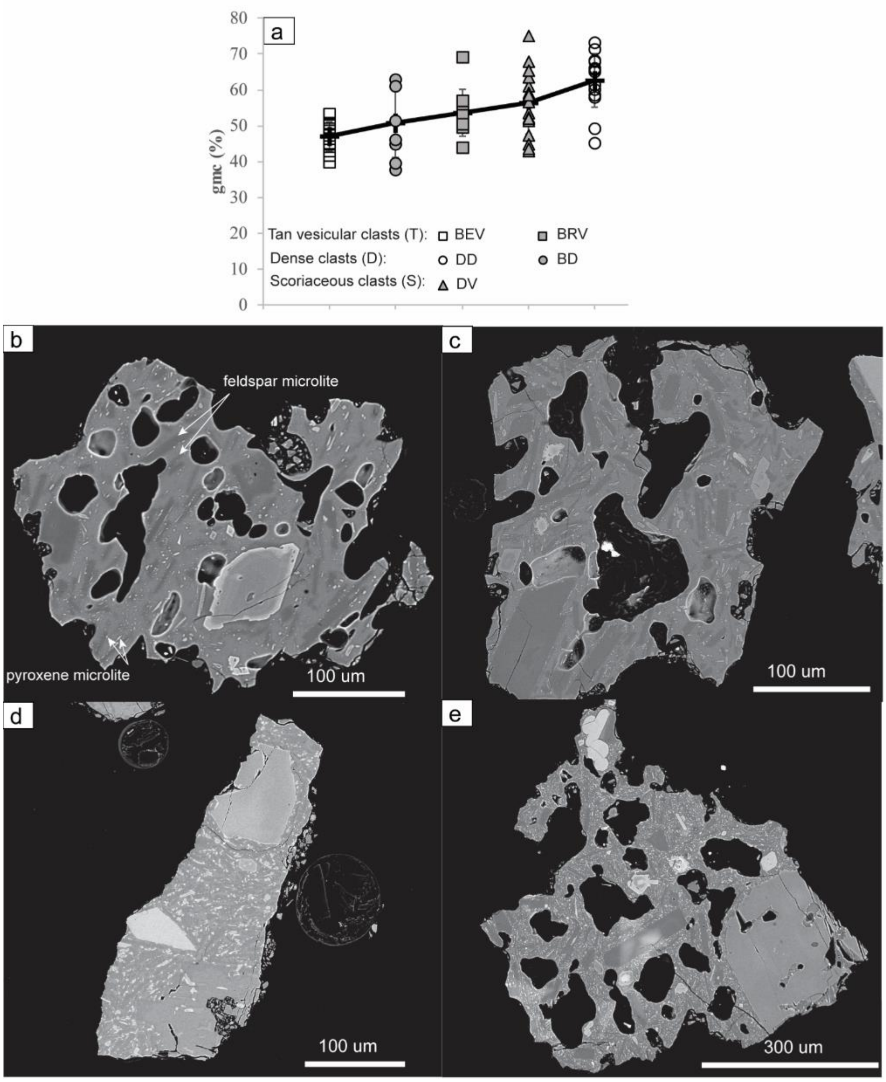

Fig. 4.7: Overview of different juvenile types, their groundmass crystallinities and textures. a) 2D-groundmass crystallinities obtained from image analysis on back-scattered electron images. Different glass types are summarised as follows: Tan vesicular juveniles comprise both beige vesicular (BEV) and brown vesicular (BRV) clasts, marked by white and grey squares, respectively. Dense clasts include beige dense (BD) and dark dense (DD) juveniles and are represented by grey and white circles, respectively. Scoriaceous juveniles (DV) are represented by triangles. Insets b) to e) show backscattered electron images where groundmass glass is of medium grey colour, whereas dark grey areas represent feldspar microlites and bright areas mark pyroxene microlites. Scale bar corresponds to 100 µm for a, b and c, while in d the scale bar represents 300 µm. b) T-type glass from T13-4, showing medium-sized coalescent and slightly deformed vesicles and large feldspar microlites. Pyroxene microlites are subordinate and overall groundmass crystallinity lies at 41.73%. c) T-type juvenile from T13-3, displaying large deformed vesicles and large feldspar microlites. Few large pyroxene microlites (long axis 30-40 µm) can be seen, while most pyroxene microlites are small (<10 µm). Groundmass crystallinity is gmc=50.50%. d) D-type microcrystalline juvenile that exhibits a high groundmass crystallinity of gmc=60.19%. Feldspar and pyroxene microlites are small and closely spaced. e) Scoriaceous juvenile from T13-4 showing both high vesicularity and high groundmass crystallinity (gmc=75%). Vesicles are large, coalescent and deformed and the groundmass is characterised by large feldspar microlites and closely spaced, groundmass-filling pyroxene microlites.

4.4.2.2 Crystals and lithics

Free crystals involve variable proportions of plagioclase, clinopyroxene and orthopyroxene. Ortho- and clinopyroxene are often euhedral to subhedral while plagioclase appears mostly fragmented. Lithics comprise accidental, oxidised and altered, orange and white-coloured lithics from hydrothermally altered areas, as well as red oxidised and dull grey fragments of lava flows or products from previous explosive eruptions, such as fragile orange-weathered pumices. Cognate lithics are present, but can only be unequivocally identified, where clast morphology is significantly altered, showing for example rounded edges or evidence of alteration.

4.4.2.3 Lateral variation

In line with the lateral variability that can be observed in deposit characteristics of individual subunits (Fig. 4.2), Fig. 4.8 illustrates the lateral variability in pyroclast assemblages.

The componentry assemblage of T13-4 varies strongly with dispersal direction, in agreement with the multi-lobate dispersal (Fig. 4.8). While juvenile clasts always constitute the main component, ranging from 54.66 to 81.16% and vesicular clasts prevail over dense clasts (Fig. 4.8) with S>T (Table 4.3), relative abundances of the juvenile classes vary between locations. The highest percentages of T-type clasts occur at Loc. 1, where they reach up to 27.53%. On the other hand, the lowest amount of T-type glass and the highest percentage of D-type clasts appear in the NE, at Loc. 2 with D=53.24% and T=11.87%. Free crystals are more common at WP250, where they constitute up to 40.22% of the 2 Φ fraction, while their abundance decreases to 24.68–29.67% at Loc. 1 (Fig. 4.8). Pyroxene abundances among the free crystals generally overshadow plagioclase (Px:Plg=1.79–4.10), but Px:Plg-ratios vary from 0.85 at Loc. 3 to 2.18–3.1 at WP290 to 1.79–2.41 at Loc. 1 (Fig. 4.8). Lithic abundances are highest at WP290, where they range from 4.82 to 12.06 %, while the lowest lithic abundances are associated with the lower bed of subunit T13-4 at WP250 (Fig. 4.2).

A similarly variable range in componentry can be observed throughout subunit T13-6, where the pyroclast assemblage differs between the NE and the SE lobes (Fig. 4.2, Fig. 4.3, Fig. 4.4). Lithic abundances are higher at Loc. 1 and WP290 (Lith=9.14–20.26%, Fig. 4.8) than in the NE (Lith=3.71–4.63%). The proportions of juvenile clasts show a similar spatially correlated range with samples at Loc. 2 and WP250 being dominated by D=51.27–53.13% and S=31.25–35.27% while T-glass is subordinate (13.45–15.63%). On the contrary, T-type glass abundances are higher in the E and SE (T=33.07% at Loc. 1). With S-type percentages ranging between 23.20 and 42.38%, vesicular clasts prevail over dense clasts in eastern directions.

The observed lateral variability in the pyroclast assemblage agrees with the multi-lobate dispersal pattern (e.g. Fig. 4.3d) and with the previously described lateral variable number of individual beds within subunits, as can be seen i.e., for T13-4 between WP290 and Loc. 1 (Fig. 4.2). This highlights the limited value of componentry analysis of individual beds and subunits when it comes to the lateral correlation of individual beds/bedsets.

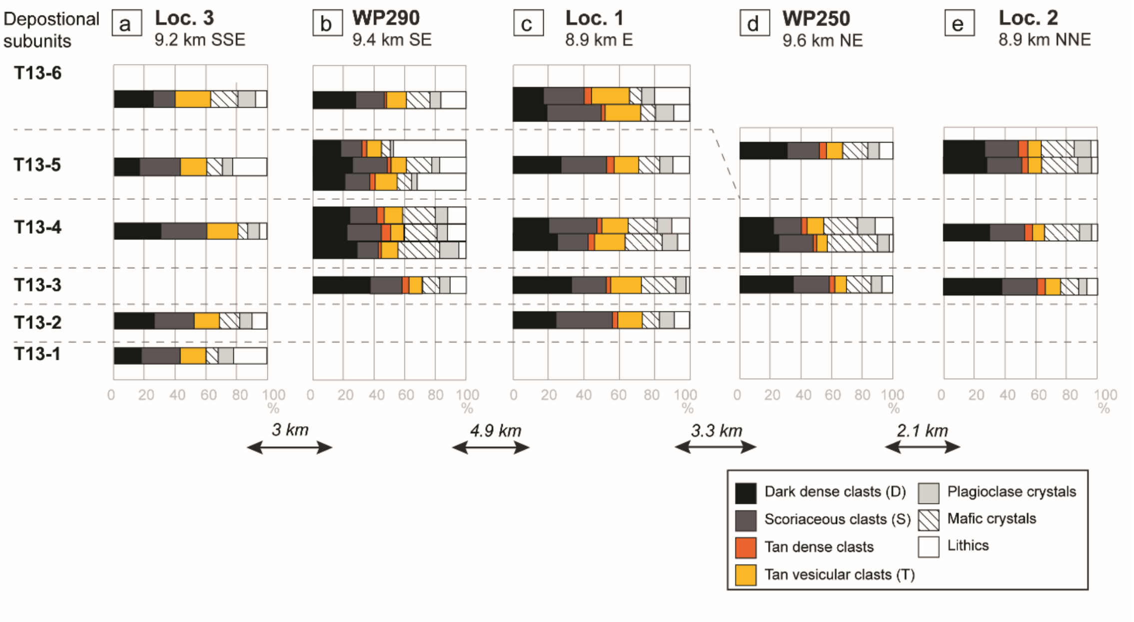

Fig. 4.8: Pyroclast assemblage obtained from point counting of the 2 Φ fraction of individual subunits from the T13-tephra sequence. Point counting data is reported for key sections to illustrate lateral variability, with locations being the same as in Fig. 4.2 and Fig. 4.1b. Where a subunit contains more than one sampled bed, the pyroclast assemblage for each sampled bed is reported. The distinguished componentry classes are: dark dense clasts (D-type, black), scoriaeous clasts (S-type, grey), tan dense clasts (orange), tan vesicular clasts (T-type, yellow), plagioclase (light grey), pyroxenes (striped), lithics (white). Note that for inset a) Loc. 3, tan dense clasts are included within the tan vesicular glass class, slightly increasing relative proportions of T clasts by ≤5.92%.

4.4.2.4 Sequence variation

Relative proportions of different componentry classes vary systematically throughout the sequence. These variations can be illustrated at Loc. 1 (Fig. 4.8) and are detailed in the following.

The componentry of T13-1 could only be quantified in its main SE-directed dispersal (Fig. 4.3b). Here, tephra assemblage is dominated by juveniles (60.26%), followed by lithics (22.12%) and free crystals (17.63%), with more plagioclase than pyroxenes (Px:Plg=0.77, Fig. 4.8). Juveniles are dominated by scoriaceous clasts (41.49%), followed by dense clasts (29.79%). Scoriaceous clasts show a range of morphologies and vesicles are generally deformed, coalescent and comprise different sizes. Dense clasts are blocky with sharp edges and show conchoidal and step-like fractures. Tan vesicular glass shows a range of morphologies dominated by fluidal, smooth surfaces. Vesicles have heterogeneous sizes and are mostly deformed and coalescent.

T13-2 shows a decrease in lithic abundance (Lith=8.79%), compared to T13-1, while juveniles increase to 73.62%. S-type clasts (43.36%) dominate over D-type (37.61%) and T-type clasts (19.03%) and show mostly isolated vesicles with ~50 μm diameter and cuspate morphologies. D-type clasts comprise blocky and chippy morphologies and show step-like fractures and irregular surfaces due to microlite crystals below the surface. T-type glass has heterogeneous vesicle distributions with deformed vesicles and smooth, fluidal surfaces (i.e., Fig. 4.6d). Both T13-1 and -2 are characterised by bimodal grain size distributions and adhering dust (Fig. 4.9k, l).

T13-3 shows an increase in free crystals (24.70%, Fig. 4.9a), while lithic abundances decrease to 2.38% (Fig. 4.9a). Crystals contain more pyroxenes over plagioclase (Px/Plg=3.16, Fig. 4.9b). Juvenile clasts show high proportions of dense clasts 48.53% compared to vesicular clasts (S=27.04%; T=24.43%). D-type clasts have blocky and chip-like morphologies with sharp edges. S-type and T-type clasts show an increased vesicularity, compared to T13-1 and T13-2, with large vesicles (70–100 μm) that are closer spaced. Vesicles appear deformed and show evidence of coalescence while some clasts show tiny vesicles with diameters <20 μm (Fig. 4.7b).

The pyroclast assemblage of T13-4 is similar to T13-3 with high abundances of free crystals that decrease within the subunit from 29.67% to 24.68% in line with decreasing

Px/Plg ratios (2.41% and 1.79%). Vesicular clasts dominate over dense clasts and increase within T13-4 (Fig. 4.9c), in line with increasing abundances of S-type clasts (Fig. 4.9d). Both S-type and T-type clasts show an increase in vesicularity, compared to previous subunits with scoriaceous clasts having large deformed and coalescent vesicles (Fig. 4.7e), while T-type glass shows generally smaller and closely spaced vesicles (i.e. Fig. 4.6g). Between the two grading cycles of T13-4 (Fig. 4.2c), vesicle deformation increases slightly with stratigraphic height.

While T13-5 is generally associated with a significant increase in lithics, this is not particularly evident at Loc. 1, where lithic abundances are similar to the underlying T13-4. Free crystals decrease only slightly to 19.57%, while juvenile clasts increase to 70.92%, in line with an increase of D-type clasts to 44.06% (Fig. 4.9c). D-type morphologies are dominated by flat, platy and blocky morphologies. S-type clasts show predominantly homogeneous, large (~100 μm), poorly deformed and coalescent vesicles with irregular to fluidal morphologies, which are often filled with fine dust. T-type clasts show heterogeneous vesicle distributions, involving both large, deformed and coalescent, as well as isolated small vesicles. Morphologies are generally fluidal to pumiceous.

In line with the previously described lateral variability of subunit T13-6, the abundance of lithic components comes with an increase from 9.14 to 20.26% (Fig. 4.9a) and a decrease in juvenile clasts from 72.31 to 65.97% between the two T13-6 beds at Loc. 1 (Fig. 4.2c). The pyroclast assemblage of T13-6 is characterised by a sudden increase in vesicular T-type clasts compared to the underlying subunits (Fig. 4.9c, d) with abundances of 28.25–33.07%. T-type glass is characterised by smooth glassy surfaces and high vesicle densities (Fig. 4.6i). Vesicles have heterogeneous distributions and are strongly deformed. S-type clasts are characterised by predominantly large (~100 μm) and slightly less deformed vesicles. The components of this unit have generally a very juvenile appearance and show no ash cover. Lithics are mainly cognate, comprising rounded dense clasts and rounded vesicular clasts with vesicle fillings as well as reddish-white, dense lithics and grey dull, dense lava fragments with orange dust cover.

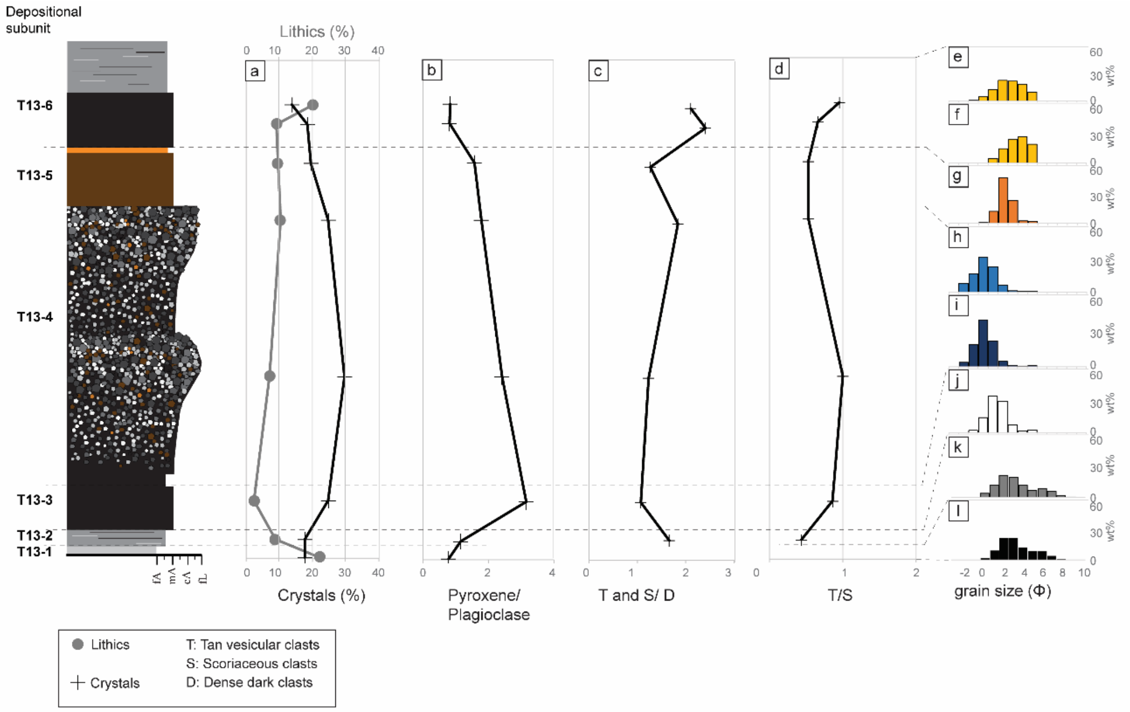

Fig. 4.9: Idealised composite profile illustrating the main variations in componentry at the representative key location Loc. 1. Componentry is shown for the 2 Φ size class. Note that data for T13-1 is taken from Loc. 3, given the limited dispersal of T13-1. a) Percentage of lithic clasts (grey) and free crystals (black) is calculated relative to total number of clasts counted per sample. b) Ratio of free pyroxenes over free plagioclase. c) Vesicular juvenile over dense juveniles with vesicular juveniles containing both tan vesicular (T) and scoriaceous (S) clasts, while D marks dense clasts. d) Variation in vesicular clast types calculated relative to total number of counted juvenile glass. Insets e to l) show grain size distributions for individual beds at Loc. 1 and at Loc. 3 for T13-1. Note the bimodality in subunits T13-1 (l) and T13-2 (k).

4.4.3 Geochemical characterisation

Andesitic to dacitic tephra is known for being affected by pre- and syn-eruptive crystallisation (Hammer et al., 2000; Gaunt et al., 2016; Di Piazza et al., 2019), including both phenocrysts (>100 µm) and groundmass microlites (<100 µm). Image analysis of the subunits at Loc. 1 (Fig. 4.2c) shows that the groundmass is highly microcrystalline (>37.8 %; average groundmass crystallinity=54.36%) with proportions of pure glass (calculated on a vesicle- and phenocryst-free base) ranging from 25 to 61.61%. The dominant microlite phases are plagioclase (27.19–56.81%), followed by pyroxene (7.26–29.42%). Interestingly, despite the different juvenile types being correlated with groundmass crystallinity (Fig. 4.7a), no clear correlation between groundmass crystallinity and glass composition can be established (Fig. 4.10).

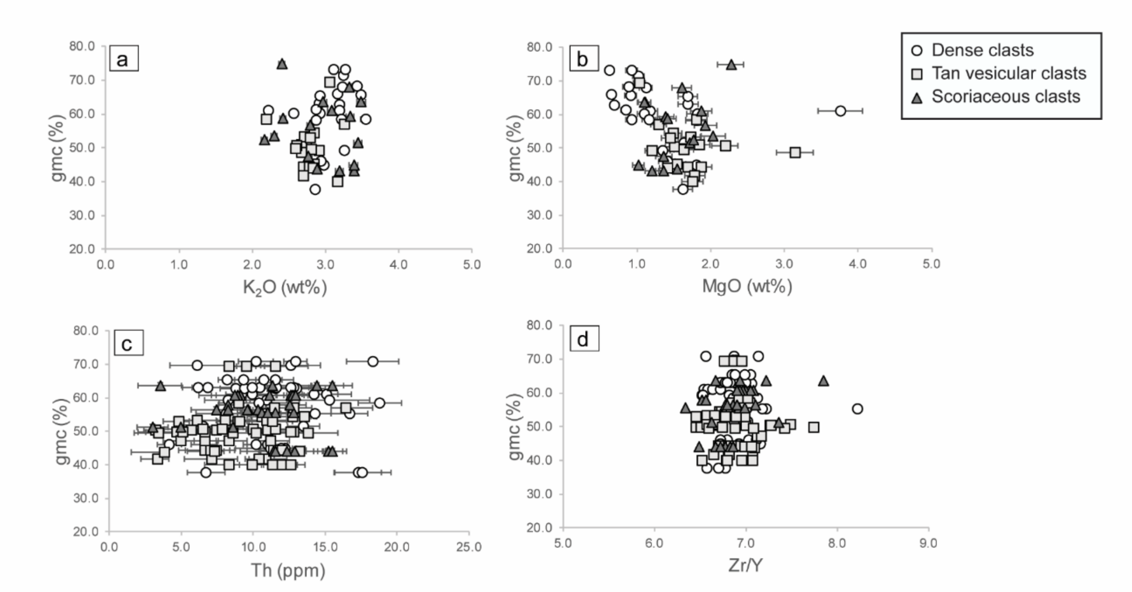

Fig. 4.10: Overall 2D-groundmass crystallinity (gmc in %, calculated on a vesicle- and phenocryst-free basis) for different componentry classes and their relationship with selected major element oxide and trace element compositions. Major element compositions are normalised on a volatile-free basis. Error bars mark respective analytical errors (see Appendix G-1 for major element data and Appendix G-2 for trace element data). Different juvenile types are represented by the following symbols: white circles- dense microcrystalline juveniles (D-type), light grey squares- tan vesicular juveniles (T-type), dark grey triangles- scoriaceous juveniles (S-type) a) Groundmass crystallinity vs K_2O. Note the constant K_2O values with increasing groundmass crystallinity. b) Groundmass crystallinity vs MgO. Note the weak negative correlation between gmc and MgO. c) Groundmass crystallinity vs Th. Thorium compositions are variable but lack an evident correlation with groundmass crystallinity. d) Groundmass crystallinity vs incompatible trace element ratio Zr/Y. Note that Zr/Y remains constant with variable gmc.

4.4.3.1 Major elements

The juvenile glass is dacitic in composition (SiO_2=62.34–69.61 wt% and K_2O=1.83–4.13 wt%) following the classification of Le Maitre et al. (2002) and falls into the medium- to high-K ranges as defined by Gill (1981). The new major element glass compositions compare well with previously published data for the Tufa Trig Formation (SiO_2=60.25–67.24 wt%; K_2O=1.82–3.29 wt%; MgO=1.44–3.52; CaO=3.7–6.9 wt%; Donoghue et al., 2007).

Major element compositions cover the same range for S-type, D-type and T-type clasts and form continuous linear arrays between wt% SiO_2 and wt% MgO, CaO and K_2O in Harker diagrams (Fig. 4.11a-f). Generally, T-type clasts show lower SiO_2 (63.26–68.44 wt%) and slightly higher MgO and CaO (MgO=0.95–3.76 wt%, CaO=3.21–5.63 wt%), compared to S-type (SiO_2=64.14–68.55; MgO=0.77–2.49 wt%; CaO=2.98–5.20 wt%) and D-type glass (SiO_2=62.34–69.61; MgO=0.48–3.76 wt%; CaO=2.73–6.18 wt%). While no clear temporal relationship can be seen between individual subunit glass compositions and eruption progression, several observations regarding individual subunits are noteworthy: Although the majority of T13-2 glass compositions span a continuous linear array between SiO_2=65.64–69.61, MgO=0.63–1.73 wt%, CaO=2.83–4.62 wt%, K_2O=2.74–3.66 wt% (Fig. 4.11), some glass compositions extend to comparably low SiO_2 (64.14–64.21 wt%) and high MgO (1.88–2.02 wt%) and CaO (4.95–5.02 wt%), highlighting a compositional gap of ~1 wt% from SiO_2~64.2 to 65.6 wt%. T13-3 glasses highlight a similar compositional gap of ~1 wt% from SiO_2~64.6 to 65.6 wt% and form a cluster at higher MgO content of 2.36–3.4 wt%, while the majority of data points shows values of SiO_2=65.41–68.83 and MgO=0.76–1.86 (Fig. 4.11a). For T13-4 juveniles the gap is less evident, but a cluster with relatively higher MgO (2.44–3.02 wt%), CaO (4.79–5.63 wt%) and slightly lower SiO_2 (63.43–64.20 wt%) and K_2O (2.17–2.57 wt%) can be observed (Fig. 4.11). Similarly, a group of T13-5 and T13-6 glasses has comparably low SiO_2 contents (=62.34–63.87 wt%) and higher MgO (1.49–3.76 wt%) and CaO values (5.01–6.18 wt%, Fig. 4.11b, d), while the majority of data points shows values between SiO_2=64.2–69.58 wt%, MgO=0.7–3.23 wt%, CaO=2.73–5.24 wt% and K_2O=1.94–3.69 wt%.

4.4.3.2 Trace element compositions

Mt. Ruapehu magmas are well known for incorporating crystals along their ascent path (Nakagawa et al., 1999; Nakagawa et al., 2002; Kilgour et al., 2013), limiting the value of bulk compositions to e.g., distinguish between different magma batches. While this problem can be avoided by obtaining spot analyses on pure glass, for glasses with high microlite densities this undertaking is often complicated by the absence of pure glass spots that are large enough (~30 μm) for trace element spot analysis. At the same time, decreasing the beam diameter to fit the available smaller glass spots (e.g., ~10 μm) would increase the analytical uncertainty. Consequently, trace element analyses represent semi bulk-rock compositions including glass and microlites. Analysis spots were selected carefully to avoid phenocrysts to minimise the influence of components incorporated during magma ascent and storage. To exclude the influence of variable microlite-glass proportions on the trace element compositions, only trace elements that are incompatible in the dominant microlite phases (plagioclase and pyroxenes) are discussed in the following (Fig. 4.11g-j). In line with this, the following two observations make us confident that bulk compositions are indeed representative of the late-stage magma and can provide useful insights into magmatic processes syn-and prior to eruption: (1) Trace element ratios show no correlation with groundmass crystallinity (Fig. 4.10c, d) and (2) analysed trace elements and representative trace element ratios exhibit a limited compositional variability, varying by ±10–15% from respective averages.

All analysed samples are enriched in large ion lithophile elements (LILE) with respect to high field strength elements (i.e., high Ba/Y in Fig. 4.11i, j). Light rare earth elements (LREE) are higher than middle (MREE) and heavy rare earth elements (HREE), as exemplified by La/Sm ratios of ≥3.5 in Fig. 4.11g, h. As can be expected for subduction-related melts, the glass shards are generally enriched in elements that are mobile in aqueous phases such as Rb or Ba, if compared to mid-ocean ridge basalts (Fig. 4.11i, j, Elliott et al., 1997). Minor syn-sequence variations involve subunits T13-2 and -3 being characterised by almost constant Zr/Y ratios of 6.78–7.18 and 6.78–7.1, while La/Sm ratios show the largest continuous range of all subunits ($La/Sm_{T13\text{-}2}$=3.53–4.21 and $La/Sm_{T13\text{-}3}$=3.93–4.67, Fig. 4.11g, Table 4.3). Similarly, Rb/Sm and Ba/Y show a continuous range of 19.16–24.54 (Rb/Sm) and 23.65–29.38 (Ba/Y) for these two subunits (Table 4.3). It is noteworthy, that these trace element ratios are less scattered in T13-4 (e.g., La/Sm=3.62–4.11, Zr/Y=6.77–6.99, Ba/Y=23.60–28.28, Rb/Sm=19.79–23.16, Table 4.3), than in samples from T13-2 and T13-3 (Fig. 4.11g, i). T13-5 shows lower Zr/Y values than subunits T13-2 to -4 with values of Zr/Y=6.54–6.67 (Fig. 4.11h), while Rb/Sm ratios vary between 20.8 and 24.5 at almost constant Ba/Y (24–25.20). Contrastingly, T13-6 shards show variable Zr/Y values of 6.52–8.23 with homogeneous La/Sm ratios (La/Sm=3.68–4.34, Fig. 4.11i). Rb/Sm ratios of T13-6 are variable (20.17–27.59), reaching higher values than observed in subunits T13-2 to -5 and Ba/Y values range between 23.90–30.72 (Table 4.3, Fig. 4.11j).

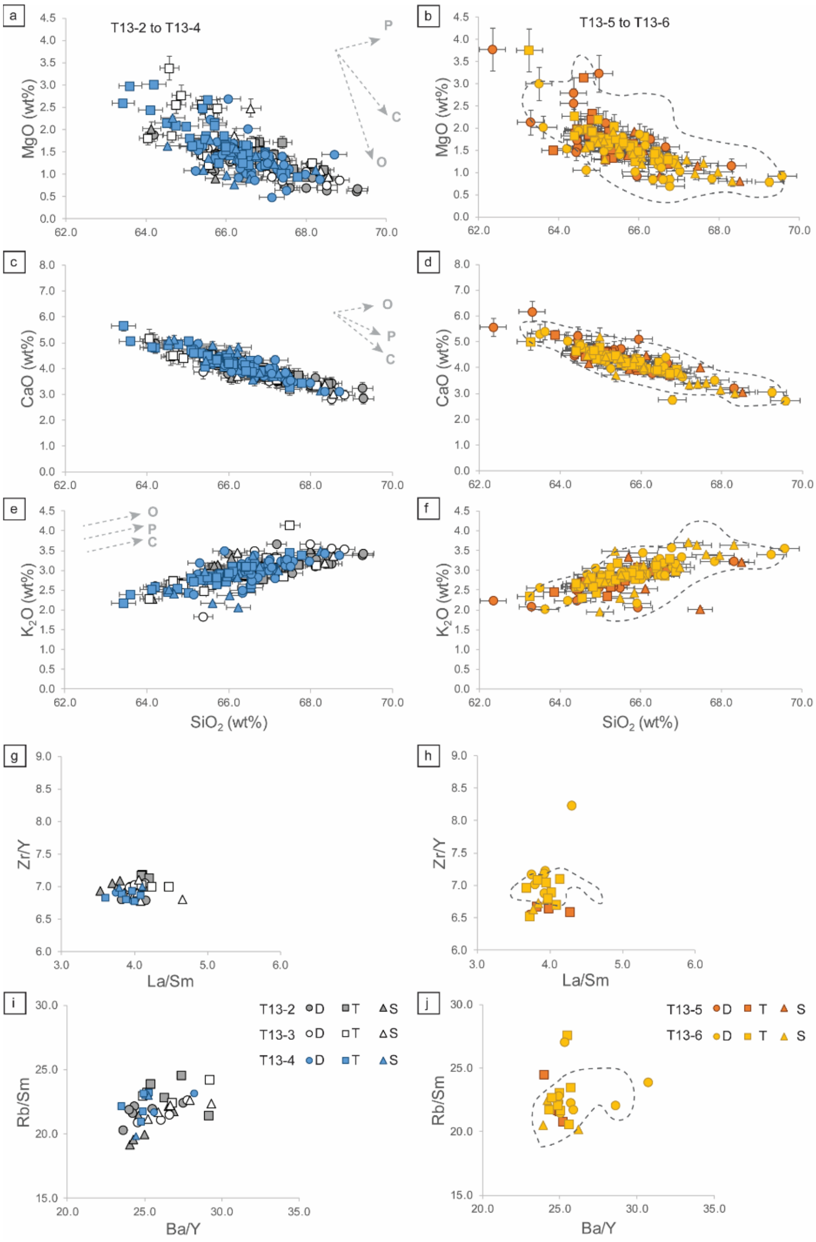

Fig. 4.11: Geochemical characterisation of individual subunit throughout the T13-sequence. Major elements are normalised on a volatile-free basis. Symbols are grouped according to their corresponding juvenile class: circles show dense juveniles, squares mark tan vesicular clasts and triangles mark scoriaceous juveniles. Individual subunits are colour-coded with T13-2 data being reported in grey, T13-3 in white, T13-4 in blue and T13-5 and -6 in orange and yellow, respectively. Note the absence of T13-1. Error bars mark accuracy for major element oxides (Appendix G-1.4). Stippled field in b, d, f, h and j mark compositional field for subunits T13-2,-3 and -4 as reported in insets a, c, e, g and i. Assuming 10% of fractionation of each phase, fractionation vectors are reported by grey dashed arrows for orthopyroxene (O), clinopyroxene (C) and plagioclase (P), following phenocryst compositions in Nakagawa et al., (1999) and Price et al., (2012). a) MgO vs SiO_2 for subunits T13-2, -3 and -4 b) MgO vs SiO_2 for subunits T13-5 and -6. c) CaO vs SiO_2 for subunits T13-2, -3 and -4. d) CaO vs SiO_2 for subunits T13-5 and -6. e) K_2O vs SiO_2 for subunits T13-2, -3 and -4. f) K_2O vs SiO_2 for subunits T13-5 and -6. g) Trace element ratios Zr/Y vs La/Sm for subunits T13-2, -3 and -4. h) Trace element ratios Zr/Y vs La/Sm for subunits T13-5 and -6. i) Trace element ratios Rb/Sm vs Ba/Y are shown for subunits T13-2, -3 and -4. j) Trace element ratios Rb/Sm vs Ba/Y are reported for subunits T13-5 and -6.

Table 4.3 (continues on next page): Main features of subunits within the T13-tephra sequence

	T13-1	T13-2	T13-3	T13-4	T13-5	T13-6
Main deposit features	Thickness <10 mm, highly fragmented, laminated	Thickness <10 mm, highly fragmented, laminated	Massive medium ash with capping finer ash, normally graded	At least two cycles of reverse grading, coarsest subunit	Variable, including massive brown ash in SE and bedset of multiple mm to cm-thick beds in ESE. Overall better sorting	Normally graded, massive ash, with capping laminated very fine ash to fine ash
Main dispersal direction	SE, <11 km	Multiple, <10 mm at 10 km	Slightly asymmetrical dispersal, mainly towards E-ESE, maximum extent 21 km	Multi-lobate, mainly towards the E with secondary lobes towards SE, NE and WSW	Multiple	Bilobate towards NE and SE, <19.9 km distance
Grain size features	Bimodal distribution with modes at 2 Φ and 6 Φ	Bimodal distribution (2 and 6 Φ modes)	Unimodal distribution, laterally variable grain size modes (1 Φ in E-NE) and 2 Φ in SE.	Unimodal distribution with modes at 0 Φ (E) and 1 Φ (SE, SSE and NE) maximum grain sizes of –3 Φ. Reverse grading. Finer NE lobe with mode at 1 Φ	Laterally variable: Bimodal with mode at 2 Φ and secondary mode at >4 Φ in SE. Unimodal in SSE (mode at 1 Φ) and in E (mode at 2 Φ)	Laterally variable and normally graded: Mode at 4 Φ in SE and E directions. Coarser in NE, with mode at 2 Φ
Median grain size (maximum clast)	fA (vcA)	fA (vcA)	mA–cA (fL)	cA–vcA (mL)	mA–cA (mL)	mA–vfA (mL)
Componentry	Juv>Lith>C	Juv>C>Lith	Juv>C>Lith	Juv>C>Lith	Juv>Lith>C	Juv>C>Lith; lithics show higher abundance to the E
Juveniles	S>D~T; D:V=0.4	S≥D>T; D:V=0.6	D>S>T; D:V=0.9 in E and 1.2–1.4 in SE and NE	D>S>T; D:V=0.5–1.3	D>S>T; D:V=0.8–0.9 but E where D:V=0.4	D>S>T (SE and NE) and S>D~T (E); D:V=1.1 to NE and 0.4–0.9 to SE-E
D-type	Blocky, rugged surface, conchoidal & step-like features	Blocky with extremely fine ash cover, sharp edges and conchoidal features, gmc=60.18–65.93%	Chippy-blocky, sharp edges and conchoidal features, gmc=51.44–65.63%	Chippy to blocky with irregular surface and small vesicles, conchoidal and step-like features, gmc=37.80–73.18%	Blocky and irregular surface, rarely fluidal and smooth, conchoidal and step-like features, gmc=58.50–61.08%	Shattered surface, conchoidal features, sharp edges, higher abundances to the E-NE, gmc=44.80–61.36%
S-type	Fluidal morphologies with smooth surface to irregular morphologies with thick bubble walls and heterogeneous, deformed and coalescent vesicles	Isolated larger vesicles, thick glassy walls, cuspate shape, few shards show fluidal morphology, gmc=53.66–68.07%	Fluidal and blocky morphologies with smooth surfaces and large isolated vesicles, slightly deformed, gmc=51.59–61.11%	Heterogeneous morphologies, generally irregular and blocky. Heterogeneous vesicles, ranging from large isolated & deformed vesicles to small, closely spaced slightly deformed vesicles, gmc=47.39–75%	Thick bubble walls and fluidal-smooth morphologies with large slightly deformed vesicles, gmc=56.73–59.22%	Glassy, heterogeneous vesicularity with deformed and coalescent vesicles, gmc=43.05–58.72%
T-type	Fluidal morphologies with smooth surface and heterogeneous vesicles (deformed and coalescent) and thick bubble walls	Small and deformed vesicles with elongated, irregular bubble walls and smooth fluidal surfaces, gmc=43.93–49.19%	Fluidal morphologies, smooth surfaces, heterogeneous vesicles, ranging from small, poorly deformed vesicles and thin bubble walls to large coalescent deformed vesicles, gmc=50.50–58.32%	Homogeneous vesicularity with closely spaced small vesicles, variably deformed, gmc=41.73–69.29%	Pumiceous with smooth surfaces and small vesicles and fluidal with large deformed vesicles, gmc=48.59–50.85%	Higher abundance to the E-SE. Glassy with high vesicle density, comprising small and strongly deformed vesicles that show disrupted shapes, gmc=39.98–57.11%

Notes: Componentry refers to relative percentages of Juv (juvenile clasts), Lith (lithics) and C (crystals), calculated to the total number of counted shards, while the different juvenile classes are calculated relative to the total number of juveniles with D: dense clasts, S: scoriaceous clasts and T: tan vesicular clasts. *Grain size and maximum grain size follow the nomenclature of White & Houghton, (2006) with vfA=very fine ash, 3 to 4 Φ; fA=fine ash, 3 to 2 Φ; mA=medium ash, 2 to 1 Φ; cA=coarse ash, 1 to 0 Φ; vcA=very coarse ash, 0 to –1 Φ; fL=fine lapilli, –1 to –2 Φ; mL=medium lapilli, –2 to –4 Φ. Major element compositions show the range of spot analyses and are reported as normalised values, re-calculated to 100 on a volatile-free basis (Appendix G-1). Trace element compositions represent the range of spot analyses, while averages are reported in Appendix G-2. Groundmass crystallinity on a vesicle and phenocryst-free basis is reported as gmc (Appendix F-1).

Table 4.3 (continued): Main features of subunits within the T13-tephra sequence

	T13-1	T13-2	T13-3	T13-4	T13-5	T13-6
Major elements	nd	SiO_2=64.14–69.61 wt%; K_2O=2.28–3.66 wt%; MgO=0.63–2.02 wt%; CaO=2.83–5.02 wt%	SiO_2=64.06–68.83 wt%; K_2O=1.83–4.13 wt%; MgO=0.76–3.37 wt%; CaO=2.78–5.15 wt%	SiO_2=63.43–68.71 wt%; K_2O=2.07–3.49 wt%; MgO=0.48–3.02 wt%; CaO=3.08–5.63 wt%	SiO_2=62.34–68.52 wt%; K_2O=2.02–3.33 wt%; MgO=0.8–3.76 wt%; CaO=3.04–6.18 wt%	SiO_2=63.26–69.58 wt%; K_2O=1.94–3.69 wt%; MgO=0.7–3.75 wt%; CaO=2.73–5.41 wt%
Trace elements	nd	La/Sm=3.53–4.21; Rb/Sm=19.16–24.54; Ba/Y=23.65–29.17; Zr/Y=6.78–7.18	La/Sm=3.93–4.67; Rb/Sm=20.89–24.22; Ba/Y=24.56–29.38; Zr/Y=6.78–7.10	La/Sm=3.62–4.11; Rb/Sm=19.79–23.16; Ba/Y=23.60–28.28; Zr/Y=6.77–6.99	La/Sm=3.72–4.28; Rb/Sm=20.8–24.5; Ba/Y=24–25.20; Zr/Y=6.54–6.67	La/Sm=3.68–4.34; Rb/Sm=20.17–27.59; Ba/Y=23.90–30.72; Zr/Y=6.52–8.23

Notes: Componentry refers to relative percentages of Juv (juvenile clasts), Lith (lithics) and C (crystals), calculated to the total number of counted shards, while the different juvenile classes are calculated relative to the total number of juveniles with D: dense clasts, S: scoriaceous clasts and T: tan vesicular clasts. *Grain size and maximum grain size follow the nomenclature of White & Houghton, (2006) with vfA=very fine ash, 3 to 4 Φ; fA=fine ash, 3 to 2 Φ; mA=medium ash, 2 to 1 Φ; cA=coarse ash, 1 to 0 Φ; vcA=very coarse ash, 0 to –1 Φ; fL=fine lapilli, –1 to –2 Φ; mL=medium lapilli, –2 to –4 Φ. Major element compositions show the range of spot analyses and are reported as normalised values, re-calculated to 100 on a volatile-free basis (Appendix G-1). Trace element compositions represent the range of spot analyses, while averages are reported in Appendix G-2. Groundmass crystallinity on a vesicle and phenocryst-free basis is reported as gmc (Appendix F-1).

4.5 Discussion

In the following, we combine the multi-parameter dataset to characterise the complexity of the deposits associated with the T13 multi-phase eruption and to discuss the implications this has for the understanding of eruption dynamics and the syn-eruptive progression of small-scale multi-phase eruptions.

4.5.1 Tephra dispersal

Individual subunits show complex tephra dispersal that is characterised by several thickness lobes in different directions, while no clear internal contacts can be correlated between different sections. Pyroclast assemblages show lateral variability for individual subunits with proportions of juvenile clasts, lithics and crystals differing between locations (Fig. 4.8). Contrastingly, grain size characteristics show less lateral variability, as has e.g. been shown for T13-4, which is characterised by low F1 and F2 throughout different locations (Fig. 4.5). This has interesting implications for syn-eruptive dispersal dynamics: (1) Subunits represent multiple semi-continuous or intermittent individual explosions of similar eruption style and intensity rather than one continuous eruption. The stratified and laminated texture of tephra deposits agrees well with instable weak eruption plumes, discontinuous magma discharge rates and intermittent short-lived eruptive activity (cf. Arrighi et al., 2001; Pioli et al., 2008; Cioni et al., 2011). (2) The prevailing north-westerly, westerly and south-westerly winds can change over timescales of few hours and exert a strong control on the eruption plume and tephra dispersal, leading to the observed SE and NE-dominated dispersal directions. Similar dispersal patterns have been previously described for both historical and prehistorical Mt. Ruapehu eruptions (Cronin et al., 2003; Pardo et al., 2012).

4.5.1.1 Tephra volume

Different methods for calculating deposit volumes give coherent values and span several orders of magnitudes. Overall, the cumulative T13 deposit volume is an order of magnitude smaller compared to the deposit volumes inferred for the subplinian to Plinian eruptions of the Bullot Formation (>0.6 km^3, Pardo et al., 2012) but agrees well with values calculated for similarly extensive dispersed multi-phase eruptions at Mt. Ruapehu (Donoghue et al., 1995; Tf6 and Tf8 after Donoghue et al., 1997; T15, Voloschina et al., 2020). A previously published deposit volume for T13 (“Tf5” in Donoghue, 1991; Donoghue et al., 1995) yields a cumulative value of 88 × 10^6 m^3 (Donoghue, 1991), which compares well with the here calculated volume estimates of 24.4 to 60.4 × 10^6 m^3. However, this previous calculation was based on a deposit dispersal that was approximated by an elliptical, single lobe and did not account for the multi-phase character of the sequence.

The comparison of our data with the most complete thickness dataset from the June 1996 Mt. Ruapehu eruption (Bonadonna et al., 2005; Bonadonna et al., 2012) suggests that the here presented thickness data resolves only the second (medial) segment of the total distribution (Fig. 4.12; Bonadonna et al., 1998; Bonadonna et al., 2005). The erupted volume obtained for the subplinian phase on June 17th 1996 is 4 × 10^6 m^3 (Bonadonna et al., 2005), compared to a total volume for the 1995–1996 sequence of <0.1 km^3 (Johnston et al., 2000). In Fig. 4.12a, deposit thicknesses for T13-4 are shifted upward compared to 1996 thicknesses, indicating higher erupted volumes of the former. The volume calculations in Bonadonna et al. (2005) are based on an in-situ or a shortly afterwards sampled dataset, thus accounting for deposits with thicknesses <10 mm, which is a resolution that is complicated to obtain for most geologically preserved deposits. In fact, while unconsolidated pyroclastic material can be identified at several northward locations, a discrete tephra deposit that can be unequivocally associated with the 1995–1996 events has not been identified yet. This concords with the suggestion that the T13-eruption involved a larger erupted volume and that the estimated deposit volume represents a minimum value. Similar statements have been previously discussed for more voluminous eruptions, where deposit volumes are known to underestimate the distal fine ash component significantly (Fierstein et al., 1992; Rose, 1993; Bonadonna et al., 2012).

Using the Mt. Ruapehu June 1996 dataset of Bonadonna and Houghton (2005), we can estimate the potentially underrepresented distal deposit volume (Fig. 4.12). Following the single segment exponential model of Pyle (1989) and Fierstein et al. (1992), the deposit thickness thinning rate is described by the k-factor in the exponential equation and is represented by the slope of the thickness distribution in a log(deposit thickness) to √(isopach area) diagram. The T13-4 and T13-6 distributions are described by k-factors of

$k_{T13\text{-}4}$= –0.117 and $k_{T13\text{-}6}$= –0.126, respectively (Fig. 4.12b, Table 4.2). These values are similar to the k-factor that describes the 2nd segment of the June 1996 thickness distribution (k_{1996}= –0.116). Based on the assumption that the two eruption phases have similar break-in-slope distances (b_{is}=28.41 km), and assuming that the k-factors for the distal segment (k_d= –0.047) are comparable for the June 1996 and the T13-4 and T13-6 phases, this would add 59–62% to the previously calculated deposit volumes for T13-4 and T13-6, respectively (Fig. 4.12).

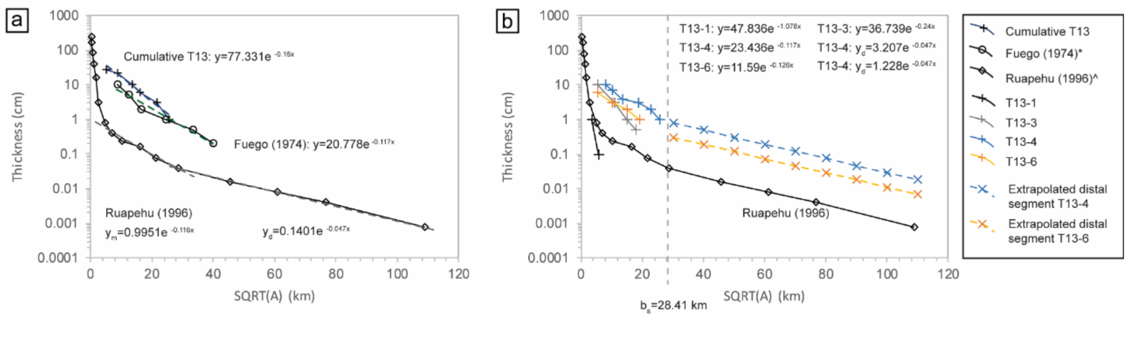

Fig. 4.12: Semi-log plot showing deposit thickness in cm vs √(isopach area A) in km. a) The distribution of the cumulative thickness for the T13-sequence (plus signs) is compared with the thickness distribution of the Fuego 1974 eruption (circles, data from Rose et al., 2008) and the distribution for the June 1996 Mt. Ruapehu eruption (data from Bonadonna and Houghton, 2005). For comparison, exponential equations that describe the exponential fitting line are reported as well. b) Thickness distribution for individual subunits: T13-1 (black plus signs), T13-3 (grey plus signs), T13-4 (blue plus signs) and T13-6 (orange plus signs). Note the steep thickness distribution for subunits T13-1 and T13-3. Assuming, that our field data represents only the medial segment (cf. Bonadonna et al., 1998), T13-4 and T13-6 show similar k-factors of $k_{T13\text{-}4}$= –0.117 and $k_{T13\text{-}6}$= –0.126 that describe the thickness thinning rate following Pyle (1989); Fierstein et al. (1992). Based on the known thickness distribution from the June 1996 Mt. Ruapehu eruption after Bonadonna and Houghton, 2005 and assuming similar break-in-slope distances (b_{is}=28.41 km) between the medial and the distal segment, we extrapolate the distal segment for subunits T13-4 and T13-6, using a distal k-factor of k_d= –0.047. Extrapolated distal segments are marked by blue and orange crosses and dashed lines for T13-4 and T13-6, respectively. The exponential equations that describe the observed medial and extrapolated distal segments are shown as well. For comparison, the June 1996 Mt. Ruapehu distribution (after Bonadonna and Houghton, 2005) is also shown.

4.5.2 Syn-eruptive variation and eruption progression

Donoghue et al. (1997) described the eruption styles associated with the Tufa Trig Formation to involve predominantly phreatomagmatic and Strombolian activity. However, the combination of the here presented field observations, pyroclast assemblage, grain size and textural characteristics suggest more complex scenarios that involve an interplay between phreatomagmatic and magmatic processes simultaneously or over short timescales. In line with this, we infer that the T13-eruption was characterised by short-lived, intermittent to semi-continuous eruptive activity, where the low intensity activity can be described as phreatomagmatic and Strombolian-type activity, while the more dispersed subunits are better approximated by violent Strombolian to subplinian-type activity. In line with this, the term *violent Strombolian* is used to describe eruptive activity that is more energetic and involves higher magma eruption rates compared to "normal" Strombolian activity, and is accordingly associated with wider dispersed deposits with high percentages of ash-sized material (cf. Walker, 1973; Arrighi et al., 2001; Pioli et al., 2008, Cioni et al., 2008a). No unequivocal evidences for plug formation or indicators typical of Vulcanian-type activity (cf. Heiken & Wohletz, 1985; Kennedy et al., 2005; Yamanoi et al., 2008; Wright et al., 2012; Suzuki et al., 2013; Miwa et al., 2009; 2013) could be identified.

In the remainder of the section we discuss the systematic variations and coherent patterns in deposit textures, pyroclast assemblage and textural characteristics to provide insights into the eruption progression and dynamics (Fig. 4.9, Fig. 4.13). We subdivide the T13-sequence in five main eruption phases: (1) opening phase, (2) semi-continuous Strombolian phase, (3) main violent Strombolian to subplinian phase, followed by a time break, (4) violent Strombolian phase and (5) violent Strombolian to subplinian phase with final ash venting.

4.5.2.1 The opening phase P1

Beds associated with subunits T13-1 and T13-2 are predominantly in the fine ash size fractions and display bimodal grain size distributions with secondary modes in the extremely fine ash fractions (Fig. 4.9). Combined with relatively high percentages of orange and white lithics of older eruptive products and the hydrothermal system, as well as densely crystallised, blocky juvenile clasts, and ubiquitous adhering dust, this is typically interpreted as an indicator for phreatomagmatic fragmentation mechanisms (Heiken et al., 1985; Wohletz et al., 2013). Groundmass crystallinities span a variable range, being generally larger than >50% for both scoriaceous and dense clasts (Fig. 4.13, Table 4.3). We interpret the laminated appearance of these subunits, together with limited bed thicknesses (<10 mm) and a maximum extent of ~11 km from source, as these subunits representing multiple small, low-intensity eruptions. Eruption styles are influenced by variable degrees of phreatomagmatic to Strombolian explosions, with individual explosions being closely spaced in time.

4.5.2.2 Violent Strombolian phase P2

The extensive dispersal of T13-3 (Fig. 4.2) highlights the importance of this phase. Tan vesicular and scoriaceous clasts show higher vesicularities and larger isolated and deformed vesicles compared to the opening phase, while at the same time percentages of dense juvenile clasts in the 2 Φ size fraction are relatively high. We interpret this as an increase in fragmentation efficiency and increasing influence of magmatic fragmentation. In line with this, relative proportions of juvenile clasts and free crystals are higher compared to the opening phase, agreeing with higher fragmentation energy and laterally consistent, massive deposit textures (Fig. 4.2). Eruption rate declines with time, resulting in an overall grain size decrease (Fig. 4.2b, c, d). Regarding the geochemical characteristics, it is noteworthy that averaged compositions for T-type glass are characterised by slightly lower SiO_2 values along with higher MgO contents, agreeing with an increase in pyroxene free crystals over plagioclase (Fig. 4.8). This suggests that a compositionally slightly less evolved magma portion was involved in this eruption phase. The slightly asymmetric dispersal in combination with laterally variable componentry and grain size modes can be related to a syn-eruptive change in wind direction distributing the pyroclastic ejecta towards different directions.

4.5.2.3 Main violent Strombolian to subplinian phase P3

The relatively coarser grain size and thickness of the beds associated with T13-4, combined with the highly vesicular nature of T-type clasts, underline an increasingly magmatic character and higher eruption intensity for this phase. At least two grading cycles indicate semi-continuous magma discharge, possibly due to fluctuations in eruption rate. The strongly irregular and extensive dispersal patterns (Fig. 4.3d, Fig. 4.4c) suggest that eruption duration must have been sufficiently long to accommodate syn-eruptive wind changes and several consecutive explosive events, suggesting that eruptive activity involved violent Strombolian to subplinian-type characteristics (cf. subplinian II in Cioni et al., 2008a). Average SiO_2 and K_2O contents decrease from SiO_2=66.77 wt% in T13-3 to 66.01 wt% in T13-4 and from K_2O=3.08 wt% to 2.77 wt% in T13-4, respectively, while CaO content increases from CaO=3.74 wt% in T13-3 to 4.33 wt% in

T13-4 (Fig. 4.13). This highlights that the melt feeding the T13-4 is slightly less evolved than the one that fed T13-3.

In line with the different types of contacts discussed in Heinrich et al. (2020), we define the contact between subunits T13-4 and T13-5 as a 3rd-order contact, implying a time break on the order of magnitude of 2–5 years. As no evidence for reworking and erosion can be identified, the timescales are probably significantly shorter, possibly in the range of months to maximum a year. For comparison, during the subplinian 11–14 October 1995 eruptions, the Crater Lake was displaced, following the precedent series of eruptions throughout 1995 (Nairn et al., 1996; Cronin et al., 2003). Subsequently, the Crater Lake refilled during the break in eruption activity between November 1995 and June 1996, only to be evaporated anew during the subplinian 17 June 1996 eruption (Scott, 2013). In agreement with these timescales, the time break within the T13-sequence was potentially long enough to allow for a Crater Lake renewal, potentially allowing for phreatomagmatic fragmentation.

4.5.2.4 Violent Strombolian phase P4

Beds associated with T13-5 exhibit similar features to T13-2 and T13-1 regarding their pyroclast assemblage but vary significantly in their deposit and dispersal characteristics, being significantly coarser and wider dispersed (Table 4.3). We interpret the numerous, laterally strongly variable beds as follows: The eruption recommences, alimented by portions of the same magma that fed the previous phases. Deposit textures suggest less continuous activity compared to P3, with multiple intermittent explosions excavating deeply into the vent system and leading to the irregular tephra dispersal. Textural characteristics lack clear indicators for phreatomagmatism. This indicates that if a Crater Lake renewal has taken place, it might have been only partially, and that during the initial explosions of this eruption phase, it has been progressively emptied again. With eruption progression, individual explosions are increasingly influenced by magmatic fragmentation overshadowing phreatomagmatic fragmentation.

4.5.2.5 Violent Strombolian to subplinian phase P5

The dispersal of the deposits associated with this eruption phase shows a characteristic bilobate pattern, suggesting a change in wind direction between at least two discrete phases. This results in the higher intensity phase being dispersed mainly towards the N, while ash-sized ejecta is dispersed towards the SE. T13-5 and -6 are closely spaced in time, as shown by the lack of a clean contact in many locations. High relative proportions of strongly vesicular juvenile clasts point towards violent Strombolian to possibly subplinian eruption styles, given the extended dispersal. We interpret the increase in SiO_2 and K_2O glass compositions relative to the previous phase (Fig. 4.13) as this subunit being likely fed by a slightly different portion from the magmatic system. The extraction and magma ascent are probably facilitated thanks to the extensive vent and conduit excavation during the previous phase and an absent Crater Lake.

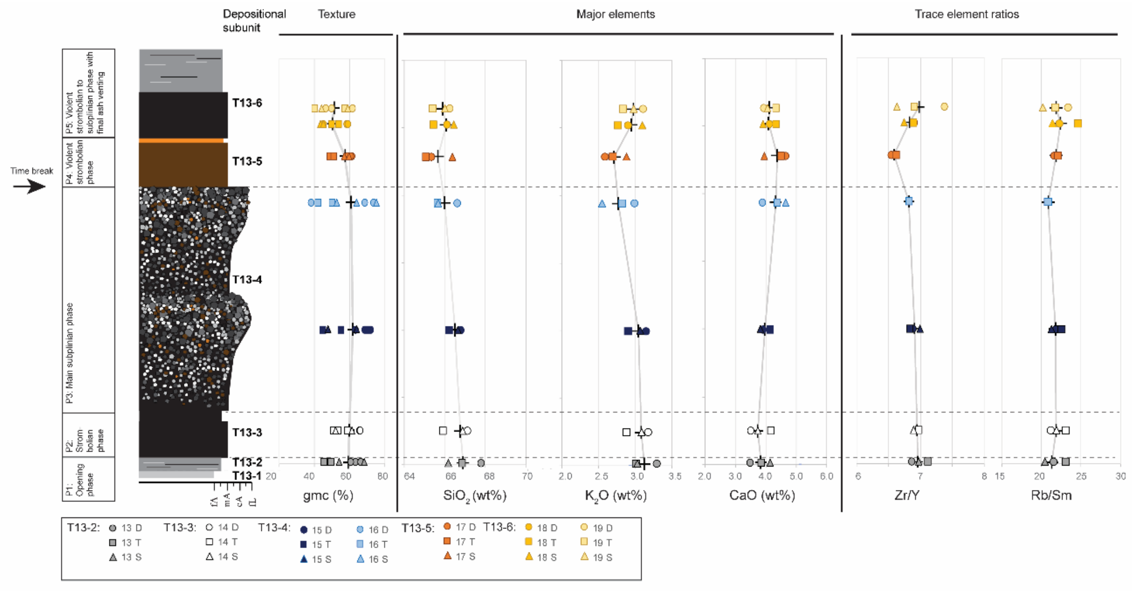

Fig. 4.13: Overview of an idealised composite stratigraphic profile of the T13-tephra sequence. The variability of selected parameters throughout the sequence is reported. Subunit averages are marked by plus signs, are connected by a grey line and are calculated based on the relative proportions of the different juvenile types. Major element compositions are normalised on a volatile-free basis. Groundmass crystallinity is shown as gmc (%). The temporal evolution of major element oxides SiO_2, K_2O and CaO is reported, showing averaged compositions for the three main juvenile classes: dense clasts (D, circles), tan vesicular clasts (T, squares) and scoriaceous clasts (S, triangles). The temporal evolution of selected trace element ratios Zr/Y and Rb/Sm is shown as well, using the same symbology as for major elements.

4.5.3 Temporal patterns in the magmatic system of an andesitic composite volcano

Mt. Ruapehu's magmatic system involves a nested shallow system at 2 to 9 km depth (Kilgour et al., 2013). Studies on crystals and melt inclusions from historical eruptions (Nakagawa et al., 1999; Nakagawa et al., 2002; Kilgour et al., 2013) and on lava flows from the past 250,000 years suggest multiple small-volume (<0.1 km^3) interconnected dikes and sills in a shallow system (Gamble et al., 1999; Price et al., 2005; Price et al., 2012; Conway et al., 2018). These small magma bodies are in a mushy state (e.g., 25–55 vol% crystals, Barth et al., 1994; Marsh, 2015) and can interact with each other prior and during eruption (Nakagawa et al., 1999; Nakagawa et al., 2002; Kilgour et al., 2013). In the following, we will examine our dataset at different timescales ranging from individual eruption sequences (months to years) to 1000s of years, discussing how our dataset fits with previously published datasets and outlining the implications for future eruption scenarios.

4.5.3.1 Temporal patterns within an eruption sequence

Several findings on timescales of individual eruption sequences can be outlined for the T13-sequence: (1) Minor systematic changes such as decreasing SiO_2 and increasing MgO and CaO throughout eruption phases P1 to P3 (Fig. 4.13) indicate that these phases were fed by a magma that becomes less evolved with eruption progression. Compositions of eruption phase P4 appear unaffected by the time break and show a further decrease in SiO_2 and K_2O and an increase in CaO compared to P1 to P3 (Fig. 4.13). Conversely, P5 eruption products shift back in composition towards higher SiO_2 and lower CaO values. (2) A compositional gap in major element oxides SiO_2, CaO and K_2O is most pronounced for the initial eruption phases P1 and P2 (subunits T13-2 and T13-3; Fig. 4.11, Fig. 4.13). This can be interpreted as these phases being fed by compositionally distinct magmas that were erupted concomitantly. On the contrary, while the same range in major element compositions can be observed in the successive phases, the range is more continuous (i.e., T13-4, Fig. 4.11), suggesting that any compositionally distinct melts were homogenised subsequently, leading to compositions that close the compositional gap. This concords with phases P1 and P2 showing a variable incompatible element ratio La/Sm, indicating that the different melts might be influenced by variable amounts of fractional crystallisation. (3) Compared to historic eruptions, groundmass glass compositions within the T13-sequence show limited variability regarding SiO_2, MgO, CaO and K_2O contents arguing for a compositionally similar magma feeding the entire eruption sequence. This contrasts with the variability in major element bulk and glass compositions, observed within the historic 1995–1996 eruption sequence (Nakagawa et al., 1999; Nakagawa et al., 2002; Kilgour et al., 2013), and for older lava flow sequences (Price et al., 2012; Conway et al., 2018), which witness distinct feeding magma batches on timescales as short as individual eruption sequences. (4) The limited variability in trace element ratios (e.g., Fig. 4.13) concurs with this and indicates that variations in e.g., fluid-mobile elements such as Rb/Sm and Ba/Y at constant Zr/Y ratios can be attributed to subduction-zone processes (i.e., signature of aqueous fluids from the subducting slab) rather than indicating major changes in the magmatic source between eruption phases. (5) Banded juvenile shards that show variations in microlite densities can be found but are not volumetrically significant, suggesting that they may represent late-stage mingling of different magma portions within the conduit rather than pre-eruptive interaction of distinct magma batches. (6) Microlite abundances show no clear covariance with glass composition, as has been observed for example in eruptions from the Bullot Formation (cf. Pardo et al., 2014), where microlite-poor glass was associated with less evolved compositions, while more evolved compositions showed higher microlite contents. This suggests that the T13-sequence was fed by a compositionally similar magma, and that there are no evident major syn-eruptive changes in the magmatic source. Contrastingly, late-stage processes controlling melt viscosity and ascent behaviour in the conduit (e.g., shallow late-stage microlite crystallisation, degassing) appear to vary between individual phases.

While different lines of evidence such as crystal textures (e.g., zoning and absorption features, Nakagawa et al., 2002; Kilgour et al., 2013) point towards complex interactions in disequilibrium, glass textures do not witness any volumetrically significant mixing nor significant indicators of compositionally significantly distinct magma bodies. Instead, major element glass compositions of individual eruption phases cluster along the same linear trend in Harker diagrams that has been described for historic eruptions (Nakagawa et al., 1999; Nakagawa et al., 2002) and for other eruptions of the Tufa Trig Formation (Donoghue et al., 2007). It can be excluded that the T13-eruption was fed by a single fractionating melt, as this would require increasingly more silicic compositions with eruption progression. Instead, the lack of a clear geochemical evolution with eruption progression suggests that individual eruption phases were fed by magmas with very similar, yet slightly different composition. Linear trends in the SiO_2 vs MgO, CaO and K_2O diagrams highlight the influence of fractional crystallisation of plagioclase and pyroxenes on magma evolution and composition (cf. arrows in Fig. 4.11a, c, e), although solely fractional crystallisation cannot explain the full compositional range (cf. Nakagawa et al., 1999). Instead, the continuous linear trends in MgO, CaO, K_2O vs SiO_2 compositions highlight the role of pre- and syn-eruptive mixing of compositionally similar melts that are affected by variable degrees of fractional crystallisation.

Based on the major and trace element data, we suggest the following scenario for the processes occurring in the magmatic system feeding the T13-sequence: Prior to eruption onset, a parental magma of intermediate composition is injected into the shallow sill-dike system (Fig. 4.14a). Here, it forms individual magma pockets that are subject to similar processes of fractional crystallisation of pyroxene and plagioclase and can interact among each other and with pre-existing residual melts (Fig. 4.14b). This accounts for the continuous and similar ranges observed in MgO, CaO, K_2O vs SiO_2 compositions for individual subunits as well as the limited trace element variability that point both towards a similar magma source. Following eruption onset, individual eruption phases are fed by these genetically related melts, progressively tapping slightly distinct melt pockets, accounting for the minor systematic variations in e.g. SiO_2, CaO, K_2O between eruption phases (Fig. 4.13). The SiO_2 decrease throughout P1 to P4 suggests an involvement of less evolved magma (Fig. 4.14b, c) that can be explained by a continuous supply (and continuous mixing) of a melt with relatively lower SiO_2 contents to the shallow system. Eruption phase P5, on the contrary, shows an increase in wt% SiO_2 and K_2O and can be attributed to a slightly more evolved melt feeding this phase. The melt erupted during P5 is still related to the parental melt feeding P1–P4 but involves a separate batch that had longer relative residence time in the shallow system, accounting for the relatively more evolved major element compositions.

These observations concord with the current understanding of Mt. Ruapehu’s magmatic system, which is described as a shallow intricate sill-dike system (Gamble et al., 1999; Price et al., 2005; Price et al., 2012). Studies on the isotopic composition of pre-historic lava flow sequences suggest that Mt. Ruapehu’s magmas represent a complex interplay between mantle-sourced and crustal melts. These melts are modified by crustal assimilation, fractional crystallisation and mixing/mingling (Price et al., 2012). It is interesting to note, that the T13 scenario contrasts with the scenario suggested for the 1995–1996 eruptions, where Nakagawa et al. (1999) identified a discrete injection of “high-T” magma into pre-existing “low-T”, shallow, highly crystallised magma batches. Similar to Price et al. (2012), Nakagawa et al. (1999) relate short-term variations in bulk and glass major element compositions between individual eruptions to the formation of separate small volume magma pockets in the shallow system. While this overall agrees with the scenario proposed for the T13-sequence, it is important to highlight that historic eruptions are linked to individual, independent, small-volume magma batches with distinct magmatic evolution (Gamble et al., 1999; Nakagawa et al., 1999; Nakagawa et al., 2002; Price et al., 2005). This differs from the limited variability in trace and major elements observed in the T13-sequence that highlight a similar magmatic evolution for the T13-feeding magma and point towards a genetic relationship for the involved individual magma batches.

Despite the constant decrease in SiO_2 contents throughout P1 to P4 (Fig. 4.13) and the variable trace element compositions between P1–P3 and P4–P5 (Fig. 4.11h, j, Fig. 4.13), there is no clear indicator for a discrete event of “fresh” magma injection throughout the T13-sequence. This leads to the conclusion that if any high-T magma was injected into the shallow magmatic system syn-eruptively, it was more continuous and has been hindered from ascending by the highly crystallised, shallow system (Nakagawa et al., 2002; Price et al., 2012; Kilgour et al., 2013). However, it cannot be excluded that small-volume magma injection at depth has progressively mixed with the previously emplaced melts, adding heat to the system and leading to a destabilisation and remobilisation of individual melt portions (Fig. 4.14b, c), thus constituting a possible internal eruption trigger (cf. Calbuco, Arzilli et al., 2019).

In line with this, the combination of the above observations implies that eruption progression of the T13 multi-phase eruption and changes in eruption style are controlled predominantly by processes in the conduit and during magma ascent, and changes in fragmentation mechanisms (e.g. magmatic vs phreatomagmatic). Accordingly, we interpret the variable heterogeneity in groundmass crystallinities between subunits (Fig. 4.13) to be caused by time-variant fluctuations in magma ascent and discharge rates, where i.e. heterogeneous cooling, stalling and degassing in the conduit lead to heterogeneous textural characteristics within the same subunit. A narrow range in groundmass crystallinity suggests comparably continuous magma discharge rates, as observed in P2. In addition to this, lateral differences in temperature, magma viscosity and volatile content within the conduit further influence the range in groundmass crystallinities and the different types of juvenile clasts (Fig. 4.14d). Similar explanations have been suggested for other small-scale eruptions (cf. Etna, Taddeucci et al., 2004; and Nakadake, Miyabuchi et al., 2008; Miyabuchi et al., 2019). A time-resolved quantitative characterisation of vesicle and microlite characteristics in combination with the analysis of volatile compositions of groundmass glass could provide better insights into the processes that control short-term changes in magma ascent rates and melt viscosity but was beyond the scope of this paper.

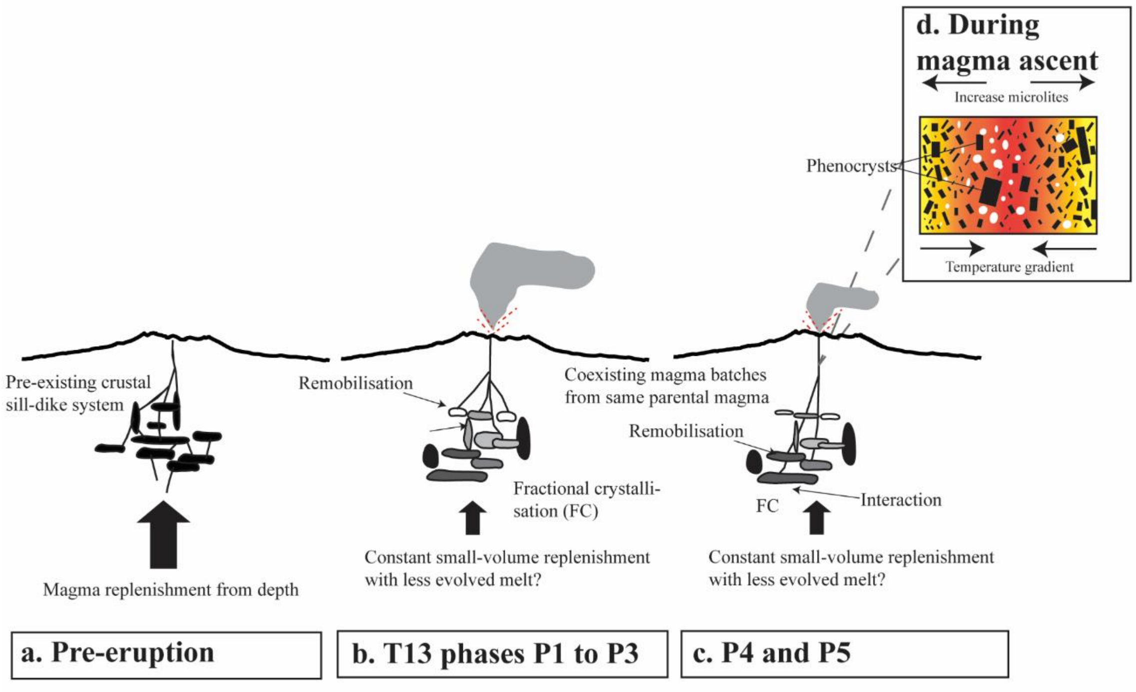

Fig. 4.14: Schematic illustration of the magmatic system feeding the T13-eruption sequence. a) Deeper parental magma arrives into pre-existing crustal, shallow sill-dike system, prior to T13-eruption onset. b) Eruption phases P1 to P3 are fed by magma with similar major and trace element composition, deriving from the same parental magma and affecting increasingly less evolved magma portions. c) After a time break, eruption recommences with P4, which involves similar major and trace element compositions to P1 to P3. Final eruption phase P5 involves slightly more evolved major element compositions compared to P4. Note that potential "fresh" magma replenishing the shallow system is not erupted but leads to a destabilisation of the magma already residing in the system. Size of magma batches and depths are not representative of actual dimensions.

4.5.3.2 Temporal patterns between eruption sequences

To discuss temporal variations between eruption sequences and over timescales of 100s to 1000s of years, we integrate our data with previous geochemical analyses of scoria, lava bombs, tephra and lava flows (Fig. 4.15). For Mt. Ruapehu, the majority of existing geochemical data was obtained on lava flows and lava bombs/scoria for both historical and prehistorical eruptions (Gamble et al., 1999; Price et al., 2005; Price et al., 2012; Conway et al., 2018). Datasets on tephra are scarce, generally characterising the ejecta only in terms of their major elements (Donoghue et al., 2007). Given that 55% of the most recent 1800-year tephra record are constituted by multi-phase eruption sequences associated with small-volume explosive eruptions (Voloschina et al., 2020), this discrepancy emphasises the need for datasets which cover periods of >1000 years and account for the currently most realistic type of eruptions. The integration of the data on selected tephra sequences within the time frame of the Tufa Trig Formation (Donoghue et al., 1997) and comparing it with the well-studied lapilli-bearing Bullot Formation (Donoghue et al., 1995; Pardo et al., 2011; Pardo et al., 2014) and the lavas of the Whakapapa Formation (Price et al., 2012; Conway et al., 2018) leads to the following observations: (1) Glass compositions of the Bullot Formation display slightly lower SiO_2 and higher CaO values (Pardo et al., 2014; Fig. 4.15), when compared to the Tufa Trig Formation. However, both average major and trace element glass compositions show limited variability over the past ~22,000 years. (2) Within the Tufa Trig Formation, the older T5 member shows distinct compositions characterised by SiO_2=60.01–64.41 wt%, CaO=5.4–7.42 wt% and K_2O=1.45–2.27 wt%, Zr/Y=6.44–6.81, Rb/Sm=15.47–18.54 and marks a feeding magma with a distinct evolution compared to the other Tufa Trig members. The multi-phase T15 eruption, conversely, which occurred shortly after T13 (530 cal BP, Voloschina et al., 2020) shows a compositional range (SiO_2=62.73–70.42, CaO=2.16–5.69 wt%, K_2O=1.53–4.13 wt%, Zr/Y=6.33–6.51, Rb/Sm=19.01–21.19) that is similar to T13-compositions, indicating similar processes in the magmatic system. (3) The most recent geologically preserved member of the Tufa Trig Formation, the T31-sequence, shows more evolved compositions with SiO_2=62.0–75.82 wt%, CaO=0.64–5.93 wt%, K_2O=2.21–4.85 wt%, Zr/Y=6.81–7.97, Rb/Sm=20–26.97. (4) Interestingly, glass compositions from the historical 1995–1996 eruptions (Nakagawa et al., 1999; Moebis et al., 2011; Kilgour et al., 2013) show lower SiO_2 and higher CaO contents and trace element ratios (Zr/Y=5.05–6.05 and Rb/Sm=16.04–21.16, Gamble et al., 1999) compared to the T13-sequence and other Tufa Trig members (e.g. T15, Fig. 4.15). These major and trace element compositions are similar to those observed in tephras associated with the Bullot Formation (Pardo et al., 2014) and the youngest lava flows from the Whakapapa Formation (Conway et al., 2018), indicating a similar magmatic source.

Mt. Ruapehu's magmatic system seems to show long-term variations that act over 100s to 1000s of years. Similar long-term variations in other long-lived, intermediate systems are generally associated with periodical replenishment of deeper magma (e.g. Ngauruhoe, Hobden, 1997; Hobden et al., 1999; Cotopaxi, Pistolesi et al., 2011; Shiveluch, Ponomareva et al., 2015). In line with this, it appears that the T5 member and the 1995–1996 eruptions mark episodes of magma replenishments (Gamble et al., 1999; Nakagawa et al., 1999). For historical activity, Gamble et al. (1999) suggested a periodicity of 20–30 years for the injection of fresh magma with volumes $<50 \times 10^6$ m^3, in line with the formation of distinct small-volume magma batches that feed individual eruptions. However, this contrasts with the limited range in compositions observed for the T13 and T15 sequences as well as with the limited variability in major and trace element compositions in Fig. 4.15. This discrepancy between historical and pre-historical eruptions with regards to geochemical datasets and eruption frequency and style, in combination with the time-variable complexity of eruption sequences during the past 1800 years (Voloschina et al., 2020), indicates that eruption behaviour at Mt. Ruapehu is time-variable. In line with similar time-resolved studies, changes in eruption behaviour over timescales of 100s to 1000s of years can be potentially related to periodic changes in the magnitude and frequency of magma influx to the shallow magmatic system. The difference between the T13-sequence and the historical eruptions could then be attributed to the former being fed by relatively more constant and more voluminous magma supply, while the latter involves the injection of discrete and small-volume magma into the crystallised shallow system. More time-resolved data on other Tufa Trig members is needed to quantify the character and periodicity of magma replenishments and to relate them to changes in eruption frequency and magnitude.

4.5.4 Limitations in characterising the deposits of small to moderate multi-phase eruptions

The preservation potential for thin fine-grained tephra is particularly low and is strongly controlled by the nature of the depositional environment (i.e., vegetation cover, slope angle, Cutler et al., 2018; Dugmore et al., 2018), both during, as well as after eruption. For multi-bed sequences, the correlation of individual beds/bedsets is complicated by limited thickness, the lack of distinct features and/or blurred or modified contacts. In addition to this, the value of individual parameters such as componentry, geochemistry and textures for correlation/fingerprinting purposes is limited by the heterogeneous textural features and homogeneous compositional signatures of individual eruption phases (cf. Cioni et al., 2008b).

In line with this, while several time-resolved studies target the characterisation of small to moderate multi-phase eruptions these studies are generally based on well documented eruption sequences, where the ejecta is sampled at regular intervals or shortly after eruption and additional information on eruption style and dynamics is available from monitoring (e.g. Taddeucci et al., 2002; Nakada et al., 2013; Miyabuchi et al., 2019). With regard to this, it is important to highlight the discrepancy in the resolution that can be obtained from the study of deposit sequences with regards to eruption style, eruption magnitude and eruption progression in comparison to in-situ sampled eruption sequences. A comparison of the T13-deposit sequence with the studies of the 2011 Shinmoedake eruptions (Nakada et al., 2013; Suzuki et al., 2013; Miyabuchi et al., 2013) and the 2014-2015 Nakadake eruptions (Miyabuchi et al., 2018; 2019) will be used to illustrate this in the following.

The 2011 Shinmoedake eruptions were characterised by a phreatomagmatic opening phase, followed by a main subplinian to vulcanian phase, a phase of lava accumulation, a vulcanian phase and final phreatomagmatic ash emission (Miyabuchi et al., 2013; Nakada et al., 2013; Suzuki et al., 2013). Individual phases (described as “stages” in Nakada et al., 2013) involved multiple explosions of similar eruption style and intensity. The 2014-2015 Nakadake activity started with magmatic explosions, dominated by intermittent Strombolian activity and ash emission, with a period of phreatomagmatic activity after water re-appeared in the vent (Miyabuchi et al., 2019). Overall, the T13-sequence compares well with these two well-described eruptions and the inferred eruption dynamics. Similar to the complex multi-lobate pattern observed for individual T13-subunits, individual eruption pulses for both the Shinmoedake and the Nakadake eruptions are dispersed towards different directions and show irregular, elongated pattern, some with multiple lobes (cf. Miyabuchi et al., 2013; 2019). It is interesting to note that at Nakadake, deposits associated with the phreatomagmatic phase were spatially limited to the most proximal 8 km (Miyabuchi et al., 2018). At Shinmoedake, only deposits associated with the subplinian phases (Unit-2, -3 and -4 in Miyabuchi et al., 2013) could be identified beyond distances of 10 km, while the depositional subunit associated with the phreatomagmatic opening phase (Unit-1 in Miyabuchi et al., 2013) could not be mapped due to limited dispersal and discontinuous appearance. Similarly, samples taken for ash characterisation in Suzuki et al. (2013), derive from maximum distances of 8 km and were taken maximal 3 days after the eruption.

For the case study of the T13-sequence, samples were taken at distances between 8 to 10 km from source. At Mt. Ruapehu, this distance has been identified as the optimum distance range, where tephra sequences are preserved in sufficient detail to account for both the lateral and temporal variability in tephra sequences and to distinguish between different types of eruptive activity (cf. Voloschina et al., 2020). The comparison of the investigated distance ranges and the proximal dispersal of low-intensity, small volume eruption styles observed at Shinmoedake and Nakadake, suggests that the T13-sequence might be biased towards more magmatically-driven phases and magnitudes above a critical threshold. The discontinuous and limited dispersal of subunits T13-1 and T13-2 agrees with that, suggesting that short-lived, low-intensity eruptive activity dominated by phreatomagmatic explosions and intermittent ash emission is potentially underrepresented in the tephra record.

While with the present resolution and the local preservation conditions it might not be possible to quantify the exact number of phases that were involved during the T13-eruption sequence, we have shown that the integration of a multi-parameter approach with high-resolution field work adds critical constraints to the complexity of prolonged multi-phase eruptions at Mt. Ruapehu. The here applied strategy proved successful in constraining the dominant phases and the eruption characteristics associated with multi-phase eruption progressions, where individual eruption phases represent several individual explosive events that are characterised by similar eruption style, mechanisms and intensity. Individual explosive events and short-lived, low-intensity, intermittent eruptive activity can currently not be further resolved geologically due to the low preservation potential of deposits on the steep, proximal volcanic slopes. However, it is important to highlight that the optimum distance range can be expected to vary between volcanic regions around the world as preservation conditions are strongly influenced by local environmental and climatic conditions. This implies that the eruption styles and magnitudes preserved in tephra sequences are potentially variable between different volcanic regions. Further research and comparisons between observed eruption sequences and tephra sequences in different climatic conditions are needed to quantify volcano-specific preservation thresholds with regards to eruption magnitude and style.

Fig. 4.15 (next page): Illustration of SiO_2, K_2O and CaO groundmass variability throughout different eruption sequences over the last 22,000 years. T13 groundmass glass is integrated with glass data on Tufa Trig tephra sequences T5, T15 and T31 and with existing literature data on the historical 1995–1996 eruptions and tephra deposits from the Bullot Formation. Note the breaks in the time axis. Compositional ranges are marked by horizontal bars, while plus signs show the average, where available. Literature data on tephra is marked by grey bars. Additional compositions obtained from the analysis of groundmass glass in lava bombs and scoriae is shown in black. Eruption ages are reported where available. Compositional ranges have been previously published as follows: [1]Mgt- Mangatoetoenui eruption (Pardo et al., 2012); Sw- Shawcroft compositions follow Pardo et al. (2012), while the age is obtained from [2]Donoghue et al. (1995); [+]ages for tephra sequences T5, T13 and T15 are from Voloschina et al., (2020); [3]Groundmass glass compositions for historical eruptions were obtained on scoriae and are described in Kilgour et al. (2013) and [4]Nakagawa et al. (2002); groundmass glass compositions on volcanic ash from historical eruptions follow [5]Moebis et al. (2011), [6]Moebis (2010) and [7]Donoghue et al. (1997). Compositions for other Tufa Trig tephra members are reported after [8]Donoghue et al. (2007), while trace element compositions for the Shawcroft and Mangatoetoenui members are published in [9]Pardo et al. (2014). Trace element compositions on lava flows from the Whakapapa Formation are reported for selected lava flows from the Crater Lake and Iwikau members, both younger than 10,000 years and follow [10]Conway et al. (2018), while trace element compositions for the historical 1995–1996 eruptions are from [11]Gamble et al. (1999).

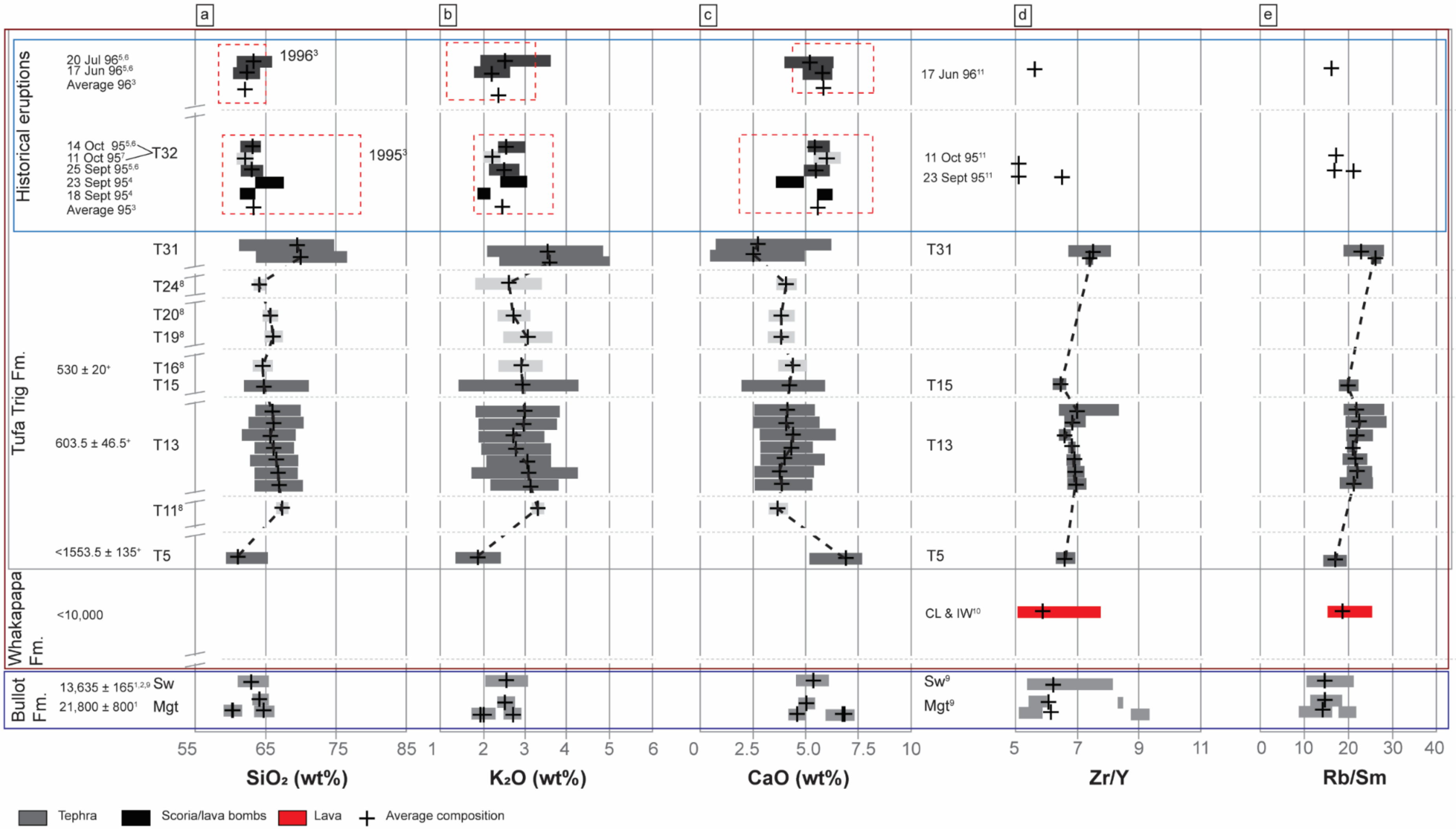

¹Pardo et al. (2012) ²Donoghue et al. (1995) ⁺Voloschina et al. (2020) ³Kilgour et al. (2013) ⁴Nakagawa et al. (2002) ⁵Moebis et al. (2011) ⁶Moebis (2010) ⁷Donoghue et al. (1997) ⁸Donoghue et al. (2007) ⁹Pardo et al. (2014) ¹⁰Conway et al. (2018) ¹¹Gamble et al. (1999)

4.6 Conclusions and outlook

Sudden changes in eruption dynamics and eruption style are well known and documented for historically observed, small to moderate multi-phase eruptions (Taddeucci et al., 2002; Cronin et al., 2003; Martin-Del Pozzo et al., 2008). However, deposit-based studies that characterise the range in depositional features and relate them to syn-eruptive variations in eruption dynamics and their key parameters are comparably scarce and tend to target observed eruptions (Taddeucci et al., 2002; Miwa et al., 2013; Miyabuchi et al., 2019). The intermittent character, lower intensity and small erupted volumes result in deposits, which represent a mixture of multiple processes acting simultaneously rather than representing a single process. Accordingly, data analysis and interpretation are complicated and depend on the quality of the investigated multi-parameter data and the available field conditions. This limits our understanding of short- and long-term patterns in eruption behaviour and hinders realistic frequency-magnitude models that form the base for hazard assessment and probabilistic eruption forecast models. With this study we present a detailed multi-parameter characterisation of a complex small-volume multi-phase eruption at a frequently active andesite volcano based on a deposit sequence. The key findings and limitations that arise from this research can be summarised as follows:

(1) The T13-tephra sequence can be subdivided into six depositional subunits, representative of five eruption phases: (1) an opening phase P1, dominated by multiple small eruptions, with major phreatomagmatic influence and characterised by low energy and eruption rates, represented by subunits T13-1 and -2. (2) A semi-continuous violent Strombolian phase P2, which is preserved in T13-3. (3) The main violent Strombolian to subplinian phase (P3, T13-4) that is characterised by prolonged duration and multiple waxing-waning cycles. This phase is followed by a time break of less than a year. (4) Then, the eruption recommences with a violent Strombolian phase P4, associated with strong excavation. (5) The last phase P5 is characterised by violent Strombolian to subplinian character with a final ash venting phase.

(2) Tephra volumes span several orders of magnitudes, involving volume estimate ranges from 3.83–8.23 × 10^5 m^3 for T13-1 to 2.41–3.69 × 10^7 m^3 for T13-4. Cumulative deposit volumes of 2.44–6.04 × 10^7 m^3 for T13 indicate that the main

phase T13-4 constitutes about 65% of the total deposit volume. A comparison with thickness distributions from similar eruptions with more complete distal datasets, suggests that the here presented deposit volumes might be underestimated by up to 62%.

(3) Lithosedimentological characteristics, pyroclast assemblage and textural features of individual subunits show lateral and temporal variability along the T13-tephra sequence. The lateral variability of componentry coupled with a limited variability in the geochemical composition advises against their use in the correlation of individual subunits without consulting additional data. However, patterns in relative proportions of individual componentry classes such as lithics or specific juvenile types (i.e., T-glass) within the sequence are coherent at individual locations, suggesting their value in a relative stratigraphic context and for understanding temporal variations throughout the eruptive sequence.

(4) Juvenile clasts constitute the main component, with relative proportions of scoriaceous, pumiceous and dense clasts varying along the stratigraphic sequence. Image analysis shows a correlation between juvenile clast types and groundmass crystallinities, with dense clasts showing the highest gmc=57.79%, followed by slightly lower values for scoriaceous (gmc=53.05%) and tan vesicular clasts (gmc=50.80%).

(5) Ash morphologies and groundmass textures display a range of characteristics and indicate a complex interplay between phreatomagmatic and magmatic processes that act simultaneously or over short timescales. Overall, the role of magmatic processes increases with eruption progression (i.e., from P1 to P3) as suggested by increasing proportions of highly vesicular glass, coarser median grain size and a decrease in the relative proportions of extremely fine ash.

(6) Geochemical compositions indicate minor systematic variations throughout the sequence and are consistent with occasional disequilibrium indicators, such as banded clasts, as well as zoned and absorbed crystals, but overall the compositional ranges are too limited to unequivocally prove the coexistence of distinct (i.e., high-T and low-T) magmatic sources, as has been seen for the historical 1995–1996 episodes (Nakagawa et al., 1999; Nakagawa et al., 2002; Kilgour et al., 2013). This suggests that the processes feeding and acting during the largest eruption of the past 1800 years were different from those involved in historical eruptions.

(7) Systematic variations between eruption phases concur with the existing understanding of a shallow, nested sill-dike system, where individual magma batches coexist and are modified by complex processes dominated by fractional crystallisation, crustal assimilation and interaction between individual magma batches. Different to historical eruptions, compositionally slightly distinct melts feeding the T13-eruption sequence appear related, originating from the same intermediate parental melt that was injected in the system prior to eruption onset.

(8) While the compositional variability appears to be minor within individual eruption sequences, the integration of the T13-sequence in a larger time framework suggests that Mt. Ruapehu's magmatic system might show variations on timescales of 100s to 1000s of years.

The key findings and limitations that arise from this study can serve as a base for further, more in-depth studies on similar geologically preserved multi-bed tephra sequences at other volcanoes. The integration of short-term data on the scale of individual eruption sequences with a high-resolution tephra record provides the opportunity to unravel both short- and long-term processes in the intricated magmatic systems that feed the most frequent eruptions on Earth. While the eruption progression of complex multi-phase eruptions appears to be mostly controlled by the shallow system, the influence of deeper, less evolved magma bodies cannot be excluded unequivocally. This has important implications for hazard and risk management, as the involved magma volumes suggest that, in an eruption scenario similar to the T13-eruption, magma migration should be detectable prior to eruption but that syn-eruptive precursory signs for upcoming phases might be absent.

References

Arrighi, S., Principe, C., & Rosi, M. (2001). Violent strombolian and subplinian eruptions at Vesuvius during post-1631 activity. *Bulletin of Volcanology, 63*(2), 126-150. doi:https://doi.org/10.1007/s004450100130

Arzilli, F., Morgavi, D., Petrelli, M., Polacci, M., Burton, M., Di Genova, D., Spina, L., La Spina, G., Hartley, M. E., Romero, J. E., Fellowes, J., Diaz-Alvarado, J., & Perugini, D. (2019). The unexpected explosive sub-Plinian eruption of Calbuco volcano (22–23 April 2015; southern Chile): Triggering mechanism implications. *Journal of Volcanology and Geothermal Research, 378*, 35-50. doi:https://doi.org/10.1016/j.jvolgeores.2019.04.006

Barth, G., Kleinrock, M., & Helz, R. (1994). The magma body at Kilauea Iki lava lake: Potential insights into mid-ocean ridge magma chambers. *Journal of Geophysical Research: Solid Earth, 99*(B4), 7199-7217. doi:https://doi.org/10.1029/93JB02804

Barsotti, S., Neri, A., Bertagnini, A., Cioni, R., Mulas, M., & Mundula, F. (2015). Dynamics and tephra dispersal of Violent Strombolian eruptions at Vesuvius: insights from field data, wind reconstruction and numerical simulation of the 1906 event. Bulletin of Volcanology, 77(7), 58. doi:https://doi.org/10.1007/s00445-015-0939-6

Beck, A. (1950). Volcanic activity at Mt. Ruapehu from August to December, 1945. *New Zealand Journal of Science and Technology, 31*, 1-13.

Bonadonna, C., Cioni, R., Pistolesi, M., Connor, C., Scollo, S., Pioli, L., & Rosi, M. (2013a). Determination of the largest clast sizes of tephra deposits for the characterization of explosive eruptions: a study of the IAVCEI commission on tephra hazard modelling. *Bulletin of Volcanology, 75*(1), 680. doi:https://doi.org/10.1007/s00445-012-0680-3

Bonadonna, C., & Costa, A. (2012). Estimating the volume of tephra deposits: A new simple strategy. *Geology, 40*(5), 415-418. doi:https://doi.org/10.1130/G32769.1

Bonadonna, C., & Costa, A. (2013b). Plume height, volume, and classification of explosive volcanic eruptions based on the Weibull function. *Bulletin of Volcanology, 75*(8), 742. doi:https://doi.org/10.1007/s00445-013-0742-1

Bonadonna, C., Ernst, G., & Sparks, R. (1998). Thickness variations and volume estimates of tephra fall deposits: the importance of particle Reynolds number. *Journal of Volcanology and Geothermal Research, 81*(3), 173-187. doi:https://doi.org/10.1016/S0377-0273(98)00007-9

Bonadonna, C., & Houghton, B. F. (2005). Total grain-size distribution and volume of tephra-fall deposits. *Bulletin of Volcanology, 67*(5), 441-456. doi:https://doi.org/10.1007/s00445-004-0386-2

Bustillos A., J., Romero, J. E., Troncoso, L., & Guevara C., A. (2016). Tephra fall at Tungurahua Volcano (Ecuador) - 1999-2014: An Example of Tephra Accumulation from a Long-lasting Eruptive Cycle. Geofísica internacional, 55, 55-67.

Bryan, C., Sherburn, S., Bibby, H., Bannister, S., & Hurst, A. (1999). Shallow seismicity of the central Taupo Volcanic Zone, New Zealand: its distribution and nature. *New Zealand Journal of Geology and Geophysics, 42*(4), 533-542. doi:https://doi.org/10.1080/00288306.1999.9514859

Cioni, R., Bertagnini, A., Santacroce, R., & Andronico, D. (2008a). Explosive activity and eruption scenarios at Somma-Vesuvius (Italy): Towards a new classification scheme. *Journal of Volcanology and Geothermal Research, 178*(3), 331-346. doi:https://doi.org/10.1016/j.jvolgeores.2008.04.024

Cioni, R., D'Oriano, C., & Bertagnini, A. (2008b). Fingerprinting ash deposits of small scale eruptions by their physical and textural features. *Journal of Volcanology and Geothermal Research, 177*(1), 277-287. doi:https://doi.org/10.1016/j.jvolgeores.2008.06.003

Cioni, R., Bertagnini, A., Andronico, D., Cole, P. D., & Mundula, F. (2011). The 512 AD eruption of Vesuvius: complex dynamics of a small scale subplinian event. *Bulletin of Volcanology, 73*(7), 789-810. doi:https://doi.org/10.1007/s00445-011-0454-3

Cioni, R., Pistolesi, M., Bertagnini, A., Bonadonna, C., Hoskuldsson, A., & Scateni, B. (2014). Insights into the dynamics and evolution of the 2010 Eyjafjallajökull summit eruption (Iceland) provided by volcanic ash textures. *Earth and Planetary Science Letters, 394*, 111-123. doi:https://doi.org/10.1016/j.epsl.2014.02.051

Conway, C. E., Gamble, J. A., Wilson, C. J., Leonard, G. S., Townsend, D. B., & Calvert, A. T. (2018). New petrological, geochemical, and geochronological perspectives on andesite-dacite magma genesis at Ruapehu volcano, New Zealand. *American Mineralogist: Journal of Earth and Planetary Materials, 103*(4), 565-581. doi:ttps://doi.org/10.2138/am-2018-6199

Cronin, S. J., Hedley, M. J., Neall, V. E., & Smith, R. G. (1998). Agronomic impact of tephra fallout from the 1995 and 1996 Ruapehu Volcano eruptions, New Zealand. *Environmental Geology, 34*(1), 21-30.

Cronin, S. J., Neall, V. E., Lecointre, J. A., Hedley, M. J., & Loganathan, P. (2003). Environmental hazards of fluoride in volcanic ash: a case study from Ruapehu volcano, New Zealand. *Journal of Volcanology and Geothermal Research, 121*, 271-291. doi:https://doi.org/10.1016/S0377-0273(02)00465-1

Cutler, N. A., Streeter, R. T., Marple, J., Shotter, L. R., Yeoh, J. S., & Dugmore, A. J. (2018). Tephra transformations: variable preservation of tephra layers from two well-studied eruptions. *Bulletin of Volcanology, 80*(11), 77. doi:https://doi.org/10.1007/s00445-018-1251-z

Di Piazza, A., Vona, A., Mollo, S., De Astis, G., Soto, G. J., & Romano, C. (2019). Unsteady magma discharge during the "El Retiro" subplinian eruption (Turrialba volcano, Costa Rica): Insights from textural and petrological analyses. *Journal of Volcanology and Geothermal Research, 371*, 101-115. doi:https://doi.org/10.1016/j.jvolgeores.2019.01.004

Donoghue, S. L. (1991). *Late Quaternary Volcanic Stratigraphy of the Southeastern Sector of the Mount Ruapehu Ring Plain New Zealand.* (Doctor of Philosophy), Massey University.

Donoghue, S. L., Neall, V. E., & Palmer, A. S. (1995). Stratigraphy and chronology of late Quaternary andesitic tephra deposits, Tongariro Volcanic Centre, New Zealand. *Journal of the Royal Society of New Zealand, 25*(2), 115-206. doi:https://doi.org/10.1080/03014223.1995.9517487

Donoghue, S. L., Neall, V. E., Palmer, A. S., & Stewart, R. B. (1997). The volcanic history of Ruapehu during the past 2 millenia based on the record of Tufa Trig tephras. *Bulletin of Volcanology, 59*, 136-146. doi:https://doi.org/10.1007/s004450050181

Donoghue, S. L., Vallance, J., Smith, I. E. M., & Stewart, R. B. (2007). Using geochemistry as a tool for correlating proximal andesitic tephra: case studies from Mt Rainier (USA) and Mt Ruapehu (New Zealand). *Journal of Quaternary Science, 22*(4), 395-410. doi:https://doi.org/10.1002/jqs.1065

Dugmore, A., Streeter, R., & Cutler, N. (2018). The role of vegetation cover and slope angle in tephra layer preservation and implications for Quaternary tephrostratigraphy. *Palaeogeography, Palaeoclimatology, Palaeoecology, 489*, 105-116. doi:https://doi.org/10.1016/j.palaeo.2017.10.002

Elliott, T., Plank, T., Zindler, A., White, W., & Bourdon, B. (1997). Element transport from slab to volcanic front at the Mariana arc. *Journal of Geophysical Research: Solid Earth, 102*(B7), 14991-15019. doi:https://doi.org/10.1029/97jb00788

Fierstein, J., & Nathenson, M. (1992). Another look at the calculation of fallout tephra volumes. *Bulletin of Volcanology, 54*(2), 156-167. doi:https://doi.org/10.1007/bf00278005

Gamble, J. A., Wood, C. P., Price, R. C., Smith, I. E. M., Stewart, R. B., & Waight, T. (1999). A fifty year perspective of magmatic evolution on Ruapehu Volcano, New Zealand: verification of open system behaviour in an arc volcano. *Earth and Planetary Science Letters, 170*, 301-314. doi:https://doi.org/10.1016/S0012-821X(99)00106-5

Gaunt, H. E., Bernard, B., Hidalgo, S., Proaño, A., Wright, H., Mothes, P., Criollo, E., & Kueppers, U. (2016). Juvenile magma recognition and eruptive dynamics inferred from the analysis of ash time series: The 2015 reawakening of Cotopaxi volcano. *Journal of Volcanology and Geothermal Research, 328*, 134-146. doi:https://doi.org/10.1016/j.jvolgeores.2016.10.013

Gill, J. (1981). *Orogenic andesites and plate tectonics*. Berlin: Springer Verlag.

Hammer, J. E., Cashman, K. V., & Voight, B. (2000). Magmatic processes revealed by textural and compositional trends in Merapi dome lavas. *Journal of Volcanology and Geothermal Research, 100*(1–4), 165-192. doi:https://doi.org/10.1016/S0377-0273(00)00136-0

Hayes, G. (2004). The Waiouru, New Zealand, earthquake swarm: Persistent mid crustal activity near an active volcano. *Geophysical Research Letters, 31*(19). doi:https://doi.org/10.1029/2004gl020709

Heiken, G., & Wohletz, K. (1985). *Volcanic Ash* Univ. of Calif. Press, Berkeley.

Heinrich, M., Cronin, S. J., & Pardo, N. (2020). Understanding multi-vent Plinian eruptions at Mt. Tongariro Volcanic Complex, New Zealand. *Bulletin of Volcanology, 82*(3), 30. doi:https://doi.org/10.1007/s00445-020-1369-7

Hobden, B. J. (1997). *Modelling magmatic trends in time and space: eruptive and magmatic history of Tongariro volcanic complex, New Zealand.* (Doctor of Philosophy), University of Canterbury.

Hobden, B. J., Houghton, B. F., Davidson, J. P., & Weaver, S. D. (1999). Small and short-lived magma batches at composite volcanoes: time windows at Tongariro volcano, New Zealand. *Journal of the Geological Society, 156*(5), 865-868. doi:https://doi.org/10.1144/gsjgs.156.5.0865

Houghton, B. F., & Nairn, I. A. (1991). The 1976–1982 Strombolian and phreatomagmatic eruptions of White Island, New Zealand: eruptive and depositional mechanisms at a 'wet' volcano. *Bulletin of Volcanology, 54*(1), 25-49. doi:https://doi.org/10.1007/BF00278204

Hurst, A. W., & McGinty, P. J. (1999). Earthquake swarms to the west of Mt Ruapehu preceding its 1995 eruption. *Journal of Volcanology and Geothermal Research, 90*(1), 19-28. doi:https://doi.org/10.1016/S0377-0273(99)00019-0

Inman, D. L. (1952). Measures for describing the size distribution of sediments. *Journal of Sedimentary Research, 22*(3).

Jarosewich, E. (2002). Smithsonian microbeam standards. *Journal of Research of the National Institute of Standards and Technology, 107*(6), 681. doi:https://doi.org/10.6028/jres.107.054

Johnston, D. M. (1997). *A chronology of the 1945 eruption of Ruapehu Volcano, New Zealand*: Institute of Geological & Nuclear Sciences.

Johnston, D. M., Houghton, B. F., Neall, V. E., Ronan, K. R., & Paton, D. (2000). Impacts of the 1945 and 1995-1996 Ruapehu eruptions, New Zealand: An example of increasing societal vulnerability. *Geological Society of America Bulletin, 112*(5), 720-726. doi:https://doi.org/10.1130/0016-7606(2000)112<720:IOTARE>2.0.CO;2

Kennedy, B., Spieler, O., Scheu, B., Kueppers, U., Taddeucci, J., & Dingwell, D. B. (2005). Conduit implosion during Vulcanian eruptions. Geology, 33(7), 581-584. doi:10.1130/g21488.1

Kilgour, G., Blundy, J., Cashman, K., & Mader, H. M. (2013). Small volume andesite magmas and melt–mush interactions at Ruapehu, New Zealand: evidence from melt inclusions. *Contributions to Mineralogy and Petrology, 166*(2), 371-392. doi:https://doi.org/10.1007/s00410-013-0880-7

Le Maitre, R., Streckeisen, A., Zanettin, B., Le Bas, M., Bonin, B., & Bateman, P. (2002). *Igneous rocks: A classification and glossary of Terms*. Cambridge, UK: Cambridge University Press.

Legros, F. (2000). Minimum volume of a tephra fallout deposit estimated from a single isopach. *Journal of Volcanology and Geothermal Research, 96*(1-2), 25-32. doi:https://doi.org/10.1016/S0377-0273(99)00135-3

Lormand, C., Zellmer, G. F., Németh, K., Kilgour, G., Mead, S., Palmer, A. S., Sakamoto, N., Yurimoto, H., & Moebis, A. (2018). Weka Trainable Segmentation Plugin in ImageJ: A Semi-Automatic Tool Applied to Crystal Size Distributions of Microlites in Volcanic Rocks. *Microscopy and Microanalysis, 24*(6), 667-675. doi:https://doi.org/10.1017/S1431927618015428

Lowe, D. J., Blaauw, M., Hogg, A. G., & Newnham, R. M. (2013). Ages of 24 widespread tephras erupted since 30,000 years ago in New Zealand, with re-evaluation of the timing and palaeoclimatic implications of the Lateglacial cool episode recorded at Kaipo bog. *Quaternary Science Reviews, 74*, 170-194. doi:https://doi.org/10.1016/j.quascirev.2012.11.022

Marsh, B. (2015). Magma chambers. In H. Sigurdsson (Ed.), *The Encyclopedia of Volcanoes (Second Edition)* (Vol. 1, pp. 184-201). Amsterdam: Academic Press.

Martin-Del Pozzo, A. L., González-Morán, T., Espinasa-Pereña, R., Butron, M. A., & Reyes, M. (2008). Characterization of the recent ash emissions at Popocatepetl Volcano, Mexico. *Journal of Volcanology and Geothermal Research, 170*(1), 61-75. doi:https://doi.org/10.1016/j.jvolgeores.2007.09.004

Miwa, T., Toramaru, A., & Iguchi, M. (2009). Correlations of volcanic ash texture with explosion earthquakes from vulcanian eruptions at Sakurajima volcano, Japan. Journal of Volcanology and Geothermal Research, 184(3), 473-486. doi:https://doi.org/10.1016/j.jvolgeores.2009.05.012

Miwa, T., Geshi, N., & Shinohara, H. (2013). Temporal variation in volcanic ash texture during a vulcanian eruption at the Sakurajima volcano, Japan. *Journal of Volcanology and Geothermal Research, 260*, 80-89. doi:https://doi.org/10.1016/j.jvolgeores.2013.05.010

Miyabuchi, Y., Ikebe, S.-i., & Watanabe, K. (2008). Geological constraints on the 2003–2005 ash emissions from the Nakadake crater lake, Aso Volcano, Japan. *Journal of Volcanology and Geothermal Research, 178*(2), 169-183. doi:https://doi.org/10.1016/j.jvolgeores.2008.06.025

Miyabuchi, Y., Hanada, D., Niimi, H., & Kobayashi, T. (2013). Stratigraphy, grain-size and component characteristics of the 2011 Shinmoedake eruption deposits, Kirishima Volcano, Japan. Journal of Volcanology and Geothermal Research, 258, 31-46. doi:https://doi.org/10.1016/j.jvolgeores.2013.03.027

Miyabuchi, Y., Iizuka, Y., Hara, C., Yokoo, A., & Ohkura, T. (2018). The September 14, 2015 phreatomagmatic eruption of Nakadake first crater, Aso Volcano, Japan: Eruption sequence inferred from ballistic, pyroclastic density current and fallout deposits. *Journal of Volcanology and Geothermal Research, 351*, 41-56. doi:https://doi.org/10.1016/j.jvolgeores.2017.12.009

Miyabuchi, Y., & Hara, C. (2019). Temporal variations in discharge rate and component characteristics of tephra-fall deposits during the 2014–2015 eruption of Nakadake first crater, Aso Volcano, Japan. *Earth, Planets and Space, 71*(1), 44. doi:https://doi.org/10.1186/s40623-019-1018-6

Moebis, A., Cronin, S. J., Neall, V. E., & Smith, I. E. (2011). Unravelling a complex volcanic history from fine-grained, intricate Holocene ash sequences at the Tongariro Volcanic Centre, New Zealand. *Quaternary International, 246*(1–2), 352-363. doi:http://dx.doi.org/10.1016/j.quaint.2011.05.035

Nairn, I. A., & Group, R. S. (1996). Volcanic eruption at a New Zealand ski resort prompts reevaluation of hazards. *Eos, Transactions American Geophysical Union, 77*(20), 189-191. doi:http://dx.doi.org/10.1029/96EO00129

Nakada, S., Nagai, M., Kaneko, T., Suzuki, Y., & Maeno, F. (2013). The outline of the 2011 eruption at Shinmoe-dake (Kirishima), Japan. Earth, Planets and Space, 65(6), 1. doi:10.5047/eps.2013.03.016

Nakagawa, M., Wada, K., Thordarson, T., Wood, C. P., & Gamble, J. A. (1999). Petrologic investigations of the 1995 and 1996 eruptions of Ruapehu volcano, New Zealand: formation of discrete and small magma pockets and their intermittent discharge. *Bulletin of Volcanology, 61*, 15-31. doi:https://doi.org/10.1007/s004450050259

Nakagawa, M., Wada, K., & Wood, C. P. (2002). Mixed Magmas, Mush Chambers and Eruption Triggers: Evidence from Zoned Clinopyroxene Phenocrysts in Andesitic Scoria from the 1995 Eruptions of Ruapehu Volcano, New Zealand. *Journal of Petrology, 43*(12), 2279-2303. doi:https://doi.org/10.1093/petrology/43.12.2279

Oishi, M., Nishiki, K., Geshi, N., Furukawa, R., Ishizuka, Y., Oikawa, T., Yamamoto, T., Nanayama, F., Tanaka, A., Hirota, A., Miwa, T., & Miyabuchi, Y. (2018). Distribution and mass of tephra-fall deposits from volcanic eruptions of Sakurajima Volcano based on posteruption surveys. *Bulletin of Volcanology, 80*(4), 42. doi:https://doi.org/10.1007/s00445-018-1215-3

Oliver, R. (1945). Further activity of Mount Ruapehu, May-July 1945. *New Zealand Journal of Science and Technology, 26*, 24-33.

Pardo, N., Cronin, S., Palmer, A., Procter, J., & Smith, I. (2012). Andesitic Plinian eruptions at Mt. Ruapehu: quantifiying the uppermost limits of eruptive parameters. *Bulletin of Volcanology, 74*, 1161-1185. doi:https://doi.org/10.1007/s00445-012-0588-y

Pardo, N., Cronin, S. J., Palmer, A. S., & Németh, K. (2011). Reconstructing the largest explosive eruptions of Mt. Ruapehu, New Zealand: lithostratigraphic tools to understand subplinian–plinian eruptions at andesitic volcanoes. *Bulletin of Volcanology, 74*(3), 617-640. doi:https://doi.org/10.1007/s00445-011-0555-z

Pardo, N., Cronin, S. J., Wright, H. M., Schipper, C. I., Smith, I., & Stewart, B. (2014). Pyroclast textural variation as an indicator of eruption column steadiness in andesitic Plinian eruptions at Mt. Ruapehu. *Bulletin of Volcanology, 76*(5), 822. doi:https://doi.org/10.1007/s00445-014-0822-x

Paton, C., Hellstrom, J., Paul, B., Woodhead, J., & Hergt, J. (2011). Iolite: Freeware for the visualisation and processing of mass spectrometric data. *Journal of Analytical Atomic Spectrometry, 26*(12), 2508-2518. doi:https://doi.org/10.1039/C1JA10172B

Pearce, N. J. G., Perkins, W. T., Westgate, J. A., Gorton, M. P., Jackson, S. E., Neal, C. R., & Chenery, S. P. (1997). A Compilation of New and Published Major and Trace Element Data for NIST SRM 610 and NIST SRM 612 Glass Reference Materials. *Geostandards Newsletter, 21*(1), 115-144. doi:https://doi.org/10.1111/j.1751-908X.1997.tb00538.x

Pioli, L., Erlund, E., Johnson, E., Cashman, K., Wallace, P., Rosi, M., & Delgado Granados, H. (2008). Explosive dynamics of violent Strombolian eruptions: The eruption of Parícutin Volcano 1943–1952 (Mexico). *Earth and Planetary Science Letters, 271*(1), 359-368. doi:https://doi.org/10.1016/j.epsl.2008.04.026

Pistolesi, M., Rosi, M., Cioni, R., Cashman, K. V., Rossotti, A., & Aguilera, E. (2011). Physical volcanology of the post–twelfth-century activity at Cotopaxi volcano, Ecuador: Behavior of an andesitic central volcano. *GSA Bulletin, 123*(5-6), 1193-1215. doi:http://dx.doi.org/10.1130/B30301.1

Platz, T., Cronin, S. J., Smith, I. E. M., Turner, M. B., & Stewart, R. B. (2007). Improving the reliability of microprobe-based analyses of andesitic glasses for tephra correlation. *The Holocene, 17*(5), 573-583. doi:https://doi.org/10.1177/0959683607078982

Ponomareva, V., Portnyagin, M., Pevzner, M., Blaauw, M., Kyle, P., & Derkachev, A. (2015). Tephra from andesitic Shiveluch volcano, Kamchatka, NW Pacific: chronology of explosive eruptions and geochemical fingerprinting of volcanic glass. *International Journal of Earth Sciences, 104*(5), 1459-1482. doi:https://doi.org/10.1007/s00531-015-1156-4

Price, R. C., Gamble, J. A., Smith, I. E. M., Maas, R., Waight, T., Stewart, R. B., & Woodhead, J. (2012). The Anatomy of an Andesite Volcano: a Time-Stratigraphic Study of Andesite Petrogenesis and Crustal Evolution at Ruapehu Volcano, New Zealand. *Journal of Petrology, 53*(10), 2139-2189. doi:https://doi.org/10.1093/petrology/egs050

Price, R. C., Gamble, J. A., Smith, I. E. M., Stewart, R. B., Eggins, S., & Wright, I. C. (2005). An integrated model for the temporal evolution of andesites and rhyolites and crustal development in New Zealand's North Island. *Journal of Volcanology and Geothermal Research, 140*(1-3), 1-24. doi:https://doi.org/10.1016/j.jvolgeores.2004.07.013

Pyle, D. M. (1989). The thickness, volume and grainsize of tephra fall deposits. *Bulletin of Volcanology, 51*(1), 1-15. doi:https://doi.org/10.1007/bf01086757

Reed, J. (1945). Activity at Ruapehu, March-April, 1945. *New Zealand Journal of Science and Technology, 26*, 17-23.

Rose, W. I. (1993). Comment on ‘another look at the calculation of fallout tephra volumes’ by Judy Fierstein and Manuel Nathenson. *Bulletin of Volcanology, 55*(5), 372-374. doi:https://doi.org/10.1007/bf00301148

Rose, W. I., Anderson, A. T., Woodruff, L. G., & Bonis, S. B. (1978). The October 1974 basaltic tephra from Fuego volcano: Description and history of the magma body. *Journal of Volcanology and Geothermal Research, 4*(1), 3-53. doi:https://doi.org/10.1016/0377-0273(78)90027-6

Rose, W. I., Self, S., Murrow, P. J., Bonadonna, C., Durant, A. J., & Ernst, G. G. J. (2008). Nature and significance of small volume fall deposits at composite volcanoes: Insights from the October 14, 1974 Fuego eruption, Guatemala. *Bulletin of Volcanology, 70*(9), 1043-1067. doi:https://doi.org/10.1007/s00445-007-0187-5

Salmon, M., Stern, T., & Savage, M. K. (2011). A major step in the continental Moho and its geodynamic consequences: the Taranaki-Ruapehu line, New Zealand. *Geophysical Journal International, 186*(1), 32-44. doi:https://doi.org/10.1111/j.1365-246X.2011.05035.x

Scott, B. J. (2013). A revised catalogue of Ruapehu volcano eruptive activity: 1830-2012. *GNS Science Report, 2013/45*.

Suzuki, Y., Nagai, M., Maeno, F., Yasuda, A., Hokanishi, N., Shimano, T., Ichihara, M., Kaneko, T., & Nakada, S. (2013). Precursory activity and evolution of the 2011 eruption of Shinmoe-dake in Kirishima volcano—insights from ash samples. Earth, Planets and Space, 65(6), 11. doi:10.5047/eps.2013.02.004

Taddeucci, J., Pompilio, M., & Scarlato, P. (2002). Monitoring the explosive activity of the July–August 2001 eruption of Mt. Etna (Italy) by ash characterization. *Geophysical Research Letters, 29*(8). doi:https://doi.org/10.1029/2001GL014372

Taddeucci, J., Pompilio, M., & Scarlato, P. (2004). Conduit processes during the July–August 2001 explosive activity of Mt. Etna (Italy): inferences from glass chemistry and crystal size distribution of ash particles. *Journal of Volcanology and Geothermal Research, 137*(1), 33-54. doi:https://doi.org/10.1016/j.jvolgeores.2004.05.011

Turner, R., & Hurst, T. (2001). Factors Influencing Volcanic Ash Dispersal from the 1995 and 1996 Eruptions of Mount Ruapehu, New Zealand. *Journal of Applied Meteorology, 40*(1), 56-69. doi:https://doi.org/10.1175/1520-0450(2001)040<0056:FIVADF>2.0.CO;2

Villamor, P., & Berryman, K. R. (2006). Evolution of the southern termination of the Taupo Rift, New Zealand. *New Zealand Journal of Geology and Geophysics*, *49*(1), 23-37. doi:https://doi.org/10.1080/00288306.2006.9515145

Voloschina, M., Lube, G., Procter, J., Moebis, A., & Timm, C. (2020). Lithosedimentological and tephrostratigraphical characterisation of small-volume, low-intensity eruptions: The 1800 years Tufa Trig Formation, Mt. Ruapehu (New Zealand). *Journal of Volcanology and Geothermal Research*, 106987. doi:https://doi.org/10.1016/j.jvolgeores.2020.106987

White, J. D. L., & Houghton, B. F. (2006). Primary volcaniclastic rocks. *Geology, 34*(8), 677-680. doi:https://doi.org/10.1130/G22346.1

Wohletz, K., Zimanowski, B., & Büttner, R. (2013). Magma-water interactions in Modeling volcanic processes: The physics and mathematics of volcanism (pp. 230-257): Cambridge University Press, New York.

Wright, H. M., Cashman, K. V., Mothes, P. A., Hall, M. L., Ruiz, A. G., & Le Pennec, J. L. (2012). Estimating rates of decompression from textures of erupted ash particles produced by 1999–2006 eruptions of Tungurahua volcano, Ecuador. Geology, 40(7), 619-622.

Yamanoi, Y., Takeuchi, S., Okumura, S., Nakashima, S., & Yokoyama, T. (2008). Color measurements of volcanic ash deposits from three different styles of summit activity at Sakurajima volcano, Japan: Conduit processes recorded in color of volcanic ash. Journal of Volcanology and Geothermal Research, 178(1), 81-93. doi:https://doi.org/10.1016/j.jvolgeores.2007.11.013

Supplementary material

Supplementary Table S4.1 (Appendix H-2): Average major and trace element groundmass composition with 2SD.

Spot data on major and trace element geochemistry is contained within Appendix G-1 and Appendix G-2, respectively.

Chapter 5

Modelling multi-phase eruptions

This chapter presents an 1800-year frequency-magnitude record for small to moderate explosive eruptions at Mt. Ruapehu and identifies four periods that are characterised by distinct eruptive behaviour and distinct eruption rates. Probabilistic models are applied to the geological multi-phase record and show how long-term eruption records can improve future eruption forecast models.

Chapter 5 contains the manuscript Probabilistic modelling of multi-phase eruptions in geological records: An example from Mt. Ruapehu, New Zealand by M. Voloschina, M. Bebbington, G. Lube, J. Procter & A. Moebis. The manuscript is submitted as a research article for publication in *Journal of Volcanology and Geothermal Research*. The format of the manuscript has been adapted to match the format of the thesis. In the following, the contributions of individual authors are outlined (DRC 16 - Statement of Contribution is contained in Appendix I-3 and on page 264):

Principal author: M Voloschina

Carried out: Field work and mapping

Laboratory analysis

Providing magnitude and tephrostratigraphical data for statistical modelling

Use of statistical models to discuss frequency-magnitude relationships

Data analysis and interpretation

Manuscript draft

Co-authors: M. Bebbington

Contributed to the study by: Developing statistical methods for multi-phase modelling

Creating age depth model using statistical methods

Editing and discussing statistical data

G. Lube

Contributed to the study by: Data discussion and interpretation

Commenting and reviewing manuscript

J. Procter

Contributed to the study by: Commenting manuscript

Data discussion and interpretation

A.Moebis

Contributed to the study by: Assistance with field and laboratory work

Probabilistic modelling of multi-phase eruptions in geological records: An example from Mt Ruapehu, New Zealand.

5.1 Abstract

Eruption forecast models are crucially dependent on the quality of the underlying eruption record and its ability to account for short- and long-term changes in eruption behaviour. Long-lived composite andesitic volcanoes are known to show changes in eruption frequency, magnitude and style at different timescales during their lifespan. Given the generally low preservation potential of the associated deposits, small to moderate explosive eruptions tend to be underrepresented in long-term eruption records and accordingly in the resulting forecast models. Mt. Ruapehu is the historically most active volcano in New Zealand with major eruptive episodes in 1945 and 1995–1996. The tephra record of the past 1800 years comprises at least thirty-one small to moderate explosive eruptions, ranging from complex multi-phase eruptions with deposit volumes of 2.14–50.71 × 10^6 m^3 to short-lived low-intensity eruptions with deposit volumes of 1.72–19.4 × 10^5 m^3. The integration of a high-resolution tephrostratigraphic framework with a refined age model and magnitude estimates for individual eruption subunits, allows to quantify time-variable pattern in frequency-magnitude behaviour and to compare these with time-variable patterns in the geochemical signature. Over the past 1800 years, four periods of distinct eruption behaviour associated with three activity regimes can be identified. (1) A low rate regime between 1300 and 610 cal BP involves an average eruption frequency of one eruption every ~125 years, and comprises mostly single-phase low to mid-intensity eruptions and indicates a break in eruptive activity between 1300 and 945 cal BP. (2) Two medium rate regimes between 1718 and 1300 cal BP and during the last 370 years have a 40 years recurrence rate, while (3) a high frequency regime (610-370 cal BP) is characterised by decadal eruptions, and involves the largest eruptions of the past 1800 years. Statistical models are applied to the geological multi-phase record and indicate consistent trends regarding the number of eruption phases and deposit volume of individual eruption phases. The here presented research uses a multi-parameter

approach to show how a detailed eruption record can be used to advance the understanding of the factors that are involved in eruption behaviour switches at long-lived andesitic volcanoes and how this information can be used to improve eruption forecast models at a frequently active volcano.

5.2 Introduction

Eruptions do not occur at instants in time. Instead they can last days, months or even decades. During prolonged eruptions, sudden changes in eruptive behaviour are common. About half of historically documented eruptions are known to contain more than one explosive eruption phase (Jenkins et al., 2007) with different eruption phases being characterised by distinct eruption styles, magnitudes and duration (Cioni et al., 2008; Barsotti et al., 2015; Torres-Orozco et al., 2018). For hazard and risk management it is crucial to forecast eruption progression during multi-phase eruptions, by being able to estimate the likelihood, style and magnitude of any potential future eruption phase(s) and the associated hazards (Bebbington and Jenkins, 2019).

For historical eruptions, the analysis of multi-phase data from the Global Volcanism Programme (GVP, Bebbington and Jenkins, 2019) has led to a categorisation of eruption behaviour, distinguishing effusive, combined effusive and explosive, and varying types/intensities of explosive behaviour. Eruption progression could then be modelled using tools from the theory of semi-Markov chains, where the likelihood of the next phase (including eruption end) is estimated based on the current state, the elapsed time in that state, and the length of the preceding quiescence. While this model was based on a dataset from 697 eruptions at 186 volcanoes, nearly three quarters of the volcanoes contributed information on three or fewer eruptions. This illustrates how eruption forecast models tend to be strongly biased by the availability of detailed historical accounts for a few volcanoes (e.g. Vesuvius, Etna) and how data quality generally decreases with age (Connor et al., 2015). Addressing this issue is critical when it comes to the identification and definition of volcanic regimes and other time-varying changes in eruption behaviour (Lerner et al., 2019).

Eruption forecasting data are, in the main, obtained either from geological records or historical accounts or observations. Depending on the model, they might focus on the eruptive history of individual volcanoes (Cronin et al., 2001; Passarelli et al., 2010; Garcia-Aristizabal et al., 2012; Damaschke et al., 2017a; 2017b) or multiple volcanoes (Martin et al., 2004; Bebbington and Marzocchi, 2011; Jaquet et al., 2012). The objective from the probabilistic analysis of such multiple eruption data can involve long-term forecasting of future eruption onsets and magnitudes (Marzocchi and Zaccarelli, 2006; Bebbington, 2014), or linking long-term variation in eruption patterns to changes in the magmatic system (Turner et al., 2011).

Obtaining representative long-term geological records of explosive eruptive activity is a complex undertaking. Often this involves merging stratigraphic observations from different sectors of the volcano to obtain the most complete record possible (Óladóttir et al., 2008; 2011; Lowe, 2011; Pardo et al., 2011; Damaschke et al., 2017b). While long-term changes in eruption frequency can be potentially better resolved in distal areas and are traditionally approached by means of sediment or marine cores, this approach potentially neglects the more frequent but usually smaller and less dispersed events with VEI ≤ 3, which nevertheless contribute greatly to volcanic risk.

Mt. Ruapehu is a frequently active andesitic volcano on the North Island of New Zealand. The tephra record comprising the eruptions of the past 1800 years is defined as the Tufa Trig Formation and includes at least 31 small to moderate eruptions of VEI~3. While the tephra record represents predominantly phreatomagmatic to magmatic explosive eruptions with deposit volumes <0.1 km^3, Voloschina et al. (2020) have shown that ~55% of these eruptions include more than one eruption phase and that eruption frequency and magnitude show time-variable patterns throughout the past 1800 years. This paper combines a refined frequency-magnitude record for the 1800 years–present eruptive record with geochemical data to quantify changes in long-term eruption behaviour and relate them to the underlying magmatic system. Subsequently, this dataset is integrated with statistical modelling and is used as a test bed for geological multi-phase modelling. Here, models for both onset times and phase volumes are developed and the phase number distribution is tested for consistency with the model of Bebbington and Jenkins (2019).

5.2.1 Geological background

The Tongariro Volcanic Centre on the North Island of New Zealand (TgVC, Fig. 5.1a) comprises the andesitic composite volcanoes Mt. Tongariro and Mt. Ruapehu and marks the southernmost extension of the Taupo Volcanic Zone (TVZ). Mt. Ruapehu is the larger of the centres, with a peak of 2797 m asl and an edifice volume of ~150 km^3 (Hackett et al., 1989). The andesitic composite volcano is considered one of New Zealand's most active volcanoes and has exhibited a range of eruption styles and magnitudes over the past 250,000 years (Gamble et al., 2003). Explosive activity is well constrained for the past ~30,000 years, based on the tephra deposits preserved in the ring plain, with a number of studies characterising the lapilli deposits associated with the voluminous Plinian eruptions of the Bullot Formation (Topping, 1973; Donoghue et al., 1995; Pardo et al., 2011; Pardo et al., 2012). These eruptions took place between 27,000 and 10,000 years BP (Donoghue et al., 1995; Pardo et al., 2011) and involve VEIs of 4 to 5, tephra volumes of >0.6 km^3 and peak eruption column heights of up to 37 km (Pardo et al., 2012).

For the last 10,000 years, a change in eruption behaviour has been noted, associated with a switch to smaller but more frequent phreatomagmatic to Strombolian eruptions (Topping, 1973; Donoghue et al., 1995; Donoghue et al., 1997). While eruptions between 10,000 and ~1800 years BP are poorly characterised in terms of frequency, magnitude and style, the tephra record overlying the Taupo Pumice (AD 232; Lowe et al., 2013) is well characterised (Donoghue et al., 1997; Voloschina et al., 2020). This formation is defined as the Tufa Trig Formation and comprises at least thirty-one discrete tephra units at a distance range of 6 to 21 km from the current vent.

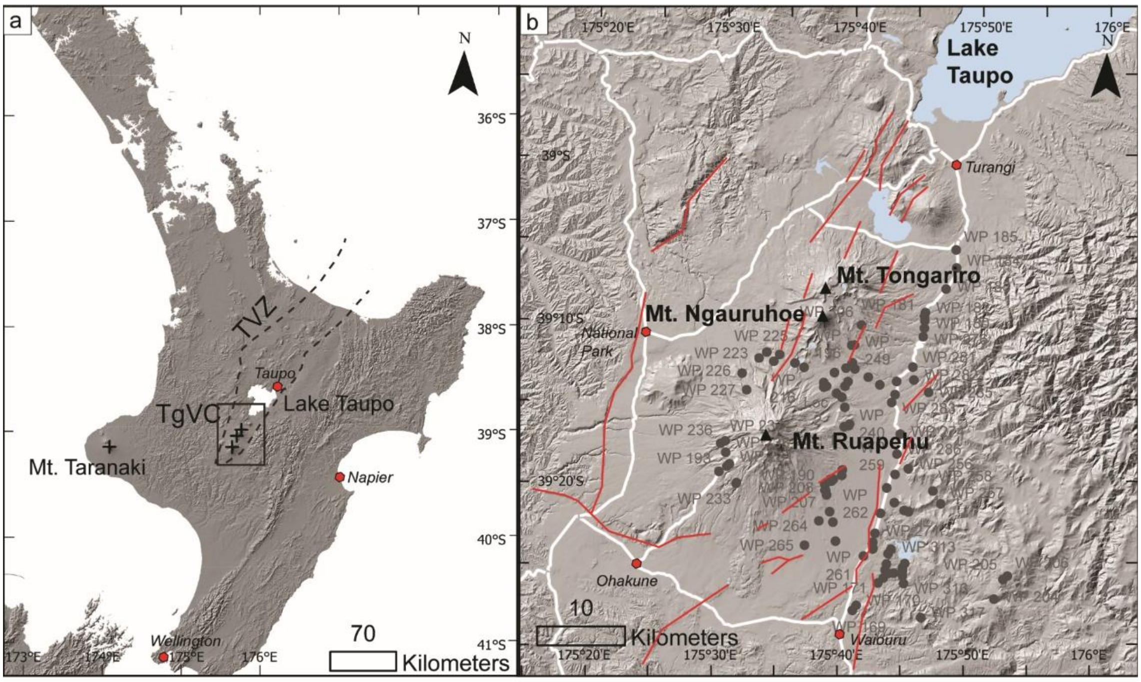

Fig. 5.1: Overview geographical setting based on a 8 m digital elevation model from the LINZ Data Service (https://data.linz.govt.nz) and is based on the LINZ Topo50 map series from 2012. a) The North Island of New Zealand. The Taupo Volcanic Zone (TVZ) is delimited following Wilson et al. (1995). The position of the Tongariro Volcanic Centre (TgVC) is marked by a box and the position of the andesitic volcano Mt. Taranaki and the rhyolitic caldera Taupo are reported for comparison. Inset b) shows an overview of the Tongariro Volcanic Centres (TgVC), which include Mt. Tongariro and Mt. Ngauruhoe to the North and Mt. Ruapehu. Field locations that were investigated for this research are marked by grey circles. The white lines represent major roads. Red lines show major fault lines and are modified after Villamor et al. (2007).

5.2.2 Tufa Trig Formation

A high-resolution study on the tephrostratigraphic and lithosedimentologial characteristics of the Tufa Trig Formation has uncovered previously unknown complexity in these small-scale eruptions, showing that tephra deposits can be grouped into three main types that are representative of different eruption types (Fig. 5.2 and Voloschina et al., 2020): (1) Single bed ash units (SBA) represent low-intensity eruptions and are characterised by the lowest preserved tephra deposit volumes in the order of magnitude of ~1×10^6 m^3. These units are generally discontinuously laminated, involve deposit thicknesses <10 mm at medial distances and are composed of highly fragmented pyroclastic material in the ash fraction (grain diameter <2 mm, Fig. 5.2b). Maximum distances at which associated tephra deposits are preserved macroscopically, are ~11 km. These units constitute ~35% of the tephras recorded in the last 1800 years at Mt. Ruapehu.

(2) Lapilli units (L) are associated with moderate intensity short-lived eruptions and involve deposit volumes of 5–10 × 10^6 m^3. The dominant grain size lies in the lapilli fraction (grain diameter ≥ 2 mm, Fig. 5.2d) and tephra dispersal is characterised by narrow distributions to distances of up to 20 km. About 10% of the tephra members of the 1800-year record can be classified as lapilli units. (3) About 55% of the geologically preserved record is constituted by multi-bed ash units (MBA, Fig. 5.2). These sequences show various degrees of complexity, involving either 2–3 subunits (Fig. 5.2a) or at least 4 subunits (Fig. 5.2c). The subunits represent individual eruption phases within a multi-phase sequence, and sharp contacts between beds can be associated with abrupt changes in eruption characteristics, such as style, dispersal, or intensity. Multi-bed ash units show an extensive dispersal around the ring plain, defining irregular multi-lobate patterns. Deposit volumes are in the order of magnitude of 15–69 × 10^6 m^3, with volumes obtained for the main phases being in the range of 4–16 × 10^6 m^3 (Voloschina et al., 2020).

5.2.3 Major historical eruptions

Per definition, the geological record of the Tufa Trig Formation also includes all historical eruptive activity sourced from Mt. Ruapehu (Donoghue et al., 1997). Since the start of historical observations in 1861, major magmatic eruptive episodes took place in 1895, 1945, 1969, 1971–1977 and 1995–1996 (Scott, 2013). The 1945 and the 1995–1996 episodes erupted the largest cumulative tephra volumes (<0.1 km^3; Johnston et al., 2000) and comprised series of multiple events ranging between small-scale phreatic and phreatomagmatic activity with deposits restricted to the summit plateau, and major subplinian events, which transported pyroclastic material up to heights of 10 km (Cronin et al., 2003) and distances of up to 200 km (Bonadonna et al., 2005).

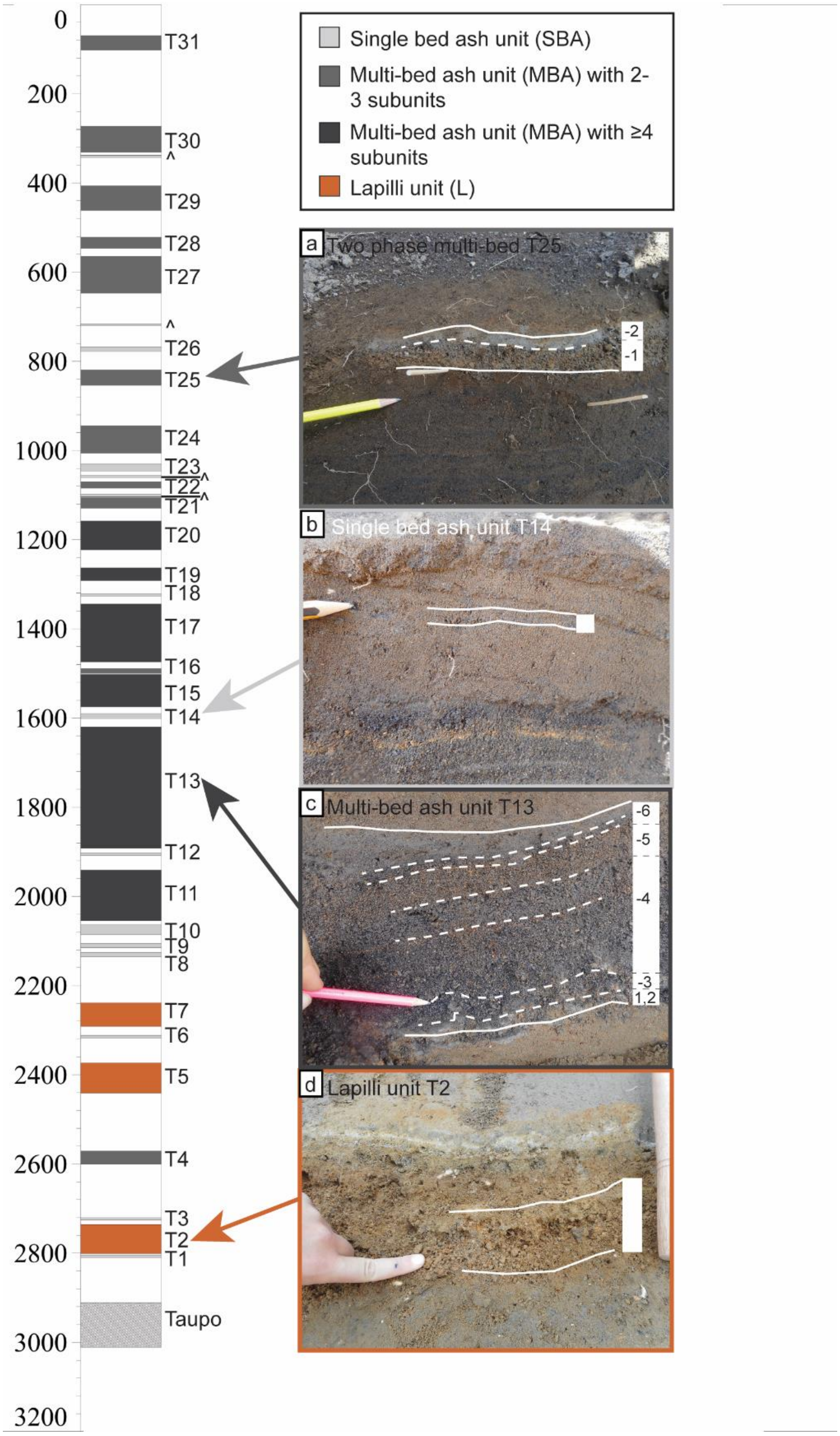

Fig. 5.2: Composite stratigraphic profile showing idealised tephra and soil thicknesses of the Tufa Trig Formation in mm at ~10 km distance from source. The three main types of deposit, classified in Voloschina et al. (2020) are reported by different colours with light grey units corresponding to single bed ash unit (SBA), medium grey units showing multi-bed ash units with 2 to 3 subunits, dark grey units representing multi-bed ash units with ≥4 subunits and orange marking lapilli units. The stratigraphic position of four uncorrelated tephra units is reported as well (“^”). Insets show images of typical tephra sequences, representative of the different lithosedimentological types.

The 1945 eruptions began in March 1945 with a small to moderate explosive eruption (Scott, 2013). With increasing activity, the Crater Lake was emptied and an emplacement of a lava dome was observed (Oliver, 1945; Scott, 2013). Ash fall was described in Taupo (~80 km NNE), Napier (~120 km E) and Wellington (~230 km SSW) on several occasions (Fig. 5.1a and Fig. 5.3a; Johnston, 1997b; Scott, 2013).

During the 1995–1996 episodes the main eruptive activity was characterised by small intermittent phreatic to phreatomagmatic and Strombolian eruptions. By Oct 11 1995, the Crater Lake had been fully displaced and a period of semi-sustained subplinian activity was observed until Oct 14 1995. Main dispersal was towards the NE (Fig. 5.3b, Oct 11 ‘95) and towards the SE (Fig. 5.3b, Oct 14 ‘95, Cronin et al., 2003) and tephra volumes were estimated at 25–30 × 10^6 m^3 and 5–10 × 10^6 m^3, respectively (Nairn et al., 1996, Cronin et al., 2003). Activity continued as ash emissions and ceased by November (Cronin et al., 2003; Scott 2013). By June 1996 the Crater Lake had refilled, so that during the violent June 17 1996 eruption, water was evaporated while a subplinian eruption plume dispersed ash up to distances of >200 km northward (Fig. 5.3b). The 1996 tephra deposit volume was calculated at 4 × 10^6 m^3, based on thickness and isomass data acquired shortly after the eruption (Bonadonna et al., 2005).

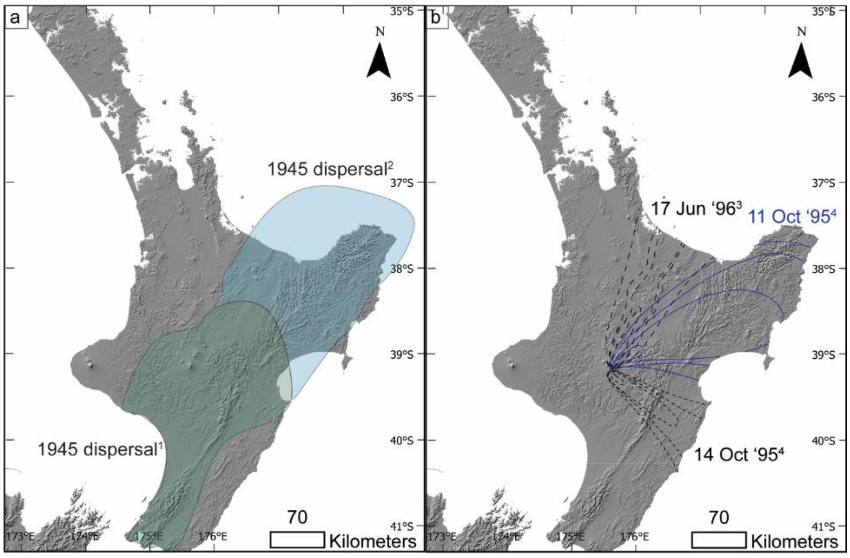

Fig. 5.3: Overview showing tephra dispersal during major historical eruption episodes at Mt. Ruapehu. Inset a) shows the dispersal of ash associated with the 1945 eruptions modified after Johnston et al. (2000) with green area marking tephra dispersal after Beck (1950), while the blue area extends the dispersal area following Johnston et al. (2000). b) Tephra dispersal for major magmatic phases during 1995-1996 episodes shows the NE-isopachs for October 11th in blue, the SE-isopachs of Oct 14th after Cronin et al. (1998) with stippled lines and the isomass dispersal from the 17 Jun 1996 subplinian phase after Bonadonna and Houghton (2005) are reported by dashed lines.

5.3 Methods

In the following, we use the recently refined tephra record presented in Voloschina et al. (2020). This record comprises 31 defined tephra members, which can be further subdivided into at least 71 depositional subunits and further four uncorrelated tephra units. This data forms the basis to create a tephra age model, which is then integrated with tephra volumes and major element data to discuss changes in the eruption behaviour for the past 1800 years. In addition to this, statistical models are applied to this record for modelling inter-eruption onset and eruption duration and deposit volume of intra-eruption sequences. The four uncorrelated units are not considered as formal members, as they have not been correlated to other locations and could be identified at only one location. However, they are included in the age model as well as in the frequency-magnitude record.

5.3.1 Linking the most recent tephra member T31 to a historical eruption

In order to constrain our age model, and thus calibrate it to the present day to enable forecasting, the top of the geologically preserved eruptive record needs to be matched to the historical record.

The 1945 and 1995–1996 eruptions constitute the largest events over the past 160 years, having erupted similar total erupted volumes of ~0.1 km^3, suggesting that they should appear in the tephra record. The 1945 eruption led to widespread ashfall, affecting large parts of the North Island (Fig. 5.3a; Johnston et al., 1995; 2000). Changing wind directions resulted in variable ashfall dispersal with a strong prevalence of westerly winds (Beck, 1950; Johnston, 1997a). As opposed to this, the main phases of the 1995–1996 episodes were characterised by prevalently NNE-NE-directed dispersal (Fig. 5.3b; Cronin et al., 2003).

The stratigraphically uppermost discrete tephra unit is T31 (Fig. 5.2) and can be identified in type locations to the North (Loc. 2, Fig. 5.1) and to the East (Loc. 1). At Loc. 2 it appears as an indistinctly laminated fine ash without distinct subunits and is overlain by 130 mm soil, while at Loc. 1 it contains at least three beds and is overlain by 480 mm soil below todays surface. Generally, the uppermost 10 to 50 cm of the profiles investigated in this study are characterised by poor compaction and are strongly disturbed by vegetation, including perturbation by roots. In many sections around the ring plain, the upper part of the profile is entirely absent or strongly reworked. Accordingly, the identification and correlation of T31 between Loc. 1 and Loc. 2 is based on the characteristic stratigraphic position of the tephra sequence, which is encompassed between todays surface and the underlying relatively thick soil sequence between T31 and T30 (Fig. 5.2).

Soil thicknesses overlying T31 at Loc. 1 and Loc. 2, suggest that the eruption responsible for this deposit is older than the 25 years that have passed since the 1995–1996 episodes. In agreement with several enhanced periods of eastward tephra dispersal during the 1945 eruptions, we relate the T31 tephra unit to the 1945 eruptions. In line with this, several locations (e.g., WP219, WP223) in the North contain lapilli-sized pumices in the roots but no quantification of their stratigraphic position is possible. We infer that these pyroclasts are associated with the 1995–1996 eruptions.

5.3.2 Tephra dispersal and volume calculations

The datasets on the thickness distribution of the individual 75 subunits of the thirty-one defined members and the four additional members differ in their detail and number of available data points. Thickness datasets for key units T2, T5, T7, T13-1, T13-3, T13-4, T13-6, T14 and for T15-3 and T15-4 are extensive and allow the construction of detailed isopachs (cf. Fig. 3.10 and Fig. 4.3). For the majority of subunits, however, thickness data is limited, involving as little as one data point for i.e., the uncorrelated subunits. In the following we use a simplified approach to approximate tephra dispersal from these limited datasets and show how this can be used to estimate tephra volumes and how these compare with volume estimates from detailed isopachs.

The simplest (and therefore easiest to reproduce) geometrical shape to approximate isopachs are ellipses (cf. Kawabata et al., 2015). This allows the construction of idealised isopachs from as little as three data points, which delimit the major and minor axis of the ellipse. Similar to Kawabata et al. (2015), we approximate one ellipse for each individual subunit, assuming that each ellipse represents an individual eruption phase.

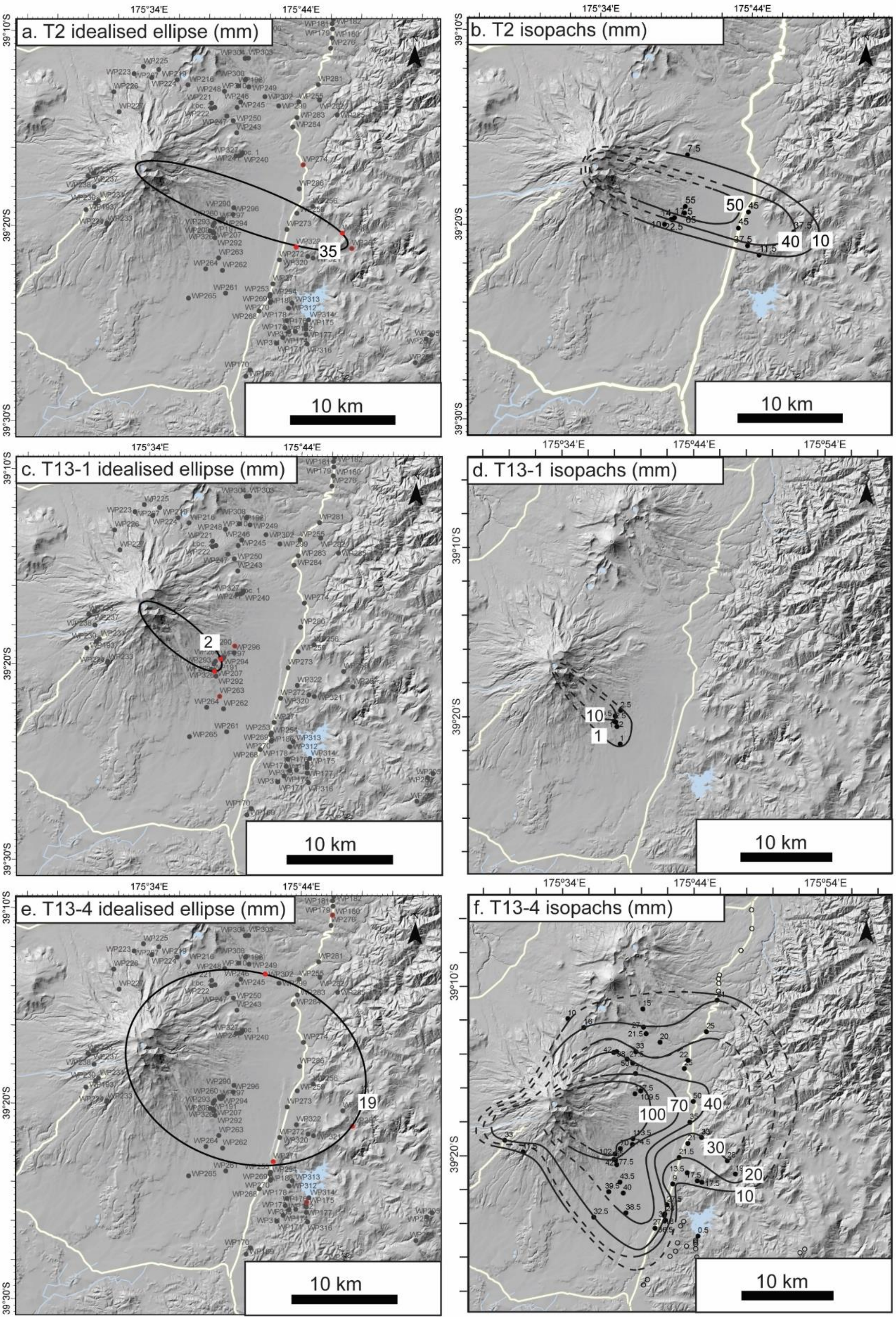

Fig. 5.4: Comparison of idealised and detailed isopachs to approximate tephra dispersal. Thicknesses are in mm. a) Lapilli unit T2 is approximated by an idealised ellipse of 35 mm thickness. b) Detailed isopachs constructed for the same unit T2 after Voloschina et al. (2020). c) Idealised ellipse of 2 mm thickness to approximate the dispersal of subunit T13-1. d) Detailed isopach for subunit T13-1 as shown in Chapter 4. e) Tephra dispersal of main subunit T13-4 approximated by an idealised ellipse and f) by detailed isopachs as shown in Chapter 4.

For units with detailed datasets, multiple isopachs can be constructed for different thicknesses, allowing to compare different methods for volume calculation (i.e., Pyle, 1989; Fierstein and Nathenson, 1992; Legros, 2000 and Bonadonna and Costa, 2013). This has been shown for selected key units in previous chapters with the difference in deposit volume estimates associated with different volume calculation methods ranging between 7.38 and 41.02 %. Conversely, for poorly constrained subunits, at best one ideal ellipse-shaped isopach can be constructed. In this case, minimum deposit volumes can be estimated by applying the minimum isopach approach of Legros (2000). Table 5.1 shows the comparison of tephra volumes obtained from the simplified ellipse-method with those obtained from detailed isopachs for key units (Fig. 5.4). For example, tephra dispersal for T2 can be approximated by a single 35 mm ellipse (Fig. 5.4a) and yields a tephra volume of 9.32×10^6 m^3. This volume compares well with the volume range of $5.17–9.52 \times 10^6$ m^3 that was obtained from detailed isopachs in Chapter 3 (Table 5.1). For T13-1 and T13-4, volumes obtained from the ellipse-methods (Fig. 5.4c, e) are slightly smaller than the values obtained from detailed isopachs (Fig. 5.4d, f) but range in the same order of magnitude (Table 5.1). This shows that the ellipse method provides a simple and reliable approach to estimate the order of magnitude for tephra volumes from poorly constrained datasets. Importantly, this approach enables us to calculate deposit volumes for the entirety of our dataset. Naturally enough, we stress that the approximate deposit volumes should be treated with caution and advise against their use as absolute volumes. For comparability, in the remainder of the paper we will only use tephra volumes obtained by the ellipse method.

Table 5.1: Deposit volumes calculated for key subunits to illustrate how volumes based on simplified ellipse compare with volumes obtained from detailed isopachs.

Subunit	Deposit type	Deposit volume in m^3 from ellipses [1]	Deposit volume in m^3 from detailed isopachs [2]
T2	L	9.32E+06	5.17–9.52E+06
T5	L	2.51E+06	4.86–6.25E+06
T7	L	3.58E+06	2.51–2.81E+06
T13-1	MBA	1.76E+05	3.83–8.23E+05
T13-3	MBA	5.09E+06	8.11–12.8E+06
T13-4	MBA	2.31E+07	2.41–3.70E+07
T13-6	MBA	1.04E+07	1.19–1.46E+07
T14	SBA	8.55E+05	1.10–1.35E+06
T15-3	MBA	4.94E+06	6.40–15.9E+06
T15-4	MBA	2.54E+06	3.63–4.89E+06

Notes: [1] Tephra dispersal approximated by idealised ellipses. Deposit volumes calculated following Legros (2000) [2] Tephra dispersal approximated by manually drawn detailed isopachs, shown in Voloschina et al. (2020) for T2, T14 and T15-3 and -4. Isopachs for T13-1, -3, -4 and -6 are discussed in Chapter 4. Deposit volumes are reported as ranges, calculated by using several methods calculated after Pyle (1989), Fierstein and Nathenson (1992), Legros (2000) and Bonadonna and Costa (2013).

5.3.3 Geochemical characterisation

Individual subunits were sampled at the representative key section Loc. 1 (Fig. 5.1b). For subunits, which do not appear at Loc. 1 (Voloschina et al., 2020), the dataset was complemented by samples from other locations to construct a record for major element compositions over the past 1800 years. Juvenile glass shards were picked manually from the 2 and 3 Φ size fractions and embedded in an epoxy plug. Major element compositions were obtained on at least ten juvenile shards for each sample. Analyses were performed at a JEOL JXA-840 electron microprobe, equipped with a Priceton Gamma Tech Prism 2000 Si(Li) energy-dispersive system at Massey University. Analytical conditions included a voltage of 15 kV, a beam current of 900 pA and counting times of 100 s. To minimise alkali loss in glass, a defocused beam of 8 to 15 µm diameter was used, depending on microlite density. Given the highly microcrystalline nature of the samples, and to exclude the contamination by microlite composition, data was subsequently filtered and discarded for the following factors: (1) MgO> 5 and <0.5 wt% (2) Al_2O_3>16 wt% (cf. Platz et al. 2007b) and (3) totals <94 wt%. Compositions were normalised to 100, excluding volatiles and averaged for each sample. Spot analyses are reported in Appendix H-3.2.

The Astimex standard minerals albite and olivine were measured regularly to monitor precision and accuracy. Accuracy is well below 5 % for SiO_2, Al_2O_3, Na_2O and MgO and slightly worse for FeO, reaching maximum values of –18%.

5.4 Results

5.4.1 Age model

Constraints for the age model include matching the stratigraphically uppermost tephra unit (T31) with the AD 1945 eruption, the well constrained age of the Burrell eruption for Unit T26, three ^{14}C ages for tephra members T13, T15 and T17 (Voloschina et al., 2020) as well as two previous ages from Moebis (2010) for T2 and T7 (Voloschina et al., 2020). Deposits associated with the Taupo eruption dated at 1718 ± 10 cal BP (Lowe et al., 2013) constrain the lower end of the record. The interpolation method of Turner et al.

(2008) is repeated 1000 times to produce realisations of the ages of the tephras (Fig. 5.5); a piecewise cubic Hermite interpolating polynomial (Fritsch and Carlson 1980) is fitted to the known dates, assuming relative ages to be a function of soil depth. The process of repeating the procedure, re-sampling the known dates randomly from within their error range, yields mean ages and standard deviations for the interpolated ages. Ages for individual tephra members were calculated using the Southern Hemisphere SHCal13 atmospheric curve (Hogg et al. 2013) and are reported in Table 5.2.

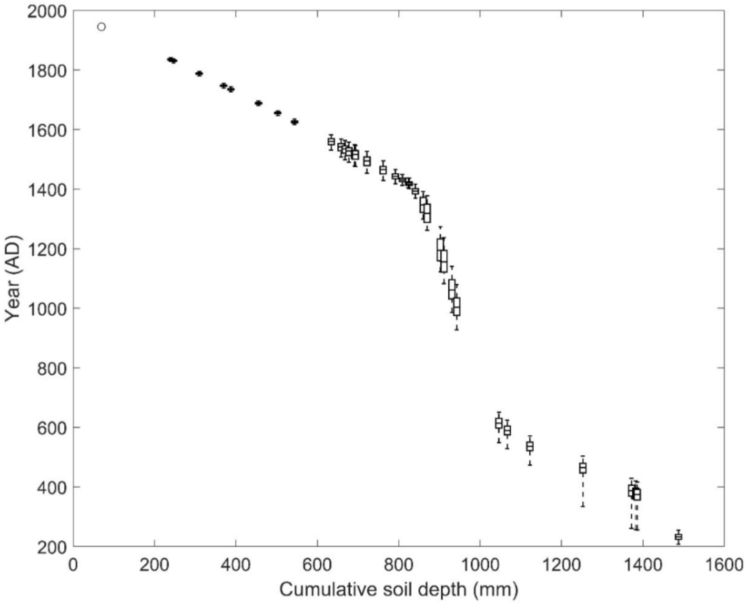

Fig. 5.5: Tephra age interpolation based on cumulative soil depth in mm. Each tephra age is indicated by a boxplot at the profile depth. The 1945 eruption (see text) is indicated by a circle.

5.4.2 Minimum volume estimates for subunits

In order to identify and analyse time-variable patterns in eruption magnitude, minimum tephra volumes were estimated for 75 individual subunits, including the four uncorrelated units. For the uncorrelated units only one data point is available, and we use this information to delimit the major axis of the ellipse, while the extent of minor axes is inferred from ellipses of units with similar dispersal characteristics (Supplementary Table S5.1). No tephra dispersal could be quantified for subunit T28-1.

Calculated tephra volumes span several orders of magnitude. Single bed ash units (SBA) are characterised by deposit volumes ranging between 1.72 × 10^5 m^3 and 1.94 ×10^6 m^3.

The uncorrelated units fall in the lowermost end of the range, showing values of 1.58–2.7 × 10^5 m^3. Lapilli units (L), associated with moderate intensity activity, have larger values for both major and minor axis, compared to single bed ash units and estimated deposit volumes range between 2.51 and 9.32 × 10^6 m^3. Multi-bed ash units (MBA) span cumulative deposit volumes ranging between 2.14–50.71 × 10^6 m^3. Individual subunits yield volumes of 1.32 × 10^5 m^3 to 23.14 × 10^6 m^3, with the most extensively dispersed subunits being approximated by more circular ellipses (e.g., Fig. 5.4e). Cumulative volumes for tephra units are shown in Table 5.2, while volumes for individual subunits are summarised in Supplementary Table S5.1. Based on this, a minimum estimate for the total cumulative volume for the tephra record of Tufa Trig Formation (excluding the 1995–1996 eruptions) yields ~0.208 km^3.

Table 5.2: Tephra units with number of subunits and estimated tephra ages. Cumulative volumes are reported for units based on idealised ellipses and are estimated following Legros (2000)

Tephra unit	Subunits	Mean age in cal BP (±SD)	Volume (m^3)	Notes	Tephra unit	Subunits	Mean age (cal BP)	Volume (m^3)
T31	3	4.8	2.14E+06	AD 1945	T17	6	519 (8)	1.80E+07
T30	2	115 (3)	7.25E+06		T16	2	530 (7)	2.18E+06
^	1	120 (3)	2.46E+05		T15	5	532 (8)	1.41E+07
T29	3	162 (3)	1.18E+07		T14	1	557 (12)	8.55E+05
T28	2	203 (3)	6.91E+06		T13	6	604 (27)	5.07E+07
T27	2	215 (3)	7.88E+06		T12	1	631 (34)	2.23E+05
^	1	262 (3)	1.58E+05		T11	4	754 (42)	1.81E+07
T26	1	295 (3)	5.76E+05	AD 1655 (Burrell)	T10	1	792 (42)	1.94E+06
T25	2	324 (4)	4.00E+06		T9	1	886 (40)	1.90E+05
T24	3	391 (13)	1.10E+07		T8	1	945 (37)	1.43E+06
T23	1	410 (16)	9.85E+05		T7	1	1337 (23)	3.58E+06
^	1	417 (16)	2.24E+05		T6	1	1362 (21)	1.45E+06
T22	2	424 (17)	2.88E+06		T5	1	1416 (21)	2.51E+06
^	1	434 (18)	2.70E+05		T4	3	1494 (38)	3.79E+06
T21	2	436 (18)	3.01E+06		T3	1	1571 (40)	1.72E+05
T20	6	457 (19)	1.33E+07		T2	1	1580 (39)	9.32E+06
T19	5	486 (16)	5.91E+06		T1	1	1584 (38)	2.15E+05
T18	1	507 (11)	3.13E+05					

5.4.3 Frequency-magnitude record

The integration of the age model with tephra volumes for individual subunits allows to quantitatively discuss time-variable patterns in Mt. Ruapehu’s eruption frequency and magnitude over the past 1800 years. Several periods characterised by different eruption behaviour can be identified: (1) The time span following the Taupo eruption from 1718 cal BP to ~1300 cal BP includes tephra members T1 to T7. Associated eruptive activity involves mostly one phase suggesting short-lived low and moderate-intensity eruptions, as indicated by single bed ash units and lapilli units. Deposit volumes range mainly between 1×10^6 and 10^7 m^3 (Fig. 5.6), while the cumulative deposit volume associated with this time span represents ~10% of the total volume erupted over the past 1800 years. (2) No macroscopic discrete tephra units were identified in the time span between ~1300 cal BP and ~950 cal BP. This interval shows particularly low soil accumulation rates of 0.2 to 0.36 mm/y, which agree well with a period associated with soil development in the Whangaehu Valley and the absence of lahar deposits (Lecointre et al., 2004; Hodgson et al., 2007). As it is typical for other areas dominated by frequent andesitic volcanism (Lowe et al. 2010), soil formation in Mt. Ruapehu’s ring plain is dominated by upbuilding processes. Accordingly, the low soil accumulation rates between T7 and T13 can be attributed to the lack of volcanic material that can be transformed into soil and indicate a hiatus in major eruptive activity. (3) The time span between 950 and 610 cal BP includes tephra members T8 to 12 and comprises individual tephra unit volumes ranging from 1×10^5 to $\geq 10^7$ m^3 and leading to a cumulative volume of 2.2×10^7 m^3. Associated deposits involve one phase with the exception of tephra member T11, which is a multi-bed unit with at least 4 subunits. (4) The following 240-year long time span (~610–370 cal BP) includes 43% of the tephra units from the tephra record and comprises members T13 to T24. This time period includes the most complex multi-bed units that were deposited over the past 1800 years, such as T13, T15, T17, T19 and T20, each containing 5 to 6 subunits. Associated tephra members show extensive dispersal around source and are characterised by tephra volumes in the order of magnitude of ~1×10^7 m^3 (Fig. 5.6) for individual tephra units. The cumulative tephra volume erupted over these 240 years represents 60% of the cumulative tephra volume erupted over the last 1800 years. (5) The past ~370 years involve slightly less frequent and less complex eruption sequences, compared to the preceding period. Nine tephra units (17 subunits) are associated with this time span, including the 1945 eruptions but excluding all other historical eruptions. Associated tephra deposits involve predominantly multi-bed ash units with 2-3 subunits. Volumes for individual tephra units range between 1×10^5 and 10^7 m^3, corresponding to a cumulative volume of ~4×10^7 m^3.

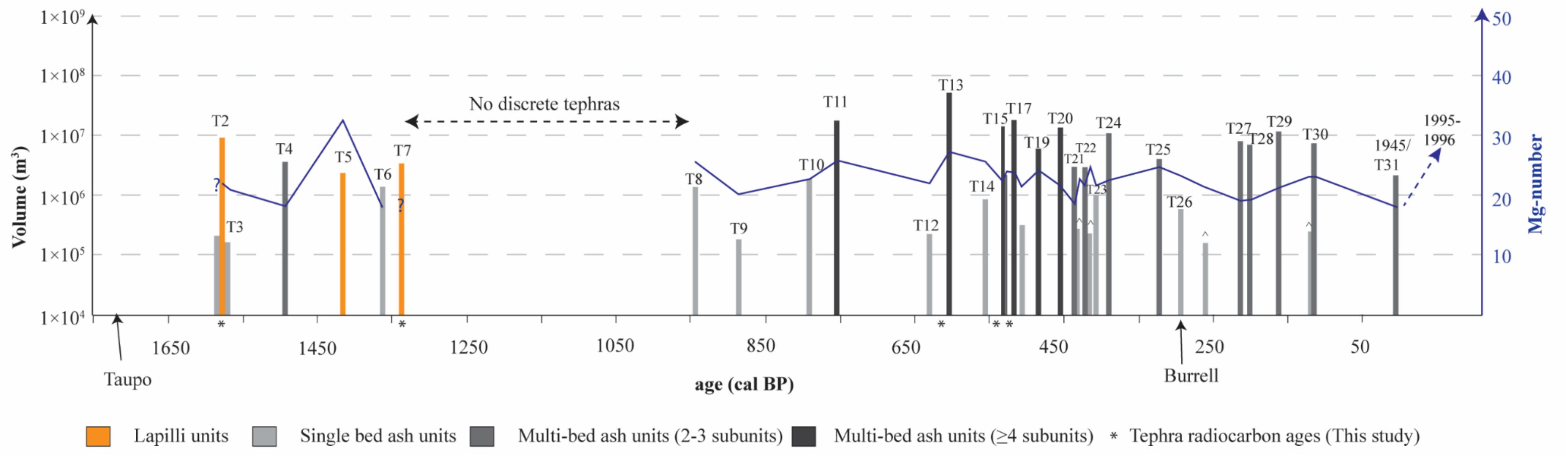

Fig. 5.6: Frequency-magnitude relationships for the Tufa Trig Formation showing tephra unit deposit volumes for individual members. Ages for members are based on the age model. Different lithosedimentological deposit types are marked by different colours with lapilli units in orange, single bed ash units in light grey, multi-bed ash units with 2-3 subunits in medium grey and multi-bed ash units with more than 4 subunits in dark grey. Time-dependent average Mg-number (Mg#) for individual tephra members is calculated as Mg#=100*MgO/(MgO+FeO$_{Tot}$) and is shown in blue. No data is available for members T1 and T7. For comparison, the Mg-number for the historical 1995-1996 eruptions is reported as well, following the dataset of Moebis et al. (2011).

5.4.4 Variation in the geochemical signature

To evaluate whether the changes in eruption frequency and magnitude are coherent with temporal variations in the geochemical signature, seventy-four samples, representative of individual subunits are characterised in terms of their major element groundmass glass composition. For comparison, compositions of four tephra samples from the 1995–1996 eruptions, published in Moebis et al. (2011) are reported as well (Fig. 5.6, Fig. 5.7). Mg-numbers are calculated as Mg#=100*MgO/(MgO+FeO$_{Tot}$) and are averaged for individual members with values ranging between Mg#=18 and Mg#=34 (Fig. 5.6). While there is no simple time-dependent trend nor an evident correlation between eruption magnitude and Mg-number, minor systematic variations can be seen, involving overall decreasing trends between e.g. T13 and T21 or between T25 and T28 (Fig. 5.6). It is worth highlighting, that the time span between 610 and 370 cal BP shows frequent changes in the Mg-number within the overall decreasing trend. Contrastingly, changes are less pronounced in e.g. the most recent 370 years with tephra members T27 to T29 having almost constant Mg-number values. Similarly, tephra members erupted before 610 cal BP do not seem to show any systematic changes in Mg-numbers. Lapilli unit T5 shows a significantly higher Mg-number of 34, compared to the other members (average Mg#=23 ± 6), and appears in a strong contrast to the low Mg-number members T4 and T6 (Mg#=19). A similar marked increase can be observed between the two major historical episodes in 1945 (T31) and 1995–1996, involving Mg#=18 and Mg#=28, respectively.

Major element compositions of groundmass glass cluster into the dacite field following the TAS classification of Le Maitre et al. (2002). Similar to the systematic patterns that can be seen in Mg-numbers, major element compositions of individual members cover the same range as the entire Tufa Trig Formation (Fig. 5.7). Overall, major elements vary between SiO_2=60.5–69.7 wt%, MgO=0.51–4.94 wt%, CaO=2.65–7.25 wt% and K_2O=1.7–4.8 wt%. Variations between subunits within individual members tend to show progressively decreasing SiO_2 and K_2O concomitant with increasing CaO and MgO (e.g., T11, T13, T17 in Fig. 5.7). For some members, the last subunit(s) show a slight increase in SiO_2 (e.g., T13, T17). Generally, the compositional variability within individual subunits is larger than the variability between subunits and/or individual members. It is noteworthy, that syn-sequence variation appears more pronounced in the multi-bed units with 4–6 subunits. Here, the Mg-number generally follows an increasing trend with eruption progression for T11, T13 and T15, while T17, T19 and T20 show relatively constant values. Multi-bed units of the past ~450 years (e.g., T24, T29, T30) show comparably little intra-sequence variation regarding both major oxide compositions as well as regarding Mg-number. In agreement with the trends indicated by the Mg-number in Fig. 5.6, T5 is characterised by compositions that are significantly distinct from the other Tufa Trig members, having an average composition of SiO_2=60.9 wt%, CaO=6.9 wt% and K_2O=1.9 wt% (Fig. 5.7, Appendix H-3.3), compared to an average composition of SiO_2=64.9 wt%, K_2O=2.9 wt% and CaO=4.4 wt% for the remaining members. In a similar manner, glass compositions of T31 differ by higher SiO_2 (66.3 wt%) and K_2O (3.1 wt%) and lower CaO (3.2 wt%) and the 1995–1996 eruptions show slightly lower SiO_2=63 wt% and K_2O (2.5 wt%) and higher CaO (5.4 wt%, Appendix H-3.3).

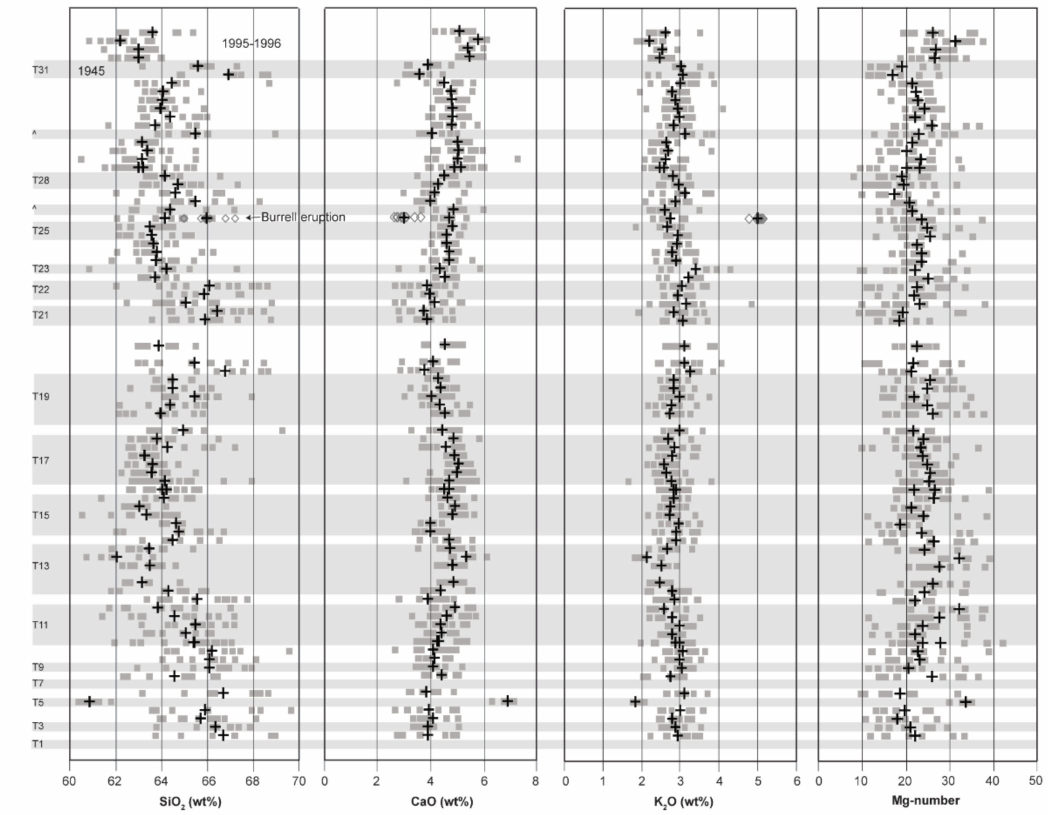

Fig. 5.7: Major element groundmass compositions for individual subunits reported relative to their stratigraphic position. Compositions for SiO_2, CaO and K_2O are normalised to 100, on a volatile-free basis. Grey squares represent individual analyses (cf. Appendix H-3.2), while plus signs show averaged compositions with number of analyses reported in Appendix H-3.3. No data is available for tephra members T1 and T7 and subunits T13-3, T19-1, T20-3, -5 and -6. Data for the historical 1995–1996 eruptions is reported as T32 and follows Moebis et al. (2011).

5.5 Statistical Modelling

In order to understand and forecast future eruption behaviour, in the following statistical models are applied to the previously introduced frequency-magnitude dataset with the aim to model inter-sequence eruption onsets (Fig. 5.8a) and intra-sequence eruption magnitude, such as deposit volume and number of eruption phases (Fig. 5.8b).

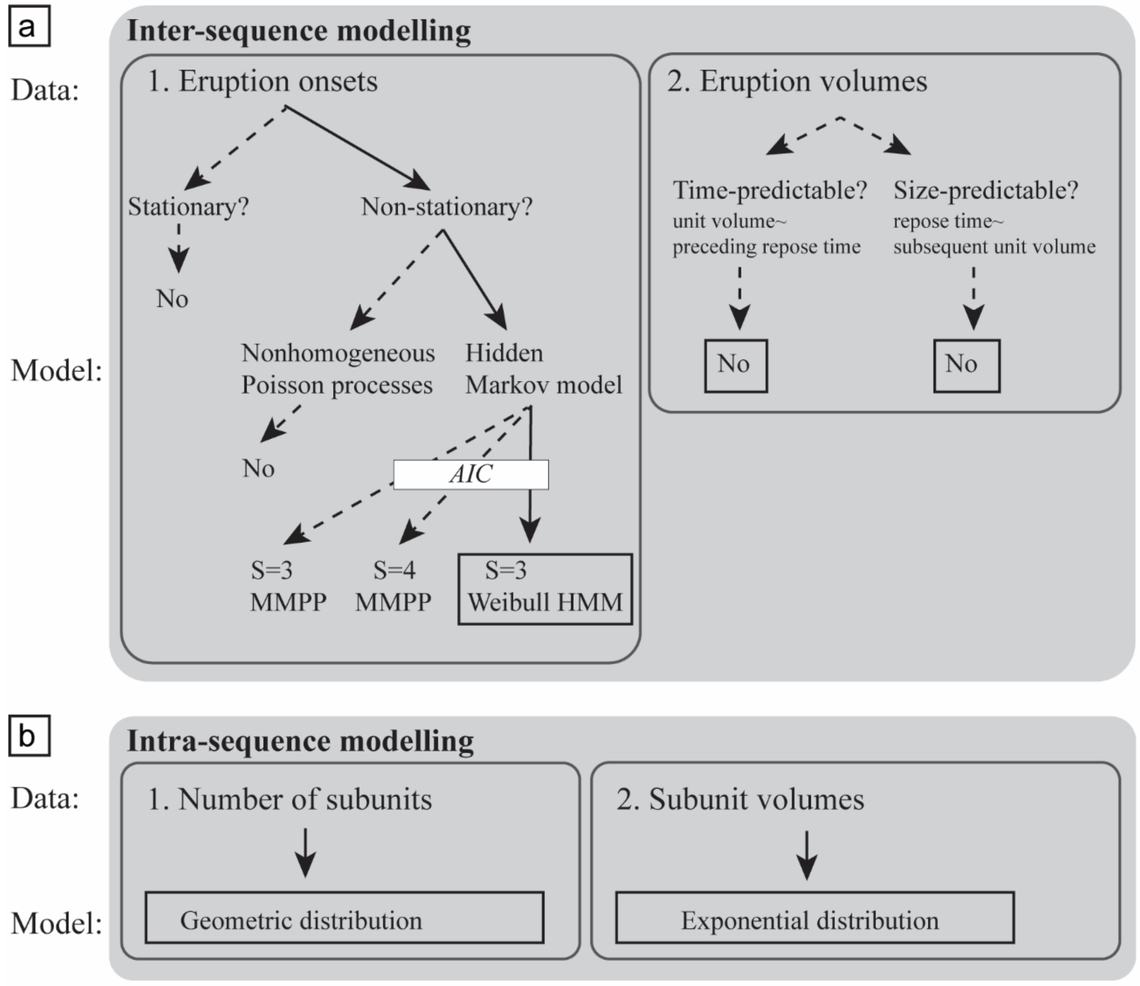

Fig. 5.8: Flow chart illustrating the data sets and models used for the statistical modelling and discussed in the following sections. Solid arrows show the employed process, while dashed lines mark potential alternatives that were discarded. The final applied model is highlighted by a box. a) Inter-sequence modelling is discussed in 5.5.1 Statistical modelling of inter-sequence onsets. Abbreviations are as follows: AIC - Akaike Information Criterion, HMM - Hidden Markov model, MMPP - Markov Modulated Poisson Process with S denoting the number of hidden states. b) Intra-sequence modelling is discussed in 5.5.2 Statistical Modelling of intra-eruption sequences.

5.5.1 Statistical modelling of inter-sequence onsets

A variety of models of differing complexities are available to describe patterns in eruption onsets, the suitability of which depends mostly on whether the data is consistent with the model assumptions. The first distinction we make is between stationary and non-stationary data (cf. Bebbington, 2013; Fig. 5.8a). In the former case, the entirety of the data is considered to be governed by the same (time-independent) process, while for non-stationary data no single process can describe all the data. The cumulative number of eruptions shows systematic variation with time compared to the linear expectation line, which would indicate stationary data (Fig. 5.9a). Therefore, the eruption record is not stationary at the 5% significance level (Fig. 5.9a) and different slopes in the data suggest systematic variation in eruption rates with time, in line with the time-variable patterns seen in Fig. 5.6.

In this case a simple renewal model (Bebbington and Lai, 1996; Turner et al., 2008) cannot be used. This means that we cannot stack (Turner et al., 2008) the age-realisations in order to analyse them. Instead the idea of Bebbington (2020) is adopted and will be applied for all following models, where the same model is fitted (i.e., with different parameter estimates) to each age-realisation and the model outputs are reported as means of individual realisations. Then, forecasts are an aggregate of forecasts from each model realisation, thus propagating the age uncertainty into forecast uncertainty.

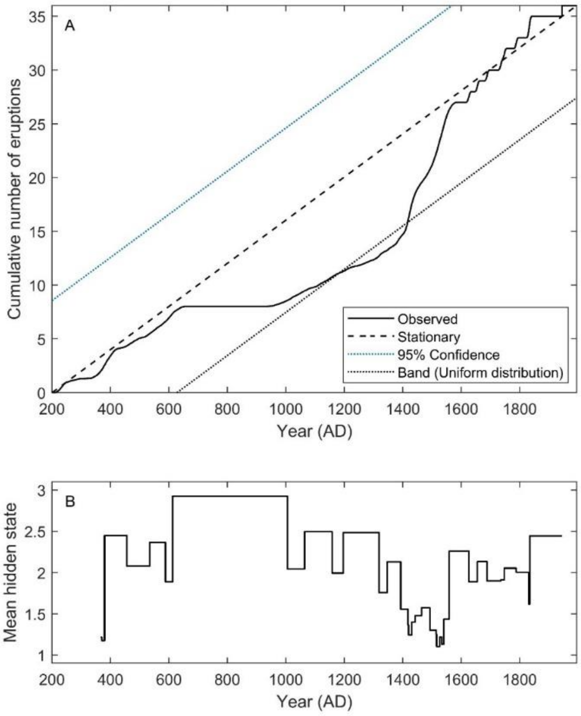

Fig. 5.9: a) The cumulative number of eruptions is shown against eruption ages in AD ages following the age model. Constant slopes indicate stationarity of the data over the duration of an unobserved hidden state. Data is obtained from averaging 1000 age realisations. b) Estimated mean hidden state path of the three-state Weibull hidden Markov model. Data represents averages of 1000 age realisations.

In Fig. 5.9a, the many periods with similar slopes represent approximately constant rate of eruptions, indicating that the system has multiple levels of activity, or `regimes’ (Bebbington, 2007; Carniel 2014). This suggests that the system can be described by a hidden Markov model (HMM; Fig. 5.8a), where activity is stationary over the duration of an unobserved hidden state and is conditional to that particular unobserved hidden state. The simplest possible model considers that the activity in each state is a Poisson process, with only the mean time between eruptions differing by state. This model is the Markov Modulated Poisson Process, or MMPP (Fig. 5.8a; Ryden, 1996). The MMPP model consists of S hidden (unobserved) states. In each state, which is described by the variable s = 1,..,S, with S being the number of states, events occur in a Poisson process of rate λ_s. We will use the renewal process variant of Bebbington (2007), where the hidden state may only change immediately after each eruption, as this best represents the changes in regime caused by eruptions. In the following, a_{ij} denotes the probability that the hidden state changes to j given that it was in state i prior to the eruption. Transition probabilities between different states are then summarised in the Markov transition matrix $A = (a_{ij})$.

Given the ambiguity in the number of regimes that can be seen in Fig. 5.9a, both three- and four-hidden state models were fit to the data, using the method outlined by Bebbington (2007). Model identifiability is established by ordering states from smallest to largest average interevent time in each realization, thus classifying states from high to low rate, based on their eruption frequency. The relative quality of a statistical model to fit a dataset can be assessed through the use of the Akaike Information Criterion (AIC; Fig. 5.8a; Akaike, 1977), which provides a tool to compare the quality of different models:

$$AIC = 2\log L - 2k \tag{5.1}$$

where logL is the loglikelihood, which measures the “goodness-of fit” of the model, and k is the number of parameters in the model. In the here discussed case the model parameters are the number of hidden states. Relatively better models avoid both under- and overfitting of the data and accordingly, would have greater likelihood while the number of model parameters is small. The AIC compensates for the better fit achieved by a larger first term by the second (penalty) term in Eq. 5.1. I.e., in a scenario where two models fit a dataset equally well and show the same loglikelihood, the model with a higher number of parameters and accordingly a higher second term would result in a lower AIC and would thus be relatively worse. In line with this, higher AICs indicate better models, with a difference of 2 between the tested models being considered significant. In previous similar studies, the AIC has been shown to be a reliable tool to estimate the model size, and accordingly the number of hidden states, that fits the data better (Bebbington, 2007). Three models are compared using the AIC (Fig. 5.8a): (1) A three-hidden state MMPP model, (2) a four-hidden state MMPP model and (3) a Weibull HMM with three hidden states. The latter is a special case of the more complex HMM model described in Bebbington (2007), which uses the Weibull interevent distribution (Bebbington and Lai, 1996) in place of the exponential distribution of the MMPP. Comparing (1) with (2) leads to inconclusive results, with 57% of realizations having a better AIC for the three-hidden state model. The average difference in AIC is 0.46, compared to the critical level of 2. On the contrary, the comparison between (1) and (3) increases the AIC by an average of 9.8, with 93% of realizations being better fit by the Weibull HMM. In line with this, the

Weibull HMM will be used in the following to characterise our dataset and the underlying hidden states. In the Weibull HMM, with S = 3, the interevent time t in State s is a Weibull random variate with density

$$f(t) = \alpha_s \beta_s^{\alpha} t^{\alpha-1} \exp\left(-\beta_s^{\alpha} t^{\alpha}\right). \tag{5.2}$$

Transition probabilities and Weibull parameters are estimated using the Expectation-Maximisation (EM) algorithm (Bebbington 2007) as

$$\mathrm{A} = \begin{pmatrix} 0.600 & 0.218 & 0.182 \\ 0.234 & 0.483 & 0.283 \\ 0.126 & 0.766 & 0.108 \end{pmatrix}. \tag{5.3}$$

The transition matrix A indicates that the state with higher average numbers of eruptions (e.g., the high rate and the medium rate state) are more persistent and are more likely to not change state. The low rate state, on the other hand, prefers to transition to the medium rate state. The Weibull parameters $\alpha = \begin{pmatrix} 5.19 & 2.95 & 47.8 \end{pmatrix}$ and $\beta = \begin{pmatrix} 0.098 & 0.022 & 0.008 \end{pmatrix}$ yield an average of (0.107 0.025 0.008) eruptions per year for the high, medium and low rate states, respectively. These regimes mark the time periods as discussed in the previous section with the low rate regime comprising the time span between 1300 and 610 cal BP, including the hiatus in eruptive activity between 1300 and 945 cal BP. The medium rate regime applies to the periods between 1718 and 1300 cal BP as well as to the most recent 370 years, while the high rate regime describes the time span between 610 and 370 cal BP.

5.5.2 Statistical Modelling of intra-eruption sequences

5.5.2.1 Number of subunits

As seen in Fig. 5.6, the number of subunits, and therefore the number of associated eruption phases is time-variant. A model that describes the phases within an eruption has been previously suggested for historical data (Bebbington and Jenkins, 2019), and will be investigated for a geological dataset in the following analogous processes. Assuming that the four tephras present at only one location consist of only one subunit, the 35 eruptions have numbers of subunits as given in Table 5.3.

Table 5.3: Number of subunits per eruption

Subunits	1	2	3	4	5	6
Eruptions	16	8	5	1	2	3

These numbers are consistent with a geometric probability distribution P for the number of subunits per eruption N (Fig. 5.8b),

$$P(N=n) = (1-q)q^{n-1} \quad n = 1,2,3,\ldots \tag{5.4}$$

where q describes the probability that a further phase occurs and is estimated using maximum likelihood as q = 0.557. The fit is tested using the Kolmogorov-Smirnov statistic derived by Best and Rayner (2003), which allows to compare an empirical (sample) distribution to an empirical distribution function and allows to validate the difference between the two. In statistical hypothesis tests, the P-value (or probability value) can assume values between 0 and 1 and indicates the probability that, if the model is true, the resulting sample from it is as likely or unlikely as the observed data. Accordingly, a P-value close to 1 provides no evidence to reject the model, whereas a small P-value suggests evidence to reject the null hypothesis. The cumulative distribution fits a geometric distribution with q = 0.557 and a high P-value = 0.876. In case the four single location tephras are omitted from the distribution, the P-value improves to 0.956, with the probability that a further phase occurs being obtained as q = 0.587 through maximum likelihood estimation.

Such a distribution for a 2-state (eruptive stage, eruption end) process is consistent with the Markov chain eruption phase model developed by Bebbington and Jenkins (2019). An extension of the Bebbington and Jenkins (2019) analysis to the complete set of observed eruptions from the GVP catalogue (Bebbington and Jenkins, in preparation) has estimated that approximately 56% of observed eruptions have multiple phases. The here obtained probability of q = 0.557 (0.587) for a further phase to occur matches this value very closely.

5.5.2.2 Volumes

An eruption process is considered to be time-predictable when the unit volume is correlated with the preceding interevent repose duration, while it is considered to be size-predictable if the interevent repose time is correlated with the subsequent unit volume (e.g., Sandri et al. 2005; Marzocchi & Bebbington 2012). We find that the eruption process is neither time- nor size-predictable (Fig. 5.8a; Sandri et al. 2005), as the correlations between the mean inter-eruption time and the previous or subsequent unit volumes are statistically insignificant as indicated by correlation coefficients of $\rho=0.095$ and $\rho=-0.109$. The correlation coefficient ρ can adopt a value between –1 and 1, with –1 denoting a negative correlation and 1 representing a positive correlation, while values close to 0 indicate insignificant correlation. The associated P-values are $P = 0.593$ for a null hypothesis of a non-time-predictable process and $P = 0.541$ assuming a non-size-predictable process, providing no evidence to reject the respective null hypotheses. Hence, we need to investigate the volumes of individual subunits within an eruption sequence. From this point we omit the four tephras for which we have only one location, and therefore much greater uncertainty in the volume estimates. The estimated volumes of the remaining subunits have properties given in Table 5.4.

Table 5.4: Summary statistics of deposit volume (km^3) by subunit number. Pooled data for subunit numbers 4-6 is included in the last row. N marks the number of subunits for the respective class. Note that T28 and T26 are excluded from these statistics.

Subunit number	N	Mean	Standard Deviation
1	29	0.00175	0.00220
2	17	0.00234	0.00123
3	10	0.00334	0.00240
4	*6*	*0.00603*	*0.00843*
5	*5*	*0.00499*	*0.00349*
6	*3*	*0.00496*	*0.00493*
4-6	14	0.00542	0.00593

Overall, the subunit deposit volumes fit an exponential distribution with mean 0.002768 km^3 (Fig. 5.10). To see if there is any pattern in the volumes erupted during a sequence, an analysis of variance is performed that symmetrise the distributions through logarithms. This yields a small P-value of 0.002, allowing us to reject the null hypothesis of equal means for all subunit numbers. Accordingly, it can be concluded that there is a statistically significant difference between subunit volumes and that subunit volumes increase with an increasing number of subunits, i.e. the volume associated with subunit number 1 < volume associated with subunit number 2 < volume associated with subunit 3 etc. Noting that the higher subunit numbers need to be aggregated because of the small sample sizes, the same test of equal means for just subunits 4, 5 and 6 produces a high P-value of 0.945, indicating that there is no significant difference between the volumes associated with these subunits. Hence, we can treat eruptions with ≥ 4 subunits as one class (see the last row in Table 5.4). Repeating the analysis of variance for four classes (subunits 1, 2, 3 and 4–6) produces a similarly small P-value < 0.001, with the average volume increasing with subunit number (Table 5.4). The exponential distribution gives a similarly satisfactory fit (Fig. 5.11) for all four classes (i.e., after grouping subunits 4–6) confirming that subunit volumes increase with eruption progression with volumes for subunits 4, 5 and 6 being statistically equal.

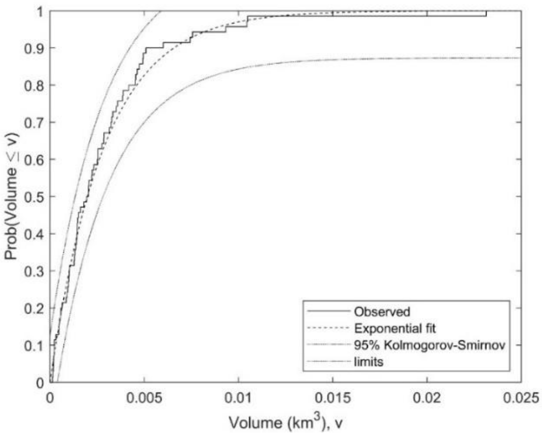

Fig. 5.10: Measured subunit volumes (all subunits), compared with an exponential distribution (mean 0.002768 km^3). The 95% significance in line with the Kolmogorov-Smirnov test is reported for comparison.

While overall unit volumes appear to not be correlated with the preceding repose length (i.e., not size-predictable process), the number of individual subunits appears to be correlated with the length of repose times (Fig. 5.12). An overall trend shows that longer inter-sequence repose periods are associated with fewer subunits, while eruptions with higher subunit numbers are associated with shorter repose periods of 20–40 years (Fig. 5.12). This agrees very well with tephrostratigraphic observations where the most complex tephra members with 4–6 subunits occur within a short time span between 610 and 370 cal BP, while the low rate regime between 1718 and ~1300 cal BP is characterised by long repose times and eruptions that involve mainly one eruption phase.

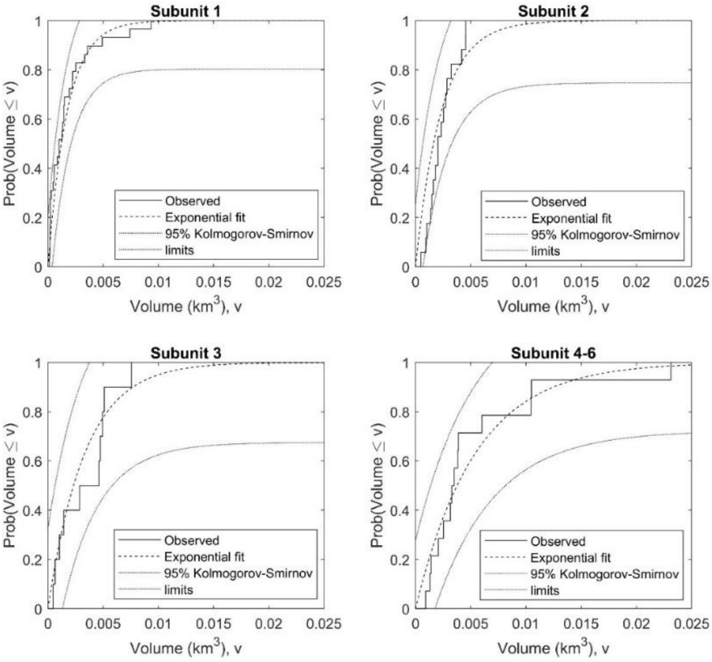

Fig. 5.11: Exponential volume distributions grouped according to their respective subunit number. Following the Kolmogorov-Smirnov test, the 95% significance limit is reported as well. Note that subunits 4-6 are grouped in inset d.

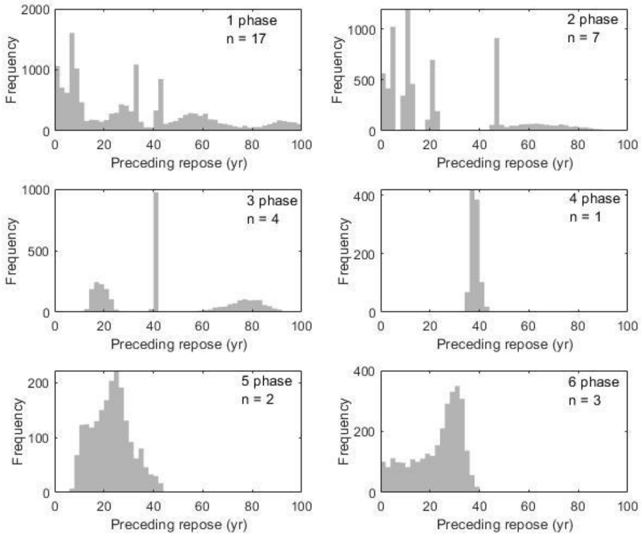

Fig. 5.12: Frequency distributions of the inter-sequence repose lengths preceding each eruption are shown for different number of phases. "n" represents the number of eruptions with that specific number of subunits.

5.6 Discussion

5.6.1 Insights into long-term variation in Mt. Ruapehu's eruption behaviour

Based on the previously introduced datasets, the 1800-year tephra record of Mt. Ruapehu shows consistent time-variable eruption behaviour, which can be described by four periods associated with three different regimes: (1) A medium rate regime between 1718 and 1300 cal BP with an average eruption frequency of one eruption every ~40 years and involves short-lived low-intensity and moderate explosive eruptions. (2) A low rate regime between 1300 and 610 cal BP, which also includes a break in eruptive activity between 1300 and 945 cal BP and has an average eruption recurrence rate of one eruption every 125 years. This period comprises mostly short-lived low-intensity eruptions. (3) A high rate regime between 610 and 370 cal BP shows decadal eruptions and includes the largest multi-phase eruptions of the past 1800 years. (4) The most recent regime (<370 years) has a medium eruption rate of one eruption every 40 years and involves mostly multi-phase eruptions with 2–3 phases.

The hidden states identified by the statistical analysis correspond to time periods that are characterised by similar eruption behaviour in terms of eruption frequency, magnitude and style, suggesting similar underlying controlling factors. In the following, we will use the previously introduced frequency-magnitude record and its combination with tephrostratigraphic and geochemical data to discuss possible physico-chemical factors that account for changes in magma extrusion rates, the magmatic system and the observed time-variant frequency-magnitude behaviour.

Mt. Ruapehu is located in a graben structure at the southernmost end of the Taupo rift system where local average extension rates are ~2.3 ± 1.2 mm/y (Villamor et al., 2006b). Rift extension is accommodated mainly by tectonic activity with subdominant dike intrusion (Gómez-Vasconcelos et al., 2017), and is considered to involve periods of accelerated fault activity in the southern extension (Villamor et al., 2007). Mt. Ruapehu's ring plain hosts several major fault lines (e.g. Rangipo Fault, Wahianoa Fault, Karioi Fault, Raurimu Fault, Villamor et al., 2006a) and in the past, periods of enhanced volcanic activity both for Mt. Ruapehu (Bullot Formation, Villamor et al., 2007; Pardo et al., 2011) and for Mt. Tongariro (Mangamate Formation, Nairn et al., 1998; Heinrich et al., 2020) have been correlated to periods with increased fault slip-rates (Gómez-Vasconcelos et al., 2016).

Based on this, a ~200-year long period of enhanced tectonic activity associated with increased rifting and enhanced dike intrusion into the shallow crustal system could account for the observed increase in eruption frequency and magnitude between 610 and 370 cal BP. This is particularly interesting, considering that the high rate regime follows a ~300-year long absence of eruptive activity between 1300 and 945 cal BP. In line with extension being mostly accommodated by activity in the normal faults that limit the Ruapehu-Tongariro grabens, major tectonic activity could be expected to be associated with the high rate period and should be preserved in contemporaneous deposit sequences (cf. Gómez-Vasconcelos et al., 2017). While evidences for tectonic activity <1718 cal BP can be found in different sectors of the ring plain, at the current stage, the stratigraphic relationships between tectonic and volcanic activity during the past 2000 years are yet poorly characterised.

At the same time, long-term variability in eruption frequency and magnitude at other volcanic systems has been seen to be associated with long-term changes in the magmatic system, such as periodic influx of deeper magma (Óladóttir et al., 2008; Ponomareva et al., 2015). A comparison of the time-variant patterns in eruption frequency, magnitude and geochemical compositions shows parallels with patterns seen at the 130 km-westward Mt. Taranaki (Turner et al., 2011; Damaschke et al., 2017). Here, variations in eruption rates and style are related to ~1500-year cycles in magma supply with each period being fed by a single, compositionally distinct magma batch (Turner et al., 2011). A slightly more complex scenario was inferred for Mt. Ngauruhoe: Here, long-term patterns in isotope and geochemical signature identify periodical recharge of the magmatic system by more mafic magma batches (Hobden et al., 2002). However, no simple relation through i.e., assimilation and/or fractional crystallisation (AFC) could be established between individual eruptions, suggesting that individual eruptions were fed by short-lived small-volume magma batches (Hobden et al., 1999; Hobden et al., 2002). Similar conclusions were obtained for the magmatic system of Mt. Ruapehu based on studies on lava flows and historical eruptions (Nakagawa et al., 2002; Price et al., 2005; Price et al., 2012) and would be consistent with the frequent systematic changes in Mg# over short timescales as observed during the high rate regime (Fig. 5.6, Fig. 5.7). In line with the previous chapter, the limited variability in glass compositions for the past 1800 years (cf. Fig. 4.15) combined with systematic changes in the Mg-number suggest a complex, multi-level magmatic system that involves periodical deep recharges with less evolved magma (Gamble et al., 1999; Price et al., 2005; Price et al., 2012). Accordingly, we suggest that the period of frequent and voluminous eruptive activity between 610 and 370 cal BP can be related to an increase in magma influx from depth, likely associated with an interval of enhanced rifting.

5.6.2 Changes in eruptive regime

Interestingly, it seems that the different regimes as indicated by the cumulative eruption frequency in Fig. 5.9a are slightly offset compared to patterns in eruption magnitude and frequency (Fig. 5.13). Similarly, an increase in Mg-number appears to herald the change to a different eruption regime (e.g., 1416, 754 and 417 cal BP in Fig. 5.6). The marked increase in Mg-number of the 1995–1996 eruptions compared to the precedent 1945 eruption highlights that there is a possibility that these eruptions might have concluded with a switch in regime. At present we appear to be most likely in the medium rate regime, and from Eq. 5.3 a transition to the higher or lower rate states is roughly equally likely. A transition to a more active period with major eruptions occurring at an average rate of one per decade, would have significant impacts on New Zealand’s economy, affecting major branches such as tourism, agriculture and energy generation (Nairn et al., 1996; Johnston et al., 2000) and directly putting the health of humans and livestock at risk (Cronin et al., 1998; 2003).

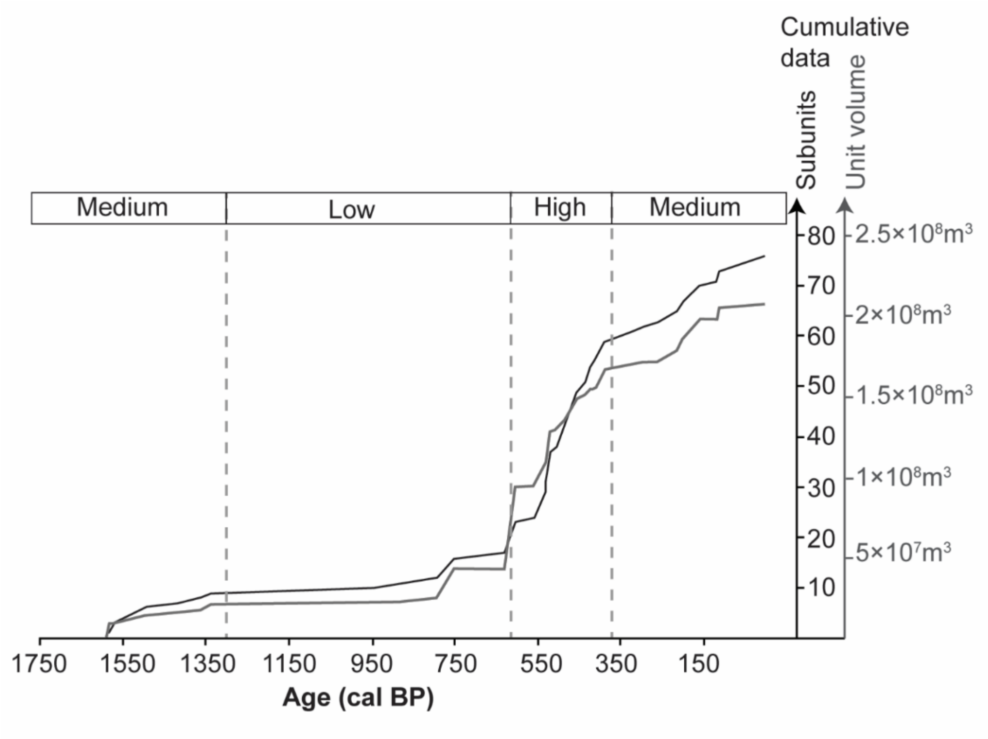

Fig. 5.13: Overview over time-variable changes in cumulative frequency and magnitude data. Ages are reported in cal BP following the previously introduced age model. The number of subunits is shown in black and deposit volumes for individual tephra units are represented by the grey curve. For comparison, the extent of the regimes as identified by previous statistical analysis is reported as well.

5.6.3 Implications for eruption forecast

The presented statistical models show that existing multi-phase models can be successfully applied to model eruption onsets and volumes for geological datasets. One interesting aspect is that the 1995–1996 eruptions of Mt. Ruapehu do not form a discrete tephra unit in the geological record yet. We can use the model and the data up to and including the 1945 eruption to see whether forecasts on the onset date are consistent with the actual onset date of the 1995–1996 eruptions. To do this, an ensemble forecast is made by simulating each of the 1000 realisations 50 times to the next event. This involves simulating if the hidden state changed from the one that, in that realisation, produced the 1945 eruption, and then simulating the appropriate Weibull random variate from the simulated state. The results are shown in Fig. 5.14 where the 1995–1996 eruptions occur at the 65th percentile of the simulated distribution, showing that their onset date is consistent with the (geological) model. Finally, assuming that the 1995–1996 eruptions are a further data point, the model can be refitted and re-simulated to estimate the distribution of time to the next such event, bearing in mind that we are now 25 years on and no commensurate (VEI 3+) eruption was observed since. The result is shown in Fig. 5.15, with a median forecast date of AD 2079. This forecast contrasts starkly with the median estimate obtained via expert elicitation (Bebbington et al., 2018) who estimated a VEI 3 eruption at AD 2031. However, a median forecast date of AD 2079 is close to the estimated median forecast date of AD 2068 for a VEI 4 eruption (Bebbington et al., 2018).

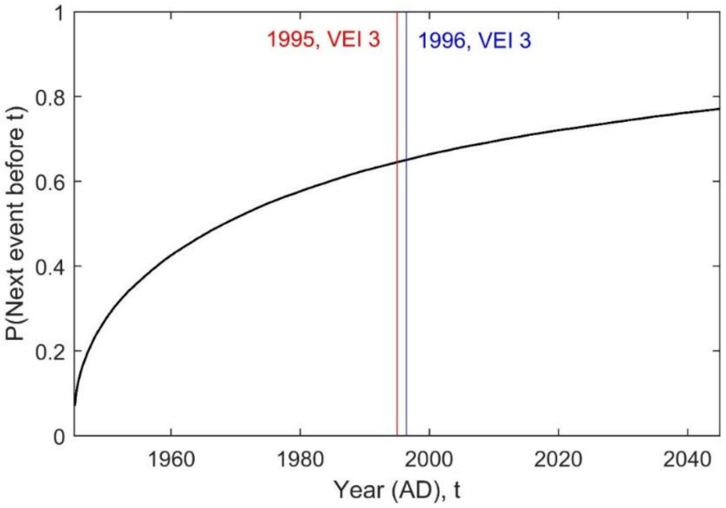

Fig. 5.14: Probability forecast of eruption onset time of the next commensurate (VEI 3+) event, starting from 1945. Based on a dataset that includes the tephra record of the Tufa Trig Formation up to and including the 1945 eruptions. Red and blue lines mark the onset date of the 1995–1996 eruptions that were classified as VEI 3.

With regards to modelling of intra-sequence progression, the applied models highlight a relationship between subunit volume and eruption progression, which is a key information for future eruption crises as it indicates that the most voluminous phase appears later in a multi-phase progression. For stakeholders and hazard management plans this implies relatively more time for potential evacuation decisions following eruption onset. On the contrary, with the existing models, no information can be obtained about the remaining volume of an ongoing phase. At this stage, this implies that the magnitude (including volume) of the upcoming phase cannot be forecasted.

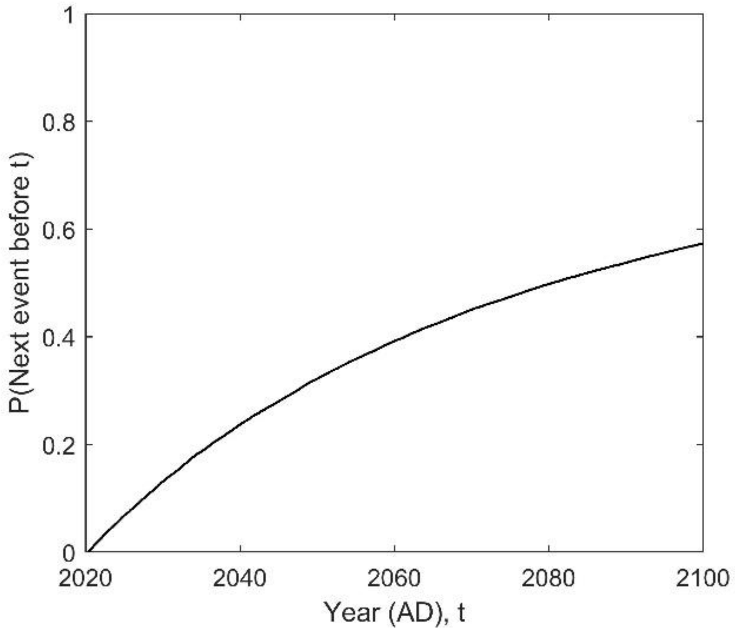

Fig. 5.15: Temporal forecast for the eruption onset of the next commensurate (VEI 3+) event, considering that no commensurate event was observed prior to AD 2020. The forecast is based on a dataset that includes the tephra record of the Tufa Trig Formation and the 1995–1996 eruptions.

5.7 Conclusions

An increasing number of studies targets the statistical modelling of eruptions with the final aim of creating eruption forecast models (Turner et al., 2008; Marzocchi & Bebbington, 2012; Damaschke et al., 2017a). Mt. Ruapehu is part of the Tongariro National Park, New Zealand, which is a popular tourist destination all year around and is surrounded by important infrastructural and agricultural entities. The recent major eruptions in 1995–1996 have highlighted the need for eruption forecast models that account for the possibility of a multi-phase character and that can constrain and forecast eruption progression.

The present study shows how the geological record can be used to create a long-term frequency-magnitude record that provides insights into time-variant pattern in eruption behaviour and highlights the influence of enhanced rifting activity and increased deep magma recharge on eruptive activity. The time period following the Taupo eruption (1718–1300 cal BP) can be classified as a medium rate regime, with an eruption every 40 years. The following regime (1300–610 cal BP) has a low average eruption rate (1/125 years) and comprises a hiatus in eruptive activity between 1300 and 945 cal BP. The time period between ~610 to ~370 cal BP is characterised by an increased eruption frequency of one eruption every ~10 years and involves the largest multi-phase eruptions of the past 1800 years, erupting 60% of the total cumulative deposit volume of the Tufa Trig Formation within only ~240 years. Short-term changes in Mg-number suggest an enhanced frequency of deep magma recharge in the nested shallow system. Finally, ~370 years ago, the state has changed to a medium rate again, which, most likely, also depicts the current state. However, given the distinct geochemical signature of the 1995–1996 eruption, there is a possibility that the next major (VEI 3+) eruption might indicate the onset of a new regime.

The here presented frequency-magnitude record is used to adapt statistical models that are based on historical datasets to geological datasets and shows that existing multi-phase models can be successfully applied to model eruption onsets and volumes from geologically preserved eruptions. However, given that the majority of statistical models crucially depends on observation frequency and quality, more studies at other volcanoes are needed to test the presented models. This is particularly evident if the geological record is compared with the historical record, which contains mostly small-volume short-lived phreatic to phreatomagmatic eruptions (Scott, 2013). Accordingly, the here presented tephra record is very likely biased towards eruption magnitudes of VEI ≥ 3 and deposit volumes of $\geq 1 \times 10^5$ m^3, implying that the true eruption frequency might be actually higher.

The multi-parameter dataset introduced in this work represents a framework for ongoing and future studies at Mt. Ruapehu and provides an important case study for eruption forecast modelling from geological records at other analogous volcanoes. Similar studies contribute not only to the understanding of the complexities associated with time-variant changes in eruption behaviour at frequently active, long-lived volcanoes but also constitute the basic framework for eruption and hazard models and decision-making during future eruption crises.

References

Akaike, H. (1977). On entropy maximization principle. In P. R. Krishnaiah (Ed.), *Applications of Statistics* (pp. 27-41).

Barsotti, S., Neri, A., Bertagnini, A., Cioni, R., Mulas, M., & Mundula, F. (2015). Dynamics and tephra dispersal of Violent Strombolian eruptions at Vesuvius: insights from field data, wind reconstruction and numerical simulation of the 1906 event. *Bulletin of Volcanology, 77*(7), 58. doi:https://doi.org/10.1007/s00445-015-0939-6

Bebbington, M. S. (2020). Temporal-volume probabilistic hazard model for a supervolcano: Taupo, New Zealand. *Earth and Planetary Science Letters, 536*, 116141. doi:https://doi.org/10.1016/j.epsl.2020.116141

Bebbington, M. (2014). Long-term forecasting of volcanic explosivity. *Geophysical Journal International, 197*(3), 1500-1515. doi:https://doi.org/10.1093/gji/ggu078

Bebbington, M. S. (2013). Models for temporal volcanic hazard. *Statistics in volcanology, 1*(1), 1. doi:http://dx.doi.org/10.5038/2163-338X.1.1

Bebbington, M. S. (2007). Identifying volcanic regimes using hidden Markov models. *Geophysical Journal International, 171*(2), 921-942. doi:https://doi.org/10.1111/j.1365-246X.2007.03559.x

Bebbington, M. S., & Jenkins, S. F. (2019). Intra-eruption forecasting. *Bulletin of Volcanology, 81*(6), 34. doi:https://doi.org/10.1007/s00445-019-1294-9

Bebbington, M. S., Stirling, M. W., Cronin, S., Wang, T., & Jolly, G. (2018). National-level long-term eruption forecasts by expert elicitation. *Bulletin of Volcanology, 80*(6), 56. doi:https://doi.org/10.1007/s00445-018-1230-4

Bebbington, M. S., & Marzocchi, W. (2011). Stochastic models for earthquake triggering of volcanic eruptions. *Journal of Geophysical Research: Solid Earth, 116*(B5). doi:10.1029/2010jb008114

Bebbington, M. S., & Lai, C. D. (1996). On nonhomogeneous models for volcanic eruptions. *Mathematical Geology, 28*(5), 585-600. doi:https://doi.org/10.1007/BF02066102

Beck, A. (1950). Volcanic activity at Mt. Ruapehu from August to December, 1945. *New Zealand Journal of Science and Technology, 31*, 1-13.

Best, D., & Rayner, J. (2003). Tests of fit for the geometric distribution. *Communications in Statistics-Simulation and Computation, 32*(4), 1065-1078. doi:ttps://doi.org/10.1081/SAC-120023878

Bonadonna, C., & Costa, A. (2013). Plume height, volume, and classification of explosive volcanic eruptions based on the Weibull function. *Bulletin of Volcanology, 75*(8), 742. doi:https://doi.org/10.1007/s00445-013-0742-1

Bonadonna, C., & Houghton, B. F. (2005). Total grain-size distribution and volume of tephra-fall deposits. *Bulletin of Volcanology, 67*(5), 441-456. doi:https://doi.org/10.1007/s00445-004-0386-2

Carniel, R. (2014). Characterization of volcanic regimes and identification of significant transitions using geophysical data: a review. *Bulletin of Volcanology, 76*(8), 848. doi:https://doi.org/10.1007/s00445-014-0848-0

Cioni, R., Bertagnini, A., Santacroce, R., & Andronico, D. (2008). Explosive activity and eruption scenarios at Somma-Vesuvius (Italy): Towards a new classification scheme. *Journal of Volcanology and Geothermal Research, 178*(3), 331-346. doi:https://doi.org/10.1016/j.jvolgeores.2008.04.024

Connor, C., Bebbington, M., & Marzocchi, W. (2015). Probabilistic volcanic hazard assessment *The Encyclopedia of Volcanoes (Second Edition)* (pp. 897-910). Amsterdam: Academic Press.

Cronin, S. J., Neall, V. E., Lecointre, J. A., Hedley, M. J., & Loganathan, P. (2003). Environmental hazards of fluoride in volcanic ash: a case study from Ruapehu volcano, New Zealand. *Journal of Volcanology and Geothermal Research, 121*, 271-291. doi:https://doi.org/10.1016/S0377-0273(02)00465-1

Cronin, S. J., Bebbington, M., & Lai, C. (2001). A probabilistic assessment of eruption recurrence on Taveuni volcano, Fiji. *Bulletin of Volcanology, 63*(4), 274-288. doi:https://doi.org/10.1007/s004450100144

Cronin, S. J., Hedley, M. J., Neall, V. E., & Smith, R. G. (1998). Agronomic impact of tephra fallout from the 1995 and 1996 Ruapehu Volcano eruptions, New Zealand. *Environmental Geology, 34*(1), 21-30.

Damaschke, M., Cronin, S. J., & Bebbington, M. S. (2017a). A volcanic event forecasting model for multiple tephra records, demonstrated on Mt. Taranaki, New Zealand. *Bulletin of Volcanology, 80*(1), 9. doi:https://doi.org/10.1007/s00445-017-1184-y

Damaschke, M., Cronin, S. J., Holt, K. A., Bebbington, M. S., & Hogg, A. G. (2017b). A 30,000 yr high-precision eruption history for the andesitic Mt. Taranaki, North Island, New Zealand. *Quaternary Research, 87*(1), 1-23. doi:https://doi.org/10.1017/qua.2016.11

Donoghue, S. L., Neall, V. E., Palmer, A. S., & Stewart, R. B. (1997). The volcanic history of Ruapehu during the past 2 millenia based on the record of Tufa Trig tephras. *Bulletin of Volcanology, 59*, 136-146. doi:https://doi.org/10.1007/s004450050181

Donoghue, S. L., Neall, V. E., & Palmer, A. S. (1995). Stratigraphy and chronology of late Quaternary andesitic tephra deposits, Tongariro Volcanic Centre, New Zealand. *Journal of the Royal Society of New Zealand, 25*(2), 115-206. doi:https://doi.org/10.1080/03014223.1995.9517487

Fierstein, J., & Nathenson, M. (1992). Another look at the calculation of fallout tephra volumes. *Bulletin of Volcanology, 54*(2), 156-167. doi:https://doi.org/10.1007/bf00278005

Fritsch, F. N., & Carlson, R. E. (1980). Monotone Piecewise Cubic Interpolation. *SIAM Journal on Numerical Analysis, 17*(2), 238-246. doi:https://doi.org/10.1137/0717021

Gamble, J. A., Wood, C. P., Price, R. C., Smith, I. E. M., Stewart, R. B., & Waight, T. (1999). A fifty year perspective of magmatic evolution on Ruapehu Volcano, New Zealand: verification of open system behaviour in an arc volcano. *Earth and Planetary Science Letters, 170*, 301-314. doi:https://doi.org/10.1016/S0012-821X(99)00106-5

Garcia-Aristizabal, A., Marzocchi, W., & Fujita, E. (2012). A Brownian model for recurrent volcanic eruptions: an application to Miyakejima volcano (Japan). *Bulletin of Volcanology, 74*(2), 545-558. doi:https://doi.org/10.1007/s00445-011-0542-4

Gómez-Vasconcelos, M. G., Villamor, P., Cronin, S., Procter, J., Palmer, A., Townsend, D., & Leonard, G. (2017). Crustal extension in the Tongariro graben, New Zealand: Insights into volcano-tectonic interactions and active deformation in a young continental rift. *GSA Bulletin, 129*(9-10), 1085-1099. doi:https://doi.org/10.1130/B31657.1

Gómez-Vasconcelos, M. G., Villamor, P., Cronin, S. J., Procter, J., Kereszturi, G., Palmer, A., Townsend, D., Leonard, G., Berryman, K., & Ashraf, S. (2016). Earthquake history at the eastern boundary of the South Taupo Volcanic Zone, New Zealand. *New Zealand Journal of Geology and Geophysics, 59*(4), 522-543. doi:10.1080/00288306.2016.1195757

Hackett, W. R., & Houghton, B. F. (1989). A facies model for a quaternary andesitic composite volcano: Ruapehu, New Zealand. *Bulletin of Volcanology, 51*(1), 51-68. doi:https://doi.org/10.1007/bf01086761

Heinrich, M., Cronin, S. J., & Pardo, N. (2020). Understanding multi-vent Plinian eruptions at Mt. Tongariro Volcanic Complex, New Zealand. *Bulletin of Volcanology, 82*(3), 30. doi:https://doi.org/10.1007/s00445-020-1369-7

Hobden, B. J., Houghton, B. F., & Nairn, I. A. (2002). Growth of a young, frequently active composite cone: Ngauruhoe volcano, New Zealand. *Bulletin of Volcanology, 64*(6), 392-409. doi:https://doi.org/10.1007/s00445-002-0216-3

Hobden, B. J., Houghton, B. F., Davidson, J. P., & Weaver, S. D. (1999). Small and short-lived magma batches at composite volcanoes: time windows at Tongariro volcano, New Zealand. *Journal of the Geological Society, 156*(5), 865-868. doi:https://doi.org/10.1144/gsjgs.156.5.0865

Hodgson, K. A., Lecointre, J. A., & Neall, V. E. (2007). Onetapu Formation: The last 2000 yr of laharic activity at Ruapehu volcano, New Zealand. *New Zealand Journal of Geology and Geophysics, 50*(2), 81-99. doi:https://doi.org/10.1080/00288300709509823

Hogg, A. G., Hua, Q., Blackwell, P. G., Niu, M., Buck, C. E., Guilderson, T. P., Heaton, T. J., Palmer, J. G., Reimer, P. J., & Reimer, R. W. (2013). SHCal13 Southern Hemisphere calibration, 0–50,000 years cal BP. *Radiocarbon, 55*(4), 1889-1903. doi:https://doi.org/10.2458/azu_js_rc.55.16783

Jaquet, O., Lantuéjoul, C., & Goto, J. (2012). Probabilistic estimation of long-term volcanic hazard with assimilation of geophysics and tectonic data. *Journal of Volcanology and Geothermal Research, 235-236*, 29-36. doi:https://doi.org/10.1016/j.jvolgeores.2012.05.003

Jenkins, S. F., Magill, C. R., & McAneney, K. J. (2007). Multi-stage volcanic events: A statistical investigation. *Journal of Volcanology and Geothermal Research, 161*(4), 275-288. doi:https://doi.org/10.1016/j.jvolgeores.2006.12.005

Johnston, D. M., Houghton, B. F., Neall, V. E., Ronan, K. R., & Paton, D. (2000). Impacts of the 1945 and 1995-1996 Ruapehu eruptions, New Zealand: An example of increasing societal vulnerability. *Geological Society of America Bulletin, 112*(5), 720-726. doi:https://doi.org/10.1130/0016-7606(2000)112<720:IOTARE>2.0.CO;2

Johnston, D. M. (1997a). *A chronology of the 1945 eruption of Ruapehu Volcano, New Zealand*: Institute of Geological & Nuclear Sciences.

Johnston, D. M. (1997b). *Physical and social impacts of past and future volcanic eruptions in New Zealand.* (Doctor of Philosophy), Massey University, Palmerston North.

Johnston, D. M., & Neall, V. E. (1995). *Ruapehu Awakens: the 1945 eruption of Ruapehu*. Palmerston North, New Zealand: Science Centre and Manawatu Museum Scientific Monograph No. 1.

Kawabata, E., Cronin, S. J., Bebbington, M. S., Moufti, M. R. H., El-Masry, N., & Wang, T. (2015). Identifying multiple eruption phases from a compound tephra blanket: an example of the AD1256 Al-Madinah eruption, Saudi Arabia. *Bulletin of Volcanology, 77*(1), 6. doi:https://doi.org/10.1007/s00445-014-0890-y

Le Maitre, R., Streckeisen, A., Zanettin, B., Le Bas, M., Bonin, B., & Bateman, P. (2002). *Igneous rocks: A classification and glossary of Terms*. Cambridge, UK: Cambridge University Press.

Lecointre, J., Hodgson, K., Neall, V., & Cronin, S. (2004). Lahar-Triggering Mechanisms and Hazard at Ruapehu Volcano, New Zealand. *Natural Hazards, 31*(1), 85-109. doi:https://doi.org/10.1023/B:NHAZ.0000020256.16645.eb

Legros, F. (2000). Minimum volume of a tephra fallout deposit estimated from a single isopach. *Journal of Volcanology and Geothermal Research, 96*(1-2), 25-32. doi:https://doi.org/10.1016/S0377-0273(99)00135-3

Lerner, G. A., Cronin, S. J., Bebbington, M. S., & Platz, T. (2019). The characteristics of a multi-episode volcanic regime: the post-AD 960 Maero Eruptive Period of Mt. Taranaki (New Zealand). *Bulletin of Volcanology, 81*(11), 61. doi:https://doi.org/10.1007/s00445-019-1327-4

Lowe, D. J., Blaauw, M., Hogg, A. G., & Newnham, R. M. (2013). Ages of 24 widespread tephras erupted since 30,000 years ago in New Zealand, with re-evaluation of the timing and palaeoclimatic implications of the Lateglacial cool episode recorded at Kaipo bog. *Quaternary Science Reviews, 74*, 170-194. doi:https://doi.org/10.1016/j.quascirev.2012.11.022

Lowe, D. J. (2011). Tephrochronology and its application: A review. *Quaternary Geochronology, 6*(2), 107-153. doi:https://doi.org/10.1016/j.quageo.2010.08.003

Lowe, D. J., & Tonkin, P. J. (2010, 1-6 August 2010). *Unravelling upbuilding pedogenesis in tephra and loess sequences in New Zealand using tephrochronology.* Paper presented at the 19th World Congress of Soil Science, Soil Solutions for a Changing Wold, Brisbane, Australia.

Martin, A. J., Umeda, K., Connor, C. B., Weller, J. N., Zhao, D., & Takahashi, M. (2004). Modeling long-term volcanic hazards through Bayesian inference: An example from the Tohoku volcanic arc, Japan. *Journal of Geophysical Research: Solid Earth, 109*(B10). doi:https://doi.org/10.1029/2004JB003201

Marzocchi, W., & Bebbington, M. S. (2012). Probabilistic eruption forecasting at short and long time scales. *Bulletin of Volcanology*, *74*(8), 1777-1805. doi:https://doi.org/10.1007/s00445-012-0633-x

Marzocchi, W., & Zaccarelli, L. (2006). A quantitative model for the time-size distribution of eruptions. *Journal of Geophysical Research: Solid Earth, 111*(B4). doi:https://doi.org/10.1029/2005JB003709

Moebis, A., Cronin, S. J., Neall, V. E., & Smith, I. E. (2011). Unravelling a complex volcanic history from fine-grained, intricate Holocene ash sequences at the Tongariro Volcanic Centre, New Zealand. *Quaternary International*, *246*(1–2), 352-363. doi:http://dx.doi.org/10.1016/j.quaint.2011.05.035

Nairn, I. A., Kobayashi, T., & Nakagawa, M. (1998). The ~10 ka multiple vent pyroclastic eruption sequence at Tongariro Volcanic Centre, Taupo Volcanic Zone, New Zealand:: Part 1. Eruptive processes during regional extension. *Journal of Volcanology and Geothermal Research, 86*(1–4), 19-44. doi:https://doi.org/10.1016/S0377-0273(98)00085-7

Nairn, I. A., & Group, R. S. (1996). Volcanic eruption at a New Zealand ski resort prompts reevaluation of hazards. *Eos, Transactions American Geophysical Union, 77*(20), 189-191. doi:http://dx.doi.org/10.1029/96EO00129

Nakagawa, M., Wada, K., & Wood, C. P. (2002). Mixed Magmas, Mush Chambers and Eruption Triggers: Evidence from Zoned Clinopyroxene Phenocrysts in Andesitic Scoria from the 1995 Eruptions of Ruapehu Volcano, New Zealand. *Journal of Petrology, 43*(12), 2279-2303. doi:https://doi.org/10.1093/petrology/43.12.2279

Óladóttir, B. A., Sigmarsson, O., Larsen, G., & Devidal, J.-L. (2011). Provenance of basaltic tephra from Vatnajökull subglacial volcanoes, Iceland, as determined by major- and trace-element analyses. *The Holocene, 21*(7), 1037-1048. doi:https://doi.org/10.1177/0959683611400456

Óladóttir, B. A., Sigmarsson, O., Larsen, G., & Thordarson, T. (2008). Katla volcano, Iceland: magma composition, dynamics and eruption frequency as recorded by Holocene tephra layers. *Bulletin of Volcanology, 70*(4), 475-493. doi:https://doi.org/10.1007/s00445-007-0150-5

Oliver, R. (1945). Further activity of Mount Ruapehu, May-July 1945. *New Zealand Journal of Science and Technology, 26*, 24-33.

Pardo, N., Cronin, S., Palmer, A., Procter, J., & Smith, I. (2012). Andesitic Plinian eruptions at Mt. Ruapehu: quantifiying the uppermost limits of eruptive parameters. *Bulletin of Volcanology, 74*, 1161-1185. doi:https://doi.org/10.1007/s00445-012-0588-y

Pardo, N., Cronin, S. J., Palmer, A. S., & Németh, K. (2011). Reconstructing the largest explosive eruptions of Mt. Ruapehu, New Zealand: lithostratigraphic tools to understand subplinian–plinian eruptions at andesitic volcanoes. *Bulletin of Volcanology, 74*(3), 617-640. doi:https://doi.org/10.1007/s00445-011-0555-z

Passarelli, L., Sandri, L., Bonazzi, A., & Marzocchi, W. (2010). Bayesian Hierarchical Time Predictable Model for eruption occurrence: an application to Kilauea Volcano. *Geophysical Journal International, 181*(3), 1525-1538. doi:https://doi.org/10.1111/j.1365-246X.2010.04582.x

Ponomareva, V., Portnyagin, M., Pevzner, M., Blaauw, M., Kyle, P., & Derkachev, A. (2015). Tephra from andesitic Shiveluch volcano, Kamchatka, NW Pacific: chronology of explosive eruptions and geochemical fingerprinting of volcanic glass. *International Journal of Earth Sciences, 104*(5), 1459-1482. doi:https://doi.org/10.1007/s00531-015-1156-4

Price, R. C., Gamble, J. A., Smith, I. E. M., Maas, R., Waight, T., Stewart, R. B., & Woodhead, J. (2012). The Anatomy of an Andesite Volcano: a Time-Stratigraphic Study of Andesite Petrogenesis and Crustal Evolution at Ruapehu Volcano, New Zealand. *Journal of Petrology, 53*(10), 2139-2189. doi:https://doi.org/10.1093/petrology/egs050

Price, R. C., Gamble, J. A., Smith, I. E. M., Stewart, R. B., Eggins, S., & Wright, I. C. (2005). An integrated model for the temporal evolution of andesites and rhyolites and crustal development in New Zealand's North Island. *Journal of Volcanology and Geothermal Research, 140*(1-3), 1-24. doi:https://doi.org/10.1016/j.jvolgeores.2004.07.013

Pyle, D. M. (1989). The thickness, volume and grainsize of tephra fall deposits. *Bulletin of Volcanology, 51*(1), 1-15. doi:https://doi.org/10.1007/bf01086757

Rydén, T. (1996). An EM algorithm for estimation in Markov-modulated Poisson processes. *Computational Statistics & Data Analysis, 21*(4), 431-447. doi:https://doi.org/10.1016/0167-9473(95)00025-9

Sandri, L., Marzocchi, W., & Gasperini, P. (2005). Some insights on the occurrence of recent volcanic eruptions of Mount Etna volcano (Sicily, Italy). *Geophysical Journal International, 163*(3), 1203-1218. doi:https://doi.org/10.1111/j.1365-246X.2005.02757.x

Scott, B. J. (2013). A revised catalogue of Ruapehu volcano eruptive activity: 1830-2012. *GNS Science Report, 2013/45*.

Topping, W. W. (1973). Tephrostratigraphy and chronology of late quaternary eruptives from the Tongariro Volcanic Centre, New Zealand. *New Zealand Journal of Geology and Geophysics, 16*(3), 397-423. doi:https://doi.org/10.1080/00288306.1973.10431368

Torres-Orozco, R., Cronin, S. J., Pardo, N., & Palmer, A. S. (2018). Volcanic hazard scenarios for multiphase andesitic Plinian eruptions from lithostratigraphy: Insights into pyroclastic density current diversity at Mount Taranaki, New Zealand. *GSA Bulletin, 130*(9-10), 1645-1663. doi:https://doi.org/10.1130/B31850.1

Tost, M., & Cronin, S. J. (2015). Linking distal volcaniclastic sedimentation and stratigraphy with the development of Ruapehu volcano, New Zealand. *Bulletin of Volcanology, 77*(11). doi:https://doi.org/10.1007/s00445-015-0977-0

Turner, M. B., Cronin, S. J., Bebbington, M. S., Smith, I. E. M., & Stewart, R. B. (2011). Relating magma composition to eruption variability at andesitic volcanoes: A case study from Mount Taranaki, New Zealand. *GSA Bulletin, 123*(9-10), 2005-2015. doi:https://doi.org/10.1130/b30367.1

Turner, M. B., Cronin, S. J., Bebbington, M. S., & Platz, T. (2008). Developing probabilistic eruption forecasts for dormant volcanoes: a case study from Mt Taranaki, New Zealand. *Bulletin of Volcanology, 70*(4), 507-515. doi:https://doi.org/10.1007/s00445-007-0151-4

Villamor, P., Van Dissen, R., Alloway, B. V., Palmer, A. S., & Litchfield, N. (2007). The Rangipo fault, Taupo rift, New Zealand: An example of temporal slip-rate and single-event displacement variability in a volcanic environment. *GSA Bulletin, 119*(5-6), 529-547. doi:https://doi.org/10.1130/B26000.1

Villamor, P., & Berryman, K. R. (2006a). Evolution of the southern termination of the Taupo Rift, New Zealand. *New Zealand Journal of Geology and Geophysics, 49*(1), 23-37. doi:https://doi.org/10.1080/00288306.2006.9515145

Villamor, P., & Berryman, K. R. (2006b). Late Quaternary geometry and kinematics of faults at the southern termination of the Taupo Volcanic Zone, New Zealand. *New Zealand Journal of Geology and Geophysics, 49*(1), 1-21. doi:https://doi.org/10.1080/00288306.2006.9515144

Voloschina, M., Lube, G., Procter, J., Moebis, A., & Timm, C. (2020). Lithosedimentological and tephrostratigraphical characterisation of small-volume, low-intensity eruptions: The 1800 years Tufa Trig Formation, Mt. Ruapehu (New Zealand). *Journal of Volcanology and Geothermal Research*, 106987. doi:https://doi.org/10.1016/j.jvolgeores.2020.106987

Supplementary material

Supplementary Table S5.1 (continues on next page): Overview of main descriptive characteristics of the ellipses that approximate tephra dispersal and are used for deposit volume calculations. "^" marks uncorrelated tephra units.

	Ellipse characteristics				Deposit volume calculations					
Tephra unit	major axis	minor axis	circularity	Aspect ratio	area (km^2)	thickness (cm)	Legros (km^3)	Legros (m^3)	Deposit type	Age (cal BP)
T31-3	9.4	2.62	0.53	3.59	19.32	2	0.0014	1425742.2		
T31-2	9.4	2.62	0.53	3.59	19.32	0.7	0.0005	499009.8		
T31-1	9.4	2.62	0.53	3.59	19.32	0.3	0.0002	213861.3	MBA	4.8
T30-2	9.72	3.94	0.68	2.47	30.03	2.1	0.0023	2326869.7		
T30-1	14.08	12.06	0.89	1.17	133.34	1	0.0049	4920172.2	MBA	115 (3)
^ 29-30	9.6	2.95	0.57	3.26	22.21	0.3	0.0002	245909.0	SBA	120 (3)
T29-3	14.26	9.15	0.84	1.56	102.45	2	0.0076	7560883.8		
T29-2	13.92	8	0.8	1.74	87.52	1	0.0032	3229377.3		
T29-1	14.24	4.85	0.6	2.93	54.3	0.5	0.001	1001908.8	MBA	162 (3)
T28-2	13.76	8.67	0.83	1.59	93.67	2	0.0069	6912846.0		
T28-1									MBA	203 (3)
T27-2	14.02	11.19	0.88	1.25	123.22	1	0.0045	4546965.6		
T27-1	9.71	2.96	0.57	3.28	22.58	4	0.0033	3332217.6	MBA (L)	215 (3)
^ 26-27	9.75	2.79	0.54	3.5	21.37	0.2	0.0002	157710.6	SBA	262 (3)
T26	10.27	3.87	0.65	2.66	31.22	0.5	0.0006	575972.1	SBA	295 (3)
T25-2	13	9.53	0.87	1.36	97.34	0.5	0.0018	1795959.9		
T25-1	9.33	3.02	0.59	3.09	22.15	2.7	0.0022	2207103.4	MBA	324 (4)
T24-3	15.09	12.05	0.88	1.25	142.77	0.9	0.0047	4741292.1		
T24-2	13.17	5.48	0.68	2.4	56.69	2	0.0042	4183648.2		
T24-1	14.92	7.87	0.78	1.9	92.26	0.6	0.002	2042725.0	MBA	391 (13)
T23	9.31	3.65	0.67	2.55	26.71	1	0.001	985488.3	SBA	410 (16)
^ 22-23	9.32	2.77	0.55	3.37	20.27	0.3	0.0002	224388.9	SBA	417 (16)
T22-2	11.97	7.94	0.85	1.51	74.6	1	0.0028	2752629.3		
T22-1	9.64	2.37	0.48	4.07	17.93	0.2	0.0001	132323.4	MBA	424 (17)
^ 21-22	9.44	3.28	0.62	2.87	24.35	0.3	0.0003	269510.2	SBA	434 (18)
T21-2	12.4	7.94	0.84	1.56	77.25	1	0.0029	2850488.1		
T21-1	9.53	2.94	0.57	3.25	21.98	0.2	0.0002	162175.5	MBA	436 (18)
T20-6	12.36	5.09	0.68	2.43	49.36	0.5	0.0009	910599.8		
T20-5	13.74	5.28	0.65	2.6	56.93	1.5	0.0032	3151075.5		
T20-4	13.26	7.7	0.81	1.72	80.14	1.3	0.0038	3844219.9		
T20-3	10	3.19	0.57	3.13	25.07	0.7	0.0006	647583.9		
T20-2	12.68	6.91	0.79	1.84	68.78	1	0.0025	2537834.4		
T20-1	13.05	5.37	0.68	2.43	55.06	1.1	0.0022	2234763.6	MBA	457 (19)
T19-5	13.37	7.25	0.79	1.84	76.08	0.5	0.0014	1403694.5		
T19-4	15.69	9.08	0.81	1.73	111.87	0.5	0.0021	2063927.7		
T19-3	10.13	5.85	0.81	1.73	46.54	0.6	0.001	1030351.3		
T19-2	12.74	8.52	0.85	1.5	85.28	0.3	0.0009	943994.3		
T19-1	10.33	7.85	0.88	1.32	63.68	0.2	0.0005	469980.5	MBA	486 (16)

Supplementary Table S5.1 (continues): Overview of main descriptive characteristics of the ellipses that approximate tephra dispersal and are used for deposit volume calculations. "^" marks uncorrelated tephra units.

	Ellipse characteristics				Deposit volume calculations					
Tephra unit	major axis	minor axis	circularity	Aspect ratio	area (km^2)	thickness (cm)	Legros (km^3)	Legros (m^3)	Deposit type	Age (cal BP)
T18	9.82	2.2	0.45	4.46	16.99	0.5	0.0003	313447.1	SBA	507 (11)
T17-6	11.29	4.47	0.66	2.53	39.63	2.4	0.0035	3509721.4		
T17-5	11.59	4.47	0.65	2.59	40.67	4	0.006	6002596.8		
T17-4	11.78	3.82	0.58	3.09	35.29	1	0.0013	1302127.2		
T17-3	12.6	8.43	0.85	1.5	83.36	1.5	0.0046	4613865.3		
T17-2	9.73	3.61	0.64	2.7	27.62	1	0.001	1019030.4		
T17-1	13.04	9.97	0.88	1.31	102.13	0.4	0.0015	1507365.0		519 (8)
T16-2	10.28	3.61	0.62	2.85	29.15	1.5	0.0016	1613452.5		
T16-1	9.99	2.78	0.53	3.59	21.8	0.7	0.0006	563068.2	MBA	530 (7)
T15-5	14	9.56	0.85	1.47	105.11	1	0.0039	3878706.6		
T15-4	21.02	8.33	0.67	2.52	137.45	0.5	0.0025	2535878.7		
T15-3	19.39	10.99	0.8	1.76	167.43	0.8	0.0049	4942533.6		
T15-2	11.64	6.22	0.78	1.87	56.84	0.7	0.0015	1468048.1		
T15-1	11.64	6.52	0.8	1.79	59.59	0.6	0.0013	1319211.9	MBA	532 (8)
T14	13.36	11.04	0.89	1.21	115.85	0.2	0.0009	855002.5	SBA	557 (12)
T13-6	22.44	13.39	0.82	1.68	235.93	1.2	0.0104	10446847.6		
T13-5	17.36	6.95	0.67	2.5	94.76	3	0.0105	10490153.4		
T13-4	23.25	18.07	0.88	1.29	330.04	1.9	0.0231	23138824.0		
T13-3	22.94	19.14	0.89	1.2	344.73	0.4	0.0051	5088273.8		
T13-2	12.72	5.32	0.69	2.39	53.13	0.7	0.0014	1372244.6		
T13-1	9.77	3.1	0.58	3.15	23.81	0.2	0.0002	175695.7	MBA	604 (27)
T12	9.71	2.64	0.52	3.68	20.14	0.3	0.0002	222960.9	SBA	631 (34)
T11-4	13.76	3.28	0.46	4.2	35.44	2.5	0.0033	3268971.0		
T11-3	12.93	7.63	0.81	1.69	77.52	1	0.0029	2860451.1		
T11-2	16.08	9.73	0.82	1.65	122.83	1	0.0045	4532427.0		
T11-1	12.59	10.18	0.89	1.24	100.65	2	0.0074	7427970.0	MBA	754 (42)
T10	9.36	3.26	0.62	2.87	23.96	2.2	0.0019	1944748.1	SBA	792 (42)
T9	10.04	3.26	0.59	3.08	25.71	0.2	0.0002	189702.9	SBA	886 (40)
T8	12.11	8.17	0.85	1.48	77.68	0.5	0.0014	1433140.7	SBA	945 (37)
T7	21.17	5.84	0.51	3.63	97.07	1	0.0036	3581919.9	L	1337 (23)
T6	12.2	8.18	0.85	1.49	78.36	0.5	0.0014	1445742.0	SBA	1362 (21)
T5	23.99	3.62	0.32	6.63	68.15	1	0.0025	2514735.0	L	1416 (21)
T4-3	9.93	3.23	0.58	3.08	25.15	0.5	0.0005	464017.5		
T4-2	9.93	3.23	0.58	3.08	25.15	2.2	0.002	2041758.2		
T4-1	12.22	7.24	0.81	1.69	69.46	0.5	0.0013	1281518.6	MBA	1494 (38)
T3	9.3	2.13	0.45	4.37	15.52	0.3	0.0002	171850.7	SBA	1571 (40)
T2	21.45	4.29	0.39	5	72.2	3.5	0.0093	9324113.4	L	1580 (39)
T1	10.18	3.64	0.63	2.79	29.12	0.2	0.0002	214868.7	SBA	1584 (38)

Additional supplementary material

Supplementary Table S5.2 (Appendix H-3.2): Spot microprobe data representing major element groundmass compositions for individual subunits.

Supplementary Table S5.3.1 (Appendix H-3.3): Averaged compositions for individual subunits with respective standard deviations.

Supplementary Table S5.3.2 (Appendix H-3.3): Compositions averaged for individual tephra members.

Chapter 6

Synthesis

This chapter revisits the hypothesis and research objectives as introduced in chapter 1. The key findings from chapters 3, 4 and 5 are summarised and the contribution of this research is brought into context of previous knowledge and current challenges in the relevant areas of interest. Furthermore, the data emerging from this research is used to address overarching research questions contributing to a wider understanding of the late Holocene history at Mt. Ruapehu.

6.1 Synthesis

Explosive volcanic eruptions of small to moderate magnitudes (VEI ≤ 3; volumes ≤ 0.1 km^3) are amongst the most common volcanic phenomena on Earth (Newhall et al., 1982; Siebert et al., 2015). Records and observations of historical eruptions of this magnitude show that, more than often, these eruptions do not occur as single eruption events but involve complex, several months- to years-long multi-phase eruption sequences (Gudmundsson et al., 2012; Bustillos et al., 2016; Miyabuchi et al., 2019). Forecasting the eruption progression of multi-phase eruptions, including sudden changes in eruption dynamics and magnitude as well as anticipating associated changes in potential hazard impacts, remain major challenges for volcanologists and decision-makers during volcanic crises. To approach these challenges, historical eruptions from the Smithsonian Global Volcanism Program (GVP) have been recently analysed by means of statistical methods (Jenkins et al., 2007; Bebbington et al., 2019). However, the observation of an overall decrease in data quality and availability with age as well as the peculiarity in the eruption behaviour of individual volcanoes hamper this approach. In particular, it becomes evident that, at this point in time, no routine application of probabilistic models manages to account for the whole range of eruption styles and magnitudes that is known for volcanic activity. However, existing probabilistic studies form an important framework for more in depth-studies at individual volcanoes. They also provide first guidelines on the detail and time-resolution that volcanological datasets ought to have in order to create robust probabilistic eruption forecasts that account for the dynamic changes in eruptive activity, both on short and on long timescales.

This PhD research aimed at adding complexity to the understanding of the short-term, long-term and multi-phase eruption behaviour at frequently active, long-lived composite volcanoes. The framework of this study consisted in the creation and analysis of a high-resolution, deposit-based eruption record for the past two millennia of New Zealand's historically most active volcano- Mt. Ruapehu. The rationale was that such a record would extend and complement the existing but short historical record and would add detail to the most recent pre-historic tephra record. The approach to accomplish this involved combining comprehensive tephrostratigraphical and lithosedimentological mapping of Mt. Ruapehu's youngest tephra formation (the <1800 years Tufa Trig Formation) along with geochemical and componentry analysis and coring to develop techniques that allow the identification, characterisation and dating of small to moderate magnitude, single-phase and multi-phase eruptions. If successful, this would reveal a first robust and sufficiently comprehensive eruption frequency-magnitude record of Mt. Ruapehu's most recent eruptive activity, which would provide the base to estimate probabilities of future activity. This dataset could then also serve to test existing probabilistic models on geological multi-phase records. Furthermore, it was anticipated that this frequency-magnitude record, in combination with data on eruption style and magma chemistry could be used to identify possible short- and long-term temporal pattern in the eruption behaviour at Mt. Ruapehu and to relate them to changes in the volcanic system.

Following a brief recapitulation of the research objectives that guided this PhD research, the remainder of this chapter aims to synthesise the main research results presented in Chapters 3, 4 and 5 and to discuss their wider implications in the context of previous knowledge and of current research challenges in this area.

6.1.1 Research objectives revisited

At the beginning of this research an overarching hypothesis was defined, stating that a detailed frequency-magnitude record, characterising information on eruption style, magnitude and eruption recurrence as well as the number and order of individual single- and multi-phase eruptions could be used to understand and identify short- and long-term patterns in eruption behaviour and could be related to time-variant changes in physico-chemical processes in the volcanic system. These time-variant patterns would form the basis for short- and long-term eruption forecasts.

Three main objectives were introduced in Chapter 1 to guide this research. They were addressed throughout Chapter 3, Chapter 4 and Chapter 5 and lead to the key findings that will be outlined in the following sections.

Objective 1: Creating a detailed frequency-magnitude record for Mt. Ruapehu, detailing eruption style, frequency and magnitude for multi-phase and single-phase eruptions over the past two millennia.

Objective 2: Characterising switches in eruption behaviour during multi-phase eruptions and relating them to changes in the source-conduit system.

Objective 3: Identifying patterns and long-term changes in eruption behaviour and the volcanic system.

6.2 Key research findings

6.2.1 A high-resolution tephra record for the last two millennia at Mt. Ruapehu and re-definition of the Tufa Trig Formation

A systematic approach to create a network of field locations, which covers different ring plain sectors was introduced and discussed in Chapter 3. In addition to the 19 tephra members that were previously defined for the Tufa Trig Formation (Donoghue et al., 1997), thirteen new members were identified, leading to an overall number of thirty-one tephra members. The high-resolution tephrostratigraphic framework and lithosedimentological analysis show that the eruption behaviour over the past 1800 years was characterised by small to moderate explosive single-phase and multi-phase eruptions, involving average tephra volumes between ~2×10^5 m^3 and 6×10^7 m^3 and ranging from low-intensity phreatomagmatic activity to complex sequences of increasingly semi-sustained magmatic, subplinian activity. The associated deposits can be grouped into three main types that have different frequencies over the past 1800 years: (1) Single bed ash units represent low-intensity, predominantly phreatomagmatic single-phase eruptions and constitute ~35% of the tephra record. (2) Moderate intensity single-phase eruptions comprise increasingly magmatic signatures and are represented by lapilli-bearing units. They form ~10% of the record. (3) Multi-bed ash units constitute ~55% of the tephra record and represent multi-phase eruptions with phases of variable intensity and magnitude. These multi-bed ash units show a variable degree of complexity and involve either 2–3 eruption phases or 4–6 eruption phases for the most complex and widespread sequences.

The re-definition of the Tufa Trig Formation not only increases the previously assumed overall eruption frequency from one eruption every ~100 years to one eruption every ~60 years but also expands the understanding of the complexity of eruptions at Mt. Ruapehu and small to moderate explosive eruptions in general. While recent small to moderate multi-phase eruptions at i.e., Eyjafjallajökull (Bonadonna et al., 2011; Dellino et al., 2012), Shinmoedake (Miyabuchi et al., 2013; Nakada et al., 2013; Suzuki et al., 2013), Nakadake (Miyabuchi et al., 2018; 2019) or the 1995–1996 eruptions at Mt. Ruapehu (Nairn et al., 1996; Cronin et al., 2003) have highlighted the dynamic character of the associated eruption sequences, few studies discuss the characteristics of the geologically preserved tephra sequences associated with this type of eruptions. Using the well-preserved tephra sequences of Mt. Ruapehu as a case study, the tephrostratigraphical and lithosedimentological analyses in Chapter 3 have highlighted that tephra sequences associated with small to moderate explosive eruptions actually represent variable eruption duration (minutes to years), variable magnitude (1×10^5 m^3 – 1×10^7 m^3 tephra volume) and variable eruption intensity (dispersal limited to the summit area vs cm-sized clasts being dispersed to distances of ~20 km). This extends the understanding of eruption behaviour at Mt. Ruapehu, which until this point, was considered to have produced predominantly small-scale phreatomagmatic to Strombolian eruptions during the past ~10,000 years (Donoghue et al., 1997). Eruption scenarios need to account for this detail and complexity in volcanic activity at Mt. Ruapehu and at other comparable volcanoes, where similar systematic mapping of small-volume tephra deposits might lead to a revision of the existing understanding of small-scale volcanic activity and the associated ranges in eruption dynamics.

6.2.2 New age constraints and stratigraphic markers for the post-Taupo eruptive history of the Tongariro Volcanic Centres

Prior to this study, few age constraints were available for the Tufa Trig Formation, with the Taupo eruption providing the lower base and only one tephra member dated (Donoghue et al., 1997). This precluded the development of a robust tephra age model and hampered the discussion of time-variant eruption behaviour over the past 1800 years. The geochemical fingerprinting that was performed during this research disproves the often cited Okataina-sourced Kaharoa eruption (AD 1314) as a stratigraphic marker (Purves, 1990; Donoghue et al., 1997) as no glass shards with rhyolitic compositions (cf., Nairn et al., 2004; Lowe et al., 2008) could be identified.

The new age constraints presented in Chapter 3 and Chapter 5 consist of new radiocarbon ages of soil underlying the members T13, T15 and T17 in the Ngamatea swamp core. They highlight that three of the most complex eruption sequences of the last 1800 years were deposited within a time span of less than 100 years. The identification of the Taranaki-sourced Burrell Lapilli being interbedded with the Tufa Trig Formation provides an additional stratigraphic marker constraining the tephra record of the past ~300 years. The correlation of the stratigraphically uppermost T31 to the historical 1945 eruption furthermore allows to compare the historical eruption record with the tephra record (as discussed in Chapter 5). These age constraints provide the framework for the probabilistic models presented and discussed in Chapter 5 and allow the identification of time-variant patterns in eruption behaviour at Mt. Ruapehu.

In addition to the value that these age constraints have for the eruption record of Mt. Ruapehu, they also contribute to the wider late Holocene chronostratigraphic framework of the Tongariro Volcanic Centre (TgVC) and the southern Taupo Volcanic Zone. While the widely dispersed Tufa Trig members T13, T15 and T17 add chronostratigraphic constraints for the time span around ~600 cal BP, the widely dispersed Burrell Lapilli helps to constrain the most recent TgVC eruption history, as it can be readily identified macroscopically as well as through major element fingerprinting.

6.2.3 Time-variable eruption behaviour at Mt. Ruapehu

The combination of the age model with the frequency-magnitude record introduced in Chapter 5 allows to quantitatively discuss time-variable patterns in Mt. Ruapehu's most recent tephra record. Over the past 1800 years eruption behaviour has varied in terms of eruption frequency, magnitude and eruption style (Fig. 5.6). Probabilistic modelling shows that the eruptive behaviour of Mt. Ruapehu can be approximated by different "regimes", which differ in their eruption rates. The 1800-year time span can be divided in four distinct time spans, which are described by three regimes: (1) The time span following the Taupo eruptions (1718–1300 cal BP) involves a medium eruption rate with one eruption every ~40 years and comprises mostly single-phase eruptions associated with single bed ash and lapilli units. (2) The subsequent time span between ~1300 and ~610 cal BP includes a ~300-year long hiatus in major eruptive activity and comprises mostly single-phase eruptions and one major multi-phase eruption. This time span is described by a low rate regime (1/125 years). (3) The time period between ~610 and ~370 cal BP has an average decadal eruption frequency and comprises ~60% of the total Tufa Trig Formation deposit volume. This time span contains the most complex and voluminous multi-phase eruptions with 5–6 phases. (4) Finally, the last 370 years show medium eruption rates (1/40 years) and include less complex multi-phase eruptions with 2 to 3 eruption phases. The time between the major historical eruption episodes in 1945 and 1995–1996 and their cumulative volumes of ≤ 0.1 km^3 (Johnston et al., 2000) compare well with the characteristics of the tephra deposits of the past 370 years. In line with this, the current regime is most likely a medium rate regime.

6.2.4 Time-variable pattern in glass compositions of the 1800-year tephra record at Mt. Ruapehu

In addition to a time-resolved frequency-magnitude record, a near continuous characterisation of the groundmass major element composition of juvenile tephra has been obtained over the past 1800 years (Chapter 5). Despite minor systematic changes within individual eruption sequences, major element groundmass compositions show limited variability over the past 1800 years. One exception to this is lapilli unit T5, which shows a distinct geochemical signature, characterised by lower SiO_2, and higher MgO and CaO. The other exception is constituted by groundmass compositions obtained for the historical 1995–1996 eruptions that are similarly characterised by relatively lower SiO_2 and higher MgO and CaO (Fig. 5.7).

Similar patterns become evident from the characterisation of selected key units in terms of their trace element characterisation, as shown in Chapter 4. Trace element compositions vary little between individual units with T5 and the 1995–1996 eruptions showing distinct compositions (Fig. 4.15). The homogeneous groundmass compositions highlight the limited value of geochemical analysis for the identification and correlation of same-source andesitic-dacitic tephra units. However, the limited variability of groundmass compositions at Mt. Ruapehu over a time span of 1800 years makes the associated tephras valuable tephrostratigraphic markers in the framework of the eruptive history of the Tongariro Volcanic Centre, where fast major element glass analysis allows to distinguish between the different volcanic sources.

6.2.5 Time-variable pattern in the Mg-number as indicator of upcoming regime changes

Interestingly and slightly contrasting to the limited variation in groundmass compositions, the Mg-number appears to show systematic time-variant patterns both within individual eruption sequences and over the time span of the Tufa Trig Formation (Fig. 5.6, Fig. 5.7). While late-stage microlite crystallisation might mask periodic magma replenishment leading to similar groundmass glass compositions, the Mg-number indicates a periodic involvement of compositionally less evolved magma. This agrees well with the textures observed in phenocrystals in Nakagawa et al. (1999) and Nakagawa et al. (2002), and the current understanding of the shallow nested sill-dike system, which constitutes the upper part of a complex multi-level plumbing system (Price et al., 2005; Price et al., 2012; Kilgour et al., 2013). Over the past 1800 years, Mg-numbers have an average of Mg#=23 ± 6, with lapilli-unit T5 showing a distinct Mg#=34, in line with the previous paragraphs. Systematic increases in the Mg-number in tephra units T5, T11 and before T23 might indicate changes in the magma replenishment, resulting in different eruption rates and are therefore associated with a regime change. In line with this, changes in the Mg-number might herald regime changes, prior to the actual regime change. In this case, the change from Mg#=18 (T31) to Mg#=28 (1995–1996), discussed in Chapter 5, suggests that there is a possibility that the next major eruption might mark the onset of another regime.

6.2.6 Characterisation of the largest multi-phase eruption of the last 1800 years – a possible worst-case scenario for future eruptions

The multi-bed ash unit T13 is a widely dispersed characteristic tephra sequence, which forms an important chronostratigraphic marker for the post-Taupo stratigraphic framework. With this unit constituting the largest eruption known for the past 1800 years, the study of the associated tephra sequence in Chapter 4 contributes to the understanding and quantification of a potential worst-case scenario for future eruption crises at Mt. Ruapehu. Based on the lithosedimentological work presented in Chapter 3 and Chapter 4, this sequence has been re-defined by identifying six depositional subunits that are representative of five eruption phases. These depositional subunits can be correlated through the various sectors of the ring plain and associated deposit volumes span several orders of magnitude from 5.6×10^5 m^3 to 3.23×10^7 m^3. Irregular multi-lobate isopachs and laterally variable componentry within individual subunits suggest that each of the subunits is composed of multiple eruption events. It also shows that the here applied high-resolution tephrostratigraphical mapping is still not fine-scaled enough to fully resolve the complexities of intra-subunit eruption progressions as they can be resolved for observed eruptions (cf. Miwa et al., 2013; Suzuki et al., 2013; Miyabuchi et al., 2018; 2019). While no single parameter proves sufficient to unequivocally correlate individual subunits laterally, it has been shown that a multi-parameter approach integrating volume calculations, grain size distribution, componentry as well as textural and geochemical analyses aids to unravelling the eruption sequence. The heterogeneity observed in the pyroclast assemblages and textural features of juvenile glass between subunits contrasts with the limited variability observed in both major element and trace element data throughout the sequence (cf. Cioni et al., 2008b). Syn-eruptive changes in eruption dynamics appear to be controlled by short-term processes in the conduit and vent, such as changes in melt ascent rates influenced by an interplay between late-stage microlite crystallisation, increasing melt viscosity and degassing efficiency and variable fragmentation mechanisms (cf. Kilgour et al., 2016; Zdanowicz et al., 2018; Miyabuchi et al., 2018; 2019; Mujin et al., 2020). Major changes in the magmatic system appear subordinate.

The T13-sequence involves multiple eruption styles and magnitudes from a series of low-energy predominantly phreatomagmatic eruptions during the opening phase to the main, semi-continuous, violent Strombolian to subplinian phase P3, which is increasingly controlled by magmatic fragmentation. Higher eruption intensities are associated with higher erupted tephra volumes and show signatures that are characteristic of deeper, less evolved magma and faster magma ascent rates, such as an increase in free pyroxenes, slightly less evolved groundmass compositions, as well as a decrease in groundmass crystallinity associated with a concomitant increase in clast vesicularity.

After a time break in the eruption progression, the eruption recommences with enhanced excavation of the vent system with the Crater Lake being evaporated and/or ejected during preceding phases. The eruption sequence concludes with a violent Strombolian to subplinian phase, fed by a magma that is slightly compositionally distinct from the preceding eruption phases and is followed by a phase of prolonged ash emission.

Following this, the worst-case eruption scenario would involve a prolonged multi-phase eruption that evolves from intermittent, low-intensity, small-volume phreatomagmatic eruptions to increasingly more continuous, violent and magmatic activity. In a scenario similar to the T13-sequence, the area at risk of tephra fall might be significantly larger than previously assumed and is subject to short-term changes in tephra dispersal. Future eruption scenarios need to take in account that a cessation in eruptive activity may potentially not mark the end of the eruption sequence but can be followed by another period of activity. Furthermore, the limited compositional variability highlights that prolonged eruption sequences might not necessarily involve the migration of deep large (detectible) magma volumes during eruption progression, suggesting that syn-eruptive precursory signals that allow the forecast of eruption progression might be scarce or involve short timescales. It is interesting to note that key characteristics of the eruption sequence (i.e., intermittent phreatomagmatic to Strombolian activity, several phases of semi-continuous magmatic activity, major break in activity) are similar for T13 and the 1995–1996 eruptions. However, the T13-sequence was significantly larger and therefore should be considered as the baseline for potential worst-case eruption scenarios.

6.2.7 Insights into the magmatic system feeding prolonged multi-phase eruptions

The identification of time-variable eruption behaviour presented in Chapter 5 aids to further unravel the processes in the magmatic system that feds prolonged multi-phase eruptions. This becomes particularly evident through the comparison of geochemical pattern observed in the largest geologically preserved T13-sequence and the largest historically observed 1995–1996 sequence, as discussed in Chapter 4. While the T13-sequence shows limited syn-sequence variation in major elements such as MgO, SiO_2, K_2O and CaO and indicates that the entire sequence was fed by a compositionally similar parental magma, major element glass compositions for the 1995–1996 eruptions are strongly variable and point towards the involvement of several distinct source magmas (Nakagawa et al., 1999; Nakagawa et al., 2002). The observation that glass compositions in the T13-sequence show limited variability, while glasses from the 1995–1996 eruptions span the entire compositional range known for Mt. Ruapehu (Gamble et al., 1999) can be attributed to differences in the magma system feeding the two multi-phase eruptions. In particular, the T13-sequence marks the first eruption sequence of a ~200-year long high rate eruption regime, while the 1995–1996 eruptions and other historical eruptions are associated with a medium rate regime. As discussed in Chapter 5, the time span from ~610 to 370 cal BP is likely associated with a period of enhanced rifting. In this context, a voluminous and more constant magma supply is expected and agrees with the entire T13-sequence originating from the same parental magma that was injected into the system prior to eruption onset (e.g., Fig. 4.14a). Systematically less evolved compositions (e.g., increasing MgO and CaO, decreasing SiO_2) with eruption progression can be related to constant deep magma influx during the T13-eruption sequence. Overall, the high rate period is associated with magma supply that differs significantly in frequency and magnitude from the magma supply inferred for historical eruptions and the associated medium rate regime. For historical timescales, discrete small-volume magma injections into the shallow crystallised system have a frequency of ~20–30 years, with individual eruptions being fed by separate small-volume magma batches (Gamble et al., 1999; Nakagawa et al., 1999; Price et al., 2012). This implies that over the past 370 years a relative decrease in the volume and frequency of magma replenishments into the shallow system can be observed. This highlights that historically observed multi-phase eruptions differ from geologically preserved multi-phase eruption sequences (e.g., T13, T15 and

T17) with regards to eruption frequency and magnitude as well as the underlying magmatic system.

6.2.8 Probabilistic modelling of small to moderate multi-phase eruptions

While recent studies have shown the relevance of multi-phase eruptions in the context of historical datasets (Jenkins et al., 2007; Bebbington et al., 2019), there are few studies that have attempted modelling eruption progression of small to moderate multi-phase eruptions based on geologically preserved records. Using the tephra record of the past 1800 years at Mt. Ruapehu, it has been shown in Chapter 5 that existing multi-phase models can be successfully applied to geological datasets. One interesting outcome from intra-sequence modelling is that the number of subunits (and accordingly eruption phases) can be approximated by a geometrical distribution with a ~56% probability of a further phase occurring. Intra-sequence subunit volumes, on the other hand, increase with subunit number and follow an exponential distribution. These two findings have important implications for eruption forecasts, as they imply that once an eruption has started, due to the “memoryless’ property of both geometrical and exponential distributions, the volume and magnitude of the potentially upcoming phase(s) are independent of the current phase, complicating predictions on eruption progression characteristics and eruption duration. In other words, in a future eruption crisis the probability of another phase following the current phase is slightly higher than the eruption containing one phase only. Furthermore, statistical models cannot provide information on the number and magnitude of potentially upcoming eruption phases. In this case, additional information from i.e., geophysical and geochemical monitoring is needed to guide risk management following eruption onset.

Overall, the preliminary analysis of the multi-phase eruptions of the Tufa Trig Formation needs to be complemented by more information on eruption behaviour during individual phases but provides a promising new framework in terms of intra-sequence modelling and future studies at Mt. Ruapehu and analogue volcanoes. The applicability of models that were inferred from historical datasets to geological datasets as discussed in Chapter 5 shows that these models can form the foundation for future research on similar long-term multi-phase datasets.

6.2.9 Implications for eruption styles associated with small to moderate explosive eruptions

The main eruption styles associated with small to moderate explosive eruptions are typically classified as periods of continuous ash emission (Cioni et al., 2008a) and Hawaiian and Strombolian for the lower magnitude ranges (Newhall et al., 1982), while higher intensity eruptions are classified as violent Strombolian (Arrighi et al., 2001), Vulcanian (Nairn et al., 1978; Newhall et al., 1982) or subplinian (Cioni et al., 2008a; Bonadonna et al., 2013). These eruption styles typically imply purely magmatic fragmentation, while phreatomagmatic fragmentation and eruption styles are generally treated separately, irrespective of the involved magnitudes (Walker, 1973; Zimanowski et al., 2015). Mixed phreatomagmatic-magmatic eruption progressions are known from i.e. Eyjafjallajökull (Gudmundsson et al., 2010; Dellino et al., 2012), Vesuvius (Barberi et al., 1992; Cioni et al., 2008a), Shinmoedake (Miyabuchi et al., 2013; Nakada et al., 2013; Suzuki et al., 2013) and Nakadake (Miyabuchi et al., 2018; Miyabuchi et al., 2019) but few studies exist on the variability of the associated deposits and pyroclast assemblage. The characterisation and classification of deposit sequences and eruption progression is also hampered by existing classification schemes and terminology being based on “ideal” scenarios to define eruption style, magnitude and the resulting deposit characteristics (cf. Walker, 1973; Newhall et al., 1982; Pyle, 1989). Contrastingly, the reality is more complicated and transient, often resulting in discrepancies between deposit characteristics and inferred eruption dynamics (cf. Cioni et al., 2008a, Bonadonna et al., 2013, 2016). The systematic tephrostratigraphic and lithosedimentological characterisation of the phreatomagmatic-magmatic eruptions of the Tufa Trig Formation presented in Chapter 3 and Chapter 4 provide the opportunity to elucidate the range in the deposit features of tephra sequences associated with mixed eruption styles of small to moderate magnitude multi-phase eruptions and to discuss the variability in the processes controlling them. For single bed ash units and lapilli-bearing units the distinction between predominantly “wet” and “dry” eruption mechanisms is facilitated by the ash-rich beds being characterised by limited dispersal, high proportions of extremely fine ash and predominant proportions of non-vesicular clasts, which are typical indicators of phreatomagmatic eruptions. On the other end, the highly vesicular lapilli-sized pyroclasts that are dispersed to distances of 20 km suggest relatively higher eruption intensity, probably related to increasingly magmatic fragmentation mechanisms. For multi-bed ash units, a univocal distinction between phreatomagmatic and magmatic processes is more convolute. In particular, the variable range and the concurrence of different juvenile clasts in individual subunits (i.e., Chapter 3, Chapter 4) including both very dense and blocky pyroclasts, as well as highly vesicular pumiceous glass suggests that the interplay of dry magmatic and phreatomagmatic fragmentation mechanisms might be complex and perhaps also more continuous than currently assumed. However, there appears to be a relationship between fragmentation mechanisms and the magnitude of the eruption that influences the proportions of juvenile and lithic components in tephras. Accordingly, smaller magnitudes appear to involve predominantly phreatomagmatic eruption mechanisms while, possibly due to their magnitude and accordingly generally higher gas contents and mass discharge rates, larger eruption phases involve an increasing proportion of magmatic activity. This might be related to increasing magma/water ratios but further investigation is needed to clarify this issue. Future detailed studies on ash morphologies and pyroclast assemblage of multi-phase eruptions, where individual phreatomagmatic, mixed and purely magmatic phases are observed and characterised could be used to identify key characteristics in the associated pyroclast assemblages that can be subsequently extrapolated to geologically preserved tephra sequences.

6.2.10 Preservation bias from merging historical datasets with geological dataset

In Chapter 5, the historical and geological eruptive records of Mt. Ruapehu were linked by associating the stratigraphically uppermost discrete T31 with the historical 1945 eruptions. The merging of the two datasets allows a comparison of historically observed eruptions with the data that was obtained exclusively from the geological record and highlights several implications regarding potential preservation biases. In Chapter 5 it has been shown that the minimum volumetric threshold for macroscopically preserved tephra deposits at medial distances ranges in the order of magnitude of 1×10^5 m^3. This agrees well with the 1945 and 1995–1996 eruptions, for which cumulative volumes have been estimated at $<1 \times 10^8$ m^3 and which, accordingly, should be preserved in the tephra record. While this is true for the 1945 eruption, the 1995–1996 eruptions do not yet appear as a discrete tephra unit in the tephra record, even though pyroclastic material associated with this eruption can be found in vegetation roots (e.g. WP219, WP223) and covering the surface i.e. at the Iwikau skifield. Considering that 25 years have passed since then, this raises important questions about the timescales and processes that are involved in the formation of upbuilding andisoils and discrete tephra deposit. The field observations lead to the following conclusions: (1) The time frames for the formation of discrete tephra units in the Tongariro National Park are longer than previously assumed and are in the order of magnitude of at least 20 years, potentially longer. The identification of a macroscopic deposit that can be unequivocally associated with the 1995–1996 eruptions, constitutes an interesting future research topic, allowing to further discuss the apparent discrepancy in eruption characteristics between geologically preserved eruption sequences and observed eruption sequences (cf. 4.5.4 Limitations in characterising the deposits of small to moderate multi-phase eruptions). (2) As discussed in Chapter 3, preservation conditions are strongly laterally variable, explaining the discontinuous appearance of pyroclastic material associated with the 1995–1996 eruptions. At the same time this confirms the value of a network of field locations that accounts for laterally variable preservation conditions. (3) While it has been shown that the 1995–1996 eruptions can be considered commensurate to the 1800-year tephra record (Fig. 5.14), this shows once again that the tephra record is biased with regard to eruption styles and magnitude. This becomes particularly evident when looking at the historically most frequently observed small phreatic to phreatomagmatic eruptions (Scott, 2013). The most recent 2007 event falls into this category and despite a deposit volume estimated at 1×10^5 m^3 (Kilgour et al., 2010), associated ashfall affected only the summit area and is not expected to be represented in the geological record of the Tufa Trig Formation. Accordingly, even though the here presented high-resolution macroscopic tephrostratigraphic study added detail to the understanding of small to moderate explosive eruptions, it is important to emphasise that this record does not include phreatic-phreatomagmatic events of the magnitude of the 2007 eruption. (4) This, in turn, highlights that, in addition to a volumetric threshold, the preservation of small volume multi-phase eruptions also depends on eruption dynamics (i.e., eruption continuity) as well as external factors (i.e., wind direction and strength) and local preservation conditions. In other words, if enough ash is deposited to bury the previously deposited ash and therefore acts as erosion protector, even small volumes may be preserved as a discrete tephra, despite showing pocketing appearance. If, on the other hand, during a period of continuous ash emission, wind patterns change over short timescales, the thin fine-grained pyroclastic material is widely distributed but subject to quick local erosion.

(5) Finally, the overall magnitude and tephra volume are comparable for e.g., 1945, 1995–1996 and the largest Tufa Trig members, each being characterised by deposit volumes of <0.1 km^3. Nonetheless, there are clear discrepancies between the datasets that underlie magnitude quantification between the two major historical eruptions and the geologically preserved eruptions. The 1995–1996 dataset for volume estimates was obtained shortly after eruptions, as it is common for historical (and observed) eruptions and includes an extensive distal dataset and proximal measurements prior to erosion. For geologically preserved datasets, this data can typically not be quantified (see 4.5.4 Limitations in characterising the deposits of small to moderate multi-phase eruptions), leading to a well-known underestimation of deposit volumes (potentially up to ~62%; 4.5.1.1 Tephra volume) compared to actual erupted volumes (Fierstein et al., 1992; Rose, 1993; Bonadonna et al., 2012). An often used approach to deal with this discrepancy involves adding a VEI-magnitude to geologically characterised eruptions (e.g. Newhall et al., 1982), which in case of the Tufa Trig Formation would lead to volcanic explosivity indices of ~4, rather than the previously assumed VEI ≤ 3. It is important to keep in mind that this regards only magnitude quantification and does not necessarily represent eruption styles. With the 1995–1996 eruptions being classified as VEI 3, this highlights that in particular the most complex multi-phase eruptions that were erupted between 610 and 370 cal BP, such as the T13-sequence, were at least one magnitude larger than the largest, historically observed eruptions. Accordingly, the 1995–1996 eruptions represent a minimum rather than a maximum scenario for potential prolonged multi-phase eruptions at Mt. Ruapehu.

6.3 Implications for the late Holocene history at Mt. Ruapehu

6.3.1 Eruption frequencies at the Tongariro Volcanic Centres

Mt. Ruapehu is located within the iconic Tongariro National Park and lies within ~20 km distance from the northward active volcanoes Mt. Ngauruhoe and Mt. Tongariro. As has been discussed in the preceding sections, understanding time-variable changes in Mt. Ruapehu’s eruptive behaviour is important for understanding the peculiarity of Mt. Ruapehu’s magmatic system and to create Mt. Ruapehu-specific robust eruption forecast models. However, for hazard models for the Tongariro National Park and for stakeholders and decision-makers it is crucial to obtain a holistic understanding of the explosive eruptive activity and associated potential hazards by comparing the eruption behaviour of the individual volcanoes in a local framework.

While Mt. Ruapehu’s late Holocene eruptive activity involved predominantly explosive activity (Greve et al., 2016; Conway et al., 2018), pre-historic eruptive activity at Mt. Tongariro has included several major periods of effusive activity (Hobden et al., 1999; Hobden et al., 2002; Greve et al., 2016; Shane et al., 2017; Shane et al., 2019). Over historical time spans (since 1846; Scott et al., 2014), small-scale eruptive activity has been observed at Red Crater, Te Maari and Mt. Ngauruhoe, involving 30 discrete eruptions sourced mostly from Red Crater and some Te Maari-sourced eruptions. The most recent eruption from Mt. Tongariro involves a hydrothermal eruption 2012 at Te Maari (Lube et al., 2014; Pardo et al., 2014; Scott et al., 2014). Tephra deposits associated with pre-historical explosive activity are sourced mainly from Mt. Ngauruhoe, where Moebis et al. (2011) identified major explosive activity for the past ~4700 years, while explosive activity at Red Crater is documented in the tephra record for the past ~300 cal BP (Fig. 6.1).

Adding the 18 Mt. Ruapehu-sourced tephras from the Mangatawai Formation (Moebis et al., 2011) and black ash-1 and -2 (Donoghue et al., 1995) from the Papakai Formation, Mt. Ruapehu’s eruptive record can be expanded to 6000 years and can be compared with Mt. Ngauruhoe’s eruptive record (Fig. 6.1a). Both the 6000-year and the 2000-year cumulative frequency records highlight short periods characterised by high eruption rates for both Ngauruhoe and Red Crater, while Mt. Ruapehu’s eruption behaviour shows overall more constant eruption rates (Fig. 6.1b). This observation could be partially influenced by the discrepancy in the definition of “eruption” between the here presented study and previous studies, such as the distinction between single-phase and multi-phase eruptions. Or, the different cumulative frequency records could indicate differences in eruption behaviour between the adjacent volcanoes. Mts. Ngauruhoe and Tongariro are characterised by more complex geomorphological expressions of the regional tectonic setting (Gómez-Vasconcelos et al., 2017) and given their relative position to the Taupo rift system it is possible that tectonic control on volcanic activity and eruption frequency is stronger compared to the more southward Mt. Ruapehu system. In the past, the peculiar tectonic setting of the TgVC volcanoes has been used to explain the ~200-year period of Plinian eruptions, known as the Mangamate Formation (Heinrich et al., 2020), while the voluminous eruptions of the Mt. Ruapehu-sourced Bullot Formation were linked to increased fault movements in the southern rift extension (Villamor et al., 2007).

This highlights that the factors that control eruption behaviour (and frequency) are different between the two composite volcanoes Mt. Ruapehu and Mt. Tongariro (including Mt. Ngauruhoe), leading to the difference in observed eruption behaviour: While eruptive activity at Mts. Tongariro and Ngauruhoe involves short periods with high-frequency eruptions, Mt. Ruapehu’s eruptive behaviour shows an overall more constant eruption frequency that involves complex multi-phase eruptions.

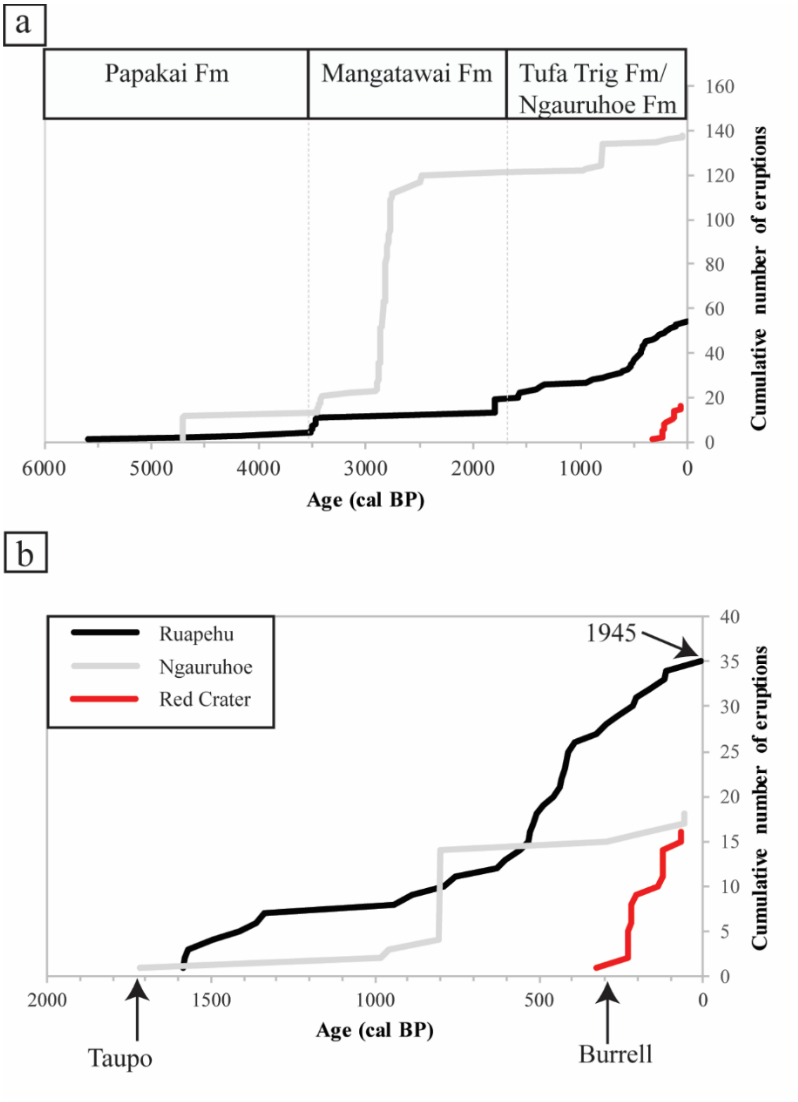

Fig. 6.1: Cumulative eruption frequency distributions for the TgVC volcanoes Mt. Ruapehu (black), Mt. Ngauruhoe (grey) and Red Crater (red). Inset a) shows explosive eruption behaviour over the past ~6000 years, while b) shows only the past 2000 years, excluding historical eruptions. Note that, for Mt. Ruapehu, the historical 1945 eruption is included in the cumulative eruption frequency.

6.3.2 Inception of Crater Lake

In line with the previous studies, it can be inferred that the presence or absence of a Crater Lake in the active vent system controls the dominant fragmentation mechanisms and accordingly the eruption style. Constraining the timing of inception of a permanent Crater Lake in the current vent system is therefore closely related to understanding the long-term eruption behaviour at Mt. Ruapehu. In the following, the tephrostratigraphic framework of the Tufa Trig Formation is combined with previously published data on the contemporaneous lahar formation (Onetapu Formation; Donoghue et al., 2001; Lecointre et al., 2004; Hodgson et al., 2007), to discuss the role of Crater Lake during the past 1800 years.

Based on the age model from Chapter 5 and existing radiocarbon constraints for lahar packages (Hodgson et al., 2007), a schematic overview is shown in Fig. 6.2. Tufa Trig members T1 to T4 coincide with the first Ona-lahar package, which comprises lahars that contain mostly hydrothermally altered and no juvenile material (Hodgson et al., 2007). Following this, Onb has been interpreted to mark the collapse of the wall containing Crater Lake and falls in a time span similar to tephra member T5. The lahars of the following Onc-package contain significant amounts of pumiceous, juvenile material (Hodgson et al., 2007) and potentially coincide with tephra members T6 and T7. Ond-lahars are characterised by dark glassy juvenile clasts and contain lake sediments (Hodgson et al., 2007). These lahars can be associated with the high frequency multi-phase eruptions including T11 to T23. Finally, One-lahars are constrained to ages <410 cal BP, thus coinciding with the time span that includes the tephra members from T24 to today (Fig. 6.2). This suggests that over the time span of the Tufa Trig Formation, Crater Lake has been less permanent than was previously assumed. In particular, the period following the Taupo eruption was characterised by both low-intensity ash-rich eruptions and higher intensity lapilli eruptions suggesting that Crater Lake was unstable and could be displaced quickly to account for the “dry” signatures observed for T2, T5 and T7. It is likely that a permanent Crater Lake started forming out following the rim collapse (Onb) of the proto Crater Lake. During the time span with no and low-intensity eruptions between T7 and T11, there was sufficient time to form out a more or less permanent Crater Lake system, as it exists today, where major eruptions and prolonged multi-phase eruption sequences are associated with periodic lake displacement and successive lake refill (Fig. 6.2).

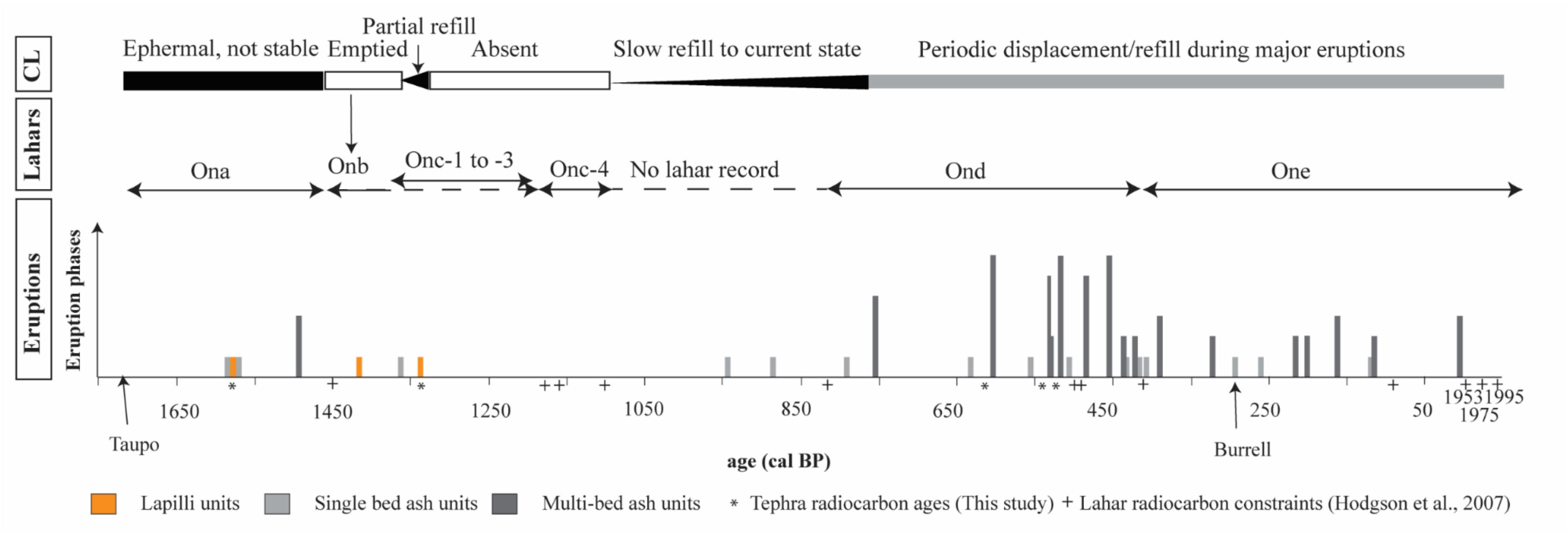

Fig. 6.2: Schematic overview of the post-Taupo timeline integrating the Tufa Trig tephra record with previously published studies on the lahar deposits of the Onetapu Formation (Donoghue et al., 2001; Lecointre et al., 2004; Hodgson et al., 2007). CL marks the evolution of Crater Lake. Radiocarbon ages are marked by stars for tephras and by plus signs for lahars and are reported in cal BP (Hodgson et al., 2007).

6.3.3 Implications for hazard assessment and future eruptions

Current eruption scenarios and response exercises at Mt. Ruapehu align with the historically most frequent observed eruptions (Scott, 2013) and are based on a short-lived, small-scale phreatic-phreatomagmatic eruption, with a strong focus on lahar hazards (Fig. 6.3). The volume of juvenile magma involved is potentially very small and the associated eruption intensity is relatively low leading to limited tephra dispersal. From the 2007 blue sky eruption it can be inferred that the main hazards comprise local ashfall affecting the summit area, small pyroclastic density currents (PDCs), snow-slurry lahars and ballistics (Lube et al., 2009; Kilgour et al., 2010). Although the affected area is comparably small, this scenario bears different risks, which are mainly influenced by the paucity of precursors, as seen during the 2007 event (Jolly et al., 2010). In future eruption crises, fast sampling and componentry analysis should aid in identifying the presence and quantity of juvenile glass to confirm or exclude this scenario. Due to the magnitude of the associated eruptive products ($\leq \sim 1 \times 10^5$ m^3), this eruption type is not represented in the tephra record and therefor no frequency information is available over long timescales.

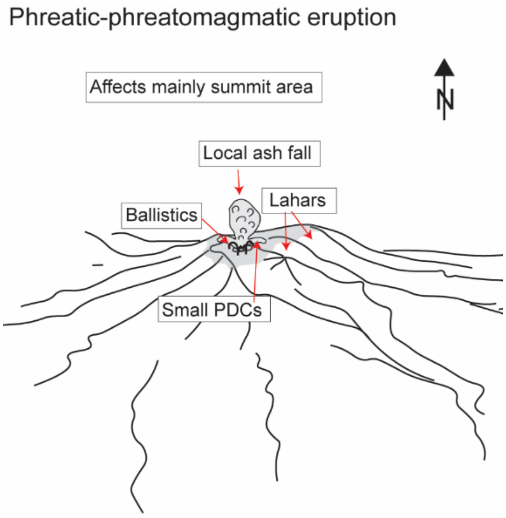

Fig. 6.3: Eruption scenario as inferred from the historically most frequent small-scale, short-lived phreatic and phreatomagmatic eruptions (Scott, 2013). Note that these eruptions typically affect the summit area.

However, following the re-defined tephra record, it becomes evident that eruption behaviour at Mt. Ruapehu is more complex and varies in key parameters such as duration, magnitude and intensity and involves both single-phase and multi-phase eruptions. For hazard management and response planning this means that in the future, additional eruption scenarios need to be considered that account for the range in the above-mentioned key parameters. In the following, three main likely eruption scenarios and their key parameters as inferred from the 1800-year tephra record are discussed and illustrated schematically in Fig. 6.4: (1) The first eruption scenario comprises a small volume low-intensity eruption (Fig. 6.4a) with minimum tephra volumes of ~1 × 10^6 m^3 and predominantly phreatomagmatic features such as high proportions of lithics and extremely fine ash and poorly vesicular clasts. Deposit characteristics of the associated single bed ash units suggest that tephra distribution is spatially limited to the Tongariro National Park area and the Rangipo Desert. Main associated hazards result from ashfall and the ejection of ballistics in the summit area. This scenario is potentially associated with small-scale lahars or snow-slurry lahars and small-scale pyroclastic density currents, as has been observed during the 2007 eruption (Lube et al., 2009; Kilgour et al., 2010). The magmatic component of this eruption type distinguishes it from the previously described phreatic-phreatomagmatic scenario, suggesting higher proportions of juvenile glass, relatively higher eruption intensity and more extensive tephra dispersal. The involved magmatic component makes it likely that magma migration prior to eruption potentially creates detectable seismic signals. However, given the small involved magma volumes, potential precursors might be short-scale or masked. (2) A second eruption scenario involves moderate intensity eruptions with tephra volumes of 5–10 × 10^6 m^3 (Fig. 6.4b). The spatially limited deposit dispersal indicates that associated eruptions are sufficiently short-lived to not be affected by syn-eruptive wind changes. Resulting main hazards are associated with airfall of lapilli-sized pyroclasts. In the investigated distance range no field evidence is available to quantify the nature and type of ballistic ejecta, but it can be assumed that the near-vent area would be affected by ballistics. The vesiculated nature of the pyroclasts and the decreasing amount of dense ash-sized pyroclast indicates the importance of magmatic over phreatomagmatic fragmentation, which is potentially associated with an absent Crater Lake. In this case, the range of associated hazards should be expanded to include dome extrusion and accordingly, potentially pyroclastic density currents (cf. Neall et al., 1999). However, in the investigated distance range, no field evidence for pyroclastic density currents could be identified. The observation, that lapilli-sized pyroclasts can reach distances >15 km, has implications for hazard management, as this scenario has the potential to significantly affect New Zealand’s State Highway 1, which passes the Rangipo Desert at ~15 km distance from the vent (Fig. 6.4b). In case of southern winds, the northward Tongariro Alpine Crossing, which is a popular tourist destination would be similarly affected (Fig. 6.4b). No comparable eruptions are known historically. This makes the discussion of the nature and timescales of precursory signals difficult, highlighting the need for detailed research to constrain the source and migration path of the magma that feeds these eruptions. However, it can be speculated that, given the volume of juvenile magma involved in this eruption, magma migration should be detectable prior to eruptions. Similarly, in line with the previously discussed ephermal nature of the Crater Lake >800 cal BP, this eruption scenario should be considered in relation with dam break events, when the Crater Lake is absent.

(3) Finally, based on the tephra record, the most likely eruption scenario involves prolonged multi-phase eruptions involving variable eruption intensities and variable number of phases (Fig. 6.4c-f). Cumulative tephra volumes range in the order of magnitude of 1–10 × 10^7 m^3, while volumes for individual eruption phases can span serval orders of magnitude (~1 × 10^5 $m^3$to ~1 × 10^7 m^3). Main hazards result from ashfall that covers extended areas, associated with the long duration of this type of eruption and the areas at risk being subject to syn-eruptive variations in wind pattern (e.g., Fig. 6.4e). In case of lake displacement with eruption progression, dome formation and the possibility of small-scale pyroclastic density currents due to dome disruption should be taken in account, although no field evidence is available to constrain the frequency and magnitude of similar events for the past 1800 years. Similarly, while the tephra record does not contain information on potential ballistic ejecta, it can be assumed that at least the summit area would be affected.

A comparison for this scenario can be drawn to the 1995–1996 eruption, which suggests that individual eruption phases are likely accompanied (or followed) by different types of lahars (Cronin et al., 1997a; Cronin et al., 1997b). However, it needs to be kept in mind, that the multi-phase eruptions preserved in the geological record are at least one magnitude larger than the 1995–1996 eruptions and that the latter therefore constitute at best an absolute minimum scenario, while a scenario similar to the T13-sequence should be considered as a potential worst-case scenario. This implies that, given the volumes involved, precursory signals indicative of magma migration can be potentially detected before eruption onset or during eruption progression. However, for the T13-eruption it has been seen, that eruption progression does not necessarily involve the discrete syn-sequence injection of "fresh" magma, suggesting that syn-eruptive precursors that herald the next phase are potentially absent. Similarly, based on the current knowledge, probabilistic forecast modelling of the potential next phase in eruption progression is limited by the statistical independence of individual phases to each other.

To conclude, while it is unlikely that future response exercises will implement prolonged eruptive activity over months to years, given the frequency of these eruptions in the 1800-year tephra record, it is crucial that the current hazard management plans are updated with regard to this worst-case scenario.

Fig. 6.4 (next page): Schematic visualisation of the main eruption scenarios as inferred from the 1800-year tephra record. For comparison, 10 and 15 km distances are indicated by red circles and the position of State Highway 1 is shown by a yellow line. Column heights are not to scale. a) Low-intensity small volume eruption resulting in single bed ash units. The extent of associated ash-rich deposits is limited to the most proximal ~10 km. b) Moderate intensity eruption leading to lapilli deposits. This type of eruptions is probably associated with the absence of Crater Lake in the active vent leading to short-lived eruptions dominated by magmatic fragmentation and the dispersal of lapilli-sized material to distances >15 km. Insets c), d), e) and f) show different phases of a multi-phase eruption leading to a multi-bed deposit. c) shows the opening phase(s), which are of low intensity and dominated by phreatomagmatic activity. Syn-eruptive changes in wind patterns lead to the dispersal of ash-sized material in different directions. d) The pre-climactic phase(s) is associated with a change in eruption intensity compared to the opening phase(s) and leads to ashfall in different directions and, depending on the eruption intensity, at different distances. d) The climactic, semi-continuous phase of the multi-phase eruption is associated with irregular multi-lobate deposits that are associated with changes in eruption intensity such as waning and waxing, multiple individual fall events and syn-eruptive changes in wind pattern. f) Following the climactic phase, a post-climactic phase emits ash over prolonged periods leading to mostly local ashfall that might affect large areas depending on the prevailing wind conditions.

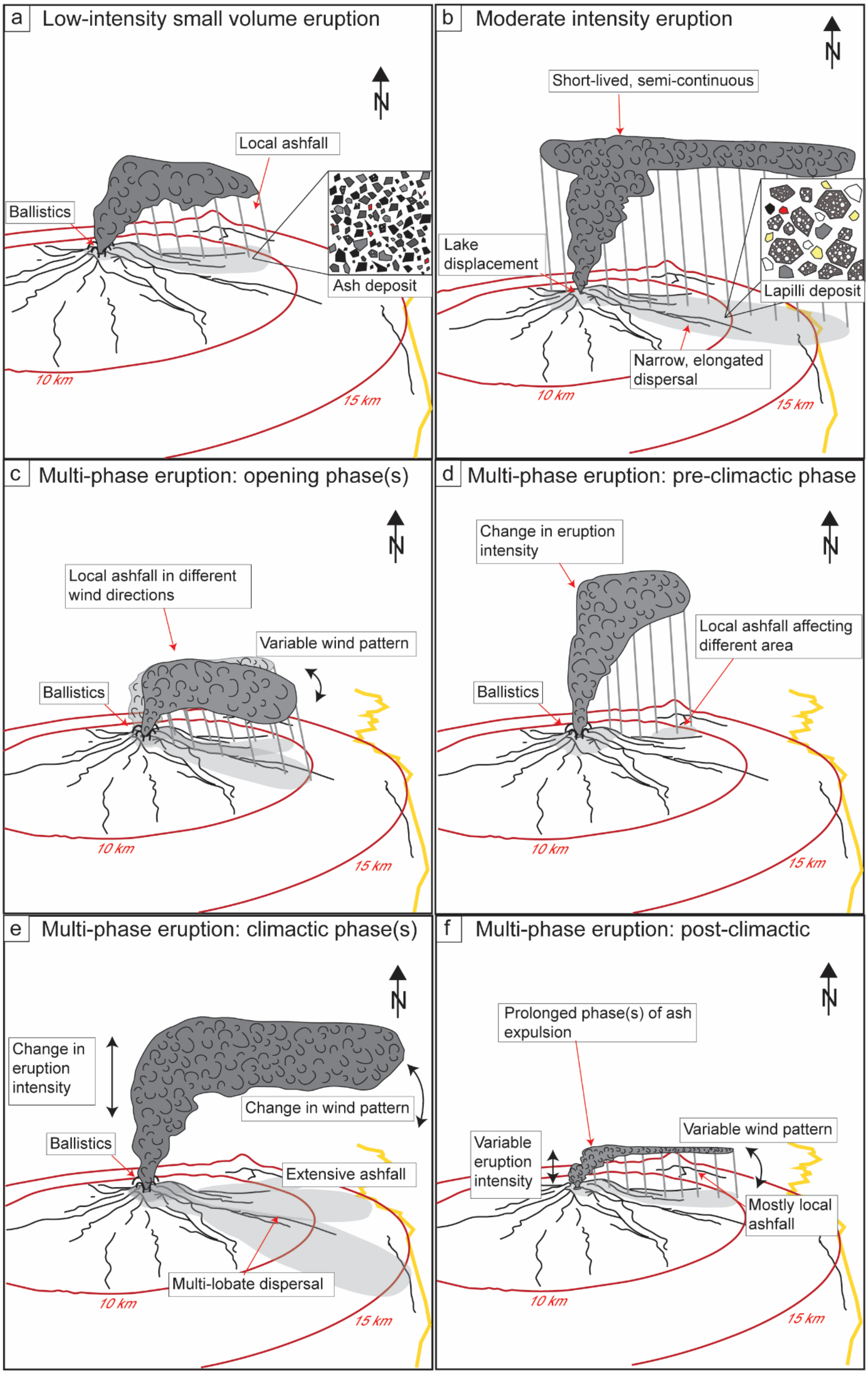
a
Low-intensity small volume eruption
Local ashfall
Ballistics
Ash deposit
10 km
15 km
N
b
Moderate intensity eruption
Short-lived, semi-continuous
Lake displacement
Lapilli deposit
Narrow, elongated dispersal
10 km
15 km
N
c
Multi-phase eruption: opening phase(s)
Local ashfall in different wind directions
Variable wind pattern
Ballistics
10 km
15 km
N
d
Multi-phase eruption: pre-climactic phase
Change in eruption intensity
Local ashfall affecting different area
Ballistics
10 km
15 km
N
e
Multi-phase eruption: climactic phase(s)
Change in eruption intensity
Ballistics
Change in wind pattern
Extensive ashfall
Multi-lobate dispersal
10 km
15 km
N
f
Multi-phase eruption: post-climactic
Prolonged phase(s) of ash expulsion
Variable wind pattern
Variable eruption intensity
Mostly local ashfall
10 km
15 km
N

6.4 Conclusive remarks

The objectives and goals that were introduced in Chapter 1 have been successfully addressed throughout the chapters of this study. In Chapter 3, a detailed tephrostratigraphic framework was combined with geochemical fingerprinting and new age constrains were introduced. Similarly, information on eruption style, frequency and magnitude for single-phase and multi-phase eruptions at Mt. Ruapehu over the past 1800 years was obtained from the lithosedimentological characterisation of key units, in line with Objective 1. Objective 2 has been addressed by investigating the multi-bed T13-tephra sequence in Chapter 4. Here, eruption progression of a characteristic prolonged multi-phase eruption was reconstructed by quantifying lithosedimentological parameters of individual subunits within the tephra sequence and by characterising syn-eruptive changes in geochemical and textural characteristics of the juvenile material. The integration of the frequency-magnitude record with a statistical age model and major element data over the past 1800 years has provided the basis for probabilistic modelling on both short- and long-term scales, highlighting the value of long-term geological multi-phase records for eruption forecast and has been discussed in Chapter 5. This has contributed to the identification of time-variable pattern in eruption behaviour and has fulfilled Objective 3. In addition, Chapter 6 presents key findings and overarching questions, outlining the contribution of this PhD research to refining eruption frequency patterns in the Tongariro National Park, to constrain the inception of a permanent Crater Lake in Mt. Ruapehu’s active vent system and to outline the implications for future eruptions and hazard assessments.

References

Arrighi, S., Principe, C., & Rosi, M. (2001). Violent strombolian and subplinian eruptions at Vesuvius during post-1631 activity. *Bulletin of Volcanology, 63*(2), 126-150. doi:https://doi.org/10.1007/s004450100130

Barberi, F., Bertagnini, A., Landi, P., & Principe, C. (1992). A review on phreatic eruptions and their precursors. *Journal of Volcanology and Geothermal Research, 52*(4), 231-246. doi:https://doi.org/10.1016/0377-0273(92)90046-G

Bebbington, M. S., & Jenkins, S. F. (2019). Intra-eruption forecasting. *Bulletin of Volcanology, 81*(6), 34. doi:https://doi.org/10.1007/s00445-019-1294-9

Bonadonna, C., & Costa, A. (2012). Estimating the volume of tephra deposits: A new simple strategy. *Geology, 40*(5), 415-418. doi:https://doi.org/10.1130/G32769.1

Bonadonna, C., & Costa, A. (2013). Plume height, volume, and classification of explosive volcanic eruptions based on the Weibull function. *Bulletin of Volcanology, 75*(8), 742. doi:https://doi.org/10.1007/s00445-013-0742-1

Bonadonna, C., Genco, R., Gouhier, M., Pistolesi, M., Cioni, R., Alfano, F., Hoskuldsson, A., & Ripepe, M. (2011). Tephra sedimentation during the 2010 Eyjafjallajökull eruption (Iceland) from deposit, radar, and satellite observations. *Journal of Geophysical Research: Solid Earth, 116*(B12). doi:https://doi.org/10.1029/2011jb008462

Bustillos A., J., Romero, J. E., Troncoso, L., & Guevara C., A. (2016). Tephra fall at Tungurahua Volcano (Ecuador) - 1999-2014: An Example of Tephra Accumulation from a Long-lasting Eruptive Cycle. *Geofísica internacional, 55*, 55-67.

Cioni, R., Bertagnini, A., Santacroce, R., & Andronico, D. (2008a). Explosive activity and eruption scenarios at Somma-Vesuvius (Italy): Towards a new classification scheme. *Journal of Volcanology and Geothermal Research, 178*(3), 331-346. doi:https://doi.org/10.1016/j.jvolgeores.2008.04.024

Cioni, R., D'Oriano, C., & Bertagnini, A. (2008b). Fingerprinting ash deposits of small scale eruptions by their physical and textural features. *Journal of Volcanology and Geothermal Research, 177*(1), 277-287. doi:https://doi.org/10.1016/j.jvolgeores.2008.06.003

Conway, C. E., Gamble, J. A., Wilson, C. J., Leonard, G. S., Townsend, D. B., & Calvert, A. T. (2018). New petrological, geochemical, and geochronological perspectives on andesite-dacite magma genesis at Ruapehu volcano, New Zealand. *American Mineralogist: Journal of Earth and Planetary Materials, 103*(4), 565-581. doi:ttps://doi.org/10.2138/am-2018-6199

Cronin, S. J., Hodgson, K. A., Neall, V. E., Palmer, A. S., & Lecointre, J. A. (1997a). 1995 Ruapehu lahars in relation to the late Holocene lahars of Whangaehu River, New Zealand. *New Zealand Journal of Geology and Geophysics, 40*(4), 507-520. doi:https://doi.org/10.1080/00288306.1997.9514780

Cronin, S. J., Neall, V. E., Lecointre, J. A., Hedley, M. J., & Loganathan, P. (2003). Environmental hazards of fluoride in volcanic ash: a case study from Ruapehu volcano, New Zealand. *Journal of Volcanology and Geothermal Research, 121*, 271-291. doi:https://doi.org/10.1016/S0377-0273(02)00465-1

Cronin, S. J., Neall, V. E., Lecointre, J. A., & Palmer, A. S. (1997b). Changes in Whangaehu river lahar characteristics during the 1995 eruption sequence, Ruapehu volcano, New Zealand. *Journal of Volcanology and Geothermal Research, 76*(1), 47-61. doi:https://doi.org/10.1016/S0377-0273(96)00064-9

Dellino, P., Gudmundsson, M., Larsen, G., Mele, D., Stevenson, J., Thordarson, T., & Zimanowski, B. (2012). Ash from the Eyjafjallajökull eruption (Iceland): Fragmentation processes and aerodynamic behavior. *Journal of Geophysical Research: Solid Earth, 117*(B9). doi:https://doi.org/10.1029/2011JB008726

Donoghue, S. L., & Neall, V. E. (2001). Late Quaternary constructional history of the southeastern Ruapehu ring plain, New Zealand. *New Zealand Journal of Geology and Geophysics, 44*(3), 439-466. doi:https://doi.org/10.1080/00288306.2001.9514949

Donoghue, S. L., Neall, V. E., & Palmer, A. S. (1995). Stratigraphy and chronology of late Quaternary andesitic tephra deposits, Tongariro Volcanic Centre, New Zealand. *Journal of the Royal Society of New Zealand, 25*(2), 115-206. doi:https://doi.org/10.1080/03014223.1995.9517487

Donoghue, S. L., Neall, V. E., Palmer, A. S., & Stewart, R. B. (1997). The volcanic history of Ruapehu during the past 2 millenia based on the record of Tufa Trig tephras. *Bulletin of Volcanology, 59*, 136-146. doi:https://doi.org/10.1007/s004450050181

Fierstein, J., & Nathenson, M. (1992). Another look at the calculation of fallout tephra volumes. *Bulletin of Volcanology, 54*(2), 156-167. doi:https://doi.org/10.1007/bf00278005

Gamble, J. A., Wood, C. P., Price, R. C., Smith, I. E. M., Stewart, R. B., & Waight, T. (1999). A fifty year perspective of magmatic evolution on Ruapehu Volcano, New Zealand: verification of open system behaviour in an arc volcano. *Earth and Planetary Science Letters, 170*, 301-314. doi:https://doi.org/10.1016/S0012-821X(99)00106-5

Gómez-Vasconcelos, M. G., Villamor, P., Cronin, S., Procter, J., Palmer, A., Townsend, D., & Leonard, G. (2017). Crustal extension in the Tongariro graben, New Zealand: Insights into volcano-tectonic interactions and active deformation in a young continental rift. *GSA Bulletin, 129*(9-10), 1085-1099. doi:https://doi.org/10.1130/B31657.1

Greve, A., Turner, G. M., Conway, C. E., Townsend, D. B., Gamble, J. A., & Leonard, G. S. (2016). Palaeomagnetic refinement of the eruption ages of Holocene lava flows, and implications for the eruptive history of the Tongariro Volcanic Centre, New Zealand. *Geophysical Journal International, 207*(2), 702-718. doi:https://doi.org/10.1093/gji/ggw296

Gudmundsson, M. T., Pedersen, R., Vogfjörd, K., Thorbjarnardóttir, B., Jakobsdóttir, S., & Roberts, M. J. (2010). Eruptions of Eyjafjallajökull Volcano, Iceland. *Eos, Transactions American Geophysical Union, 91*(21), 190-191. doi:https://doi.org/10.1029/2010EO210002

Gudmundsson, M. T., Thordarson, T., Höskuldsson, Á., Larsen, G., Björnsson, H., Prata, F. J., Oddsson, B., Magnússon, E., Högnadóttir, T., Petersen, G. N., Hayward, C. L., Stevenson, J. A., & Jónsdóttir, I. (2012). Ash generation and distribution from the April-May 2010 eruption of Eyjafjallajökull, Iceland. *Scientific Reports, 2*(1), 572. doi:https://doi.org/10.1038/srep00572

Heinrich, M., Cronin, S. J., & Pardo, N. (2020). Understanding multi-vent Plinian eruptions at Mt. Tongariro Volcanic Complex, New Zealand. *Bulletin of Volcanology, 82*(3), 30. doi:https://doi.org/10.1007/s00445-020-1369-7

Hobden, B. J., Houghton, B. F., Davidson, J. P., & Weaver, S. D. (1999). Small and short-lived magma batches at composite volcanoes: time windows at Tongariro volcano, New Zealand. *Journal of the Geological Society, 156*(5), 865-868. doi:https://doi.org/10.1144/gsjgs.156.5.0865

Hobden, B. J., Houghton, B. F., & Nairn, I. A. (2002). Growth of a young, frequently active composite cone: Ngauruhoe volcano, New Zealand. *Bulletin of Volcanology, 64*(6), 392-409. doi:https://doi.org/10.1007/s00445-002-0216-3

Hodgson, K. A., Lecointre, J. A., & Neall, V. E. (2007). Onetapu Formation: The last 2000 yr of laharic activity at Ruapehu volcano, New Zealand. *New Zealand Journal of Geology and Geophysics, 50*(2), 81-99. doi:https://doi.org/10.1080/00288300709509823

Jenkins, S. F., Magill, C. R., & McAneney, K. J. (2007). Multi-stage volcanic events: A statistical investigation. *Journal of Volcanology and Geothermal Research, 161*(4), 275-288. doi:https://doi.org/10.1016/j.jvolgeores.2006.12.005

Johnston, D. M., Houghton, B. F., Neall, V. E., Ronan, K. R., & Paton, D. (2000). Impacts of the 1945 and 1995-1996 Ruapehu eruptions, New Zealand: An example of increasing societal vulnerability. *Geological Society of America Bulletin, 112*(5), 720-726. doi:https://doi.org/10.1130/0016-7606(2000)112<720:IOTARE>2.0.CO;2

Jolly, A. D., Sherburn, S., Jousset, P., & Kilgour, G. (2010). Eruption source processes derived from seismic and acoustic observations of the 25 September 2007 Ruapehu eruption—North Island, New Zealand. *Journal of Volcanology and Geothermal Research, 191*(1–2), 33-45. doi:https://doi.org/10.1016/j.jvolgeores.2010.01.009

Kilgour, G., Blundy, J., Cashman, K., & Mader, H. M. (2013). Small volume andesite magmas and melt–mush interactions at Ruapehu, New Zealand: evidence from melt inclusions. *Contributions to Mineralogy and Petrology, 166*(2), 371-392. doi:https://doi.org/10.1007/s00410-013-0880-7

Kilgour, G., Mader, H., Blundy, J., & Brooker, R. (2016). Rheological controls on the eruption potential and style of an andesite volcano: A case study from Mt. Ruapehu, New Zealand. Journal of Volcanology and Geothermal Research, 327, 273-287. doi:https://doi.org/10.1016/j.jvolgeores.2016.08.001

Kilgour, G., Manville, V., Pasqua, F. D., Graettinger, A., Hodgson, K. A., & Jolly, G. E. (2010). The 25 September 2007 eruption of Mount Ruapehu, New Zealand: Directed ballistics, surtseyan jets, and ice-slurry lahars. *Journal of Volcanology and Geothermal Research, 191*(1–2), 1-14. doi:http://dx.doi.org/10.1016/j.jvolgeores.2009.10.015

Lecointre, J., Hodgson, K., Neall, V., & Cronin, S. (2004). Lahar-Triggering Mechanisms and Hazard at Ruapehu Volcano, New Zealand. *Natural Hazards, 31*(1), 85-109. doi:https://doi.org/10.1023/B:NHAZ.0000020256.16645.eb

Lowe, D. J., Shane, P. A. R., Alloway, B. V., & Newnham, R. M. (2008). Fingerprints and age models for widespread New Zealand tephra marker beds erupted since 30,000 years ago: a framework for NZ-INTIMATE. *Quaternary Science Reviews, 27*(1), 95-126. doi:https://doi.org/10.1016/j.quascirev.2007.01.013

Lube, G., Breard, E. C. P., Cronin, S. J., Procter, J. N., Brenna, M., Moebis, A., Pardo, N., Stewart, R. B., Jolly, A., & Fournier, N. (2014). Dynamics of surges generated by hydrothermal blasts during the 6 August 2012 Te Maari eruption, Mt. Tongariro, New Zealand. *Journal of Volcanology and Geothermal Research, 286*, 348-366. doi:https://doi.org/10.1016/j.jvolgeores.2014.05.010

Lube, G., Cronin, S. J., & Procter, J. N. (2009). Explaining the extreme mobility of volcanic ice-slurry flows, Ruapehu volcano, New Zealand. *Geology, 37*(1), 15-18. doi:https://doi.org/10.1130/g25352a.1

Miwa, T., Geshi, N., & Shinohara, H. (2013). Temporal variation in volcanic ash texture during a vulcanian eruption at the Sakurajima volcano, Japan. Journal of Volcanology and Geothermal Research, 260, 80-89. doi:https://doi.org/10.1016/j.jvolgeores.2013.05.010

Miyabuchi, Y., Hanada, D., Niimi, H., & Kobayashi, T. (2013). Stratigraphy, grain-size and component characteristics of the 2011 Shinmoedake eruption deposits, Kirishima Volcano, Japan. Journal of Volcanology and Geothermal Research, 258, 31-46. doi:https://doi.org/10.1016/j.jvolgeores.2013.03.027

Miyabuchi, Y., Iizuka, Y., Hara, C., Yokoo, A., & Ohkura, T. (2018). The September 14, 2015 phreatomagmatic eruption of Nakadake first crater, Aso Volcano, Japan: Eruption sequence inferred from ballistic, pyroclastic density current and fallout deposits. *Journal of Volcanology and Geothermal Research, 351*, 41-56. doi:https://doi.org/10.1016/j.jvolgeores.2017.12.009

Miyabuchi, Y., & Hara, C. (2019). Temporal variations in discharge rate and component characteristics of tephra-fall deposits during the 2014–2015 eruption of Nakadake first crater, Aso Volcano, Japan. *Earth, Planets and Space, 71*(1), 44. doi:https://doi.org/10.1186/s40623-019-1018-6

Moebis, A., Cronin, S. J., Neall, V. E., & Smith, I. E. (2011). Unravelling a complex volcanic history from fine-grained, intricate Holocene ash sequences at the Tongariro Volcanic Centre, New Zealand. *Quaternary International, 246*(1–2), 352-363. doi:http://dx.doi.org/10.1016/j.quaint.2011.05.035

Mujin, M., & Nakamura, M. (2020). Late-stage groundmass differentiation as a record of magma stagnation, fragmentation, and rewelding. Bulletin of Volcanology, 82, 1-17.

Nairn, I. A., & Group, R. S. (1996). Volcanic eruption at a New Zealand ski resort prompts reevaluation of hazards. *Eos, Transactions American Geophysical Union, 77*(20), 189-191. doi:http://dx.doi.org/10.1029/96EO00129

Nairn, I. A., & Self, S. (1978). Explosive eruptions and pyroclastic avalanches from Ngauruhoe in February 1975. *Journal of Volcanology and Geothermal Research, 3*(1), 39-60. doi:https://doi.org/10.1016/0377-0273(78)90003-3

Nairn, I. A., Shane, P. R., Cole, J. W., Leonard, G. J., Self, S., & Pearson, N. (2004). Rhyolite magma processes of the ∼AD 1315 Kaharoa eruption episode, Tarawera volcano, New Zealand. *Journal of Volcanology and Geothermal Research, 131*(3), 265-294. doi:https://doi.org/10.1016/S0377-0273(03)00381-0

Nakada, S., Nagai, M., Kaneko, T., Suzuki, Y., & Maeno, F. (2013). The outline of the 2011 eruption at Shinmoe-dake (Kirishima), Japan. Earth, Planets and Space, 65(6), 1. doi:10.5047/eps.2013.03.016

Nakagawa, M., Wada, K., Thordarson, T., Wood, C. P., & Gamble, J. A. (1999). Petrologic investigations of the 1995 and 1996 eruptions of Ruapehu volcano, New Zealand: formation of discrete and small magma pockets and their intermittent discharge. *Bulletin of Volcanology, 61*, 15-31. doi:https://doi.org/10.1007/s004450050259

Nakagawa, M., Wada, K., & Wood, C. P. (2002). Mixed Magmas, Mush Chambers and Eruption Triggers: Evidence from Zoned Clinopyroxene Phenocrysts in Andesitic Scoria from the 1995 Eruptions of Ruapehu Volcano, New Zealand. *Journal of Petrology, 43*(12), 2279-2303. doi:https://doi.org/10.1093/petrology/43.12.2279

Neall, V. E., Houghton, B. F., Cronin, S. J., Donoghue, S. L., Hodgson, K. A., Johnston, D. M., Lecointre, J. A., & Mitchell, A. R. (1999). Volcanic Hazards at Ruapehu Volcano. *Ministry of Civil Defense, Volcanic Hazards Information Series No. 8*.

Newhall, C. G., & Self, S. (1982). The volcanic explosivity index (VEI) an estimate of explosive magnitude for historical volcanism. *Journal of Geophysical Research: Oceans, 87*(C2), 1231-1238. doi: https://doi.org/10.1029/JC087iC02p01231

Pardo, N., Cronin, S. J., Németh, K., Brenna, M., Schipper, C. I., Breard, E., White, J. D. L., Procter, J., Stewart, B., Agustín-Flores, J., Moebis, A., Zernack, A., Kereszturi, G., Lube, G., Auer, A., Neall, V., & Wallace, C. (2014). Perils in distinguishing phreatic from phreatomagmatic ash; insights into the eruption mechanisms of the 6 August 2012 Mt. Tongariro eruption, New Zealand. *Journal of Volcanology and Geothermal Research, 286*, 397-414. doi:http://dx.doi.org/10.1016/j.jvolgeores.2014.05.001

Price, R. C., Gamble, J. A., Smith, I. E. M., Maas, R., Waight, T., Stewart, R. B., & Woodhead, J. (2012). The Anatomy of an Andesite Volcano: a Time-Stratigraphic Study of Andesite Petrogenesis and Crustal Evolution at Ruapehu Volcano, New Zealand. *Journal of Petrology, 53*(10), 2139-2189. doi:https://doi.org/10.1093/petrology/egs050

Price, R. C., Gamble, J. A., Smith, I. E. M., Stewart, R. B., Eggins, S., & Wright, I. C. (2005). An integrated model for the temporal evolution of andesites and rhyolites and crustal development in New Zealand's North Island. *Journal of Volcanology and Geothermal Research, 140*(1-3), 1-24. doi:https://doi.org/10.1016/j.jvolgeores.2004.07.013

Purves, A. (1990). *Landscape ecology of the Rangipo Desert.* (Master), Massey University, Palmerston North.

Rose, W. I. (1993). Comment on 'another look at the calculation of fallout tephra volumes' by Judy Fierstein and Manuel Nathenson. *Bulletin of Volcanology, 55*(5), 372-374. doi:https://doi.org/10.1007/bf00301148

Scott, B. J. (2013). A revised catalogue of Ruapehu volcano eruptive activity: 1830-2012. *GNS Science Report, 2013/45*.

Scott, B. J., & Potter, S. H. (2014). Aspects of historical eruptive activity and volcanic unrest at Mt. Tongariro, New Zealand: 1846–2013. *Journal of Volcanology and Geothermal Research*, *286*, 263-276. doi:http://dx.doi.org/10.1016/j.jvolgeores.2014.04.003

Shane, P., Cocker, K., Coote, A., Stirling, C. H., & Reid, M. R. (2019). The prevalence of plagioclase antecrysts and xenocrysts in andesite magma, exemplified by lavas of the Tongariro volcanic complex, New Zealand. *Contributions to Mineralogy and Petrology, 174*(11), 89. doi:https://doi.org/10.1007/s00410-019-1626-y

Shane, P., Maas, R., & Lindsay, J. (2017). History of Red Crater volcano, Tongariro Volcanic Centre (New Zealand): Abrupt shift in magmatism following recharge and contrasting evolution between neighboring volcanoes. *Journal of Volcanology and Geothermal Research, 340*, 1-15. doi:https://doi.org/10.1016/j.jvolgeores.2017.04.008

Siebert, L., Cottrell, E., Venzke, E., & Andrews, B. (2015). Earth's Volcanoes and Their Eruptions: An Overview. In H. Sigurdsson (Ed.), *The Encyclopedia of Volcanoes (Second Edition)* (pp. 239-255). Amsterdam: Academic Press.

Suzuki, Y., Nagai, M., Maeno, F., Yasuda, A., Hokanishi, N., Shimano, T., Ichihara, M., Kaneko, T., & Nakada, S. (2013). Precursory activity and evolution of the 2011 eruption of Shinmoe-dake in Kirishima volcano—insights from ash samples. Earth, Planets and Space, 65(6), 11. doi:10.5047/eps.2013.02.004

Villamor, P., Van Dissen, R., Alloway, B. V., Palmer, A. S., & Litchfield, N. (2007). The Rangipo fault, Taupo rift, New Zealand: An example of temporal slip-rate and single-event displacement variability in a volcanic environment. *GSA Bulletin, 119*(5-6), 529-547. doi:https://doi.org/10.1130/B26000.1

Walker, G. P. (1973). Explosive volcanic eruptions—a new classification scheme. *Geologische Rundschau, 62*(2), 431-446.

Zdanowicz, G., Boudon, G., Balcone-Boissard, H., Cioni, R., Mundula, F., Orsi, G., Civetta, L., & Agrinier, P. (2018). Geochemical and textural constraints on degassing processes in sub-Plinian eruptions: case-study of the Greenish Pumice eruption of Mount Somma-Vesuvius. Bulletin of Volcanology, 80(4), 38. doi:10.1007/s00445-018-1213-5

Zimanowski, B., Büttner, R., Dellino, P., White, J. D., & Wohletz, K. H. (2015). Magma–water interaction and phreatomagmatic fragmentation *The Encyclopedia of Volcanoes (Second Edition)* (pp. 473-484). Amsterdam: Academic Press.

Chapter 7

Conclusions

This chapter summarises the specific findings of this PhD research and presents an outlook for future research topics.

7.1 Conclusions

With this research the overarching hypothesis introduced in Chapter 1 has been confirmed, showing how a high-resolution tephra record can contribute information on eruption frequency, magnitude and style and how it improves the understanding of the eruption dynamics associated with small to moderate multi-phase eruptions at Mt. Ruapehu. Changes in eruption behaviour can be related to physico-chemical processes in the volcanic system, acting on different timescales and provide insights into the factors that control changes in eruption behaviour at a frequently active, long-lived andesitic volcano. In conclusion, the specific findings of the here presented PhD research can be summarised as follows:

- The previously existing eruption record of Mt. Ruapehu of the past 1800 years has been expanded to now include at least 31 correlated tephra members.
- The 31 tephra members have been shown to be all Mt. Ruapehu-sourced. It has been shown that they can be grouped into three main deposit types, which vary in their deposit texture, lithosedimentological characteristics and pyroclast assemblages and are representative of different eruption styles and magnitudes.
- *Single bed ash units* represent small volume low-intensity eruptions of predominantly phreatomagmatic eruptions and constitute 35% of the 1800-year record. Associated deposit volumes range in the order of magnitude of ~1–10 × 10^5 m^3.
- *Lapilli units* constitute 10% of the Tufa Trig Formation and contain vesicular, cm-sized pyroclasts that are distributed up to 20 km from source. They show evidence for dry magmatic fragmentation and are associated with a higher eruption

intensity than the small volume low-intensity eruptions that deposit single bed ash units. Deposit volumes are estimated to 5–10 × 10^6 m^3.

- *Multi-bed ash units* constitute 55% of the tephra record and are associated with multi-phase eruptions of variable complexity. Cumulative unit volumes are in the order of magnitude of 15–70 × 10^6 m^3 with individual subunits showing variable volumes between 4–37 × 10^6 m^3.
- The T13-tephra sequence marks the largest eruption of the past two millennia and constitutes a realistic worst-case scenario for future eruptions, involving a prolonged, months to years long, multi-phase eruption with at least five eruption phases of variable eruption intensity and magnitude.
- The T13-sequence had an opening phase that involved mostly phreatomagmatic eruptions and became increasingly magmatic and more violent with eruption progression.
- Pyroclast assemblages and pyroclast characteristics suggest an interplay of variably dominant phreatomagmatic and magmatic fragmentation mechanisms during each eruption phase within the multi-phase sequence.
- Irregular multi-lobate isopachs in combination with lateral variance in the pyroclast assemblages show that individual phases of the T13-sequence represent several individual fall events.
- Syn-sequence major and trace element compositions show a limited variability and involve minor systematic changes. Major and trace element glass compositions cannot be used to correlate individual subunits.
- The entire T13-sequence was fed by compositionally slightly different magma batches originating from a compositionally similar parental magma. This differs from the compositional heterogeneity that was observed for e.g. the historical 1995–1996 eruptions.
- Changes in syn-eruptive eruption behaviour can be related to shallow processes in the conduit, such as late-stage microlite crystallisation and variations in magma viscosity, degassing and magma ascent rates.
- New age constraints involve dating tephra members T13, T15 and T17 and the geochemical identification of the AD 1655 Burrell Lapilli as a stratigraphic marker and are integrated within a statistical age model.
- Over the past two millennia, Mt. Ruapehu’s eruptive behaviour shows time-variant pattern regarding eruption frequency and magnitude.

- The past 1800 years can be subdivided into four periods, which can be described by three regimes: the time span between 1718–1300 cal BP involves a medium eruption rate with one eruption every ~40 years while the time span between 1300–610 cal BP has a low eruption rate of one eruption every ~125 years. The period between 610 and 370 cal BP has a high eruption frequency with one eruption every 10 years, while the last 370 years are associated with a medium eruption rate again.
- The most complex and voluminous multi-phase eruptions, involving 5–6 eruption phases occur between 610 and 370 cal BP and constitute 60% of the cumulative tephra volume of the Tufa Trig Formation.
- Major element groundmass compositions show limited variability over the past 1800 years, while systematic changes in the Mg-number might herald upcoming regime changes.
- Statistical modelling successfully approximates pattern in multi-phase eruptions from the detailed 1800-year record and provides a framework for future eruption forecast modelling of small to moderate multi-phase eruption progressions.
- Assuming that we are currently in a medium rate regime, based on eruption forecast models the next eruption with a magnitude equal or larger than those preserved in the Tufa Trig tephra record has a median forecast date of AD 2079.
- The here presented tephra record most likely involves a preservation bias, representing only deposit volumes $\geq 1 \times 10^5$ m^3 and magnitudes of VEI ≥ 3. Consequently, small-volume, short-lived phreatic to phreatomagmatic eruptions, as frequently observed historically, are significantly underrepresented.
- Historical multi-phase eruptions such as the 1995–1996 eruptions differ from geologically preserved multi-phase eruptions such as T13, T15 and T17 in magnitude, geochemical characteristics and the feeding system. A full explanation of this difference still needs further work, but seems to be related to changes in the magnitude and rate of magma supply over the past ~610 years.
- A comparison of eruption frequencies for the Tongariro Volcanic Centres Mt. Ruapehu, Mt. Ngauruhoe and Red Crater for the past 6000 and 2000 years shows that the eruptive activities at Mt. Ngauruhoe and Red Crater are characterised by short-time (<100 years) periods of high frequency activity, possibly due to a greater tectonic control on magma intrusion in the northern volcanic systems. In comparison, Mt. Ruapehu's eruptive activity appears to be distributed more

evenly throughout the past 2000 years, with individual eruptions varying in magnitude and complexity.

- The integration of the tephra record with existing studies on lahar deposits shows that a permanent Crater Lake in the active vent system probably only formed over the last ~800 years. Contrastingly, in the time span between the Taupo eruption and ~800 cal BP, Crater Lake was periodically emptied during major magmatic eruptions and refilled only partially.
- Based on the tephra record and historical observations, four main eruption scenarios can be defined and need to be implemented in future eruption plans and hazard management: (1) a small-scale, short-lived phreatic to phreatomagmatic eruption; (2) a small volume low-intensity eruption; (3) a moderate intensity eruption and (4) a prolonged multi-phase eruption with phases of variable intensity and magnitude.

This research highlights the importance of systematic mapping to capture the lateral and temporal complexities associated with deposits from small to moderate explosive single- and multi-phase eruptions. This highlights the need for comprehensive time-resolved datasets with the here presented approaches illustrating the minimum detail that is needed to unravel eruption dynamics from geologically preserved tephra sequences associated specifically with mixed phreatomagmatic-magmatic eruptions, and with small to moderate explosive eruptions, in general. The application of statistical models to geological multi-phase sequences provides an important step towards more comprehensive and realistic eruption forecast models that can account for sudden changes in eruption dynamics during multi-phase eruptions. This will aid in decision-making during future eruption crises not only at Mt. Ruapehu but globally.

7.2 Future perspectives

From the here conducted research a number of possible future research avenues arises, which are outlined in the following:

(1) In the framework of this study the focus was set on the explosive eruptions of the last 1800 years at Mt. Ruapehu. While the main associated hazards with small-scale ash-rich eruptions lead to widely dispersed ashfall, this is generally not directly life-threatening.

In contrast with this, Mt. Ruapehu's 1800-year eruptive history is known to be associated with major lahars, involving volumes of 10^5 to $>10^7$ m^3 (Lecointre et al., 2004; Hodgson et al., 2007). Similarly, while dome formation was observed during the 1945 eruption, there is little geological information on the associated hazards, such as e.g., pyroclastic density currents (PDCs). In future studies, the here presented framework of explosive eruptions can be used to further develop methods to identify and integrate other hazards that are related to multi-phase eruptions.

(2) The Tufa Trig Formation is known to be interbedded with deposits sourced from other volcanoes, such as the Ngauruhoe Formation, sourced from Ngauruhoe, Red Crater and Te Maari (Moebis, 2010; Moebis et al., 2011). These relationships are yet poorly constrained, as until this point the distinction between the two formations was complicated by their similar field appearance. The detail added to the Tufa Trig Formation members allows for more tephra members to be used as stratigraphic markers within the context of the eruptive history of the TgVC and will allow to expand the understanding of overall frequency and magnitude pattern in the Tongariro National Park.

(3) Further analysis focusing on the characterisation of vesicularity, porosity and crystallisation of lapilli units T2, T5 and T7 is needed to understand how and why they are different to the other Tufa Trig Formation members. Potential future studies could contribute to quantify their source, ascent and fragmentation mechanisms. It is particularly interesting to see, how these mechanisms vary between T2, T5 and T7 and is of great importance as these poorly characterised eruptions are potentially associated with previously poorly considered hazards at Mt. Ruapehu, such as e.g., dome disruption and pyroclastic density currents.

(4) For comparable, historically documented multi-phase eruptions, detailed textural analysis of ash time-series has aided in quantifying the late-stage processes taking place within the conduit. In line with this, future studies on vesicle and microlite characteristics could advance our understanding of the processes that control ascent rates and fragmentation mechanisms with eruption progression. A comparison of textural data between the pyroclasts associated with the three main deposit types will be of particular interest to understand differences in fragmentation mechanisms and ascent rates.

(5) The time span between 610 and 370 cal BP shows high eruption frequencies of one eruption every decade and is associated with the largest and most intricate multi-phase eruptions of the past 1800 years, such as T13 and T15–T17. While in the here presented research, tephra member T13 has been analysed in detail, future studies could target the entire time span, identifying and characterising the parameters that change throughout T13 to T24 in comparison to the encompassing regimes. For the time span of the Bullot Formation, Pardo (2012) and Villamor et al. (2007) have suggested that changes in the local stress regime, such as decreasing fault-slip rates could control the shallow magmatic system and therefore eruption behaviour. With the newly defined regimes in Chapter 5, future studies could establish similar links on smaller timescales between eruptive activity and tectonic activity for the past 1800 years.

(6) While both the Bullot Formation from 27,000 to 10,000 years and the most recent 1800 years are well understood now, it can be hypothesised that research that covers the time span between 10,000 and 1800 cal BP will provide further insights into the long-term changes occurring in Mt. Ruapehu's magmatic system. Given that this time span is also associated with the frequent eruptions from Mts. Ngauruhoe and Tongariro (Moebis, 2010; Moebis et al., 2011), the integration of the eruptive records from the TgVC would contribute to the understanding of the mechanisms that control eruption behaviour in the southern Taupo Volcanic Zone. This could, for example, be approached through long-term isotope analysis, as it has been partially done for Mt. Ngauruhoe (Hobden et al., 1999).

(7) Finally, while the limitations of existing eruption classification schemes with regards to small to moderate explosive eruptions have been outlined in the previous chapters, future comparably detailed studies on similar tephra sequences at other volcanoes would add quantitative data to develop new and improve existing eruption classification schemes. One possible approach could be that eruption classifications focus more on the type of activity, which can be inferred from deposits rather than quantifying solely parameters such as magnitude and intensity. This could improve the characterisation of individual phases of multi-phase eruptions and would aid in creating more dynamic forecast models that can account for the dynamic evolution during eruption progressions.

References

Hobden, B. J., Houghton, B. F., Davidson, J. P., & Weaver, S. D. (1999). Small and short-lived magma batches at composite volcanoes: time windows at Tongariro volcano, New Zealand. *Journal of the Geological Society*, *156*(5), 865-868. doi:https://doi.org/10.1144/gsjgs.156.5.0865

Hodgson, K. A., Lecointre, J. A., & Neall, V. E. (2007). Onetapu Formation: The last 2000 yr of laharic activity at Ruapehu volcano, New Zealand. *New Zealand Journal of Geology and Geophysics, 50*(2), 81-99. doi:https://doi.org/10.1080/00288300709509823

Lecointre, J., Hodgson, K., Neall, V., & Cronin, S. (2004). Lahar-Triggering Mechanisms and Hazard at Ruapehu Volcano, New Zealand. *Natural Hazards, 31*(1), 85-109. doi:https://doi.org/10.1023/B:NHAZ.0000020256.16645.eb

Moebis, A. (2010). *Understanding the Holocene explosive eruption record of the Tongariro Volcanic Centre, New Zealand.* (Doctor of Philosophy), Massey University, Palmerston North.

Moebis, A., Cronin, S. J., Neall, V. E., & Smith, I. E. (2011). Unravelling a complex volcanic history from fine-grained, intricate Holocene ash sequences at the Tongariro Volcanic Centre, New Zealand. *Quaternary International*, *246*(1–2), 352-363. doi:http://dx.doi.org/10.1016/j.quaint.2011.05.035

Pardo, N. (2012). *Andesitic Plinian eruptions at Mt. Ruapehu (New Zealand): from lithofacies to eruption dynamics.* (Doctor of Philosophy), Massey University, Palmerston North.

Villamor, P., Van Dissen, R., Alloway, B. V., Palmer, A. S., & Litchfield, N. (2007). The Rangipo fault, Taupo rift, New Zealand: An example of temporal slip-rate and single-event displacement variability in a volcanic environment. *GSA Bulletin, 119*(5-6), 529-547. doi:https://doi.org/10.1130/B26000.1

List of appendices

All appendices are compiled on a CD, enclosed with the printed PhD thesis.

A- Field data

Appendix A-1 Field locations (.docx) Overview coordinates of field locations investigated in this research.

Appendix A-2 Composite soil thicknesses (.xlsx) Composite soil thicknesses used for age model in Chapter 5.

Appendix A-3 Stratigraphic profiles (.docx) Stratigraphic profiles of key sections and additional sections that were used for correlation.

Appendix A-4 Correlations (.docx) Correlations of individual tephra members in different dispersal directions NNE, E and SE.

B- Radiocarbon dates

Appendix B-1 Loc. 3 Charcoal (.pdf) Radiocarbon dating of Charcoal at Loc. 3, cited in Chapter 3.

Appendix B-2 Ngamatea Swamp_T13 (.pdf) Radiocarbon dating of organic material in soil underlying T13 in a core taken at WP251 (Ngamatea Swamp, Waiouru). Cited in Chapter 3.

Appendix B-3 Ngamatea Swamp_T15 and 17 (.pdf) Radiocarbon dating of organic material in soil underlying members T15 and T17 in a core taken at WP251 (Ngamatea Swamp, Waiouru). Cited in Chapter 3.

C- Tephra volumes

Appendix C-1 Thickness and volumes T2_T5_T7 (.xlsx) Thickness, max. clast and location data used for isopach and isopleth construction for lapilli units T2, T5 and T7. Volume calculations are reported as well. T2 volume is cited in Chapter 3.

Appendix C-2 Thickness and volumes T13 (.xlsx) Thickness, max. clast and location data used for isopach and isopleth construction for multi-bed member T13. Volume calculations are reported as well. T13 volume is cited in Chapter 4.

Appendix C-3 Thickness and volumes T14 (.xlsx) Thickness, max. clast and location data used for isopach and isopleth construction for representative single bed ash unit T14. Volume calculations are reported as well. T14 volume is cited in Chapter 3.

Appendix C-4 Thickness and volumes T15 (.xlsx) Thickness, max. clast and location data used for isopach and isopleth construction for representative multi-bed member T15. Volume calculations are reported as well. T15 volume is cited in Chapter 3.

D- Grain size characteristics

Appendix D-1 Grain size Loc. 1 (.xlsx) Grain size characteristics for samples representative of individual subunits at Loc. 1. Data is used in Chapter 3.

Appendix D-2 Grain size Loc. 2 (.xlsx) Grain size characteristics for samples representative of individual subunits at Loc. 2. Data is used in Chapter 3.

Appendix D-3 Grain size Loc. 3 (.xlsx) Grain size characteristics for samples representative of individual subunits at Loc. 3. Data is used in Chapter 3.

Appendix D-4 Grain size misc (.xlsx) Grain size characteristics for various samples taken at different locations. Data is cited in Chapter 3.

Appendix D-5 Grain size T13 (.xlsx) Grain size characteristics for samples representative of individual subunits of multi-bed unit T13. Data is cited in Chapter 4.

Appendix D-6 Laser particle analysis T13 (.xlsx) Laser particle analysis data for T13 subunits at Loc. 3. Data is cited in Chapter 4.

E- Componentry

Appendix E-1 to -5 Componentry (.pdf) Componentry analysis data for key units cited in Chapter 3 and 4:

E-1 Grain size-related variation

E-2 Lapilli units T2 and T7 (WP296)

E-3 Multi-bed ash unit T13 (Loc. 3, WP290, Loc. 1, WP250, Loc. 2)

E-4 Single bed ash unit T14 (Loc. 3 and Loc. 1)

E-5 Multi-bed ash unit T15 (Loc. 3, WP290, Loc. 1, WP250, Loc. 2 WP219)

F- Image analysis

Appendix F-1 Texture analysis (.xlsx) Area measurements of textural analysis and calculated relative proportions of individual phases and groundmass crystallinity, used in Chapter 4.

Appendix F-2 Scanning electron microscope images for representative juveniles from subunit T13-2, used for textural analysis.

Appendix F-3 Scanning electron microscope images for representative juveniles from subunit T13-3, used for textural analysis.

Appendix F-4 Scanning electron microscope images for representative juveniles from subunit T13-4, used for textural analysis.

Appendix F-5 Scanning electron microscope images for representative juveniles from subunit T13-5, used for textural analysis.

Appendix F-6 Scanning electron microscope images for representative juveniles from subunit T13-6, used for textural analysis.

G- Geochemistry

Appendix G-1 VUW_major elements (.xlsx) Major element data obtained at the Victoria University Wellington microprobe for key units T5, T13, T15 and T31, used in Chapter 4.

Appendix G-2 Trace element data (.xlsx) Trace element data from LA-ICP-MS analysis for key units T5, T13, T15 and T31, used in Chapter 4.

Appendix G-3 MU_major elements (.xlsx) Major element data obtained at the Massey University microprobe for key locations Loc. 1, Loc. 2 and Loc. 3 to verify the source of individual subunits. Used in Chapter 3 and Chapter 5.

H- Supplementary material for publications

Appendix H-1 Supplementary material Chapter 3 (available at https://doi.org/10.1016/j.jvolgeores.2020.106987)

> Supplementary Table S3.2 (.xlsx) Averaged groundmass glass major element compositions for individual subunits of the Tufa Trig Formation, obtained from electron microprobe analysis
>
> Supplementary Table S3.3 (.xlsx) Compilation of re-normalised groundmass glass major element compositions a) for Taranaki-sourced Burrell Lapilli after Platz et al. (2007a) and b) for the Tongariro Volcanic Centres (TgVC) after Moebis et al. (2011).

Appendix H-2 Supplementary material Chapter 4

> Supplementary Table S4.1 (.xlsx) Average major and trace element groundmass composition with 2SD.

Appendix H-3 Supplementary material Chapter 5

> Supplementary Table S5.2 Spot analysis (.xlsx): Spot microprobe data representing major element groundmass compositions for individual subunits
>
> Supplementary Table S5.3 Averages (.xlsx): Averaged compositions for individual subunits (Supplementary Table S5.3.1) and for individual tephra members (Supplementary Table S5.3.2).

I- Statements of contribution

I-1 Chapter 3 Statement of contribution (.pdf)

I-2 Chapter 4 Statement of contribution (.pdf)

I-3 Chapter 5 Statement of contribution (.pdf)

In addition, appendices I-1 to I-3 are attached on the following pages.

I-1 Chapter 3 Statement of contribution

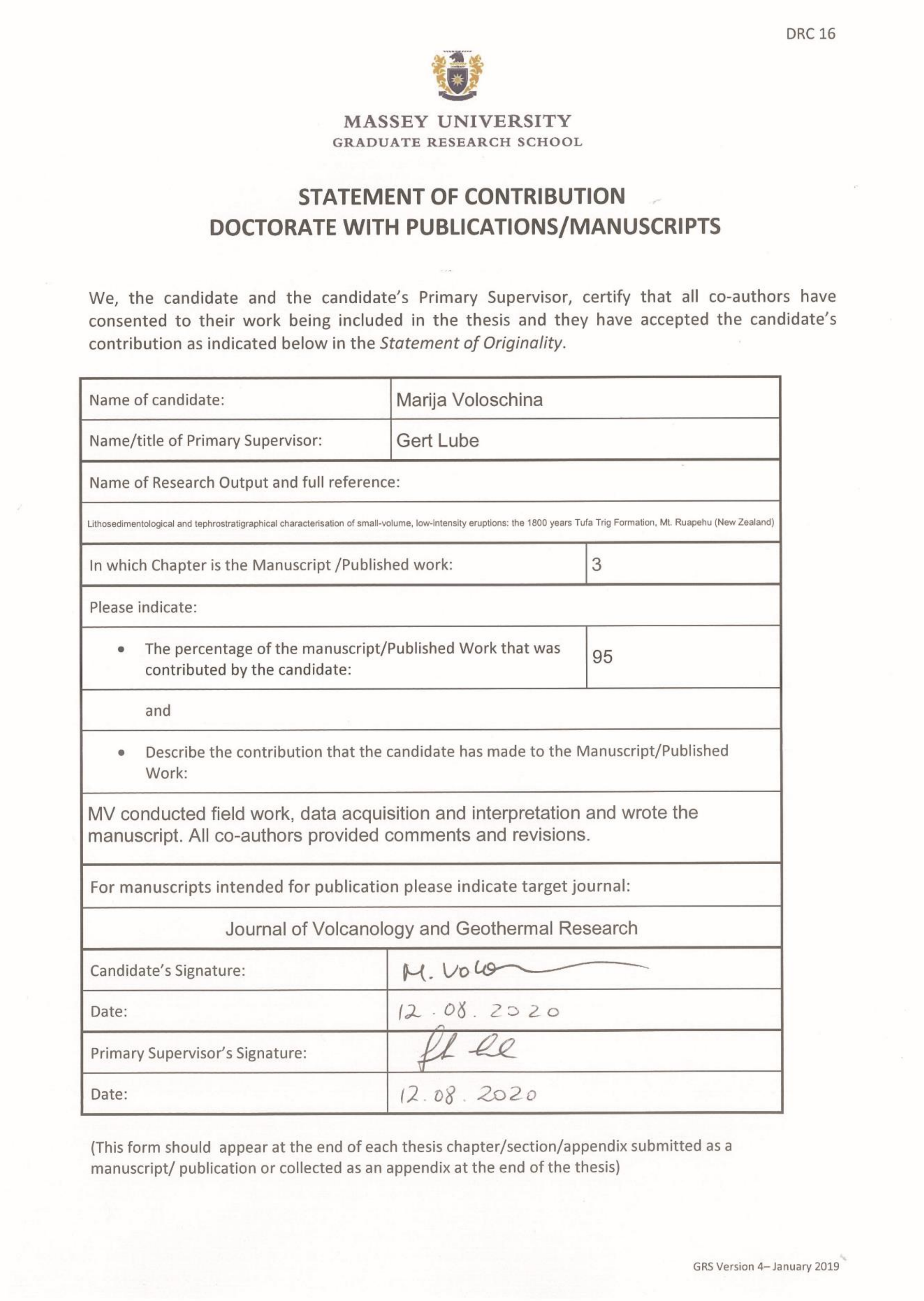

DRC 16

MASSEY UNIVERSITY
GRADUATE RESEARCH SCHOOL

STATEMENT OF CONTRIBUTION
DOCTORATE WITH PUBLICATIONS/MANUSCRIPTS

We, the candidate and the candidate's Primary Supervisor, certify that all co-authors have consented to their work being included in the thesis and they have accepted the candidate's contribution as indicated below in the *Statement of Originality*.

Name of candidate:	Marija Voloschina
Name/title of Primary Supervisor:	Gert Lube
Name of Research Output and full reference:	
Lithosedimentological and tephrostratigraphical characterisation of small-volume, low-intensity eruptions: the 1800 years Tufa Trig Formation, Mt. Ruapehu (New Zealand)	
In which Chapter is the Manuscript /Published work:	3
Please indicate:	
• The percentage of the manuscript/Published Work that was contributed by the candidate:	95
and	
• Describe the contribution that the candidate has made to the Manuscript/Published Work:	
MV conducted field work, data acquisition and interpretation and wrote the manuscript. All co-authors provided comments and revisions.	
For manuscripts intended for publication please indicate target journal:	
Journal of Volcanology and Geothermal Research	
Candidate's Signature:	M. Volo
Date:	12.08.2020
Primary Supervisor's Signature:	
Date:	12.08.2020

(This form should appear at the end of each thesis chapter/section/appendix submitted as a manuscript/ publication or collected as an appendix at the end of the thesis)

GRS Version 4– January 2019

I-2 Chapter 4 Statement of contribution

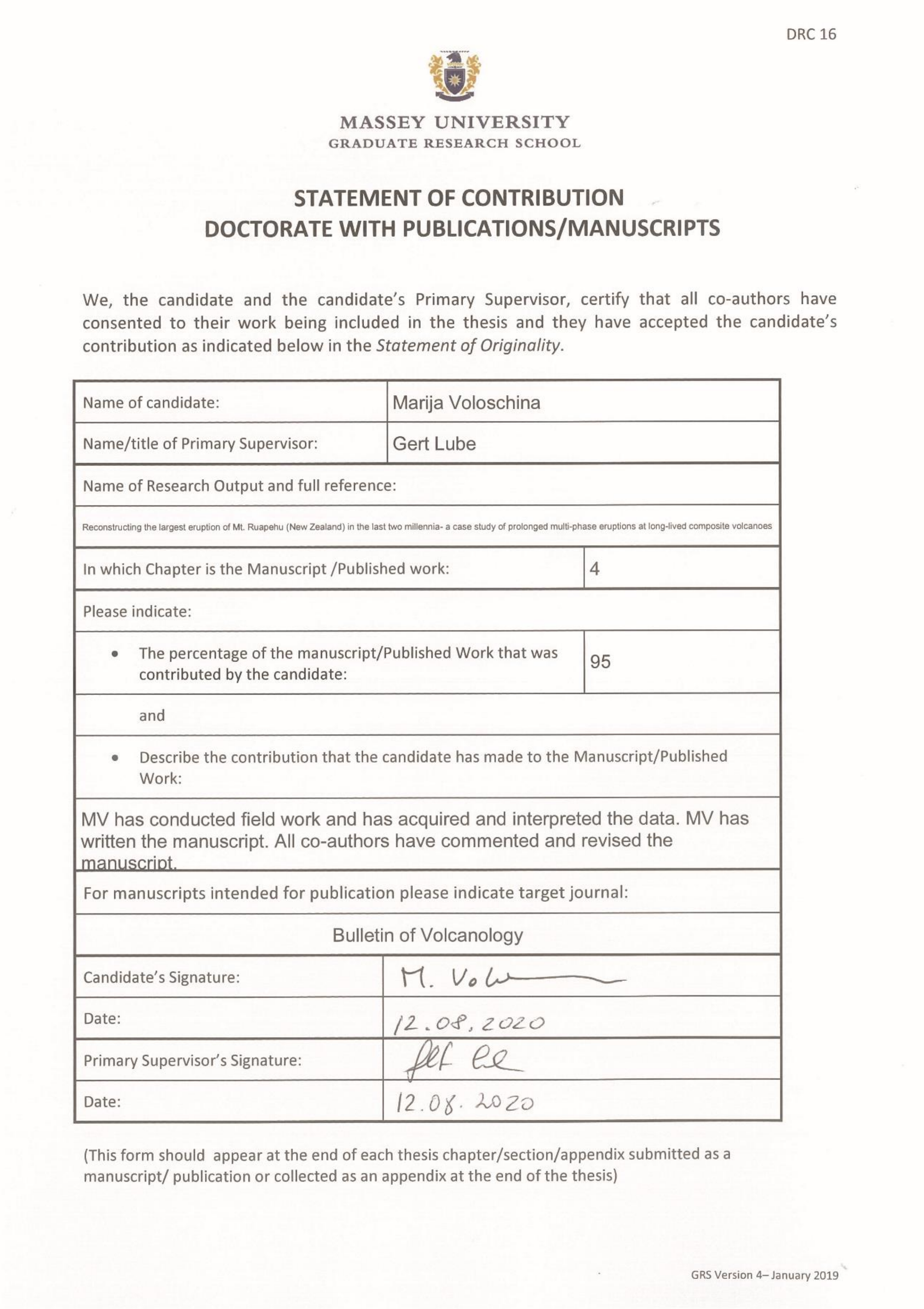

DRC 16

MASSEY UNIVERSITY
GRADUATE RESEARCH SCHOOL

STATEMENT OF CONTRIBUTION
DOCTORATE WITH PUBLICATIONS/MANUSCRIPTS

We, the candidate and the candidate's Primary Supervisor, certify that all co-authors have consented to their work being included in the thesis and they have accepted the candidate's contribution as indicated below in the *Statement of Originality*.

Name of candidate:	Marija Voloschina
Name/title of Primary Supervisor:	Gert Lube
Name of Research Output and full reference:	
Reconstructing the largest eruption of Mt. Ruapehu (New Zealand) in the last two millennia- a case study of prolonged multi-phase eruptions at long-lived composite volcanoes	
In which Chapter is the Manuscript /Published work:	4
Please indicate:	
• The percentage of the manuscript/Published Work that was contributed by the candidate:	95
and	
• Describe the contribution that the candidate has made to the Manuscript/Published Work:	
MV has conducted field work and has acquired and interpreted the data. MV has written the manuscript. All co-authors have commented and revised the manuscript.	
For manuscripts intended for publication please indicate target journal:	
Bulletin of Volcanology	
Candidate's Signature:	M. Vo
Date:	12.08.2020
Primary Supervisor's Signature:	
Date:	12.08.2020

(This form should appear at the end of each thesis chapter/section/appendix submitted as a manuscript/ publication or collected as an appendix at the end of the thesis)

GRS Version 4– January 2019

I-3 Chapter 5 Statement of contribution

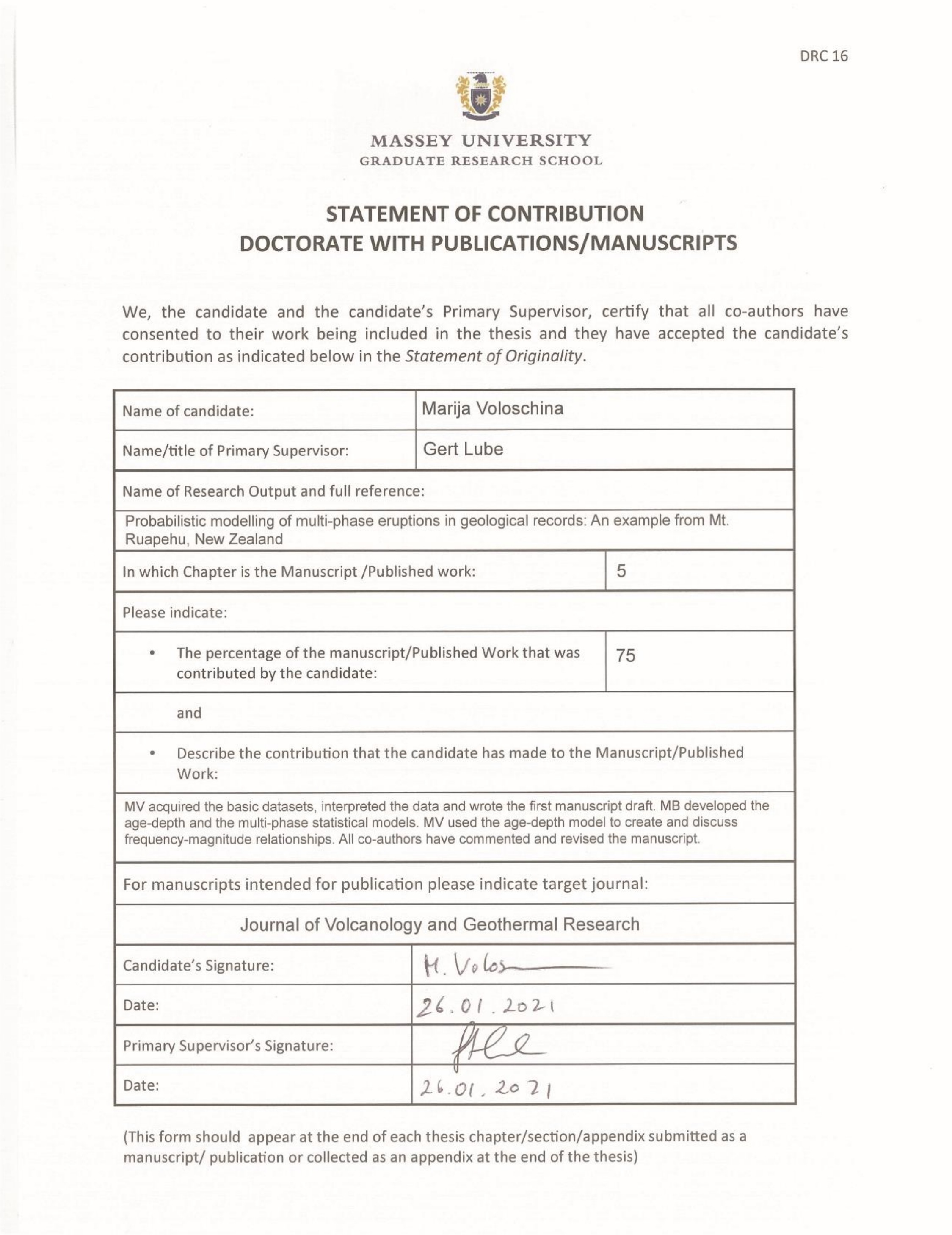

DRC 16

MASSEY UNIVERSITY
GRADUATE RESEARCH SCHOOL

STATEMENT OF CONTRIBUTION
DOCTORATE WITH PUBLICATIONS/MANUSCRIPTS

We, the candidate and the candidate's Primary Supervisor, certify that all co-authors have consented to their work being included in the thesis and they have accepted the candidate's contribution as indicated below in the *Statement of Originality*.

Name of candidate:	Marija Voloschina
Name/title of Primary Supervisor:	Gert Lube
Name of Research Output and full reference:	
Probabilistic modelling of multi-phase eruptions in geological records: An example from Mt. Ruapehu, New Zealand	
In which Chapter is the Manuscript /Published work:	5
Please indicate:	
• The percentage of the manuscript/Published Work that was contributed by the candidate:	75
and	
• Describe the contribution that the candidate has made to the Manuscript/Published Work:	
MV acquired the basic datasets, interpreted the data and wrote the first manuscript draft. MB developed the age-depth and the multi-phase statistical models. MV used the age-depth model to create and discuss frequency-magnitude relationships. All co-authors have commented and revised the manuscript.	
For manuscripts intended for publication please indicate target journal:	
Journal of Volcanology and Geothermal Research	
Candidate's Signature:	H. Volos
Date:	26.01.2021
Primary Supervisor's Signature:	
Date:	26.01.2021

(This form should appear at the end of each thesis chapter/section/appendix submitted as a manuscript/ publication or collected as an appendix at the end of the thesis)